STRUCTURAL SYSTEMS

RESEARCH PROJECT

Report No.
SSRP–16/08

CFS Test Program
Report #2

Earthquake and fire performance of a mid-rise cold-formed steel framed building – test program and test results: *Final Report*

by

Xiang Wang, Tara Hutchinson, Gilbert Hegemier, Srikar Gunisetty
(UCSD)

Praveen Kamath, Brian Meacham
(WPI)

Final Report

May 2018

Department of Structural Engineering
University of California, San Diego
La Jolla, California 92093-0085

University of California, San Diego

Department of Structural Engineering

Structural Systems Research Project

Report No. SSRP-16/08

Earthquake and fire performance of a mid-rise cold-formed steel framed building – test program and test results: *Final Report*

by

Xiang Wang, Tara Hutchinson, Gilbert Hegemier, Srikar Gunisetty
(University of California, San Diego)

Praveen Kamath, Brian Meacham
(Worcester Polytechnic Institute)

Department of Structural Engineering

University of California, San Diego

La Jolla, California 92093-0085

May 2018

DISCLAIMER

The work that provided the basis for this publication was supported by funding under a Grant with the U.S. Department of Housing and Urban Development, Office of Policy Development and Research. The substance and findings of the work are dedicated to the public. The author and publisher are solely responsible for the accuracy of the statements and interpretations contained in this publication. Such interpretations do not necessarily reflect the views of the Government.

ACKNOWLEDGEMENTS

This project is a collaboration between two academic institutions (University of California, San Diego and Worcester Polytechnic Institute), two government or institutional granting agencies (Department of Housing and Urban Development and the California Seismic Safety Commission) and more than fifteen industry partners (a complete list of industry sponsors may be found in Appendix A). It is noted that although UCSD led the overall test program, this team's primary focus was on the earthquake testing phases, while WPIs primary focus was on the fire testing phases. For sake of harmony and flow in the present report, herein both testing phases are presented. We also thank the Jacobs School of Engineering and Department of Structural Engineering at UCSD for matching support of this effort. Industry sponsors include the California Expanded Metal Products Co. (CEMCO) and Sure-Board, who each provided financial, construction, and materials support. Specific individuals that dedicated significant time on behalf of this effort included Fernando Sesma (CEMCO), Kelly Holcomb, Carleton Elliot and Tyler Elliot (Sure-Board), Harry Jones (DCI Engineers), Diego Rivera (SWS Panels), Doug Antuma (Rivante), Larry Stevig (State Farm Insurance), Tim Reinhold and Warner Chang (Insurance Institute for Business and Home Safety), Steve Helland (DPR Construction), Rick Calhoun (Walters & Wolf), and Jesse Karnes (MiTek). We appreciate the efforts of these individuals and their colleagues at their respective firms.

Regarding the test program, the technical support of NHERI@UCSD staff, namely, Robert Beckley, Jeremy Fitcher, Dan Radulescu, and Alex Sherman, are greatly appreciated. The authors are also grateful to Professor Yehuda Bock and graduate student Dara Goldberg from the Scripps Institute of Oceanography at UCSD for providing the Global Positioning System and related technical support, and Professor Falko Kuester and his students from the Department of Structural Engineering at UCSD for collecting aerial video footage and LiDAR image data of the test specimen. Experiments performed at the National Institute of Standards and Technology (NIST), led by Dr. Matthew Hoehler, supported the planning of this test program, and are greatly appreciated. Technical input to this report regarding the physical observations to appliances and other installed equipment were provided by Pat Boyer, Jack Jordan, and Larry Stevig of State Farm Insurance and Warner Chang of IBHS. These entities also kindly supplied appliances and provided support during the test program. In addition, the authors also greatly appreciate UCSD

Department of Environment, Health & Safety, and the San Diego Fire Department for providing the necessary approvals and fire department participation during the fire-testing phase of this effort. The above continuous support is gratefully acknowledged. Findings, opinions, and conclusions are those of the authors and do not necessarily reflect those of the sponsoring organizations.

EXECUTIVE SUMMARY

A substantial growth in the use of cold-formed steel (CFS) framed construction has recently been observed, notably in high seismic regions in the western United States. Structural systems of this kind consist of light-gauge framing members (e.g., studs, tracks, joists) attached with sheathing materials (e.g., wood, sheet steel). CFS-framed structures can offer lower installation and maintenance costs than other structural types, particularly when erected with prefabricated assemblies. They are also durable, formed of an inherently ductile material of consistent behavior, lightweight, and manufactured from recycled materials. Compared to other lightweight framing solutions, CFS is non-combustible, an important basic characteristic to minimize fire spread. While these lightweight systems provide the potential to support the need for resilient and sustainable housing, the state of understanding regarding their structural behavior in response to extreme events, in particular earthquakes and ensuing hazards, remains relatively limited.

To this end, a unique research collaboration between academia, government, and industry was formed to contribute to understanding the earthquake and post-earthquake fire behavior of mid-rise CFS-framed buildings. Led by the University of California, San Diego (UCSD), with partnerships from Worcester Polytechnic Institute, government and state agencies, and more than 15 industry sponsors, the centerpiece of this project involved full-scale earthquake and fire testing of a full-scale six-story CFS wall braced building. The test building was constructed on the world's largest outdoor shake table – the Large High Performance Outdoor Shake Table (LHPOST) at UCSD. Within a three-week test program, the building was subjected to seven earthquake tests of increasing motion intensity. Earthquake motions were scaled to impose service, design, and maximum credible earthquake (MCE) demands onto the test building. Subsequently, live fire tests were conducted on the earthquake-damaged building at two select floors. Finally, for the first time, the test building was subjected two post-fire earthquake tests, including a low-amplitude 'aftershock' and an extreme near-fault target MCE-scaled motion. In addition, low-amplitude white noise and ambient vibration data were collected during construction and test phases to support identification of the dynamic state of the test building.

During the earthquake test phases, the building was outfitted with more than 250 analog sensors, a Global Positioning System (GPS) system, and an array of more than 40 digital video

cameras to record the response of the building and its structural components. Between the two earthquake test phases, thermocouples were installed in various locations of the fire test compartments. Sacrificial video cameras were also installed to collect visual data regarding smoke or fire spread. To augment data measured using conventional techniques, remote sensing systems, namely, unmanned aerial vehicles (UAVs) and Light Detection and Ranging (LiDAR), were utilized to record high-resolution imagery (images and videos) or dense point clouds for analyzing the response and behavior of the test building at the various stages of the test program.

This report is the second in a series devoted to this experimental research project. While the first report (*rapid release report*) delivered initial findings of the building response and the observed physical damage during the earthquake and fire tests to seek immediate understanding from the program and stimulate discussions for future data analysis/reporting, this report (*final report*) presents a comprehensive and detailed study of the performance of the full-scale CFS building under this unique multi-hazard test program (earthquake and ensuing fire tests). In this report, the global responses of and the local response of the shear walls during the earthquake tests as well as the temperature response of the building during the fire tests are discussed in detailed. Physical damage to the structural systems and nonstructural components at various stages throughout the test program is summarized and associated with the extreme-event demands of the building. In addition, this report also involves a comprehensive system identification study to understand the evolution of the dynamic characteristics of the test building using the low-amplitude vibration data collected from the experimental program. Supplemental materials regarding the test building design and construction as well as the material specifications are documented in the companion report (the third in this series).

TABLE OF CONTENTS

LIST OF FIGURES

LIST OF TABLES

NOTATION AND UNITS

Notation

The following list summarizes the notation used throughout this report.

Acronym	Definition
AISI	American Iron and Steel Institute
ASCE	American Society of Civil Engineers
AV	Ambient Vibration
CFS	cold-formed steel
DE	design earthquake
GPS	global positioning system
IDR	interstory drift ratio
IR	interstory rotation
LiDAR	light detection and ranging
MCE	maximum considered earthquake
PFA	peak floor acceleration
PIDR	peak interstory drift ratio
PIR	peak interstory rotation
PRDR	peak roof drift ratio
PSD	power spectra density
RDR	roof drift ratio
RMS	root mean square
SLE	serviceability level earthquake
UAV	unmanned aerial vehicle
USGS	United States Geological Survey
WN	white noise

Variable	Definition
a_p	component amplification factor
V_b	base shear
$\tilde{V}_b$	normalized base shear
V_s	story shear

M_o	overturning moment
$\tilde{M}_o$	normalized overturning moment
W	building total weight
δ	floor relative displacement
δ_{up}	shear wall uplift displacement
Δ	floor absolute displacement
γ	shear panel shear distortion
Ω	structural amplification factor

Units

The international system of units (SI) is used throughout this report as the primary unit system. However, the United States (US) customary units are used in Chapter 2 as the secondary unit system to facilitate discussion of building design and construction details, since participants of this project were primarily comprised of entities of the United States. The following conversion factors are provided for convenience:

Quantity	SI unit	US customary unit	Conversion factor
Length	Meter (m) Centimeter (cm) Millimeter (mm)	foot (ft) inch (in)	1 m = 3.28084 ft 1 m = 100 cm 1 m = 1000 mm 1 ft = 12 in
Force	Kilonewton (kN)	kilopound (kips)	1 kN = 0.224809 kips
Stress	Megapascal (MPa)	kilopound per square inch (ksi)	1 MPa = 0.145038 ksi
Volume	Liter (L)	gallon (gal)	1 L = 0.264172 gal

1 INTRODUCTION

1.1 Background and Motivation

A substantial growth in the use of cold-formed steel (CFS) framed construction has recently been observed, notably in high seismic regions in the western United States (Figure 1.1). Structural systems of this kind consist of light-gauge framing members (e.g., studs, tracks, joists) attached with sheathing materials (e.g., wood, sheet steel). CFS-framed structures can offer lower installation and maintenance costs than other structural types, particularly when erected with prefabricated assemblies. They are also durable, formed of an inherently ductile material of consistent behavior, lightweight, and manufactured from recycled materials. Compared to other lightweight framing solutions, CFS is non-combustible, an important basic characteristic to minimize fire spread. While these lightweight systems provide the potential to support the need for resilient and sustainable housing, the state of understanding regarding their structural behavior in response to extreme events, in particular earthquakes and ensuing fire hazards, remains relatively limited.

To address the need for understanding the earthquake and post-earthquake fire behavior of mid-rise CFS-framed buildings, a unique multidisciplinary test project was conducted on the Large High Performance Outdoor Shake Table (LHPOST) at the University of California, San Diego (UCSD) between April and July 2016. Central to this research is the system-level earthquake and live fire testing of a full-scale six-story CFS wall braced building. In a three-week test program, the building was subjected to seven earthquake tests of increasing motion intensity. Earthquake motions were scaled to impose service, design, and maximum credible earthquake (MCE) demands onto the test building. Subsequently, live fire tests were conducted on the earthquake-damaged building at two select floors. Finally, the test building was subjected to two post-fire earthquake tests, including a low-amplitude 'aftershock' and an extreme near-fault target MCE intensity motion.

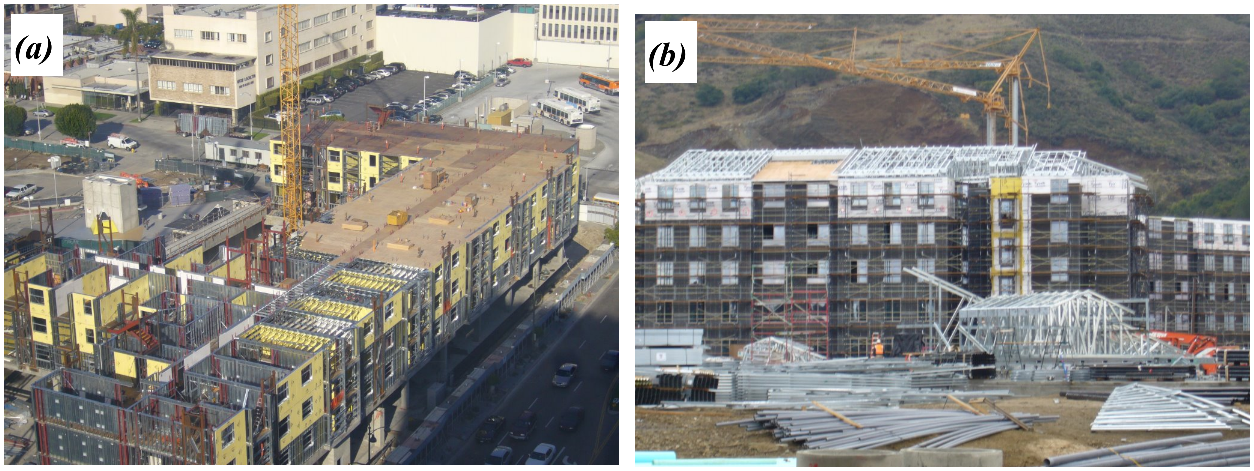

Figure 1.1. Cold-formed steel construction in high seismic regions: (a) six-story building at downtown Los Angeles, and (b) five-story building at San Luis Obispo (photos courtesy of K. Holcomb).

With an ultimate goal of achieving sustainable and resilient housing communities via the use of CFS-framed buildings, findings from this experimental project are intended to provide useful guidance to the practitioners in the following aspects: (i) evaluating the seismic and post-earthquake fire performance, (ii) supporting advancement of engineering models for use in current design practice, (iii) contributing to next-generation design codes, and (iv) improving construction and design practices.

1.2 Previous Experimental Studies

In conjunction with increased use of cold-formed steel (CFS) framed construction, experimental studies of the seismic behavior of these light-frame systems have advanced substantially in the past few decades. These experimental studies contributed significantly for advancing the understanding regarding the seismic response of CFS-framed shear wall components and structural systems. A brief overview of recent research efforts is summarized in this section.

1.2.1 Component-level Tests

The work conducted by Serrette et al. (1997) represents one of the first experimental efforts in the North America that characterized the seismic response of wood-sheathed CFS-framed shear walls. This research forms the initial basis for codified design of CFS structural systems (e.g., AISI (2007, 2013)). Rogers and his colleagues extended the wood-sheathed CFS-framed shear wall tests (Branston et al. 2006) by varying sheathing materials or framing details. Their experimental studies included pseudo-static tests of CFS-framed steel strap shear walls (Al-Kharat and Rogers, 2007) and steel-sheet shear walls (Balh et al., 2014), as well as pseudo-dynamic tests of two-story steel-sheet shear wall assemblies (Shamim et al. 2013). In addition, recent experimental studies incorporated testing of CFS shear wall sheathed with steel-sheet (Yu, 2010, Zhang et al., 2017) and the CFS shear walls sheathed with oriented strand board (OSB) panels (Liu et al., 2014).

Figure 1.2. Component-level testing of a steel sheathed cold-formed steel shear wall (Balh et al., 2014).

Meanwhile, similar experimental efforts have also occurred outside of the North America. Pseudo-static testing of wood-sheathed CFS shear walls were conducted by Fülöp and Dubina (2004a) and Landolfo et al. (2006), whereas fastener tests were conducted by Fiorino et al. (2007). Their research has significantly advanced seismic design guidelines for CFS building systems in Europe (Dubina, 2006; Fülöp and Dubina, 2004b; Fiorino et al. 2009).

1.2.2 System-level Tests

The component-level experimental studies have significantly advanced the understanding regarding the seismic behavior of the major load resistance components in CFS-framed buildings. However, investigation of the system-level performance of such buildings appears largely lacking. To date, research of this kind, to the authors' knowledge, has been very limited.

The shake table testing of a two-story low-rise CFS wall framed building conducted at the then NEES@Buffalo represented the only system-level experiment study of its kind in the North America (Peterman et al., 2016a and 2016b). This test program involved multi-stage test phases with the test building varied in the construction details (e.g., presence of exterior sheathing, interior partition walls, and etc.). The test building was subjected to a series of white noise vibration and earthquake tests at each phase of the test program until the test building suffering pronounced damage at the maximum considered earthquake in the final test stage.

Figure 1.3. System-level shake table testing of a two-story CFS building (Peterman et al., 2016a).

1.3 Scope of the Report Series

A rich set of data has emerged from this unique system-level building experimental program. Investigation of the test data has been focused on the following aspects: (1) system identification of the test building, (2) seismic behavior of the test building and the shear walls under the earthquake tests, and (3) fire test results the implications of fire effects on the structural behavior of the building. The results and findings from this full-scale CFS building test program are presented in three reports in a series as follows:

- Wang, X., Hutchinson, T.C., Hegemier, G., Gunisetty, S., Meacham, B., and Kamath, P (2016). "Earthquake and fire performance of a mid-rise cold-formed steel framed building –

test program and test results: *Rapid Release Report*." *SSRP-2016/07*, Dept. of Structural Engineering, Univ. of California, San Diego, La Jolla, CA.

- Wang, X., Hutchinson, T.C., Hegemier, G., Gunisetty, S., Meacham, B., and Kamath, P (2016). "Earthquake and fire performance of a mid-rise cold-formed steel framed building – test program and test results: *Final Report*." *SSRP-2016/08*, Dept. of Structural Engineering, Univ. of California, San Diego, La Jolla, CA.
- Wang, X., Hutchinson, T.C., Hegemier, G., and Gunisetty, S. (2016). "Earthquake and fire performance of a mid-rise cold-formed steel framed building – supplemental materials: *Final Report*." *SSRP-2016/09*, Dept. of Structural Engineering, Univ. of California, San Diego, La Jolla, CA.

The first report (*rapid release report*), which was published within a few months following the completion of the test program, synthesized several initial findings of the building response and the observed physical damage during the earthquake and fire tests to gain immediate understanding from the test program and stimulate discussions for further data analysis/reporting. The second report (*the present report*) expands the initial findings by conducting a systematic study of the experimental results of the full-scale CFS test building under this unique multi-hazard test program (earthquake and ensuing fire tests). In this report, the global responses of the test building and the local response of the shear walls during the earthquake tests are discussed in detailed. The temperature response of the fire compartments during the fire tests and the fire-induced effects on the building are also studied. Physical damage of the structures and its contents at various stages throughout the test program is documented and associated with the earthquake and fire hazard demands. In addition, this report involves a comprehensive system identification study to explore the evolution of the dynamic characteristics of the test building using the low-amplitude vibration data collected at various stages during the construction and test phases. Supplemental materials regarding the test building design and construction as well as the material specifications are documented in the companion report (the third in this series).

In conjunction with the full-scale CFS building experiments conducted at UCSD, a separate CFS shear wall test effort was undertaken at the National Institute of Standards and Technology (NIST) in June 2016. The experimental study involved a combination of reversed cyclic quasi-static loads and live thermal loading tests of six shear wall specimens constructed to replicate those of the full-scale CFS test building. Results from these component-level tests provided useful information for understanding the potential for degradation in wall capacity under earthquake-fire scenarios. Major findings from this component shear wall experimental study are briefly summarized in Chapter 6 of the present (second) report. Interested readers may also refer to the full test report (Hoehler and Smith, 2016) for detailed discussions of the component-level shear wall tests.

1.4 Report Organization

This report, the second of the report series, is organized into nine chapters as follows:

- **Chapter 2: Building Design and Construction**

  This chapter provides a comprehensive description of aspects related to test building design and construction. These include the seismic design of the test building, test motion selection strategies and the related pre-test numerical simulation effort, detailed description of the various structural and nonstructural components of the test building, and a brief summary of building construction.
- **Chapter 3: Test Protocol**

  This chapter discusses the test protocol for the three separate phases, namely, *pre-fire earthquake*, *fire*, and *post-fire earthquake* test phases, during the three-week test program. In addition, the low-amplitude vibration tests conducted during the construction and test phases are documented in this chapter. Lastly, this chapter concludes by discussing the characteristics of the earthquake input motions and the shake table tracking performance.
- **Chapter 4: Monitoring Systems**

  This chapter describes the various monitoring systems for the earthquake tests (e.g., analog sensors, Global Positioning System (GPS), and digital video camera system) as well as the fire tests (thermocouples, video cameras). In addition, this chapter briefly discusses the remote sensing systems (unmanned aerial vehicles (UAVs) and light detection and ranging (LiDAR) system) that augmented the data collected using the conventional sensors.
- **Chapter 5: System Identification Results**

  This chapter presents a comprehensive system identification study to explore the evolution of the modal characteristics (e.g., natural periods, damping ratios, and mode shapes) of the test building at the various stages of the test program using data collected from low-amplitude vibration tests. In particular, the story stiffness and frequency loss of the test building estimated using the vibration data provide quantified metrics for assessing the building damage during the test program.

- **Chapter 6: Pre-fire Earthquake Test Results**

  This chapter discusses the global building response as well as local shear wall responses during the pre-fire earthquake test sequence. In particular, these responses are compared with those measured during the pre-fire earthquake tests to characterize the effect of prior earthquake-fire damage on the behavior of the test building. In addition, the chapter provides a detailed summary of the observed physical damage of the test building at different stages during of the pre-fire earthquake test sequence.

- **Chapter 7: Fire Test Results**

  This chapter summarizes the compartment temperature responses of individual fire tests as well as the fire-induced flame and smoke propagation behavior during these tests. This chapter concludes with a brief summary of the fire-induced damage to the structural and nonstructural systems of the test building.

- **Chapter 8: Post-fire Earthquake Test Results**

  This chapter discusses the global building responses as well as local shear wall responses during the post-fire earthquake test sequence. In particular, these responses are compared with those measured during the pre-fire earthquake tests to characterize the effect of prior earthquake- and fire-induced damage on the behavior of the test building. In addition, the chapter provides a detailed summary of the physical damage of the test building at its final damage state.

- **Chapter 9: Conclusions**

  This chapter summarizes of the major findings in Chapter 5 through Chapter 8 regarding the measured response as well as the behavior of the test building during the earthquake and fire test program as well as the modal characteristics of the test building at the various stages during the test program identified using system identification techniques.

Supplemental materials are organized into eight appendices as follows:

- **Appendix A: Project Participants**
  This appendix lists the academic institutions, government and non-profit granting agencies, as well as industry partners participated in this multidisciplinary experimental project.
- **Appendix B: Shake Table Specifications**
  This appendix summarizes the major specifications of the Large High-Performance Outdoor Shake Table (LHPOST) test facility at UCSD.
- **Appendix C: Test Protocols**
  This appendix provides the detailed daily protocols for individual dynamic testing dates (including three test days in the construction phase and four test days in the test phase). The appendix also summarizes the complete test protocol of the ambient vibration data collected throughout the entire test program.
- **Appendix D: Input Earthquake Motions**
  This appendix provides detailed comparisons of the time histories and the spectra responses between the target and achieved motions for individual earthquake tests.
- **Appendix E: Analog Sensors Instrumentation Plans**
  This appendix provides the detailed instrumentation plans of five different types of analog sensors installed on the test building during the construction and earthquake test phases.
- **Appendix F: Video Cameras Instrumentation Plans**
  This appendix provides the detailed instrumentation plans of the video camera system during the pre-fire and post-fire earthquake test phases.
- **Appendix G: Acceleration Double Integration Procedures**
  This appendix presents the detailed procedures for obtaining the displacements from double integration of the measured accelerations as well as the results validated against direct displacement measurements.
- **Appendix H: Door Installation and Damage Photos**
  Photographs of the as-installed door conditions and the associated damage are documented in this appendix.

1.5 Project Team

To realize this multidisciplinary experimental research project, two universities, two (federal and state) government agencies, non-profit granting agencies, and more than 15 industry partners participated. The academic team was comprised of faculty, postdoctoral and student researchers from the University of California, San Diego (lead academic institution) and Worcester Polytechnic Institute (Table A.1 in Appendix A). The Department of Housing and Urban Development and California Seismic Safety Commission, alongside numerous industry partners, provided the financial and material resources needed to support the test program. The unique support and leadership of industry sponsors in this effort were essential to advancing the test program. (Tables A.2 and A.3 in Appendix A).

2 BUILDING DESIGN AND CONSTRUCTION

The first three sections of this chapter summarize the major tasks associated with test preparation stage, including test building design, test motion selection, and pre-test numerical simulation. Subsequently, details regarding the structural system of the test building and the nonstructural systems are discussed in Section 2.4 and 2.5, respectively. Section 2.6 discusses the estimated building weight and its floor distributions. Lastly, the chapter concludes by summarizing the building construction with the emphasis on panelized (prefabricated) construction in Section 2.7.

2.1 Building Design

The test building was designed as a CFS framed building in the high seismic region near downtown Los Angeles (coordinates: 34.0423N and 118.2641W). The hypothetical site corresponds to a NEHRP Site Class D (stiff soil) condition, with the mapped spectral accelerations of S_{DS} = 1.53 g and S_{D1} = 0.81 g (Figure 2.1). The overall building design complied with current code provisions within ASCE 7-10 *Minimum Design Loads for Buildings and Other Structures* (ASCE, 2010), AISI S100 *North American Specification for the Design of Cold-formed Steel Structural Members* (AISI, 2012), and AISI S213 *North American standard for cold-formed steel farming—Lateral design* (AISI, 2007).

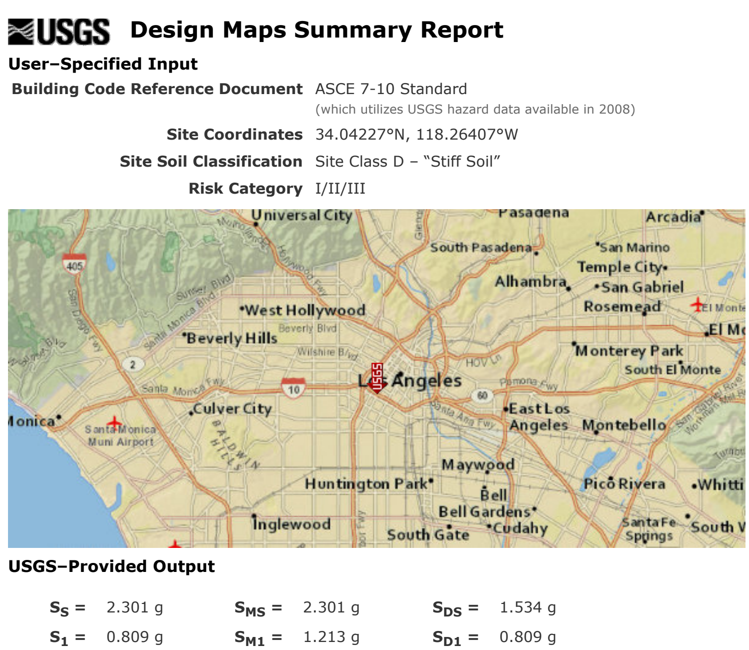

Figure 2.1. Site-specific mapped spectral accelerations.

As shown in Figure 2.2, the six-story test building had a uniform plan dimension of 10.4 m × 7.3 m (34 ft × 24 ft) at each floor, occupying almost the entire 12.2 m × 7.6 m (40 ft × 25 ft) shake table footprint. The total height of the building was 19.2 m above the shake table platen (a floor-to-floor height of 3.1 m (10 ft) for all stories and a 1.2 m-tall (4 ft tall) parapet on the roof perimeter). The seismic design considered uniformly distributed dead and live loads of 1.5 kN/m^2 (32 psf) and 1.9 kN/m^2 (40 psf) at each floor, respectively (note that live loads on the roof was taken as 1.0 kN/m^2 (20 psf)). Consequently, the effective seismic design weight of the test building was assumed as 1420 kN (320 kips). According to ASCE 7-10 (ASCE, 2010), the CFS wall braced building was designed with a response modification factor R of 6.5, an overstrength factor Ω of 3.0, and a deflection amplification factor C_d of 4.0. The code-based fundamental period of the test building T was determined as 0.43 sec considering a total building height of 18.3 m (60 ft) excluding the parapets. The base shear coefficient C_s of the test building was consequently determined as 0.236 and resulted in an effective seismic design base shear V_b of 334 kN (75 kips). The estimated maximum inelastic story drift of the building was ~1.0% (with a deflection amplification factor C_d of 4.0, which was lower than the allowable story drift of 2.0% as prescribed in ASCE 7-10 (ASCE, 2010).

As shown in Figure 2.2b, the building had a symmetric floor plan with a 1.2 m (4 ft) wide corridor oriented along the longitudinal centerline and a room at each quadrant of the building. Two transverse partition walls were located 0.6 m (2 ft) west of the transverse centerline (level 2 through level 6), each separating the two rooms on the same side of the corridor. However, no partition walls were installed at the first level due to insufficient attachment condition to the shake table platen. The exterior façade of the building provided four partial-height window openings (one at each room) and two full-height corridor openings (at each end of the corridor) at each level (Figure 2.2a). Dropped (partial-height) soffits were constructed on the corridor openings at the level 2 and level 6 to attain the anticipated ventilation condition for the fire tests. To account for the live loads and the weight of certain architectural features excluded from the construction (e.g., flooring, exterior façade finishing), four mass plates were installed on the floor diaphragm at each floor from the second floor through the roof (Figure 2.2b). Each mass plate had a dimension of 3.0 m × 1.8 m (10 ft × 6 ft) and an estimated weight of ~16.5 kN (3.7 kips).

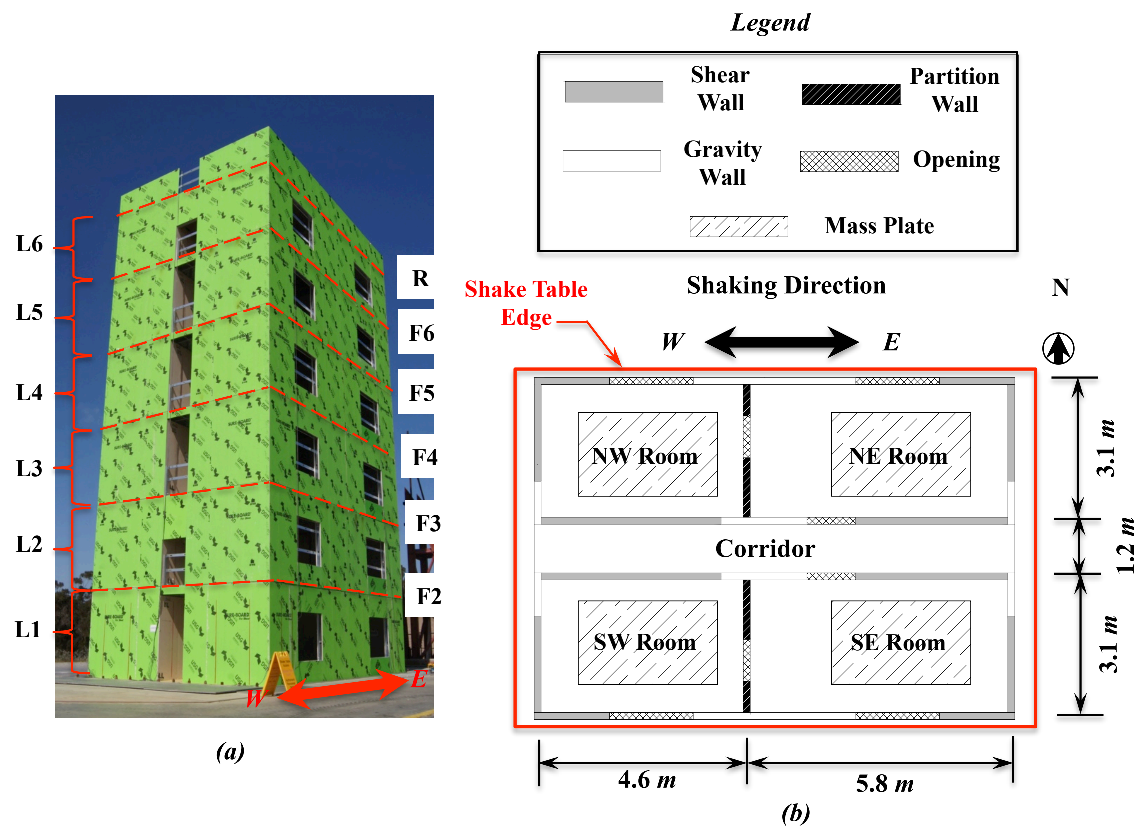

Figure 2.2. Test building: (a) isometric view, and (b) building plan layout (typical of floor 2 to 6, note that floor 1 is identical sans the transverse partition walls).

In addition to partition walls, the test building was outfitted with another two types of nonstructural systems: doors and household appliances. The building included four doors (one each on the two corridor walls and the two transverse partition walls) at each level from level 2 through level 6 but only two doors at level 1 due to the absence of partition walls (Figure 2.2b). In addition, a variety of household appliances (e.g., gas and electric range units, water heaters, wall-mounted television sets, and etc.) were installed at level 1 and level 6. Details of these nonstructural systems are discussed in Section 2.5.

2.2 Test Motion Selection

During the test preparation stage, the research team proposed to select earthquake test motions based on the following criteria: (a) inclusion of multiple intensity levels in the earthquake test protocol, (2) design event representative of strong earthquakes in California, and (3) inclusion of earthquake events with motion characteristics (e.g., near-fault pulse effect, strong durations) different from that of the design level test motion. According to these selection criteria, four seed motions from three earthquake events were chosen for the test protocol. The earthquake and motion characteristics of the (unscaled) seed motions are summarized in Table 2.1. The acceleration histories and the associated pseudo-acceleration and displacement spectra of these seed motions are presented in Figure 2.3. As shown in the table, three seed motions were selected from earthquake events in California (motions CNP196 and RRS228 from the 1994 M_w=6.7 Northridge earthquake, while motion RIO 360 from the 1992 M_w=7.0 Cape Mendocino earthquake), while the remaining motion (CUREW) from the 2010 M_w=8.8 Maule earthquake in Chile – a large-magnitude subduction earthquake. Therefore, the strong duration of motion CUREW was significantly longer than the other three records (Figure 2.3a). It is also noted that motion RRS228 differed fundamentally from the other three records in the spectral characteristics, since it contains a large-amplitude spectral peak (even larger than its short period spectral accelerations) in the period range between 0.5 and 1 second (see Figure 2.3a), while the pseudo-acceleration spectra of other three motions drops considerably when the period exceeds ~ 0.5 second. This is due to the fact that motion RRS represented a near-fault record containing a long period velocity pulses at ~1.2 second.

Table 2.1. Summary of the earthquake and motion characteristics of the seed motions.

Seed record	Event, Year	M_w	Station	R_{rup} (km)	PGA (g)	PGV (cm/sec)	PGD (cm)	$S_{a,avg}$ (g)	$S_{a,1}$ (g)	$D_{s,5\text{-}95}$ (sec)
CNP196	Northridge, 1994	6.7	Canoga Park	14.7	0.39	60.4	12.5	1.01	0.49	10.6
RIO360	Cape Mendocino, 1992	7.0	Rio Dell Overpass	14.3	0.55	45.4	5.2	1.47	0.39	10.9
CUREW	Maule, Chile, 2010	8.8	Curico	N/A	0.41	32.6	5.2	0.92	0.42	51.6
RRS228	Northridge, 1994	6.7	Rinaldi Receiving Station	6.5	0.86	147.9	41.8	1.83	1.85	9.1

Notes: M_w – moment magnitude; R_{rup} – rupture distance; PGA – peak ground acceleration; PGV – peak ground veloctiy; PGD – peak ground displacement; $S_{a,avg}$ – short-period spectral acceleration averaged between $0.5T_1$ and $1.5T_1$ (T_1 taken as the code-based building period of 0.43); $S_{a,1}$ – spectral acceleration at T=1 sec; $D_{s,5\text{-}95}$ -- strong motion duration.

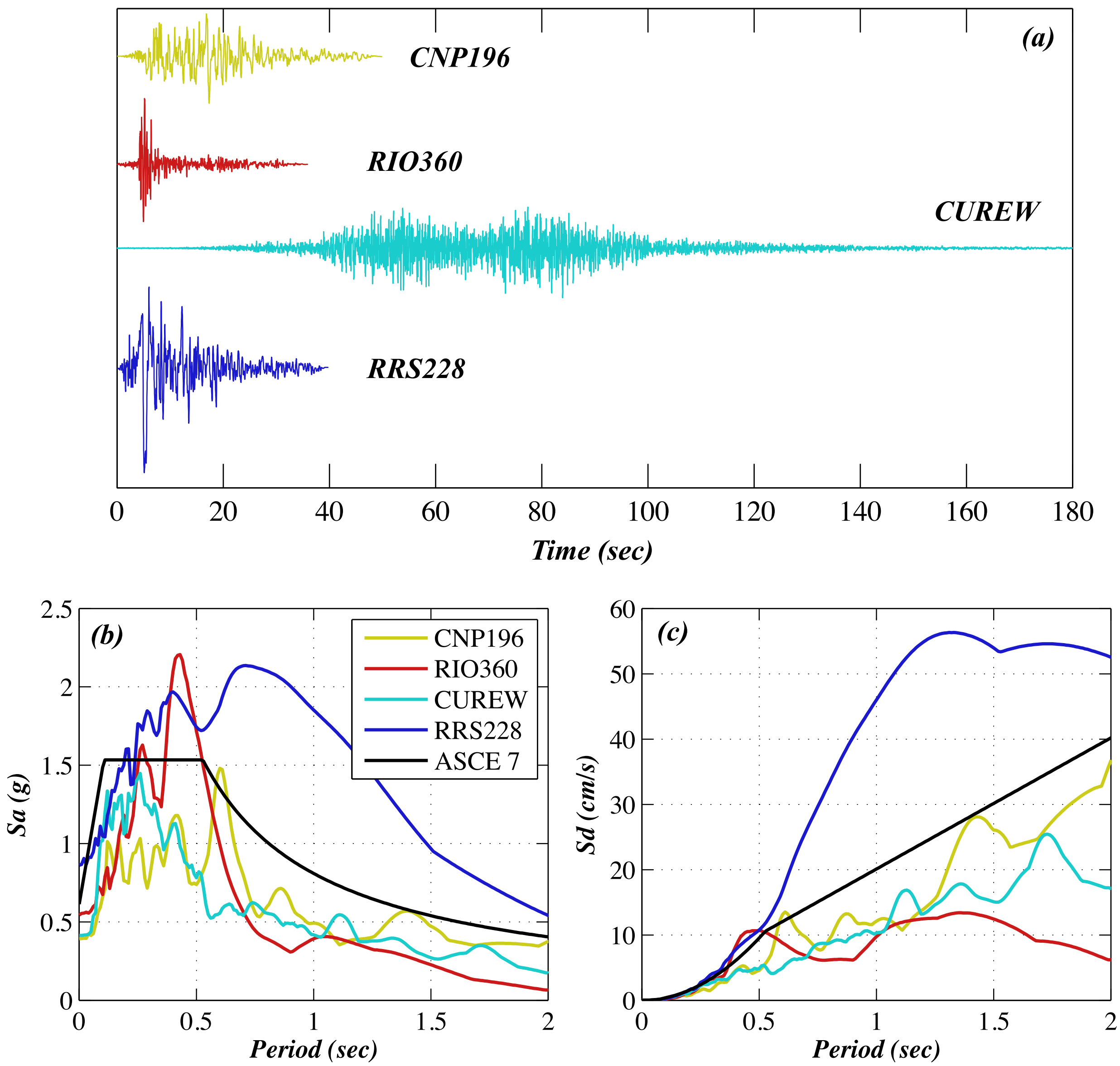

Figure 2.3. Seed motions: (a) acceleration time histories, (b) pseudo-acceleration spectra (ξ = 5%), and (c) displacement spectra (ξ = 5%).

According to the site-specific spectral accelerations (Figure 2.1), the seed motions were amplitude-scaled to four different earthquake intensity levels: (1) serviceability level (25% design level), (2) 50% design level, (3) 100% design level, and (4) maximum considered earthquake (MCE) level (150% design level). It is noted that seed motion scaling did not involve spectral matching in an effort to preserve the frequency contents of the seed motions. To ensure that a specific motion conforms to a design event characterized by the acceleration spectrum as stipulated by ASCE 7-10 (ASCE, 2010), the scaling factor of an input motion was determined as the ratio of the averaged spectral acceleration of the seed motion within a period range between half and one and a half times the building fundamental period associated (in the direction of shaking) and the averaged spectral acceleration of the design spectrum in the same period range.

The building fundamental period was initially taken as the code-based fundamental period of 0.43 second for motion scaling but adjusted to the actual period determined using the white noise test data on individual test dates (see detailed results in Section 3.2). Since the shifted period modified the scale factor of the test motions, this effect was accounted for each input motions. Table 2.2 illustrates the motion scale factor calculated based on different building period values for the design level motion (CNP196). As shown in the table, using the actual period of the building resulted in about 9% increase of the scale factor compared to that calculated using the code-based period.

Table 2.2. Scale factor calculated based on two different buidling period values.

Building period T_1 (sec)	$S_{a,avg}^{motion}$ (g)	$S_{a,avg}^{design}$ (g)	Scale Factor
0.43 (code-base period)	1.00	1.49	1.49
0.30 (actual period)	0.95	1.53	1.62

$S_{a,avg}^{motion}$ – motion spectral acceleration averaged between $0.5T_1$ and $1.5T_1$;

$S_{a,avg}^{motion}$ – design spectral acceleration averaged between $0.5T_1$ and $1.5T_1$;

2.3 Pre-test Numerical Simulation

2.3.1 Modeling Strategies

In an effort to predict the seismic response characteristics of the test building and support test motion selection during the test preparation stage, a numerical effort was conducted to develop a lumped-spring element based model using OpenSees (McKenna et al., 2016). The simplified model involved several assumptions: (a) the lateral load bearing system incorporated only the shear walls while the gravity walls not explicitly considered, (b) the floor diaphragm was considered as axially rigid, and (3) the force-displacement behavior of the shear wall was lumped into a concentrated shear spring (uplift and flexural deformation not explicitly modeled). As shown in Figure 2.4, each shear wall was modeled using two rigid beams connected by a shear spring (zero-length element) at mid-height to represent the lateral force displacement behavior in the horizontal direction (vertical and rotational stiffness were considered as rigid). Separate shear walls along the wall line were subsequently connected using rigid link constraints to ensure the deformation compatibility of the shear walls on the same wall line. The building mass at each floor was assigned to the shear wall nodes based on the tributary areas associated with the shear walls (detailed discussion of the actual building inertial weight is summarized in Section 2.6). It is noted that the numerical model of building developed using the above assumptions essentially represents a shear-beam structure under lateral loads.

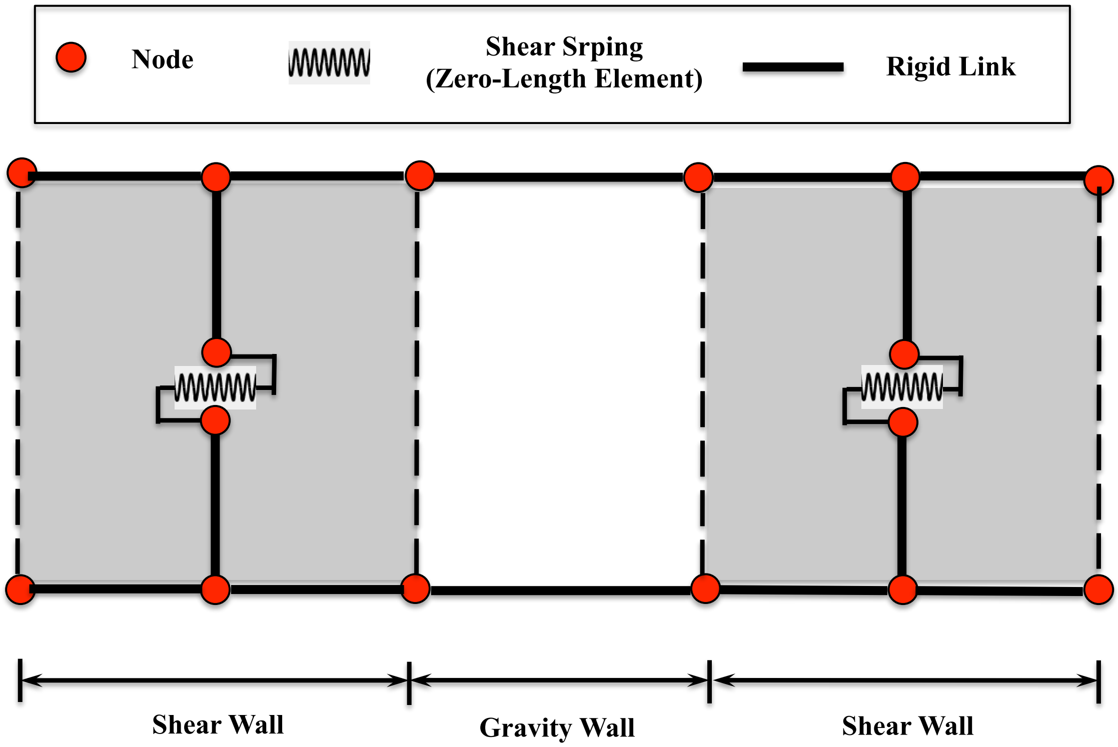

Figure 2.4. Schematics of the modeling details of a combined shear wall and gravity wall assembly.

The lateral force displacement behavior of the shear spring was modeled using *Pinching4* materials. The parameters of *Pinching4* materials were calibrated using the shear wall component test data provided by the manufacturer. Figure 2.5 presents the hysteretic response of a shear wall specimen and the derived backbone curve. As shown in the figure, the monotonic force displacement response of each shear wall was simplified as a multi-linear curve with four control points: (1) the first point defines the elastic limit of the shear wall response (~ 40% peak strength), (2) the second point corresponds to ~ 80% peak strength, (3) the third point corresponds to the attainment of peak strength, and (4) the fourth points define the attainment of ultimate deformability (twice the displacement at the peak point). Since the force displacement response was comparable in the positive and negative loading directions, the idealized backbone curve was defined as symmetric using the averaged response of the two loading directions.

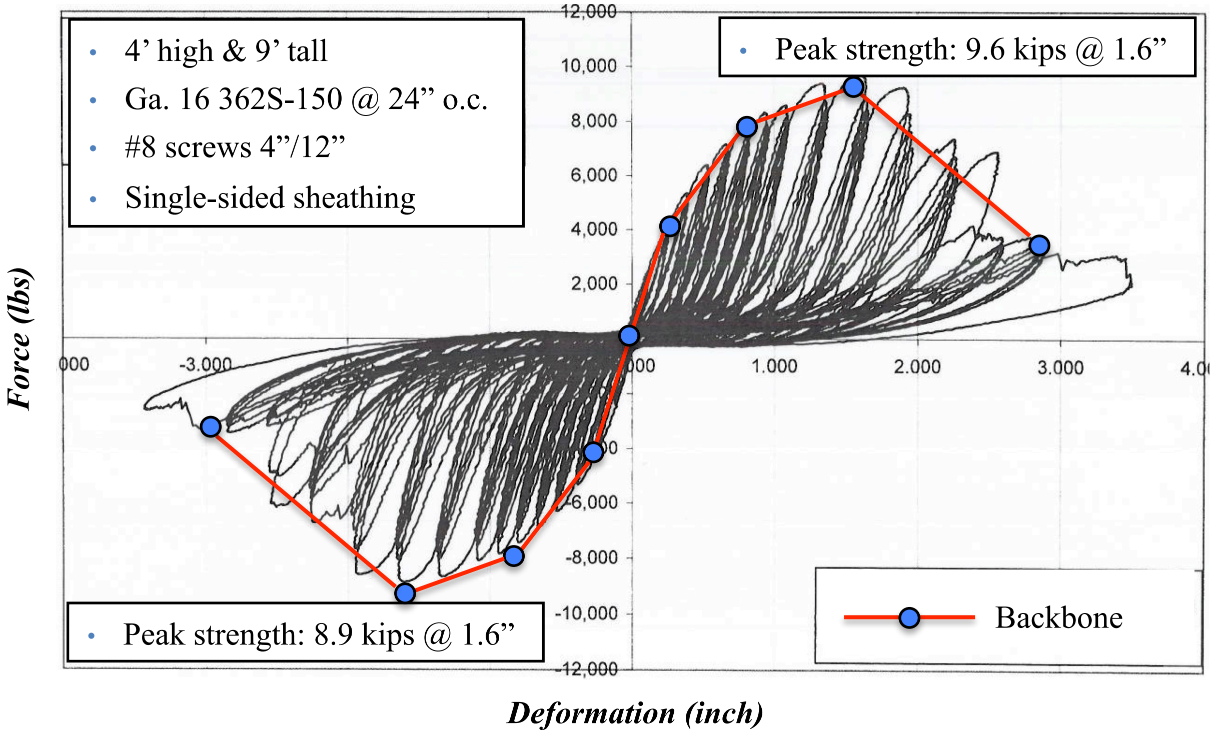

Figure 2.5. Force displacement response of a shear wall specimen and the idealized backbone curve (test data courtesy of Kelly Holcomb).

Since the dimension of the shear wall specimens for the component tests (1.2 m (4 ft) in length and 2.7 m (9 ft) in height) differed from those of the shear walls used in the full-scale test building, the shear force obtained using the component test results was converted to form the backbone curves of test building shear walls based on length scaling. An additional scale factor of 1.2 was applied to account for the fact that the stronger stud sections and the presence of gypsum boards of the shear walls in the full-scale test building. Although the component test data provided useful information regarding the seismic behavior of the shear walls, it is noted that these test specimens differed from the shear walls of the test building in several important aspects (e.g., wall length and aspect ratio, presence of tie-down system, steel framing members, and etc.). Detailed characterization of the effects of these design variables on the shear wall behavior requires further component-level experimental studies. In this regard, it is understood that the intent of pre-test numerical simulation was qualitative assessment of the performance of the test building to support decision making on test planning instead of precise prediction of the seismic response of the test building.

2.3.2 Modeling Results

Pre-test numerical simulation included eigenvalue analysis, nonlinear static (pushover) analysis, and nonlinear dynamic (time history) analysis. Figure 2.6 presents the building periods obtained from the eigenvalue analysis as well as the pushover curve of the building. As shown in Figure 2.6a, the predicted building fundamental (first mode) period in the longitudinal direction was 0.45 second. Although the value agrees well with the code-based period of 0.43 second, it was later found that the test building appeared much stiffer than the periods predicted by the numerical model. This is due to the fact that the shear springs calibrated using the component test results underestimated the stiffness of the shear walls in the full-scale test building as a result of the uncertainty related to the variation of the shear wall details.

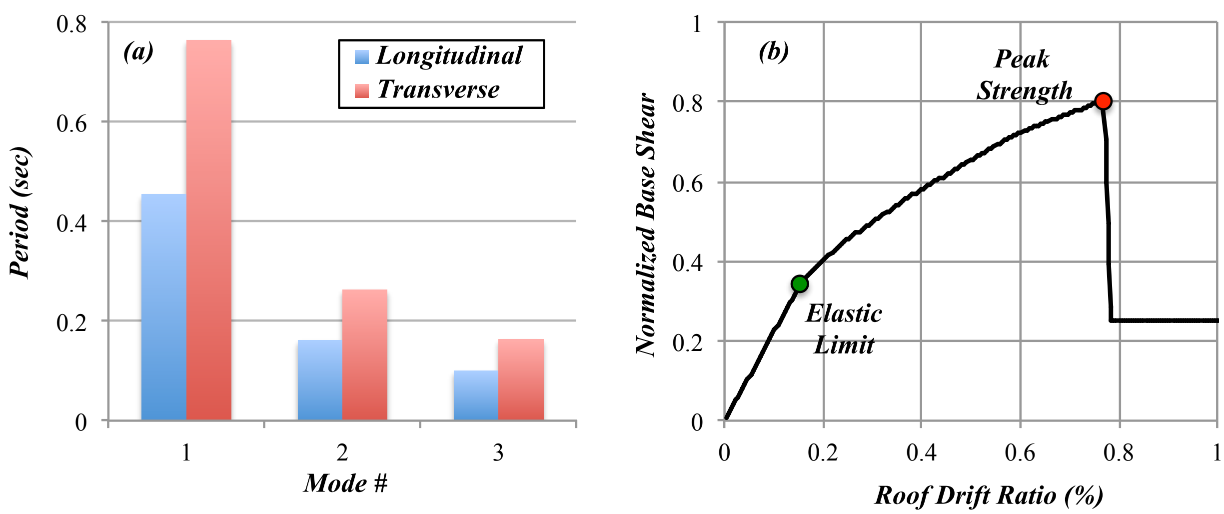

Figure 2.6. Pre-test modeling results: (a) building periods, and (b) pushover curve.

Figure 2.6b illustrates the pushover curve (base shear normalized by total building weight vs roof drift ratio). The lateral force pattern was assumed to follow the design shear distribution using the equivalent lateral force procedure. As shown in the figure, the building response remains linear when the roof drift ratio remains lower than 0.2%, and the corresponding base shear reaches about 30% of the total weight of the building. The building reaches its peak strength at a roof drift ratio of about 0.75%, with the base shear attaining as much as 80% of the total weight of the building. It implies that this light-frame structure is characterized by very high strength relative to its weight compared to other structural types (e.g., reinforced concrete or steel moment frame). The base shear dropped almost immediately following the attainment of the peak strength, due to the following two reasons: (1) the component test results do not reveal very high post-peak ductility for this type of shear walls, and, (2) the shear-type building model is likely to localized the inelastic deformation within a single story in the post-peak loading range.

In the pre-test simulation, nonlinear time history analysis was also conducted to estimate the seismic response of the test building. As shown in Figure 2.7, the input motions included four different intensity levels: service level motions (25% CNP, 25% RIO, and 25% CUR), 50% design level (50% CNP), design level (100% CNP), and maximum considered earthquake (MCE) level (150% CNP). The motion sequence was applied sequentially with a 10-second free vibration appended between individual test motions to allow for identification of the building fundamental period at the end of free vibration (denoted by the red circle markers). Rayleigh damping was incorporated into the model to account for the energy dissipation effects of the building in the dynamic analysis. The damping ratio associated with the first two longitudinal modes was taken as 5% for the service level motions and 3% for the above-the-service level motions

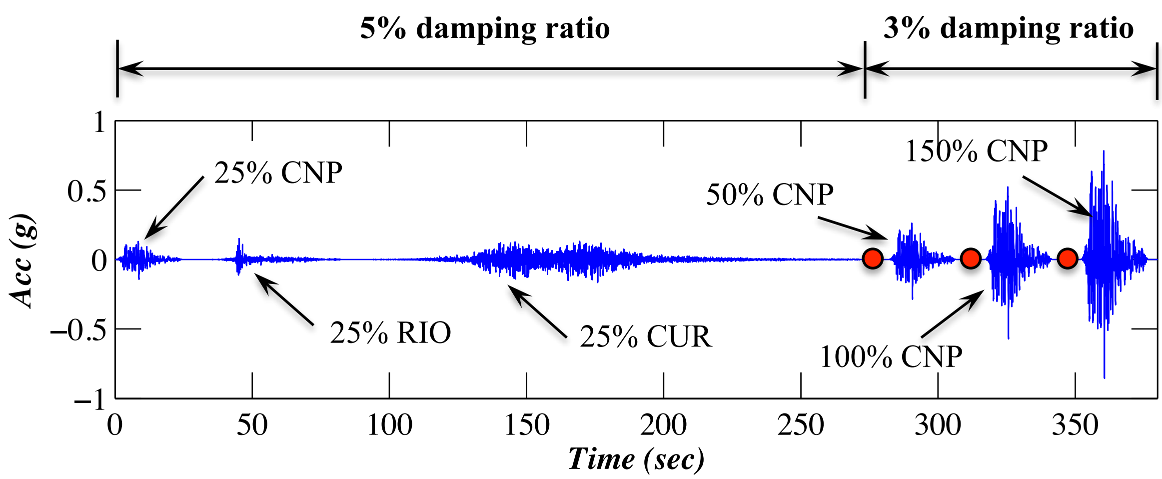

Figure 2.7. Test motion sequence for pre-test nonlinear dynamic analysis.

Figure 2.8 presents the peak roof drift ratios (PRDRs) associated with service level, 50% design level, and design level motions (results for the MCE level motion were excluded due to excessive inelastic displacement localization at the first level) as well as the building fundamental period at the completion of each intensity level (shown as the red circle markers in Figure 2.7). The predicted PRDR was 0.1% and 0.2% for the service level and 50% design level motions, which was lower than and comparable to the elastic limit from the pushover results. Meanwhile, the building fundamental period remained identical to its initial value of 0.45 second following the service level motions and increased slightly (by about 20%) following the 50% design level motion. As the predicted PRDR increased considerably and achieved 0.8% during the design level motion (100% CNP), the building underwent considerable fundamental period elongation (nearly 100% increase of its fundamental period relative to its initial value).

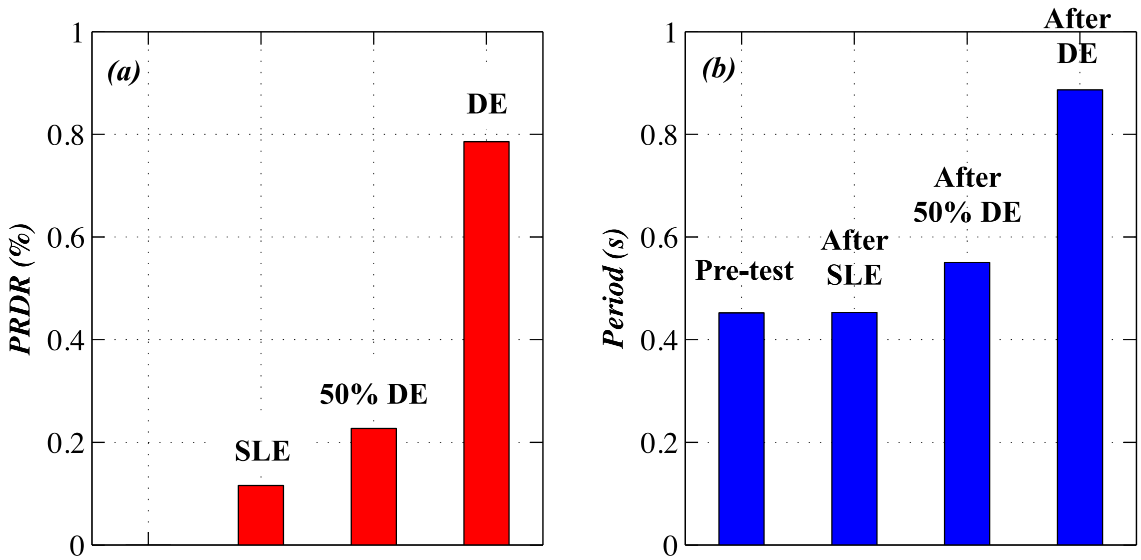

Figure 2.8. Nonlinear time history analysis results: (a) peak roof drift ratio, and (b) building fundamental period evolution.

Figure 2.9 presents the predicted building peak floor accelerations (PFAs) and peak interstory drift ratios (PIDRs) for seed motion CNP scaled to three distinct intensity levels (service level, 50% design level, and design level motions). The predicted PFA achieved their largest values at the roof level during all three motions, with a peak value of 0.4 g, 0.9 g, and 1.7 g, respectively (Figure 2.9a). The roof accelerations achieved an amplification factor of about 3 (relative to their input accelerations) at all three intensity levels, which correlates well with the code provisions (ASCE, 2010). On the other hand, the predicted PIDR was the largest at the first level at all intensity levels, with the corresponding value of 0.15%, 0.35%, and 1.1%, respectively (Figure 2.9b). Consistent with those observed from the predicted PRDR results, the predicted PIDR demands in comparison with the component test results demonstrate that the shear walls remained essentially elastic during the service level and 50% design level motions but may likely achieve the drift limit associated with the shear wall peak strength during the design level motion. However, it was later found that the shear wall behavior calibrated using the component test results underestimated the stiffness and strength of the shear walls in the test building as a result of the discrepancies of shear wall details as previously discussed. Since the model assumed a fairly uniform story stiffness distribution along the height of the building, it overestimated the PIDR demands at the lower two levels, where their actual stiffness was remarkably larger than those of the remaining levels due to the presence of large-diameter tie-down rods (details are discussed later in Section 2.4).

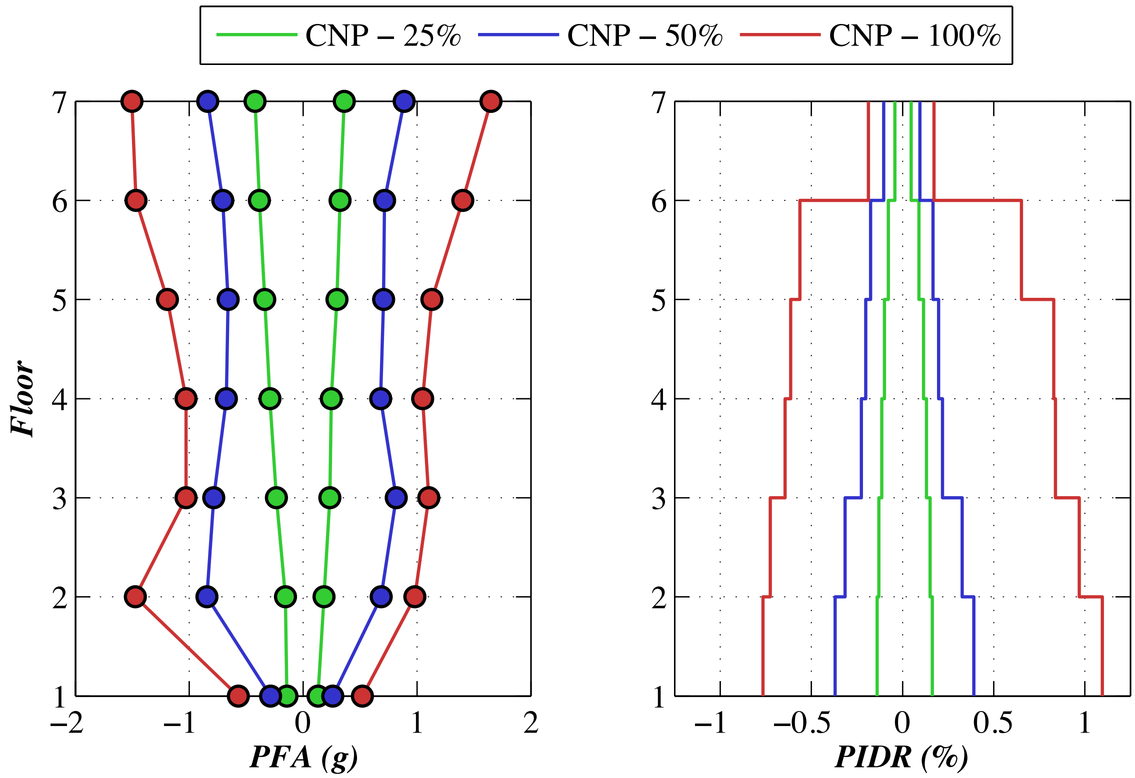

Figure 2.9. Nonlinear time history analysis results: (a) peak floor acceleration, and (b) peak interstory drift ratio.

2.4 Structural System

The structural system of the test building consisted of repetitively framed steel sheathed CFS shear walls to resist both vertical and lateral loads as well as gravity walls that were detailed to resist only vertical loads. The horizontal structural system consisted of floor diaphragms that transfer the floor level lateral and vertical loads to the vertical structural system. To resist the uplifting forces induced by seismic lateral loads, a continuous tie-down rod system was embedded in the shear wall framing. The tie-down rods were sandwiched between the compression studs (welded CFS stud packs) to carry the vertical uplift loads during the lateral loads in an event of earthquake. In addition, the building was attached to the shake table platen using tie-down rods to facilitate a fixed boundary condition at its base. The building-to-table tie-down system and the major structural components are discussed in this section.

2.4.1 Shake Table Tie-down System

To ensure a fixed boundary condition at the base of the building, the bottom tracks at the first level were attached to the shake table platen using a total of 80 large-diameter threaded steel rods. Figure 2.10 shows the plan layout of the shake table tie-down system The tie-down rods were spaced at ~0.6 m (2 ft) along the longitudinal and transverse wall lines, which are placed to align with the 0.6 m x 0.6 m (2 ft × 2 ft) grid tie-down holes of the shake table platen. Depending on the specific location, the individual tie-down rods differed in several aspects such as diameter, post-tensioning condition, and length. These rod specifications are summarized in Table 2.3.

Table 2.3. Summary of the shake table tie-down rods.

Rod diameter	Post-tensioning condition	Tie-down hole depth	Location (color code) [1]	Quantity
46 mm (1-3/4”)	**Post-tensioned**	Blind	Corner shear walls (red)	16
		2.1 m	Corridor shear walls (red)	8
46 mm (1-3/4”)	Non post-tensioned	Blind	Exterior shear walls and gravity walls (green)	16
46 mm (1-3/4”)	Non post-tensioned	2.1 m	Corridor shear walls and gravity walls (blue)	28
36 mm (1-3/8”)	Non post-tensioned	1.2 m	Exterior shear walls and gravity walls (yellow)	12
Total				**80**

[1] refer to Figure 2.10 for tie-down rod plan layout.

It is noted that post-tensioning was applied to 24 rods located within the shear walls (a pair per wall for a total of 12 shear walls). The post-tensioned rods all consisted of a diameter of 64 mm (1-3/4”) and a prestress level of about 667 kN (150 kips), which was less than 50% ultimate strength of the rods. These post-tensioned rods were each connected to the continuous shear wall tie-down rods that spanned over all levels of the building. Details of the shear wall tie-down rod system are discussed later in this section.

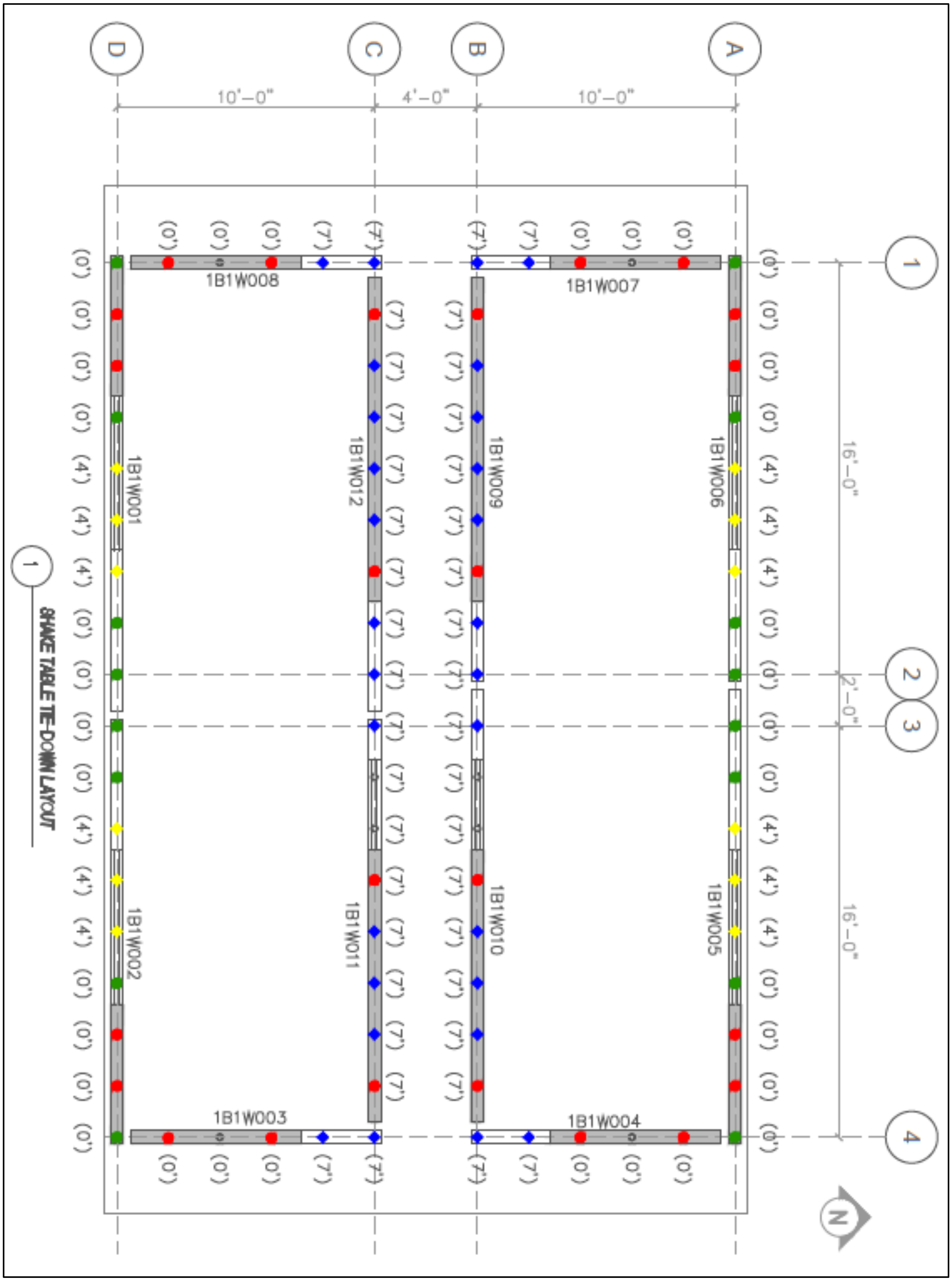

Figure 2.10. Shake table tie-down system plan layout.

2.4.2 Shear Walls

As illustrated in Figure 2.2b, two longitudinal shear walls were placed along each (east and west) end of the corridor wall lines. The wall length was 4.0 m (13 ft) for the west corridor wall segments and 3.3 m (11 ft) for the east corridor wall segments (Figure 2.11a). In addition, L-shaped shear walls with a length of ~1.6 m (5'-4") in the longitudinal direction and ~2.1 m (7 ft) in the transverse direction were placed at the four corners of the building (Figure 2.11c and d). The total shear wall length was 21.3 m (70 ft) in the longitudinal (shaking) direction and 8.6 m (28 ft) in the transverse direction. It is noted that the corridor shear walls were designed as the primary lateral load resisting elements in the direction of shaking, while the corner shear walls were assumed to resist transverse and torsion loads during the earthquake tests.

The shear walls were framed using standard framing members (e.g., studs, tracks). Sheathing materials utilized load-resisting structural panels on the exterior (or corridor) side and 16 mm (5/8") thick regular gypsum boards on the room side. The structural panels were fabricated using 16 mm (5/8") thick gypsum boards (or) bonded with a layer of 0.686 mm (0.027") thick (22 ga.) sheet steel to provide shear resistance to the shear wall assemblies. For the corridor shear walls, vertical studs utilized 600S200-68 at 610 mm (24") o.c at the first level and 600S200-54 at 610 mm (24") o.c at all the remaining levels. The (top and bottom) tracks were all constructed using of 600T200-54, with the exception of the first level bottom tracks that used 600T200-97. In addition, the chord studs (in a double stud pattern) at the edge of the door and opening windows were constructed using 600S200-68. The structural panels of the corridor walls were attached to framing using #8 self-tapping metal screws at 406 mm (16") o.c in field but different spacing on boundary: 76 mm (3") o.c. for the lower three levels, 102 mm (4") for level 4, and 152 mm (6") o.c for the upper two levels (the screw spacing details are illustrated in Figure 2.12). Additionally, the gypsum boards were attached to the framing by #8 drywall screws at a spacing of 152 mm (6") o.c. on boundary and 406 mm (16") o.c in field. The details of the corner shear walls were similar to those of the corridor shear walls, except: (1) vertical studs utilized 600S200-54 at 610 mm (24") o.c at all levels, (2) the structural panels utilized 16 mm (5/8") thick moisture-resistant gypsum boards instead of regular gypsum boards since they were located on the building exterior, and (3) the screw spacing on the boundary was 152 mm (6") o.c on the boundary and 406 mm (16") o.c in field at all levels. It is also shown in Figure 2.11 that all the corridor and corner shear walls contained a pair of tie-down subassemblies (consisting of tie-down rods and compression posts) as part of the building tie-down system. Details of the building tie-down system are discussed in the next subsection.

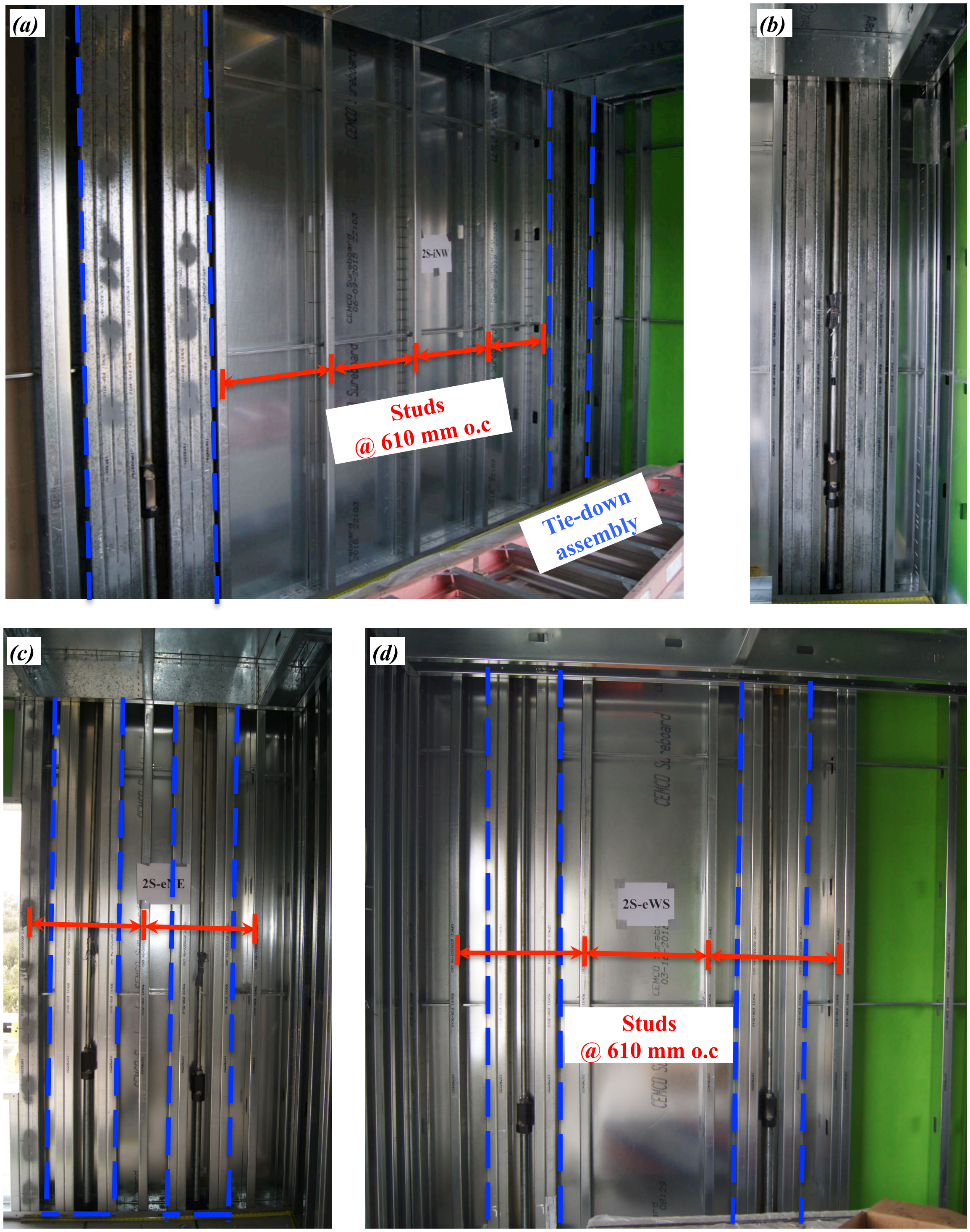

Figure 2.11. Shear walls framing at level 2: (a) corridor wall, (b) corridor wall tie-down subassembly, (c) longitudinal corner wall, and (d) transverse corner wall (all photos view from room side).

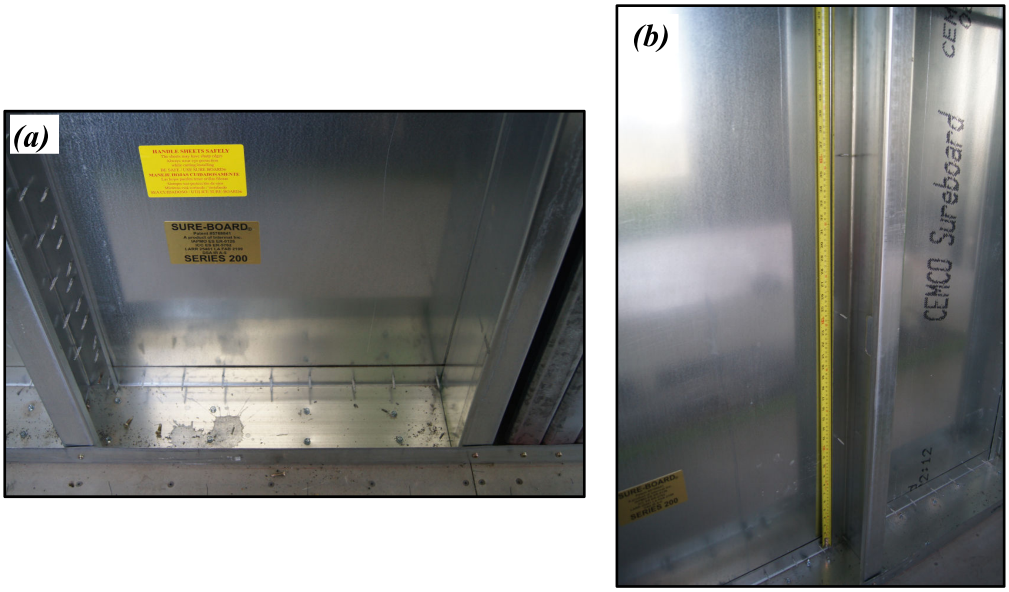

Figure 2.12. Corridor shear wall screw spacing details: (a) screws on boundary, and (b) screws in field.

2.4.3 Shear Wall Tie-down System

The tie-down system was embedded within the shear walls and spanned vertically over all levels of the building to resist the uplift forces. As shown in Figure 2.11, each shear wall included a pair of tie-down subassemblies comprised of: (a) steel rods connected by couplers, and (b) compression posts made of built-up stud packs. The details of the tie-down rods and compression posts varied by shear wall location and the building level, due to the differences in their uplift force demands of individual walls. Figure 2.13 illustrates the corridor shear wall tie-down assemblies at three select levels. Complete details of the tie-down assemblies are summarized in Table 2.4.

Two different types of steel rods were used for the tie-down system: (a) all-thread rods, and (b) Z-rods (threaded at both ends to facilitate coupler connection but unthreaded in the middle span). These steel rods were fabricated using either ASTM A36 (plain finish) or ASTM A193 Grade B7 (zinc-coated) steel material. It is noted that the steel rods were all 3.0 m (10 ft) in length and spanned over the entire level at intermediate levels (level 2 through level 5) (Figure 2.13a), while the rods consisted of three segments at level 1 (Figure 2.13a) and two segments at level 6 (Figure 2.13a). The tie-down rods were connected by couplers with double nuts located about 0.6 m (2 ft) above the floor level (Figure 2.14b), and each rod was fastened to the floor using a bearing plate connection (Figure 2.14c). Additionally, the compression posts were constructed as multiple-stud built-up packs with the following details: (a) 25 mm (1”) long welds at every 305 mm (12”) on the stud flanges if the studs were placed in a face-to-back configuration, and (b) two #8 self-tapping metal screws at every 305 mm (12”) on the web if placed in a back-to-back configuration. The stud section type and quantity of the built-up packs also varied dependent on the level and shear wall location.

Table 2.4. Details of shear wall tie-down system.

Level #	*Type of shear wall*	*Steel rod specification*	*Length (m)*	*Compression post*
1	*Corridor wall*	46 mm dia. transition rod (lower segment) 43 mm dia. A36 all-thread rod (middle segment) 43 mm dia. B7 all-thread rod (upper segment – extending ~0.6 m into level 2)	0.6 0.9 1.8	(10) 600S200-97
	Corner wall	46 mm dia. transition rod (lower segment) 43 mm dia. A36 all-thread rod (middle segment) 43 mm dia. B7 all-thread rod (upper segment – extending ~0.6 m into level 2)	0.6 0.9 1.8	(4) 600S200-68
2	*Corridor wall*	43 mm dia. B7 Z rod (extending ~0.6 m into level 3)	3.0	(8) 600S200-97
	Corner wall	29 mm dia. A36 Z rod (extending ~0.6 m into level 3)	3.0	(4) 600S200-54
3	*Corridor wall*	36 mm dia. A36 all-thread rod (extending ~0.6 m into level 4)	3.0	(8) 600S200-97
	Corner wall	25 mm dia. A36 all-thread rod (extending ~0.6 m into level 4)	3.0	(4) 600S200-54
4	*Corridor wall*	29 mm dia. B7 Z rod (extending ~0.6 m into level 5)	3.0	(8) 600S200-97
	Corner wall	19 mm dia. A36 Z rod (extending ~0.6 m into level 5)	3.0	(4) 600S200-54
5	*Corridor wall*	29 mm dia. A36 all-thread rod (extending ~0.6 m into level 6)	3.0	(8) 600S200-54
	Corner wall	16 mm dia. A36 all-thread rod (extending ~0.6 m into level 2)		(4) 600S200-54
6	*Corridor wall*	16 mm dia. A36 Z rod (lower segment) 16 mm dia. A36 Z rod (upper segment)	1.8 0.3	(4) 600S200-54
	Corner wall	16 mm dia. A36 Z rod (lower segment) 16 mm dia. A36 Z rod (upper segment)	1.8 0.3	(4) 600S200-54

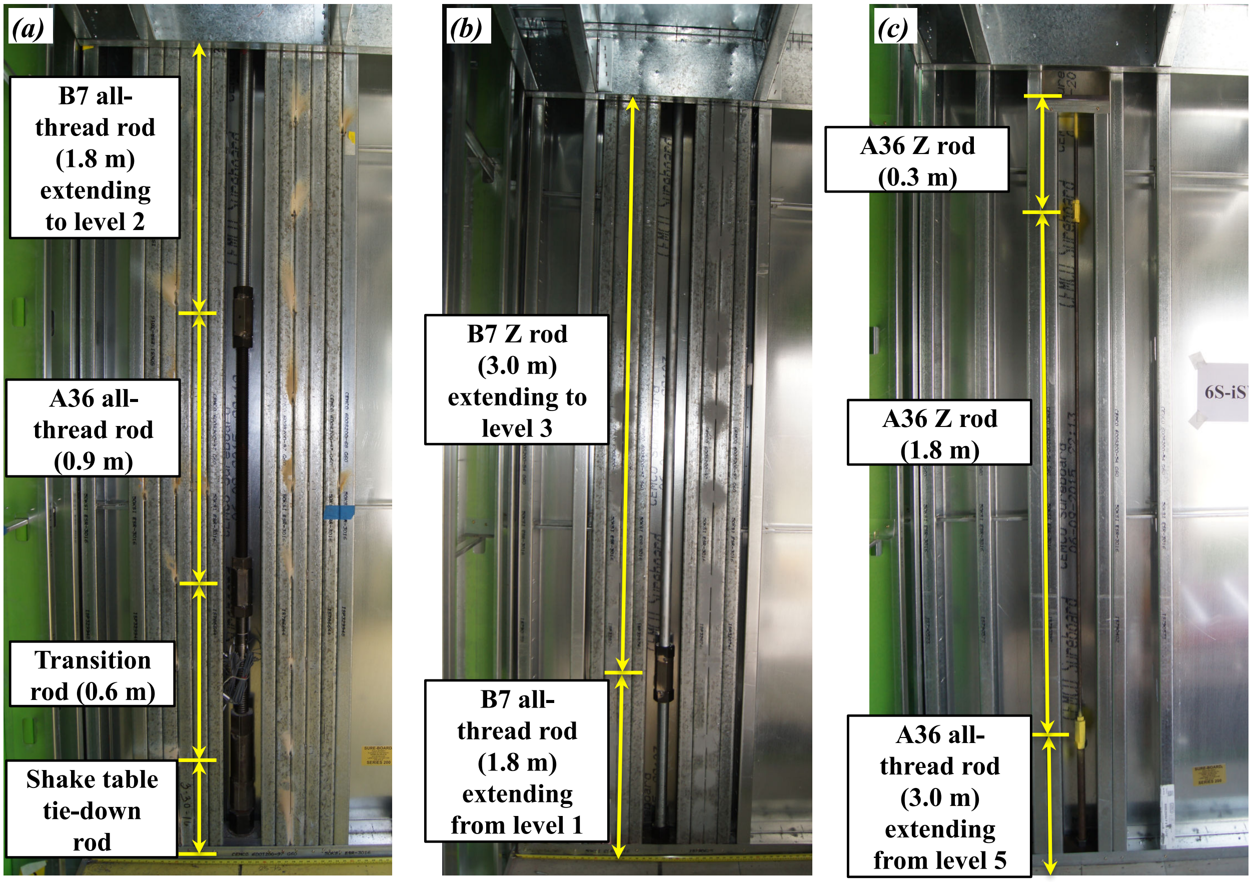

Figure 2.13. Corridor shear wall tie-down assemblies: (a) level 1, (b) level 2, and (c) level 3.

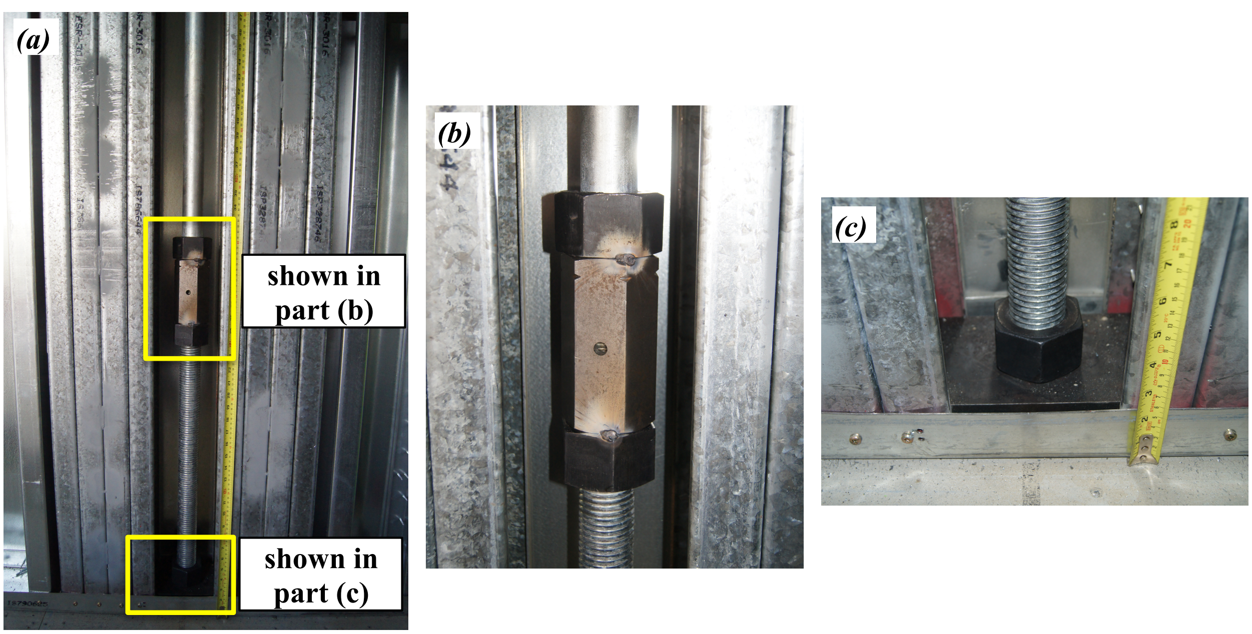

Figure 2.14. Tie-down connection details: (a) tie-down assembly (b) coupler and double lock nut connection, and (c) floor level base plate connection details.

2.4.4 Gravity Walls

The gravity walls were located between the window openings at the building exterior as well as between the two corridor shear walls (Figure 2.2b). Since the gravity walls were intended to resist only vertical forces rather than lateral shear forces, they differed from the shear walls in two important aspects: 1) gypsum panels were used as the sheathing material on both sides of the framing, and 2) absence of tie-down assembly in the framing as they are not intended to carry the uplift force induced by lateral seismic loads. As a result, the (unit-length) shear strength of the gravity walls was significantly lower than those of the shear walls.

As shown in Figure 2.15a, the gravity wall framing was constructed using 600S200-54 at 610 mm (24”) o.c for intermediate studs and 600S200-68 for chord studs. It is noted that the prefabricated wall panel joints were located in the gravity walls (on both exterior and corridor walls) that contained several closely spaced vertical studs between the studs at the regular spacing. As shown in Figure 2.15b, the regularly spaced studs were aligned with the floor joists, while additional panel edge studs formed the boundary elements of the prefabricated wall panels. The top and bottom tracks were all made of 600T200-54 (with the exception of the bottom tracks at the first level that utilized 600T200-97) and spanned over the entire length of the prefabricated wall panel. The sheathing material utilized (a) 16 mm (5/8”) thick regular gypsum boards on the corridor side and building interior, and (b) 16 mm (5/8”) thick moisture-resistant gypsum boards on the building exterior. The sheathing panels were all attached to steel framing using #8 drywall screws at a spacing of 152 mm (6”) o.c. on boundary and 406 mm (16”) o.c in field.

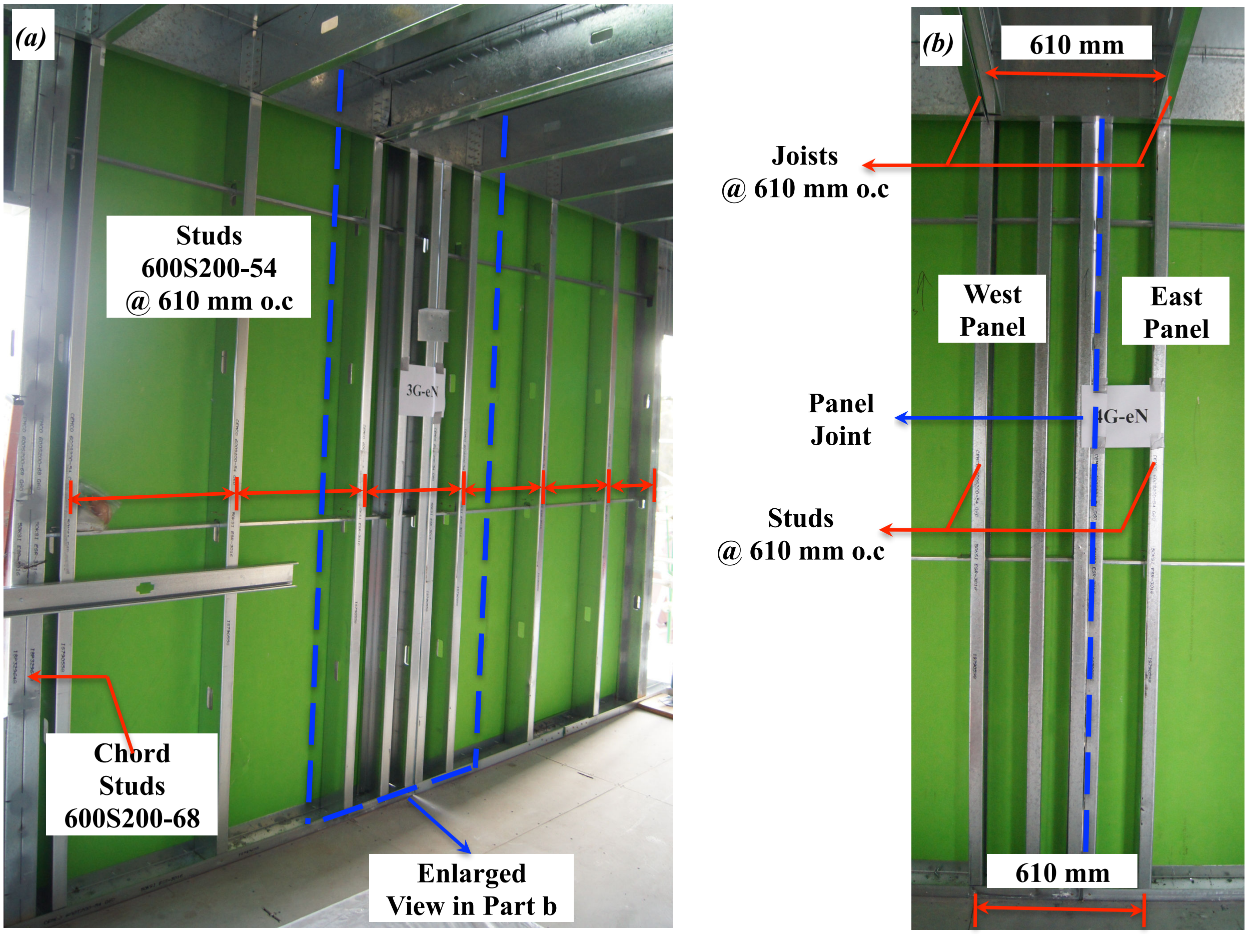

Figure 2.15. Exterior gravity wall (between the window openings): (a) steel framing, (b) wall panel joint (both view from building interior).

2.4.5 Floor Diaphragm

The floor and roof diaphragms were constructed as a ledger framing system. They were connected to the vertical wall systems by attaching the diaphragm joists to the flange of the wall studs via a combination of rim track and clip angle solution. The diaphragm joists were oriented perpendicular to the longitudinal direction of the building (direction of shaking), resulting in a clear span of ~2.9 m (9'-6") for the room span and ~1.1 m (3'-6") for the corridor span.

Regardless of span length, the diaphragm framing were constructed using 1000S200-54 at 610 mm (24") o.c for the joists (aligned with the vertical wall studs) and 1000T200-54 for the rim tracks at all floors of the building including the roof (Figure 2.16). The joist was connected to the rim track using 7-1/2"×2"×2" angles with (5) #10 metal screws vertically spaced over the flange (Figure 2.17a). All the diaphragms contained mid-span blocking or bracing (Figure

2.17b). In particular, these stiffening strategies were intended to strengthen the local stiffness of the diaphragm since the mass plates were anchored to the floor at these locations.

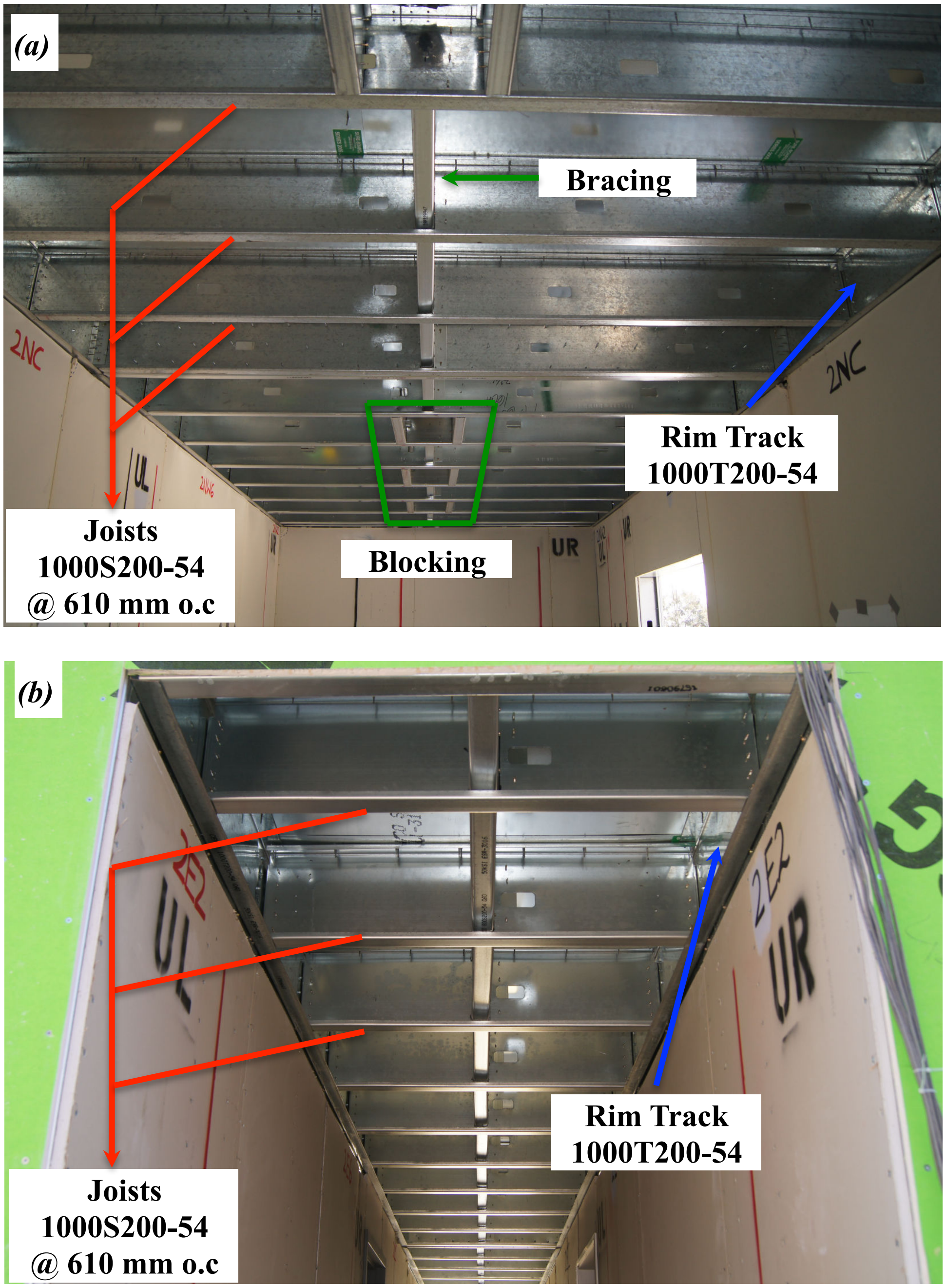

Figure 2.16. Floor diaphragm: (a) room span, and (b) corridor span.

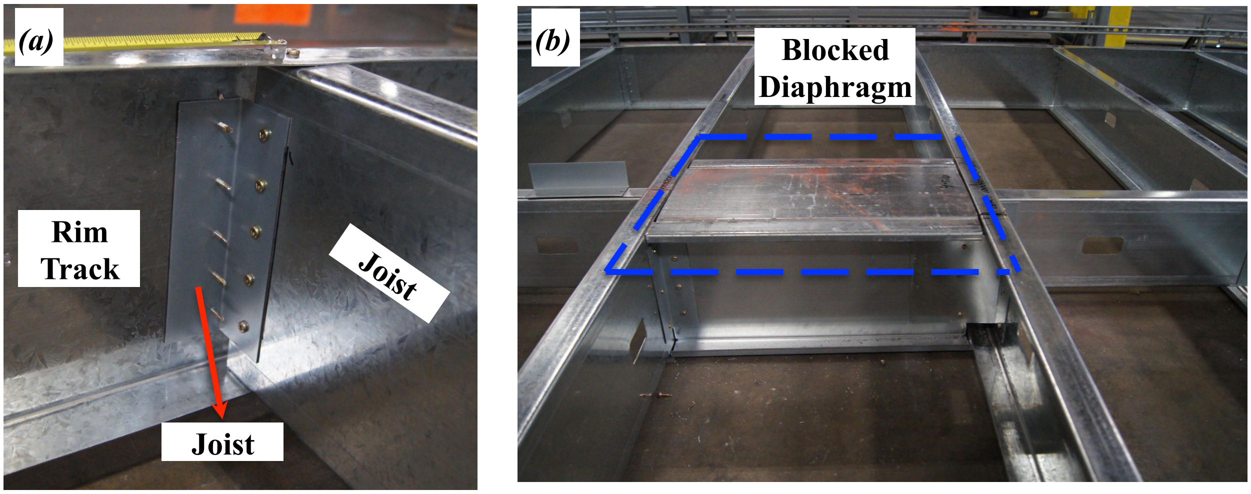

Figure 2.17. Floor diaphragm framing details: (a) joist to rim track connection, and (b) mid-span blocking of the room diaphragm.

The floor sheathing consisted of fiber reinforced cement boards bonded with a layer of 0.838 mm (0.033”) thick (20 ga.) sheet steel. The thickness of cement boards was 14 mm (9/16”) at floor 2 through 6 and 11 mm (7/16”) at the roof. The floor sheathing was attached to the upperside of the joists and rim tracks using #8 drywall screws at 152 mm (6”) o.c both in field and on boundary. In addition, the underside of floor 3 and roof was sheathed with 16 mm (5/8”) thick regular gypsum panels to provide compartmentalized fire test environments. The gypsum panels were attached to the underside of the joists and rim tracks using #8 drywall screws at 152 mm (16”) o.c both in field and on boundary.

2.5 Nonstructural Systems

The nonstructural systems incorporated in test building are categorized into the following three types: 1) interior partition walls, 2) doors, and 3) household appliances. These nonstructural systems are described in the following subsections.

2.5.1 Partition Walls

The test building consisted of two partition walls in the transverse direction of the building from level 2 to level 6, which were located ~0.6 m (2 ft) west of the transverse centerline (see Figure 2.2b). It is however noted that no partition walls were installed at the first level due to insufficient attachment conditions on the shake table platen. These non-load bearing walls separated the building interior into four separated rooms. Each partition wall involved a door opening for accessing the room on the west side of the building.

The partition wall spanned from the lower floor to the underside of the upper floor diaphragm joists at a height of ~2.8 m (9'-2"). As shown in Figure 2.18a, the steel framing of all partition walls utilized 362VS125-33 at 610 mm (24") o.c for both intermediate studs and chord studs. The partition wall framing were constructed using regular tracks 362T150-33 at the bottom tracks and slotted tracks 362CST250-33 with a slot length of 38 mm (1.5") at the top. The sheathing material utilized 16 mm (5/8") thick regular gypsum panels attached to the framing on both sides using #8 drywall screws at a spacing of 152 mm (6") o.c. on boundary and 406 mm (16") o.c in field (Figure 2.18b).

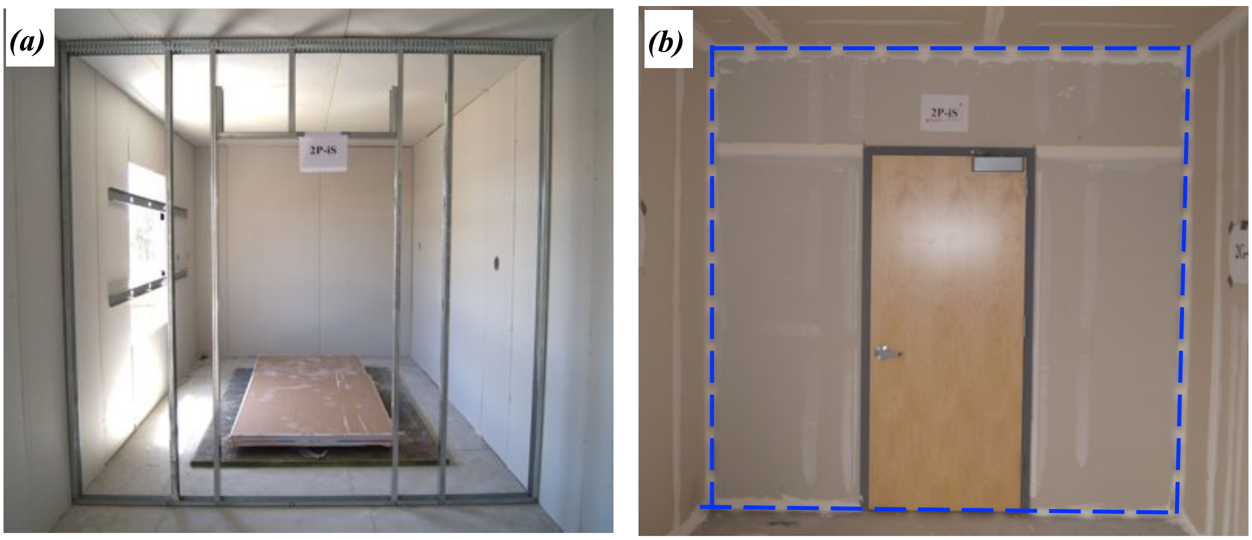

Figure 2.18. Interior partition wall: (a) CFS framing, and (b) finished wall.

2.5.2 Doors

As shown in Figure 2.19, the building included four doors at level 2 through level 6, namely, two at the corridor and on two on transverse partition walls. Level 1 consisted of only two doors (at the corridor) due to the absence of interior partition walls. All the corridor doors and the ones on the south partition walls were single-swing doors (Figure 2.20a-b) with typical opening dimension of about 1.0 m (3'-6") in width and 2.2 m – 2.5 m (7'-3" – 8'-3") in height. In contrast, the doors on the north partition walls employed the form of double-swing door (Figure 2.20c), single-swing door with a side lite frame (Figure 2.20d), and sliding door with a side lite frame (Figure 2.20e). Consequently, they required an opening width twice as much as that of a single-swing door. In addition, it is noted that the doors at level 2 and 6 were fire-rated doors since these two levels were selected as fire test floors. According to the NFPA 80 standards

(NFPA, 2013), the doors at level 2 had a 60-minute fire rating and those at level 6 had a 20-minute fire rating. Detailed descriptions of the door types, opening dimensions, and fire resistance ratings are summarized in Table 2.5.

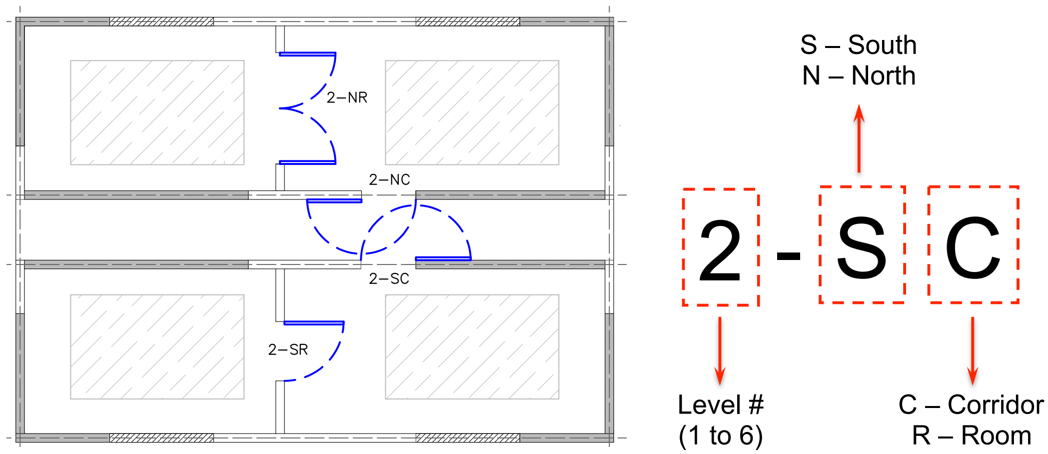

Figure 2.19. Plan layout of the doors (level 2, typical of levels 3-6) and the nomenclature.

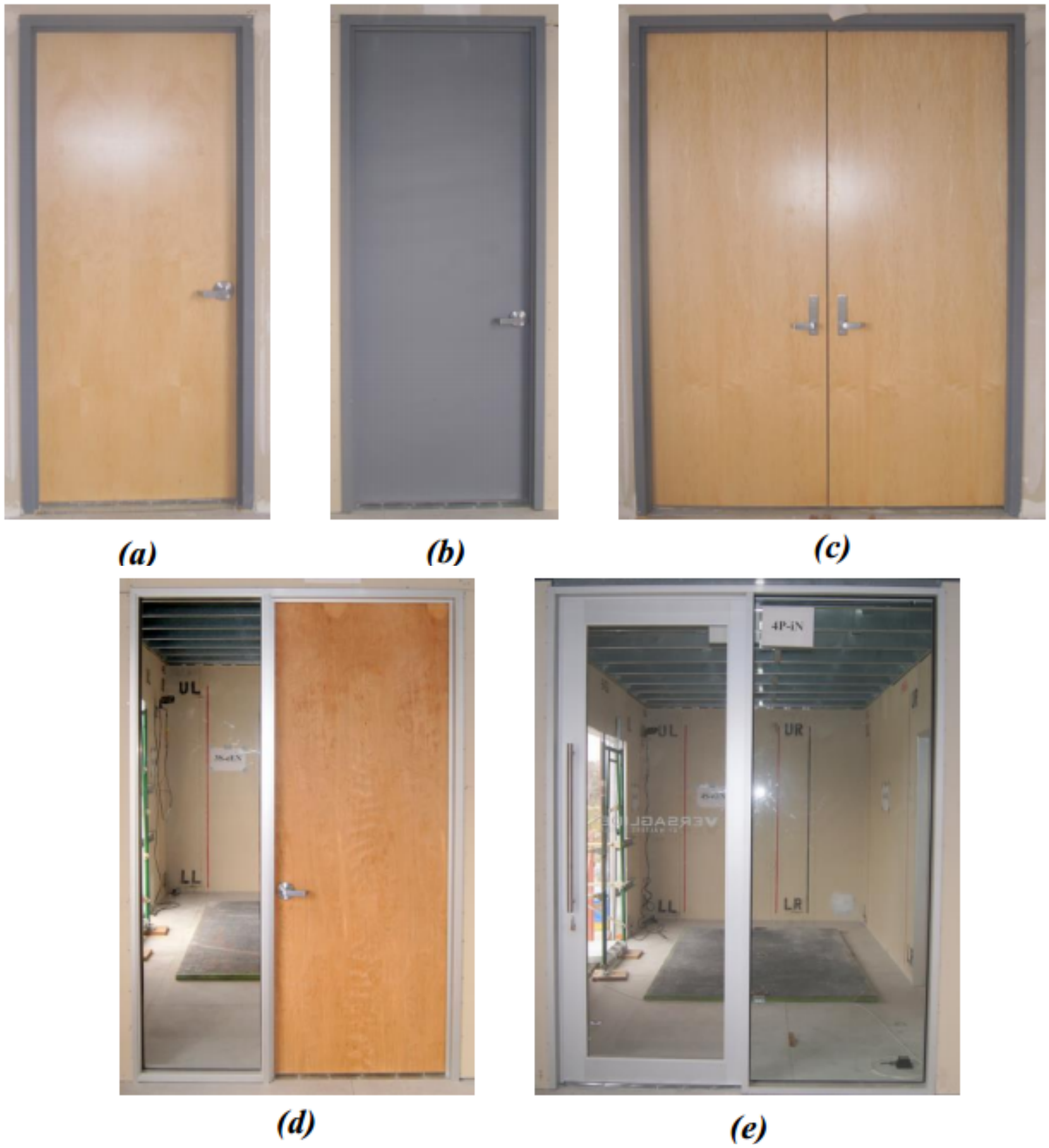

Figure 2.20. Typical door types: (a) single-swing wood door (1.0 m × 2.2 m), (b) single-swing metal door with a 20-minute fire rating (1.0 m × 2.5 m), (c) double-swing wood door (2.0 m × 2.5 m) (d) single-swing wood door with a side lite frame (1.6 m × 2.5 m) (e) sliding door with a side lite frame (2.0 m × 2.7 m).

Table 2.5. Detailed descriptions of the doors.

Level	*Short name* [1]	*Description*	*Opening width and height* (m x m)	*Fire rating* (min)
1	1-NC	Single-swing wood door with an aluminum frame	1.0 × 2.5	N/A
	1-SC	Single-swing hollow metal door with a hollow metal frame	1.0 × 2.5	N/A
2	2-NR	Double-swing hollow metal door with a hollow metal frame	2.0 × 2.2	60
	2-NC	Single-swing wood door with an aluminum a frame	1.0 × 2.2	60
	2-SC	Single-swing wood door with a hollow metal frame	1.0 × 2.2	60
	2-SR	Single-swing wood door with a hollow metal frame	1.0 × 2.2	60
3	3-NR	Single-swing wood door with an aluminum side lite frame	1.6 × 2.1	N/A
	3-NC	Single-swing wood door (vision lite) with an aluminum frame	1.0 × 2.2	N/A
	3-SC	Single-swing hollow metal door (vision lite) with a hollow metal frame	1.0 × 2.2	N/A
	3-SR	Single-swing hollow metal door with a hollow metal frame	1.0 × 2.5	N/A
4	4-NR	Single-sliding hollow metal door (vision lite) with an aluminum side lite frame	2.0 × 2.7	N/A
	4-NC	Single-swing wood door with an aluminum frame	1.0 × 2.2	N/A
	4-SC	Single-swing wood door with a hollow metal frame	1.0 × 2.2	N/A
	4-SR	Single-swing wood door with a hollow metal frame	1.0 × 2.2	N/A
5	5-NR	Double-swing wood door with an aluminum frame	1.9 × 2.2	N/A
	5-NC	Single-swing wood door with a hollow metal frame.	1.0 × 2.2	N/A
	5-SC	Single-swing hollow metal door with a hollow metal frame	1.0 × 2.2	N/A
	5-SR	Single-swing hollow metal door with a hollow metal frame.	1.0 × 2.2	N/A
6	6-NR	Double-swing wood door with a hollow metal frame	2.0 × 2.5	20
	6-NC	Single-swing wood door (vision lite) with an aluminum frame	1.0 × 2.2	20
	6-SC	Single-swing hollow metal door (vision lite) with a hollow metal frame.	1.0 × 2.2	20
	6-SR	Single-swing hollow metal door with a hollow metal frame.	1.0 × 2.5	20

[1] 1-6 = level number; NC = north corridor; NR = north room; SC = south corridor; SR = south room.

2.5.3 Appliances

The test building featured a realistic household environment at level 1 and level 6, which housed common household appliances and fire safety devices. The purpose of incorporating these items in the test program was to assess the gas-related fire ignition potential of typical residential settings in an event of earthquake. The appliances installed in the building included gas and electric ranges, water heaters, wall-mounted television sets, and safety devices such as seismic gas shutoff valves. A complete list of the appliance and safety devices and the associated specifications are summarized in Table 2.6.

Table 2.6. Appliances and their associated specifications.

Appliance legend	*Description*	*Dimensions* (m)	*Weight* (kg)
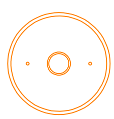	Gas water heater (Make: Envirotemp)	0.50 (Dia.) × 1.55 (H)	61.2 (empty) 213.3 (full)
	Electric water heater (Make: Whirlpool)	0.53 (Dia.) × 1.26 (H)	40.8 (empty) 193.0 (full)
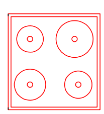	Gas range (Make: Kenmore)	0.52 (D) × 0.76 (W) × 1.21 (H)	76.2
	Electric range (Make: Kenmore)	0.72 (D) × 0.76 (W) × 1.21 (H)	63.5
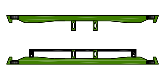	HDTV (Make: RCA)	0.09 (D) × 1.40 (W) × 0.80 (H)	21.5
	HDTV (Make: Samsung)	0.09 (D) × 1.37 (W) × 0.80 (H)	23.0
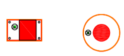	SGSV (Model 300)	0.10 (D) × 0.12 (W) × 0.10 (H)	0.9
	SGSV (Model AGV-75)	0.07 (D) × 0.04 (W) × 0.0 (H)	0.5

Notes: Dia. – diameter; D – depth; W – width; H – height.

Figure 2.21 illustrates the appliances and safety device plan layout at level 1 and level 6. The building was outfitted with two electric range units in the southwest compartment and two gas range units in the southeast compartment at each level. These units were placed on a ~ 2.4 m × 2.4 m (8 ft × 8 ft) elevated wood-framed platform with resilient tile flooring (see Figure 2.22a). The two ranges in the same compartment were placed in a side-by-side configuration, one as an unrestrained unit and the other restrained at its base (Figure 2.22a). Furthermore, a total of six water heaters (three gas water heaters and three electric water heaters) were installed in north compartments at level 1 and level 6, respectively (Figure 2.22b). The four braced water heaters each utilized a different bracing strategy to attach them to the adjacent wall framing (e.g., plumbers tape, off-the-shelf strap, and combined conduit and plumbers tape). With the exception of the one in the northwest compartment of level 6, all the remaining three water heaters were filled with water or sand to their respective operating weight capacity. In addition, two high-definition television sets were mounted on the corridor walls at level 1 (Figure 2.22c).

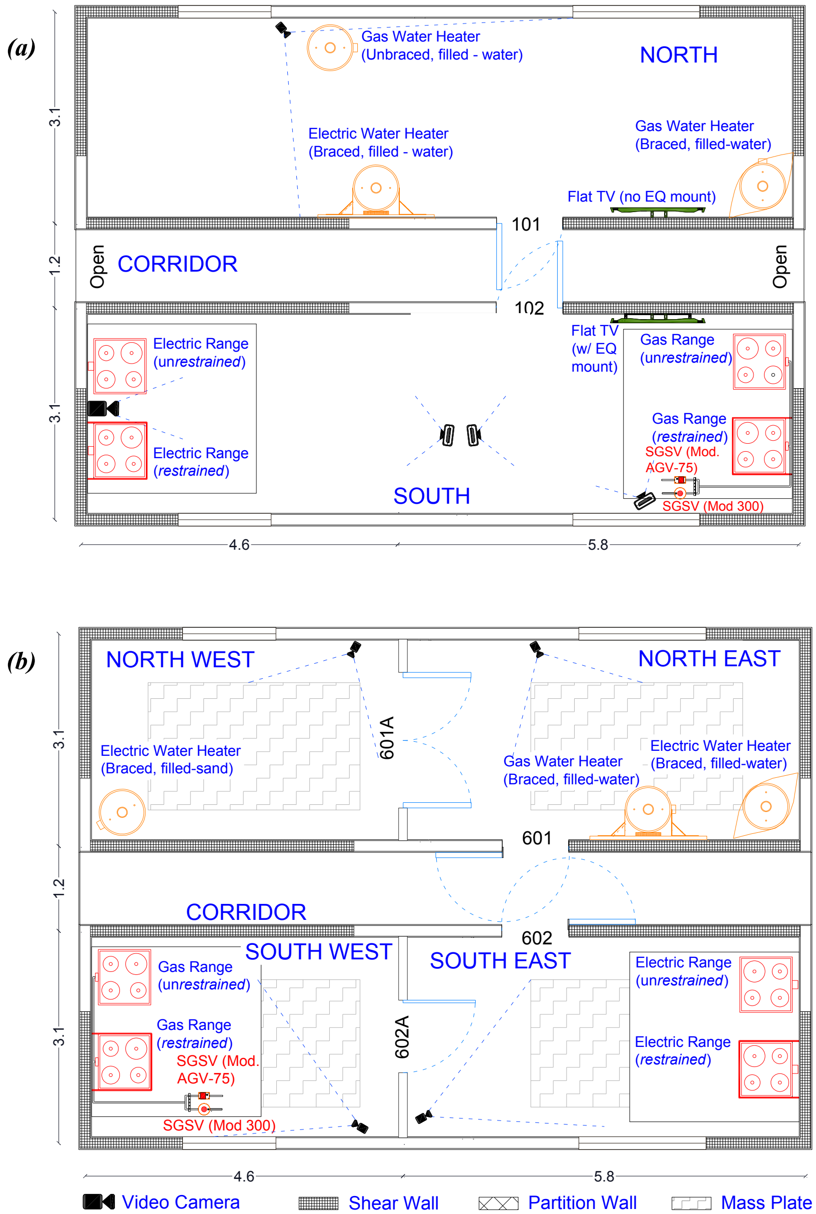

Figure 2.21. Appliance plan layout: (a) level 1, and (b) level 6 (note the hatched pattern on level 6 dilineates the outline of the mass plates, and elevated wood-framed platform was placed over the mass plates).

Two gas piping assemblies were installed in the southeast compartment at level 1 and southwest compartment at level 6 (Figure 2.22d). Each assembly consisted of two different seismic gas shutoff valves connecting to flexible piping to a floor-mounted gas supply pipe, reflecting the typical installation conditions of residential construction. These safety devices were designed as emergency gas shutoff devices in the event of earthquakes, and therefore they were air-pressurized during all the seismic tests to simulate their functionality. It is also noted that a network of six video cameras was installed within these appliance compartments to monitor their seismic response during the earthquake tests.

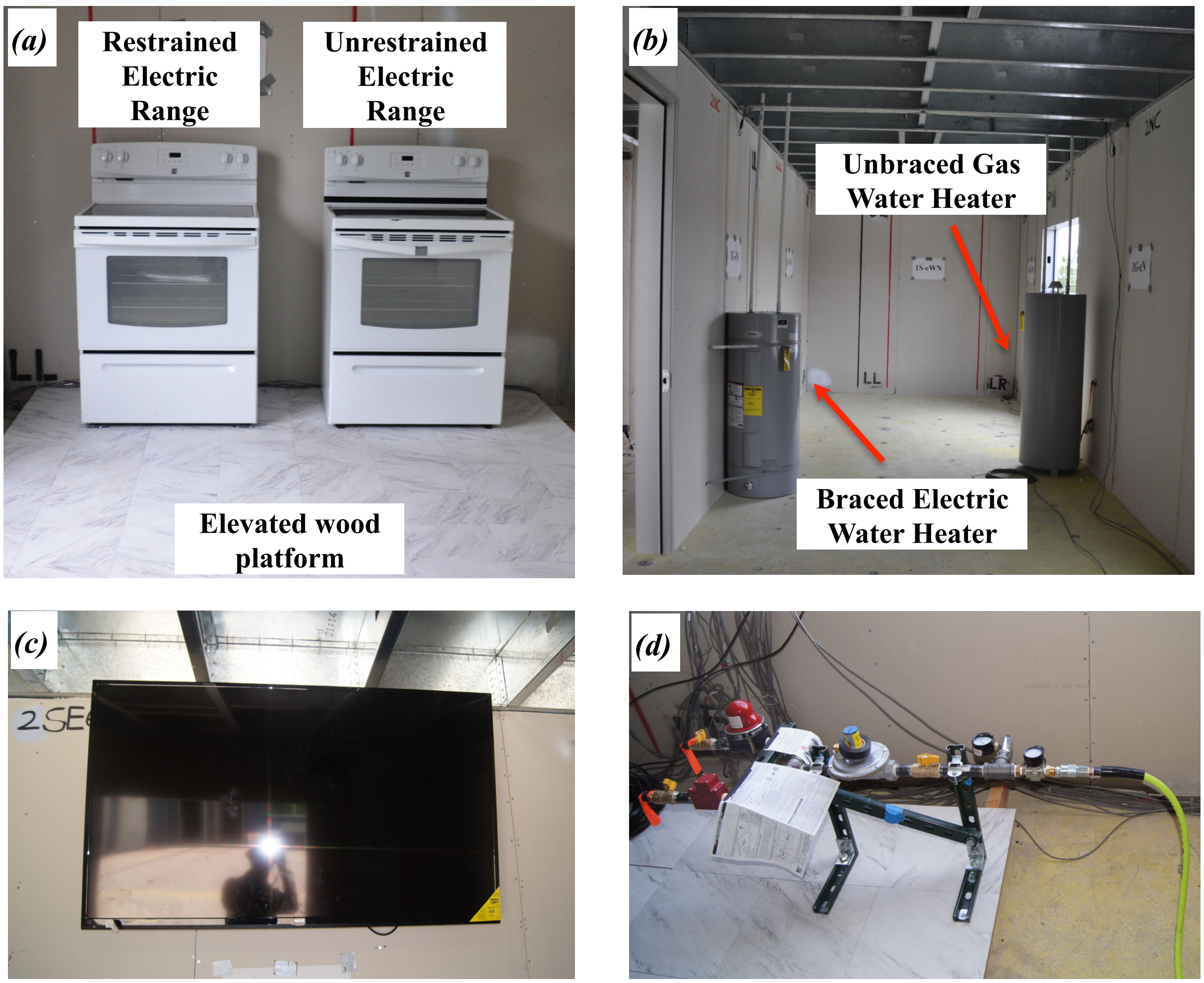

Figure 2.22. Photographs of appliances at level 1: (a) electric range units, (b) water heaters, (c) wall-mounted television set, and (d) gas piping assembly with seismic gas shutoff valves.

2.6 Estimated Building Weight

The total weight of the building including its nonstructural components was estimated using the reaction force measurements of the six vertical actuators and two hold-down struts underneath the shake table platen. These measurements were available when the table was empty and at multiple stages during the construction and test phase. Consequently, the total building weight is calculated as the difference of the total vertical force measured by the shake table at the completion of the building construction compared to that measured while the shake table was empty.

The weight of the empty table was estimated as 1715 kN (385 kips) at the time of motion tuning. The weight of the building, on the other hand, was estimated using the same set of measurements recorded during individual earthquake tests. The variations of the estimated building weight during different earthquake tests were low (ranged between 1145 kN and 1175 kN). In this regard, the actual weight of the test building including its nonstructural components was determined using the averaged value of 1160 kN (260 kips). While the actual weight of the test building was ~260 kN (60 kips) lower than that used for the design, this was anticipated as the difference accounted for the reduction of live loads (reduction factor of ~0.6) in the event of an earthquake.

The total building weight estimated using the shake table measurements was subsequently compared with hand calculation results (summation of the weight of all the structural and nonstructural components). Table 2.7 summarizes the hand calculation results of the total building weight and the weight tributary to each floor. The total (vertical) weight of the building, was determined as 1153 kN (259 kips) by hand calculation and agreed well with that determined using the table measurements (difference < 1%). As a result, the floor distribution of the vertical weight is used with no further adjustment. It is also noted that the inertial (seismic) weight reported in the table accounts for the fact that the appliances were not rigidly fixed to the building. Therefore, the total inertial weight of the building excluded the weight of the appliances.

Table 2.7. Estimated building weight and floor distributions (unit in kN).

Floor #	Wall	Floor diaphragm	Mass plate	Tie rods	Appliances	Weight (vertical)	Weight (inertial)
R	58.4	47.2	65.8	0.0	0.0	171.5	171.5
6	78.3	29.0	65.8	1.3	8.9	183.4	174.5
5	78.3	29.0	65.8	2.0	0.0	175.1	175.1
4	78.3	29.0	65.8	2.7	0.0	175.9	175.9
3	79.5	47.2	65.8	4.2	0.0	196.7	196.7
2	78.3	29.0	65.8	6.9	0.0	180.0	180.0
1	39.1	0.0	0.0	22.0	9.3	70.4	61.1
Total	490.3	210.5	395.0	38.9	18.2	**1153.0**	**1134.7**

2.7 Construction

With the exception of the stick-framed structural walls at the first level, the structural system (i.e., wall and floor systems) at all remaining levels (level 2 through 6) was constructed using prefabricated panels. These panels were categorized as either wall panels or floor panels. The diaphragm at each floor consisted of six prefabricated segments, namely, two corridor segments and one segment for each for the four rooms (Figure 2.23,). The segments at the east end were about 1.2 m (4 ft) longer than those at the west end, resulting in an offset of 0.6 m (2 ft) for the transverse panel joints west of the transverse building centerline. It is also noted that the partition wall were installed along the transverse panel joists. The wall system (shear walls and gravity walls) at each level consisted of a total of twelve prefabricated segments: eight longitudinal and four transverse wall segments (Figure 2.24). The vertical joints of all the longitudinal panels were located within the gravity wall span (both corridor and exterior walls).

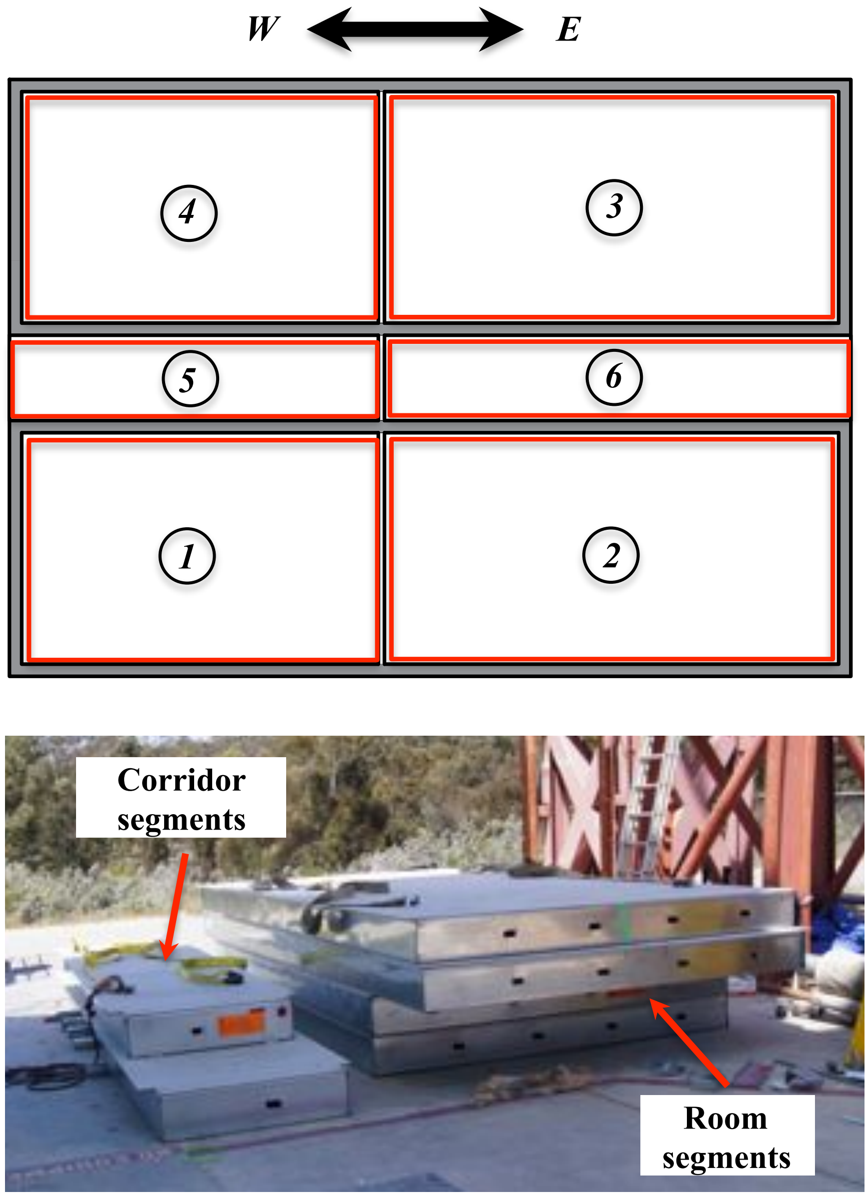

Figure 2.23. Diaphragm panel pattern (top) and photographs of the prefabricated diaphragm segments prior to installation (bottom) (room segments #1 – #4 and corridor segments #5 and #6).

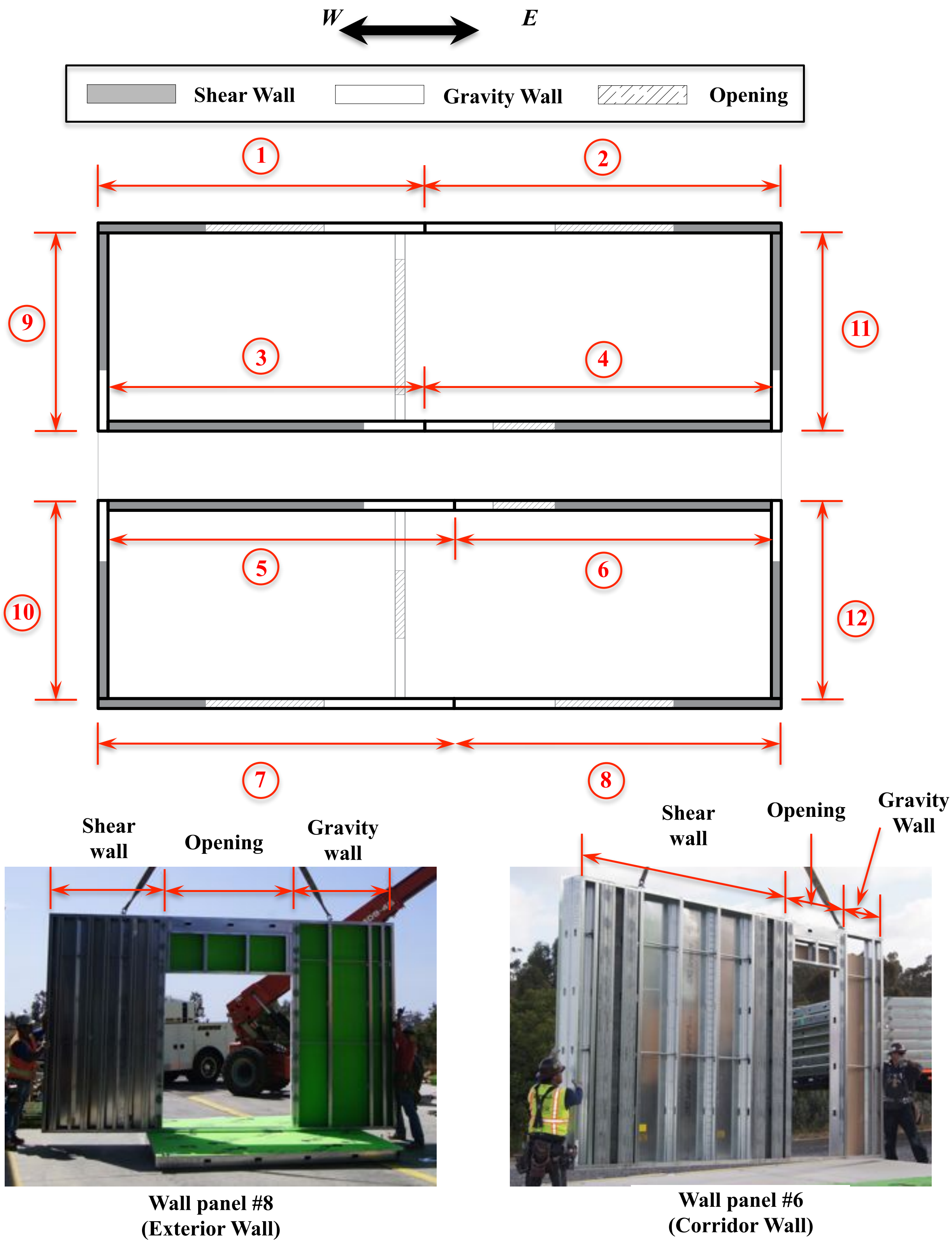

Figure 2.24. Prefabricated wall panel pattern (top) and sample prefabricated wall segments in elevation view (bottom).

Construction of the test building commenced on April 15, 2016 with the shake table platen tie-down installation. A total of 80 large-diameter steel rods were used to attach the first-level bottom tracks to the shake table at a space at 0.6 m (2 ft) along the bottom tracks (Figure 2.25a). Subsequently, the first-level wall system was stick-framed across a period of four days (Figure 2.25b). Following completion of the stick-framed wall system at the first level, building construction significantly expedited as a result of highly efficient panelized construction (Figure 2.25c). Construction of the upper levels progressed at a rate of one level per day. Erection of the building skeleton was completed on April 27, 2016 (within a total of nine days) (Figure 2.25d).

It is noted that the mass plate was installed on the building in conjunction with the building skeleton erection phase. Figure 2.25e shows the layout of the mass plates (one at each quadrant) at the roof of the building, which represented the typical mass configuration of all other floors during the earthquake tests. These mass plates were attached to the floor diaphragms building erection. The attachment details of the mass plates are shown in in Figure 2.26. In addition, a temporary platform stair tower was installed on the northeast side of the building to support access to the test building during the interior construction phase as well as the test phase. It is noted that the stair tower was detached from the building during all the earthquake and low-amplitude white noise tests and re-attached to the building at the completion of test sequence on each test date.

Interior construction commenced immediately following the completion of the building erection. Activities related to interior construction included: 1) installation of interior gypsum panels (structural walls, nonstructural walls, and ceiling) (Figure 2.27a), 2) installation of interior partition walls (Figure 2.27b), 3) door installation, and 4) appliance installation (on the first and sixth floors) (Figure 2.27c and d). These activities spanned about an entire month and the interior installation was completed at the beginning of June 2016. The building demolition began on July 11, 2016 (a week following the completion of the test program) and finished on July 20, 2016. Interested readers are referred to the video links [1,2] of the building construction and demolition time lapses.

[1] Construction time lapse available at https://www.youtube.com/watch?v=IFq7Nv_020c.
[2] Demolition time lapse available at https://www.youtube.com/watch?v=ElOiksCJUKM.

Figure 2.25. Construction of the test building: (a) building tie-down system (April 16, 2016), (b) in-situ installation of first-story wall system (April 19, 2016), (c) installation of a prefabricated wall panel at the third story (April 23, 2016), (d) completion of building skeleton erection (hoisting the last piece of roof panel) (April 27, 2016), and (e) roof mass plate layout prior to the earthquake tests (June 10, 2016).

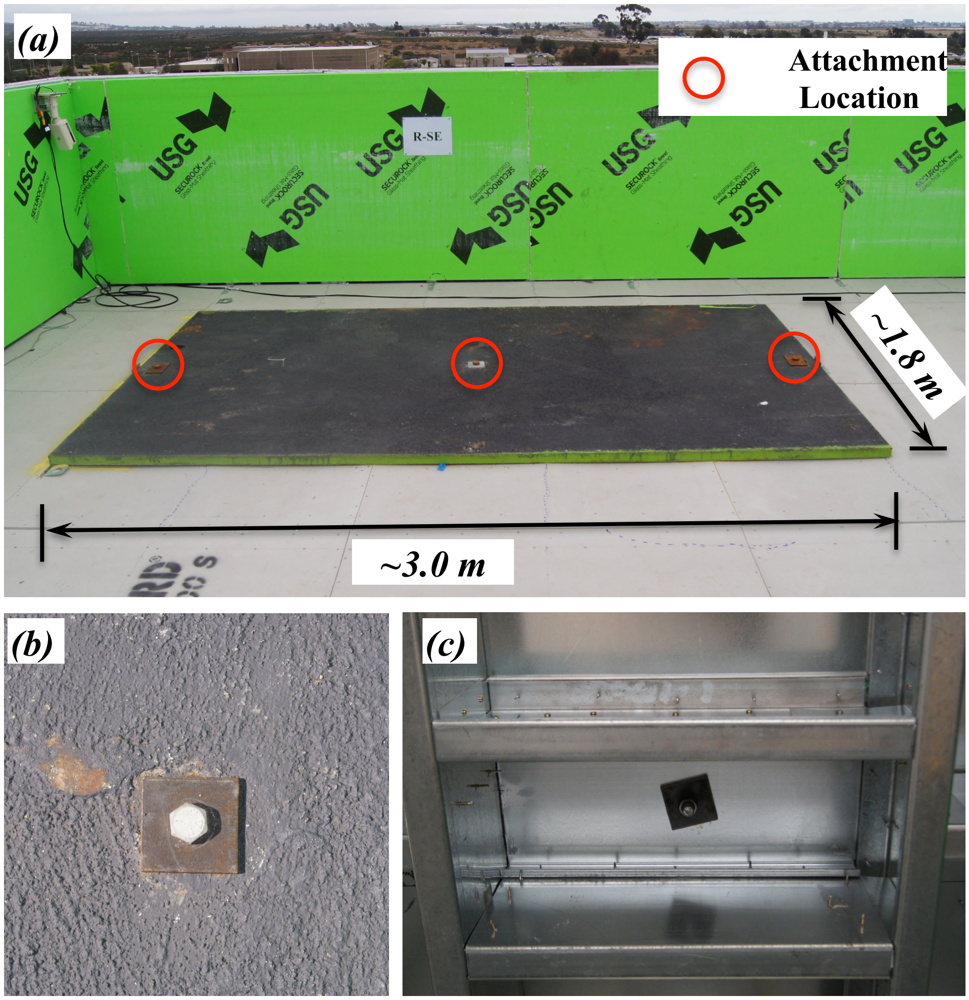

Figure 2.26. Steel mass plate and the connection details: (a) roof mass plate, (b) top connection, and (c) bottom connection.

Figure 2.27. Interior construction and installation: (a) gypsum panel installation (May 19, 2016), (b) partition wall framing installation (May 28, 2016), (c) elevated wood platform installation (June 2, 2016), and (d) appliances hoisting (June 2, 2016).

3 TEST PROTOCOL

The three-week test program consisted of a sequence of nine earthquake tests and six fire tests between June 13 and July 1, 2016. During the first week (pre-fire test phase), the building was subjected to seven earthquakes with increasing input motion intensity in three test days (June 13, 15, and 17, 2016). Subsequently, live fire tests were conducted on the earthquake-damaged building at the second and sixth levels in three consecutive days (June 27–29, 2016). The test program concluded with two post-fire earthquake tests on the final test day at the end of the third week (July 1, 2016). To complement the earthquake and fire test sequence, low-amplitude vibration test data collected using different excitation sources, namely, white noise base excitation, (tire) impact, and ambient vibration, were conducted throughout the construction and test phases. It is noted that all the earthquake and white noise excitations were applied at the base of the test building in the east-west direction using the single-axis shake table, whose axis coincided with the longitudinal axis of the building.

3.1 Dynamic Test Protocol during Construction Phase

Following the completion of the structural skeleton erection, low-amplitude white noise tests were conducted on three days during the building construction phase. These tests allowed for investigation on the dynamic characteristics of the building at the various stages during the construction. As summarized in Table 3.1, the test building contained a total of five states (denoted as C1–C5), which are characterized by varied roof mass plate layouts and interior construction aspects (e.g., attachment condition of the interior gypsum wall panels, partition wall installation state, and opened or closed doors). The roof mass plates were temporarily configured in non-symmetric layouts at states C1 and C2 to explore their effect on the dynamic characteristics of the building, while the layout at states C3–C5 represented the baseline configuration with a symmetric mass distribution (one mass plate at each quadrant). It is noted that the last two states during the construction phase (C4 and C5) represented the building at the completion of all construction activities. Vibration tests conducted during the construction phase included pulse (with a target peak acceleration of 0.08 g) and banded (0.25-25 Hz) white noise base excitations applied on the building using the LHPOST. As shown in Table 3.1, white noise tests consisted of input excitations of two distinct amplitude levels with root-mean-square (RMS) accelerations of 1.5% g and 3.0% for each configuration (note that a white noise test with an amplitude of 5.0% g RMS was conducted only at state C1). Shock tests were conducted on the second test day of the construction phase by impacting the building roof in different directions. In addition, ambient vibration data were collected throughout the construction and the test phase (between May 5 and July 1, 2016) to monitor the evolution of building dynamic characteristics.

Table 3.1. White noise tests performed during the construction phase and the associated building characteristics (note that 2× = double mass plate, 1× = single mass plate).

Date	*State*	*Interior construction status*	*Roof mass layout*
May 5, 2016	C1	minimally attached interior gypsum; partition wall installation partially completed; doors not installed	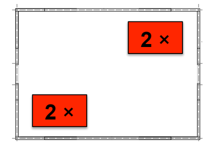
May 16, 2016	C2	minimally attached interior gypsum; partition wall installation partially completed; doors partially installed	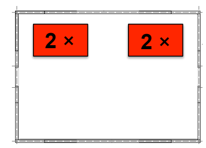
	C3		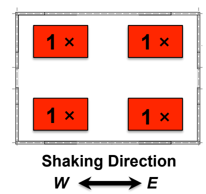
June 9, 2016	C4	fully attached interior gypsum; partition wall installation completed; all doors open	
	C5	fully attached interior gypsum; partition wall installation completed; all doors closed	

Table 3.2. White noise test sequence and the building configuration

Date	*Test* [1]	*Short name*	*Configuration*
May 5, 2016	1.5% g RMS WN (4 min)	WN:C1-A	**C1**
	3.0% g RMS WN (4 min)	WN:C1-B	
	5.0% g RMS WN (4 min)	WN:C1-C	
May 16, 2016	1.5% g RMS WN (3 min)	WN:C2-A	**C2**
	3.0% g RMS WN (3 min)	WN:C2-B	
	1.5% g RMS WN (3 min)	WN:C3-A	**C3**
	3.0% g RMS WN (3 min)	WN:C3-B	
June 9, 2016	1.5% g RMS WN (3 min)	WN:C4-A	**C4**
	3.0% g RMS WN (3 min)	WN:C4-B	
	1.5% g RMS WN (3 min)	WN:C5-A	**C5**
	3.0% g RMS WN (3 min)	WN:C5-B	

RMS = root mean square; WN = white noise test.

Figure 3.1 shows the acceleration time histories of two white noise tests (conducted in May 5, 2016) at the target root-mean-square (RMS) amplitude of 1.5% g and 3% g, respectively. It is noted that the amplitudes of the achieved input motions at both tests were smaller than their corresponding target values, with an amplitude reduction of about 25%~30%. This observation was representative of all the white noise tests conducted during the construction and test phases.

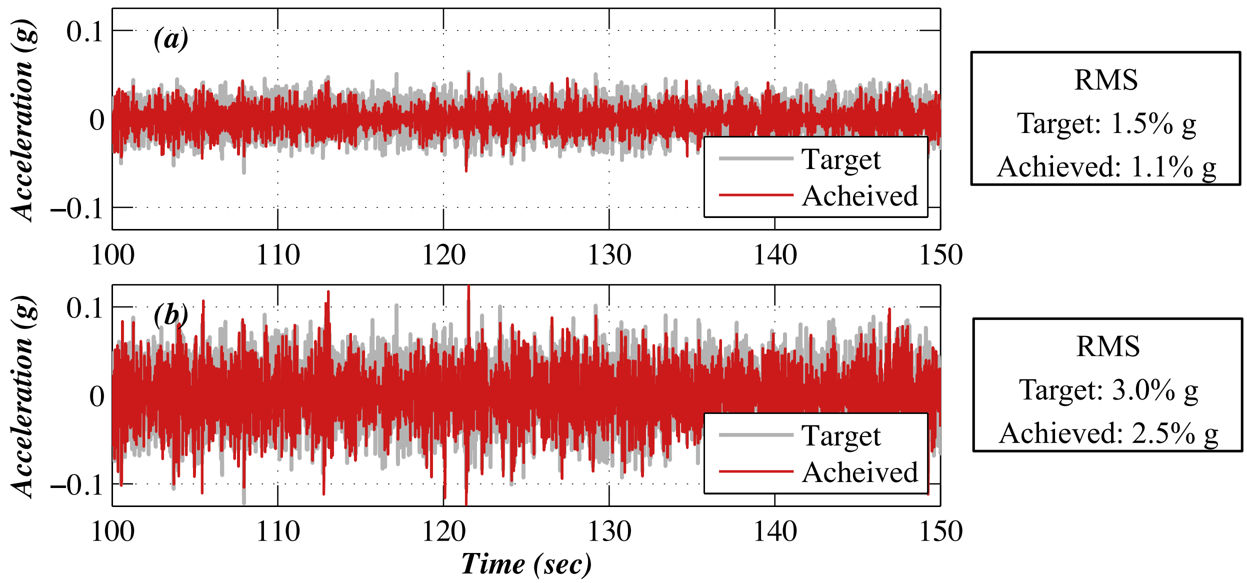

Figure 3.1. Input acceleration time histories of white noise tests: (a) WN:C1-A, and (b) WN:C1-B (May 5, 2016).

3.2 Dynamic Test Protocol during Test Phase

3.2.1 Earthquake Input Motions

As shown in Table 3.3, the test building was subjected to a sequence of seven earthquake motions prior to and two motions following the fire test phase. The input earthquake motion records adopted in the test program were selected from four historical earthquake events, namely: Rio Dell Overpass from the 1992 Cape Mendocino earthquake, Canoga Park and Rinaldi Receiving Station both from the 1994 Northridge earthquake, and Curico from the 2010 Maule earthquake in Chile. With the exception of the Curico motion that was recorded from a long-duration subduction event in Chile, the remaining three motions were recorded from strong earthquakes that occurred in California in the past few decades. Each input motion was amplitude-scaled to its targeted intensity level, which was defined as the spectral acceleration averaged between half and one and a half times the building fundamental period associated with the longitudinal vibration (the direction of shaking). Spectral matching was not involved in motion scaling in an effort to preserve the frequency contents of the original recorded motions.

As shown in Table 3.4, low-amplitude vibration base excitation tests were conducted before and after each earthquake test for the purpose of identifying the building dynamic characteristics evolution during the test phase. The white noise test sequence consistently contained two amplitude levels (1.5% g and 3% g RMS) before and after each earthquake test (except that only 1.5% g RMS white noise tests were conducted following EQ1 and EQ2). It is noted, however, that no white noise test was conducted following the last earthquake test (EQ9) provided the severity and extant of structural damage of the building at the end of the test program. Table 3.4 also defines the building state related to and the physical inspection conducted at the different stages throughout the test phase. Since multiple earthquake tests were conducted at three out of four test days, detailed physical damage inspections were conducted only following the completion of all tests of the test day, while rapid inspections were conducted between the earthquake tests primarily for the purpose of examining the condition of critical structural components (e.g., mass plate anchorage, tie-down rod connections).

Table 3.3. Earthquake test protocol

Date	*Station – Earthquake (Performance target)*	*Short Name*
June 13, 2016 (Test day 1)	Rio Dell Overpass – 1992 Cape Mendocino earthquake (service level)	EQ1:RIO-25
	Canoga Park – 1994 Northridge earthquake (service level)	EQ2:CNP-25
	Curico– 2010 Maule earthquake, Chile (service level)	EQ3:CUR-25
June 15, 2016 (Test Day 2)	Canoga Park – 1994 Northridge earthquake (service level)	EQ4:CUR-25
	Canoga Park – 1994 Northridge earthquake (50% design level)	EQ5:CNP-50
	Canoga Park – 1994 Northridge earthquake (design level)	EQ6:CNP-100
June 17, 2016 (Test Day 3)	Canoga Park – 1994 Northridge earthquake (MCE level)	EQ7:CNP-150
Fire test phase (June 27-29, 2016)		
July 1, 2016 (Test Day 4 – post-fire earthquake tests)	Rio Dell Overpass – 1992 Cape Mendocino earthquake (service level)	EQ8:RIO-25
	Rinaldi Receiving Station– 1994 Northridge earthquake (MCE level)	EQ9:RRS-150

Table 3.4. White noise test sequence and the associated building states

Date	*Dynamic Test*	*Test Name*	*State*	*Inspection*
June 13, 2016	1.5% g RMS WN	WN:S0-A	S0	Pre-EQ1
	3.0% g RMS WN	WN:S0-B		
	EQ1:RIO-25 (service level motion)			
	1.5% g RMS WN	WN:S1-A	S1	
	EQ2:CNP-25 (service level motion)			
	1.5% g RMS WN	WN:S2-A	S2	Rapid
	EQ3:CUR-25 (service level motion)			
	1.5% g RMS WN	WN:S3-A1	S3	
	3.0% g RMS WN	WN:S3-B1		Post-EQ3
June 15, 2016	1.5% g RMS WN	WN:S3-A2	S3	
	3.0% g RMS WN	WN:S3-B2		
	EQ4:CNP-25 (service level motion)			
	1.5% g RMS WN	WN:S4-A	S4	—
	3.0% g RMS WN	WN:S4-B	S4	Rapid
	EQ5:CNP-50 (50% design level motion)			
	1.5% g RMS WN	WN:S5-A	S5	—
	3.0% g RMS WN	WN:S5-B	S5	
	EQ6:CNP-100 (design level motion)			
	1.5% g RMS WN	WN:S6-A1	S6	—
	3.0% g RMS WN	WN:S6-B1	S6	Post-EQ6
June 17, 2016	1.5% g RMS WN	WN:S6-A2	S6	—
	3.0% g RMS WN	WN:S6-B2	S6	
	EQ7:CNP-150 (MCE level motion)			
	1.5% g RMS WN	WN:S7-A	S7	—
	3.0% g RMS WN	WN:S7-B	S7	Post-EQ7
Fire Test Phase (June 27-29, 2016)				
July 1, 2016	1.5% g RMS WN	WN:S8-A	S8	Pre-EQ8
	3.0% g RMS WN	WN:S8-B		
	EQ8:RIO-25 (service level aftershock)			
	1.5% g RMS WN	WN_E:S9-A	S9	—
	3.0% g RMS WN	WN_E:S9-B		—
	EQ9:RRS-150 (near-fault MCE level motion)			Post-EQ9

Notes: RMS = root mean square; WN = white noise test; EQ = earthquake test.

Figure 3.2 shows the acceleration and displacement time histories of the achieved input earthquake motions. The 5% damped elastic response spectra of the achieved motions are shown in Figure 3.3. The peak acceleration, velocity, displacement, spectral acceleration at the building fundamental period, and strong motion duration of each achieved input motion are summarized in Table 3.5. It is noted that the strong motion duration of all earthquake input motions ranged between 10 and 20 seconds, with the exception of the subduction event (EQ3) that had a strong duration of over 50 seconds. It is clearly indicated that the first seven earthquake motions (pre-fire test sequence) were applied at increasing intensity to progressively damage the building. The achieved peak input accelerations of the motions increased from 0.15 g to 0.9 g, whereas the fundamental period spectral accelerations increased from 0.3 g to 2.0 g. The last two test motions (post-fire test sequence) were intended to represent a service-level aftershock event (EQ8 – replicating EQ1) and a near-fault extreme earthquake event (EQ9) with an achieved peak input acceleration above 1.0 g.

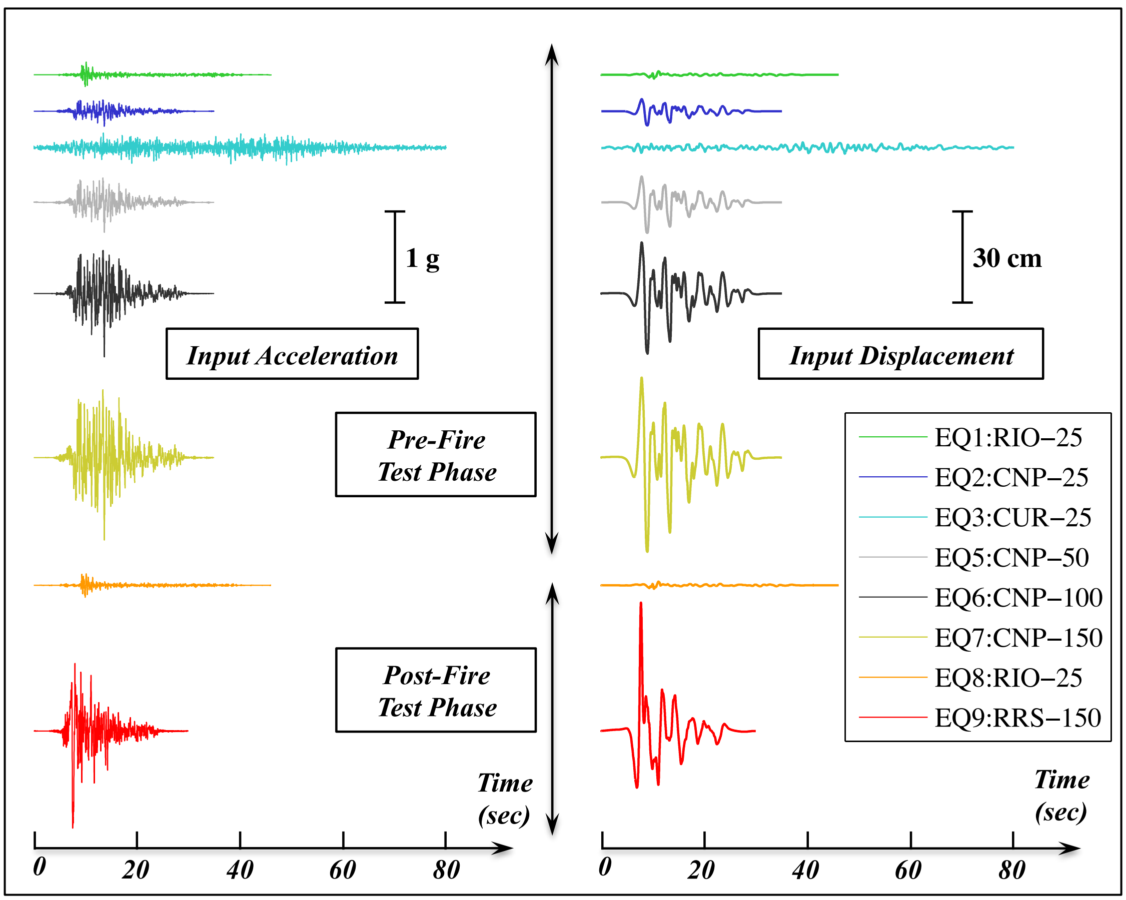

Figure 3.2. Acceleration and displacement time histories of the achieved input motions.

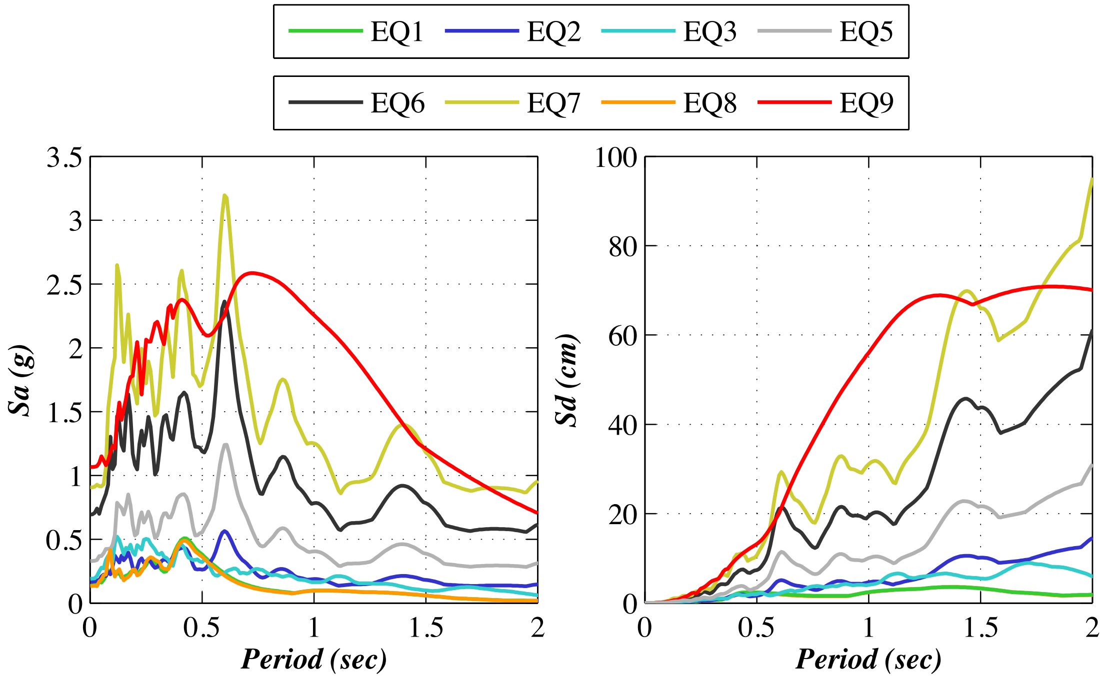

Figure 3.3. Elastic response spectra of achieved motions (ξ = 5%): (a) pseudo-acceleration spectra, and (b) displacement spectra.

Table 3.5. Summary of select characteristics of achieved earthquake input motions

Test Motion	*PIA (g)*	*PIV (cm/s)*	*PID (cm)*	*Sa(T₁,5%) (g)*	*$D_{s,5\sim95}$ (sec)*
EQ1:RIO-25	0.14	10.98	1.29	0.28	20.1
EQ2:CNP-25	0.17	22.14	4.68	0.32	11.4
EQ3:CUR-25	0.19	11.39	1.90	0.34	53.7
EQ4:CNP-25	0.17	23.41	5.00	0.35	11.9
EQ5:CNP-50	0.33	45.96	10.05	0.67	11.1
EQ6:CNP-100	0.69	90.61	19.77	1.37	10.4
EQ7:CNP-150	0.91	131.90	31.00	2.01	11.2
EQ8:RIO-25	0.13	10.30	1.20	0.09	16.7
EQ9:RRS-150	1.07	176.20	42.60	2.54	7.2

PIA – peak input acceleration; PIV – peak input velocity; PID – peak input displacement; $Sa(T_1,5\%)$ – elastic spectral acceleration of the input motion (T_1 represents the fundamental period of the building in the direction of shaking); $D_{s,5\sim95}$ – strong motion duration.

3.2.2 Earthquake Motion Tracking Performance

In an attempt to optimize the match between the achieved and target motions, all input earthquake motions were tuned at their intended intensities using an iterative time history matching technique called on-line iteration (OLI) method (Luco et al., 2008). It is noted that the motion OLI was conducted while the shake table was in an empty state (prior to the building construction). Figure 3.4 – Figure 3.6 compare the acceleration time histories and the corresponding pseud-acceleration and displacement spectra of three input motions, respectively. The three earthquake motions were scaled to different intensity levels using the same seed record (component 196 of Canoga Park records –1994 Northridge earthquake): (a) EQ2:CNP-25 (service level), (b) EQ6:CNP-100 (design level), and (c) EQ7:CNP-150 (MCE level). In overall, the time histories and the spectra of the achieved motions at all three intensity levels agree well with those of the target motions.

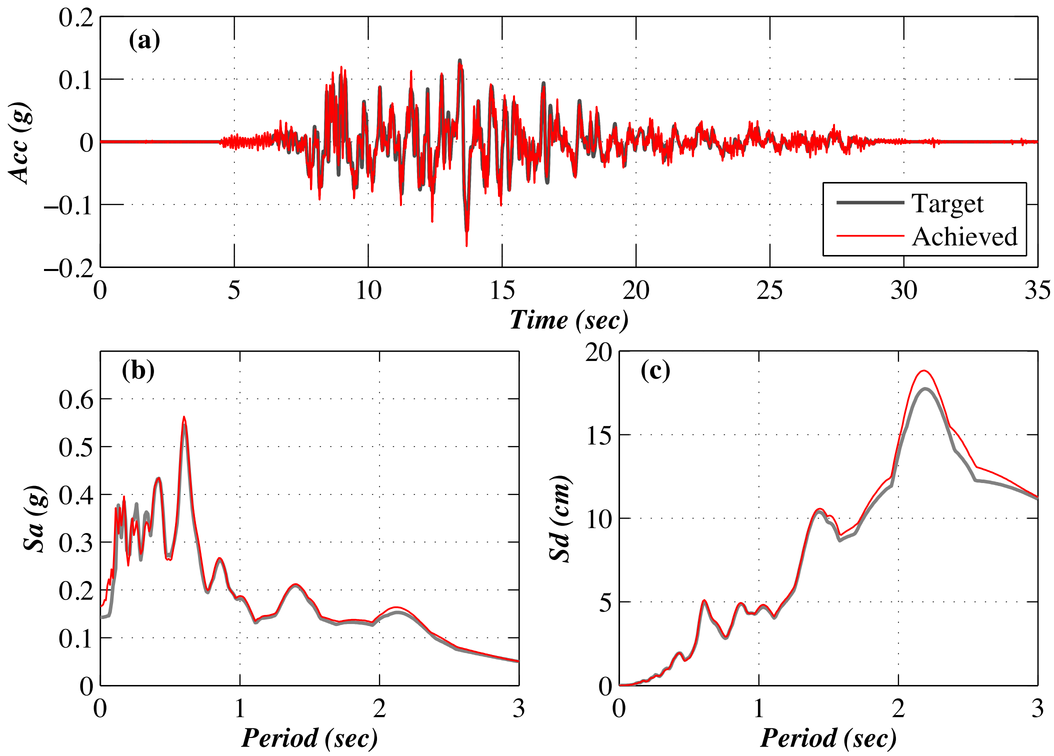

Figure 3.4. EQ2:CNP-25 – target and achieved input motion comparison: (a) acceleration time histories, (b) acceleration spectra (ξ = 5%), and (c) displacement spectra (ξ = 5%).

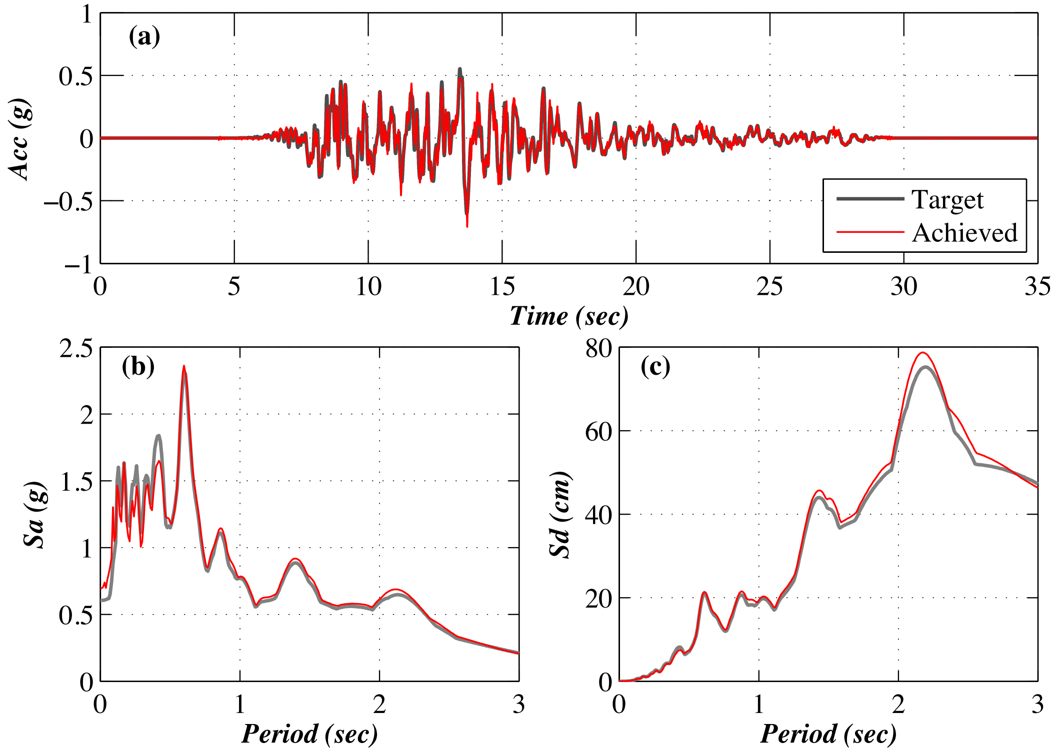

Figure 3.5. EQ6:CNP-100 – target and achieved input motion comparison: (a) acceleration time histories, (b) acceleration spectra (ξ = 5%), and (c) displacement spectra (ξ = 5%).

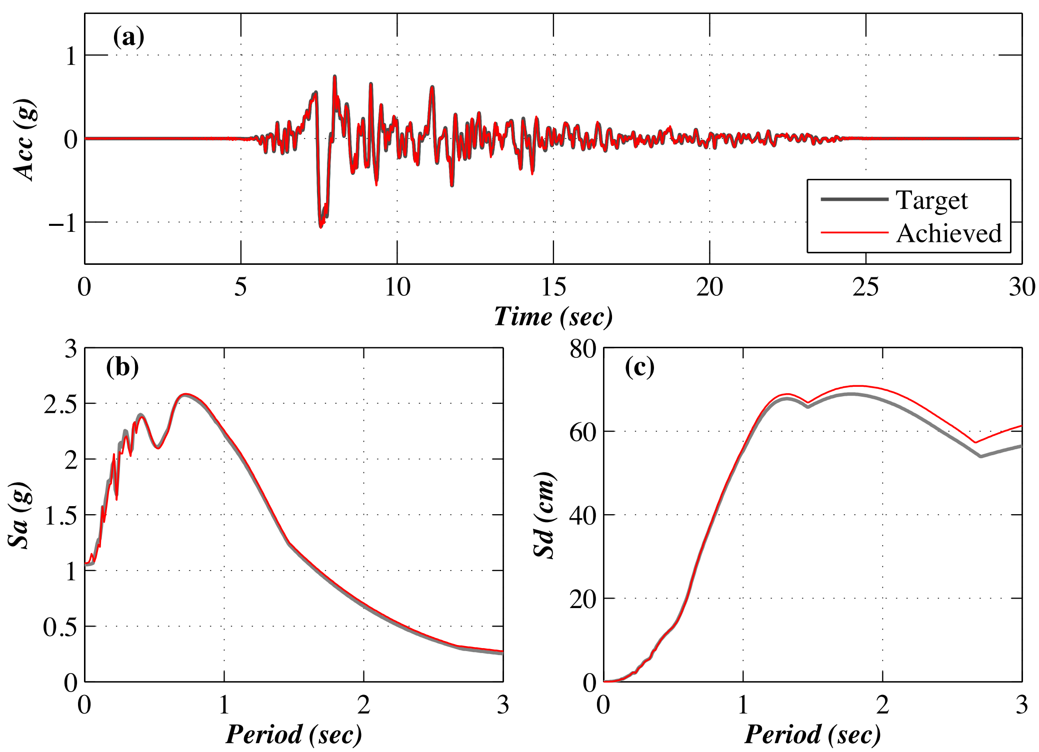

Figure 3.6. EQ7:CNP-150 – target and achieved input motion comparison: (a) acceleration time histories, (b) acceleration spectra (ξ = 5%), and (c) displacement spectra (ξ = 5%).

Key motion parameters of the target and achieved input motions are compared to evaluate the tracking performance of the shake table. Figure 3.7 compares the peak input accelerations, peak input velocities, peak input displacements (both maxima and minima), while the averaged spectral accelerations, spectral velocities, and spectral displacements (averaged between 0.2 and 0.8 second) of the target and achieved motions are compared in Figure 3.8. It is clearly shown hat these key parameters of the achieved motions agree reasonably well with those of the target motions, since the scattered points are located in the vicinity of the identity lines (gray dashed lines). This demonstrates that the shake table performed satisfactorily in reproducing the input earthquake motions.

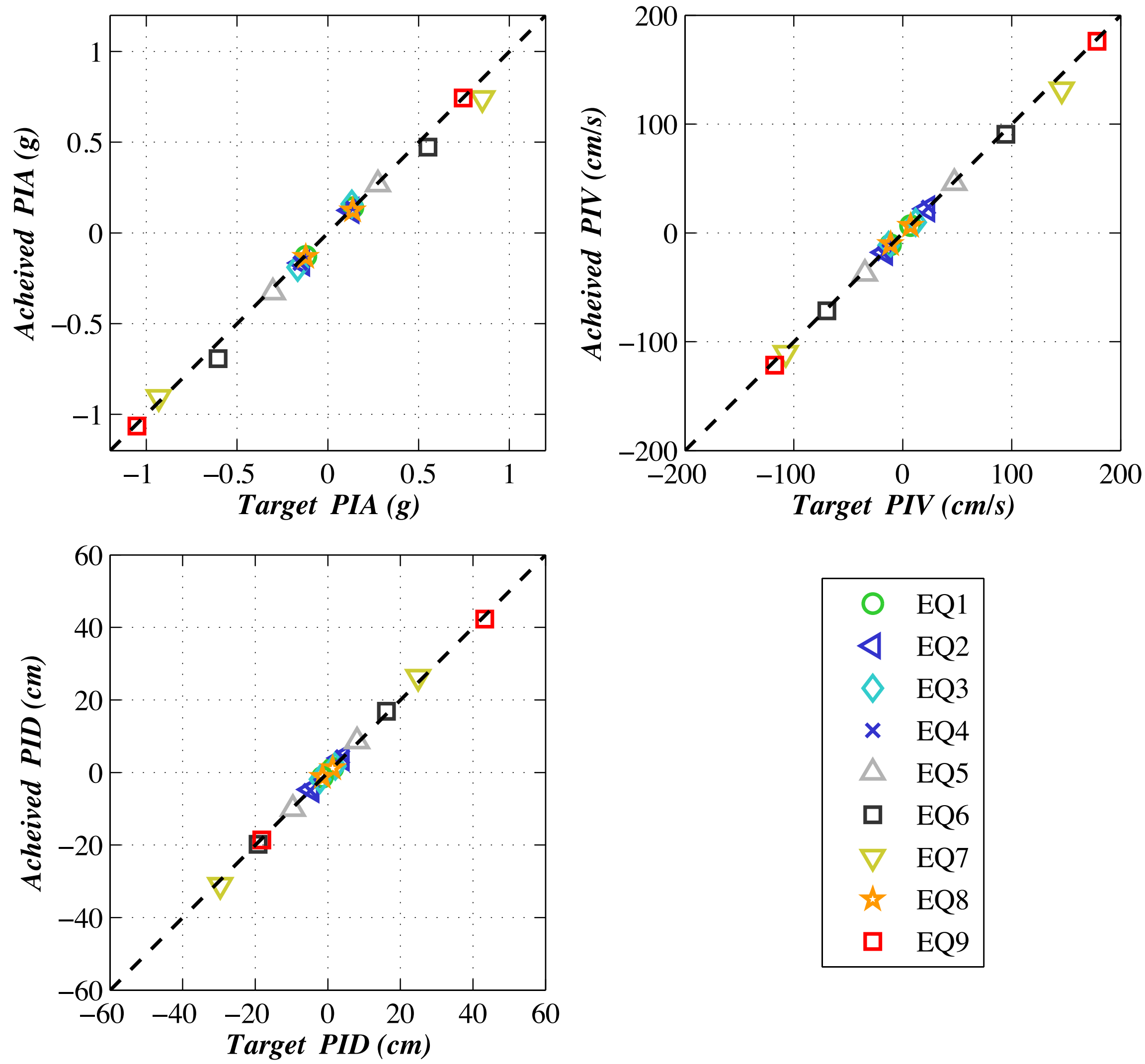

Figure 3.7. Comparison of target and achieved input motion parameters: (a) peak input accelerations, (b) peak input velocities, and (c) peak input displacements.

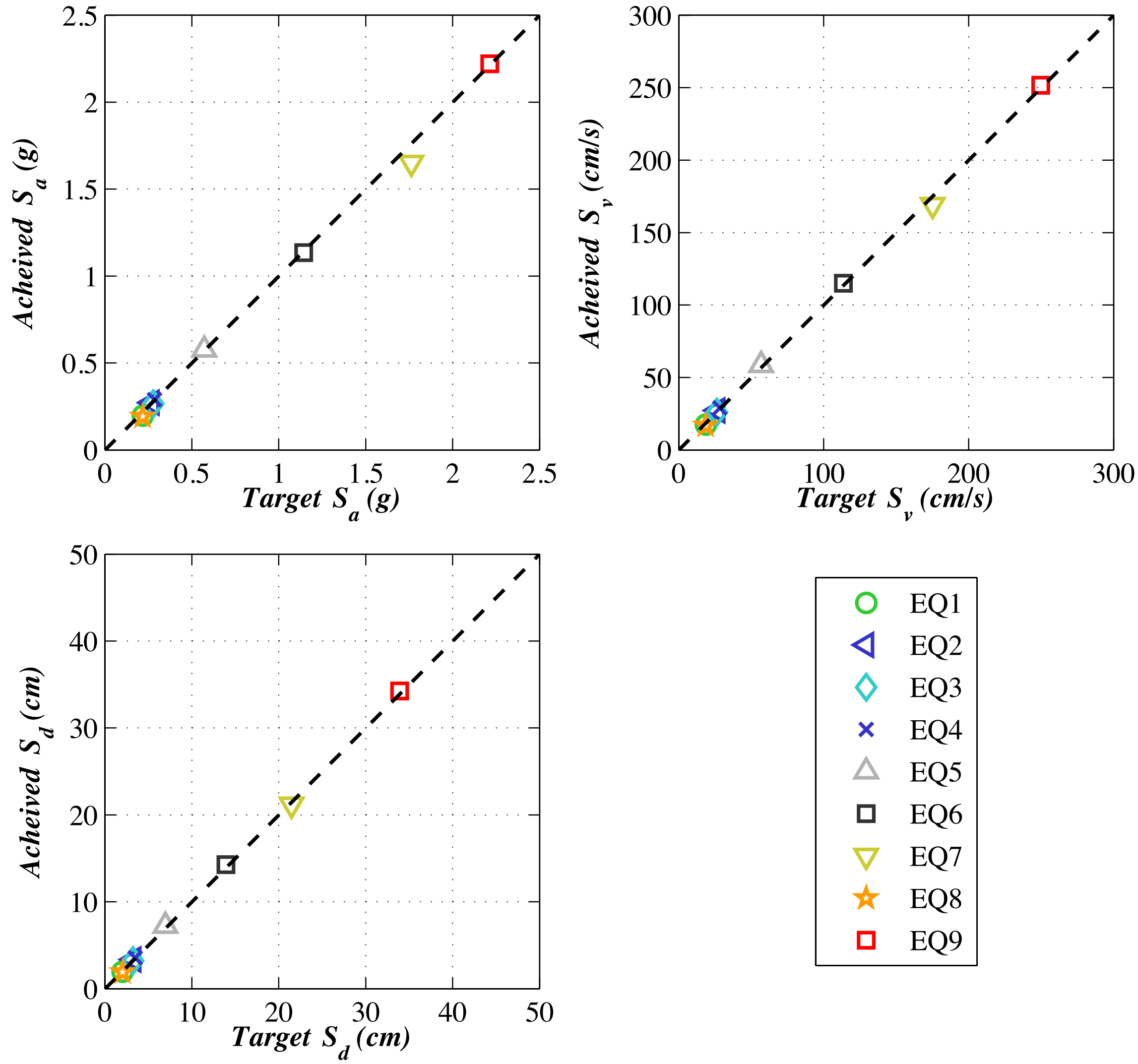

Figure 3.8. Comparison of target and achieved input motion parameters: (a) averaged spectral accelerations (ξ = 5%), (b) averaged spectral velocities (ξ = 5%), and (c) averaged spectral displacement (ξ = 5%).

Figure 3.9 summarizes the error metrics of the key motion parameters. The relative error of a specific motion parameter is determined as the absolute error (difference between the target and achieved motion) divided by the specific target motion parameter (denoted in percentage). While as large as 15% for the peak input accelerations, the errors of all other parameters appeared much smaller (< 10%). In addition, the relative errors of the motion parameters appeared larger for EQ1:RIO-25, EQ3-CUR-25, and EQ8:RIO-25 compared to those of the remaining motions. This is attributed to the low amplitudes (in the root-mean-square sense) of these service-level motions characterized with very long duration of non-significant shaking. This tends to lead to convergence difficulties for the OLI process.

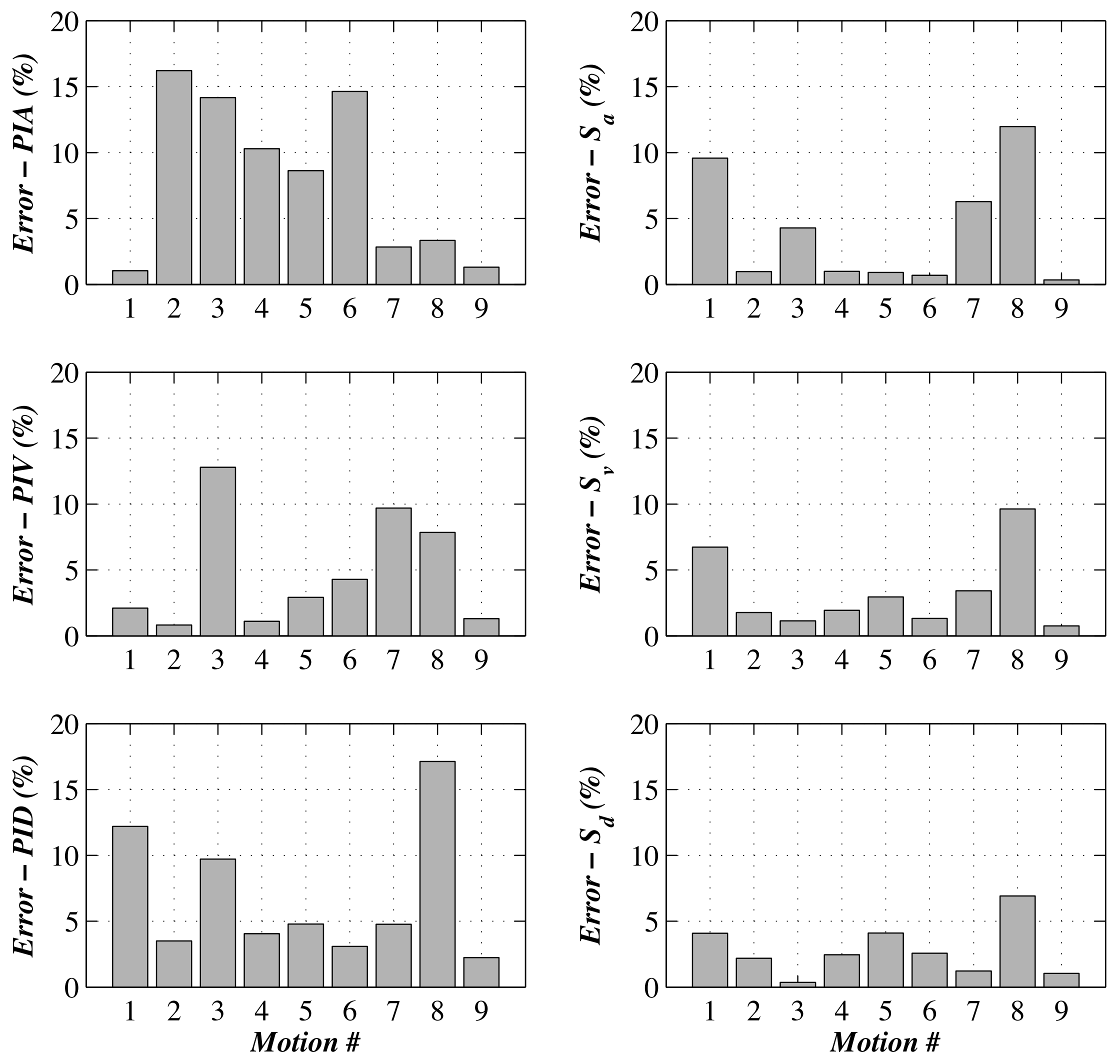

Figure 3.9. Error metrics of key motion parameters.

3.3 Fire Test Protocol

Following the pre-fire earthquake test sequence (EQ1–EQ7), the building was subjected to six compartment fire tests on three consecutive days at level 2 (four tests) and level 6 (two tests). Table 3.6 summarizes the fire test protocol. All the fire test compartments represented a 60-minute fire resistance rating construction in their undamaged condition. However, it is noted that the pre-fire earthquake tests induced gypsum damage to the fire test compartments. The severity of the damage differed significantly at the two levels, as a result of different seismic drift demands. Damage to the level 2 gypsum panels occurred in the form of crushed and gapped panel joints as the drift demands exceeded 1% during the pre-fire earthquake tests, while level 6 sustained only minor damage (joint tape cracks and incipient corner crushing) due to much smaller drift demands.

Figure 3.10 schematically illustrates the test sequence and the locations of the fire test compartments are in. It is noted that the same amount of fuel (84 liters) for all fire tests with an expected fire size of 2.16 megawatt. The major variables considered in the fire tests involved compartment space, ventilation characteristics, and pre-fire seismic damage. In addition, the atmospheric conditions during the specific fire test may also affect the actual burn duration and fire size.

Table 3.6. Fire test protocol

Test Date	Test #	Test Name	Location	Fire Characteristics
June 27th, 2016 (Fire Test Day 1)	1	L2-SW-T1	Level 2 – Southwest	*Fuel*: n-Heptane *Quantity*: 12 liters / pan *# of Pans*: 6 *Expected heat release rate*: 2.16 Mw
	2	L2-SE-T2	Level 2 – Southeast	
June 28th, 2016 (Fire Test Day 2)	3	L2-NW-T3	Level 2 – Northwest	
	4	L2-C-T4	Level 2 – Corridor	
June 29th, 2016 (Fire Test Day 3)	5	L6-C-T5	Level 6 – Corridor	
	6	L6-SW-T6	Level 6 – Southwest	

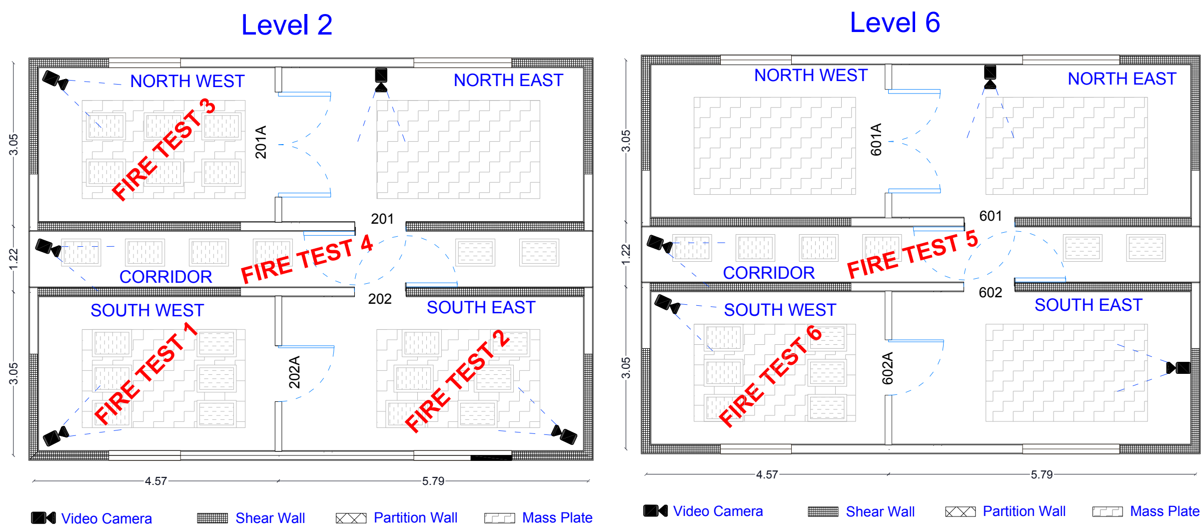

Figure 3.10. Fire test sequence and fire compartment location (level 2 and level 6).

Figure 3.11 shows the three-dimensional schematics of the fire test compartments. The dimensions of the compartments and openings are summarized in Table 3.7. It is noted that the compartments located on the west side had a plan dimension of 4.4 m × 2.9 m (Compartment 1, 3, and 6, Figure 3.11a and c), while the compartments on the east side were 5.6 m × 2.9 m (Compartment 2, Figure 3.11b). In addition, the corridor had an interior dimension of 10.4 m × 1.1 m (Compartment 4 and 5, Figure 3.11d). The floor-to-ceiling height of all the fire test compartments was 2.8 m. The window opening dimension was ~1.6 m × 1.5 m for the west compartments and 1.8 m × 1.5 m for the east compartments. The corridors consisted of two openings at the east and west ends that were partially enclosed with gypsum panels during the fire tests to contain the wind flow and ensure safety of fire ignition. As a result, the dimensions were 1.1 m × 0.9 m on the west end and 1.1 m × 1.8 m on the east end during the fire tests.

The two fire test floors (level 2 and 6) each consisted of four fire-rated doors, two on the transverse partition walls and two on the corridor walls (Figure 3.10). This resulted in the one-door configuration for the three compartments on the west side of the building (Compartment 1, 3, and 6) and the two-door configuration for the one on the east side (Compartment 2) and the corridors (Compartment 4 and 5). The opening dimension was ~1.8 m × 2.1 m for the door on the north partition wall and ~0.9 m × 2.1 m for the remaining three doors (two on the corridor walls and one on the south partition wall). It is noted that while the window and corridor openings provided sufficient ventilation on fire development, all the doors were closed during the fire tests.

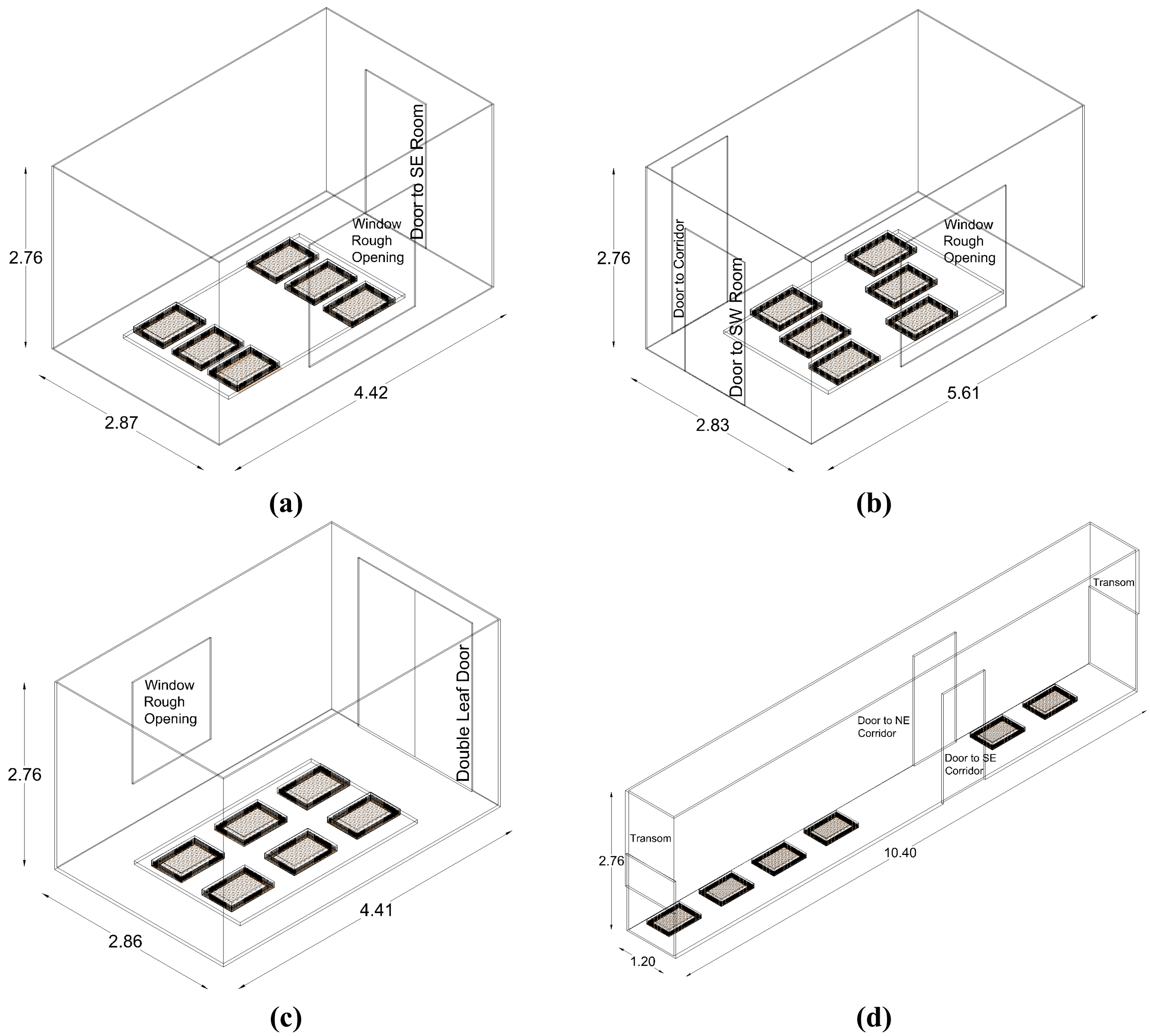

Figure 3.11. Three-dimensional schematics of the fire compartments: (a) southwest compartment, (b) southeast compartment, (c) northwest compartment, and (d) corridor (note: dimensions specified in the figure represent as-measured interior dimension, unit in meter).

Table 3.7. Summary of fire test compartment and opening dimensions.

Test # (location)	*Dimensions – Compartment*					*Dimensions – Opening*			
	L (m)	*W (m)*	*H (m)*	*Area (m^2)*	*Volume (m^3)*	*Opening type*	*W (m)*	*H (m)*	*Area (m^2)*
1 (L2-SW)	4.4	3.0	2.8	12.3	34.5	Door	0.9	2.1	2.0
						Window	1.6	1.5	2.4
2 (L2-SE)	5.6	3.0	2.8	16.2	45.5	Door	0.9	2.1	2.0
						Door	0.9	2.1	2.0
						Window	1.8	1.5	2.8
3 (L2-NW)	4.4	3.0	2.8	12.8	35.7	Door	1.8	2.1	3.8
						Window	1.6	1.5	2.4
4 (L2-C)	10.0	1.1	2.8	10.9	30.6	Door	0.9	2.1	2.0
						Door	0.9	2.1	2.0
						Corridor end	1.1	0.9	1.0
						Corridor end	1.1	1.8	1.9
5 (L6-C)	10.0	1.1	2.8	10.9	30.6	Door	0.9	2.1	2.0
						Door	0.9	2.1	2.0
						Corridor end	1.1	0.9	1.0
						Corridor end	1.1	1.8	1.9
6 (L6-S)	4.4	3.0	2.8	12.8	35.7	Door	0.9	2.4	2.2
						Window	1.6	1.5	2.4

4 MONITORING SYSTEM

The building was outfitted with more than 250 analog sensors, a Global Positioning System (GPS) system, and an array of more than 40 digital video cameras to record the behavior of the structural components and building in the earthquake tests. Between the two earthquake test phases, thermocouples were installed in various locations of the fire test compartments. Sacrificial video cameras were also installed to collect visual data regarding smoke or fire spread. In addition, remote sensing systems, such as unmanned aerial vehicles (UAVs) and light ranging and detection (LiDAR) systems, were employed to collect imagery and point cloud data at various stages during the construction and test phases. In addition, a building reference system was developed to facilitate building interior and exterior documentation. The key aspects of these monitoring systems are discussed in details in this chapter. Detailed drawings of the analog sensor instrumentation plan and documented in Appendix E, whereas those of the video camera instrumentation plan are documented in Appendix F.

4.1 Building Reference Systems

To facilitate building interior and exterior documentation during construction and test phases, a nomenclature system of the building and its structural components (e.g., walls and floor joists) was developed at the early stage of the construction phase (shortly following the completion of interior gypsum installation). The nomenclature adopted for the building reference system formed the basis of the analogue sensor and video camera nomenclature. Therefore, the building reference system is discussed at the beginning section of the chapter.

Plan Layout and Wall Lines

Consistent with the prefabricated floor panel layout, the building floor plan was divided into six segments. As shown in Figure 4.1, each segment was assigned a unique number from 1 to 6 (1–4 stand for the four rooms, 5–6 stand for corridor). The transverse boundary of the east and west segments was divided by the partition walls. These indices are used later in the analog sensor nomenclature to define the locations of accelerometers and strain gages. In addition, the four longitudinal wall lines were each assigned a unique letter from A to D starting from the northernmost wall line (A and D – exterior walls, B and C – corridor walls). The wall line indices are used in the analog sensor nomenclature to define the locations of the displacement transducers (string potentiometers and linear potentiometers) installed on the shear walls.

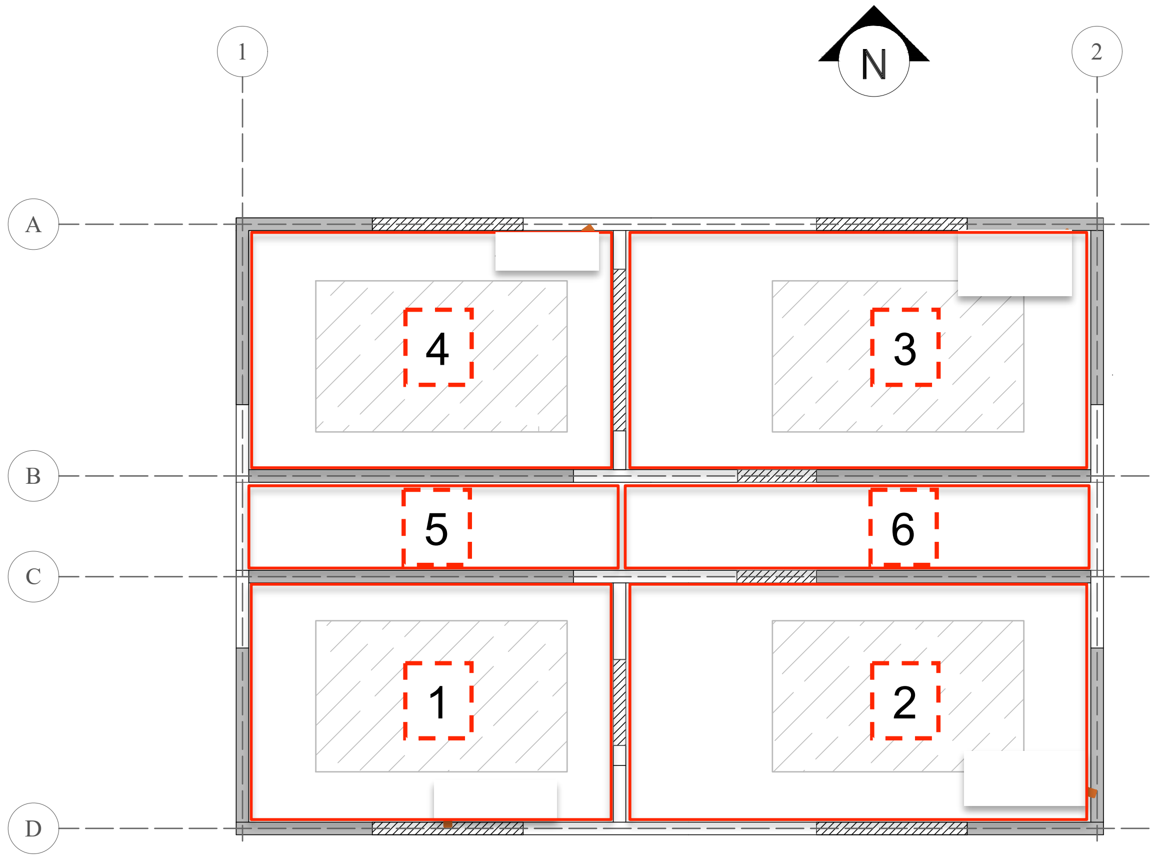

Figure 4.1. Floor plan and wall line indices.

Wall System

To facilitate photo documentation of the wall system, individual walls (i.e., shear walls, gravity walls, and partition walls) were each assigned a unique short name using a combination of numbers and letters (Figure 4.2). In addition, the interior gypsum sheathing of the shear wall was annotated using vertical red lines to represent the tie-down rod locations and vertical black lines to indicate the boundary between the shear wall and gravity wall. In addition, capitalized letters were used to indicate the specific wall corners (e.g., UL for upper left corner). Figure 4.3 schematically illustrates the annotations for the shear wall sheathing.

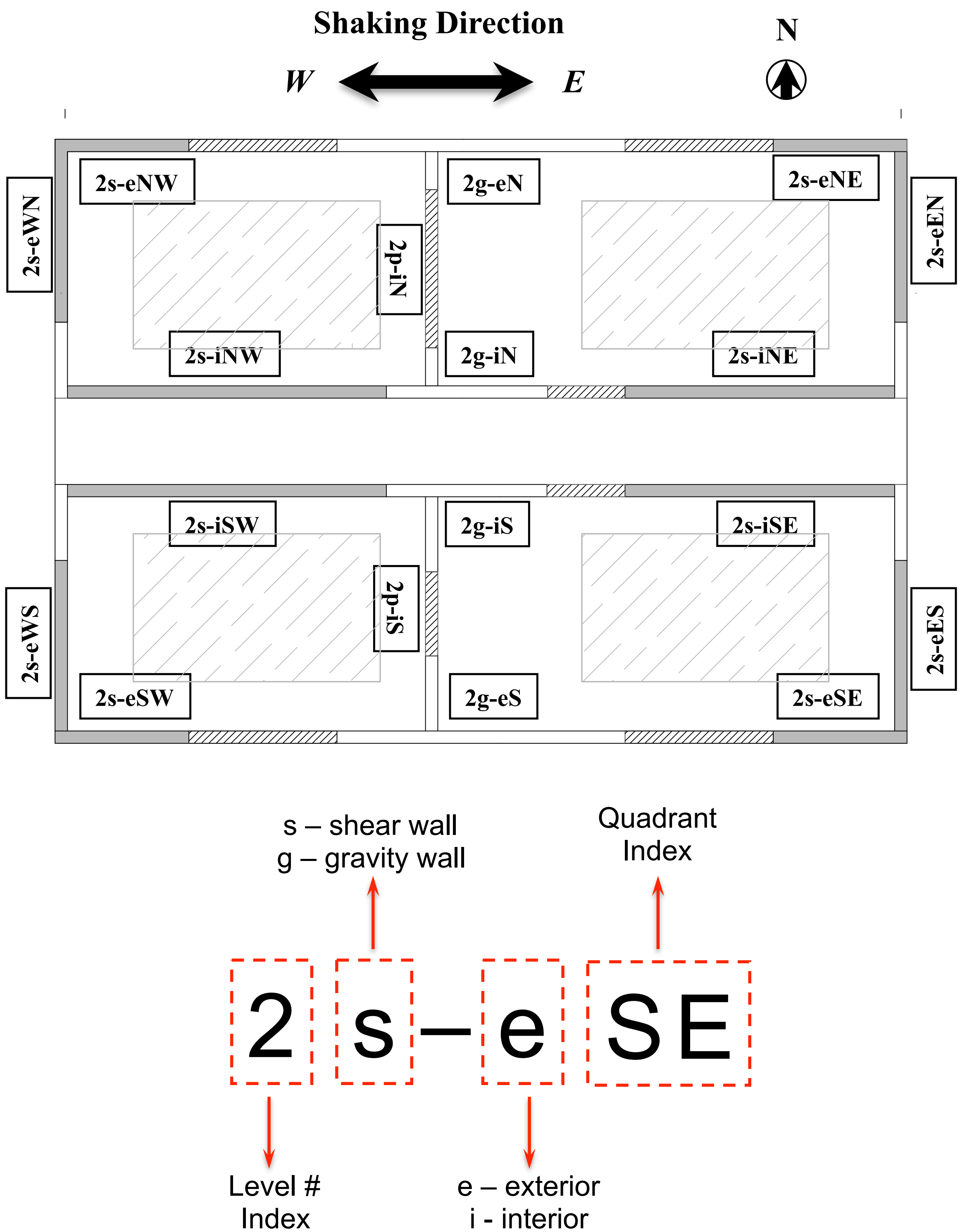

Figure 4.2. Wall system nomenclature.

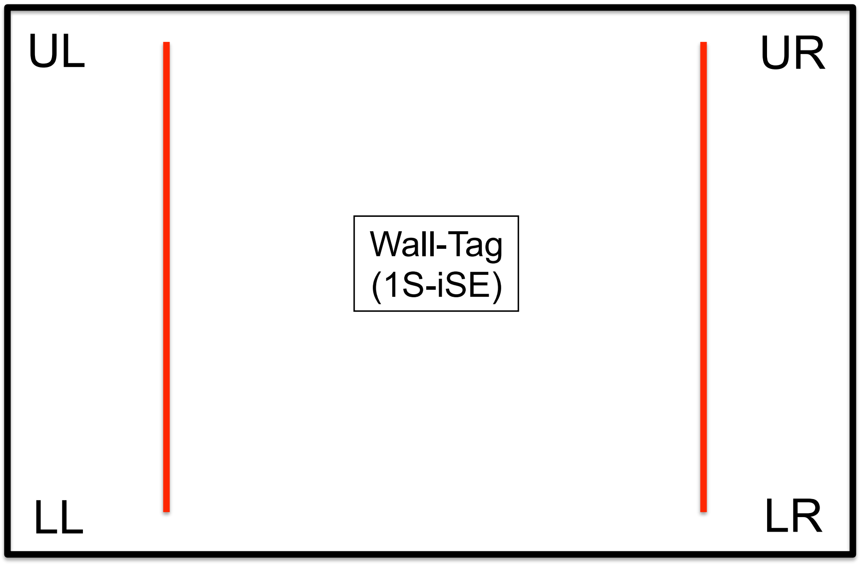

Figure 4.3. Schematic illustration of shear wall sheathing annotations.

Floor Joist Nomenclature

The floor joists were all spaced at 0.6 m on center (expect the end spans), resulting in a total of 19 joists along the longitudinal direction of the building (Figure 4.4). A nomenclature system was used to define the floor joists at floor 2, 4, 5, and 6 (joists at the remaining two floors were enclosed within the gypsum ceiling). At each of the north, corridor, and south span, the joist reference system included five joists at every fourth joist, starting from the second joist on the west end to the second joist at the end. These joists were each assigned with a unique name using a combination of numbers and letters as shown in Figure 4.4.

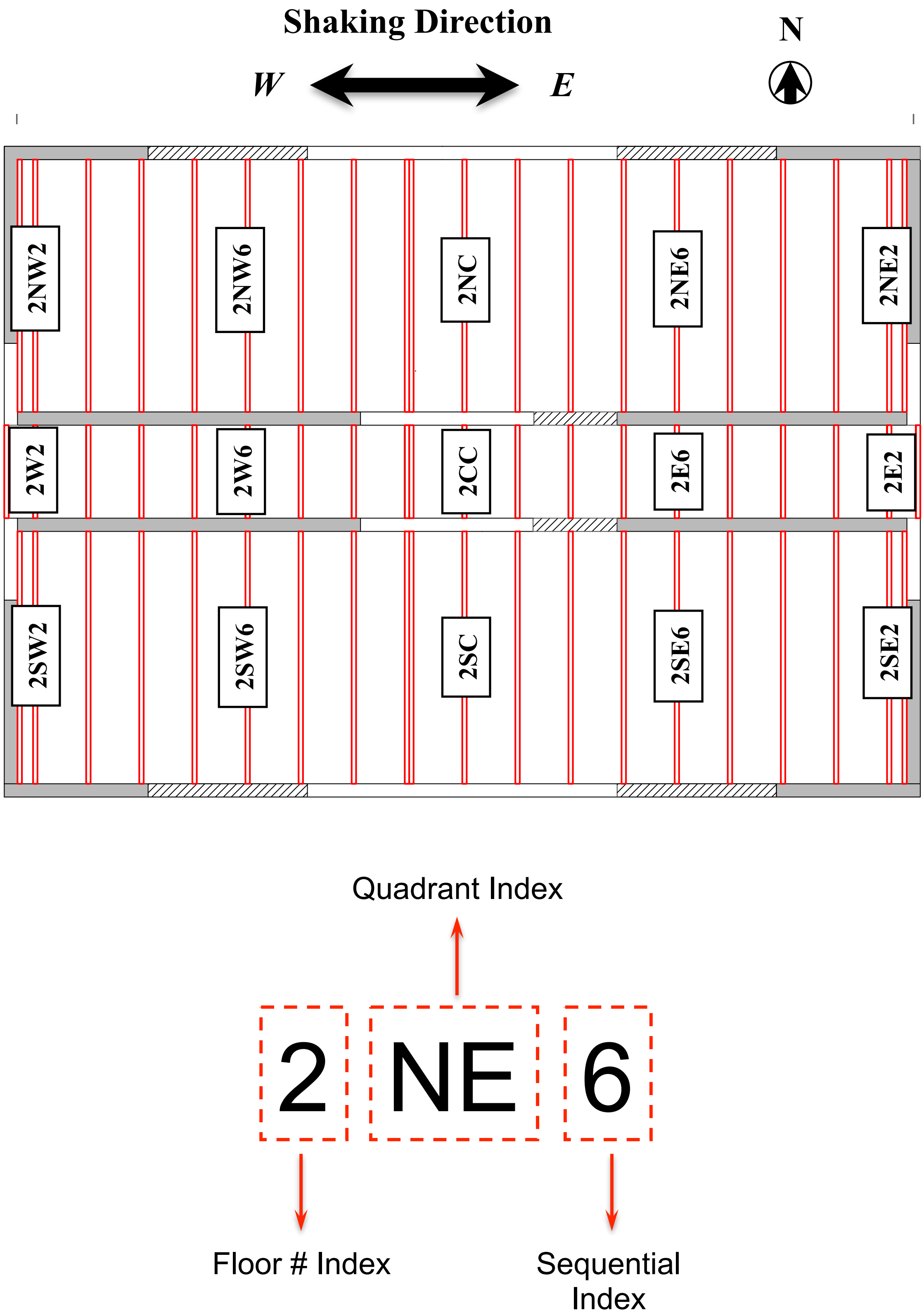

Figure 4.4. Floor joist nomenclature.

4.2 Earthquake Test Phase

The response of the test building was documented using four types of monitoring systems during the earthquake test phase: (a) analog sensors, (b) video cameras, (c) a global positioning system (GPS), and (d) still cameras. The essential characteristics of individual monitoring systems are discussed in detailed in this section. Complete instrumentation plan of the analog sensors is documented in Appendix E, while those of the video camera system in Appendix F.

4.2.1 Analog Sensors

During the earthquake test phase, the seismic response of the test building was monitored with a dense array of analog sensors consisting of accelerometers, displacement transducers (string potentiometers and linear potentiometers), and strain gauges. Table 4.1 summarizes the five different types of analog sensors and the specific responses measured by different sensors. With the exception of the Kinemetrics accelerometers that collected data using a standalone data acquisition system at a sampling rate of 200 Hz, all remaining analog sensors were connected to a multi-node distributed data acquisition system at a sampling rate of 240 Hz.

Table 4.1. Summary of the analog sensors and the measured responses.

Sensor type	Sensor index[1]	Type of measurements
Accelerometer (MEMS)	A	Floor accelerations on all floors; equipment accelerations at floor 6
Accelerometer (Kinemetrics)	n/a	Floor accelerations at floor 2, 4, 6, and roof
String potentiometer	S	Shear wall distortion at levels 1, 2, and 4; floor displacements at lower 4 floors
Linear potentiometer	L	Shear wall uplift at levels 1, 2, and 4; floor joist displacements at floor 2
Strain gage	G	Tension rod strains at levels 1, 2, and 4, compression post strains at level 1

[1] Sensor index (single-character index) used in sensor nomenclature.

The analog sensors were installed progressively during the construction during the test phase, resulting a total of four configurations at different stages during the test program (two for construction phase and two for test phase). Table 4.2 summarizes the sensor number counts for the four configurations. It is noted that some sensors (e.g., displacement transducers at level 2) were removed prior to the fire tests, while a smaller amount of sensors were damage during the fire tests (e.g., string potentiometers installed on the exterior side of the shear walls). Consequently, the total number of analog sensors during the post-fire earthquake tests became less than that of the pre-fire test sequence.

Table 4.2. Analog sensor number counts at the four different configurations.

Configuration	*Type of sensor*					*Total*
	Accel. (MEMS)	*Accel. (Kinemetrics)*	*String pot.*	*Linear pot.*	*Strain gage*	
C1 – construction phase (May 5 – 15, 2016)	25	0	0	1	12	38
C2 – construction phase (May 15 – June 9, 2016)	57	0	0	1	12	70
E1 – pre-fire test phase (June 10 – 17, 2016)	68	12	71	39	67	256
E2 – post-fire test phase (July 1, 2016)	59	0	52	22	59	192

Accelerometers (MEMS)

The test building was instrumented with an array of 68 uniaxial MEMS accelerometers at all floor including the roof at the earthquake test phase. Figure 4.5 shows the accelerometer plan layout at the second floor (also typical of the third floor and roof) and the associated nomenclature. From the second floor through the roof, each floor consistently consisted of eight accelerometers measuring horizontal floor accelerations: (a) six in the longitudinal direction (four corners and two ends of the corridor), and (b) two in the transverse direction (northeast and northwest) (Figure 4.7a-b). In contrast, the first floor (shake table platen) consisted of only four accelerometers, namely, two in the longitudinal direction (northwest and southwest) and the remaining two in the transverse direction (northeast and northwest). Second floor, third floor, and roof each included four extra accelerometers: two at the ends of the corridor (Figure 4.7b) to measure the vertical accelerations and two at the center of the mass plate in the southwest room measuring longitudinal and vertical accelerations (Figure 4.7c). In addition, three accelerometers were installed on top the water heater at the sixth floor measuring their longitudinal accelerations (Figure 4.7d), as well as one accelerometer collocated with the GPS station at the approximate center of the roof. Since the MEMS accelerometers was installed on the building at several stages during the construction phase, the instrumentation plan varied at the low-amplitude vibration test dates.

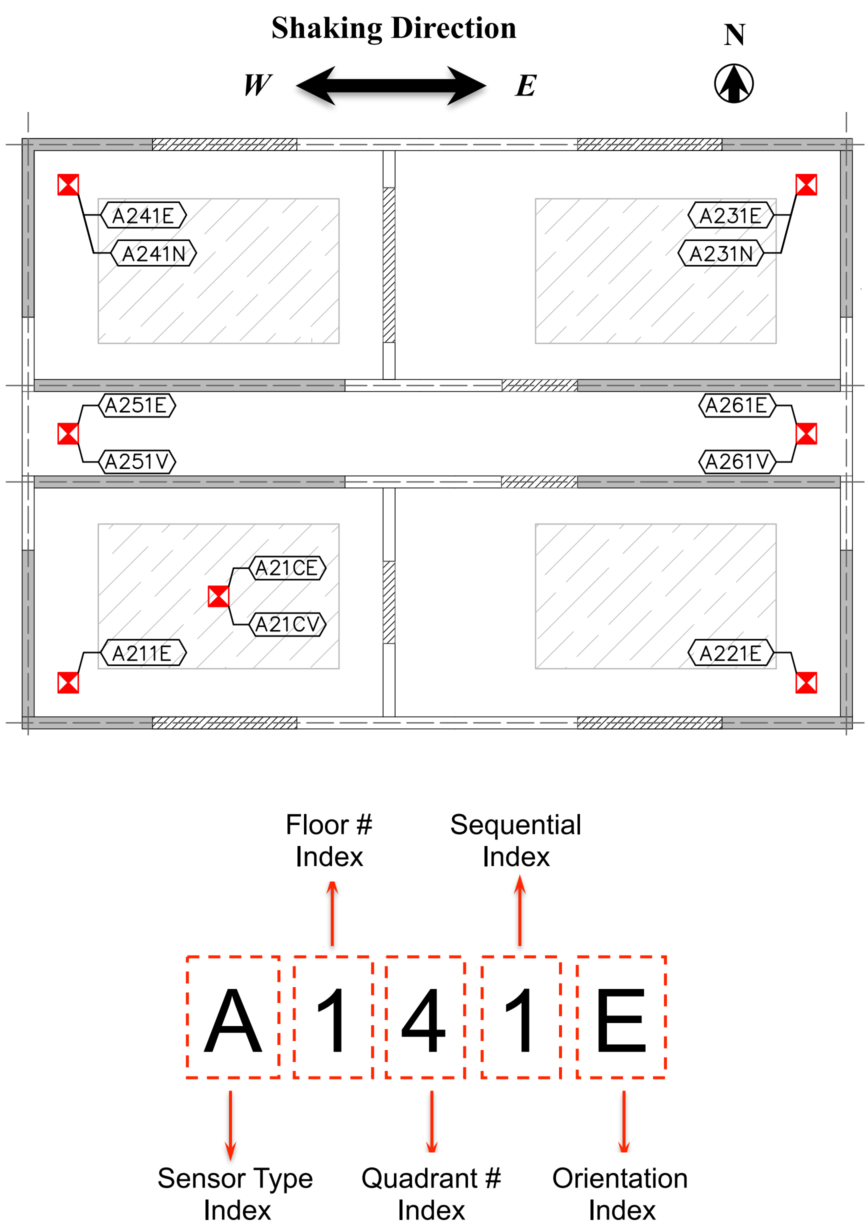

Figure 4.5. MEMS accelerometers plan layout at floor 2 (also typical of floor 3 and roof) and the nomenclature.

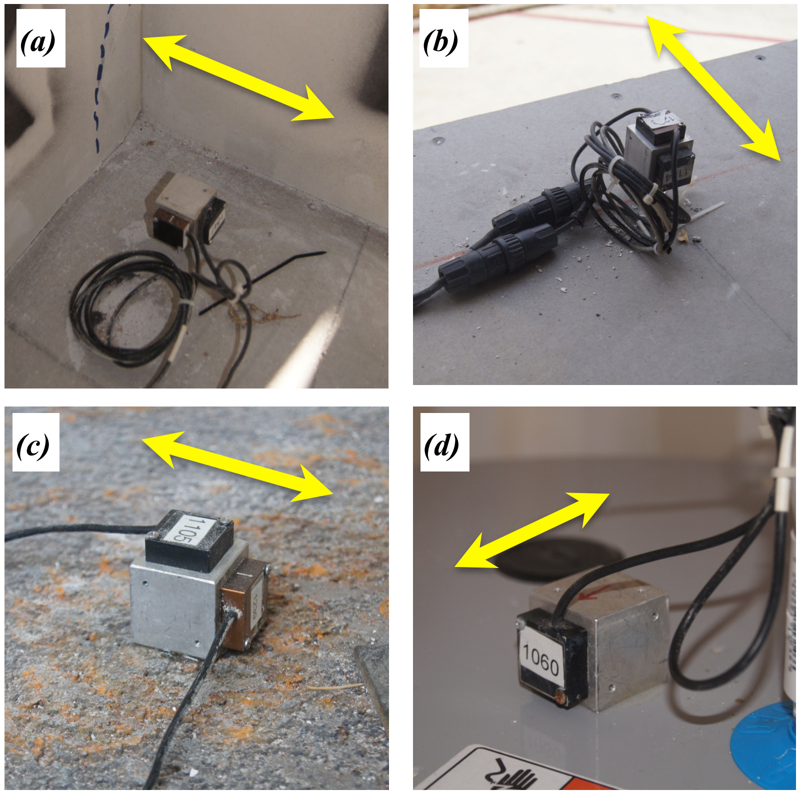

Figure 4.6. MEMS accelerometers with different mounting conditions: (a) floor corner, (b) end of corridor, (3) mass plate, and (4) top of water heater (arrow denotes the direction of shaking).

Accelerometers (Kinemetrics)

To complement the MEMS accelerometer array, the test building was deployed with a total of 12 uniaxial Kinemetrics accelerometers at four select floors: floor 2, floor 4, floor 6, and roof. As shown in Figure 4.7, these floors each consisted of two accelerometers oriented in the longitudinal direction (the ones close to the corridor) and one accelerometer in the transverse direction (the one at the south). Figure 4.8 schematically illustrates the layout of Kinemetric accelerometers in the southwest room of the second floor.

The Kinemetric accelerometers were all connected to a stand-alone data acquisition system that recorded data at a sampling rate of 200 Hz. As a result of larger dynamic range and the digital-to-analog conversion bit depth, data collected using Kinemetric accelerometers contained lower noise floor compared to data collected by MEMS accelermoters. Therefore, Data collected using this system were primarily used in the system identification study, in particular when the structural responses were very smaller in amplitude (e.g., < 0.001 g in ambient vibration). It is noted that the Kinemetric accelerometers were deployed to record data only during the pre-fire earthquake test phase, since they were installed on the building only prior to the beginning of the pre-fire earthquake test phase but removed from the building prior to the fire test phase.

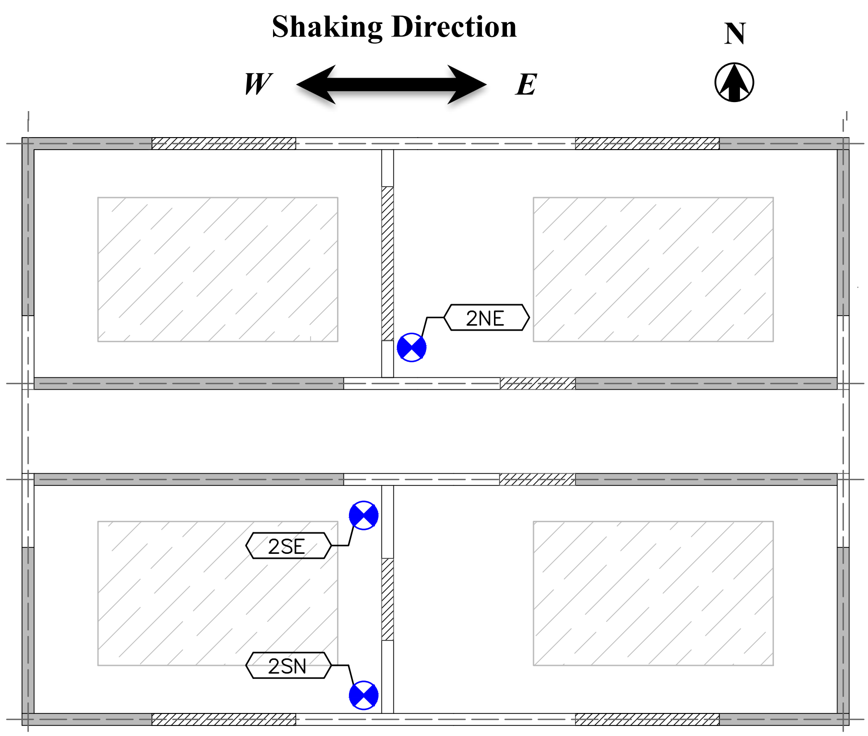

Figure 4.7. Kinematrics accelerometer plan layout at floor 2 (also typical of floor 4, floor 6, and roof).

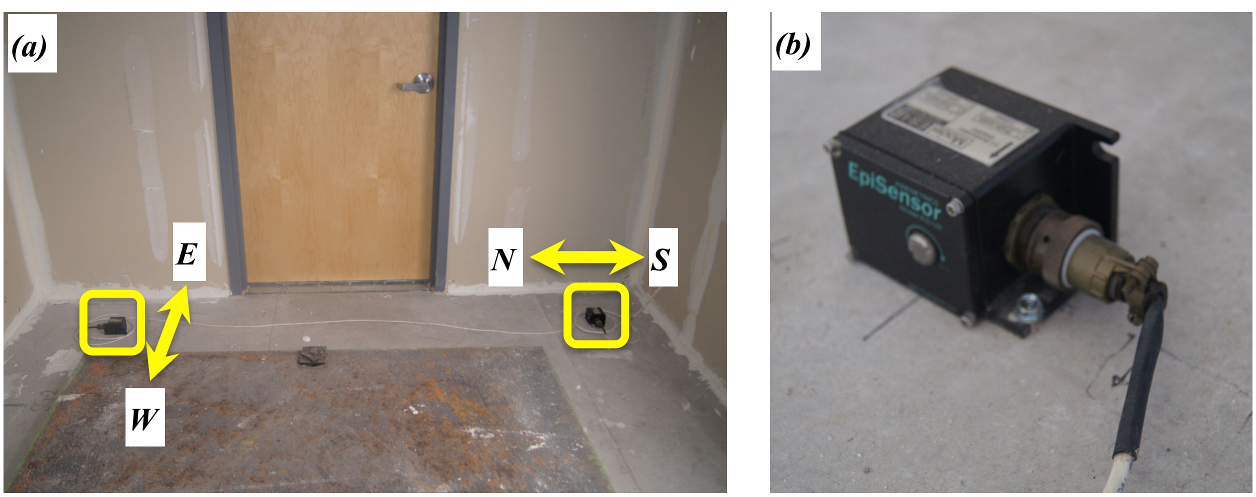

Figure 4.8. Kinemetrics accelerometers: (a) sensor layout in the southwest room at floor 2 (arrow denotes sensor orientation), (b) close-up sensor view.

Displacement Transducers

The test building was instrumented with two types of displacement transducers, namely, string potentiometers and linear potentiometers. Displacement transducers were primarily used for measuring local shear wall displacement response. In addition, four linear potentiometers were used to measure the joist displacements at the panel interface, whereas four string potentiometers to used to measure the floor displacements.

As shown in Figure 4.9, three corridor shear walls and three corner shear walls at each of the lower two levels (level 1 and 2) were instrumented with displacement transducers. Level 4 contained one less instrumented shear walls, since the northeast corner wall at level 4 was not instrumented. The instrumented walls each involved four string potentiometers to measure the shear distortions of the structural panels (Figure 4.10a-b) and a pair of linear potentiometers measuring the uplift displacements of the shear wall (Figure 4.10e). All the string potentiometers were mounted to the structural panel side using aluminum brackets. The vertically oriented string potentiometers were mounted at the upper corners of the wall (Figure 4.10c), while those oriented diagonally were mounted at the lower corners (Figure 4.10d). The angle of the diagonal strings differed depending on shear wall dimensions (see details in Appendix E). In addition, a pair of linear potentiometers was mounted at the two lower corners of each wall using aluminum angles (Figure 4.10e). They were installed on the structural panel (corridor) side for the corridor walls (same side as string potentiometers) and on the gypsum panel (interior) side for the corner walls (opposite side to string potentiometers).

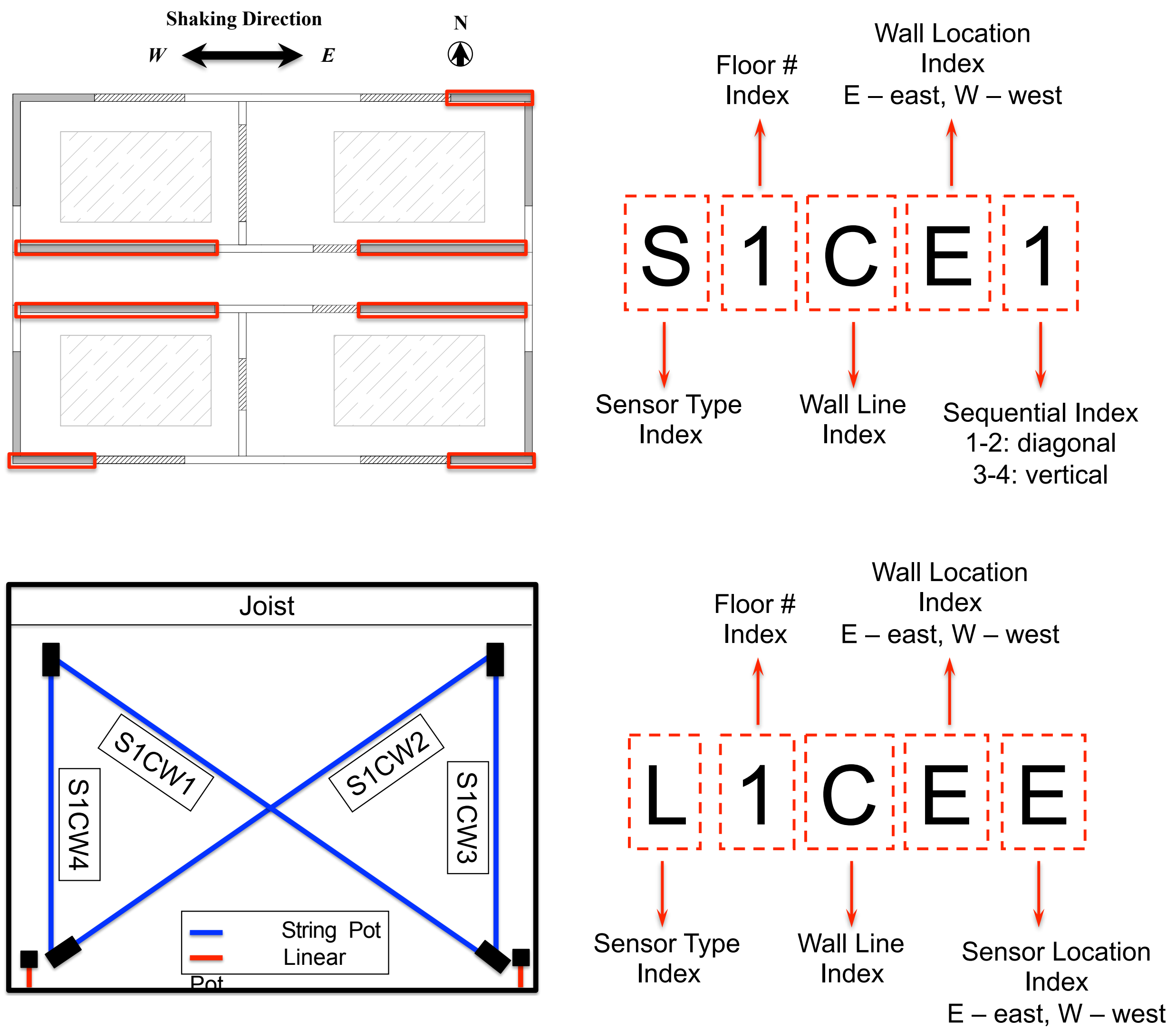

Figure 4.9. Plan layout of instrumented shear walls typical of level 1, 2, and 4 (note that the northeast corner wall at level 4 not instrumented).

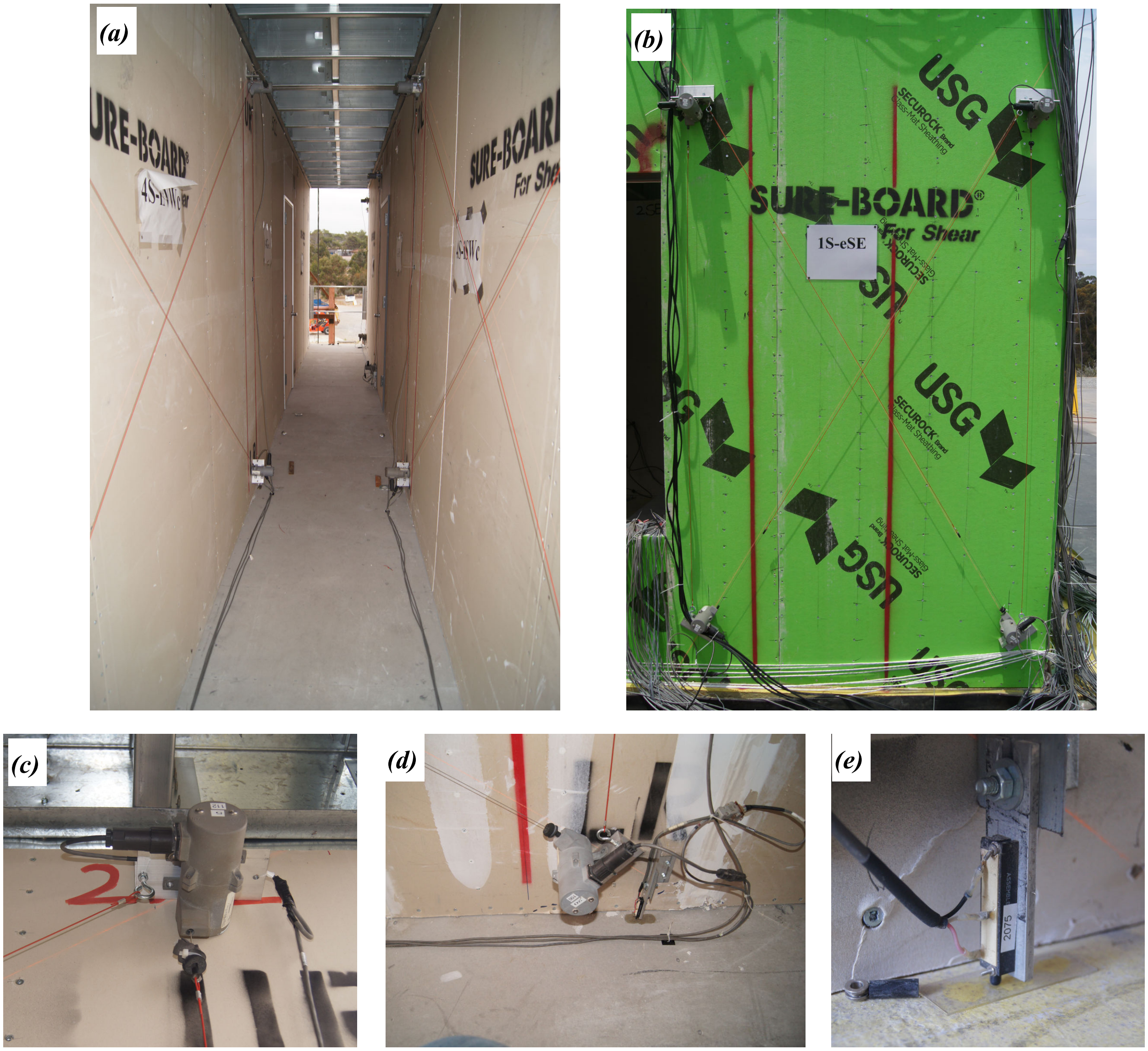

Figure 4.10. Shear wall displacement transducers: (a) string potentiometers installed on the corridor wall, (b) string potentiometers installed on the corner wall, (c) string potentiometer at the upper corner, (d) string potentiometer at the lower corner (e), linear potentiometer at the base of shear wall.

The floor panel interface was instrumented with linear potentiometers at the underside of the joists at floor 2 to measure the relative displacements between the prefabricated panels (Figure 4.11). It is noted that floor 2 was the only location that allowed such measurements, since partition walls were installed at full height in the same location on the floors above. In addition, three string potentiometers were installed on a reference frame (safety tower) and connected to the east end of the corridor at the lower three floors (one more string potentiometer was added to floor 4 during the post-fire earthquake test phase). These sensors measured the absolute floor displacements in the longitudinal directions (Figure 4.12).

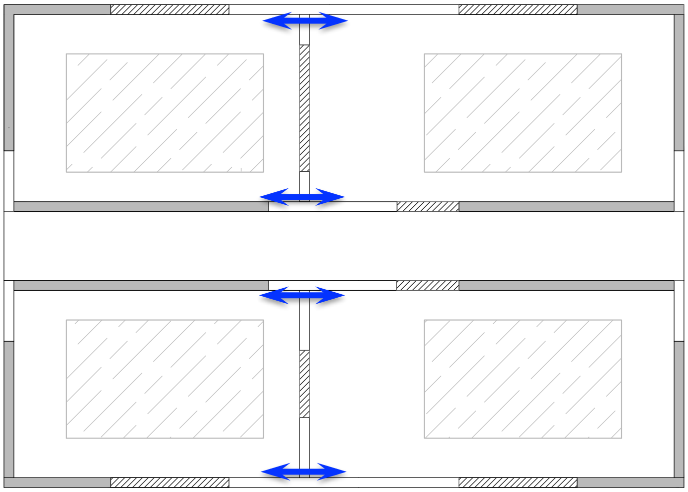

Figure 4.11. Linear potentiometers measuring the joist displacements at floor 2: instrumentation layout (left), and close-up sensor view (right).

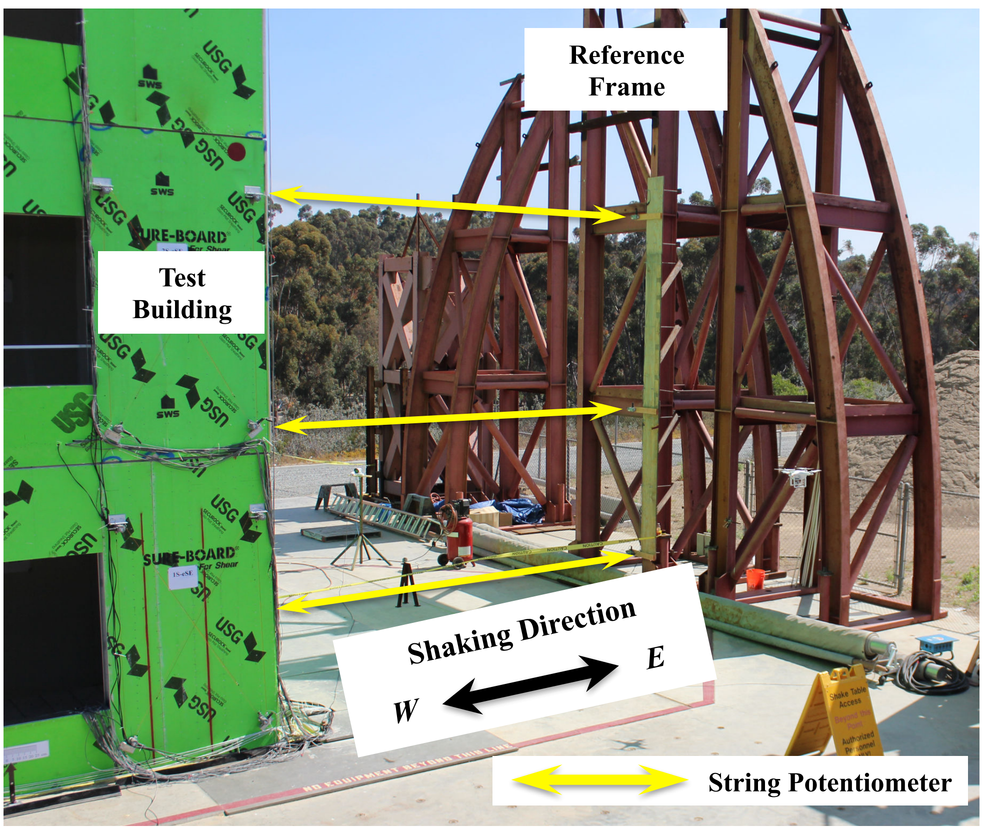

Figure 4.12. Photographs of string potentiometers measuring the floor displacements (pre-fire earthquake test phase).

Strain Gages

As shown in Figure 4.13, a total of 67 strain gages were installed on the shear wall tie-down rods (level 1, 2, and 4) as well as the compression posts (at level 1) (one strain gage malfunctioned after the installation and therefore not connected to the data acquisition system). It is noted that The tie-down rods utilized standard strain gages (Type FLA), whereas the compression posts utilized high yield strain gages (Type YFLA). Tie-down rod strain gages at level 1 was installed on the non-threaded segment of the transition rod (Figure 4.14a), while those at level 2 and 4 were installed on the Z-rods at about 0.45 m above the coupler connections (Figure 4.14b-c) (refer to Section 2.3.2 for details of the shear wall tie-down rod system).

The tie-down rods of the longitudinal shear walls on the south side (level 1, 2, and 4) were all instrumented with two strain gages, while only one strain gage was instrumented on each of the rods in the transverse and northeast corner walls (level 1 and 2). In addition, the compression posts of the two longitudinal corridor walls on the south side and the southeast corner wall at level 1 were each instrumented with two strain gages. As shown in Figure 4.15, one strain gage was installed on each side of the built-up section pack, although the exact location varied depending on specific section layout. It is noted that compression post strain gages were all installed in-situ and was limited by inadequate space for installation due to closely spaced framing studs.

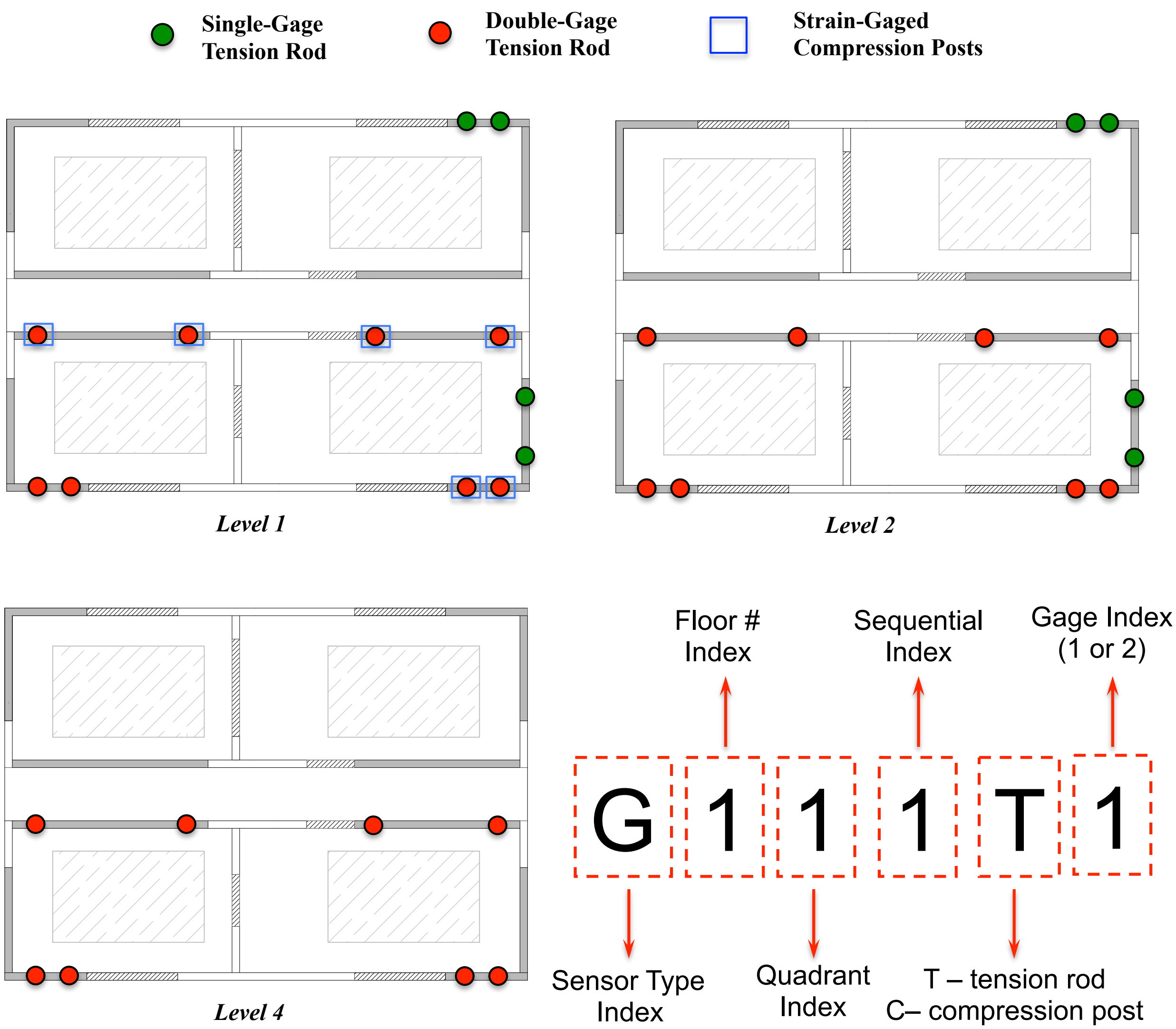

Figure 4.13. Strain gages instrumentation plan and associated nomenclature.

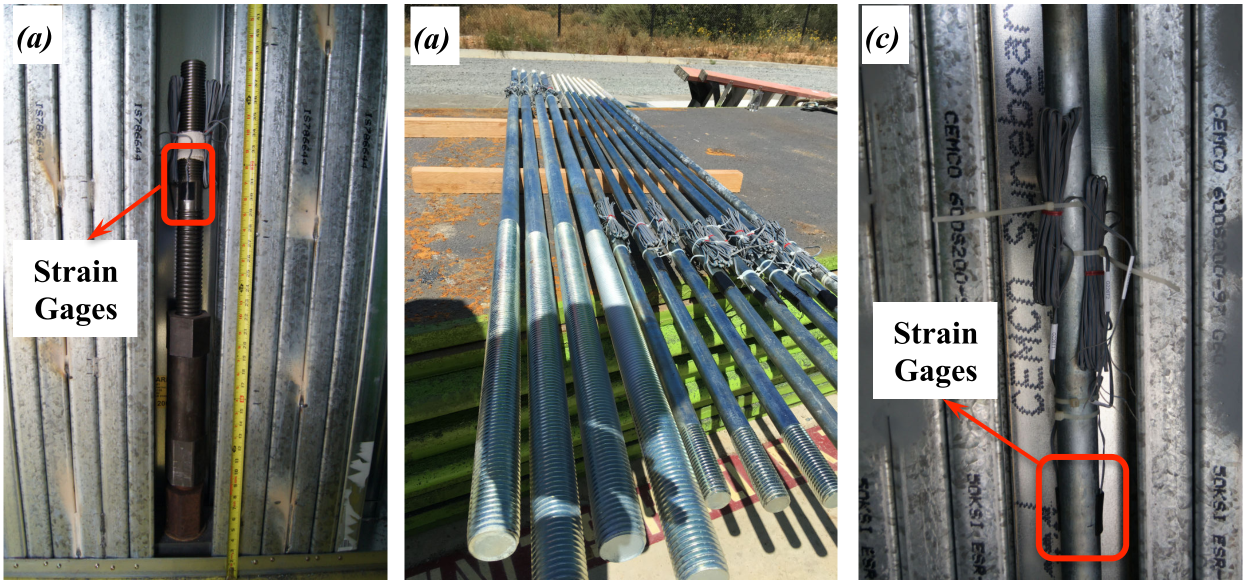

Figure 4.14. Tie-down rod strain gages: (a) transition rod at level 1, (b) pre-installed strain gaged tie-down rod, and (c) strain gaged tie-down rod (level 2).

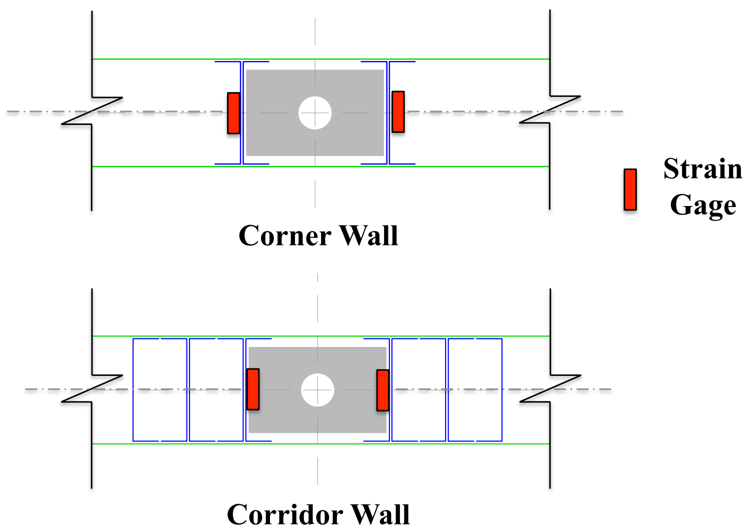

Figure 4.15. Schematic illustration of compression post strain gages.

4.2.2 Video Cameras

Complementing data collected using analog sensors, a dense network of video cameras was developed to visually monitor the building interior and exterior during the earthquake test phase. The video monitoring system consisted of four different types of cameras, namely, GoPro cameras, coax cameras, IP cameras, and high definition (HD) camcorders. All the coax and IP cameras were connected to an automatic digital video recording system, while the GoPro cameras and HD camcorders recorded videos in built-in memory cards. The GoPro and coax cameras were primarily used to monitor the structural components and contents in the building interior, whereas the HD camcorders and IP cameras were used to capture the exterior view of the building. As shown in Figure 4.16, each camera was assigned with a unique name depending on the camera type, location, and camera view. The locations and specifications of the different video cameras are summarized in Table 4.3.

The camera layouts and views were varied at different stages during the test program, resulting in a total of four configurations for different earthquake tests (Table 4.4). Due to damage to the video cables during the fire tests, the total number of cameras reduced moderately for the post-fire earthquake test sequence. Figure 4.17 shows the camera layouts at the lower two levels, and the typical camera views are illustrated in Figure 4.18.

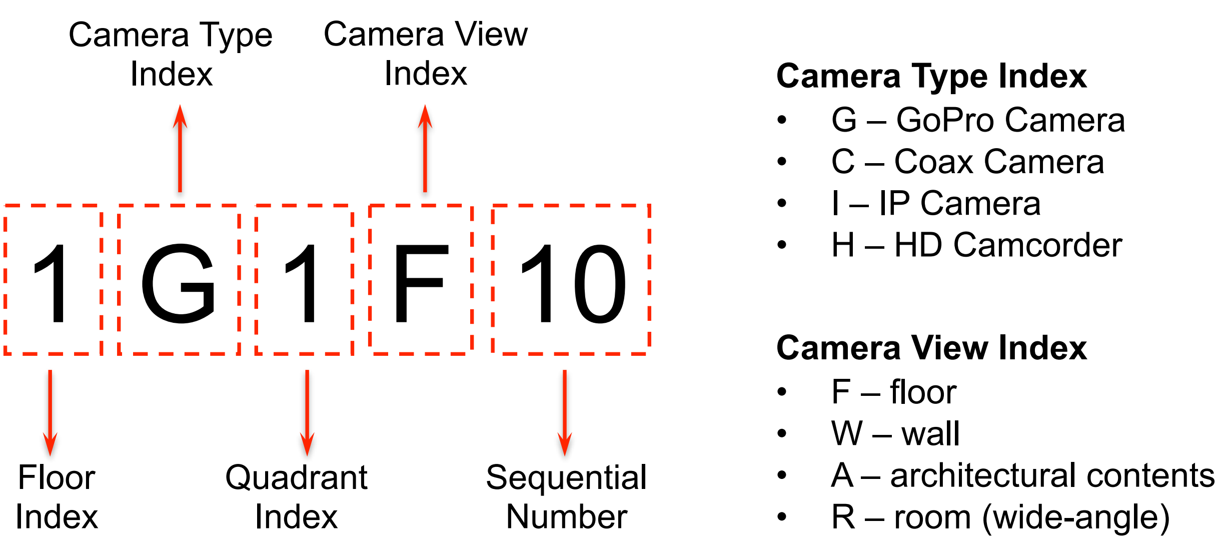

Figure 4.16. Camera nomenclature.

Table 4.3. Summary of the video camera views and specifications.

Camera type[1]	*Camera locations*	*Specifications*	*Schematic*
GoPro* (G)	Interior views of structural components and contents at the lower two levels	HD Hero4 12 MP, 4K UHD	
		HD Hero3 12 MP, 4K UHD	
Coax (C)	Interior views of structural components and contents at level 3 through the roof	2 MP, 2.8 to 12 mm Variable-focal lens, 1080p (1920 x 1080)	
		2.1 MP, 2.8 to 12 mm Auto Iris Variable-focal lens, 960H CCTV Format & 1080p AHD format.	
IP (I)	Exterior building views	Axis Pl405-IP Camera 2 MP, HDTV 1080p/2 resolution.	
High definition camcorders * (H)	Exterior building views	5.3 MP, full HD resolution.	

[1] letter in the parenthesis denotes the camera type index used in nomenclature
* denotes that the cameras were triggered manually

Table 4.4. Configuration of the video camera system.

Configuration #	*Camera type*				*Total*
	GoPro	*Coax*	*HD Camcorder*	*IP*	
Configuration 1 (EQ 1-3, pre-fire)	12	22	4	/	38
Configuration 2 (EQ 4-5, pre-fire)	14	28	3	/	45
Configuration 3 (EQ 6-7, pre-fire)	/	28	4	2	34
Configuration 4 (EQ 8-9, post-fire)	12	9	3	2	26

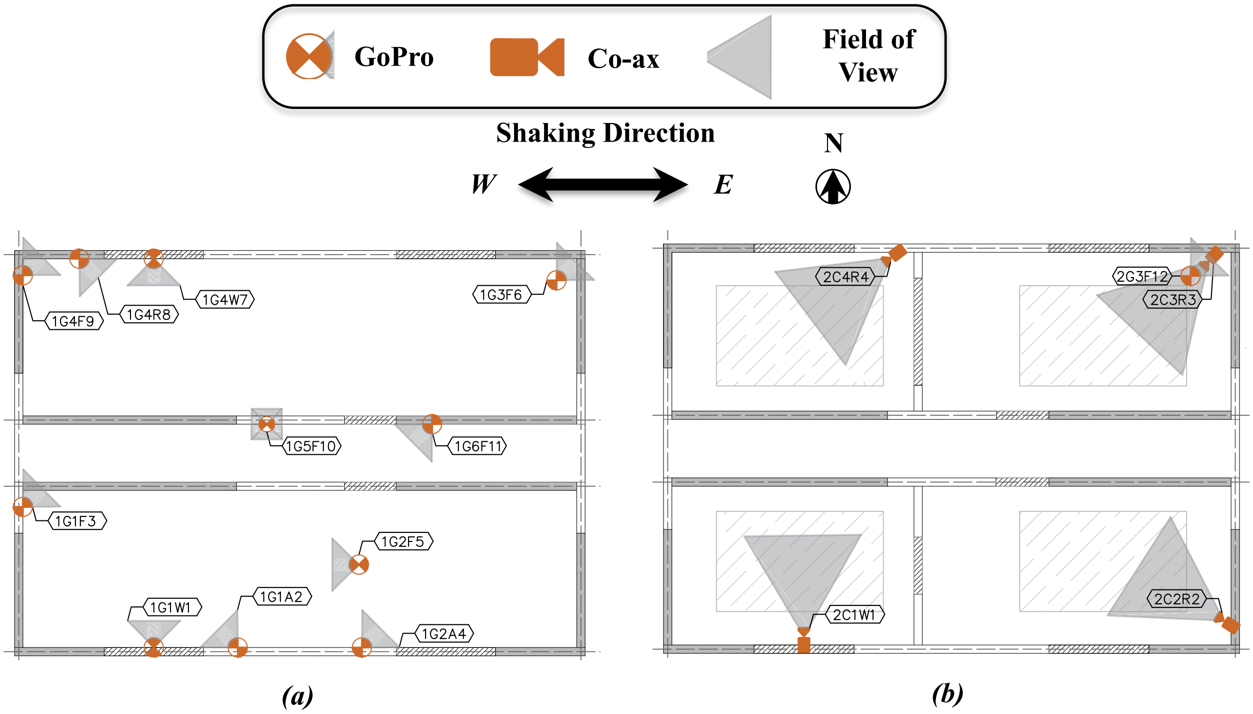

Figure 4.17. Plan layout of video cameras (configuration 2): (a) level 1, and (b) level 2.

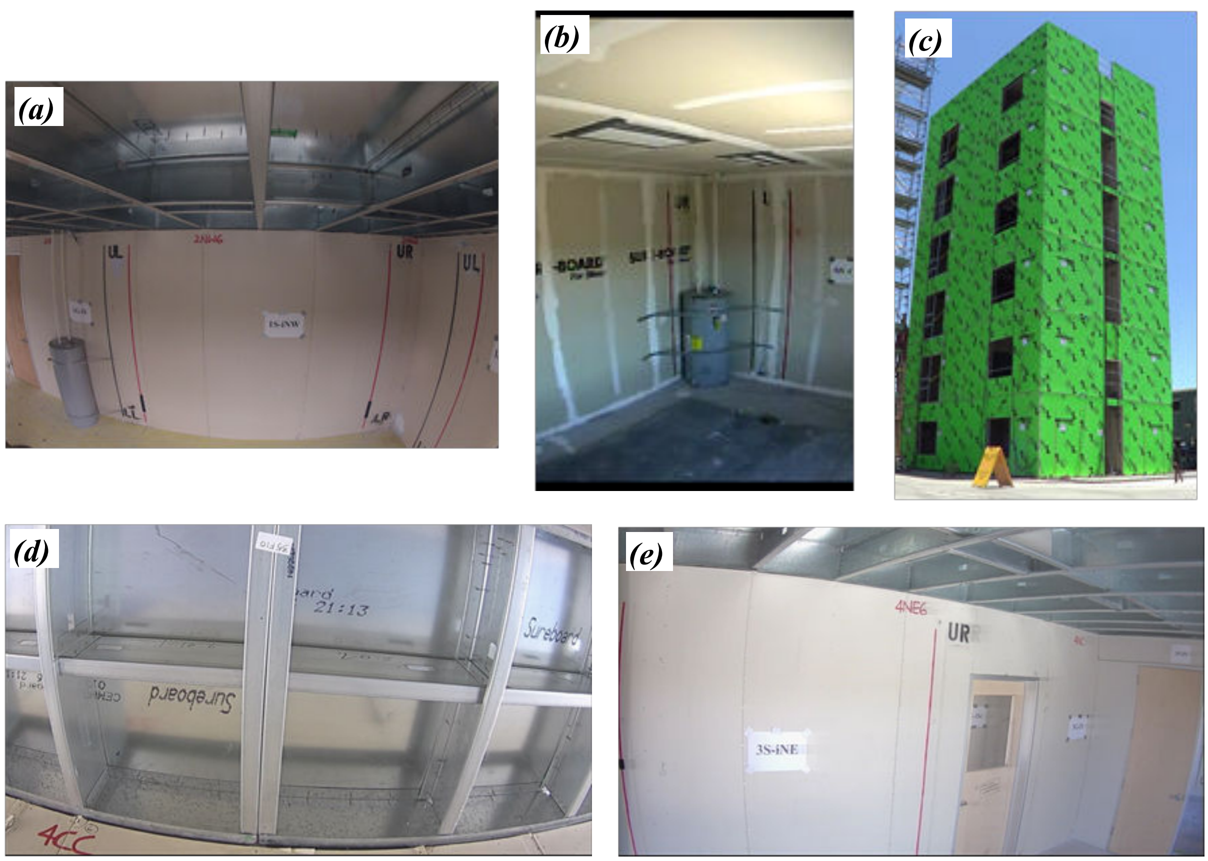

Figure 4.18. Typical camera views: (a) level 1 corridor shear wall, (b) water heater at level 6, (c) building exterior, (d) corridor joist interface at floor 4, (5) level 3 corridor wall.

4.2.3 Global Positioning System (GPS)

GPS system installation and data acquisition was a collaborative effort between the project team and researchers from Scripps Institute of Oceanography at UCSD. A total of five GPS stations were deployed at different locations of the test building during the pre-fire earthquake test sequence: three stations on the roof, namely, at the southwest and northwest corners as well as the approximate center of the roof and one station each at the west end of the corridor on the third and fifth floors. In addition, one static ground reference station was placed approximately 50 m to the west of the building (off the shake table). Figure 4.19 illustrates the plan layout of the roof GPS stations and their support conditions.

The GPS receivers were temporarily removed from the building during the fire test phase and the three roof stations were reinstalled during the post-fire test phase (the mid-level stations were not reinstalled due to the issue related to signal reception). Since it was observed from drone footage that the stations at the two corners of the roof underwent apparent high-frequency vibrations (arguably due to movement at the base of the supports), these two stations were repositioned during the post-fire test phase with modified support conditions (while the station the roof center remained at the same location).

The GPS system provided direct displacement measurements of the building roof at a sampling frequency of 10 Hz. The error of the GPS measurements was about 0.5 cm. Importantly, data collected by GPS system provided reliable measurements for capturing the residual displacements of the test building as well as benchmark results for validating the displacements derived from double integration of the acceleration responses as well as. Additional information regarding the GPS system is available in the report by Goldberg and Bock (2016).

4.2.4 Still Cameras

Photographs were taken during the construction and testing phase by the project research team and industrial collaborators. Photographs taken at various inspection stages formed an image database with systematic documentation of (a) construction progress as well as the as-built details of the structural components (e.g., shear wall framing, floor joists), and (b) physical damage of the building at various stages during the test program.

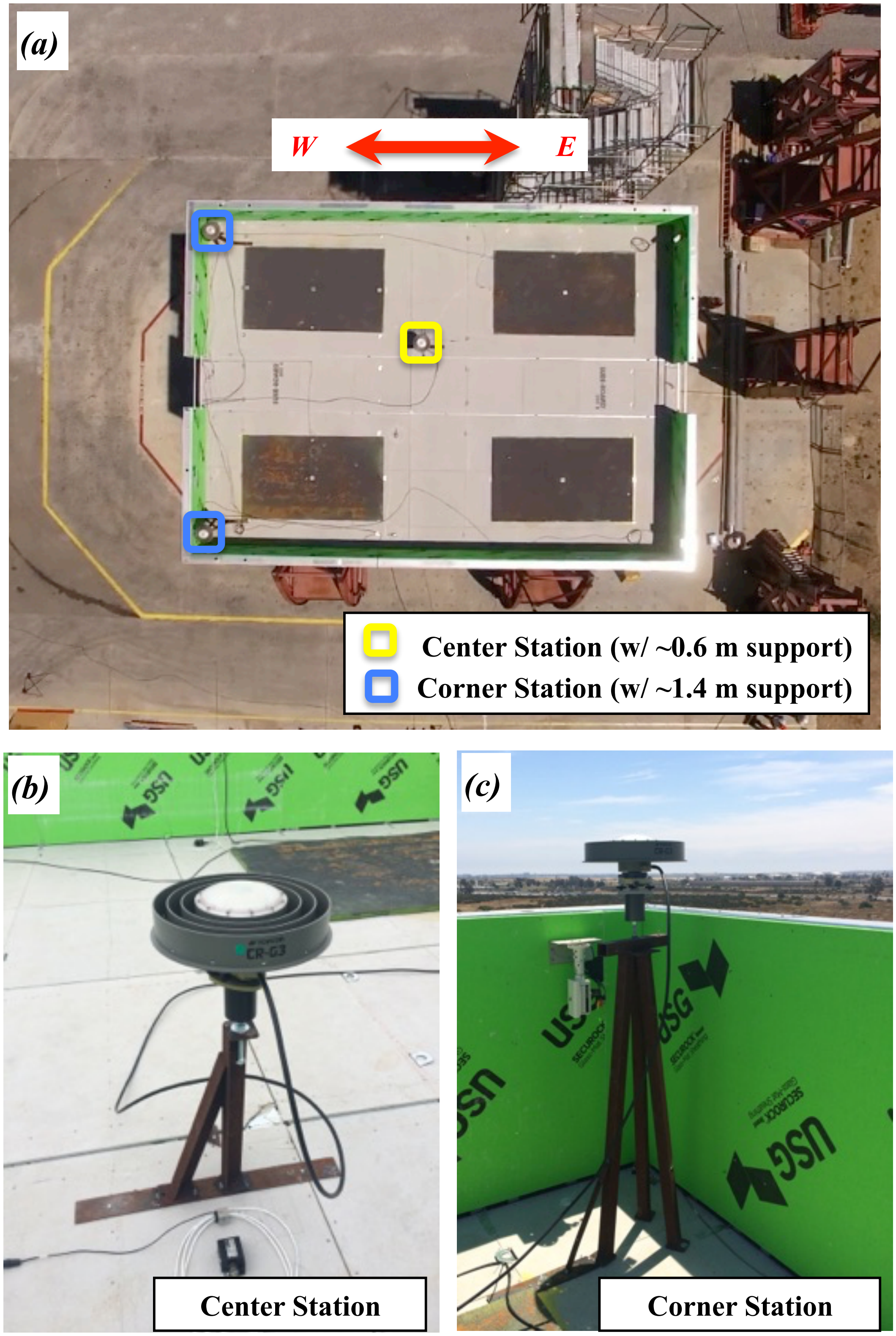

Figure 4.19. GPS monitoring system: (a) roof layout of GPS stations (pre-fire test phase), (b) center station, and (c) corner station.

4.3 Fire Test Phase

During the fire test phase, a portable data acquisition system was deployed on the test building to collect fire test data. The system was placed on the floor below the fire compartment floor for individual tests. Instrumentation consisted of two major sensing systems: (1) analog sensors (thermocouples) to measure the temperature response at various locations inside and outside of the fire compartment, and (2) an array of video cameras deployed in the building interior and exterior to visually capture flame extension, leakage, and smoke propagation.

4.3.1 Temperature Sensors

To measure the temperature response of the fire compartments and adjacent space, the test building was instrumented with a total of 233 thermocouples (Type K thermocouples with 24 gauge wires). The thermocouples were configured in two major forms: a) 9 thermocouple trees (each consisting of 6 thermocouples), and (b) 186 individual thermocouples. During individual fire tests, temperature data were recorded for a minimum of one hour from ignition at a sampling frequency of 1 Hz.

- *Thermocouple trees* were configured by vertically placing the thermocouples on a threaded rod at the desired locations along the height. The rod was mounted to the ceiling joist flange using #8 drywall screws. The thermocouple trees were fire-protected by wrapping 3 mm thick ceramic blankets on the threaded rods. The purpose of thermocouple trees was to measure the compartment temperature profiles along the vertical direction.
- *Individual thermocouples* were deployed all over the compartments at the locations of interest. The locations were decided at the completion of the pre-fire earthquake test sequence when drywall cracks and gaps were fully developed. The thermocouples were intended to measure the temperature propagation in the cracks. Data collected by individual thermocouples were used for understanding the temperature build-up in the stud cavities, joist cavities, and door frames. Excessive temperature at these locations may compromise the strength and stiffness of the structural framing and jeopardize the structural stability of the light-gauge framing systems.

Table 4.5 summarizes the thermocouple instrumentation plan associated with individual fire test. As shown in the table, the four tests conducted at level 2 included a larger amount of thermocouples compared to the two tests at level 6. Since the building sustained more severe damage to the interior gypsum drywalls at level 2, more thermocouples were placed along the cracks or inside of the gaps. In addition, the thermocouple layouts associated with individual fire tests are schematically shown in Figure 4.20 through Figure 4.25, respectively.

Table 4.5. Summary of thermocouple number and location.

Test	Location	TC ID	Number	Location
1	South West Compartment, Level 2	T1 - T5	5	Fire Stop
		T6 - T 10	5	Joint Crack (Window)
		T11 - T13, T15, T19	5	Stud Cavity
		T14, T32 - T35	5	Joist Cavity
		T16 - T18	3	Joint Crack (Wall)
		T20 - T25	6	TC Tree - Crack
		T26 - T31	6	TC Tree - Center
2	South East Compartment, Level 2	T1 - T5	5	Fire Stop
		T6, T18 - T20, T24, T42-T44	8	Joint Crack (Wall)
		T7 - T11, T14, T15	7	Joint Crack (Door)
		T27, T28, T30, T32-T34	6	Joint Crack (Window)
		T12, T13, T16	3	Door Frame Cavity
		T17, T21-T23, T25, T26	6	Stud Cavity
		T29, T31, T35	3	Stud Cavity (Window)
		T51 - T54	4	Joist Cavity
		T36 - T41	6	TC Tree - Crack
		T45 - T50	6	TC Tree - Center
3	North West Compartment, Level 2	T1-T3, T11	4	Joint Crack (Wall)
		T13, T16, T17	3	Stud Cavity
		T10, T14, T18, T25-T28	7	Joist Cavity
		T12, T15	2	Stud Cavity (Window)
		T4-T9	6	TC Tree - Crack
		T19 - T24	6	TC Tree - Center
4	Corridor, Level 2	T7-T9, T16-T21, T34-T37, T42-T56	28	Joint Crack (Wall)
		T10-T15, T38-T41, T57 -T64	18	Joint Crack (Door)
		T65-T68	4	Joist Cavity
		T22-T27	6	TC Tree - Crack
		T1-T6, T28-T33	12	TC Tree - Center
5	South West Compartment, level 6	T13, T26 (SE)	2	Joist Cavity
		T7-T12	6	TC Tree - Crack
		T1-T6	6	TC Tree - Center
6	Corridor, Level 6	T25-T30	6	Joist Cavity
		T1-T4 (NE)	4	Stud Cavity
		T7-T12	6	TC Tree - Crack
		T1-T6, T13-T18, T19-T24	18	TC Tree - Center
TOTAL			**233**	

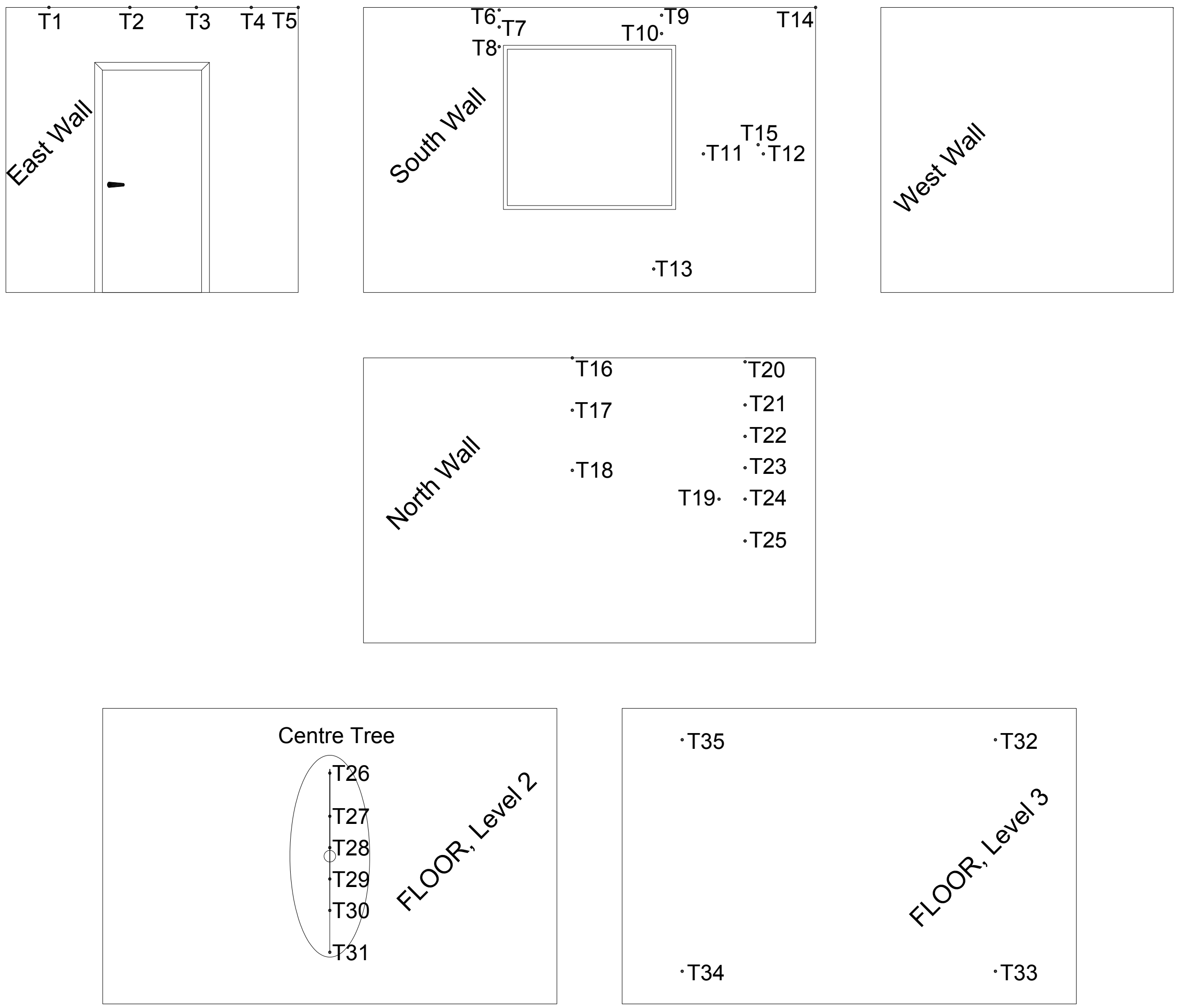

Figure 4.20. Thermocouple layout of level 2 southwest compartment and adjacent space – Fire Test 1.

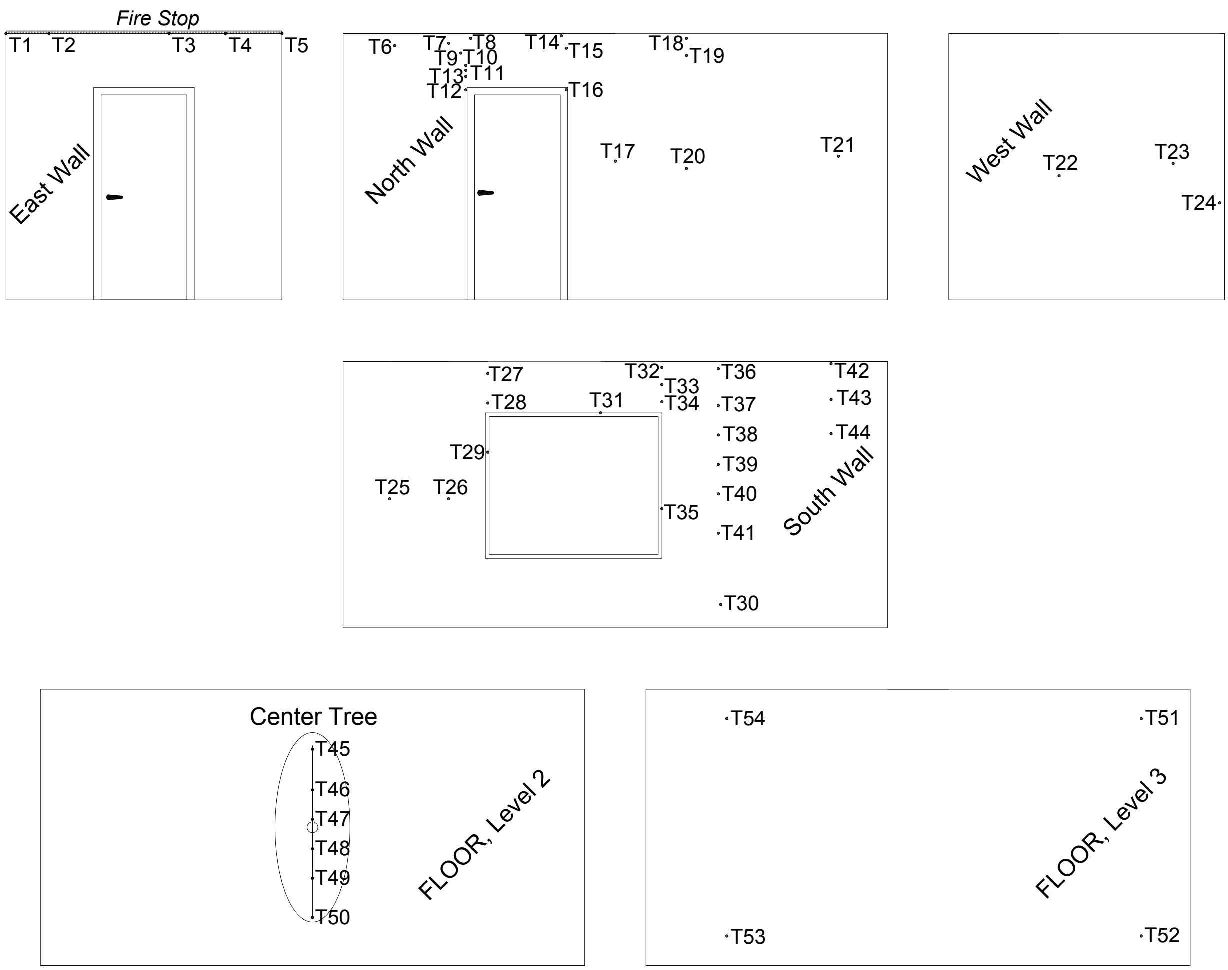

Figure 4.21. Thermocouple layout of level 2 southeast compartment and adjacent space – Fire Test 2.

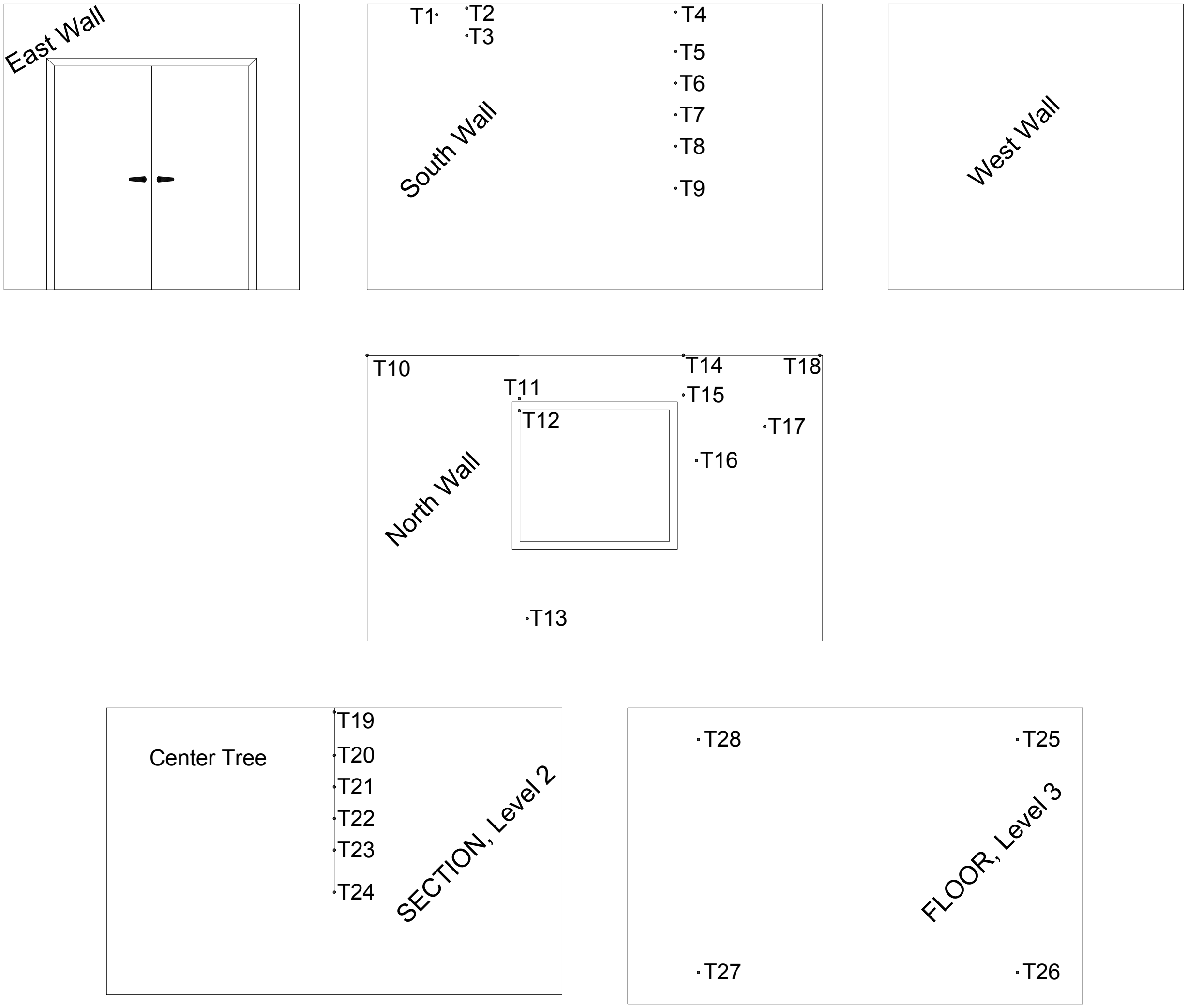

Figure 4.22. Thermocouple layout of level 2 northwest compartment and adjacent space – Fire Test 3.

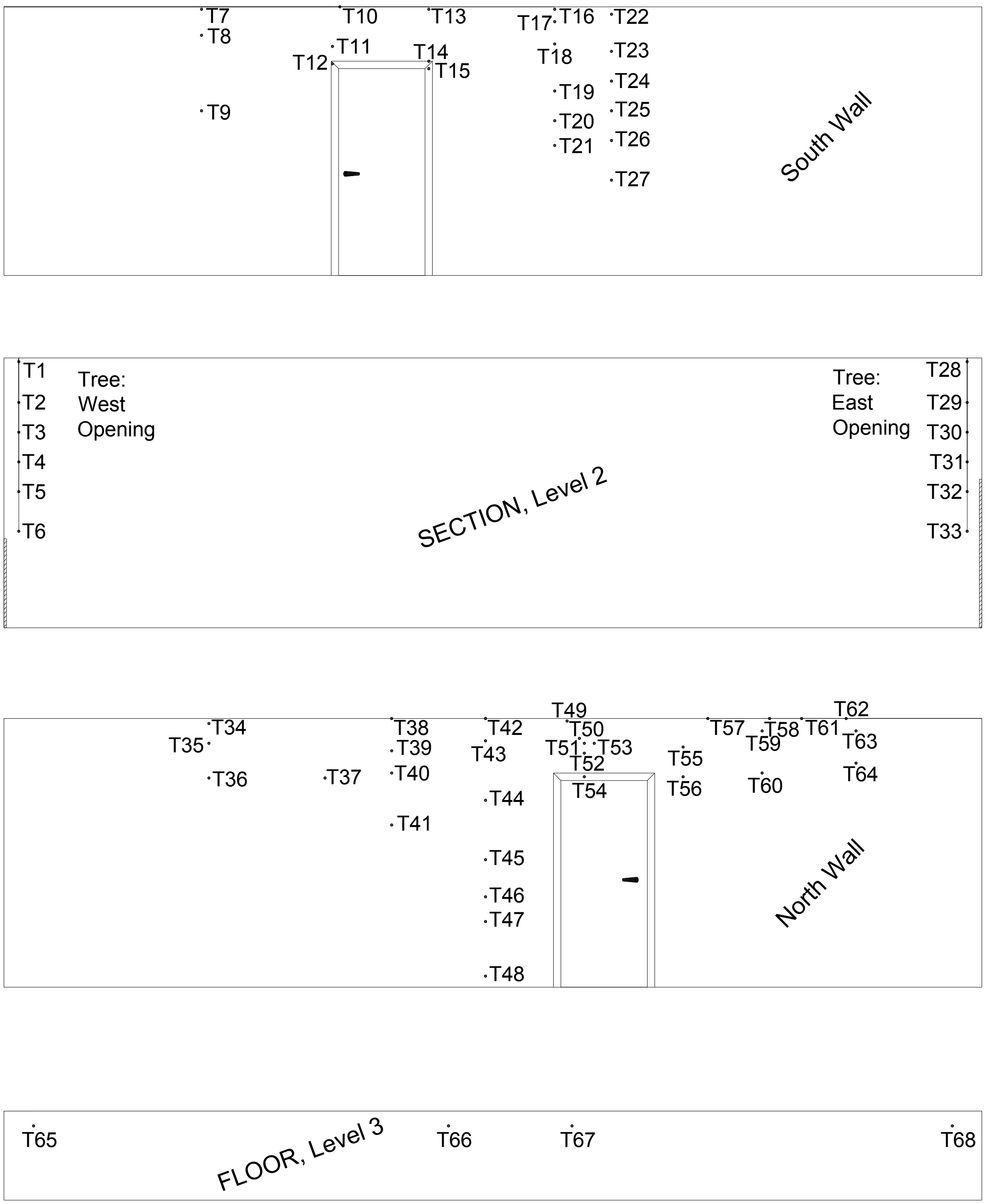

Figure 4.23. Thermocouple layout of level 2 corridor and adjacent space – Fire Test 4.

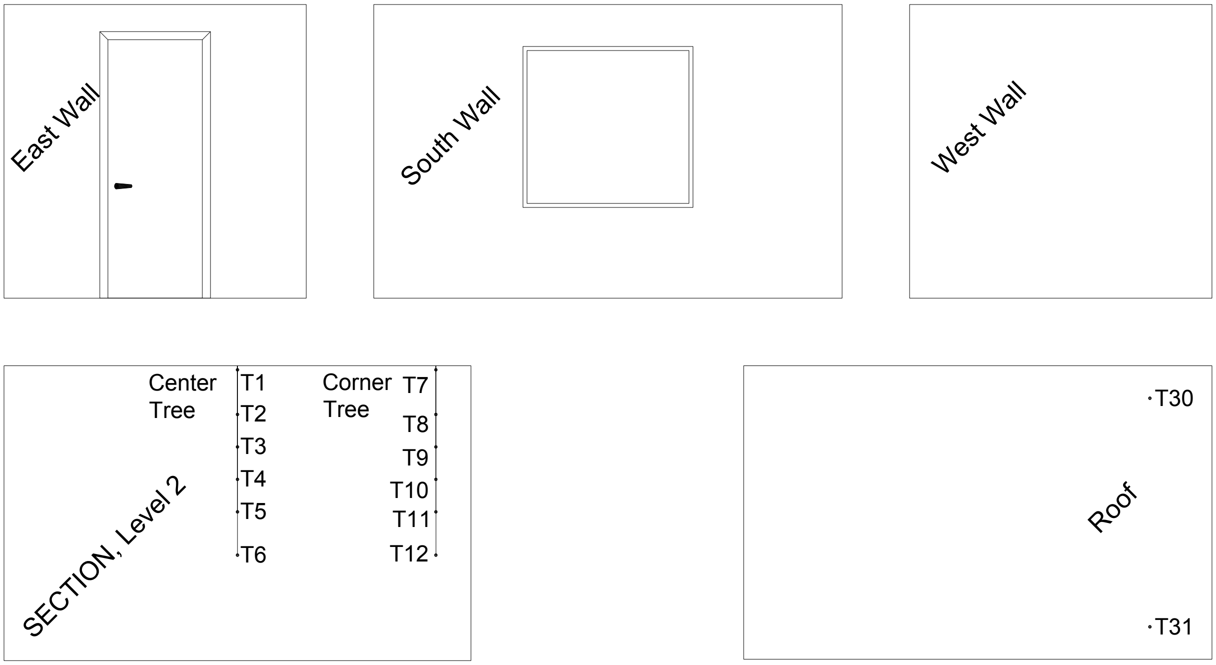

Figure 4.24. Thermocouple layout of level 6 southwest compartment and adjacent space – Fire Test 5.

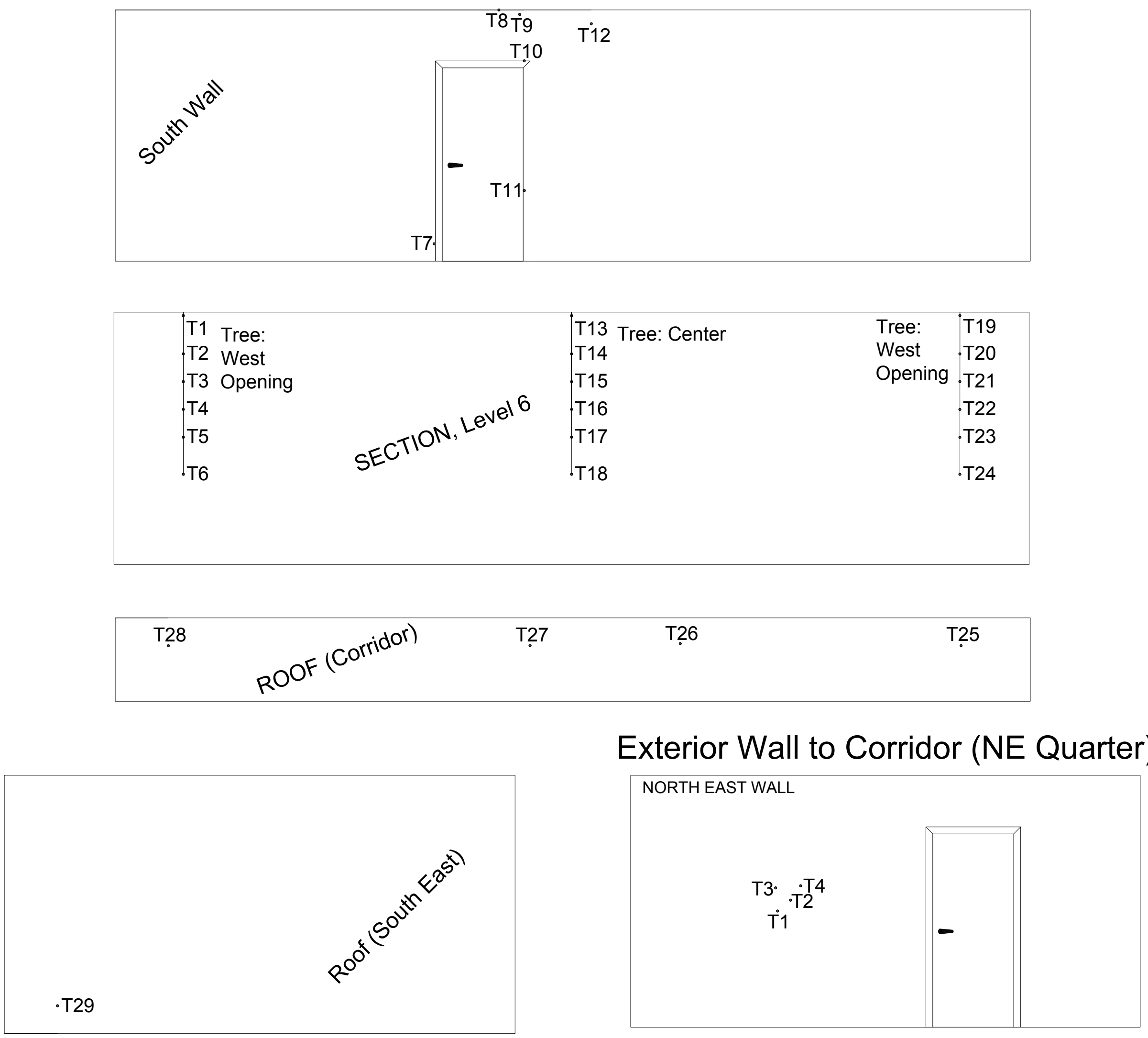

Figure 4.25. Thermocouple layout of level 6 corridor and adjacent space – Fire Test 6.

4.3.2 Video Cameras

Each fire compartment was equipped with a 1080p high-fidelity video camera to record the burning and physical condition of the building interior during the fire tests. The camera was positioned with a field of view on the window openings and fire rated doors. In addition, cameras were installed in the adjacent rooms and the corridor to capture the smoke propagation and the performance of the fire rated doors during the fire tests. In addition, global view cameras were set up on the building exterior to capture the flame extensions through the openings. Table 4.6 summarizes the locations of video cameras in different fire tests as well as their conditions following the fire tests (also refer to Chapter 7 for video cameras locations).

Table 4.6. Video camera locations and their post-test conditions.

Fire Test #	*Camera ID*	*Location*	*Post-test condition*
1	FT1-VC_01	South West Compartment	Destroyed
	FT2-VC_02	South East Compartment	Saved
	FT1-VC_03	Corridor	Saved
	FT1-VC_04	North East Compartment	Saved
	FT1-VC_G	External - South Elevation	Saved
2	FT2-VC_01	South East Compartment	Destroyed
	FT2-VC_02	Corridor	Saved
	FT2-VC_03	North East Compartment	Saved
	FT2-VC_G	Exterior - South Elevation	Saved
3	FT3-VC_01	North West Compartment	Destroyed
	FT3-VC_02	Corridor	Saved
	FT3-VC_03	North East Compartment	Saved
	FT3-VC_G	External - North Elevation	Saved
4	FT4-VC_01	Corridor	Destroyed
	FT4-VC_02	North East Compartment	Saved
	FT4-VC_G-1	External - West Elevation	Saved
	FT4-VC_G-2	Mobile (GoPro)	Saved
5	FT5-VC_01	Corridor	Destroyed
	FT5-VC_02	South East Compartment	Saved
	FT5-VC_03	South West Compartment	Saved
	FT5-VC_04	South West Compartment	Saved
6	FT6-VC_01	South West Compartment	Destroyed
	FT6-VC_02	South East Compartment	Destroyed
	FT6-VC_G	External - South Elevation	Saved

4.3.3 Still Cameras

Periodic images were taken during the fire tests from the building exterior to study the flame characteristics and temporal fire growth (with the focus on side flame extensions). These image data allowed for estimating the flame height and extensions, which may be useful for numerical validation of dynamic fire modeling.

4.3.4 Miscellaneous Data

Other types of data of interest, such as atmospheric temperature, pressure, relative humidity and wind velocity, were collected on individual test dates.

4.4 Remote Sensing Systems

Throughout the test program, unmanned aerial vehicles (UAVs) were employed to collect static and dynamic imagery data using high-resolution on-board cameras. As shown in Table 4.7, a total of 13 videos were recorded during six earthquake tests (EQ4 through EQ9) using three copters, namely, P3P1, P3P2, and SOLO. The metadata of the video cameras are summarized in Table 4.8. The responses of the building were recorded from two strategic viewpoints, including four top-view videos (with building roof in the scene) and five elevation-view videos (with north face of the building in the scene). These videos provide a unique set of imagery data for quantitatively tracking the building dynamic displacements during the earthquakes.

Table 4.7. UAV video footage and the camera view for the earthquake tests.

Test date	*Earthquake test*	*Copter*	*Camera view*
June 15, 2016	EQ4	P3P1	North Side
		P3P2	South Side
	EQ5	P3P1	North Side
		P3P2	Top View
	EQ6	P3P1	North Side
		P3P2	Water Heater
June 17, 2016	EQ7	P3P1	North Side
		P3P2	Top View
July 1, 2016	EQ8	P3P2	North Side
		P3P1	Top View
		SOLO	West Side
	EQ9	P3P2	Top View
		SOLO	Isometric View

Table 4.8. Metadata of the on-board video cameras.

On-board camera	*Manufacturer*	*Model*	*Resolution*	*Sensor size*	*35mm equivalent focal length (mm)*
P3P1	DJI	Phantom 3 Professional	3840x2160	1/2.3"	20
P3P2	DJI	Phantom 3 Professional	3840x2160	1/2.3"	20
SOLO	GoPro	Hero 3 Silver	1920x1080	1/2.3"	21.9

As shown in Table 4.9, still aerial images were also taken at various stages during the construction and test phases using three cameras: P3P1, QX1, and SL1. The metadata of the on-board still cameras are summarized in Table 4.10. These imagery datasets are used to document the building construction progress and surface damage of the building at different stages of the test phase, respectively.

Table 4.9. UAV static image dataset during the construction and test phases.

Phase	*Date*	*Dataset*	*Camera*
Construction phase	2016.04.15	Day 0 (empty table)	QX1
	2016.04.18	Day 1	QX1
	2016.04.19	Day 2	QX1
	2016.04.20	Day 3	QX1
	2016.04.21	Day 4	QX1
	2016.04.22	Day 5	QX1
	2016.04.23	Day 6	QX1
	2016.04.25	Day 7	QX1
	2016.04.26	Day 8	SL1
	2016.04.27	Day 9	SL1
	2016.04.28	Day 10	QX1
Pre-fire earthquake test phase	2016.06.14	post-EQ3 (incomplete)	P3P1
	2016.06.15	post-EQ3	P3P1
		post-EQ4	P3P1
		post-EQ6	P3P1
	2016.06.17	post-EQ6	P3P1
		post-EQ7	P3P1
	2016.06.24	post-EQ7	P3P1
Fire test phase	2016.06.27	post-fire test 1	P3P1
		post-fire test 2	P3P1
	2016.06.28	post-fire test 3	P3P1
		post-fire test 4	P3P1
	2016.06.29	post-fire test 5	P3P1
		post-fire test 6	P3P1
Post-fire earthquake test phase	2016.07.01	post-EQ8	P3P1
		post-EQ9	P3P1
		post-EQ9	P3P1
		Site area	P3P1

Table 4.10. Metadata of the on-board still cameras.

Camera	*Manufacturer*	*Model*	*Resolution (MP)*	*Sensor size*	*35mm equivalent focal length*
P3P1	DJI	Phantom 3 Professional	12	1/2.3"	20
QX1	Sony	QX1	20	APS-C	30
SL1	Canon	EOS Rebel SL1	18	APS-C	16

5 SYSTEM IDENTIFICATION RESULTS

Low-amplitude vibration tests using various excitation sources (e.g., ambient excitations, white noise base excitations) were conducted throughout the construction and the test phases. Using data collected from these low-amplitude vibration tests, this chapter presents a comprehensive system identification study to explore the evolution of modal parameters of the test building (i.e., natural frequencies, damping ratios, and mode shapes) throughout the experimental program. The modal parameters of the building are estimated using frequency-domain and four different time-domain system identification methods. Importantly, the frequency and story stiffness loss of the test building estimated using the vibration data provide quantified damage metrics for assessing the conditions of the test building at various stages during the earthquake and fire test sequence. Agreement between the evolution of the identified modal parameters and the progression of physical damage demonstrates the effectiveness of the vibration-based system identification techniques for structural damage assessment and health monitoring.

5.1 Low-amplitude Vibration Tests

5.1.1 Test Protocol

The vibration tests considered in the system identification study involve white noise (WN) base excitation tests in the construction and test phases as well as ambient vibration (AV) tests in the test phase. The amplitude of WN tests, measured in terms of the root-mean-square (RMS) acceleration of the target base excitation, was selected as either 1.5% g RMS or 3.0% g RMS (except one with an amplitude of 5.0% g RMS on the first test date of the construction phase). For the purpose of brevity, the WN tests are hereafter referred to as 1.5% g or 3.0% g WN tests. All the WN tests, except those conducted on the first test date of the construction phase (with a duration of 240 seconds), had a duration of 180 seconds. In contrast, the duration of the AV tests was much longer than those of the WN tests, with typical data length of 1200-1440 seconds.

Construction Phase

WN tests were performed on three select dates following the completion of the structural skeleton erection. As shown in Table 5.1, the test building contained a total of five states (denoted as C1–C5) at the three test dates, each associated with WN tests performed at amplitude of both 1.5% g and 3.0% g. The different states are characterized by varied roof mass plate layouts and interior construction aspects (e.g., attachment condition of the interior gypsum wall panels, partition wall installation state, and opened or closed doors). The roof mass plates were temporarily configured in non-symmetric layouts at states C1 and C2 to explore their effect on the dynamic characteristics of the building, while the layout at states C3–C5 represented the baseline configuration with a symmetric mass distribution (one mass plate at each quadrant). It is noted that the last two states during the construction phase (C4 and C5) represented the building at the completion of all construction activities. Therefore, these two states were essentially identical with the initial (reference) state defined as the beginning of the test phase (see discussions in the next section).

Table 5.1. White noise tests performed during the construction phase and the associated building characteristics (note that 2× = double mass plate, 1× = single mass plate).

Date	*State*	*Interior construction status*	*Roof mass layout*
May 5, 2016	C1	minimally attached interior gypsum; partition wall installation partially completed; doors not installed	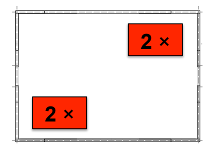
May 16, 2016	C2	minimally attached interior gypsum; partition wall installation partially completed; doors partially installed	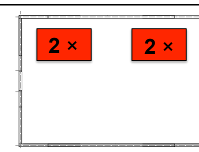
	C3		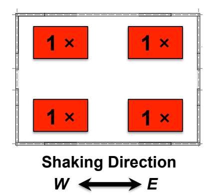
June 9, 2016	C4	fully attached interior gypsum; partition wall installation completed; all doors open	
	C5	fully attached interior gypsum; partition wall installation completed; all doors closed	

Test Phase

Figure 5.1 illustrates the timeline of the low-amplitude vibration test sequence throughout the test phase. A total of eleven states (S0–S10) are defined over the timeline, each corresponding to a specific damage condition of the test building. In addition, the availability of the low-amplitude vibration data recorded by different data monitoring systems at each state is annotated by different symbols (see detailed discussions in the following section). It is noted that state S0 is defined as the reference state for comparing the evolution of the modal parameters at all subsequent states (i.e., S1 through S10). It is noted that states S3 and S6 appear twice on different test dates, since no damage occurred between the end of one test date and the beginning of following test date. The WN tests were conducted before and after each earthquake test except at state S10 due to the severity of building damage. In contrast, the AV tests occurred at only four key stages throughout the test phase, namely, the beginning and the end of the pre-fire (states S1 and S7) as well as the post-fire earthquake test phase (states S8 and S10). Additional details regarding the vibration test protocol are available in Appendix C.

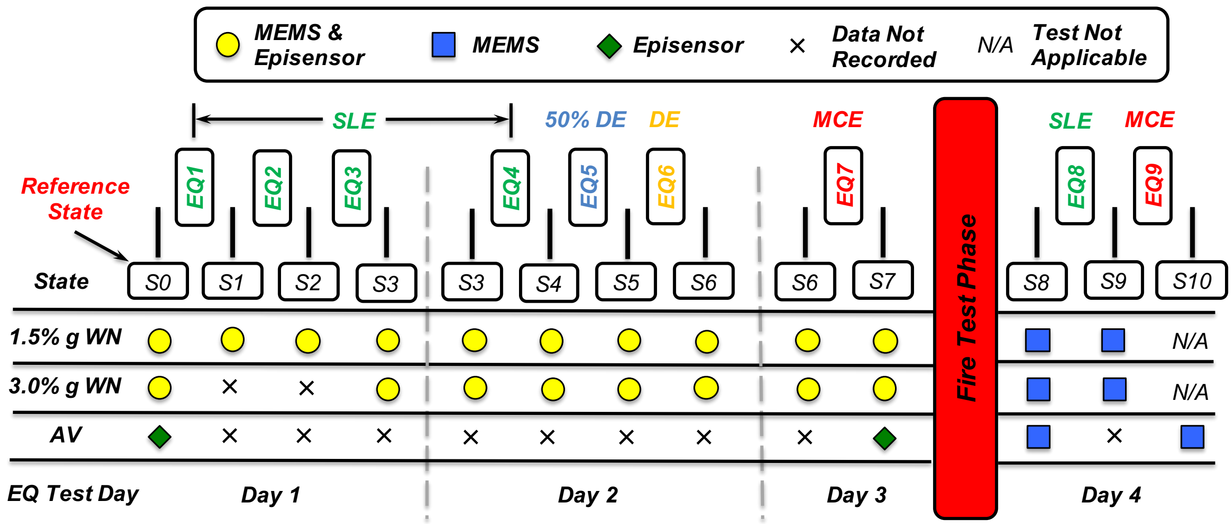

Figure 5.1. Timeline of low-amplitude vibration test protocol during the test phase.

5.1.2 Instrumentation

The floor accelerations of the building were measured by two separate monitoring systems: (1) a dense array of uniaxial MEMS accelerometers (Model 4000A) sampling data at a frequency of 240 Hz (Figure 5.2a), and (2) a relatively sparse array of uniaxial Kinemetric force balance accelerometers (Model ES-U2) sampling data at a frequency of 200 Hz (Figure 5.2b). The MEMS accelerometers were distributed at the four corners and two corridor ends at all floors as well as the table platen (the first floor), although the sensor numbers varied at different stages during the construction and test phase (ranged between 25 accelerometers at the beginning of the construction phase and 68 accelerometers at the test phase). In addition, the MEMS accelerometers had a measurement range of ±10 g and frequency bandwidth of 0–350 Hz. Accelerations recorded by the MEMS system were digitized using 16-bit analog-to-digital converters, resulting in a quantization noise ~4×10^{-4} g.

The Kinematic system consisted of only three accelerometers (two in the longitudinal direction and one in the transverse direction) at each of four select floors (floor 2, 4, 6, and roof) excluding the table platen (12 accelerometers in total). It was deployed to the building only at the pre-fire earthquake test phase. Different from the MEMS system, the Kinemetric accelerometers had a measurement range of ±4 g and frequency bandwidth of 0–200 Hz. Accelerations recorded by the Kinemetric system were digitized using 24-bit analog-to-digital converters, resulting in a quantization noise $<1\times10^{-6}$ g that were much smaller than that of the MEMS system. Additional details regarding the instrumentation plans of the two different accelerometer systems are available in Appendix E.

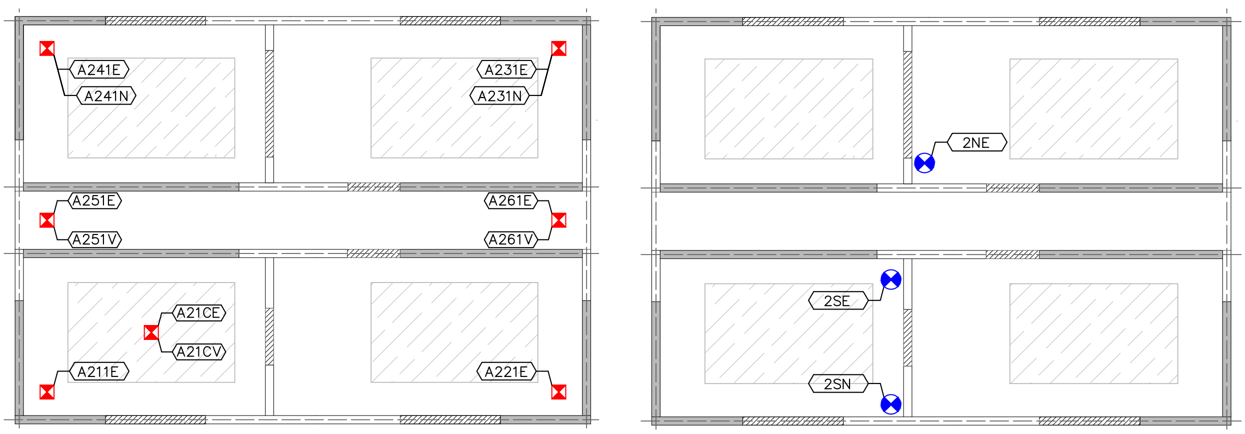

Figure 5.2. Accelerometer plan layout: (a) *MEMS array* (typical of all floors including roof), and (b) *Kinemetric array* (typical of floor 2, 4, 6 and roof).

WN data were collected by the MEMS system at all five states (C1–C5) during the construction phase as well as all except the last states (S0–S9) during the test phase (see Figure 5.1). The Kinemetric system also collected WN data at the pre-fire earthquake test phase (S0–S7), however no accelerometers were installed on the table platen to record the WN base excitations. As a result, WN data collected by the MEMS system are considered as the primary dataset due to its completeness availability of WN input excitations and consistency (i.e. availability throughout the construction and test phases). In addition, AV data were collected by the Kinemetric system during the pre-fire earthquake test phase (states S1 and S7) and by the MEMS system during the post-fire earthquake test phase (states S8 and S10). It is noted that the AV data collected at state S10 provides the only dataset for identifying the modal characteristics of the building at its final state, since conducting WN base excitation tests at this state was deemed unsafe due to severity of damage sustained by the building.

5.1.3 Accleration Response

To demonstrate the time- and frequency-domain characteristics of the WN input excitations, Figure 5.3 presents the acceleration histories of the shake table platen recorded during the WN test at state S0 (reference state) as well as the associated power spectral densities (PSDs). The PSD is estimated using the Welch's method (Welch, 1967), in which the acceleration (with a duration of 3 minutes) is divided into 20 equal segments with a 50% overlap. Since the input excitation was applied only along the longitudinal direction, the amplitude of the table acceleration in transverse directions was significantly smaller (about 5%) than its longitudinal counterpart. It is noted that the lack of comparable amplitudes of the building response during the WN tests resulted in very low participation of the building transverse vibration and tends to pose difficulties for identifying the transverse modes of the building.

Comparison of the PSDs indicates that while the input excitation in the transverse direction remained broadband over the frequency range of interest (i.e., 0.25–25 Hz), its longitudinal component contained a resonance peak at around 10 Hz, due to the oil column resonance effect of the shake table hydraulic system (typical of all WN input excitations throughout the test program). This effect was also reported in previous system identification studies on full-scale structures tested on the same experimental facility (Moaveni et al., 2011; Astroza et al., 2016).

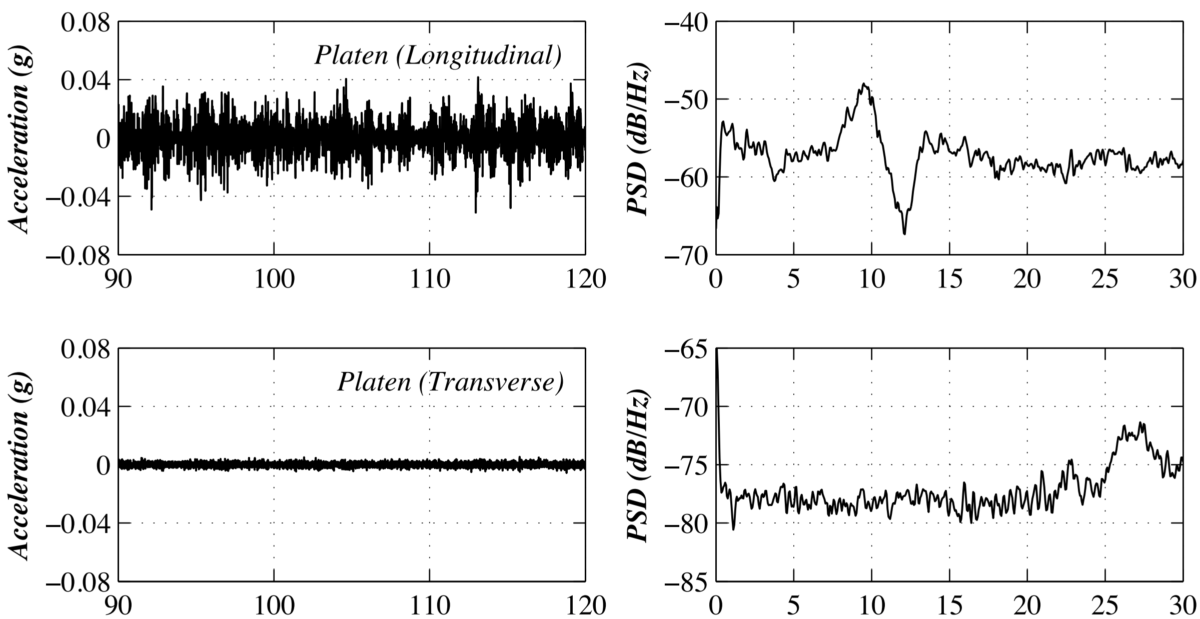

Figure 5.3. Table platen acceleration histories and associated power spectral densities (PSDs) at the reference state (S0) during the 1.5% g white noise (WN) test (recorded by MEMS system).

Figure 5.4 compares the roof acceleration time histories of the building recorded during the WN and AV tests at state S0 (reference state) as well as the associated PSDs estimated using the Welch's method. Since the WN excitation was applied along the longitudinal axis of the building, the amplitude of the transverse acceleration was significantly smaller than (as low as 5%) its longitudinal counterpart (Figure 5.4a). The PSD indicates that the dominated spectral peaks of both the longitudinal and transverse responses were associated with the longitudinal and torsional vibration of the building, while the spectral peaks related to the transverse vibration are barely observable.

The acceleration responses of the building during the AV test (Figure 5.4b) differed from those of the WN test in several aspects: (1) smaller amplitude in both the longitudinal and transverse directions (about two orders of magnitude lower than the longitudinal building responses during the WN tests), (2) comparable amplitude in the two directions, and (3) longer duration of the recorded data (10 minutes or longer for AV tests compared to 3 minutes for WN tests). Due to the comparable amplitude of acceleration responses in the longitudinal and transverse directions, the spectral peaks of PSD in the two directions are associated with apparently distinct frequencies. In addition, the spectral peaks estimated from the AV data are characterized by sharper peak amplitude and narrower bandwidth compared to those of the WN tests.

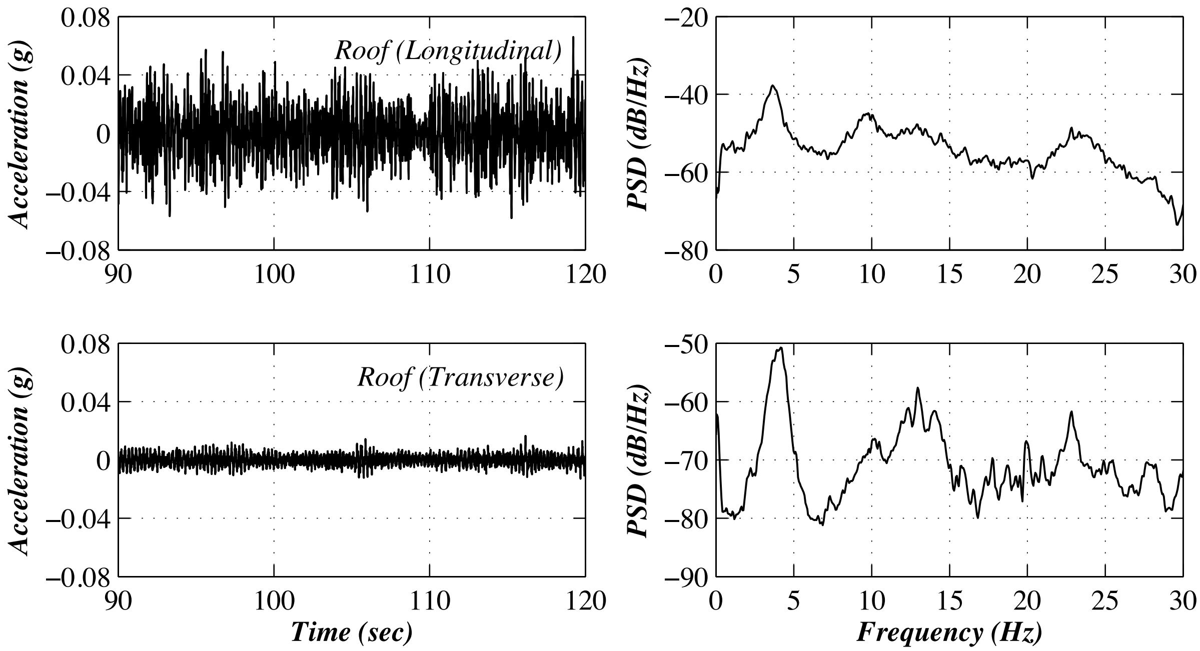

(a)

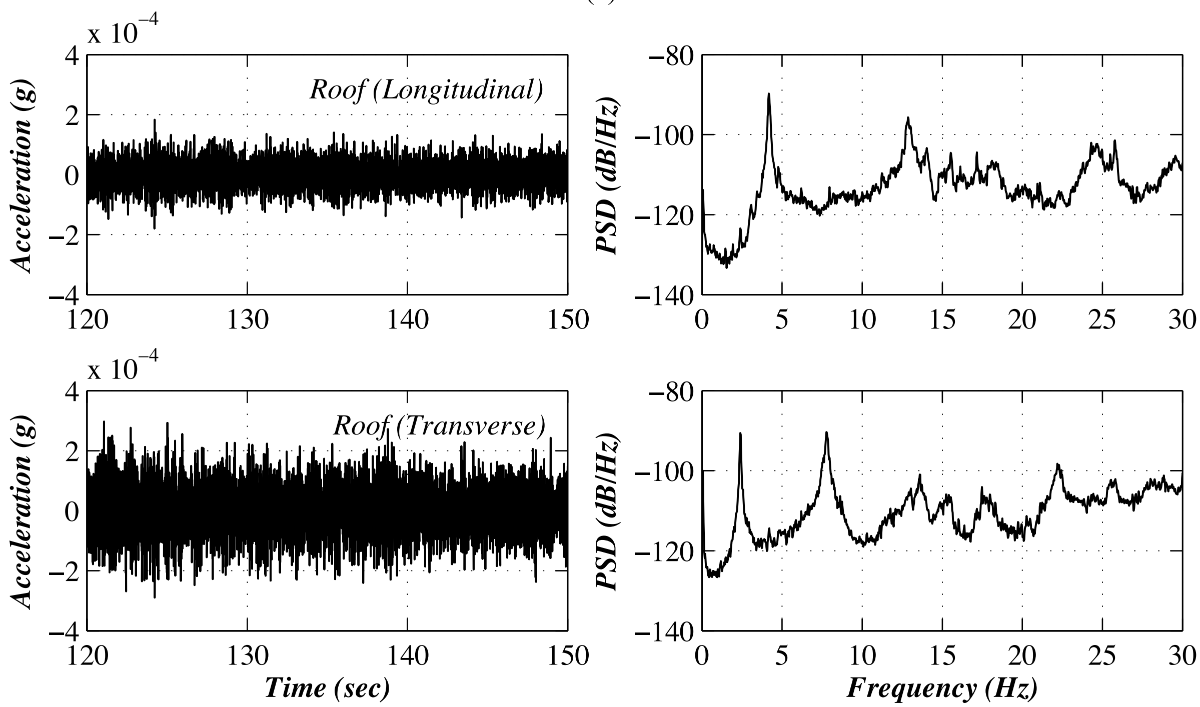

(b)

Figure 5.4. Roof acceleration time histories and the associated power spectral densities (PSDs) at the reference state (S0): (a) 1.5% g white noise (WN) test (recorded by MEMS system), and (b) ambient vibration (AV) test (recorded by Kenemetric system)

5.2 Frequency-Domain Analysis

In the frequency-domain method, the test building is considered as a single-input single-output (SISO) system. The absolute longitudinal acceleration of the table platen is taken as input, whereas the averaged (e.g., longitudinal and transverse directions) or resultant (torsional direction taken as the differential between two channels) accelerations of the roof are considered as output. Frequency-domain identification of the building modal parameters involves: (1) estimating the frequency response function (FRF), also referred to as transfer function, using the input (table platen) and output (roof) accelerations, and (2) extracting the modal parameters by fitting the estimated FRF using the Rational Fraction Polynomial method (Richardson and Formenti, 1982).

The FRF $H(f)$ is estimated as the quotient of cross power spectral density of the input and output over the auto power spectral density of the input:

$$H(f) = \frac{S_{xy}(f)}{S_{xx}(f)} \qquad \text{Eq. 5.1}$$

where $S_{xy}(f)$ is the cross power spectral density of the input and output, and $S_{xx}(f)$ is the auto power spectral density of the input. These spectral densities are both estimated using the Welch's method (Welch, 1967), which involves spectral averaging to mitigate the effect of noise and Hanning windowing to reduce the effect of spectral leakage.

Figure 5.5 presents the FRFs identified from the 1.5% g WN test at *State S0* (reference state). Each row presents the amplitude and phase of the FRF associated with the output accelerations in the three directions (i.e., longitudinal, transverse, and torsional). The FRF associated with the roof longitudinal response (first row) contains three apparent spectral peaks (i.e., 3.5~4 Hz, 12~13 Hz, and 22~24 Hz), since the phase plot at each of these frequency ranges is characterized with a 90-degree phase shift. These peaks correspond to the frequencies of the first three vibration modes in the longitudinal direction. Conversely, since the transverse and torsional building responses were very low in amplitude as a result of the unidirectional input excitations, identification of the vibration modes in these directions (second and third rows) becomes difficult absent apparent spectral peaks other than those associated with the longitudinal vibrations. In this regard, the primary purpose of the frequency domain identification is to extract the longitudinal vibration modes of the building and provide useful information for more rigorous time-domain identification techniques as discussed later in this chapter.

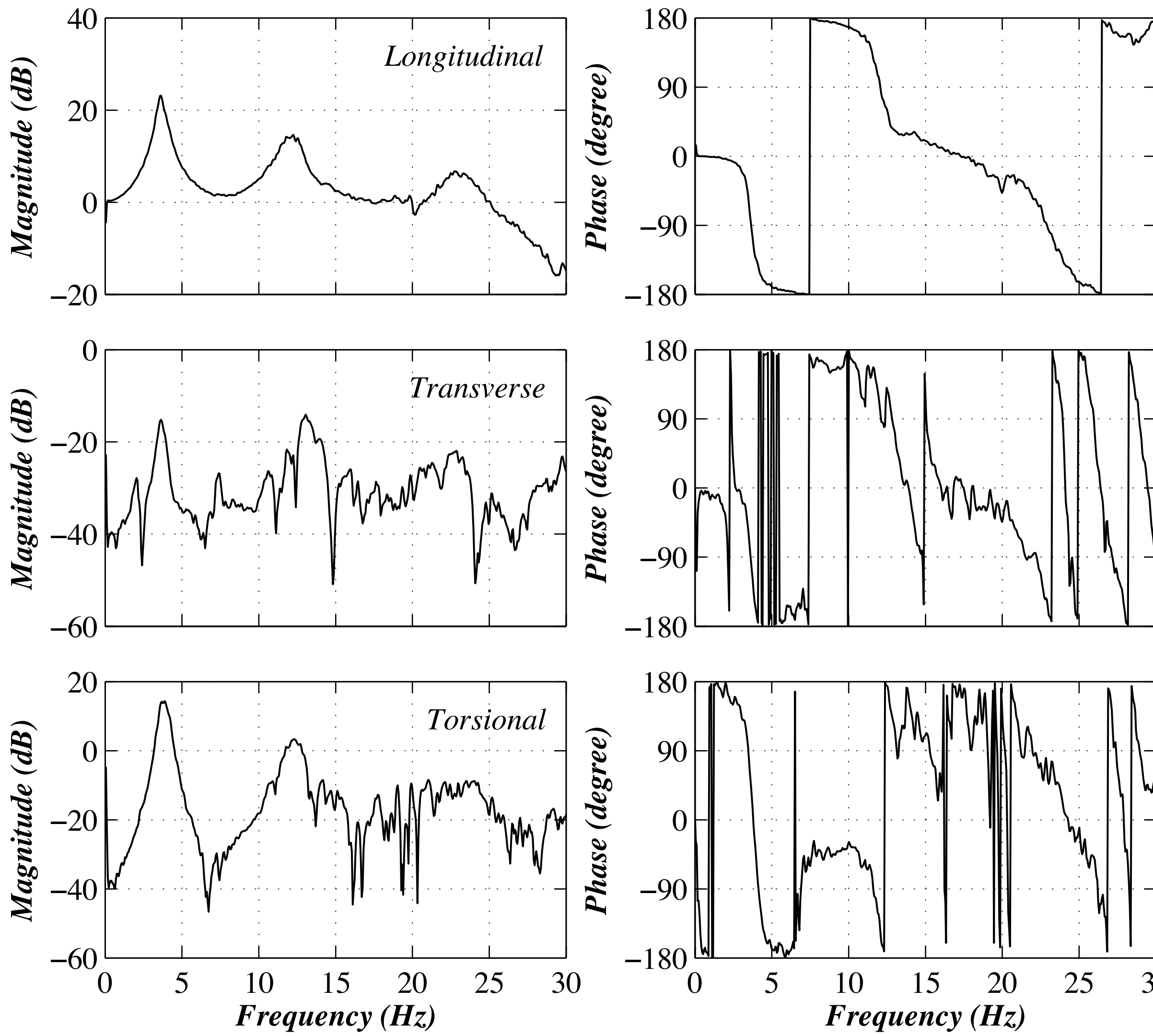

Figure 5.5. Amplitudes and phase response of the FRFs estimated using the 1.5% g white noise (WN) test at S0 (reference state).

Construction Phase

Table 5.2 summarizes the natural frequencies and damping ratios of the building longitudinal vibration modes identified from the WN data associated with the five configurations (C1–C5) in the construction phase. The variations in different configurations involved roof mass plate layout, interior gypsum attachment and door installation conditions, and etc. (refer to details in Table 5.1). Comparison of the results for the WN input excitations at the two distinct amplitude levels (1.5% g and 3.0% g) clearly demonstrates the amplitude dependency of the modal parameters. The natural frequencies reduced by about 10% and the damping ratios increased by as much as 30~50% as the amplitude of the input excitations increased from 1.5% g to 3.0% g.

Table 5.2. Natrual frequencies and damping ratios of the building longitudinal modes during the construction phase.

Test date	*Building configuration*	*RMS Amp.(g)*	*Natural frequency (Hz)*			*Damping ratio (%)*		
			1-L	*2-L*	*3-L*	*1-L*	*2-L*	*3-L*
May 5, 2016	C1	1.5%	3.51	11.42	22.41	6.2	5.7	5.1
		3.0%	3.28	10.90	n/a	8.8	6.9	n/a
		5.0%	2.99	10.37	n/a	10.7	8.2	n/a
May 16, 2016	C2	1.5%	3.63	11.57	22.47	5.6	5.6	5.0
		3.0%	3.28	10.92	21.65	7.6	6.8	5.8
	C3	1.5%	3.54	11.75	22.44	6.5	5.7	5.1
		3.0%	3.28	10.90	21.67	7.8	6.9	5.8
June 9, 2016	C4	1.5%	3.93	12.54	23.91	4.2	5.0	3.7
		3.0%	3.65	12.07	23.58	6.0	6.2	4.3
	C5	1.5%	3.93	12.54	23.52	5.1	4.5	3.6
		3.0%	3.63	12.11	22.70	6.6	5.6	4.3

Notes: duration of the white noise test was 4 minutes for C1 and 3 minutes for all the remaining configurations; n/a indicates no apparent spectral peak.

In comparison with C1 (completion of the structural skeleton erection), the natural frequencies of the building increased by about 10% at the completion of interior construction (C4 and C5). The increase of natural frequencies was primarily attributed to the stiffness contribution from the interior gypsum sheathing, since these gypsum panels were fully attached to the shear walls between May 18 and 23, 2016). In contrast, the natural frequencies at the first three configurations (C1–C3) differed only slightly (< 3%), indicating that the variation of the roof mass layout did not significantly modify the building dynamic characteristics. Additionally, the door conditions (C4 with all doors open vs. and C5 with all doors closed) barely affected the modal characteristics of the building, since the modal properties remained essentially identical under the two configurations.

Test Phase

Table 5.3 summarizes the natural frequencies and damping ratios of the building longitudinal vibration modes from the WN test data during the test phase. To demonstrate the effect of damage progression on the modal characteristics of the test building, Figure 5.6 illustrates the FRFs between the longitudinal roof (output) and table platen (input) accelerations under the WN tests at four select states (S0, S3, S6, and S7) during the pre-fire test phase. Since the building sustained only limited damage (<0.1% PRDR) at the serviceability level test sequence (states S1 and S3), the FRF contained three distinct spectral peaks associated with the first three longitudinal vibration modes. The progression of structural damage during the design level (EQ6 with a PRDR of 0.7%) and MCE level (EQ7 with a PRDR of 1.5%) tests resulted in remarkable frequency shift (reduction) of the spectral peaks as well as smaller magnitude and broader bandwidth for these peaks (indicative of increased damping ratios). For the 1.5% g WN tests, the spectral peak of the first longitudinal mode shifted from ~4 Hz at state S0 to less than 2 Hz at state S7, while its magnitude decreased from ~25 dB at state S0 to ~15 dB at state S7. It is also noted that the spectral peaks of the higher modes became less identifiable at states S6 and S7 due to the progression of structural damage. However, the natural frequencies the building did not underwent further reduction following the fire tests (between S7 and S8), indicating no appreciable loss of building stiffness during the fire tests. This may be explained by the fact that the impact of fire damage on the building stiffness did not exceed that of the seismic damage induced by the pre-fire earthquake sequence.

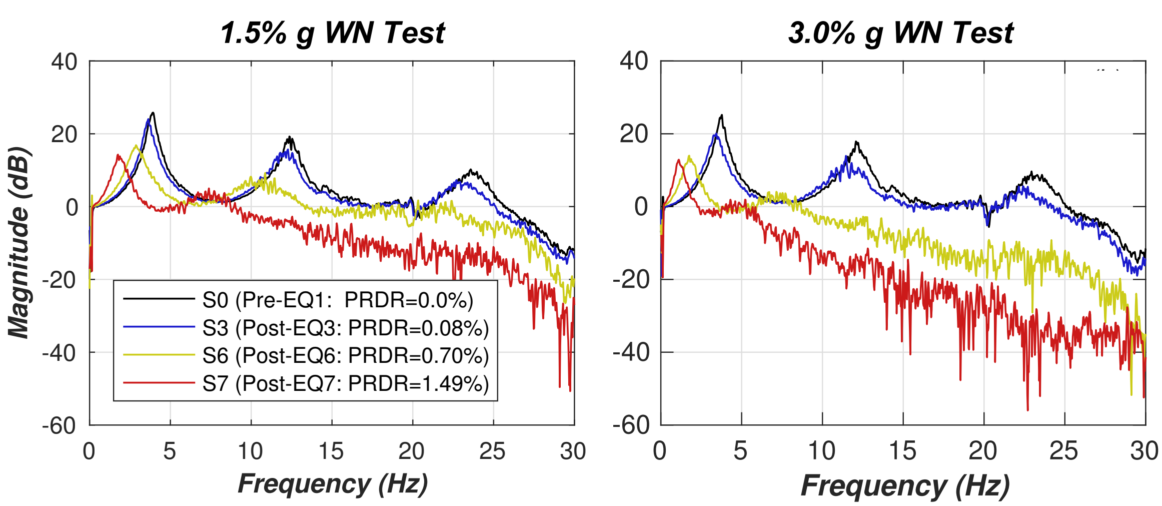

Figure 5.6. Magnitude of frequency response functions (FRFs) under the white noise (WN) tests at four select states of the test phase.

Table 5.3. Natural frequencies and damping ratios of the longitudinal vibration modes during the test phase.

Test date	*Building state*	*RMS Amp.(g)*	*Natural frequency (Hz)*			*Damping ratio (%)*		
			1-L	*2-L*	*3-L*	*1-L*	*2-L*	*3-L*
June 13, 2016	S0 (Pre-EQ1)	1.5%	3.9	12.4	23.6	5.2	4.3	3.7
		3.0%	3.6	12.3	22.7	6.9	5.8	4.4
	S3 (Post-EQ3)	1.5%	3.7	12.1	23.0	6.2	4.9	3.8
		3.0%	3.4	11.5	22.4	9.6	6.9	4.6
June 15, 2016	S3 (Pre-EQ4)	1.5%	3.8	12.2	23.6	6.2	4.7	3.7
		3.0%	3.4	11.5	22.4	9.2	6.8	4.7
	S4 (Post-EQ4)	1.5%	3.7	12.1	22.9	6.5	4.7	3.9
		3.0%	3.4	11.5	22.4	10.0	7.1	4.7
	S5 (Post-EQ5)	1.5%	3.3	11.5	22.4	9.4	6.6	4.5
		3.0%	2.8	10.9	n/a	13.6	9.6	n/a
	S6 (Post-EQ6)	1.5%	2.2	8.6	n/a	14.7	10.8	n/a
		3.0%	1.8	7.1	n/a	19.0	15.5	n/a
June 17, 2016	S6 (Pre-EQ7)	1.5%	2.2	8.6	18.6	13.9	10.7	8.4
		3.0%	1.8	7.4	n/a	17.7	14.9	n/a
	S7 (Post-EQ7)	1.5%	1.6	n/a	n/a	20.1	n/a	n/a
		3.0%	1.1	n/a	n/a	20.6	n/a	n/a
Fire test phase (June 27-29, 2016)								
July 1, 2016	S8 (Pre-EQ8)	1.5% g	1.6	6.7	n/a	17.5	15.1	n/a
		3.0% g	1.1	n/a	n/a	17.9	n/a	n/a
	S9 (Post-EQ8)	1.5% g	1.5	6.0	n/a	16.7	15.3	n/a
		3.0% g	1.1	n/a	n/a	18.3	n/a	n/a

Notes: duration of all white noise tests was 3 minutes; n/a indicates no apparent spectral peak.

5.3 Time-Domain Analysis

5.3.1 Methods and Procedures

In the time-domain system identification study, the modal parameters (i.e., natural frequencies, damping ratios, and mode shapes) of the test building during the low-amplitude vibration tests are analyzed using two input-output methods, (1) Deterministic-Stochastic Subspace Identification (DSI) method (Van Overschee and De Moor, 1996) and (2) Observer/Kalman Filter Identification combined with Eigensystem Realization Algorithm (OKID-ERA) method (Juang and Pappa, 1985; Juang et. al., 1995), as well as two output-only methods, (3) Data-

Driven Stochastic Subspace Identification (SSI-DATA) method (Van Overschee and De Moor, 1996; Peeters and De Roeck, 2001) and (4) multiple-reference Natural Excitation Technique combined with Eigensystem Realization Algorithm (NExT-ERA) method (James et. al., 1993). Each of these time-domain methods considers the test building as a linear time-invariant (LTI) state space model, in which all sources of energy dissipation are represented by linear viscous damping. In addition, these methods assume the excitation sources of the vibration tests to be broadband stationary excitations. The use of different system identification methods provides intra-method and inter-method comparisons to evaluate the consistency of the estimated modal parameters as well as the robustness of these methods when their underlying assumptions are not strictly satisfied (e.g., linear time-invariant system, broadband excitation, stationary response). Discussion of the theoretical background and implementation details of these system identification methods is outside of the scope of this paper. Interested readers are referred to relevant literature for comprehensive review of the time-domain identification methods.

The use of input-output or output-only methods depends on the type of vibration test as well as data collected by specific monitoring system. The output-only methods are used in conjunction with all AV data and WN data collected by the Kenemetric system, since the system input was either unknown or not recorded in these data. In contrast, the input-output methods are used in conjunction with WN data collected by the MEMS system. Specifically, the system input is taken as the averaged longitudinal acceleration of the table platen, whereas the system output involves two longitudinal accelerations (northwest and southwest corners) and two transverse accelerations (northwest and northeast corners) at all floors of the building from the second floor to the roof, resulting in a total of 24 output channels. In the data pre-processing procedures, the raw acceleration response recorded by each channel is first decimated to 80 Hz to reduce the computational costs and subsequently filtered using a 4th order band-pass Butterworth filter (with cut-off frequencies at 0.25 Hz and 25 Hz). It is noted that the Nyquist frequency of the processed data of 40 Hz remains sufficiently large to involve all the vibration modes that contribute noticeably to the building response.

To distinguish structural modes from spurious (mathematical) modes in the SID results, stability diagrams are employed to examine the consistency of identified modal parameters over a consecutive sequence of model orders (Heylen et al. 1995). In this study, the stability thresholds of the identified modal parameters (i.e., frequency, damping ratio, and modal assurance criterion (MAC)) are defined as the following:

$$\left|\frac{f_i - f_{i+1}}{f_{i+1}}\right| \le 0.02 \qquad \text{Eq. 5.2a}$$

$$\left|\frac{\xi_i - \xi_{i+1}}{\xi_{i+1}}\right| \le 0.05 \qquad \text{Eq. 5.2b}$$

$$1 - \mathrm{MAC}(\phi_i, \phi_{i+1}) \le 0.02 \qquad \text{Eq. 5.2c}$$

where f_i, f_{i+1}, ξ_i, and ξ_{i+1} are the identified natural frequencies and damping ratios for models of two consecutive orders, MAC(ϕ_i, ϕ_{i+1}) is the modal assurance criterion (Allemang and Brown, 1982) of a pair of mode shape vectors at two consecutive model orders. The identified modes are considered as stable when the triple convergence criteria (frequency, damping ratio, and MAC) are satisfied for at least six consecutive model orders (note that the model order increases with an increment of two) (Heylen et al. 1995).

5.3.2 White Noise Test Results

Using WN data collected by the MEMS system, the modal parameters of the building are identified by the input-output (DSI and OKID-ERA) and output-only methods (SSI-DATA and NExT-ERA). Figure 5.7 shows the stability diagram of the modal parameters identified from the 1.5% g WN test at *State S0* (reference state) by the DSI (input-output) method. The mode orders range from 60 to 140 in the stability diagram. According to the convergence criteria as mentioned above (0.02, 0.05, and 0.02 for frequency, damping ratio, and MAC), a total of four modes (two modes around 4 Hz and the other two between 12 and –14 Hz) are identified as stable within the majority of the mode order range. These modes correspond to the longitudinal and torsional vibration modes of the building. Since the minimum model order to identify all the modes is 90, the modal parameters (i.e., frequencies, damping ratios, and mode shapes) of the stabilized modes are obtained by averaging the results obtained from model order 90 through 100 (a total of six consecutive model orders). Furthermore, two transverse vibration modes (one around 2 Hz and the other slightly less than 8 Hz) are also identified as stable modes. However, since the amplitude of the WN input excitation was much lower in the transverse direction, the stabilized transverse modes span only a limited number of model orders. It is noted that the stability thresholds are more difficult to satisfy for the transverse modes (1-T and 2-T), since the transverse vibration of the building may not be sufficiently excited during the WN tests due to the much lower amplitude of input excitations in this direction.

Figure 5.8 illustrates the mode shapes of the six stabilized modes and the corresponding polar plot representations of the complex-valued mode shapes at *State S0* (reference state) by the DSI (input-output) method. The real-valued mode shapes of the building are obtained using the method proposed by Imregun and Ewins (1993). Absent substantial stiffness and mass irregularities for the test building, the first three identified modes correspond to the first transverse (1-T), longitudinal (1-L), and torsional (1-To) vibration modes, whereas the last three identified modes correspond to the second transverse (2-T), longitudinal (2-L), and torsional (2-To) vibration modes. In addition, the polar plots indicate that all the identified modes are nearly classically damped because the mode shape components are nearly collinear.

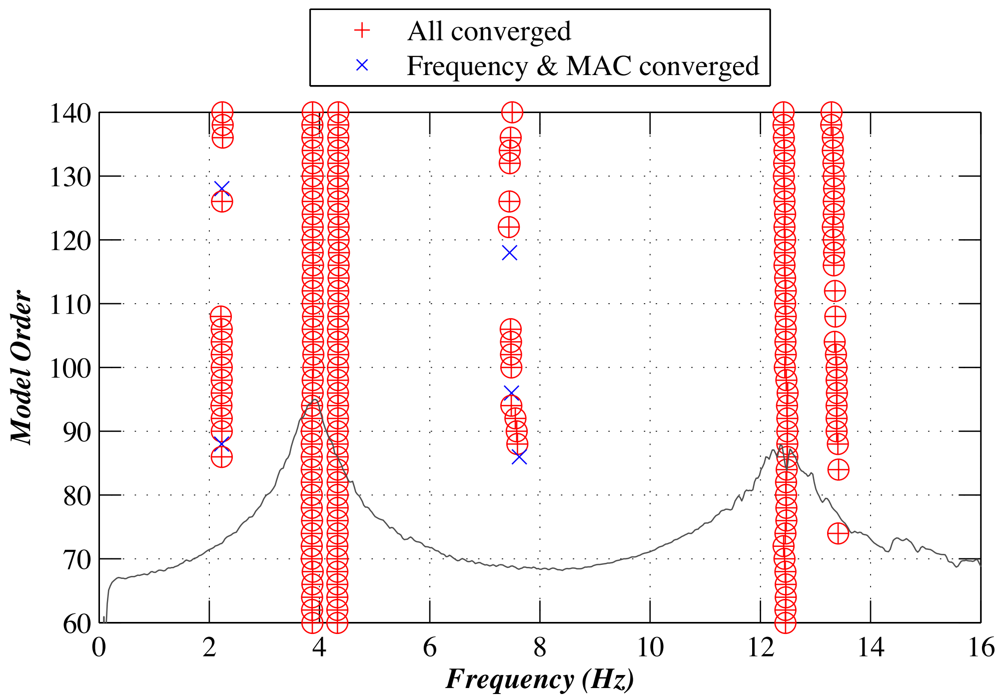

Figure 5.7. Stabilized modes identified from the 1.5% g white noise (WN) test at State S0 (reference state).

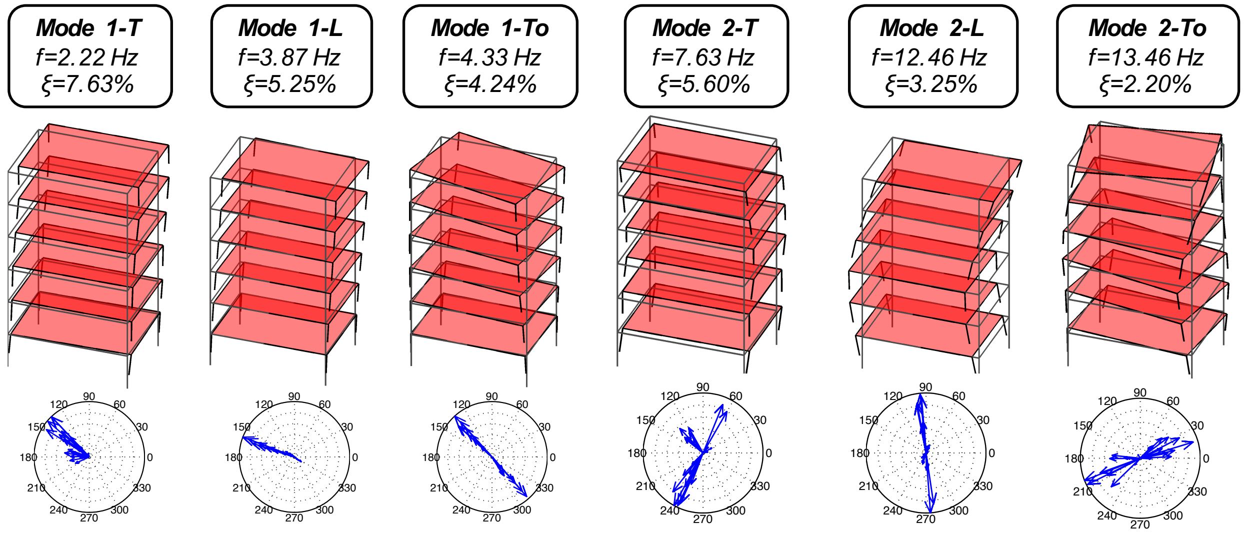

Figure 5.8. Identified mode shapes and the polar plot representation of the mode shape vectors identified from the 1.5% g white noise (WN) test at State S0 (reference state).

To validate the effectiveness of the system identification methods, Figure 5.9 compares the measured longitudinal floor accelerations of three select floors (floor 2, floor 4, and roof) with the corresponding responses predicted using the state-space models identified from the 1.5% g WN tests at three select states (S0, S7, and S8) during the test phase. Agreement between the measured and predicted responses demonstrates that the identified state-space models are capable of replicating the dynamic responses of the test building at the various states over the test program (RMS errors range between 0.003 g and 0.005 g). It is also observed that the measured floor accelerations at states S7 and S8 became apparently smaller than their counterparts at state S0 (reference state) as a result of building period elongation induced by the structural damage accumulated throughout the pre-fire test sequence (EQ1–EQ7). As the building damage progressed, discrepancies between the measured and predicted responses at states S7 and S8 increased slightly as a result of increased nonlinearity of the building response (RMS errors 20%–30% larger than those at the reference state).

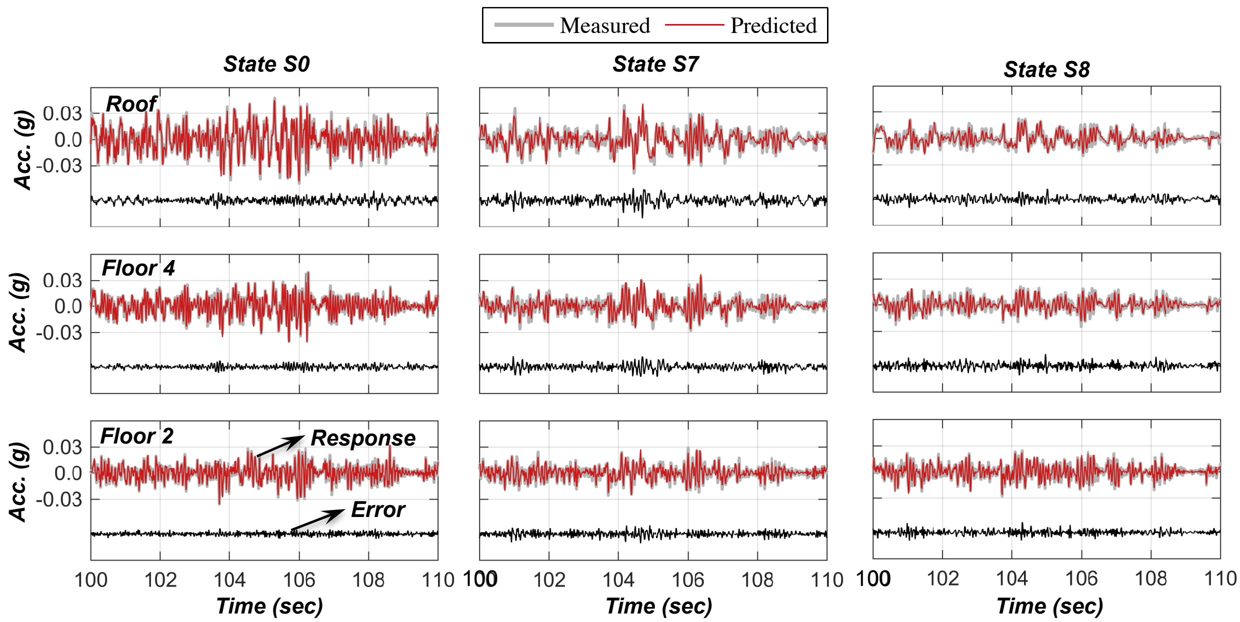

Figure 5.9. Comparison of measured and predicted longitudinal floor accelerations during the 1.5% g white noise (WN) tests at three select states: S0 (reference state, beginning of pre-fire test phase), S7 (end of pre-fire test phase), and S8 (beginning of post-fire test phase).

Construction Phase

The modal parameters of the test building during the pre-test phase were identified using the four system identification methods (two input-output and two output-only methods). The white noise test data was all recorded using the MEMS system at all five configurations (C1–C5). In the identification algorithms, the system input was taken as the averaged longitudinal acceleration recorded on the table platen, while the system output consisted of floor accelerations measured at every floor from the second floor through the roof. Since the instrumentation plan evolved during the pre-test phase, the system output for the first configuration (C1) varied slightly from the remaining configurations (C2 – C5). In specific, the output floor accelerations involved three channels (two longitudinal and one transverse) for the first configuration (C1) and four channels (two longitudinal and two transverse) for the remaining configurations (C2 – C5).

Figure 5.10 summarizes the natural frequencies of the longitudinal (1-L and 2-L) and torsional (1-To and 2-To) modes identified using both the input-output and output-only SID methods at all five states (C1–C5). The corresponding damping ratios are presented in Figure 5.11. Detailed results of the identified modal parameters are summarized in Table 5.4 and Table 5.5. It is noted that the modal parameters of transverse modes (1-T and 2-T) are not reported, since these modes can not be consistently identified due to lack of comparable amplitudes between the longitudinal and transverse excitations during the WN tests. As clearly shown in Figure 5.10, the natural frequencies identified using the different SID methods are in reasonable agreement at all five states (<5% errors among different methods). In contrast, the identified damping ratios are subjected to much larger method-to-method variability (Figure 5.11), as the highest and the lowest damping ratios identified using different methods may vary by 50%–100%. It is also observed that the damping ratios of the fundamental modes (1-L and 1-To) tend to be larger than those of their respective higher modes (2-L and 2-To). This is likely due to the greater hysteretic energy dissipation associated with the fundamental modes as a result of larger modal contribution, which is represented as equivalent viscous damping in the time-domain identification methods.

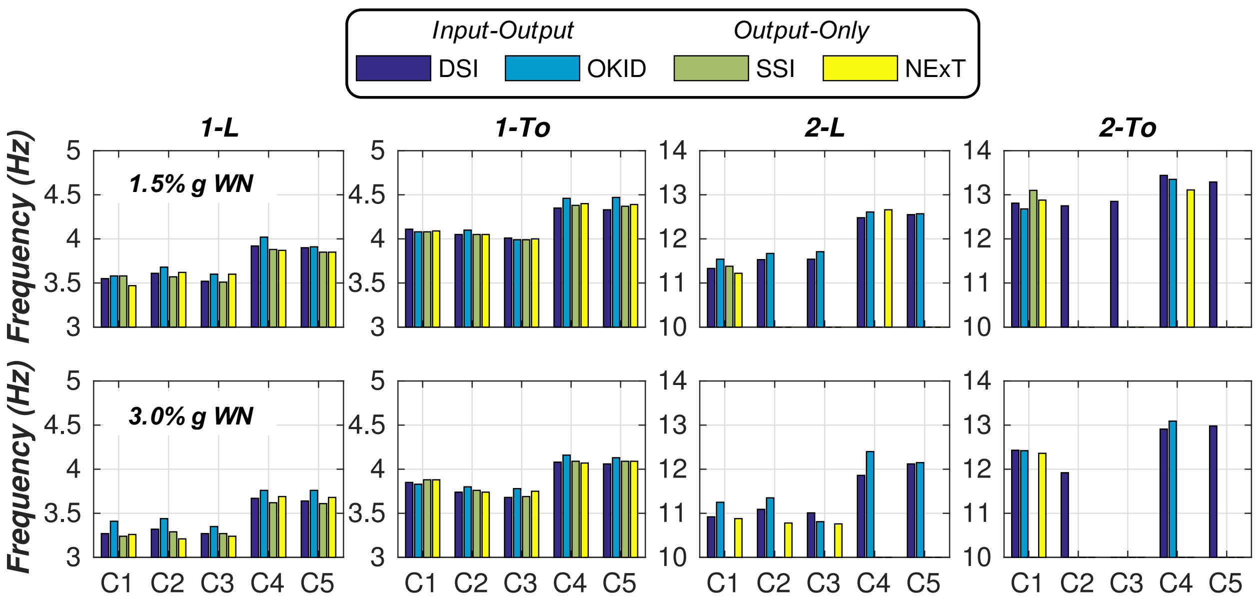

Figure 5.10. Natural frequencies identified from the white noise (WN) data during the construction phase using four system identification methods.

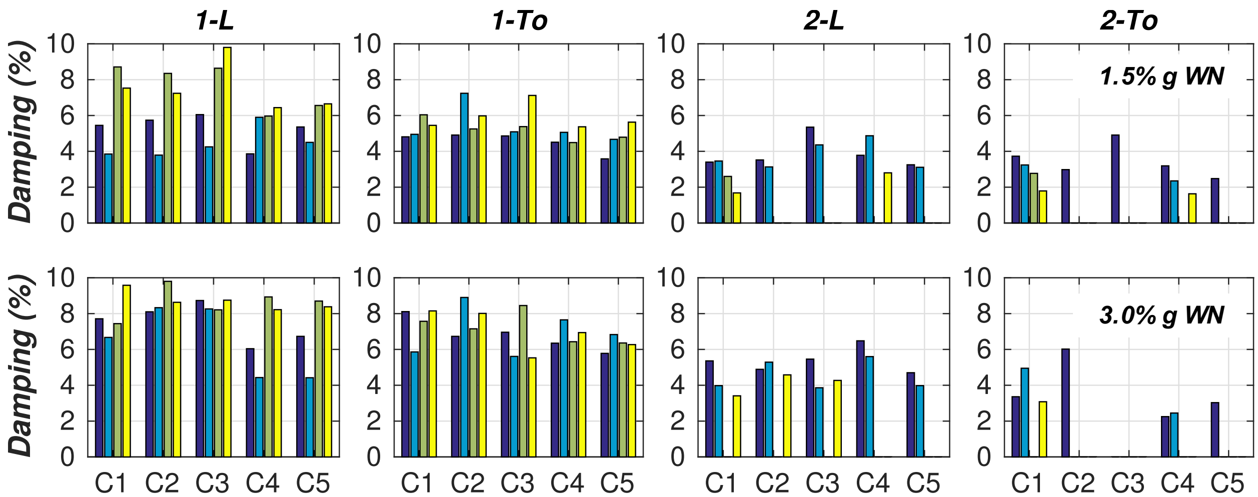

Figure 5.11. Damping ratios identified from the white noise (WN) data during the construction phase using four system identification (SID) methods.

In terms of the performance of different SID methods, all the input-output (DSI and OKID-ERA) and output-only (SSI-DATA and NExT-ERA) methods are capable of identifying the fundamental modes of the test building (1-L and 1-To). However, the output-only methods appear less effective than the input-output methods for the higher mode (2-L and 2-To) identification. This is due to the fact the WN base excitations contained a dominant spectral peak at around 10 Hz due to the oil column resonance effect of the shake table hydraulic system [25], while the output-only methods assume the input as ideal broadband white noise with perfectly flat spectra over the entire frequency domain. Neglecting the oil column resonance in the output-only methods poses difficulties for identifying the higher modes (2-L and 2-To) whose frequencies (11–13 Hz) fall into the resonance peak region (~10 Hz).

As shown in Figure 5.10, the natural frequencies (about 3.7 Hz for mode 1-L and 12.1 Hz for mode 2-L during the 3.0% g WN tests) at states C4 and C5 (completion of interior construction) were about 10% higher than those at states C1–C3 (about 3.3 Hz for mode 1-L and 11.0 Hz for mode 2-L during the 3.0% g WN tests). The increase of the natural frequency is indicative of the stiffness contribution from the fasteners that attached the interior gypsum panels to the CFS framing and the completion of partition wall installation. In contrast, the limited variation of the natural frequencies (< 3%) at the first three states (C1–C3) demonstrates that modifying the roof mass layout does not appreciably affect the modal characteristics of the building. Similarly, the nearly identical natural frequencies between states C4 and C5 indicate negligible stiffness contribution of the door system, despite a relatively large amount of doors (22 in total) installed in the building, given its relatively small footprint. As shown in Figure 5.11, the damping ratios appeared to be smaller at states C4 and C5 (5.5% – 5.8% for model 1-L at the 1.5% g WN tests) compared to those at states C1–C3 (6.3% – 7%), however the variability of the damping ratios within first three states or the last two states was as large as the frequency differences between these two stages. In addition, the natural frequencies and damping ratios appear to be dependent on the amplitudes of the WN excitations. As the WN amplitude increases from 1.5% g to 3.0% g, the average natural frequencies reduce slightly (about 5% – 10%), while the average damping ratios increase moderately (typically 20% – 30%).

Table 5.4. Natural frequencies and damping ratios identified from the 1.5% g white noise (WN) test data during the construction phase.

Cfg.	*Method*	*Natural frequency (Hz)*						*Damping ratio (%)*					
		1-T	*1-L*	*1-To*	*2-T*	*2-L*	*2-To*	*1-T*	*1-L*	*1-To*	*2-T*	*2-L*	*2-To*
C1	DSI		3.55	4.11		11.33	12.81		5.45	4.81		3.40	3.73
	OKID		3.58	4.08		11.54	12.68		3.85	4.95		3.46	3.24
	SSI		3.58	4.08		11.38	13.10		8.71	6.04		2.60	2.77
	NExT		3.47	4.09		11.22	12.88		7.53	5.45		1.68	1.79
C2	DSI		3.61	4.05	7.13	11.57	12.75		5.74	4.91	6.55	3.72	2.98
	OKID		3.68	4.10		11.67			3.79	7.24		3.13	
	SSI		3.57	4.05					8.35	5.25			
	NExT		3.62	4.05					7.24	5.98			
C3	DSI		3.52	4.01	6.95	11.54	12.85		6.05	4.86	4.29	5.35	4.91
	OKID		3.60	3.99		11.71			4.25	5.09		4.36	
	SSI		3.51	3.99					8.64	5.38			
	NExT		3.60	4.00					9.80	7.12			
C4	DSI	2.24	3.92	4.35	7.72	12.48	13.44	6.04	3.86	4.51	6.36	3.78	3.19
	OKID		4.02	4.46		12.61	13.35		5.90	5.06		4.87	2.35
	SSI		3.88	4.38					5.97	4.49			
	NExT		3.87	4.40		12.66	13.11		6.44	5.37		2.80	1.63
C5	DSI		3.90	4.33		12.55	13.29		5.36	3.58		3.25	2.48
	OKID		3.91	4.47		12.57			4.50	4.67		3.11	
	SSI		3.85	4.37					6.56	4.79			
	NExT		3.85	4.39					6.65	5.63			

Table 5.5. Natural frequencies and damping ratios identified from 3.0% g white noise (WN) test data during the construction phase.

Cfg.	*Method*	*Natural frequency (Hz)*						*Damping ratio (%)*					
		1-T	*1-L*	*1-To*	*2-T*	*2-L*	*2-To*	*1-T*	*1-L*	*1-To*	*2-T*	*2-L*	*2-To*
C1	DSI	1.97	3.27	3.85		10.92	12.43	9.98	7.71	8.11		5.36	3.36
	OKID		3.41	3.83		11.25	12.42		6.67	5.86		3.98	4.95
	SSI		3.24	3.88					7.44	7.57			
	NExT		3.26	3.88		10.88	12.36		9.58	8.15		3.41	3.08
C2	DSI	2.00	3.32	3.74	6.73	11.09	11.92	9.04	8.10	6.73	7.39	4.89	6.02
	OKID		3.44	3.80		11.35			8.33	8.90		5.29	
	SSI		3.29	3.76					9.80	7.15			
	NExT		3.21	3.74		10.78			8.63	8.01		4.58	
C3	DSI	2.00	3.27	3.68	6.74	11.01		10.82	8.73	6.96	6.67	5.46	
	OKID		3.35	3.78		10.81			8.26	5.61		3.86	
	SSI		3.27	3.69					8.21	8.45			
	NExT		3.24	3.75		10.76			8.75	5.53		4.27	
C4	DSI	2.15	3.67	4.08	7.34	11.86	12.91	7.91	6.04	6.35	4.88	6.48	2.25
	OKID		3.76	4.16		12.40	13.09		4.43	7.65		5.60	2.45
	SSI		3.62	4.09					8.93	6.43			
	NExT		3.69	4.07					8.22	6.94			
C5	DSI	2.17	3.64	4.06	7.33	12.12	12.98	7.63	6.73	5.78	4.92	4.70	3.03
	OKID		3.76	4.13		12.15			4.42	6.83		3.98	
	SSI		3.61	4.09					8.70	6.36			
	NExT		3.68	4.09					8.38	6.27			

Test Phase

The WN tests conducted during the test phase allowed for investigating the evolution of modal parameters of the building and subsequent correlation with the progression of physical damage. Table 5.3 summarizes the natural frequencies and damping ratios of the building identified using the four different system identification methods from the 1.5% g WN data during the test phase. The same results for the 3.0% g white WN data are summarized Table 5.4. For the purpose of brevity, discussion of the modal parameters herein focuses on results identified using the DSI (input-output) method, since it outperforms the output-only methods in the higher mode identification.

Figure 5.12 presents the modal parameters of the longitudinal (1-L and 2-L) and torsional (1-To and 2-To) modes identified from the test phase WN data using the DSI method. This figure shows that the progression of physical damage leads to reduction of the natural frequencies and increase of the damping ratios for all four identified modes (i.e., 1-L, 1-To, 2-L, 2-To). The modal parameters of all the identified modes remained nearly constant at *States S0–S4* (serviceability level earthquake sequence). Reduction of the natural frequencies initiated at *State S5* (following EQ5: 50% design event) and became more pronounced at *State S6* (following EQ6: design event) and S7 (following EQ7: MCE event). Since the longitudinal structural walls (in parallel with the shaking direction) suffered much more severe damage than that of the transverse walls, the natural frequencies of the longitudinal modes (1-L and 2-L) reduced more significantly than those of the torsional modes (1-To and 2-To). In addition, the damping ratios of all the identified modes increased sharply at *States S5 and S6* and remained stable at *State S7*. Following the pre-fire test sequence, the identified modal parameters remained essentially stable over the last three states (*S7–S9*), indicating that the fire tests and the post-fire serviceability earthquake test (EQ8) did not induce substantial damage to the building. As opposed to the natural frequencies and damping ratios, the mode shapes appear less sensitive to the physical damage, since the MAC values (between the reference state and subsequent states) of the longitudinal modes (1-L and 2-L) remained sufficiently close to unity (> 0.95) throughout the test sequence, although the values were slightly lower (but remained larger than 0.9) for the torsional modes (1-To and 2-To).

Consistent with those observed from the construction phase WN data, the natural frequencies and damping ratios are also found to be dependent on the amplitude of the WN excitations. At all ten states (*S0–S9*) during the test phase, increasing the WN amplitude from 1.5% g to 3.0% g consistently reduces the natural frequencies (about 10%) and increases the damping ratios (typically 20%–30% but exceeded 50% in several cases). In addition, the damping ratios of the fundamental modes (1-L and 1-To) appear larger than those of their respective higher modes (2-L and 2-To). At *States S0–S4* (serviceability level test sequence), the identified damping ratios exceeded 5% for the first longitudinal mode (1-L), as opposed to only about 3% for the second longitudinal mode (2-L).

Table 5.6. Natural frequencies and damping ratios identified from 1.5% g RMS white noise test data during the test phase.

State	*Method*	*Natural frequency (Hz)*						*Damping ratio (%)*					
		1-T	*1-L*	*1-To*	*2-T*	*2-L*	*2-To*	*1-T*	*1-L*	*1-To*	*2-T*	*2-L*	*2-To*
S0	DSI	2.22	3.87	4.33	7.63	12.46	13.46	7.83	5.25	4.24	5.60	3.25	2.20
	OKID		3.92	4.33		12.48	13.64		4.33	4.32		2.73	2.51
	SSI		3.82	4.36		12.63	13.59		7.44	5.63		5.17	3.12
	NExT		3.94	4.38			13.54		7.15	4.61			2.06
S3	DSI	2.18	3.71	4.25	7.52	12.26	13.27	4.84	6.22	4.45	4.29	3.61	2.22
	OKID		3.79	4.35		12.31	13.35		4.26	5.49		2.32	1.68
	SSI		3.72	4.27					8.09	5.51		5.36	
	NExT		3.79	4.28		12.82			7.41	6.42		2.93	
S3	DSI	2.19	3.72	4.27	7.39	12.27	13.37	6.00	6.44	4.20	2.72	3.53	3.20
	OKID		3.76	4.31		12.34			6.90	4.78		2.98	/
	SSI		3.72	4.30					6.89	4.35			
	NExT		3.82	4.22			13.47		6.77	5.45			1.69
S4	DSI	2.19	3.70	4.22	7.37	12.24	13.47		6.75	4.13	3.03	3.22	2.81
	OKID		3.71	4.25		12.35	/		5.56	5.01		3.69	/
	SSI		3.69	4.25			13.31		8.26	5.17			2.07
	NExT		3.76	4.23			13.43		7.31	6.21			1.74
S5	DSI	2.10	3.33	4.00	7.17	11.47	12.62		9.43	6.12	5.81	5.50	2.67
	OKID		3.44	3.99		11.79	/		9.86	4.01		2.76	/
	SSI		3.31	3.99			12.42		11.60	7.03			3.33
	NExT		3.34	4.00		11.81	12.53		9.70	6.16		2.94	3.09
S6	DSI	1.85	2.23	3.17		8.74	10.89	8.84	14.67	9.10		9.45	7.11
	OKID		2.27	3.20			/		16.74	9.03			/
	SSI		2.17	3.12		8.47	11.11		14.53	8.68		6.58	5.82
	NExT		2.22	3.15		8.58			15.57	10.33		6.03	
S6	DSI	1.87	2.31	3.25		8.98	11.28	11.16	14.42	9.78		9.32	7.18
	OKID		2.35	3.11		/	/		15.14	9.50		/	/
	SSI		2.20	3.22		8.54	11.09		16.93	10.53		10.70	5.49
	NExT		2.31	3.26		8.45			15.42	10.56		8.35	
S7	DSI		1.58	2.47		6.19	9.05		16.69	10.31		14.34	8.05
	OKID		1.57	2.52		6.02	/		17.69	8.96			/
	SSI		1.50	2.44		5.80	9.12		20.63	10.97		20.79	9.63
	NExT		1.56	2.44		5.92			15.09	8.61		16.68	
Fire test phase (June 27-29, 2016)													
S8	DSI		1.59	2.50		6.21	9.15		18.07	10.38		17.06	8.18
	OKID		1.57	2.48		6.39	/		19.52	10.49		15.41	/
	SSI		1.62	2.48		6.22	9.14		18.74	11.03		13.41	7.96
	NExT		1.52	2.51		6.19			15.93	14.02		13.84	
S9	DSI		1.56	2.46		5.91	9.08		16.05	10.78		16.47	7.64
	OKID		1.52	2.38		6.03	/		21.28	11.36		15.94	/
	SSI		1.56	2.44		5.95	9.15		18.15	10.52		16.00	8.44
	NExT		1.50	2.47					16.75	14.58			

Table 5.7. Natural frequencies and damping ratios identified from 3.0% g RMS white noise test data during the test phase.

State	*Method*	*Natural frequency (Hz)*						*Damping ratio (%)*					
		1-T	*1-L*	*1-To*	*2-T*	*2-L*	*2-To*	*1-T*	*1-L*	*1-To*	*2-T*	*2-L*	*2-To*
S0	DSI	2.14	3.63	4.06	7.30	12.08	12.74	6.44	6.52	6.20	4.23	5.66	4.52
	OKID		3.62	4.10		12.22	12.89		6.54	7.79		4.81	2.98
	SSI		3.58	4.08					9.87	6.45			
	NExT		3.64	4.03					9.45	7.56			
S3	DSI	2.10	3.41	3.95	7.25	11.61	12.45	8.45	9.06	7.97	5.66	5.20	4.39
	OKID		3.48	4.07		11.86			6.85	8.41		4.84	
	SSI		3.37	3.97					11.93	8.22			
	NExT		3.35	3.93					11.10	5.11			
S3	DSI	2.15	3.42	3.95	7.11	11.66	12.53	6.21	8.86	7.52	3.61	5.80	5.21
	OKID		3.59	3.96		11.97	/		8.84	6.24		3.52	/
	SSI		3.47	3.98			12.52		9.84	7.64			5.18
	NExT		3.40	3.97			12.50		10.18	9.02			4.39
S4	DSI	2.09	3.38	3.90	7.12	11.66	12.40	8.62	10.06	7.23	4.05	6.42	5.30
	OKID		3.45	3.92		11.99	/		10.38	7.04		3.45	/
	SSI		3.36	3.88			12.31		12.08	7.58			5.53
	NExT		3.31	3.91			12.27		10.17	8.29			3.87
S5	DSI		2.96	3.65	6.81	10.83	12.16		15.14	9.85	4.29	8.32	5.60
	OKID		2.99	3.68		10.90	/		15.89	6.81		10.80	/
	SSI		2.95	3.63			12.38		15.94	10.61			5.18
	NExT		2.95	3.70					17.72	10.88			
S6	DSI		1.85	2.82		7.36			16.51	12.20		19.60	
	OKID		1.94	2.64		/	/		18.35	9.04		/	/
	SSI		1.82	2.78		7.51			20.35	12.45		19.06	
	NExT		1.83	2.84					15.42	12.17			
S6	DSI		1.92	2.87		7.31	/		16.05	13.32		17.14	
	OKID		2.05	2.62			/		18.62	8.68			/
	SSI		1.93	2.83		7.78			19.58	12.03		17.42	
	NExT		2.00	2.91					17.54	11.87			
S7	DSI		1.17	2.15		4.85			17.84	14.07		17.69	
	OKID		1.11	2.25			/		18.52	10.18			/
	SSI		1.16	2.16		4.85			14.24	10.90		17.86	
	NExT		1.07	2.08		4.91			18.98	12.81		19.95	
Fire test phase (June 27-29, 2016)													
S8	DSI		1.17	2.14		4.94			17.43	13.60		13.47	
	OKID		1.10	2.21			/		20.85	10.96			/
	SSI		1.16	2.10		5.17			12.87	10.09		21.65	
	NExT		1.15	2.11		4.92			17.78	13.77		17.61	
S9	DSI		1.13	2.10		4.88			17.21	13.66		14.50	
	OKID		1.11	2.07			/		20.49	13.70			/
	SSI		1.12	2.09		5.16			14.21	11.43		21.21	
	NExT		1.12	2.04		4.78			18.81	11.99		20.98	

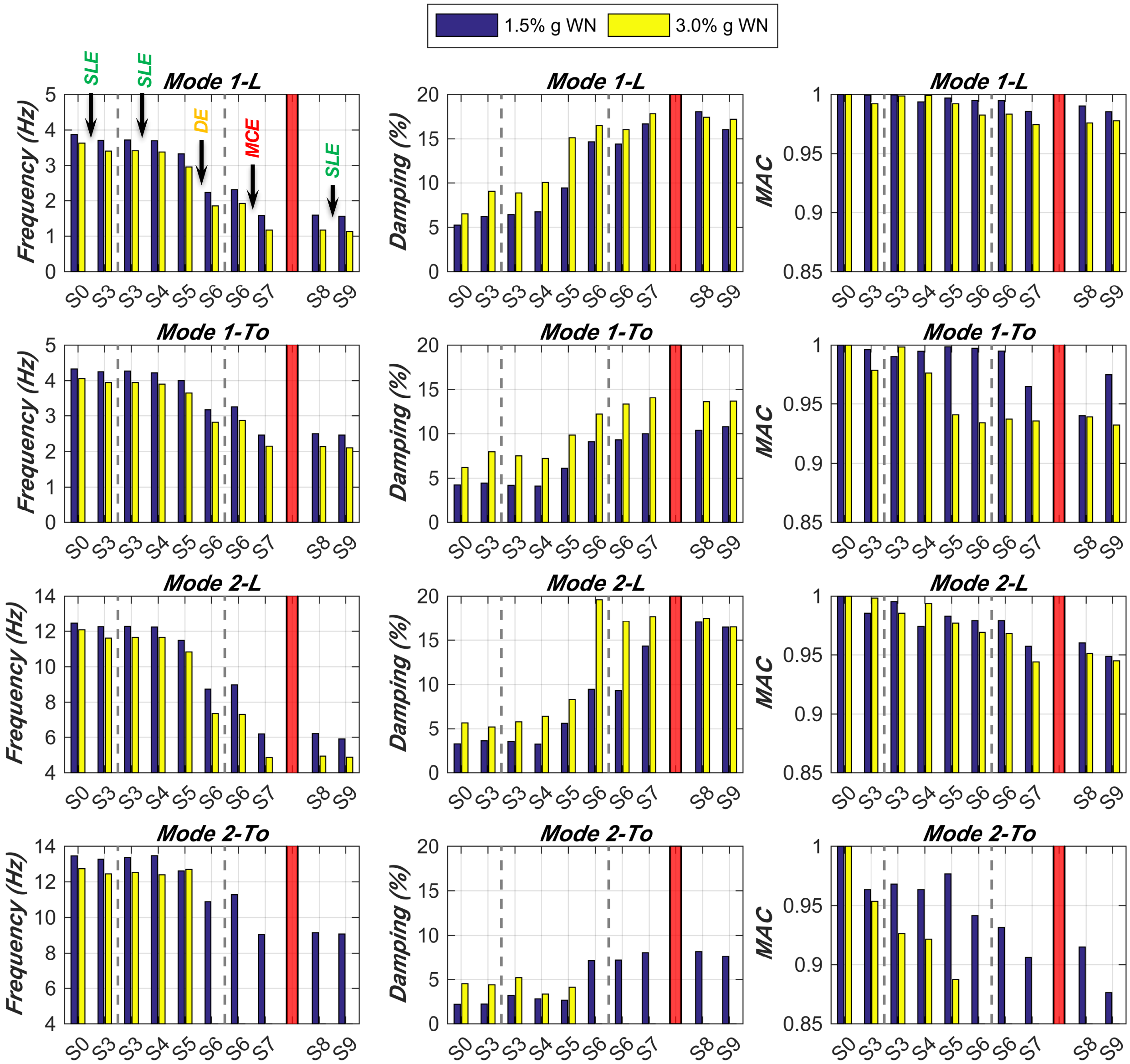

Figure 5.12. Modal parameters identified from the white noise (WN) data during the test phase (dashed vertical lines divide earthquake test dates, vertical red bar denotes the fire test phase, SLE – serviceability level, DE – design level, MCE – maximum considered earthquake level).

5.3.3 Ambient Vibration Test Results

Ambient vibration (AV) data was collected at four key stages during the test phase: (a) prior to the earthquake tests (June 9, 2016 – *State S0*), (b) following the completion of all pre-fire earthquake tests (June 17, 2016 – *State S7*), (c) following the completion of fire tests and prior to post-fire earthquake tests (June 30, 2016 – *State S8*), and (d) following the completion of the final post-fire earthquake tests (July 1, 2016 – *State S10: Final State*). Each of the four AV datasets contained a duration ranging between 10 and 12 minutes. Note that the data were collected using the Kinemetric system at the pre-fire test phase (*States S1* and *S7*) and by the MEMS system at the post-fire test phase (*States S8* and *S10*). Since the input excitations of the AV tests were unknown, the modal parameters of the test building are identified using the two output-only methods (SSI-DATA and NExT-ERA).

Figure 5.13 compares the natural frequencies and damping ratios of the test building identified from the AV data using the two output-only system identification methods. Detailed results of the identified modal parameters are summarized in Table 5.8. It is noted that a total of five stable vibration modes are identified using data collected during the pre-fire test phase (states S0 and S7). These modes correspond to the first transverse, longitudinal, and torsional modes (1-T, 1-L, and 1-To) and the second transverse and longitudinal modes (2-T and 2-L). The second torsional mode (2-To) is not identified using the pre-fire test phase AV data, which is likely due to the relatively sparse layout of the Kinemetric system (only a total of 12 accelerometers distributed at four floors). The natural frequencies and damping ratios identified using the two methods are in reasonable agreement at the first three states (*S0*, *S7*, and *S8*). In addition, Table 5.9 summarizes the modal assurance criteria (MAC) for the mode shape pairs identified using the two output-only methods. The identified mode shape pairs are consistent, since all corresponding MAC values are close to unity (except for the first torsional mode with a MAC value of 0.92). The lower MAC value for the torsional vibration modes is likely attributed to the close proximity of the Kinemetric accelerometers to the floor center of geometry.

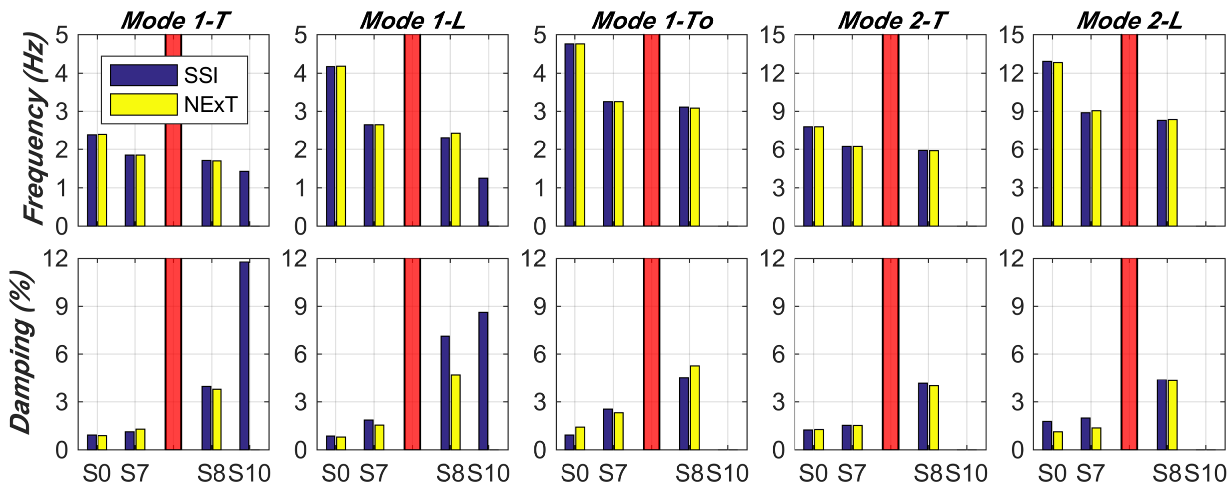

Figure 5.13. Natural frequencies and damping ratios identified from the ambient vibration (AV) data during the test phase (vertical red bar denotes the fire test phase).

Table 5.8. Natural frequencies and damping ratios identified from the ambient vibration (AV) test data.

State	*Method*	*Natural frequency (Hz)*						*Damping ratio (%)*					
		1-T	*1-L*	*1-To*	*2-T*	*2-L*	*2-To*	*1-T*	*1-L*	*1-To*	*2-T*	*2-L*	*2-To*
S0	SSI	2.39	4.17	4.76	7.79	12.92	n/a	0.95	0.89	0.95	1.26	1.79	n/a
	NExT	2.40	4.18	4.76	7.79	12.83	n/a	0.91	0.83	1.44	1.29	1.15	n/a
S7	SSI	1.85	2.65	3.25	6.22	8.89	n/a	1.15	1.88	2.55	1.55	2.00	n/a
	NExT	1.85	2.65	3.25	6.22	9.04	n/a	1.32	1.57	2.33	1.54	1.39	n/a
S8	SSI	1.71	2.31	3.11	5.92	8.28	10.39	3.95	7.11	4.52	4.15	4.39	3.89
	NExT	1.70	2.43	3.08	5.89	8.36	10.35	3.78	4.69	5.26	4.01	4.33	5.40
S10	SSI	1.43	1.25	n/a	n/a	n/a	n/a	11.76	8.62	n/a	n/a	n/a	n/a
	NExT	n/a	n/a	n/a	n/a	n/a	n/a	n/a	n/a	n/a	n/a	n/a	n/a

Notes: test data were recorded by Kinemetric system for S0 and S7 and by MEMS system for S8 and S10.

Table 5.9. Modal assurance criteria (MAC) for the mode shapes identified using the two output-only system identification methods.

State	*Modal assurance criteria (MAC) value*					
	1-T	*1-L*	*1-To*	*2-T*	*2-L*	*2-To*
S0	1.00	1.00	0.92	1.00	0.97	n/a
S7	1.00	1.00	0.97	1.00	1.00	n/a
S8	1.00	0.96	1.00	0.98	0.92	0.95

Notes: test data were recorded by Kinemetric system for S0 and S7 and by MEMS system for S8.

Compared with those at the reference state (*S0*), the frequencies at the end of the pre-fire test phase (*State S7*) reduced by 30%–40% for the longitudinal modes (1-L and 2-L) and by about 20% for the remaining modes (1-T, 1-To, and 2-T). The damping ratios increased substantially (by as much as 100%) for the first longitudinal mode (1-L) but slightly less for the other modes. The natural frequencies dropped only slightly (<10%) from *State S7* (prior to the fire tests) to *State S8* (following the fire tests). These observations are consistent with those found from the WN test results. It is noted, however, that the damping ratios at *State S8* became substantially larger than those at *State S7*. This is in direct contradiction to the observation gathered from the WN tests, in which the modal parameters remained similar before and after the fire tests. It is therefore believed that the abrupt increase of the damping ratios identified using AV data before and after the fire tests may be attributed to the use of different data monitoring systems.

Due to severity of damage sustained by the building at the final state (*S10*), the first longitudinal and transverse modes (1-L and 1-T) are the only two stable modes identified using the SSI method. While the frequency of mode 1-T decreased by only about 15% (from 1.71 sec at *State S8* to 1.43 sec at *State S10*), the frequency of mode 1-L reduced significantly (from 2.31 sec at state S8 to 1.25 sec at state S10, by about 50%). This indicates the occurrence of mode crossing between modes 1-L and 1-T, since the frequency of mode 1-L became even lower than that of mode 1-T at the final state (*S10*). Figure 5.14 compares the mode shape components of modes 1-L and 1-T at the beginning and end of the post-fire test phase (*States S8* and *S10*). While the mode shape of mode 1-T remained consistent between *States S8* and *S10* (with a MAC value of 0.98), the mode shape of mode 1-T at state S10 differed significantly from that at state S8 (with a MAC value of only 0.85). The mode shape of mode 1-L was characterized by non-proportionally large deflection concentrated at level 2 for the longitudinal components as well as large-amplitude transverse components (about 50% the longitudinal component at the roof) at the final state (*S10*). This remarkable difference clearly reveals the formation of soft story mechanism at level 2 at the end of post-fire test phase (see Chapter 8).

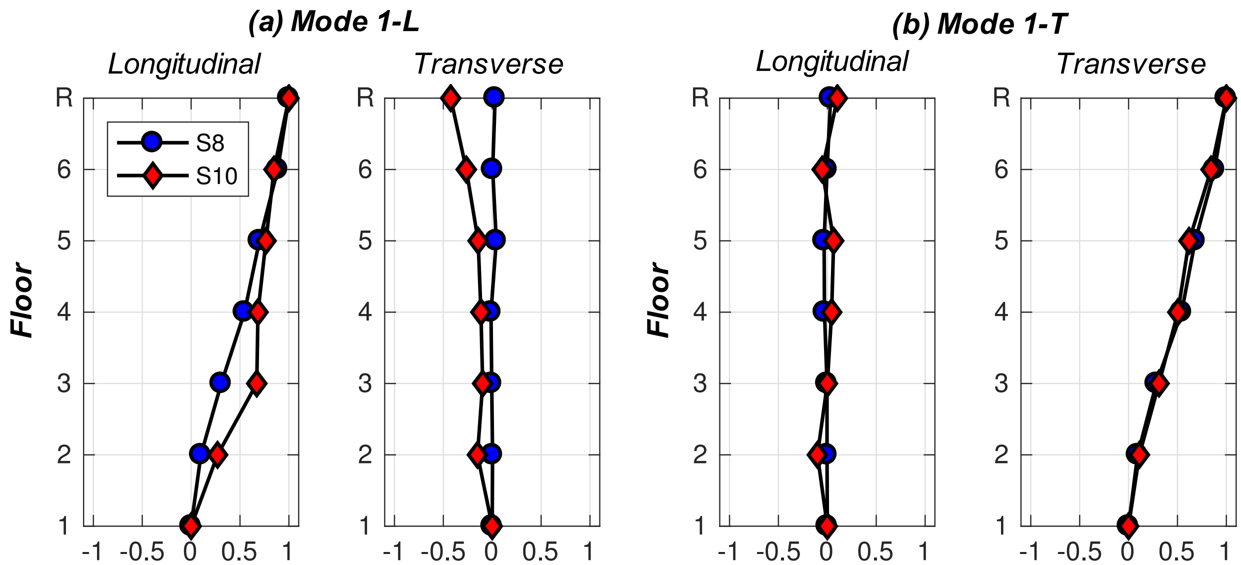

Figure 5.14. Comparison of the mode shape components of (a) mode 1-L and (b) mode 1-T between states S8 and S10 (beginning and end of the post-fire test phase).

5.4 Frequency Loss and Damage Assessment

Since the natural frequencies identified using different system identification methods tend to be more consistent than the damping ratios, the frequency loss is adopted as a (global) damage metric to quantitatively assess the progression of the building damage during the test program. In this study, the frequency loss of a specific vibration mode (in unit of percentage) is defined as the frequency difference between the subsequent state (i.e., *S1* through *S9*) and the reference state (*S0*) normalized by the frequency of the reference state. Figure 5.15 presents the frequency losses of two longitudinal (1-L and 2-L) and two torsional (1-To and 2-To) vibration modes during the test phase (from both the AV and WN tests). The evolution of frequency loss of all vibration modes correlates well with the progression of physical damage observed at different inspection stages during the test program (detailed summary of structural damage is available in Chapter 6). Since damage occurred only in the form of local gypsum crushing and incipient screw withdrawal during the serviceability level earthquake test sequence (EQ1–EQ4), the frequency losses remained sufficiently small (5%–10%) for all modes at states *S1–S4*. As the structural walls of the building sustained extensive damage at all but the uppermost levels following the design level (EQ6) and MCE level (EQ7) tests, the frequency losses increased substantially at *States S6 and S7* (attaining 50%–60% for modes 1-L and 2-L). Despite the fire damage to the gypsum sheathing at levels 2 and 6, no apparent frequency loss occurred following the fire tests

(*State S8*). This is explained by the fact that the earthquake-induced damage accumulated during the pre-fire test phase (EQ1–EQ7) outweighed the effect of fire-induced damage. In addition, the post-fire serviceability level test (EQ8) did not induce further frequency loss due to its low drift demands (PIDR < 0.2%).

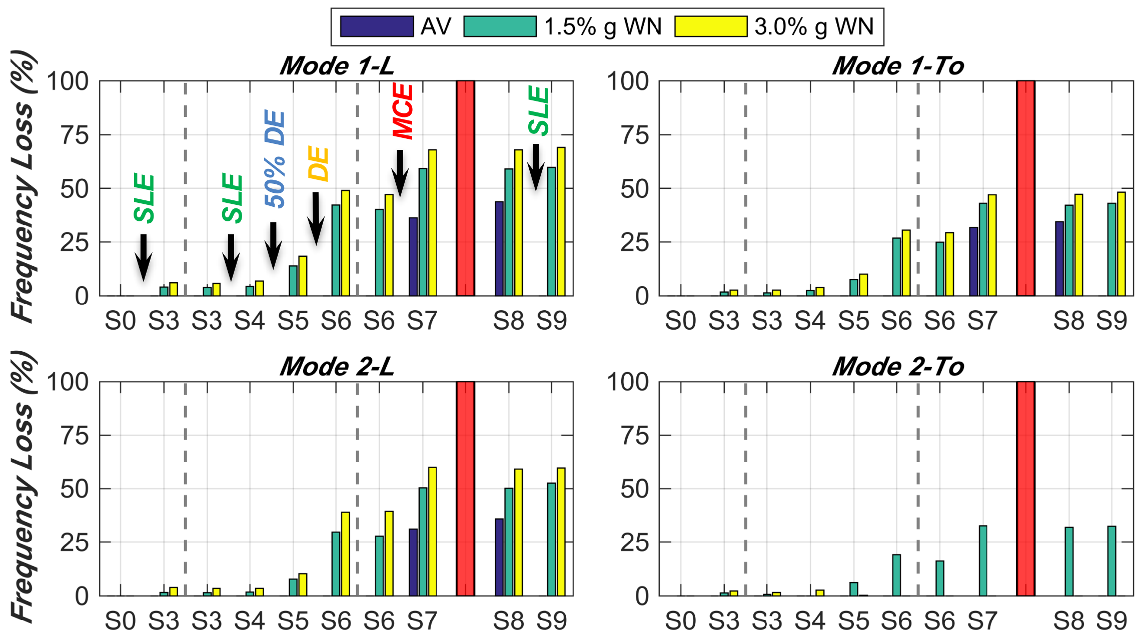

Figure 5.15. Frequency loss of the estimated using the ambient vibration (AV) and white noise (WN) data at the test phase (dashed vertical lines divide earthquake test dates, vertical red bar denotes the fire test phase, SLE – serviceability level, DE – design level, MCE – maximum considered earthquake level).

Comparison of the frequency loss results associated with different vibration excitation sources indicates that the frequency losses are also dependent on the excitation amplitudes of the vibration tests. Regardless of specific modes, the frequency loss tends to be higher when obtained from vibration tests with larger excitation amplitudes. At *State S7* (end of pre-fire test phase), for instance, the frequency losses of modes 1-L and 2-L associated with the 1.5% g WN test were about 10% lower than those of the 3.0% g WN test. The frequency losses for the AV test were even lower (about 50% those of the 3.0% g WN test), since the structural responses during the AV test were about two magnitudes smaller than those during the 3.0% g WN test. In addition, the frequency losses of the longitudinal modes (1-L and 2-L) were more significant that those of the torsional modes (1-To and 2-To). This is due to the fact that the longitudinal structural walls (in parallel with the shaking direction) sustained much more severe damage than that of the transverse walls as well as the larger amplitude of the WN excitations in the longitudinal direction.

5.5 Story Stiffness Estimation and Shear Beam Model

Since the interstory drift demands were low (<0.02 cm) during the WN tests, it is reasonable to assume that the building sustained no damage and its response remained linear during these tests. Consequently, the equivalent story stiffness of the building in the longitudinal direction (direction of shaking) can be estimated using least-square linear fitting of the shear force versus interstory drift response. In this case, the story shear force of a specific level is calculated as the summation of the inertial forces (product of lumped floor mass and absolute floor acceleration) at floor levels above, while the interstory drift is obtained by double-integrating the (absolute) floor accelerations at two adjacent floors to obtain the corresponding (absolute) floor displacements and subsequently subtracting these floor displacements to obtain the differential displacements between adjacent floors. Figure 5.16 illustrates the measured story shear versus interstory drift response (black) of all levels (level 1–6) and the fitted lines (red) during the 1.5% g WN test at state S0 (reference state). The slopes of the fitted lines represent the estimated story stiffness of the corresponding levels. It is observed that while the story stiffness of the upper four levels (ranged between 1300–1600 kN/cm) remained comparable, they were notably smaller than those of the story stiffness of level 1 and 2 (>2200 kN/cm) due to the use of larger-diameter steel tie-down rods in the shear walls at the lower two levels (refer to Section 2.4). The estimated story stiffnesses (upper four levels) appear reasonable when compared with those determined using pseudo-static test results of the corridor shear wall specimens in the component level wall tests (Hoehler and Smith, 2016). By applying a length scale factor to the initial secant stiffness of the shear wall specimen (based on the ratio between the total shear wall length of the test building and that of the wall specimen), the derived story stiffness ranges between 800–1000 kN/cm. It is noted that the smaller story stiffness obtained using the shear wall specimen test results is attributed to the fact that the drift (~0.3 cm) used for determining the shear wall initial secant stiffness is much larger than the achieved story drift of the test building during the WN tests (<0.02 cm).

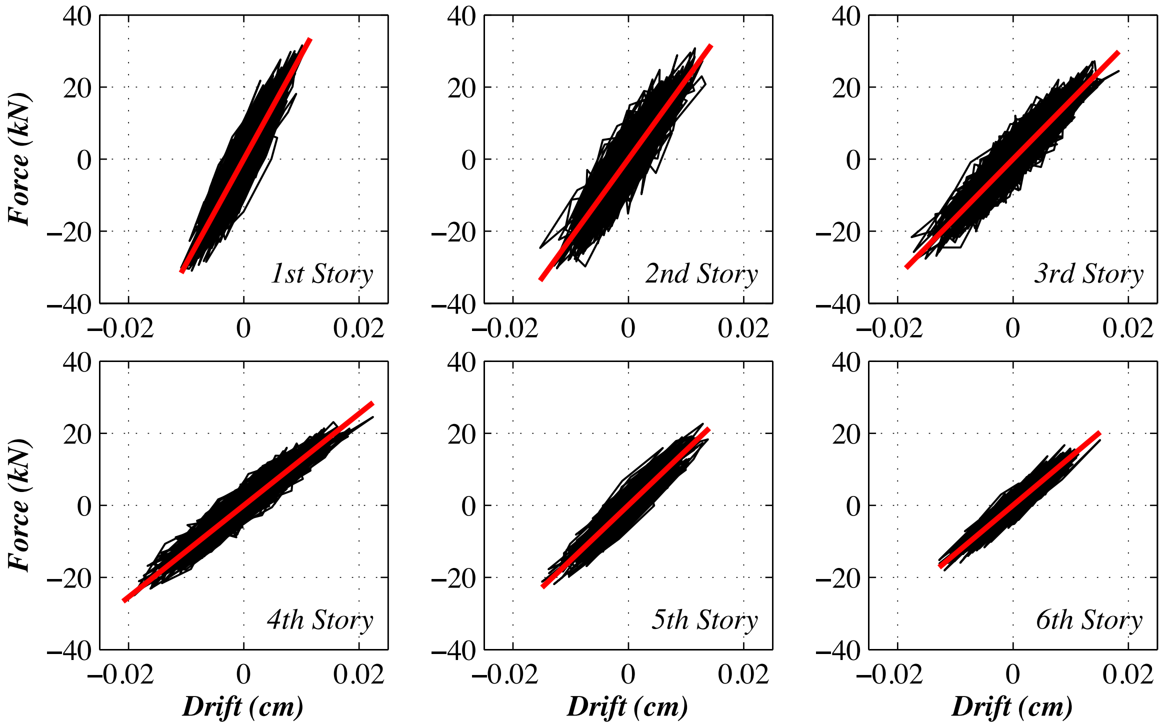

Figure 5.16. Story shear vs interstory drift response during the 1.5% g white noise (WN) test at the reference state (red lines determined using least-square linear fitting).

Figure 5.17 shows the normalized equivalent story stiffness of the building estimated using the test phase WN data, while the detailed results of the identified equivalent story stiffness are summarized in Table 5.10 and Table 5.11. The normalized story stiffness, quantified as a percentile number, represents the ratio of the story stiffness at the subsequent state (i.e., *S1* through *S9*) to that of the reference state (*S0*). The story stiffness degradation correlates well with the evolution of the natural frequencies (see Figure 5.15). While the story stiffness at all levels reduced only slightly (~10%) during the serviceability level test sequence (states *S1*–*S4*) as a result of low seismic drift demands (PIDR <0.1%), stiffness degradation continued to occur at state *S5* (following EQ5: 50% design event) and was appreciable at states *S6* (following EQ6: design level test) and *S7* (following EQ7: MCE level test). Following the pre-fire test phase, the story stiffness remained stable for the last three states (*S7*–*S9*) without substantial stiffness reduction. In addition, the stiffness degradation at level 6 (~65% at state *S7*, end of pre-fire test phase) was slightly smaller than those of the remaining levels (> 80% at state *S7*). This is consistent with the distribution of observed physical damage, since level 6 sustained less severe damage, where the PIDR was less than 0.7% during the pre-fire test phase.

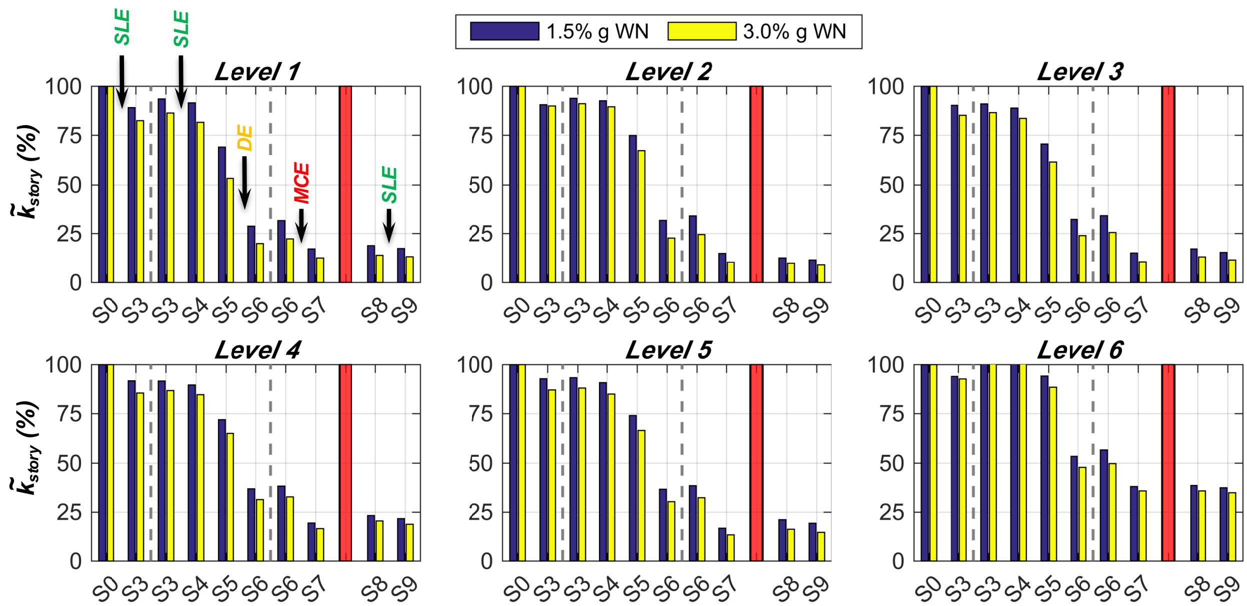

Figure 5.17. Normalized story stiffness of the building estimated using the white noise (WN) data during the test phase (dashed vertical lines divide earthquake test dates, vertical red bar denotes the fire test phase, SLE – serviceability level, DE – design level, MCE – maximum considered earthquake level).

Table 5.10. Story stiffness estiamted using the 1.5% g white noise (WN) data during the test phase.

Test date	*Building state*	*PIDR[1] (%)*	*Story stiffness (kN/cm)*					
			L1	*L2*	*L3*	*L4*	*L5*	*L6*
June 13, 2016	S0	0.0	2905.7	2204.2	1628.2	1271.7	1525.4	1346.4
	S3	0.08	2594.5	1999.3	1472.1	1168.1	1417.1	1266.5
June 15, 2016	S3	0.08	2721.6	2071.2	1484.5	1166.6	1425.8	1429.3
	S4	0.09	2663.6	2042.9	1450.6	1142.1	1386.9	1428.7
	S5	0.19	2005.5	1650.3	1149.2	914.8	1128.8	1268.6
	S6	0.70	834.8	698.5	525.3	467.7	557.1	719.1
June 17, 2016	S6	0.70	918.1	748.9	554.8	484.9	584.5	763.7
	S7	1.49	501.2	328.7	246.8	248.8	258.2	510.4
Fire test phase (June 27-29, 2016)								
July 1, 2016	S8	1.49	547.7	278.8	280.5	296.5	323.1	517.0
	S9	1.49	506.0	255.4	250.9	276.4	296.3	501.4

Note: PRDR denotes the accumulated PRDR during all the earthquake tests prior to the specific state.

Table 5.11. Story stiffness estiamted using the 3.0% g white noise (WN) data during the test phase.

Test date	*Building state*	*PRDR[1] (%)*	*Story stiffness (kN/cm)*					
			L1	*L2*	*L3*	*L4*	*L5*	*L6*
June 13, 2016	S0	0.0	2714.2	2075.6	1469.5	1133.9	1392.2	1228.8
	S3	0.08	2243.6	1868.9	1255.3	972.0	1214.6	1139.9
June 15, 2016	S3	0.08	2349.8	1893.1	1275.7	986.3	1227.9	1323.6
	S4	0.09	2221.5	1861.8	1231.6	962.4	1185.9	1303.8
	S5	0.19	1445.5	1395.9	903.9	737.4	926.0	1088.9
	S6	0.70	541.2	472.1	352.6	354.7	420.8	588.4
June 17, 2016	S6	0.70	605.3	508.5	374.9	370.0	448.5	612.3
	S7	1.49	341.5	216.4	156.4	189.1	188.5	438.9
Fire test phase (June 27-29, 2016)								
July 1, 2016	S8	1.49	378.0	200.7	192.9	232.7	228.5	439.1
	S9	1.49	358.5	183.9	170.5	214.2	206.7	427.7

Note: PRDR denotes the accumulated PRDR during all the earthquake tests prior to the specific state.

Given the estimated equivalent story stiffness of each level and the mass lumped at each floor (refer to Section 2.6), the natural frequencies of the longitudinal vibration modes of the building can be estimated by considering the building as a shear beam model (SBM). Figure 5.18 compares the natural frequencies of the longitudinal modes (f1-L and f2-L) estimated using the SBM with those identified using the DSI method from the test phase WN data (detailed results comparisons are summarized in see Table 5.12). This comparison indicates that the first longitudinal mode frequencies derived using the SBM agree reasonably well with those identified using the DSI method (<5% errors), whereas the SBM moderately underestimates the frequency of the second longitudinal model (by 10–20%). Additionally, Figure 5.18 also compares the frequency ratios of the first two longitudinal modes f_{2-L}/f_{1-L} (last column of the figure) during the test phase (*States S0–S9*). The figure reveals that the frequency ratios determined from the SBM are consistent with the DSI results (all ratios close to 3) at *States S0–S4* (serviceability level test sequence). As structural damage became pervasive following the design event EQ6 (associated with *States S6–S9*), the frequency ratios determined by the DSI results rose to about 4, while the values remained close to 3 for those derived from the SBM. Previous analytical studies indicate that the frequency ratio of the first two vibration modes is 3 for pure shear beam structures and 6 for pure flexural beam structures. These observations imply that while the shear beam model may be effective to capture the dynamic response of the building when damage remained limited (*States S0–S4*), the building response is likely to follow a combined shear-flexural mode as damage becomes more pervasive (*States S6–S9*).

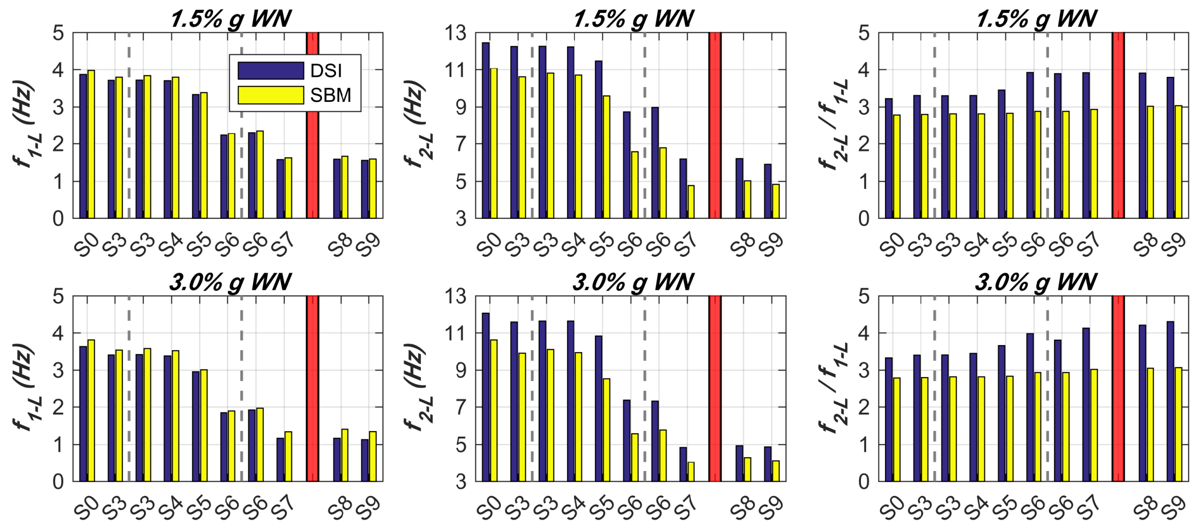

Figure 5.18. Comparison of the frequencies of the first and second longitudinal modes estimated using the shear beam model (SBM) and deterministic stochastic identification (DSI) method (dashed vertical lines divide earthquake test dates, vertical red bar denotes the fire test phase).

Table 5.12. Comparison of the frequencies of the first and second longitudinal modes identified using the shear beam model and system identification method.

Building state	*Mode 1-L*						*Mode2-L*					
	1.5% g RMS			*3.0% g RMS*			*1.5% g RMS*			*3.0% g RMS*		
	f_{model} (Hz)	*f_{DSI} (Hz)*	*Error (%)*	*f_{model} (Hz)*	*f_{DSI} (Hz)*	*Error (%)*	*f_{model} (Hz)*	*f_{DSI} (Hz)*	*Error (%)*	*f_{model} (Hz)*	*f_{DSI} (Hz)*	*Error (%)*
S0	3.98	3.87	2.84	3.81	3.63	4.96	11.08	12.46	11.08	10.62	12.08	12.09
S3	3.79	3.71	2.16	3.54	3.41	3.81	10.61	12.26	13.46	9.91	11.61	14.64
S3	3.84	3.72	3.23	3.58	3.42	4.68	10.81	12.21	11.47	10.11	11.66	13.29
S4	3.80	3.70	2.70	3.52	3.38	4.14	10.70	12.18	12.15	9.94	11.66	14.75
S5	3.38	3.33	1.50	3.01	2.96	1.69	9.59	11.49	16.54	8.55	10.83	21.05
S6	2.28	2.23	2.24	1.90	1.85	2.70	6.58	8.97	26.64	5.58	7.36	24.18
S6	2.36	2.31	2.16	1.97	1.92	2.60	6.79	8.98	24.39	5.78	7.31	20.93
S7	1.63	1.58	3.16	1.34	1.17	14.53	4.78	6.23	23.27	4.05	4.85	16.49
Fire test phase (June 27-29, 2016)												
S8	1.67	1.59	5.03	1.41	1.17	20.51	5.04	6.22	18.97	4.31	4.89	11.86
S9	1.59	1.57	1.27	1.35	1.16	16.38	4.84	6.15	21.30	4.14	4.91	15.68

Notes: f_{model} – frequency obtained using shear beam model; f_{DSI} – frequency identified using DSI method.

5.6 Summary

During the full-scale cold-formed steel (CFS) building test program, the test building was subjected to a multi-hazard scenario including earthquake, post-earthquake fire, and finally post-fire earthquake loading with companion low-amplitude vibration tests using different sources of excitations, including ambient vibration (AV) and white noise (WN) base excitation tests. These low-amplitude vibration tests were conducted throughout the construction and test phases. The vibration data is used herein to systematically study the evolution of the modal properties (i.e. natural frequencies, damping ratios, and mode shapes) of the test building. The modal properties are analyzed using frequency-domain as well as four state-of-the-art time-domain system identification (SID) methods, including two input-output (OKID-ERA and DSI) and two output-only (SSI-DATA and NExT-ERA) methods. Regarding the modal parameters of the test building identified from the low-amplitude vibration test sequence during the construction and test phases, key findings are summarized as follows:

1. The natural frequencies identified using the different time-domain system identification methods are in reasonable agreement (<5% error amongst different methods), while the identified damping ratios are subjected to much larger method-to-method variability.
2. Installation of interior gypsum panels on the CFS wall framing and the interior partition wall increased the natural frequencies of the test building by about 10% as a result of the stiffness contribution of the gypsum-to-framing fasteners.
3. The progression of building damage resulted in reduced natural frequencies and increased damping ratios. The frequency losses remained sufficiently small (<10%) during the serviceability level earthquake test sequence but increased substantially following the design level (as much as 40%) and MCE level tests (exceeded 50%) due to much larger seismic drift demands. However, the fire tests and post-fire serviceability level earthquake test induced no substantial frequency losses to the earthquake-damaged building. The evolution of the identified modal parameters correlates well with the progression of physical damage observed during the earthquake-fire test program, demonstrating the effectiveness of the SID methods for structural damage assessment and health monitoring.
4. The natural frequencies and damping ratios are dependent on the amplitudes of the vibration excitations. Increasing the excitation amplitude tends to reduce the natural frequencies but

increase the damping ratios. Increasing the root-mean-square (RMS) amplitude of the WN excitations from 1.5% g to 3.0% g results in a reduction of the natural fequencies by about 10% and an increase of the damping ratios by more than 30%. Furthermore, the frequency losses are also dependent on the amplitudes of the test excitations. Higher frequency loss is observed when the amplitude of the excitation becomes larger. The frequency losses associated with the WN tests at a RMS amplitude of 3.0% g are about 10% larger than the corresponding losses obtained from the 1.5% g WN tests. It is therefore important to note that the use of inconsistent excitation amplitudes at different states may result in biased damage assessment observations.

5. Given the story stiffness estimated from the WN tests and the lumped floor mass, the natural frequencies of the first two longitudinal modes of the building are determined by considering the mid-rise CFS test building as a shear beam model and subsequently compared with those identified using the DSI method. The comparison reveals that while the shear beam model may be sufficient for capturing the dynamic characteristics of the test building in its initial states with limited damage, its response is likely to follow a combined shear-flexural mode when damage becomes extensive.

6 PRE-FIRE EARTHQUAKE TEST RESULTS

The primary focus of this chapter is to investigate the measured response of the test building as well as summarize the associated physical damage of the structural components and the nonstructural systems during the pre-fire earthquake test sequence (EQ1–EQ7). In parallel with the system-level experiments conducted at UCSD, a series of CFS shear walls were tested was conducted in the National Fire Research Laboratory at the National Institute of Standards and Technology (NIST) to investigate the effects of fire loads on the component-level seismic behavior of shear walls. These component-level test results provided valuable guidance for post-fire earthquake testing of the full-scale building, and therefore they are first discussed in this chapter. Subsequently, the global responses of the test building (e.g., floor accelerations, interstory drifts, residual displacements, story shear forces) and the local responses of individual shear walls (e.g., structural panel shear distortion, tie-down rod forces, wall uplifting displacement) during the pre-fire earthquake tests are discussed in detail. Lastly, this chapter summarizes the physical damage of the test building and its nonstructural systems (e.g., partition walls, appliances, and doors) during the pre-fire earthquake test sequence.

6.1 Shear Wall Component Tests

The objective of the component CFS shear wall tests was to experimentally investigate the influence of the fire loads on the lateral load resistance of the shear walls with their design and construction details replicating those in the UCSD full-scale test building. The findings provided useful information regarding the selection of the earthquake motion for the post-fire earthquake test phase and estimation of the lateral strength of the fire-damaged shear walls at the fire test floors. Details of the NIST shear wall tests are available in the full report of Hoehler and Smith (2016).

A total of fourteen tests were conducted on six 2.7 m (9 ft) × 3.7 m (12 ft) shear wall specimens designed to mimic the lateral behavior of shear walls along the second floor corridor of the six-story test building. The dimensional details of the specimens are given in Figure 6.1. The test setup was informed by ASTM E2126-11 (ASTM, 2011), however deviations were made as required by the test program. Table 6.1 provides an overview of the NIST test program.

Table 6.1. NIST shear wall component test program

Test name	*Specimen*	*Description*	*Loading rate / Amplitude*
CFS01a	CFS01	Monotonic pushover	Push @ 2.54 mm/minute
CFS01b		10 minute burn	Multiple steps to 1900 kW
CFS02	CFS02	Cycling to failure	1.52 mm/second
CFS03a	CFS03	Cycling to 1 % drift	1.52 mm/second
CFS03b		13 minute 20 second burn	Step to 1900 kW
CFS03c		Continue cycling until failure	1.52 mm/second
CFS04a	CFS04	Cycling to 1.8 % drift	1.52 mm/second
CFS04b		13 minute 20 second burn	Step to 1900 kW
CFS04c		Continue cycling until failure	1.52 mm/second
CFS05a	CFS05	13 minute 20 second burn	Step to 1900 kW
CFS05b		Cycling to failure	1.52 mm/second
CFS06a	CFS06	Cycling to 1 % drift	1.52 mm/second
CFS06b		26 minute 40 second burn	Step to 1900 kW
CFS06c		Continue cycling until failure	1.52 mm/second

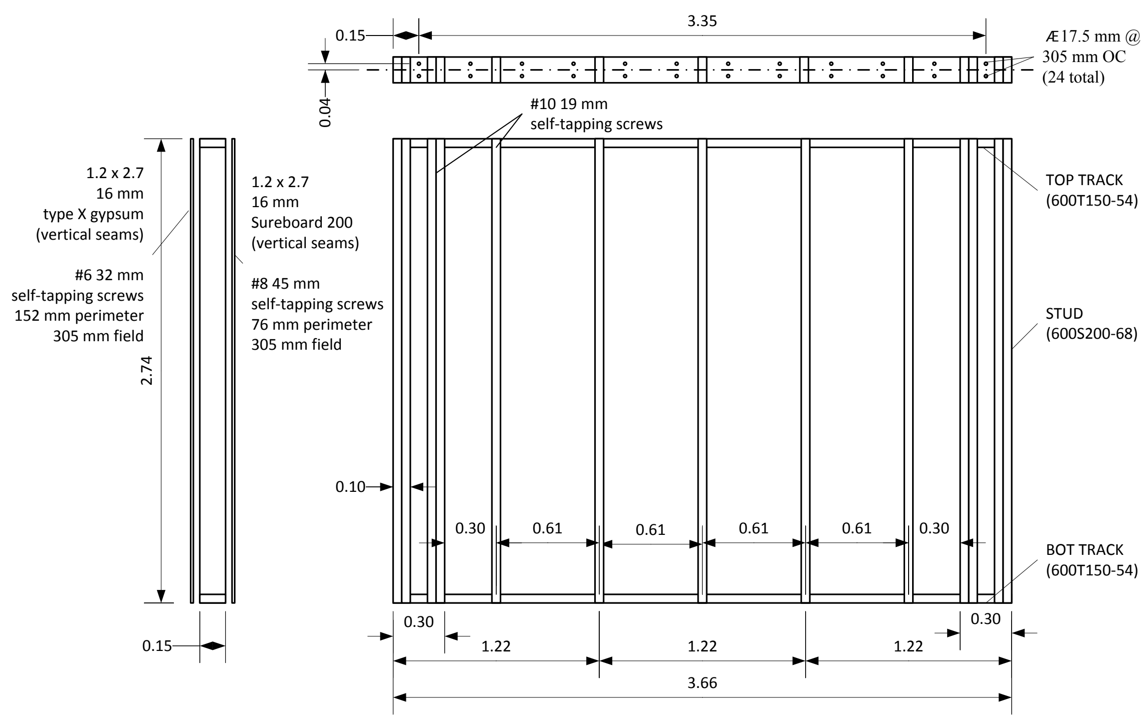

Figure 6.1. NIST shear wall specimen geometry (units in meters unless noted).

The key findings from the NIST tests that pertain to the UCSD full-scale test building are summarize by the enveloping curves (backbones) extracted from the peak values of applied force versus wall drift for the five cyclic tests shown in Figure 6.2. The portions of the curves indicated by dashed lines represent the mechanical response in the post-fire test stage. It is noted that the measured drift ratios are slightly smaller than the prescribed primary cycle drift amplitudes, which were controlled by the actuator displacement.

Test CFS02 represents the stiffness and capacity of the wall under ambient conditions. Test CFS05 represents the stiffness and capacity of the specimen after the steel sheathed side has been subjected to the investigated fire load for 13 minutes 20 seconds. The reduction in peak load capacity was 35 % (in compression) and the response was roughly symmetric for tension and compression cycles. The reduction in the peak load was accompanied by a shift in failure mode of the specimens from local buckling of the sheet steel (Figure 6.3a) to global buckling of the sheet steel (Figure 6.3b) for the unburned (CFS02) and burned (CFS05) walls, respectively. The fire severely damaged the gypsum on the burn side reducing the stiffness of the shear panels out-of-plane and creating a 16 mm standoff between the screw heads and the sheet steel; the thickness of the lost gypsum. This, in effect, changed the specimen to a plain sheet steel shear wall with reduced constraint around the panel boundaries. The global buckling mode is consistent with observations of the seismic response of laterally loaded steel sheathed steel stud walls (i.e. walls without gypsum), where the added bonded gypsum is not present to restrain the buckling evolution (Shamim et al., 2013). Pre-damaging the specimen by reversed shear cycling to 1 % (CFS03) or 1.8 % (CFS04) drift ratio prior to the fire loading had no noticeable influence on the residual load bearing capacity of the wall. The fire load alone was the trigger to shift the load-displacement behavior between that for a sheet steel wall with adhered gypsum (CFS02) to that for a sheet steel wall without adhered gypsum (CFS05). Doubling the burn time to 26 minutes 40 seconds (CFS06) caused additional reduction (11 % to 18 % in compression and tension, respectively) of the post-fire lateral load bearing capacity. This is likely due to the damage to the nonstructural gypsum board on the back side (cold side) of the wall during the longer burn, which was not present in the shorter tests.

The NIST test results indicated that the post-fire lateral capacity of the six-story building could be estimated using the capacity for an equivalently designed plain sheet steel shear wall. While the capacity was reduced from the pre-fire capacity (by approximately 35 %), the strength was predictable and repeatable. Additionally, the NIST results suggested that a soft-story mechanism would develop on the second floor of the UCSD test building where fire tests were to be performed.

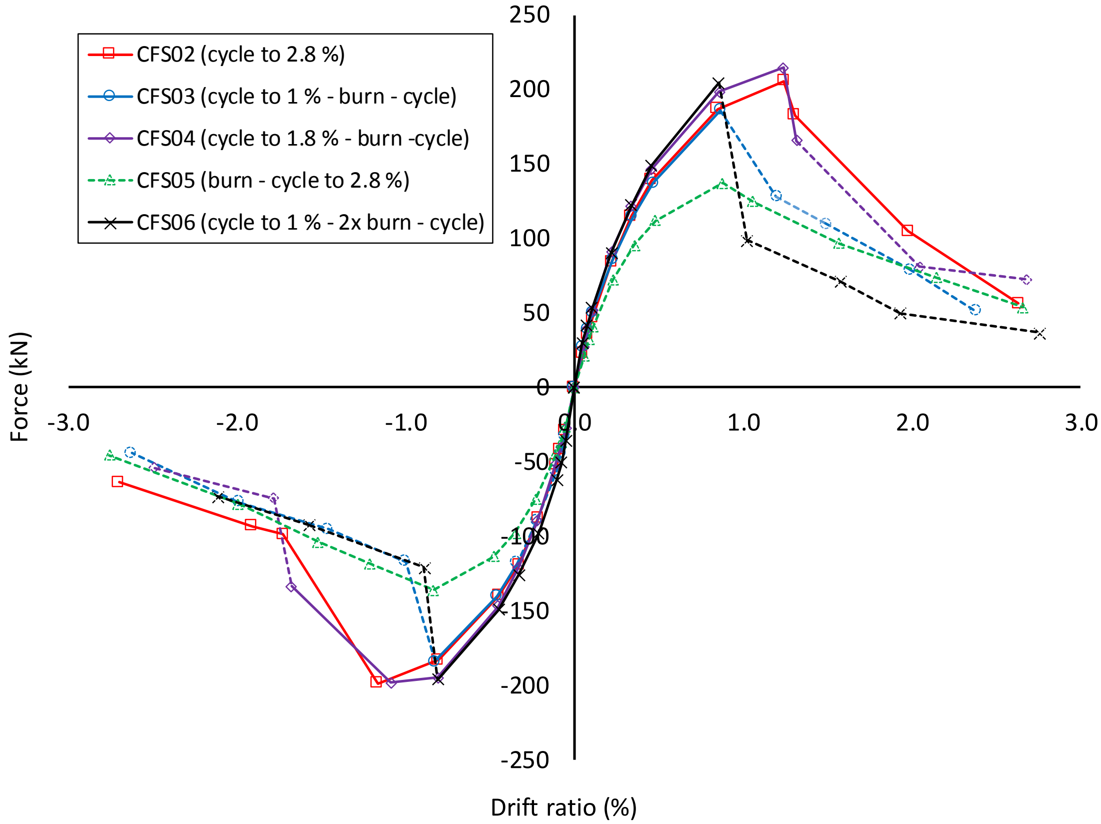

Figure 6.2. Backbone curves for CFS02 to CFS06.

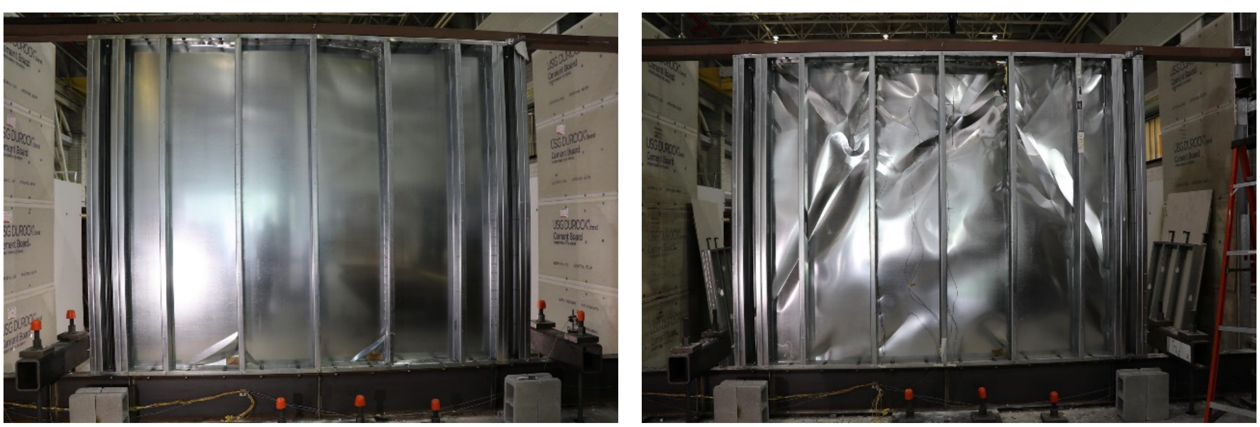

(a) (b)

Figure 6.3. Photograph of back of steel sheathed side of wall after mechanical loading to 2.8 % drift; nonstructural gypsum removed: (a) unburned wall; (b) wall after burning.

6.2 Global Building Response

6.2.1 Data Processing Procedures

Double Integration of Accelerations

Limited by the dimension and height of the test building, direct displacement measurements were only available at several locations, namely, the GPS measurements at the roof and the string potentiometer measurements at the lower three floors at the east corridor ends. In this regard, the floor displacements of the building are determined from double integration of the corresponding floor accelerations, while direct displacement measurements are employed to validate the double integration results (details of the double integration procedures are available in Appendix G). The interstory drift ratios are subsequently calculated as the differential displacements between two sequential floors normalized by the story height.

The uncertainty of the accelerations measured with MEMS accelerometers is sufficiently low (decimation error < 4×10^{-4} g). The uncertainty of displacements measured by string potentiometers also remains comparatively low (decimation error on the order of millimeter), while those measured by GPS were slightly higher (estimated error of about 0.5 cm). The floor displacements and interstory drifts, however, are subjected to larger uncertainties since they are obtained by double integrating the measured accelerations. It is reported that the relative errors of the integrated displacements may range between 5% and 10%, depending on the level of building nonlinearity during the earthquake excitations (Skolnik and Wallace, 2010).

Figure 6.4 compares the directly measured roof absolute displacement histories and those obtained using double integration method during the two MCE events (EQ7:CNP-150 and EQ9:RRS-150). It is noted that the direct displacements are determined by combining the collocated GPS (at the roof center) and accelerometer measurements using the method proposed by Bock et al. (2011). While the integrated roof displacement agrees well with the direct measurement during EQ7:CNP-150 when the residual displacement remained small (~0.5 cm) (Figure 6.4a), it becomes ineffective for EQ9:RRS-150 as it does not capture the large residual displacement (Figure 6.4b). As a result, the floor displacements and IDRs for EQ9:RRS-150 requires further processing (discussed later in Chapter 8). Additional validation results of the double integration method are available in Appendix G.

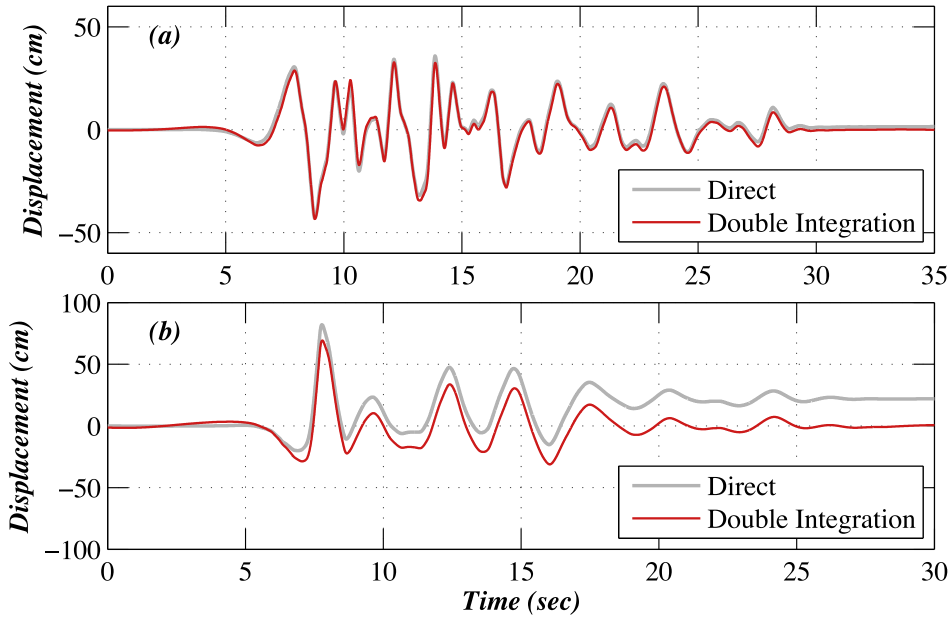

Figure 6.4. Comparison of roof absolute displacement histories determined using direct measurement and double integration: (a) EQ7:CNP-150, and (b) EQ9:RRS-150.

Floor Corner and Center Responses

With the assumption of the rigid in-plane movement of the floor diaphragm, the floor accelerations of an arbitrary location can be completely described using two translational and one torsional component with respect to the floor center of geometry. It is noted that the mass distribution of the building was nearly symmetrical at all floors (the transverse partition walls that were slightly of the centerline were the only source of non-symmetry). Therefore, the center of mass is considered to be identical with the center of geometry at all floors (hereafter simply referred to as the center or centroid).

As shown in Figure 6.5, the floor accelerations were measured at the four corners in the longitudinal direction and two in the transverse direction at every floor (floor 2 – roof). These accelerations allowed the use of least square method to determine the floor center accelerations in the longitudinal, transverse, and rotational directions. Specifically, a total of six corner measurements are used to calculate the three unknown floor center accelerations at each time instance. This strategy is also used for calculating floor displacements and interstory drift ratios of the floor center.

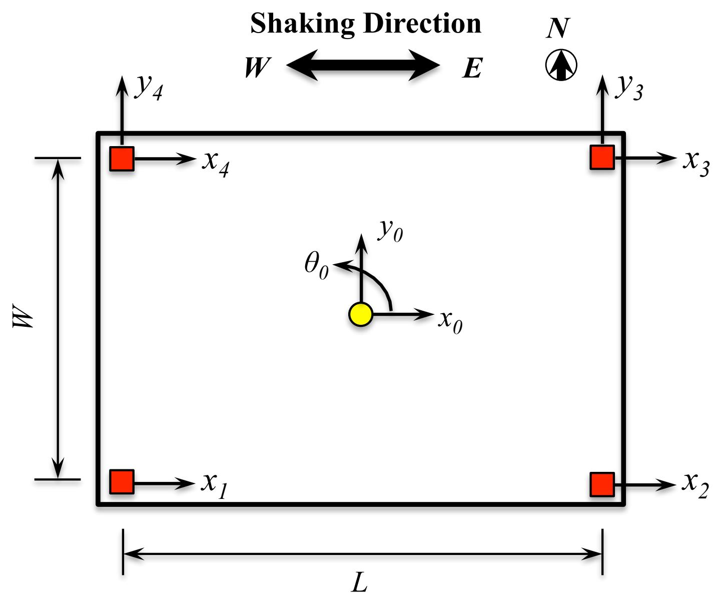

$$\underbrace{\begin{Bmatrix} x_1 \\ x_2 \\ x_3 \\ x_4 \\ y_3 \\ y_4 \end{Bmatrix}}_{Y} = \underbrace{\begin{bmatrix} 1 & 0 & W/2 \\ 1 & 0 & W/2 \\ 1 & 0 & -W/2 \\ 1 & 0 & -W/2 \\ 0 & 1 & L/2 \\ 0 & 1 & -L/2 \end{bmatrix}}_{H} \underbrace{\begin{Bmatrix} x_0 \\ y_0 \\ \theta_0 \end{Bmatrix}}_{X}$$

$$X = (H^T H)^{-1} H^T Y$$

Figure 6.5. Least square method for determining the floor center responses from corner responses.

Figure 6.6 illustrates the roof absolute accelerations at the corners and the center accelerations during the design event (EQ6:CNP-100). Since the longitudinal accelerations did not differ significantly at the four corners (*x1–x4*), the center acceleration is almost identical to those of the corners (Figure 6.6a). Conversely, the transverse accelerations at the opposite corners (*y3* and *y4*) were comparable in magnitude but opposite in directions, resulting in considerably smaller acceleration at the center compared with each of the corner responses (Figure 6.6b). This indicates that the transverse building accelerations were characterized by its torsional response. Figure 6.6c compares the torsional accelerations estimated using the least square method with those calculated using different sensor measurements (e.g., the difference of *y3* and *y4* or the difference of *x4* and *x1* divided by the distance between the sensors). The agreement of the torsional acceleration calculated using different methods further collaborates the fact that the transverse accelerations were primarily attributed to the torsional effect. In addition, Figure 6.7 presents the roof relative displacements at the center and the corner accelerations during the design event (EQ6:CNP-100). Likewise, the longitudinal displacements at the four corners were consistent, while the transverse displacements at the corners were dominated by the torsional response (equivalent magnitude but opposite in directions).

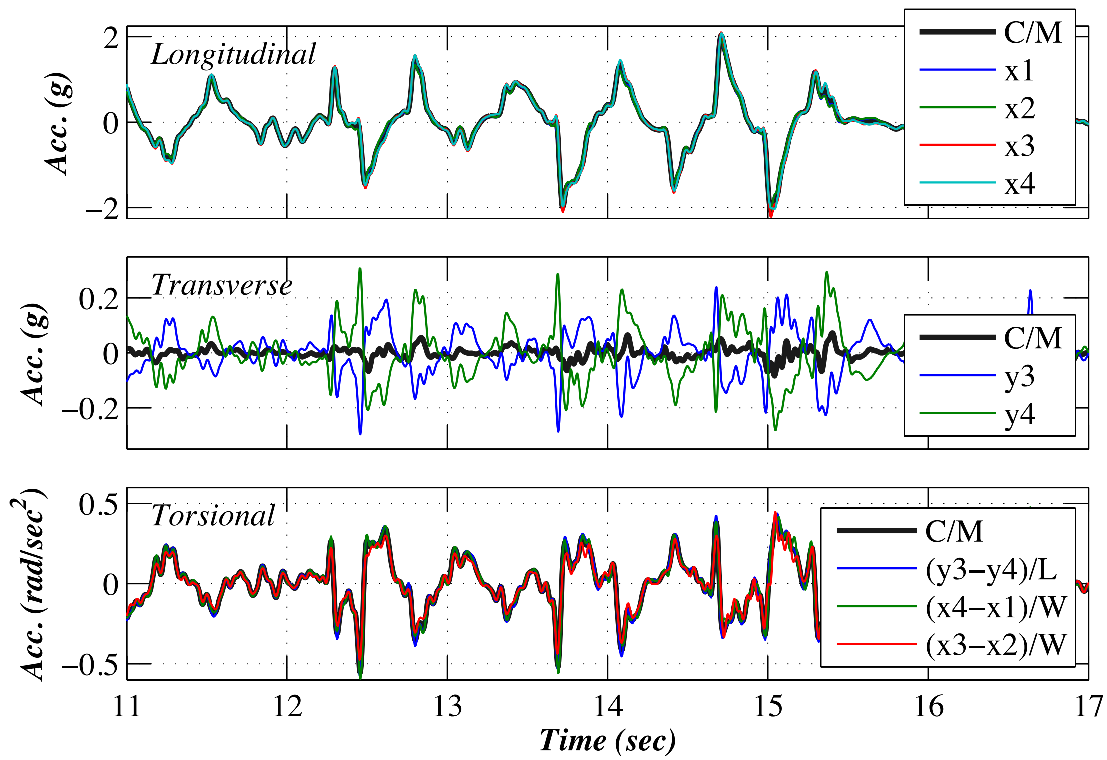

Figure 6.6. Roof absolute accelerations at the corners and the center: (a) longitudinal, (b) transverse, and (c) torsional.

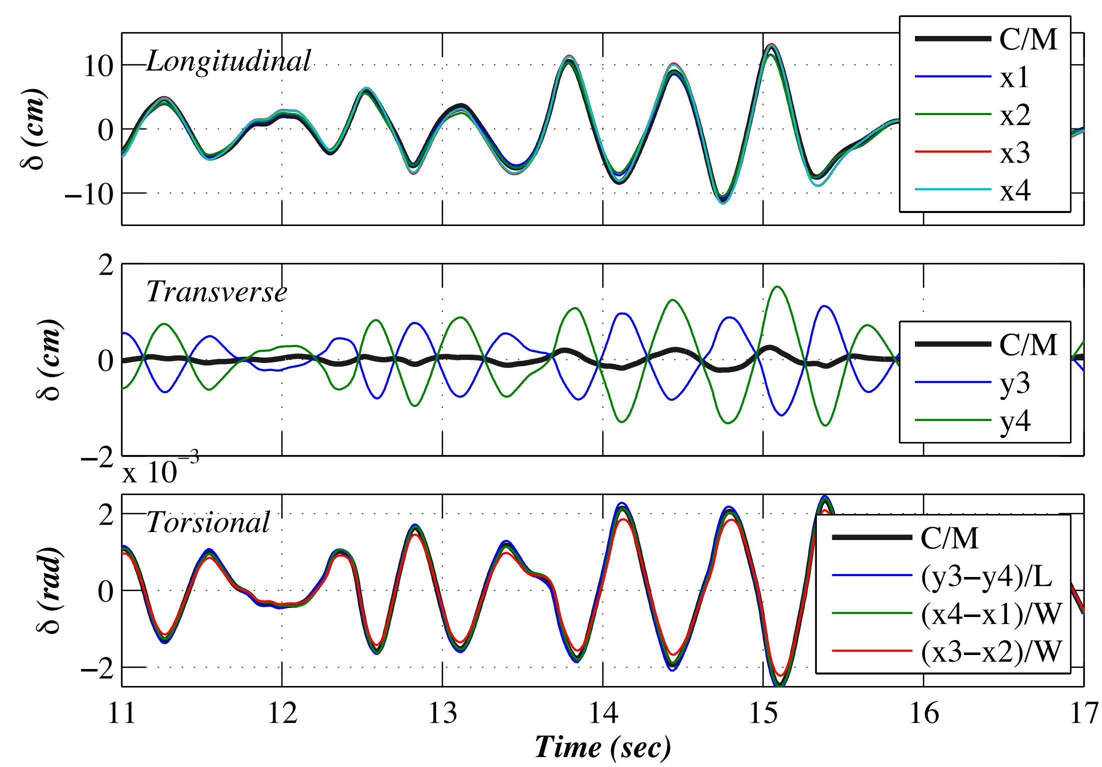

Figure 6.7. Roof relative displacements at the corners and the center: (a) longitudinal, (b) transverse, and (c) torsional.

Base Shear and Overturning Moment

Since no load cells were installed to measure to the building force demands, the base shear is determined using the inertial forces of all floors considering the dynamic equilibrium of the superstructure (Figure 6.8). The inertial force at an individual floor is calculated as the product of the floor mass and the absolute floor acceleration at the center (obtained using least square method). This assumption is considered reasonable provided the fact that the vertically distributed mass of the wall systems was much smaller than the mass concentrated at the floor level (refer to Section 2.6). In addition, the base shear is also determined using the dynamic equilibrium of the shake table platen by subtracting the forces of the hydraulic actuators from the inertial force of the shake table platen (Figure 6.8). This alternative method provides an effective means to cross validate the results obtained from the inertial forces of the superstructure. Figure 6.9 compares the base shear of the building obtained using the two methods during two select earthquake tests (EQ2:CNP-25 and EQ6:CNP-100). Agreement between the base shear forces calculated using the two methods validates the effectiveness of base shear calculations. However, since the measured actuator forces often contained high frequency noise, the base shear force V_b and overturning moment M_o presented later in this chapter are calculated using the floor inertial forces as follows:

$$V_b(t) = \sum_{i=2}^{N} -m_i a_i(t) \qquad \text{Equation 6.1a}$$

$$M_o(t) = \sum_{i=2}^{r} \left(-m_i h_i a_i(t) + w_i \delta_i(t)\right) \qquad \text{Equation 6.1b}$$

where m_i and w_i denote the lumped floor mass and the weight of the ith floor, $a_i(t)$ and $\delta_i(t)$ denote the absolute floor acceleration and relative floor displacement histories of the ith floor, and N is the total number of floors. In addition, the normalized base shear $\tilde{V}_b$ and overturning moment $\tilde{M}_o$ are defined as:

$$\tilde{V}_b = V_b / \sum_{i=2}^{N} w_i \qquad \text{Equation 6.2a}$$

$$\tilde{M}_o = M_o / \sum_{i=2}^{N} w_i h_i \qquad \text{Equation 6.2b}$$

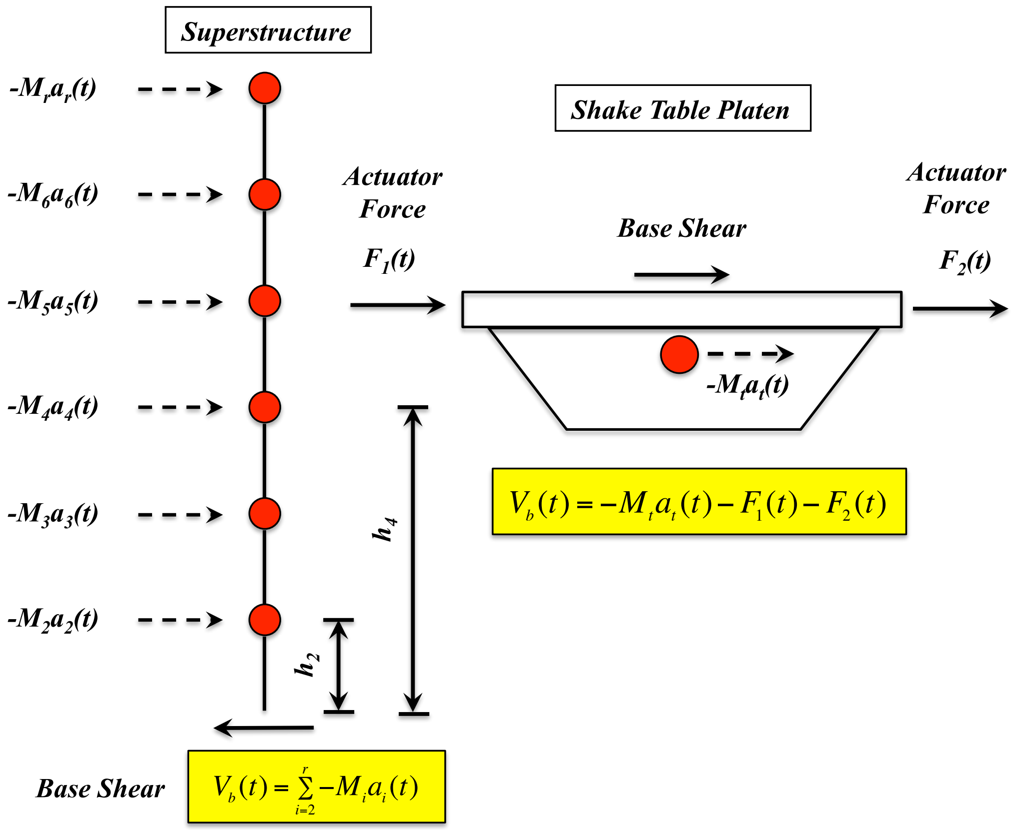

Figure 6.8. Schematic illustration of base shear and story shear calculation.

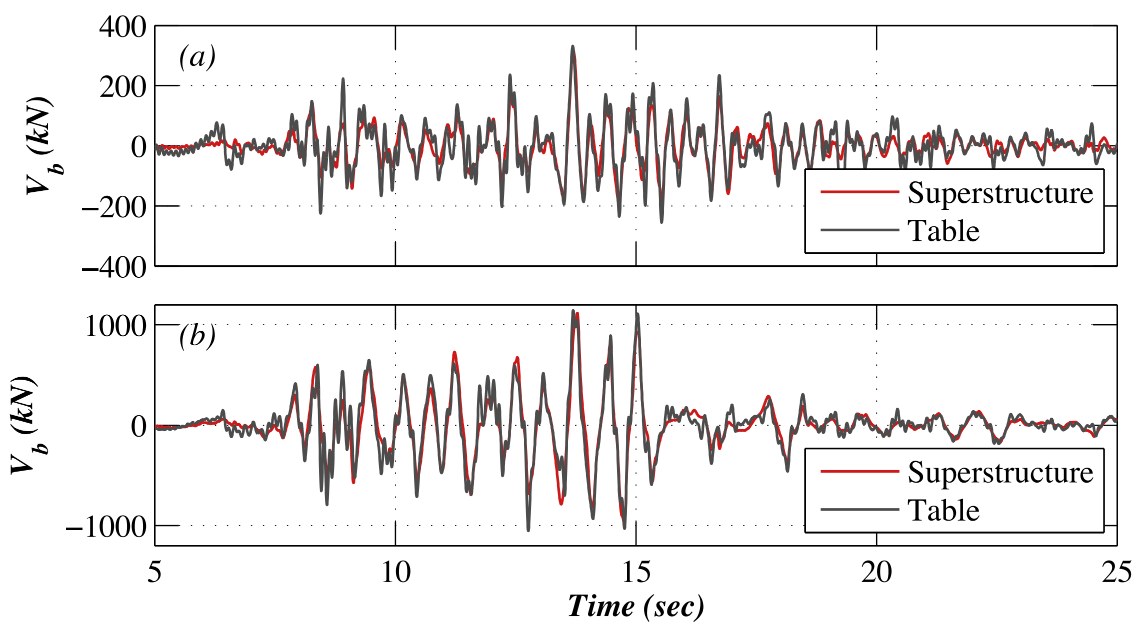

Figure 6.9. Comparison of base shear calculated using the two different method: (a) EQ2:CNP-25, and (b) EQ6:CNP-100.

6.2.2 Building Response

This section presents the global building responses during the pre-fire earthquake sequence (EQ1–EQ7). These responses include: (1) floor accelerations, (2) floor displacements, (3) interstory drift ratios (IDR), (4) roof drift ratios (RDRs), and (5) base shear and story shear forces. The accelerations presented later in this chapter denote absolute accelerations unless otherwise noted, whereas the displacements may represent either absolute displacements (relative to the ground – stationary reference) or relative displacement (relative to the first floor or table platen). For the purpose of consistency, the floor accelerations, relative floor displacements, and IDRs are presented using the follow systematic strategies:

- Time histories at the corners of all floors (levels) for EQ6:CNP-100 (design event);
- Time histories at the center of all floors (levels) for three tests with the identical target earthquake motion but different intensity levels: EQ2:CNP-25 (SLE), EQ6:CNP-100 (design event), and EQ7:CNP-150 (MCE);
- Peak response (maxima and minima) for six tests in the pre-fire earthquake sequence except for EQ4:CNP-25 (which essentially repeated EQ2:CNP-25).

Floor Absolute Accelerations

The floor absolute accelerations measured at the corners from floor 2 to roof during EQ6:CNP-100 (design event) are presented in Figure 6.10 through Figure 6.15, respectively. The measured accelerations are all filtered using a 4th order band-pass Butterworth filter with cut-off frequencies at 0.15 Hz and 30 Hz. Each figure contains two transverse accelerations (first row) and four longitudinal accelerations (second and third rows). The annotated text in each plot denotes the location and orientation of the response (e.g., *2-NW-T* indicates the transverse acceleration at the northwest corner of floor 2). In addition, the color circles represent the time instances associated with the maximum and minimum accelerations at the center the floor.

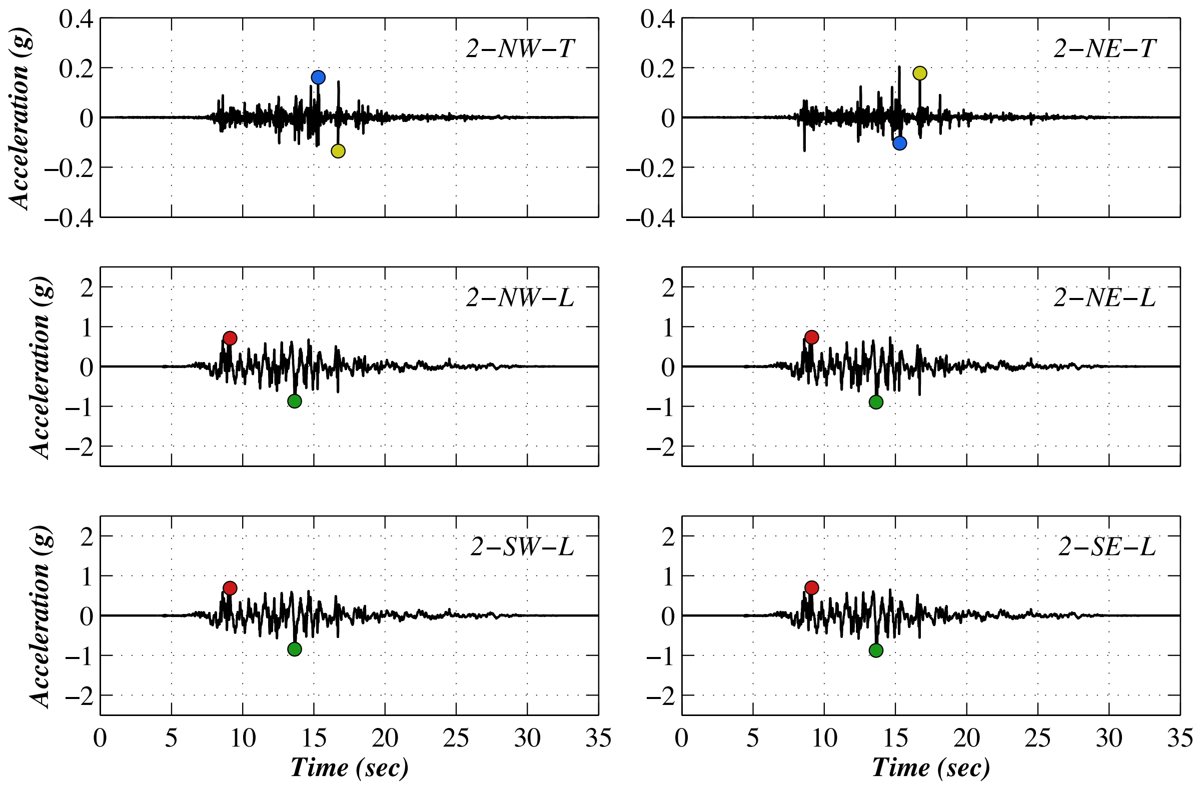

Figure 6.10. Measured corner accelerations at floor 2 – EQ6:CNP-100.

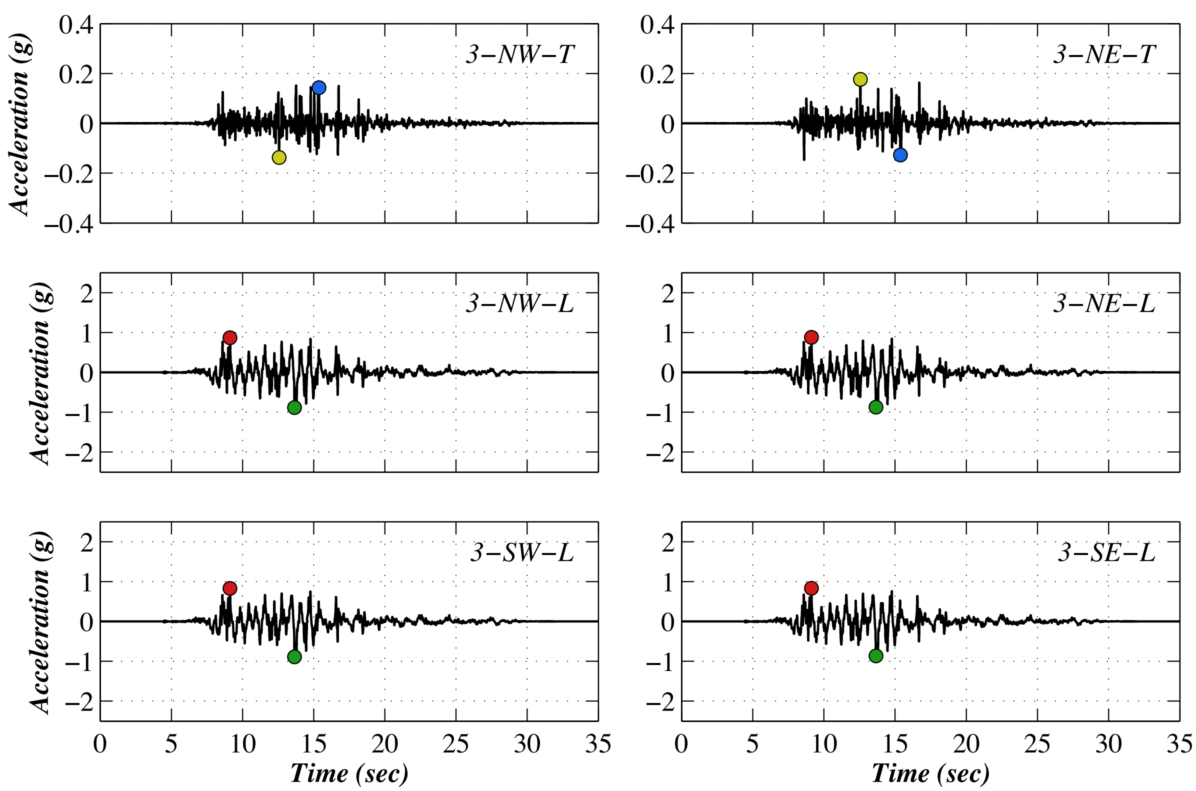

Figure 6.11. Measured corner accelerations at floor 3 – EQ6:CNP-100.

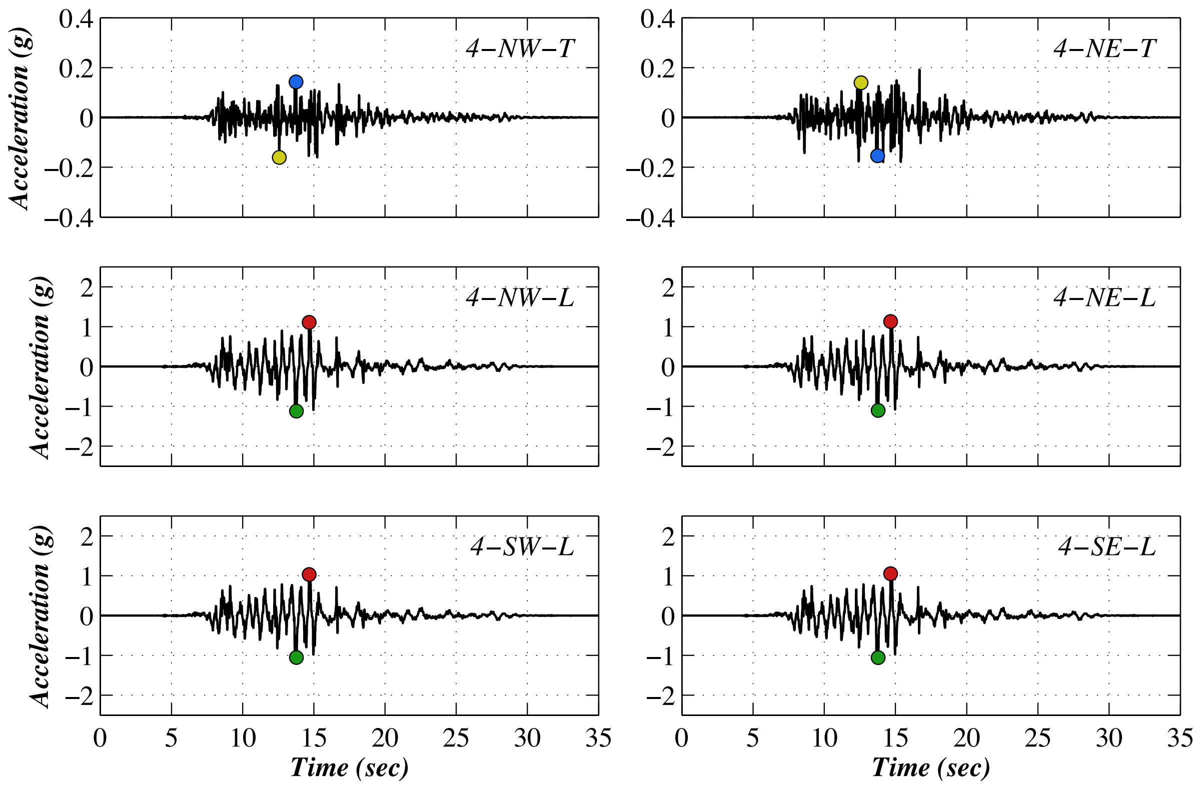

Figure 6.12. Measured corner accelerations at floor 4 – EQ6:CNP-100.

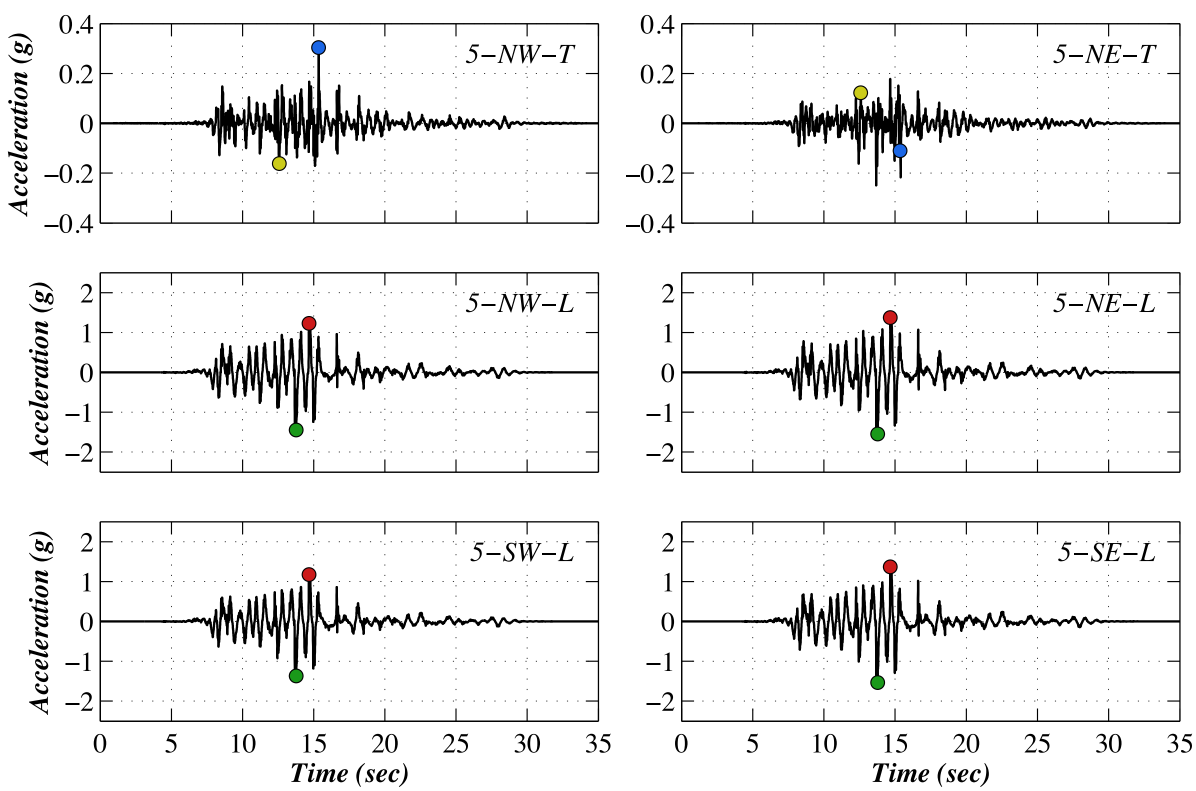

Figure 6.13. Measured corner accelerations at floor 5 – EQ6:CNP-100.

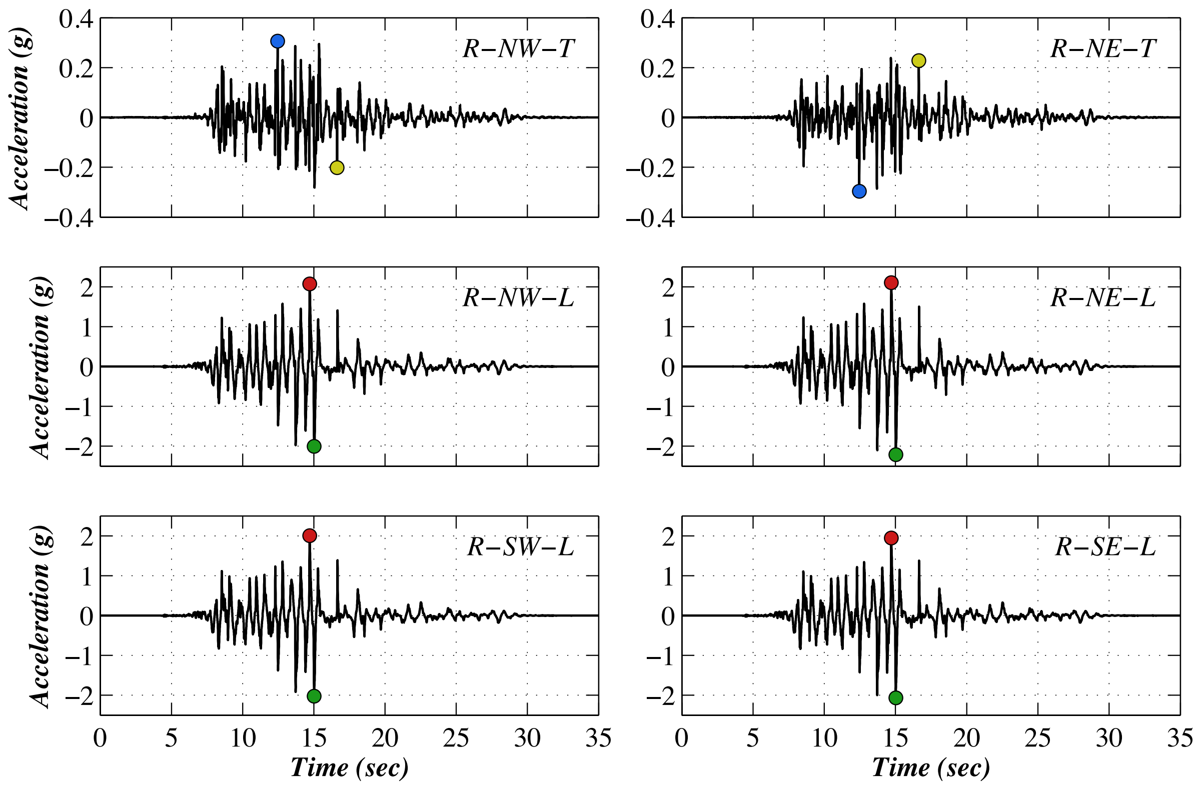

Figure 6.14. Measured corner accelerations at floor 6 – EQ6:CNP-100.

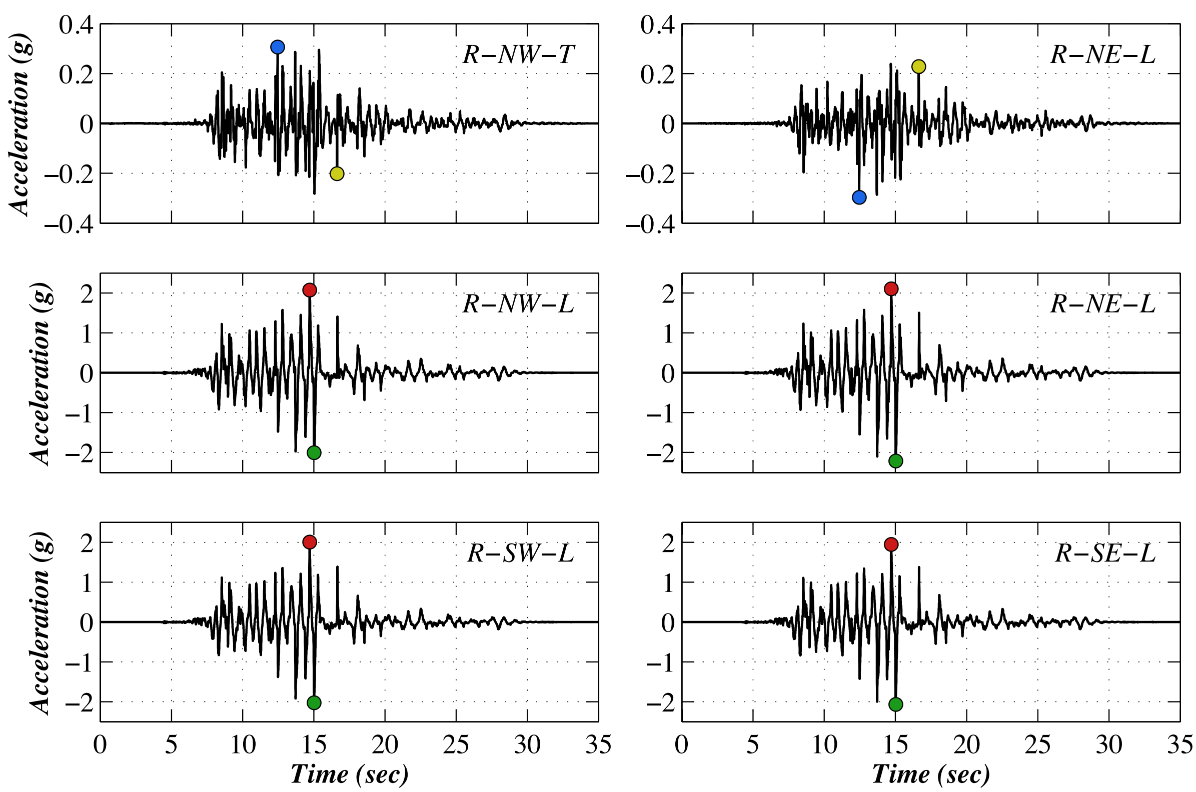

Figure 6.15. Measured corner accelerations at roof – EQ6:CNP-100.

Figure 6.16 through Figure 6.18 present the floor accelerations at the center from floor 1 (table platen) to roof during three select earthquake tests, namely, EQ2:CNP-25 (SLE), EQ6:CNP-100 (design event), and EQ7:CNP-150 (MCE), respectively. In these figures, each row contains the accelerations in the three directions (i.e., longitudinal, transverse, and torsional) at a specific floor. It is noted that the unit of the torsional accelerations (rad/sec^2) differs from that of the longitudinal and transverse accelerations (in unit of *g*). The annotated text in each plot denotes the floor number and orientation of the time history response (e.g., *2-T* indicates the transverse acceleration of floor 2). The color circles represent the time instances of the maximum (red) and minimum (green) responses to facilitate comparing the phase correlation of the responses at different floors or levels.

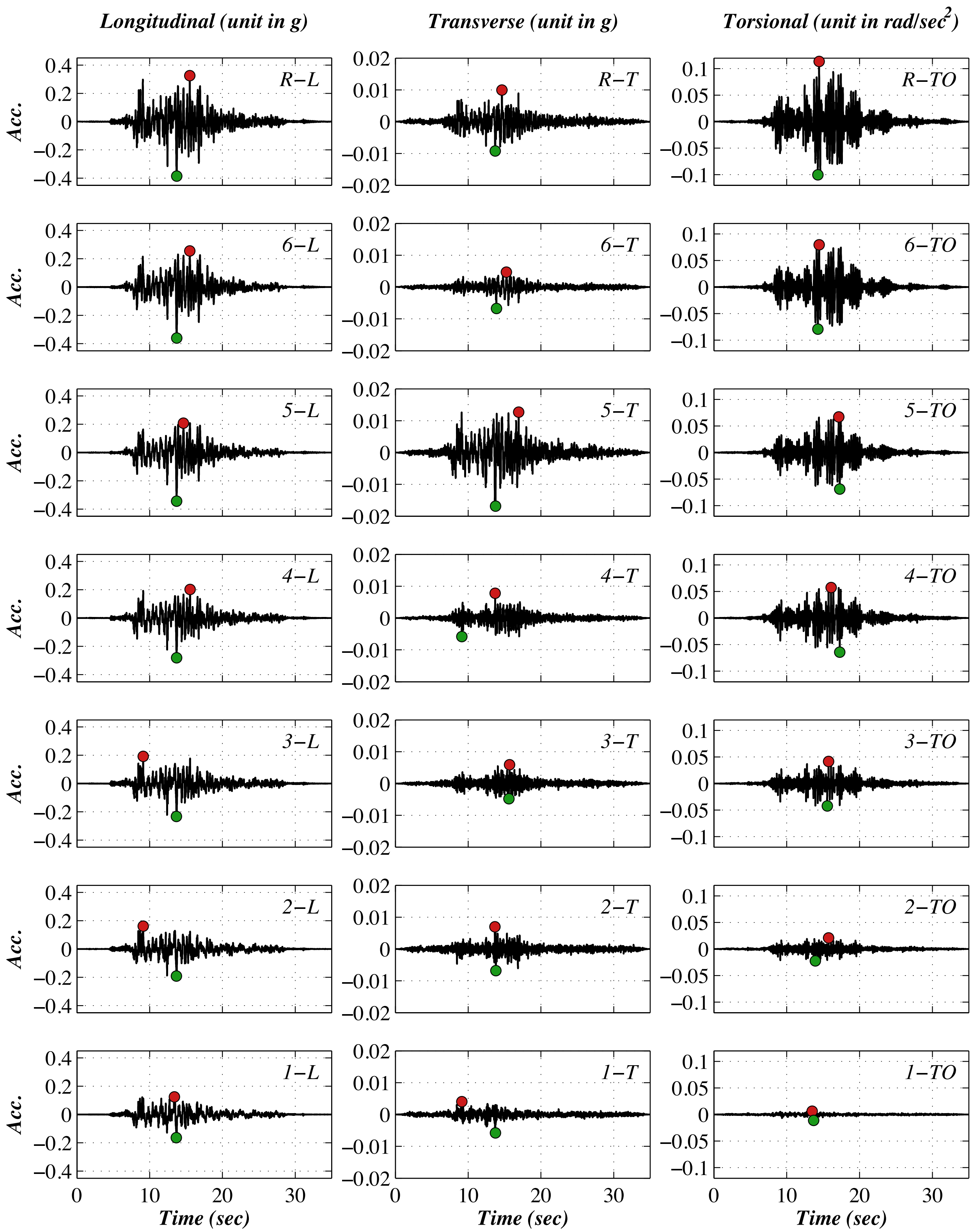

Figure 6.16. Measured floor center accelerations – EQ2:CNP-25.

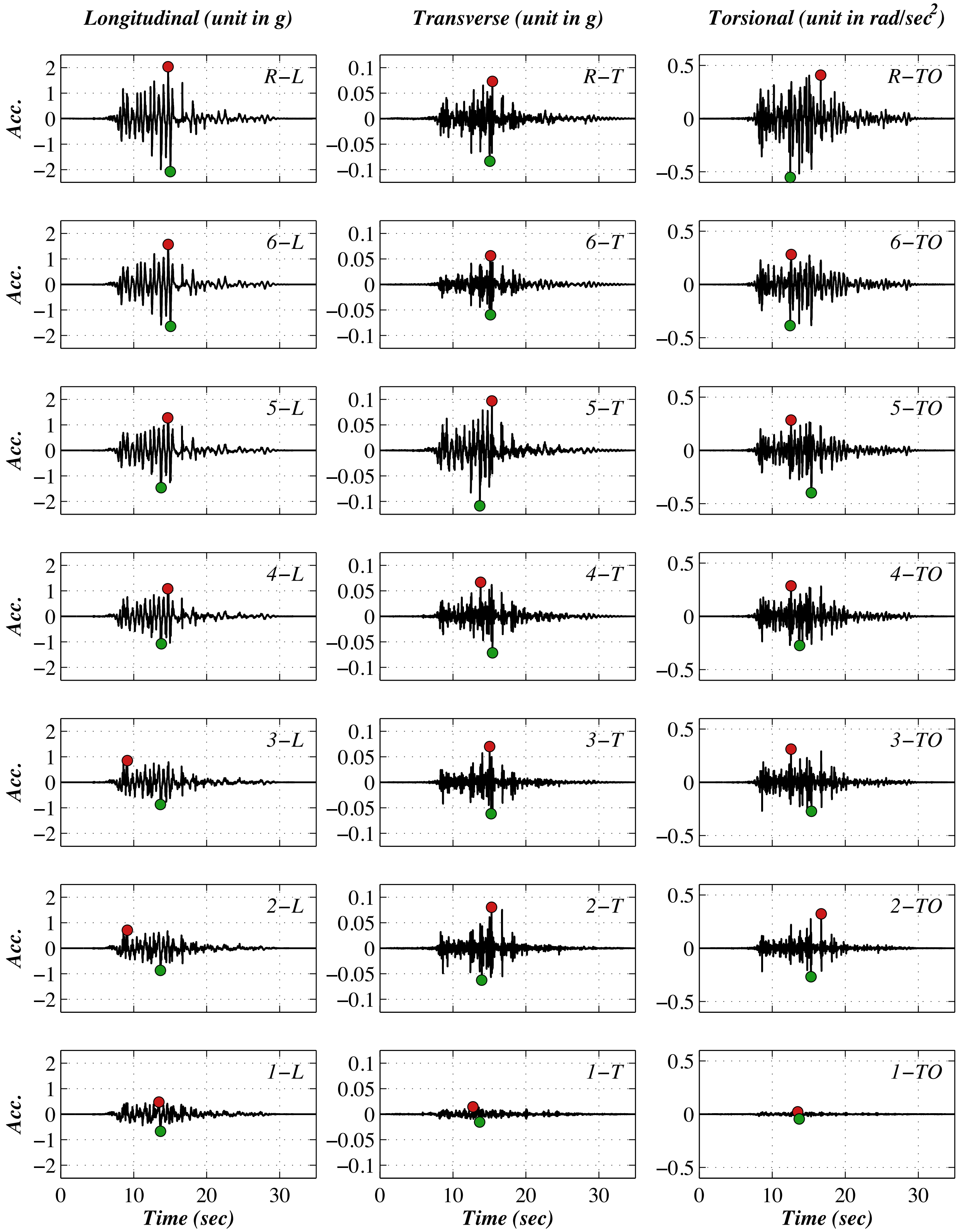

Figure 6.17. Measured floor center accelerations– EQ6:CNP-100.

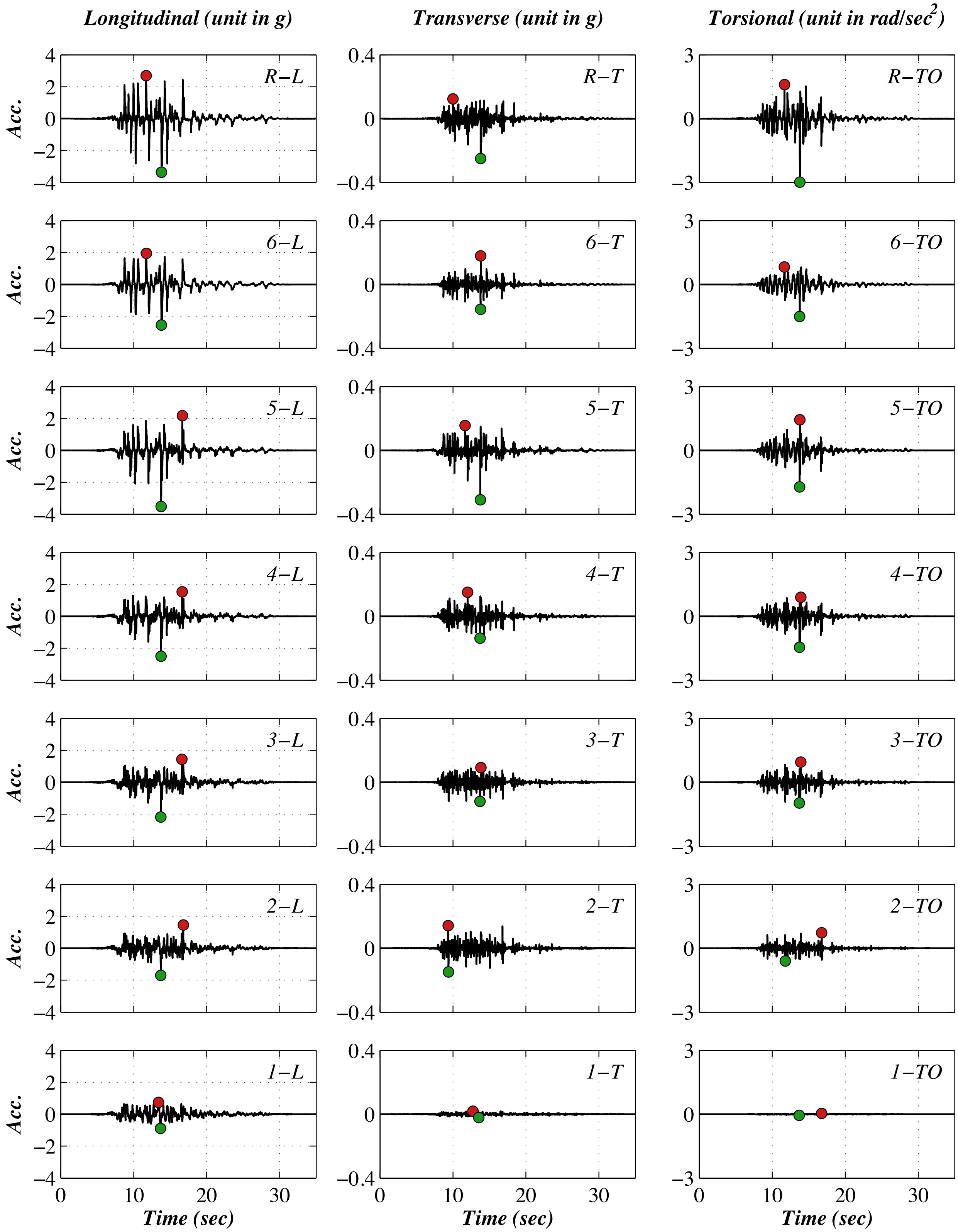

Figure 6.18. Measured floor center accelerations – EQ7:CNP-150.

Figure 6.19 presents the peak floor acceleration (PFA) distribution along the height of the building in the pre-fire earthquake sequence (in the longitudinal, transverse, and torsional directions). The peak accelerations correspond to those with respect to the floor centers. Except for EQ7, the longitudinal floor accelerations increased monotonically up the height of the building with their largest values at the roof. While relatively small during the service level earthquakes (< 0.5 g), the longitudinal peak roof accelerations achieved about 2 g during the design event (EQ6) and exceeded 3.5 g during the MCE event (EQ7). The transverse accelerations reached only < 10% of their longitudinal counterparts in all the pre-fire earthquake tests (Figure 6.20a). To facilitate the torsional and longitudinal acceleration comparison (for consistency in unit), the torsional accelerations are multiplied by the building width to represent the translational accelerations induced by the torsional effect. As shown in Figure 6.20b, the torsion-induced accelerations in the longitudinal direction were 20% – 30% that at the center of the floor up to the design event (EQ6) but reached as much as 60% at the roof during the MCE event (EQ7).

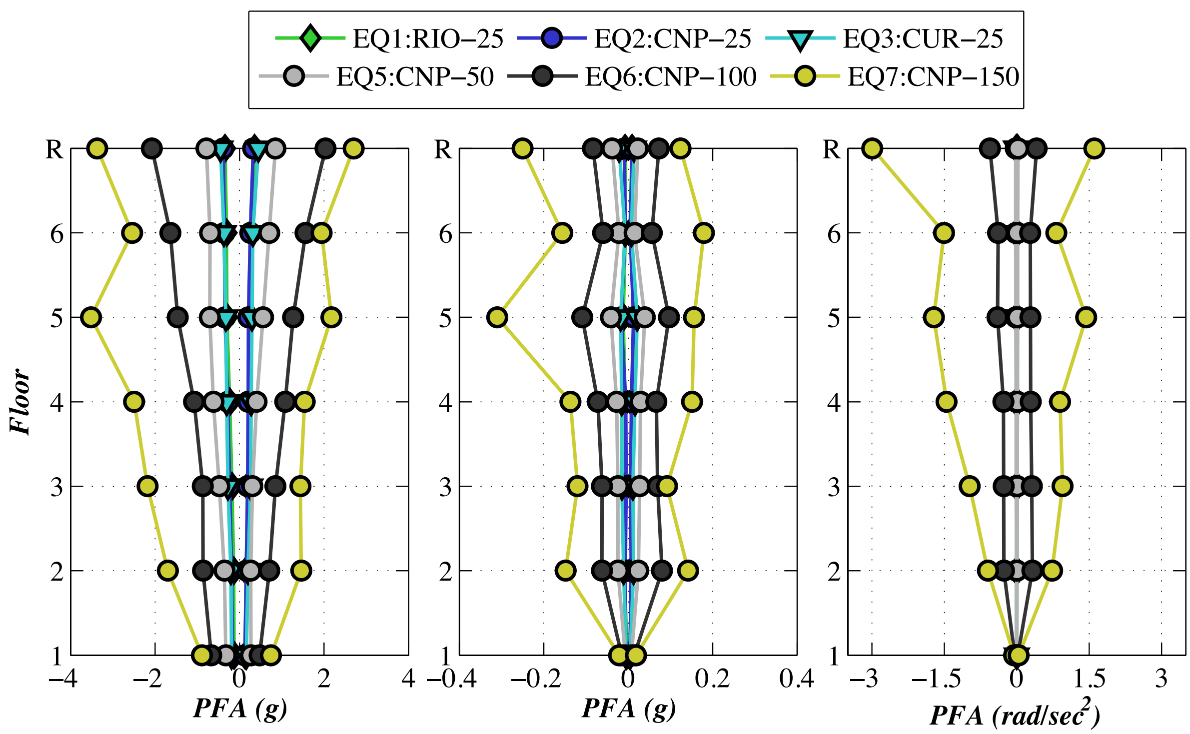

Figure 6.19. Peak floor accelerations (PFAs) measured during the pre-fire earthquake tests: (a) longitudinal, (b) transverse, and (c) torsional.

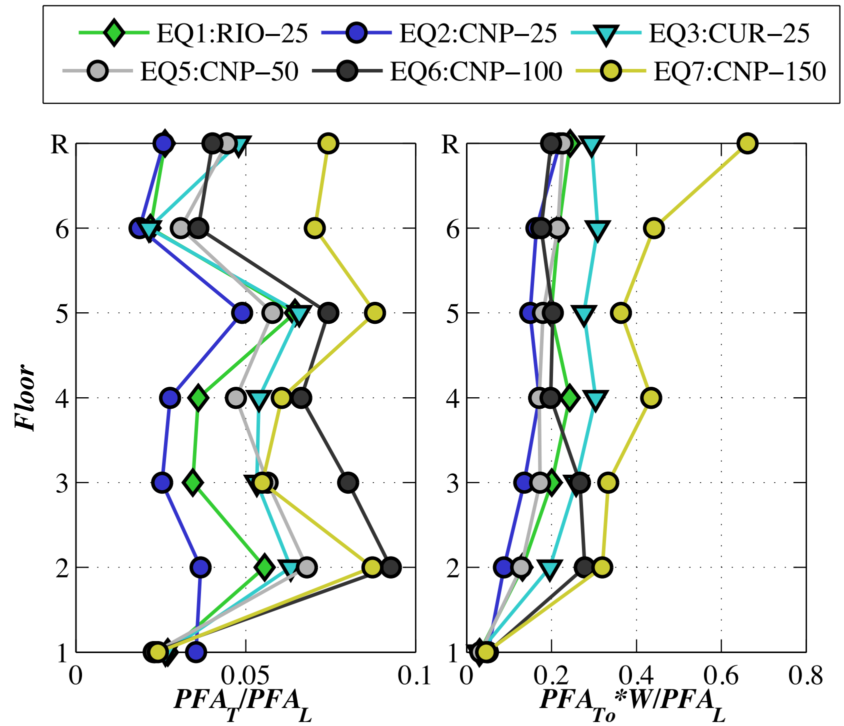

Figure 6.20. (a) Ratio of transverse and longitudinal peak floor accelerations, and (b) ratio of torsion-induced peak floor accelerations in the longitudinal direction and longitudinal peak floor accelerations during the pre-fire earthquake tests.

Floor Relative Displacements

The floor relative displacements at the corners from floor 2 to roof during EQ6:CNP-100 (design event) are presented in Figure 6.21 through Figure 6.26, respectively. Each figure contains two transverse displacements (first row) and four longitudinal displacements (second and third rows). In addition, the floor relative displacements at the center from floor 1 (shake table platen) to roof during three select earthquake tests, namely, EQ2:CNP-25 (SLE), EQ6:CNP-100 (design event), and EQ7:CNP-150 (MCE), are presented in Figure 6.27 through Figure 6.29, respectively. It is noted that the unit of torsional displacements (rad) differs from that of longitudinal and transverse displacements (cm).

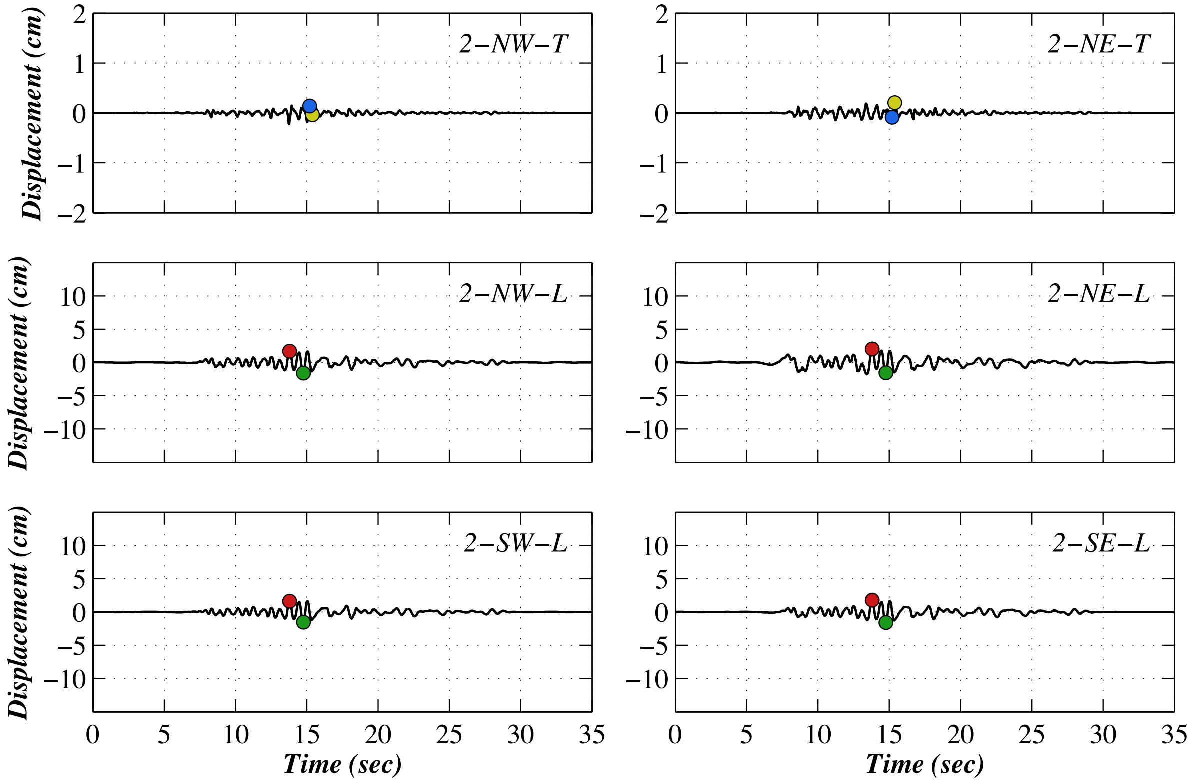

Figure 6.21. Measured corner relative displacements at floor 2 – EQ6:CNP-100.

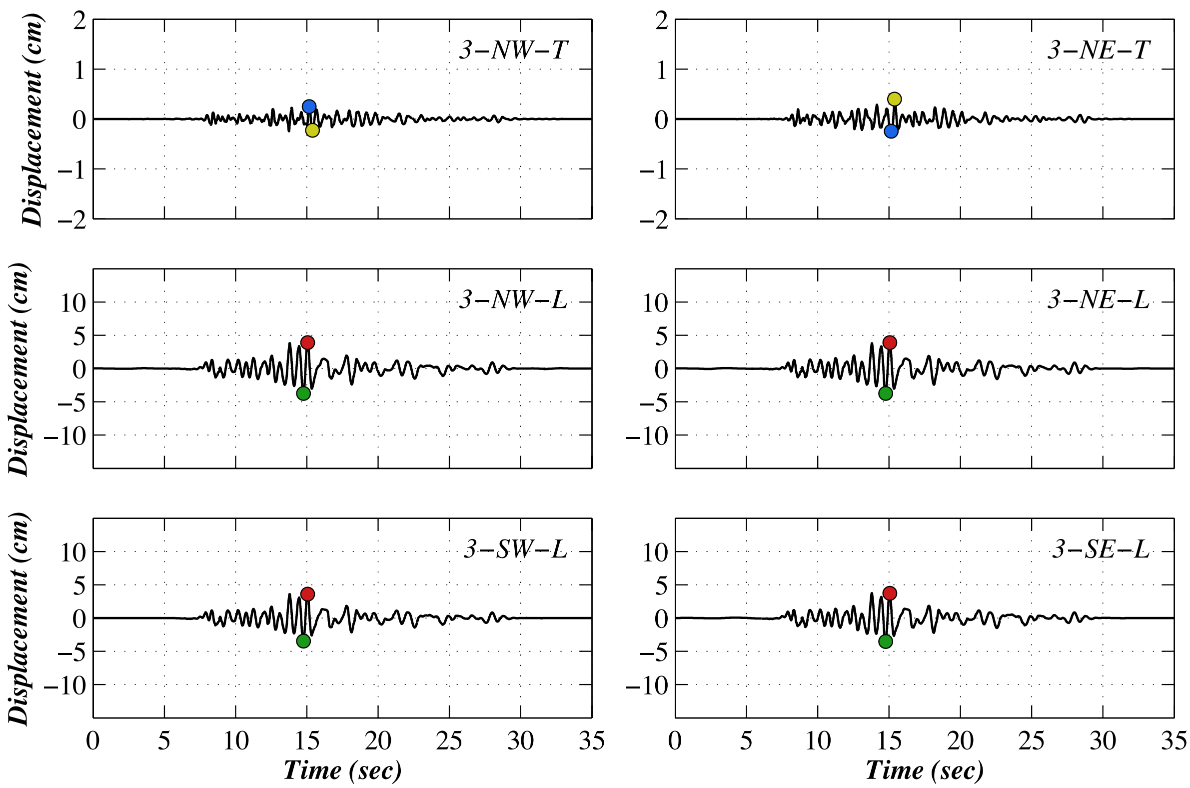

Figure 6.22. Measured corner relative displacements at floor 3 – EQ6:CNP-100.

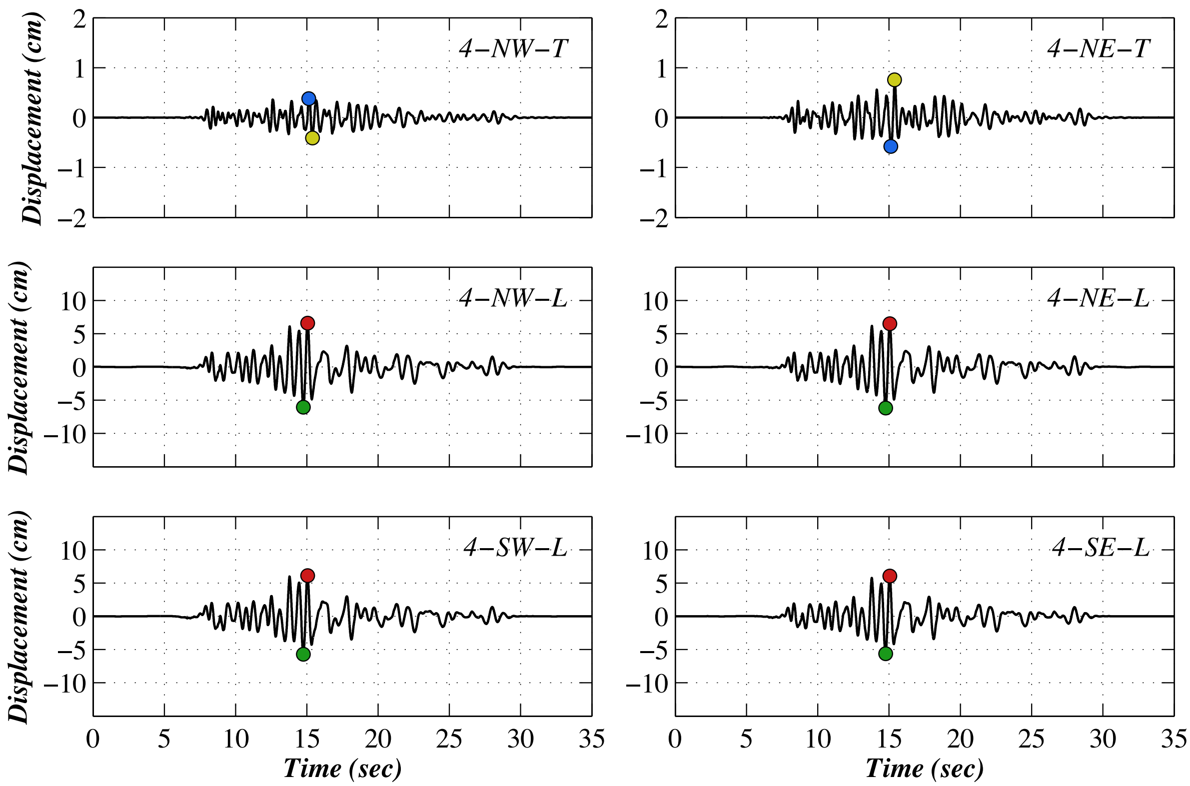

Figure 6.23. Measured corner relative displacements at floor 4 – EQ6:CNP-100.

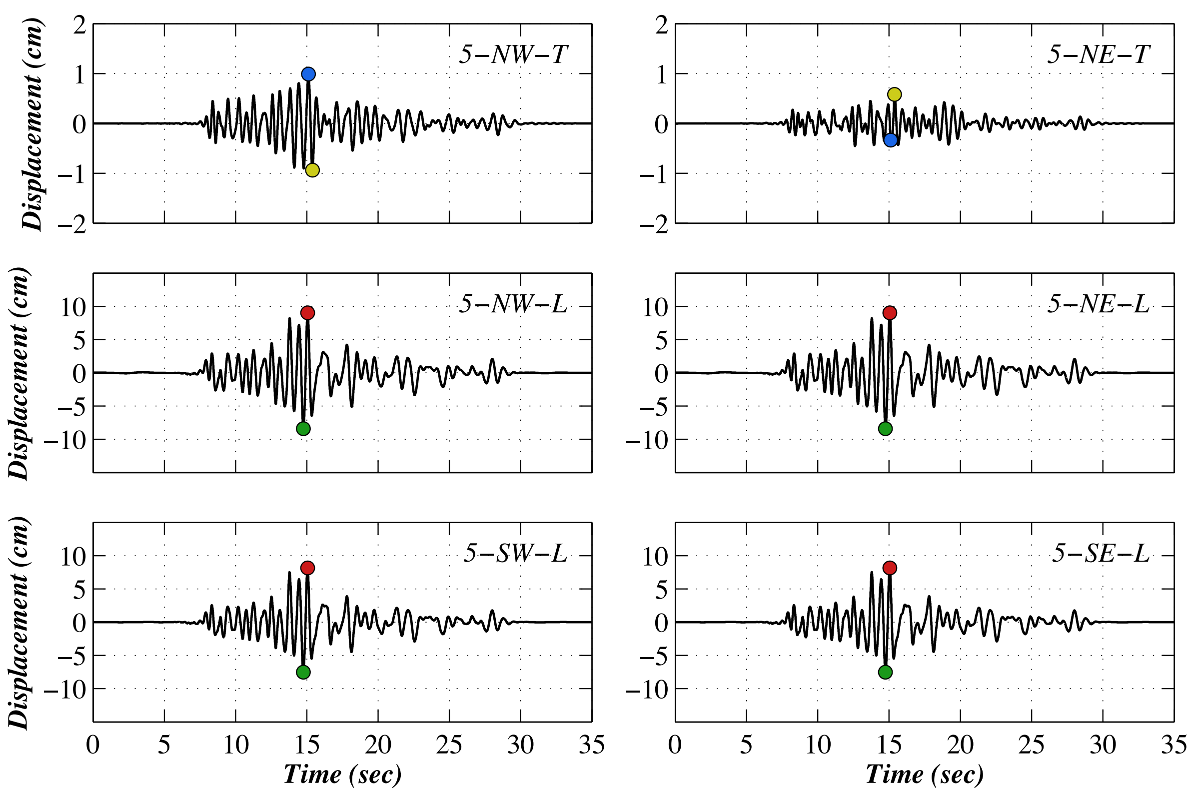

Figure 6.24. Measured corner relative displacements at floor 5 – EQ6:CNP-100.

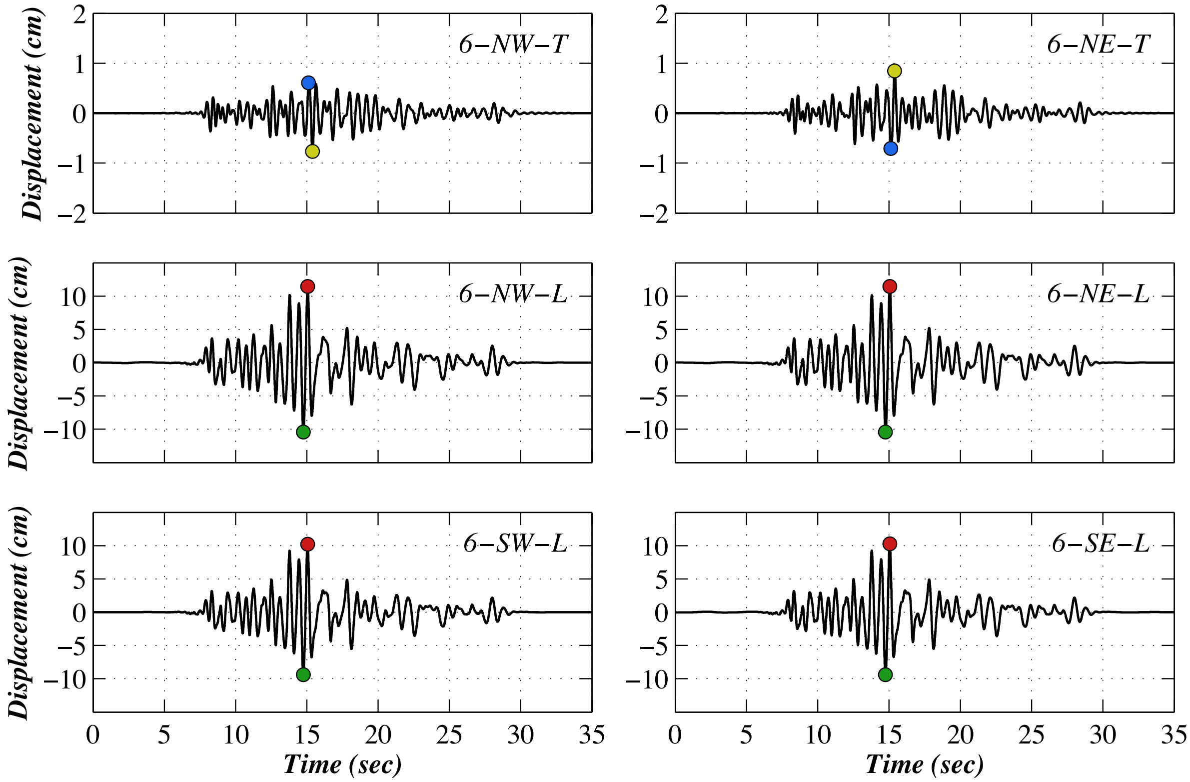

Figure 6.25. Measured corner relative displacements at floor 6 – EQ6:CNP-100.

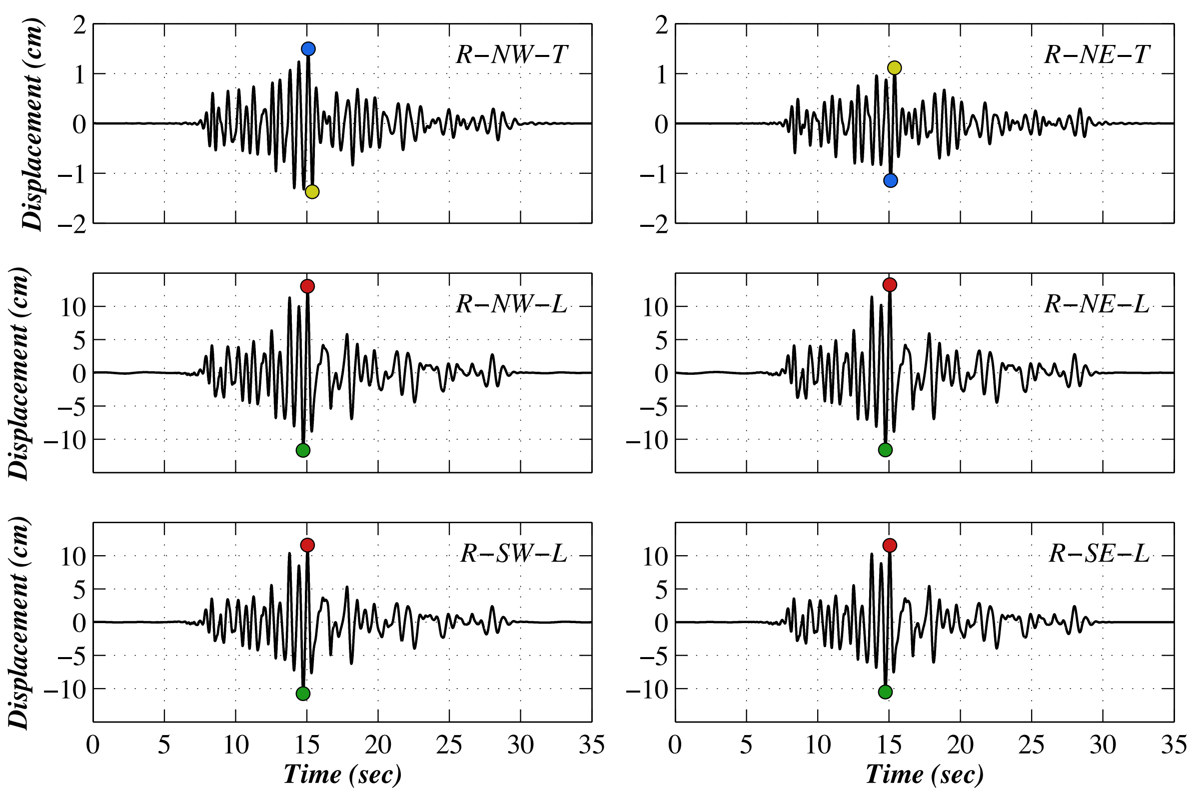

Figure 6.26. Measured corner relative displacements at roof – EQ6:CNP-100.

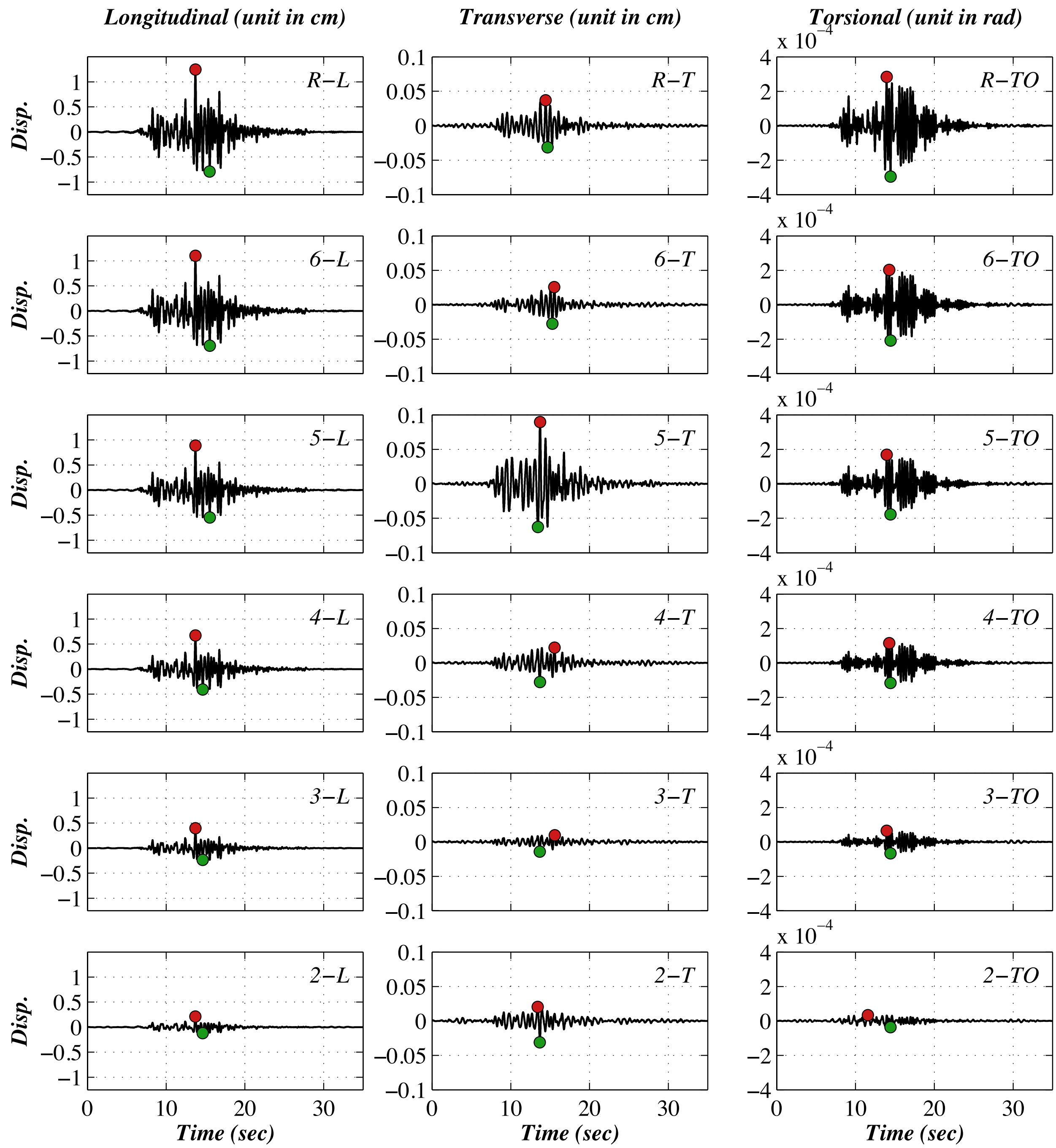

Figure 6.27. Measured relative floor center displacements– EQ2:CNP-25.

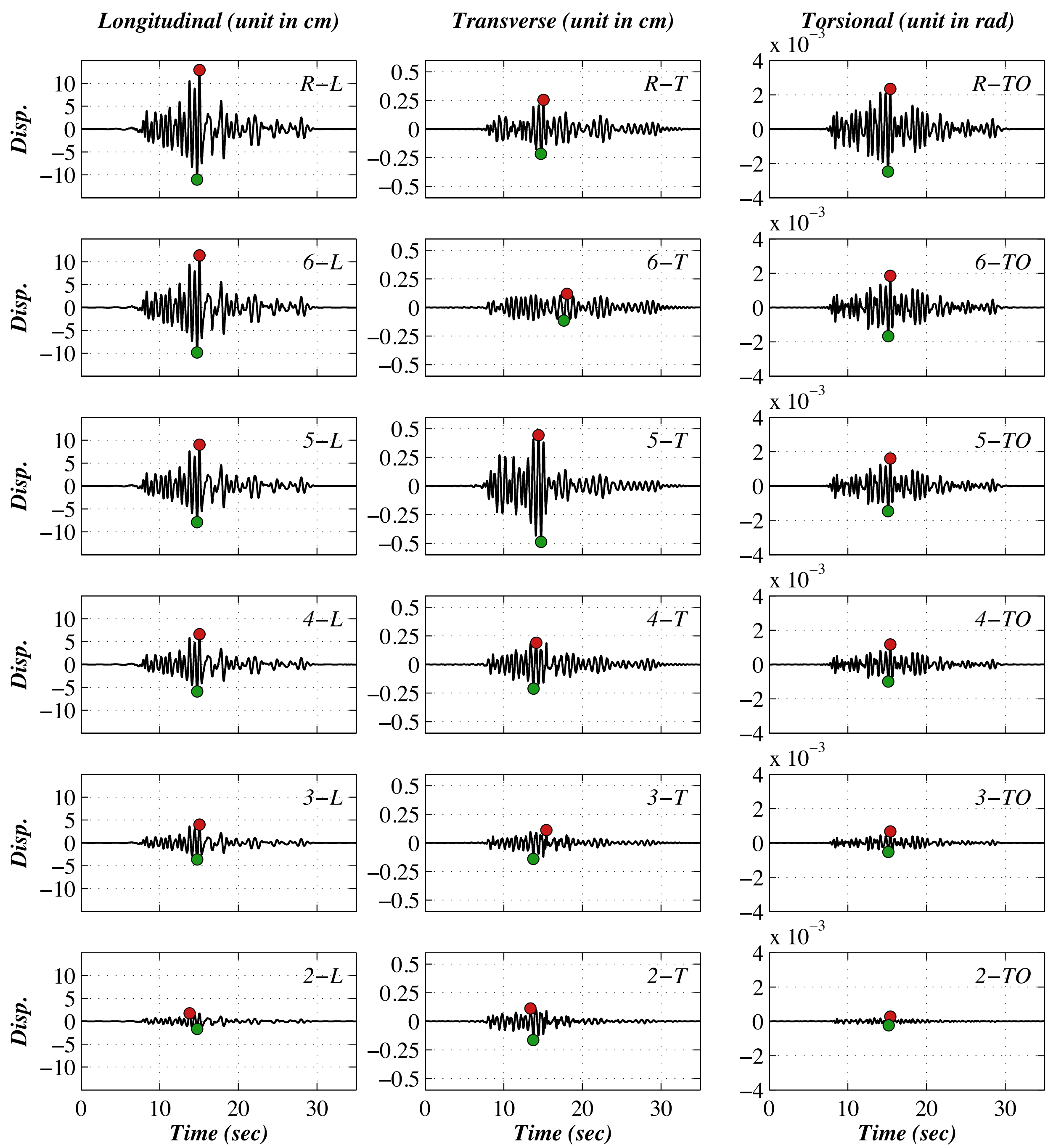

Figure 6.28. Measured relative floor center displacements – EQ6:CNP-100.

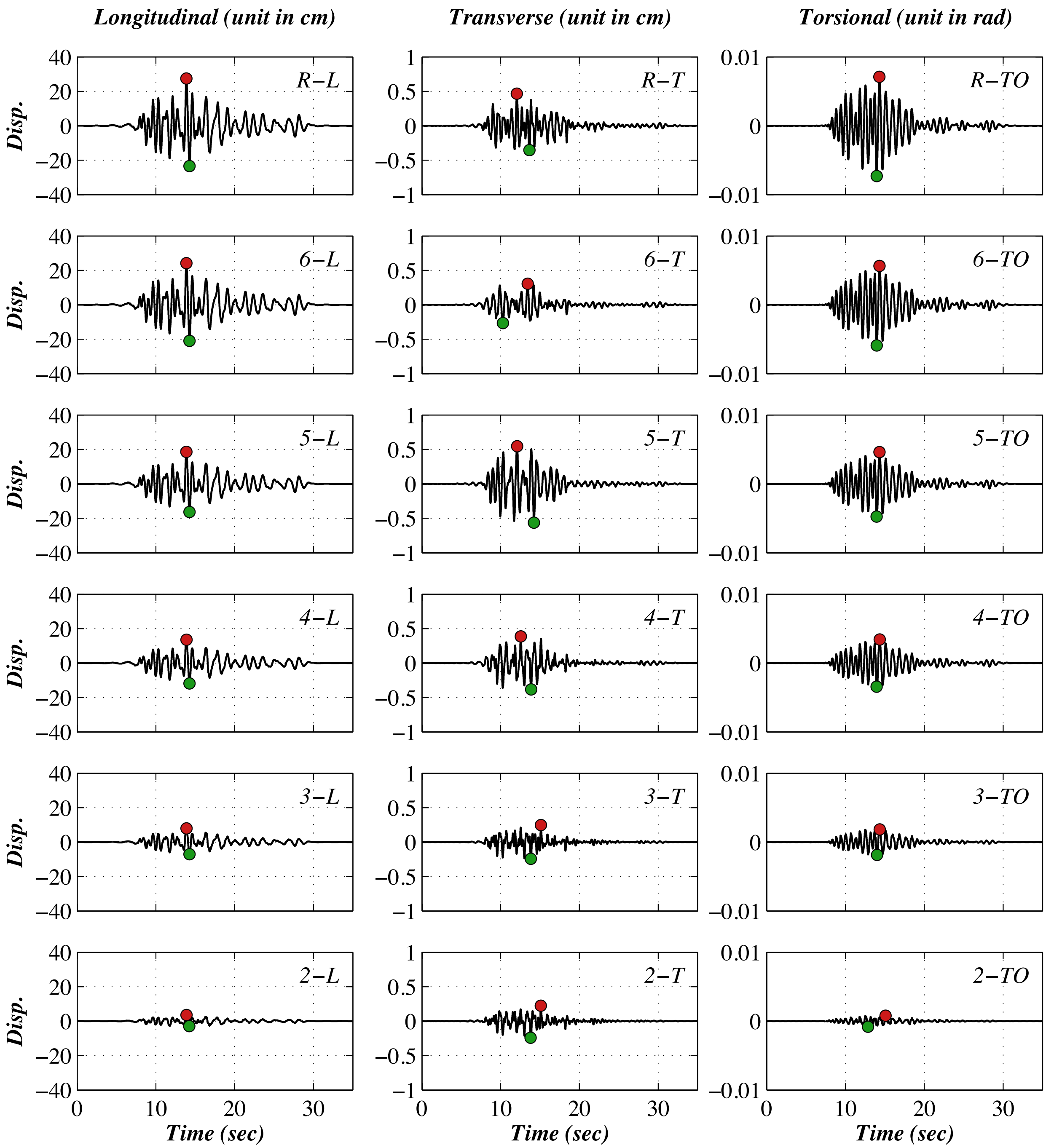

Figure 6.29. Measured relative floor center displacements – EQ7:CNP-150.

Interstory Drift Ratios

The interstory drift ratios (IDRs) at the corners at all six levels during EQ6:CNP-100 (design event) are presented in Figure 6.30 through Figure 6.35, respectively. Each figure contains two transverse responses (first row) and four longitudinal responses (second and third rows). In addition, the longitudinal and transverse IDRs at the center of all levels as well as the interstory rotations (IRs) during three select earthquake tests, namely, EQ2:CNP-25 (SLE), EQ6:CNP-100 (design event), and EQ7:CNP-150 (MCE), are presented in Figure 6.36 through Figure 6.38, respectively. It is noted that the unit of IR (rad) differs from that of the longitudinal and transverse IDRs (%).

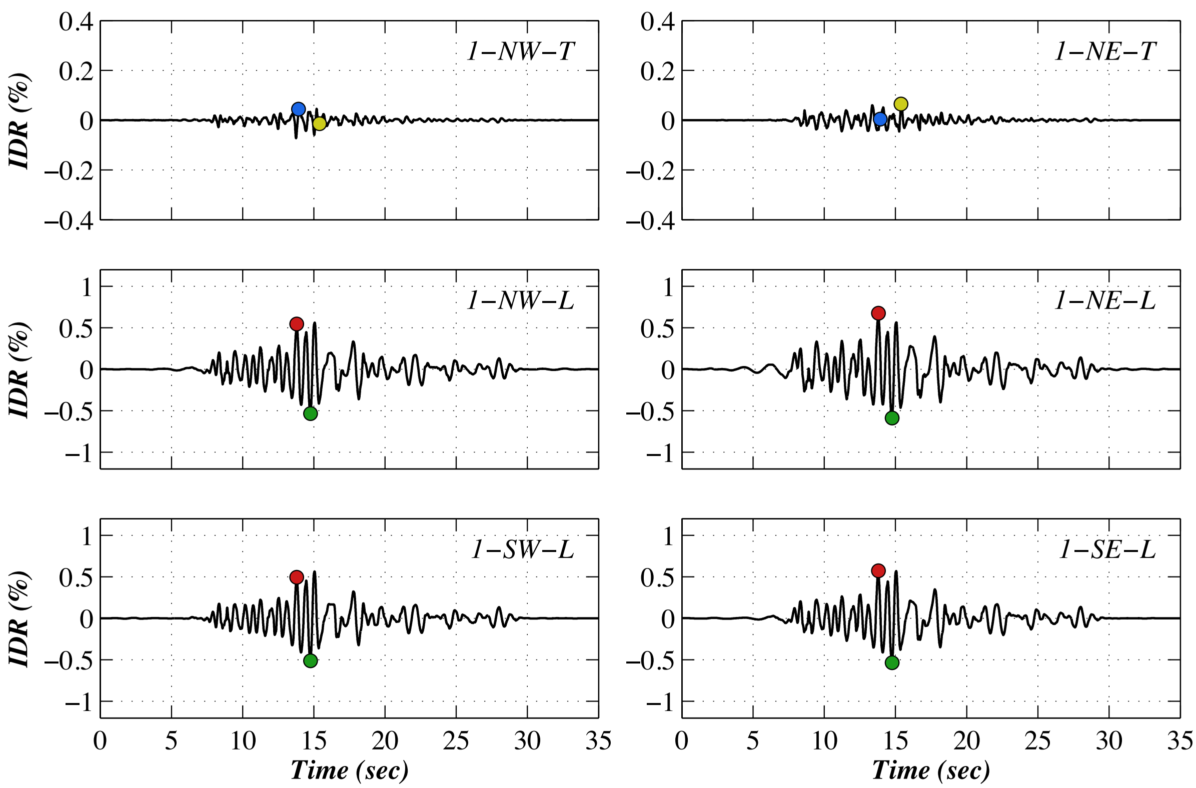

Figure 6.30. Measured corner interstory drift ratio at level 1 – EQ6:CNP100.

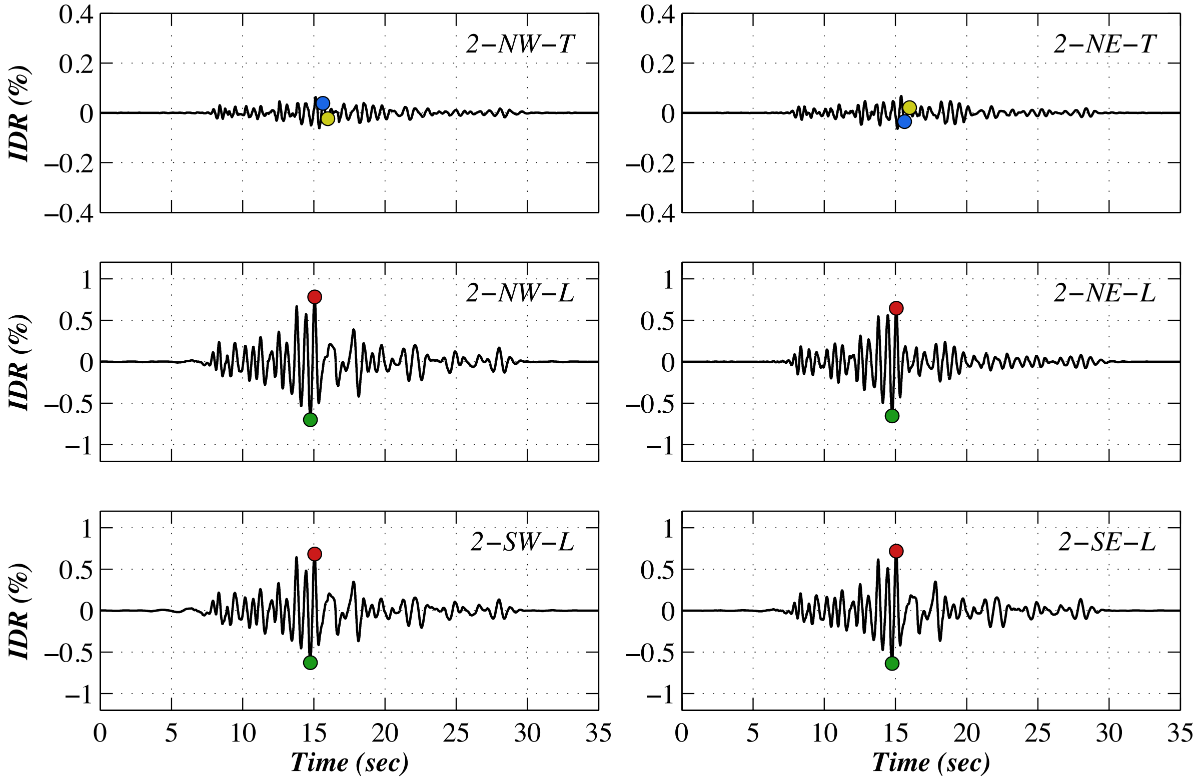

Figure 6.31. Measured corner interstory drift ratio at level 2 – EQ6:CNP100.

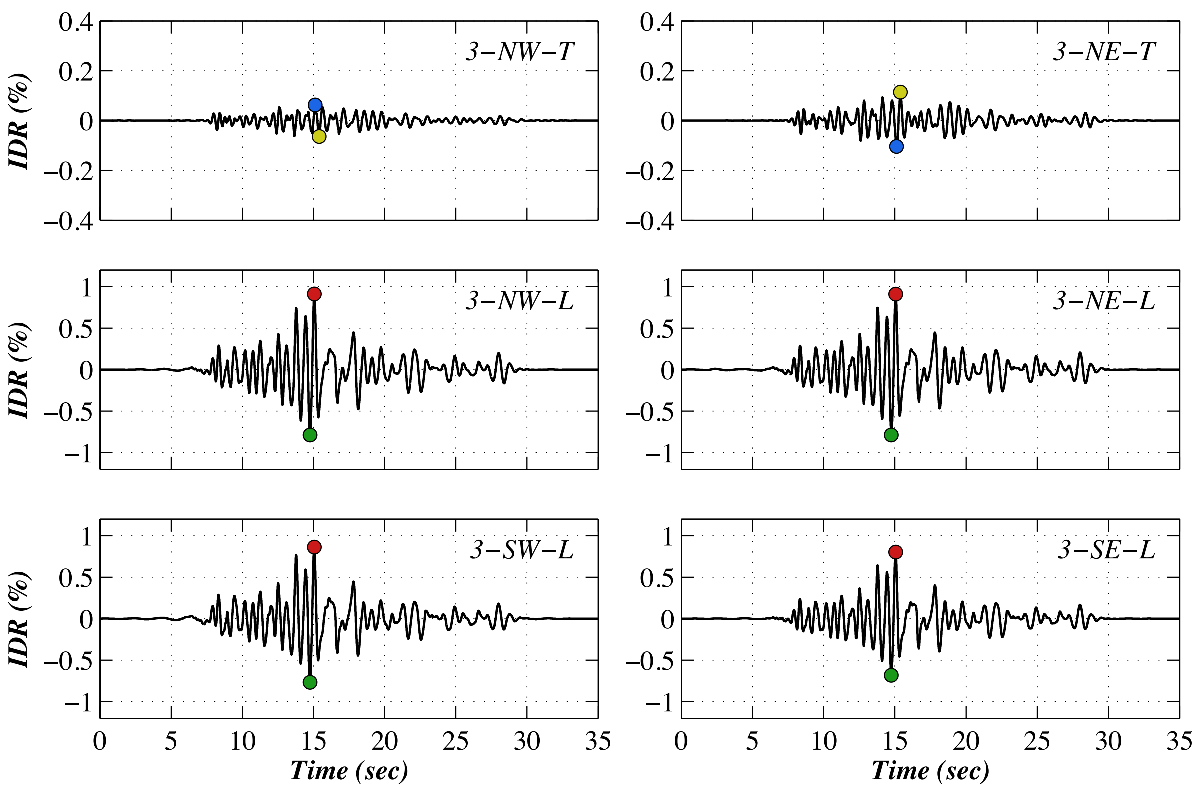

Figure 6.32. Measured corner interstory drift ratio at level 3 – EQ6:CNP100.

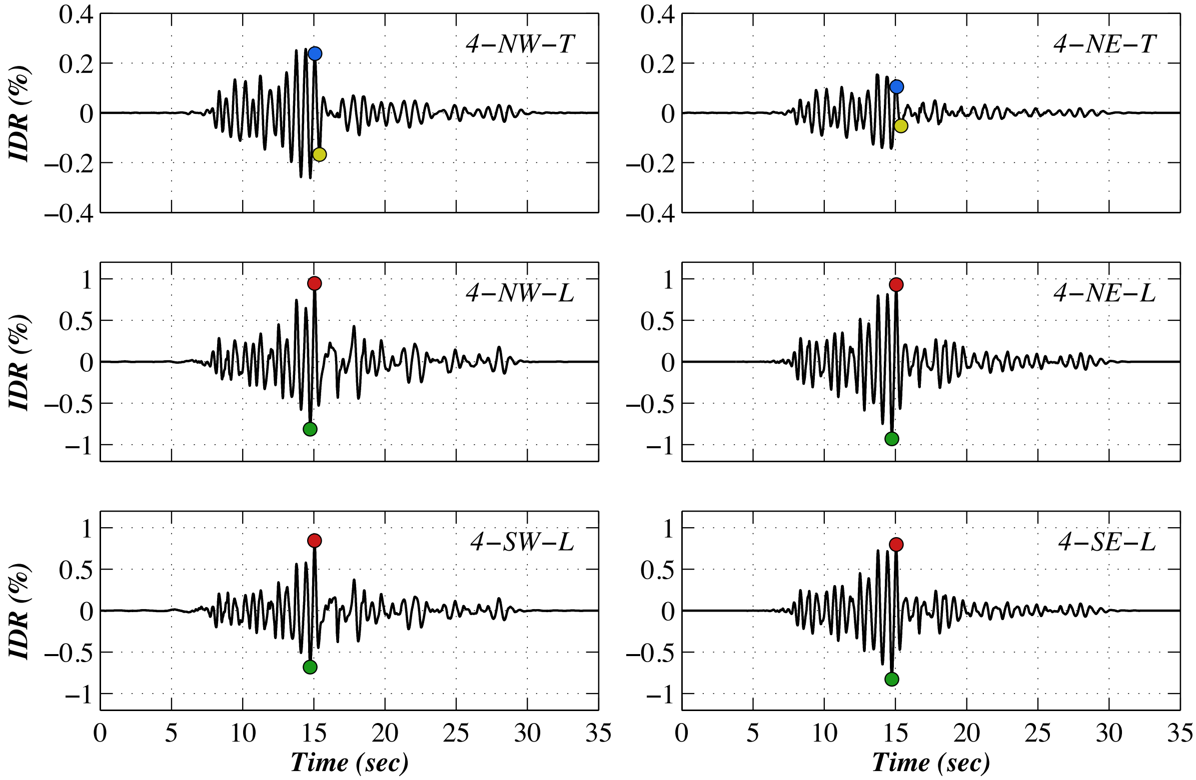

Figure 6.33. Measured corner interstory drift ratio at level 4 – EQ6:CNP100.

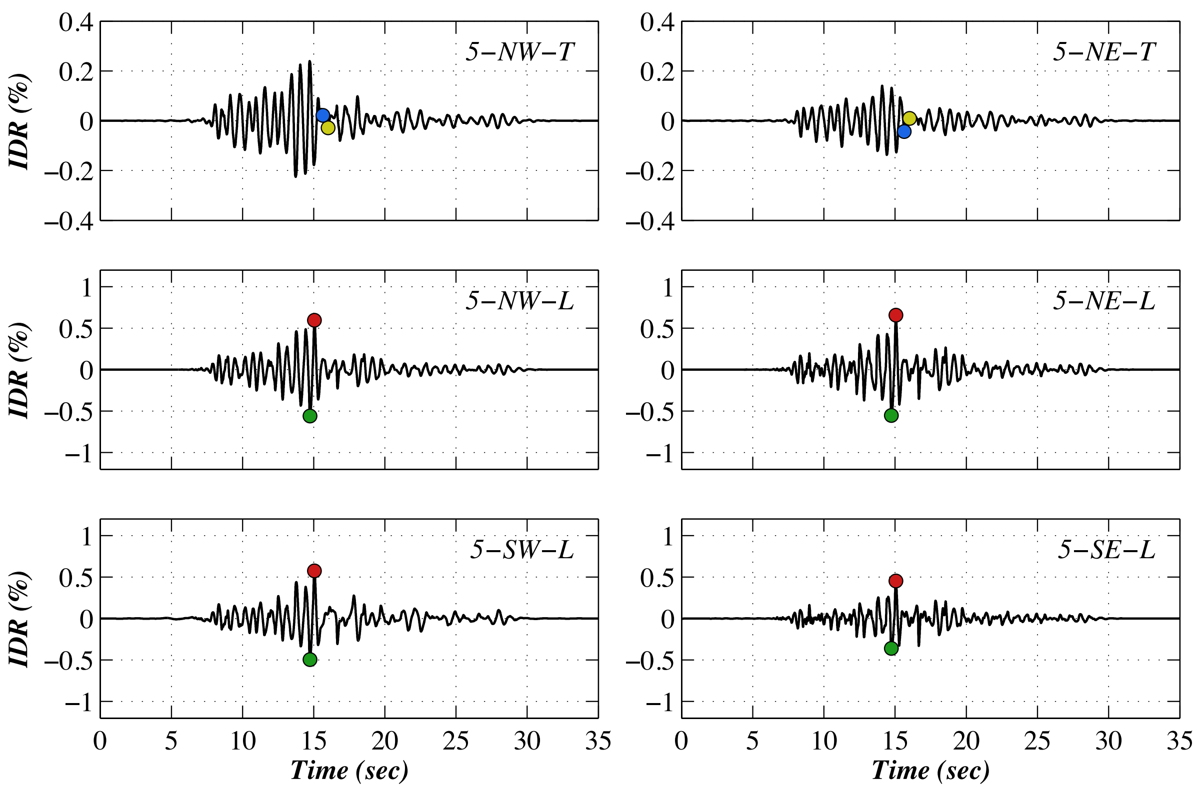

Figure 6.34. Measured corner interstory drift ratio at level 5 – EQ6:CNP100.

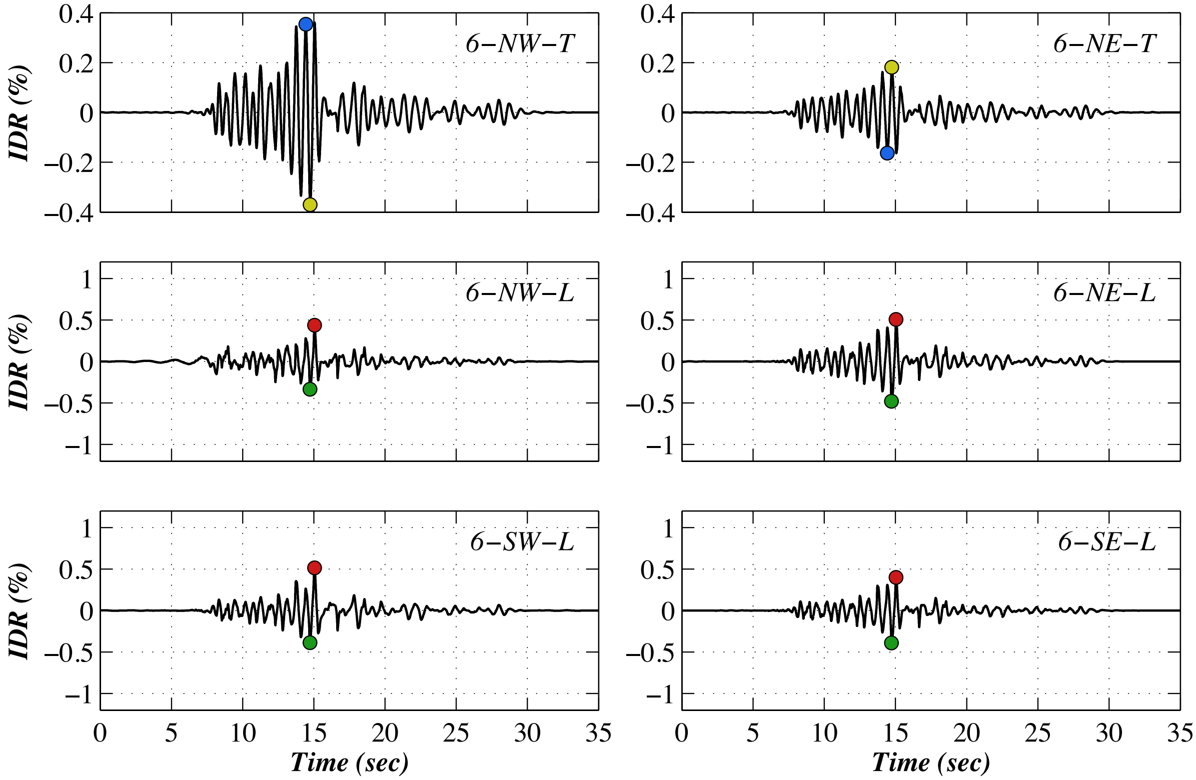

Figure 6.35. Measured corner interstory drift ratio at level 6 – EQ6:CNP-100.

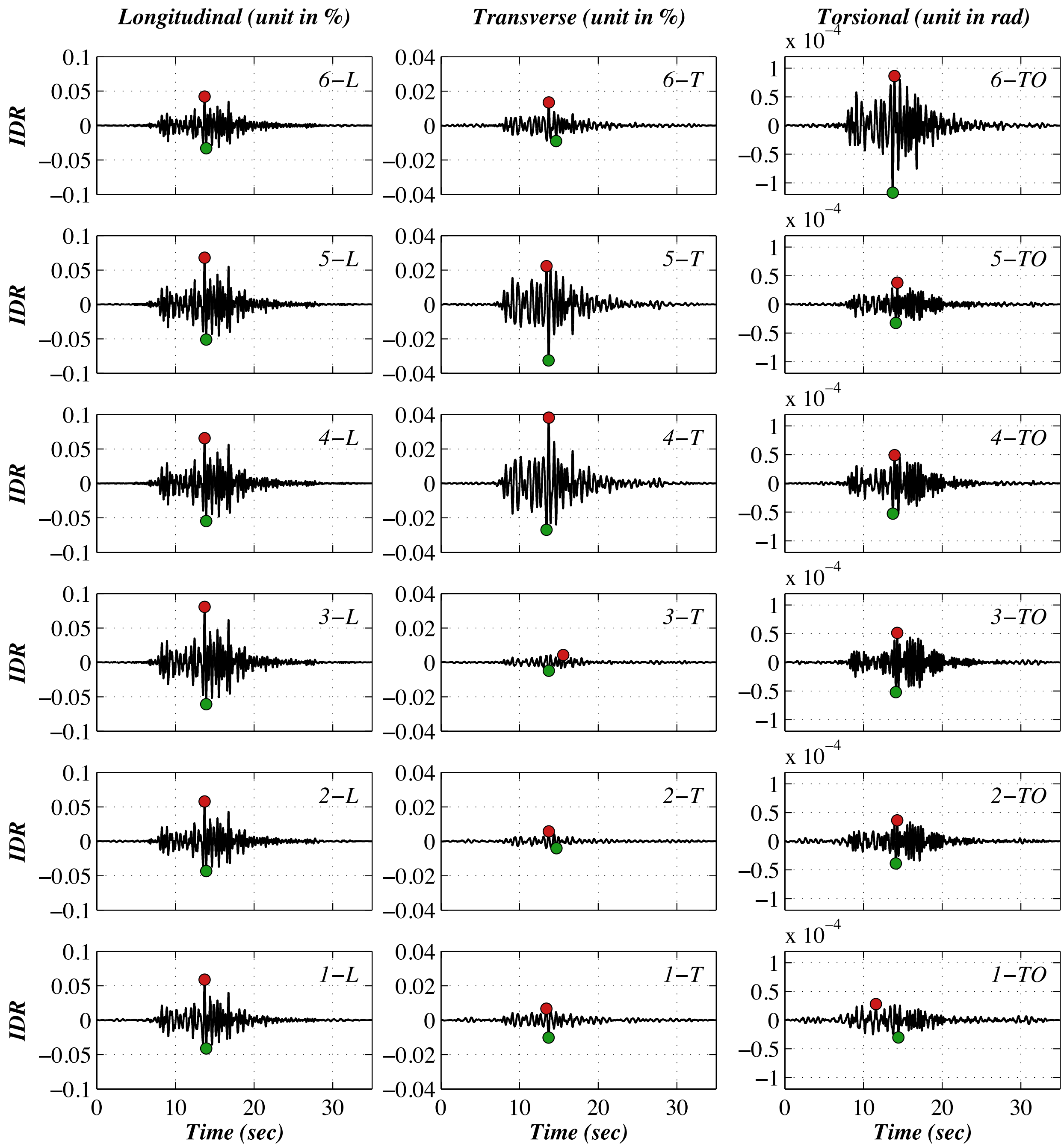

Figure 6.36. Measured floor center interstory drift ratios – EQ2:CNP-25.

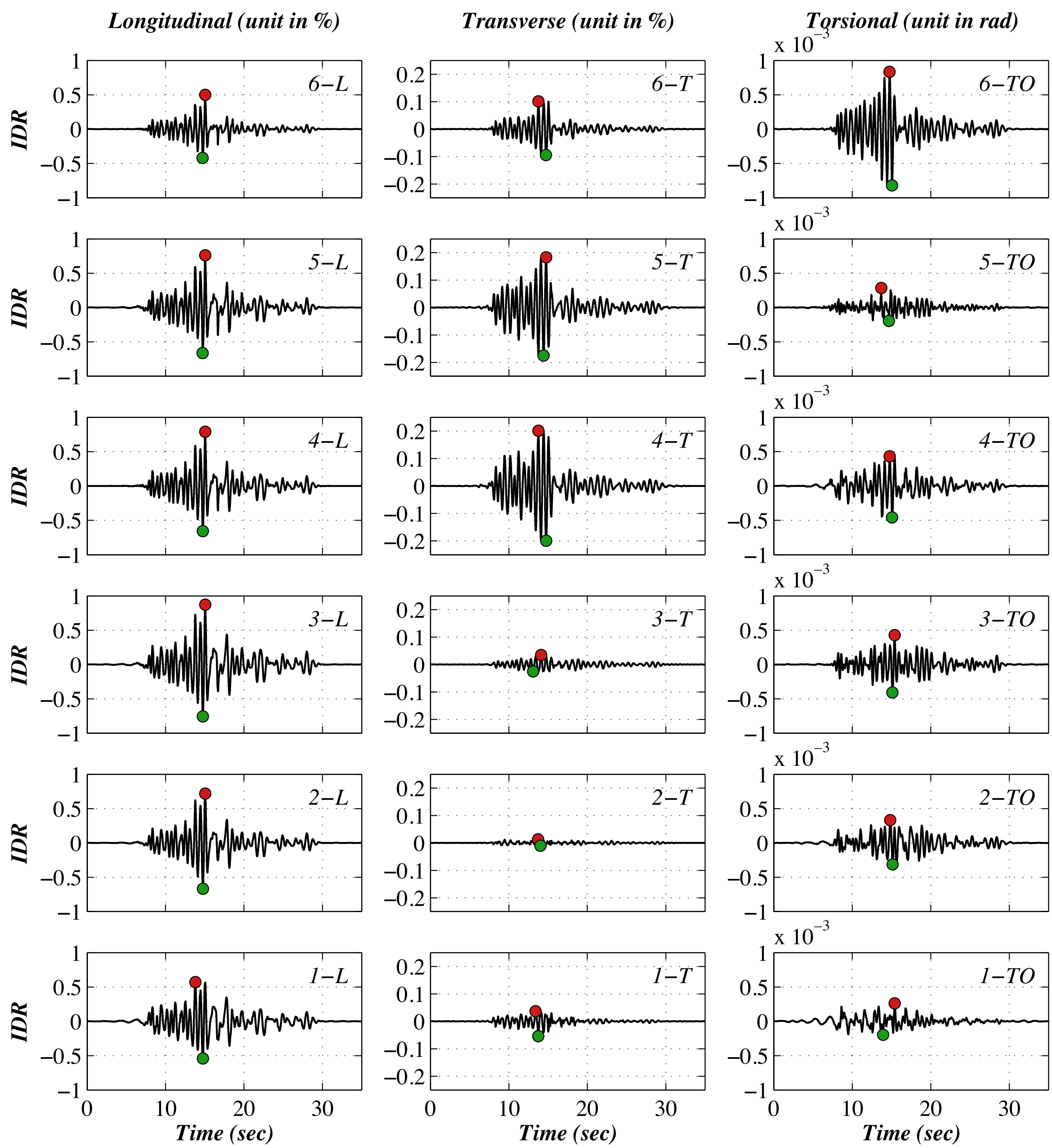

Figure 6.37. Measured floor center interstory drift ratios – EQ6:CNP-100.

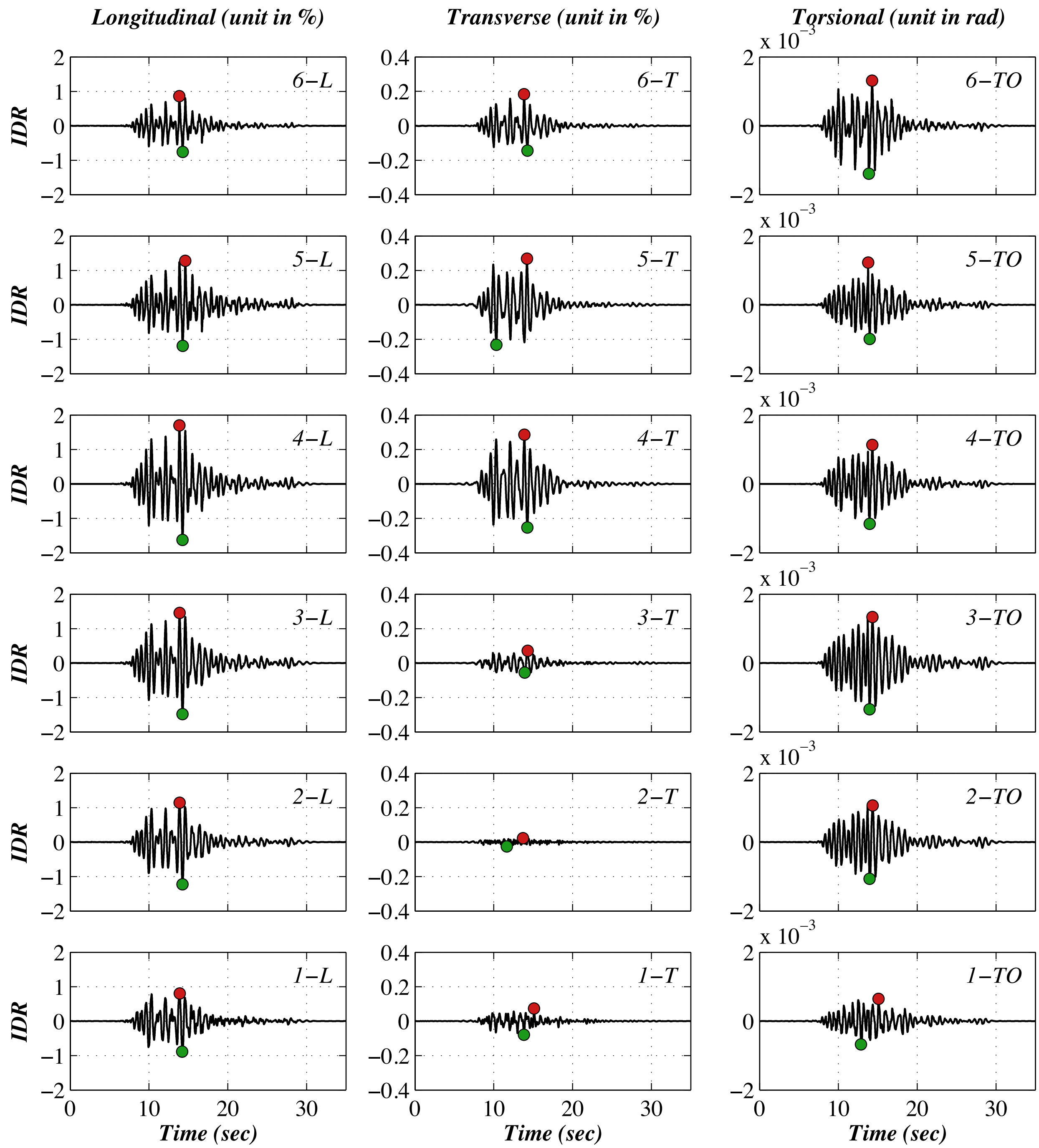

Figure 6.38. Measured floor center interstory drift ratios – EQ7:CNP-150.

Figure 6.39 presents the peak interstory drift ratios (PIDRs) in the longitudinal and transverse directions as well as the peak interstory rotation (PIRs) along the height of the building in the pre-fire earthquake test sequence. The PIDRs correspond to those associated with the floor centers. The largest longitudinal PIDRs occurred at the building mid-height (level 4) during all pre-fire earthquake tests. While relatively small during the service level earthquakes (< 0.1%), the longitudinal PIDRs achieved about 1% during the design event (EQ6) and exceeded 1.5% during the MCE event (EQ7). The transverse PIDRs at the upper three levels appeared considerably larger than those at the lower levels, while the PIR consistently achieved the largest values at the top level (level 6).

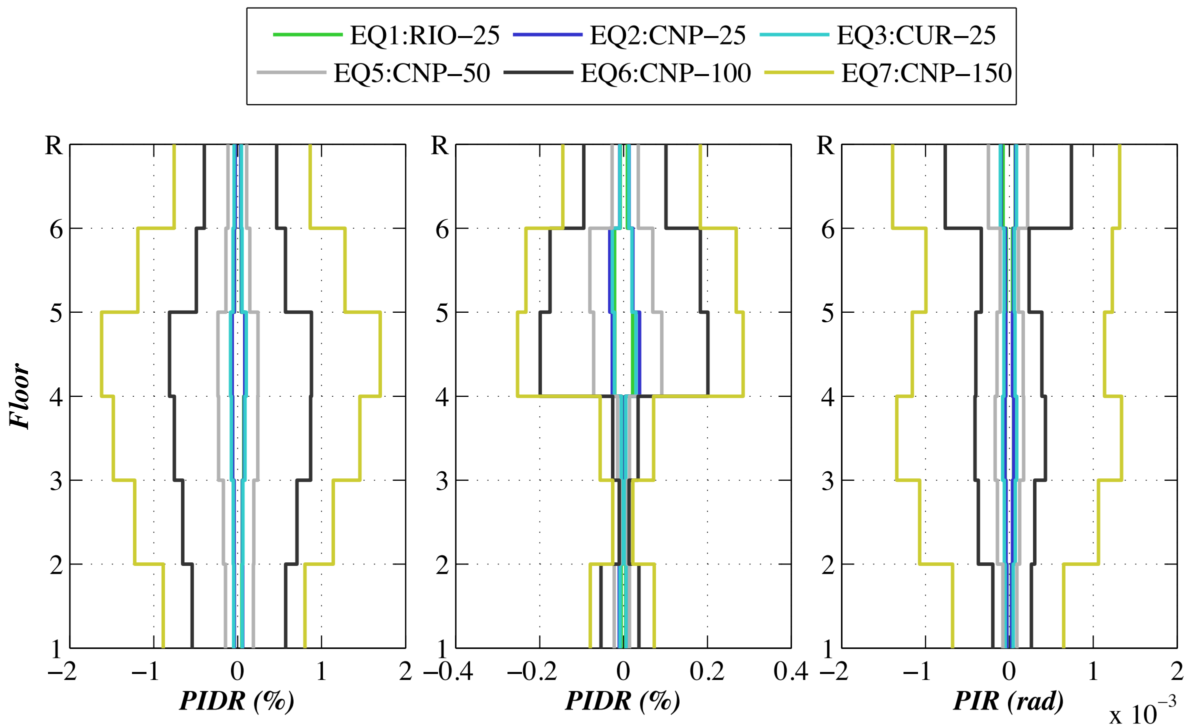

Figure 6.39. Measured peak interstory drift ratios (a) longitudinal, (b) transverse, and (c) peak interstory rotation in the pre-fire earthquake sequence.

Roof Drift Ratios

Figure 6.40 presents the time histories of the longitudinal roof drift ratios (RDRs) during EQ2:CNP-25 (SLE), EQ6:CNP-100 (design event), and EQ7:CNP-150 (MCE). The RDR is defined as the ratio between the differential displacements of the roof relative to that of the table platen divided by the total building height (~18.3 m). The absolute roof displacements were obtained using direct measurements from the roof GPS (center station), while the absolute displacements of the shake table platen were measured by the string potentiometer. As shown in

Figure 6.41, the longitudinal RDR was relatively small (< 0.1%) during the service level sequence (EQ1-EQ4) but increased to about 0.8% during the design event (EQ6) and attained ~1.5% for the MCE event (EQ7). In addition, the residual roof displacements can be also obtained using the direct GPS measurements at the roof (center station), which is determined as the differences between the averaged displacements at the beginning and end of an individual earthquake test (using a two-second window). During the pre-fire test phase, the building observed no apparent residual roof displacement up to design event (EQ6), since the calculated residual displacements at the roof remained smaller than 0.5 cm (lower than the noise floor of GPS measurements). The roof residual displacement attained ~1.5 cm following the MCE event (EQ7), corresponding to a roof drift ratio of ~0.1%.

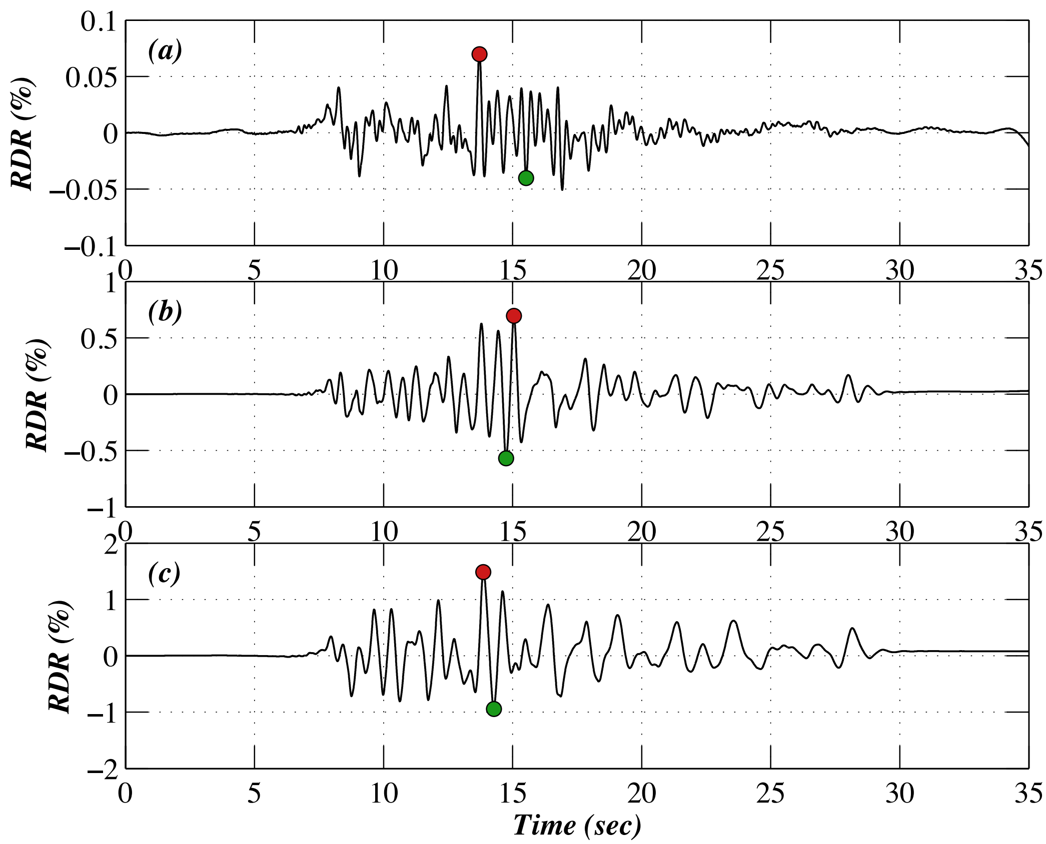

Figure 6.40. Roof drift ratio time histories: (a) EQ2:CNP-25, (b) EQ6:CNP-100, and (c) EQ7:CNP-150.

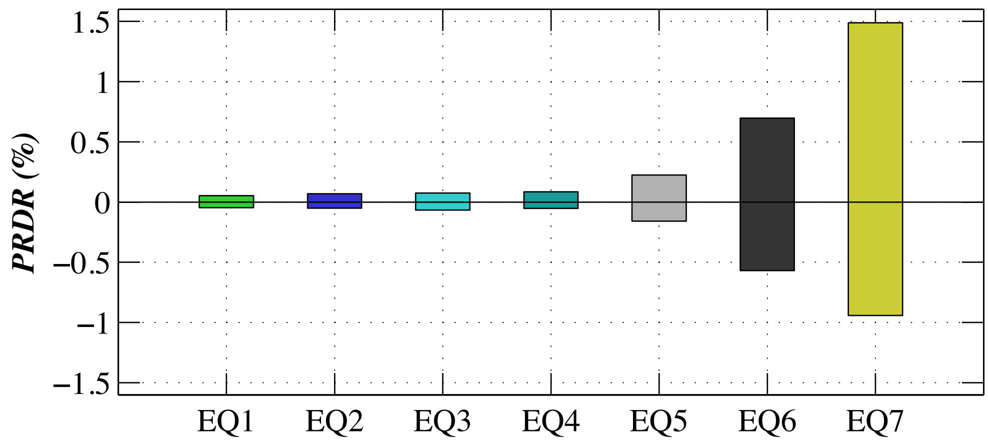

Figure 6.41. Peak roof drift ratios measured during the pre-fire earthquake tests.

Base Shear, Overturning Moment, and Story Shear Response

Figure 6.42 and Figure 6.43 illustrate the normalized base shear and overturning moment time histories during three select earthquake tests, namely, EQ2:CNP-25 (SLE event), EQ6:CNP-100 (design event), and EQ7:CNP-150 (MCE event), respectively. The circles in the plots represent the time instances when the maximum and minimum roof drift ratios were attained. The peak (maximum and minimum) base shear and overturning moment of the building during the pre-fire earthquake tests are summarized in Figure 6.44. The base shear and overturning moment increased almost in proportion with the motion intensity up to the design event (EQ6). The shear force and overturning moment measured during the MCE event (EQ7) remained comparable to that of the design event (EQ6) despite an increase of motion intensity by about 50%. This may be accounted by the fact that all the shear walls attained their peak strength during the design event (EQ6). It is noted that the peak base shear (story shear at level 1) attained as much as 100% of the total building weight during the design event (EQ6) and the MCE event (EQ7), highlighting the overstrength effects of the test building.

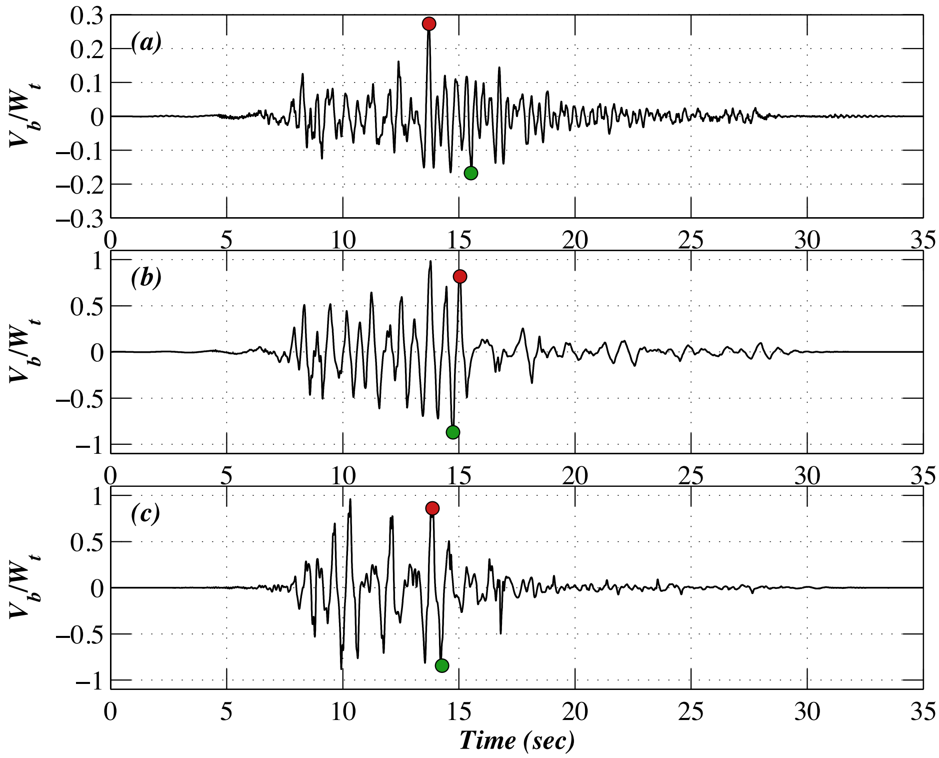

Figure 6.42. Normalized base shear histories: (a) EQ2:CNP-25, (b) EQ6:CNP-100, and (c) EQ7:CNP-150.

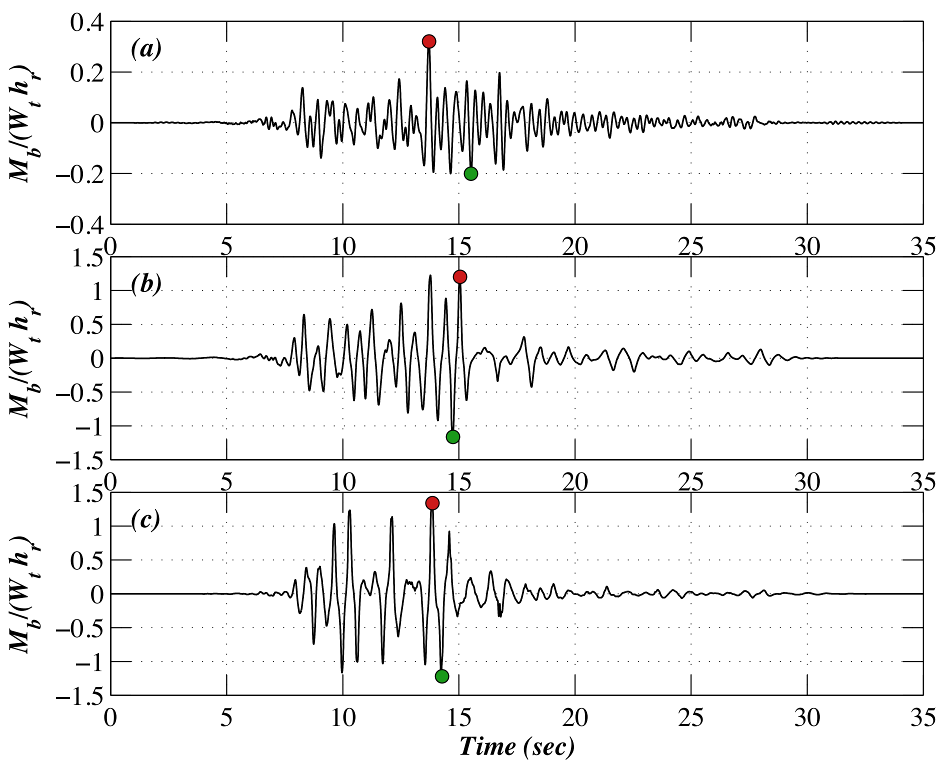

Figure 6.43. Normalized overturning moment histories: (a) EQ2:CNP-25, (b) EQ6:CNP-100, and (c) EQ7:CNP-150.

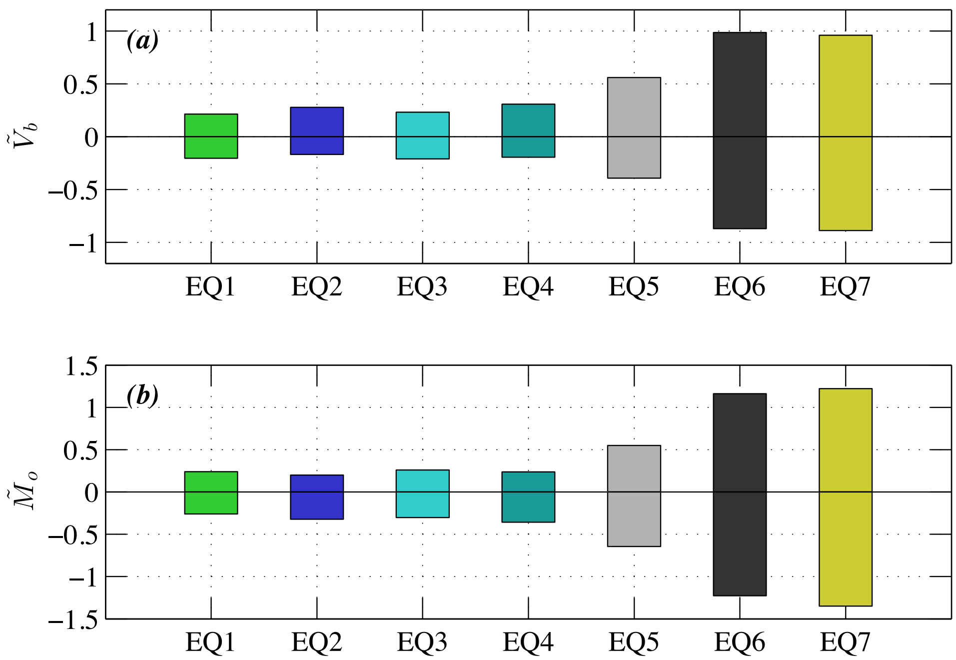

Figure 6.44. (a) Normalized peak base shear, and (b) normalized peak overturning moment during the pre-fire earthquake test sequence.

The story shear vs IDR hysteretic responses during the three select earthquake tests are presented in Figure 6.45 through Figure 6.47. The story shear accounts for the contributions of all the (corridor and corner) shear walls and gravity walls (even their contributions are not considered as significant) at the specific level, while the IDR is taken as those with respect to the floor center. The circles in the plots represent the time instances when the maximum and minimum PIDRs are attained. The story force vs IDR hysteretic responses were literally elastic at all levels during the service level event (EQ2) with the story shear force achieving ~300 kN at the lower two levels. Due to the increased motion intensity during the design event (EQ6) and MCE event (EQ7), the hysteretic responses became highly nonlinear as evident by the significant pinched hysteretic loops. Since the shear walls attained their peak strength during the design event (EQ6), the hysteretic behavior during MCE event (EQ7) reflected the post-peak behavior that the wall stiffness was small at low lateral load range but gradually regained stiffness as the lateral load increased.

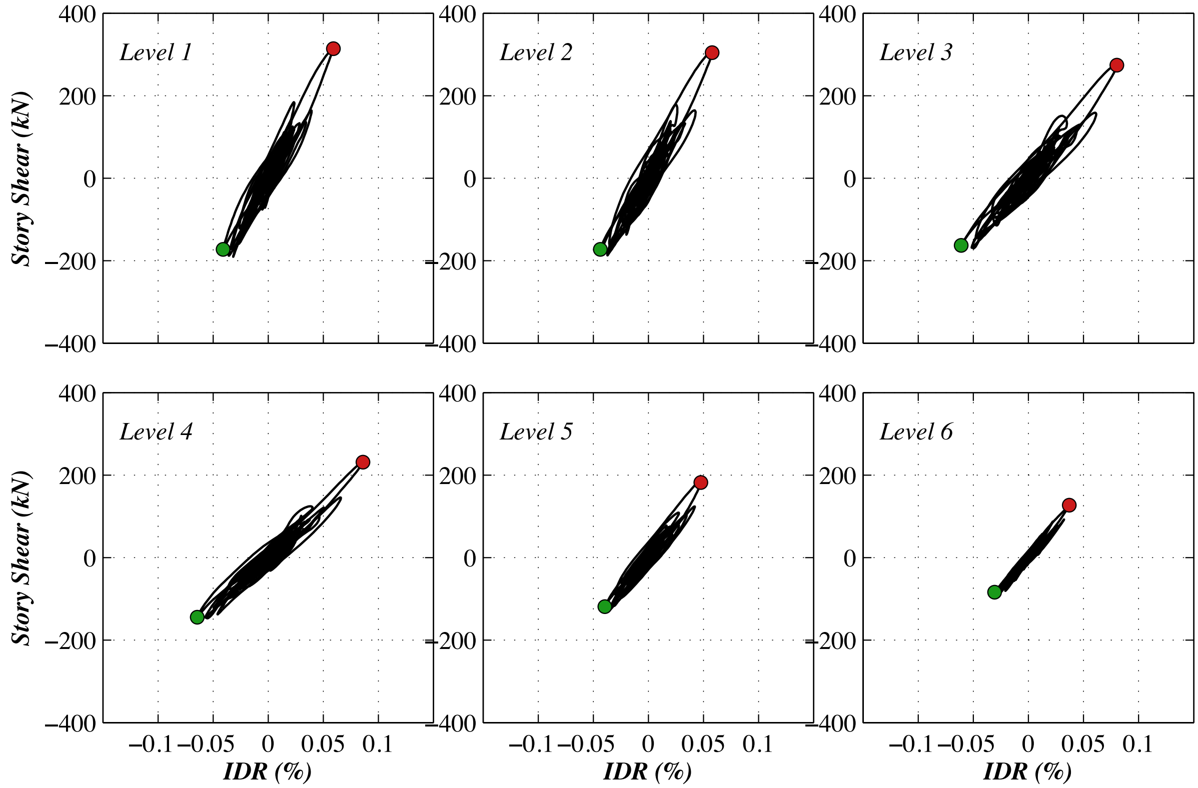

Figure 6.45. Story shear vs. interstory drift ratio (IDR) response – EQ2:CNP-25.

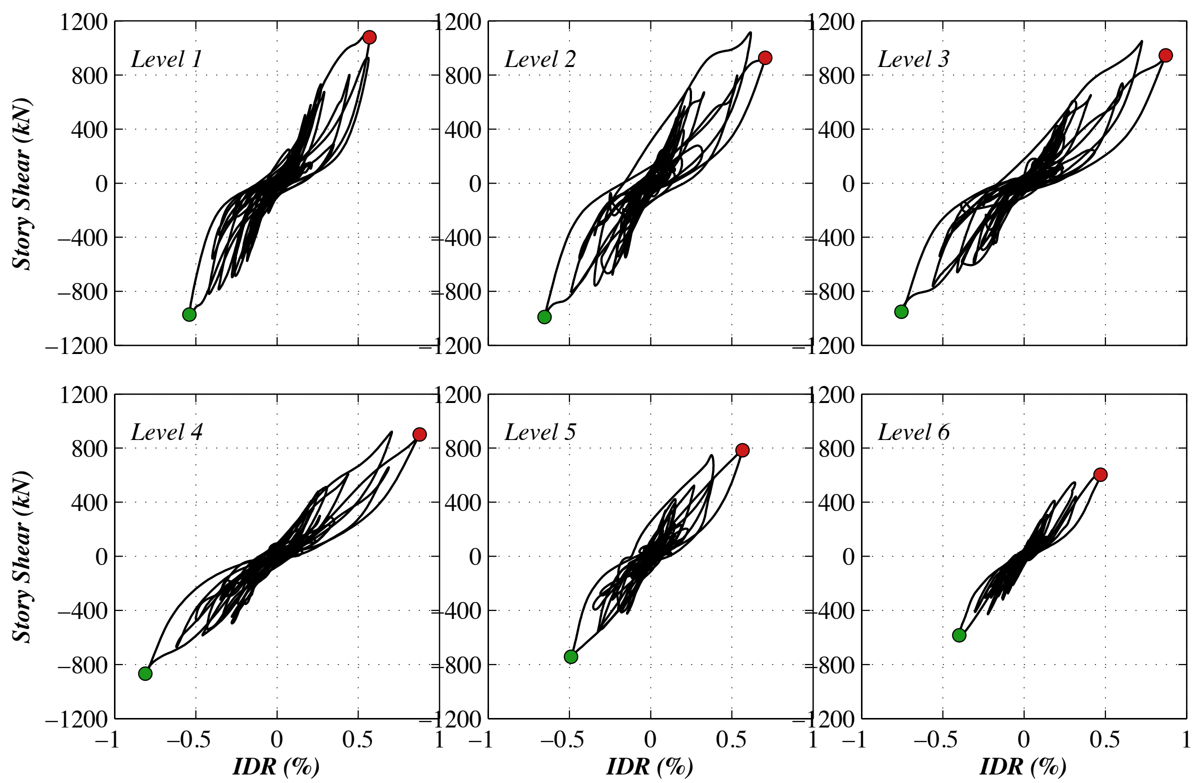

Figure 6.46. Story shear vs. interstory drift ratio (IDR) response – EQ6:CNP-100.

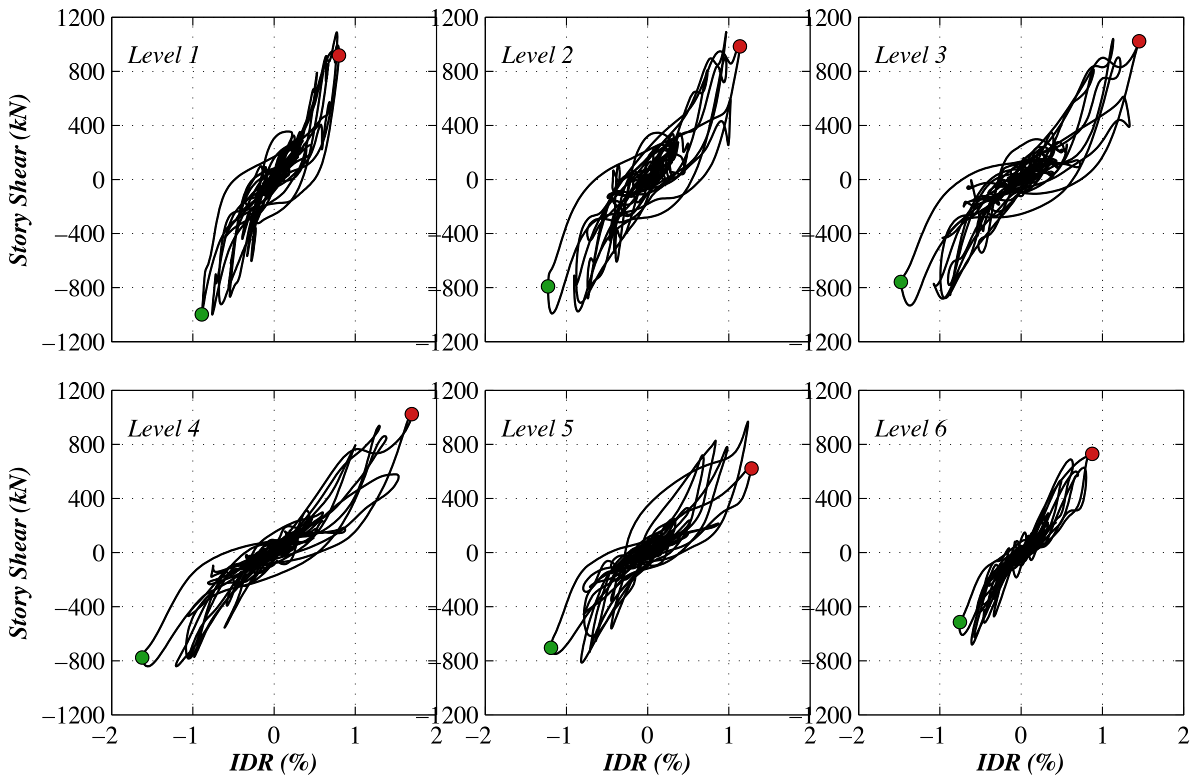

Figure 6.47. Story shear vs. interstory drift ratio (IDR) response – EQ7:CNP-150.

Estimated Story Stiffness and Building Period under Service Level Test Sequence

Since the story shear vs IDR response remained essentially linear during the service level sequence (EQ1 – EQ4) (see Figure 6.45), the equivalent story stiffness of all levels of the building can be estimated by linear curve fitting to the story shear vs IDR response during these tests. The fitted line is determined using least square linear regression on the measured hysteretic response (note that data with PIDR < 0.01% are excluded from regression). Given the estimated story stiffness at all levels of the building, the dynamic characteristics (fundamental period and the effective modal mass) of the building can be determined using eigenvalue analysis with the building idealized as a simplified shear beam model with its mass lumped at individual floors. Details regarding the floor mass distributions are discussed earlier in Section 2.6.

Figure 6.48 presents the measured (black) story shear vs PIDR responses and the fitted lines (red) of the test building during EQ2:CNP-25. The slope of the fitted line represents the estimated story stiffness at each level. Figure 6.49 summarizes the estimated story stiffness during all three service level tests (EQ1 – EQ3) as well as the story stiffness of all levels normalized by their corresponding stiffness associated with the first earthquake test (EQ1:RIO-

25). As shown in Figure 6.49a, the story stiffness at all levels reduced slightly (< 20%) during the service level sequence (EQ1 – EQ3). Notably, the story stiffness of the upper levels were only 50% and 60% those of the lower two levels (Figure 6.49b). Since the framing studs and screw spacing the shear walls at the lower levels remained almost identical, the distinctive differences of the story stiffness between the lower two levels and level 3 are likely attributed to the tie-down system details (use of large diameter tie-down rods and more studs for the compression post stud packs).

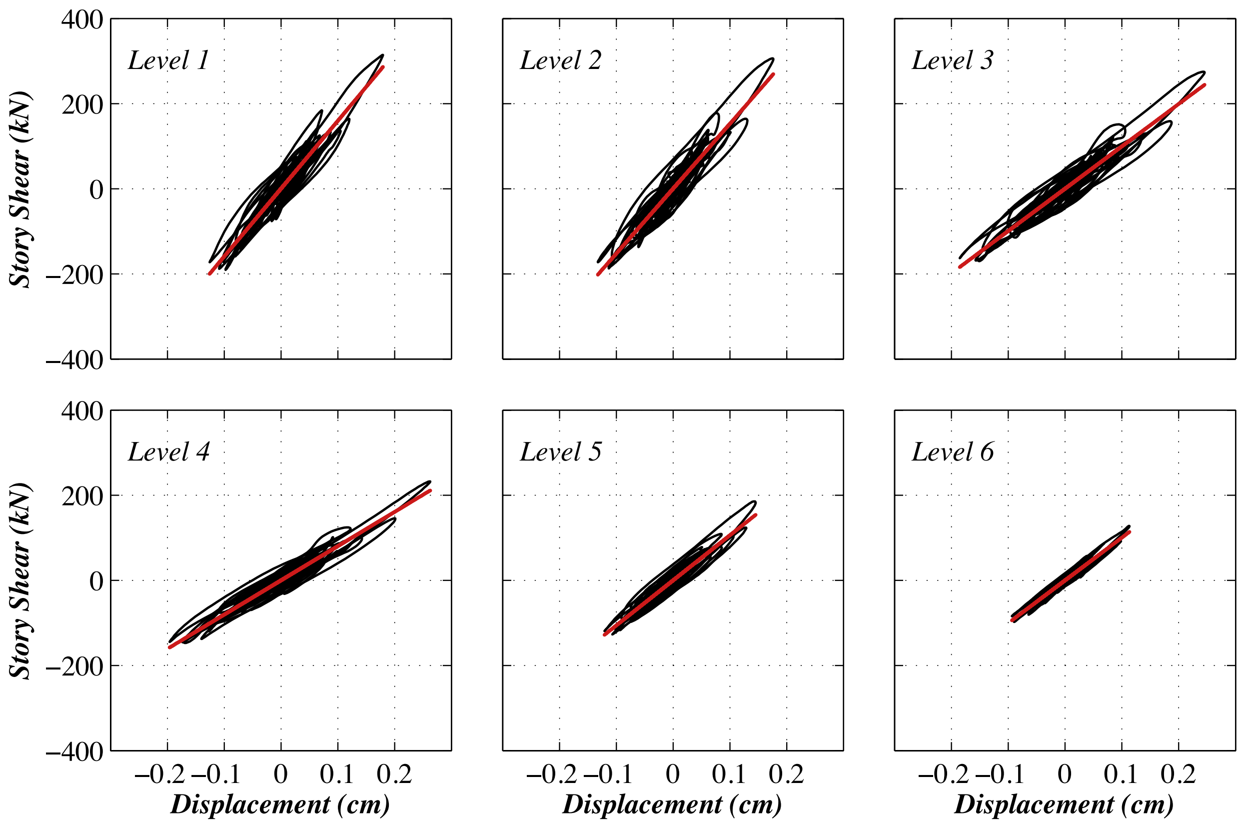

Figure 6.48. Measured story shear vs story displacement response (black) and the fitted linear response (red) – EQ2:CNP-25.

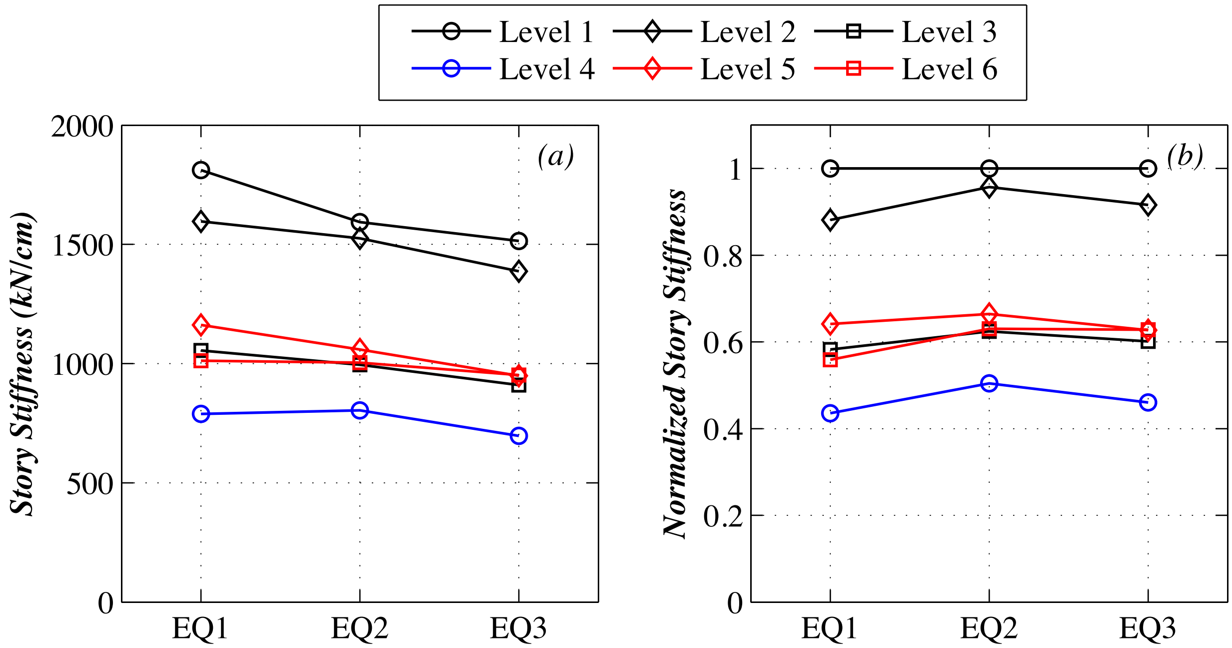

Figure 6.49. (a) Estimated story stiffness and (b) normalized story stiffness during the service level test sequence (EQ1 – EQ3).

Table 6.2 summarizes the fundamental period of the building (in the longitudinal direction) and the effective normalized modal mass during the service level test sequence (EQ1 – EQ3). As shown in the table, the estimated fundamental period was about 0.3 second and the effective modal mass of about 80% of the total mass of the building during the first three service level tests. The estimated periods are consistent with those identified from the white noise tests, which ranged between 0.26 ~ 0.29 second (refer to Chapter 5 for detailed results). However, it is important to note that the estimated fundamental period as identified during the service level tests differed notably from (more than 25% smaller than) the code-specified period of 0.43 second as considered in the seismic design.

Table 6.2. Esitmated building fundamental period during the service level earthquake tests

Test	*T_1 (sec)*	*M_{eff} (%)*
EQ1:RIO-25	0.31	79.7
EQ2:CNP-25	0.32	80.7
EQ3:CUR-25	0.33	80.1

6.2.3 Result Discussions

Summary of Global Response

The key building responses during the pre-fire earthquake tests are summarized in Table 6.3. These include peak floor accelerations (PFAs), peak inter-story drift ratios (PIDRs), peak roof drift ratios (PRDRs), residual roof drift ratios (RDR_{res}), and peak base shear forces normalized by the total building weight ($\tilde{V}_b$). Figure 6.50 and Figure 6.51 presents the building PFA and PIDR during the *service level* events (EQ1—EQ3) and the *above-the-service-level* events (EQ5—EQ7), respectively. The seismic demands of the building were relatively low during the service-level earthquakes, with the largest PIDR ~0.1% and PFA < 0.5 g. As the motion intensity increased, the largest PIDR reached about 1.0% during the design event (EQ6) and above 1.5% during the MCE event (EQ7). It is noted that the largest PIDR occurred at the mid-height of building (level 4) throughout the pre-fire earthquake test sequence. The PIDR distribution over the height of the building is consistent with building physical observations as discussed later. In addition, the PFA increased almost monotonically up the height of the building during the pre-fire tests (except for EQ7), indicating a fundamental-mode dominant structural response in these earthquake tests.

Table 6.3. Peak building responses during the earthquake tests

Test Motion	*PFA (g) / [Floor #]*	*PIDR (%) / [Level #]*	*PRDR (%)*	$\tilde{V}_b$	*RDR_{res} (%)*
EQ1:RIO-25	0.35 [R]	0.08 [L4]	0.05	0.21	0.0
EQ2:CNP-25	0.38 [R]	0.09 [L4]	0.07	0.27	0.0
EQ3:CUR-25	0.45 [R]	0.10 [L4]	0.08	0.23	0.0
EQ4:CNP-25	0.43 [R]	0.10 [L4]	0.09	0.30	0.0
EQ5:CNP-50	0.85 [R]	0.24 [L4]	0.19	0.56	0.0
EQ6:CNP-100	2.07 [R]	0.89 [L4]	0.70	0.99	0.02
EQ7:CNP-150	3.77 [R]	1.70 [L4]	1.49	0.97	0.08

PFA – peak floor acceleration; PIDR – peak interstory drift ratio; PRDR – peak roof drift ratio; $\tilde{V}_b$ – normalized base shear; RDR_{res} – residual roof drift ratio.

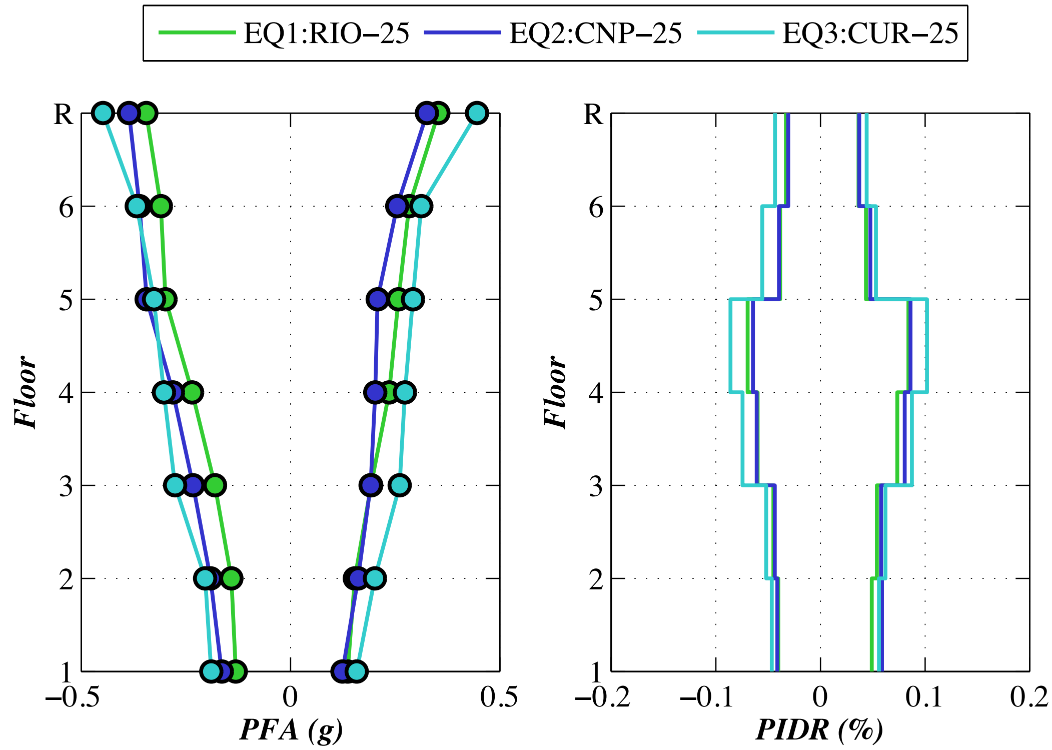

Figure 6.50. Building peak responses during the *service level tests*: (a) peak floor accelerations, and (b) peak interstory drift ratios.

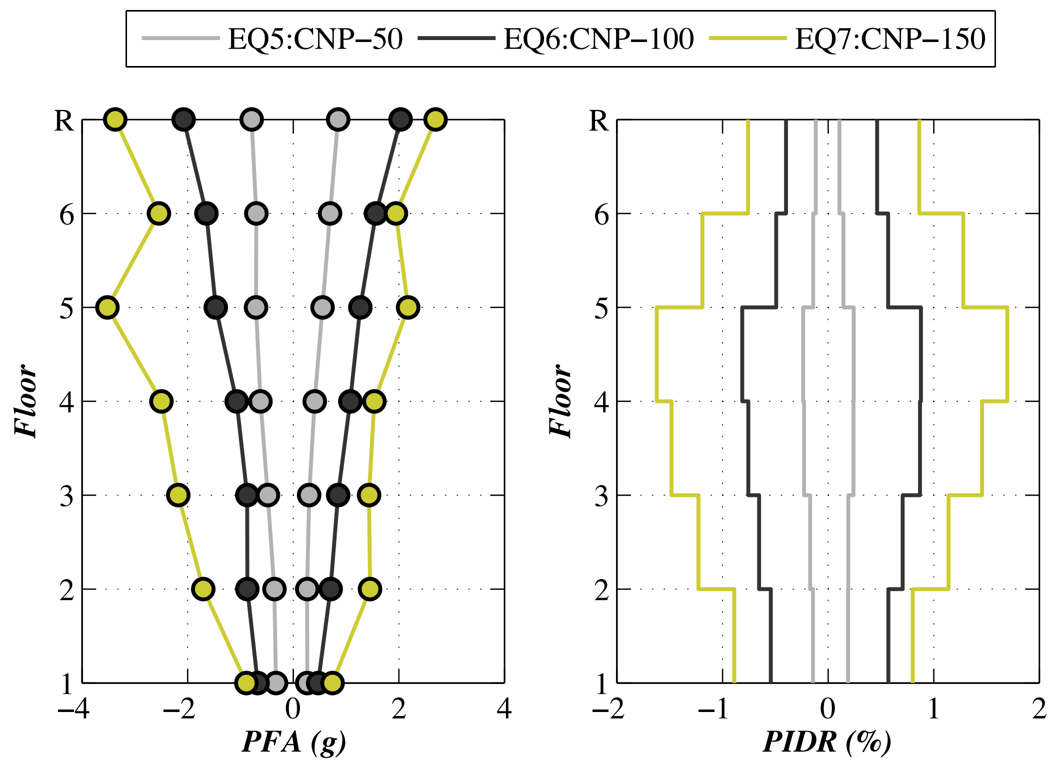

Figure 6.51. Building peak responses during the *above-service-level tests*: (a) peak floor accelerations, and (b) peak interstory drift ratios.

Figure 6.52 presents the normalized peak base shear vs peak roof drift ratio (PRDR) response during the pre-fire earthquake test sequence. As shown in the figure, the relation between peak base shear and PRDR was almost linear up to the 50% design event (EQ5). During the design event (EQ6), the base shear increased in proportional to the motion intensity and became twice as large as that for the 50% design event (EQ5), however the PRDR became three times as large as that of the 50% design event (EQ5). This is indicative of the onset of nonlinear response of the test building. The PRDR continued to rise during the MCE event (EQ7), while the base shear demand remained similar with that of the design event (EQ6).

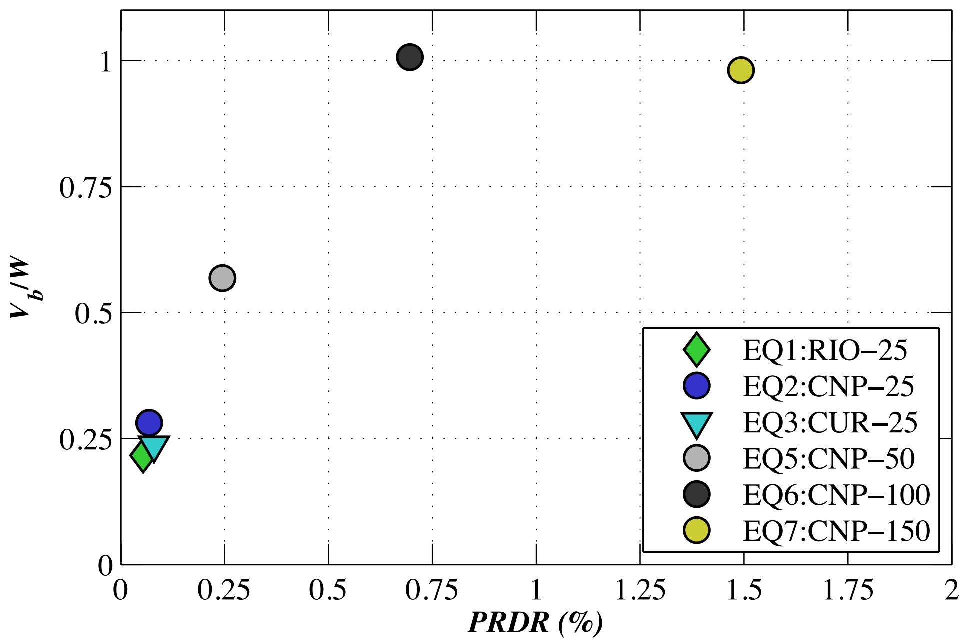

Figure 6.52. Peak normalized base shear forces vs peak roof drift ratio.

Floor Response Dispersion

Despite the input motions were all applied along its longitudinal axis, torsional response of the building was observed during the earthquake tests. The torsional behavior introduced dispersion to the building response at different corners. To quantify these effects, Figure 6.53 and Figure 6.54 compare the peak longitudinal floor responses (PFAs and PIDRs) measure at the four corners and the responses at the floor centers during EQ6:CNP-100 (design event) and EQ7:CNP-150 (MCE), respectively. The red circles represent the corner responses, whereas the floor center responses are shown as the solid black lines. It is evident that the interstory drift ratio responses were more scattered than the acceleration responses. In addition, the interstory drift ratios at the upper floors varied more significantly compared with those at the lower floors, which may be attributed to the larger torsional response at the upper levels.

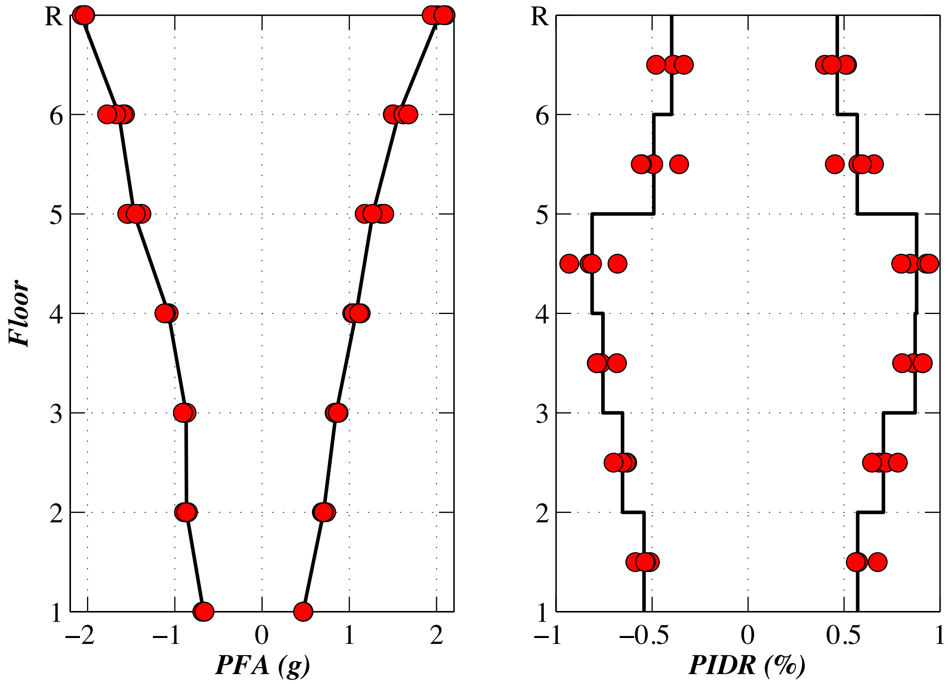

Figure 6.53. Comparison of peak longitudinal building responses at the corners and the center – EQ6:CNP-100: (a) PFA, and (b) PIDR.

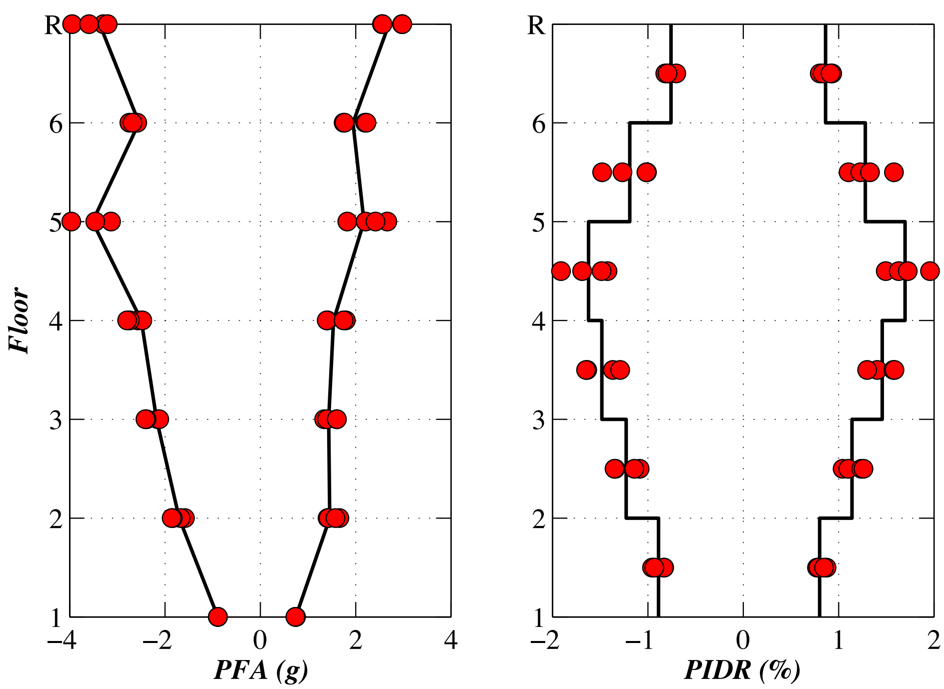

Figure 6.54. Comparison of peak floor responses measured at the corners with the responses of the floor center – EQ7:CNP-150: (a) PFA, and (b) PIDR.

Figure 6.55 summarizes the coefficients of variation (COVs) of the peak building responses of the corners during the pre-fire earthquake test sequence. The COV is determined as the ratio between the standard deviation of the four corner responses and the corresponding response of the floor center. The figure reveals that the dispersions of both the PFAs and PIDRs remained largely independent of motion intensity, although the PFAs were less scattered than the PIDRs (smaller COVs).

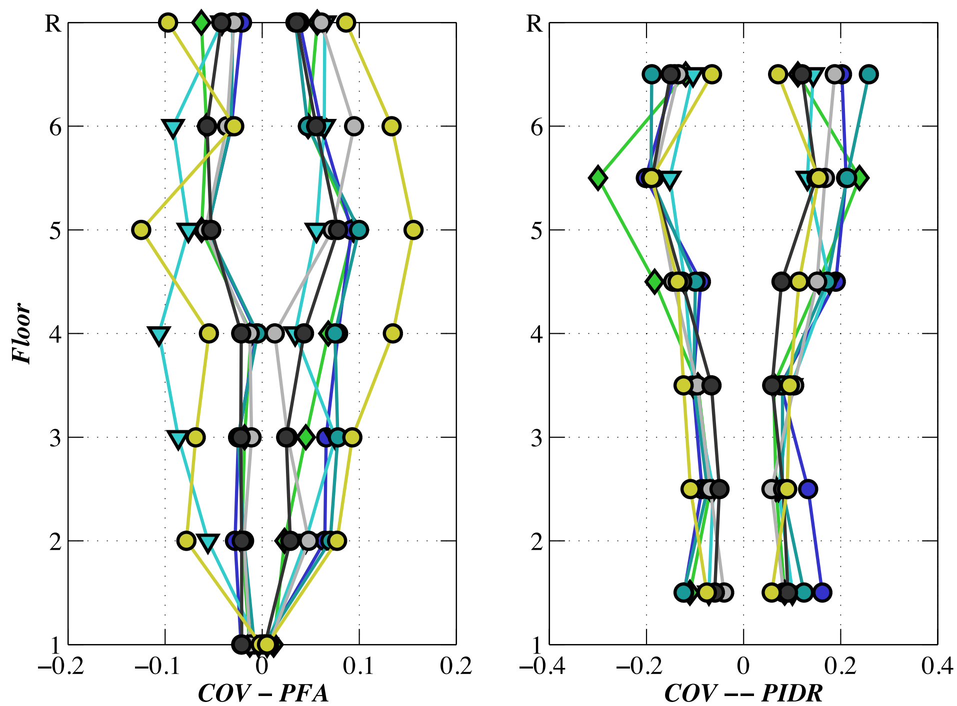

Figure 6.55. Coefficients of variation (COV) of the peak building responses of the corners: (a) PFA, and (b) PIDR.

Floor Acceleration Amplification

Figure 6.56 presents the floor acceleration amplification factors Ω during the pre-fire earthquake sequence. The amplification factor is determined as the ratio between the peak acceleration achieved at each floor and the peak input acceleration achieved by the table platen. According to ASCE 7-10 (ASCE, 2010) code provisions, the amplification factor is empirically defined as 1+2z/h (z/h denotes the normalized building height), which assumes a linear distribution along the building height from 1.0 at the base to 3.0 at the roof. During the service level sequence (EQ1-EQ3) (Figure 6.56a), the acceleration amplification factors increased monotonically up the height of the building with the largest values ranging between 2.0 and 2.5 at the roof (slightly lower than the code-specified value of 3.0). The amplification factors continued to rise during the

50% design event (EQ5) and design event (EQ6) in response to the increased motion intensity (Figure 6.56b). The floor amplification effect during the design event (EQ6) agrees well with the code-specified distribution along the building height (attained an amplification factor of about 3). Conversely, the floor amplification factors observed during the MCE event (EQ7) became significantly larger than the code-specified distribution at all floors (Figure 6.56b). This is attributed to the presence of the acceleration spikes measured during this test.

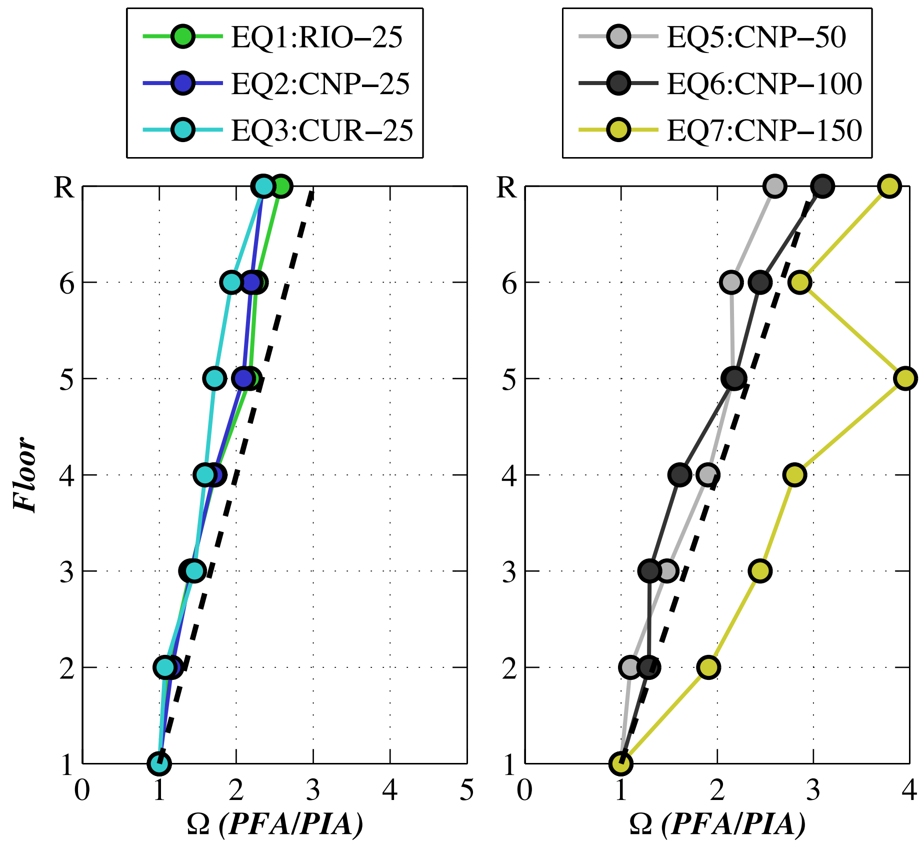

Figure 6.56. Acceleration amplification factors of the test building: (a) *service level tests*, and (b) *above-the-service level tests*.

Floor Response Spectra and Component Amplification Effect

The floor response spectra (FRS) associated the pre-fire earthquake sequence are illustrated in Figure 6.57 (service level tests) and Figure 6.58 (above-the-service level tests). The FRS are defined as the 5% damped elastic pseudo-acceleration spectra calculated using the achieved floor accelerations in the longitudinal direction. As shown in the figures, the observed spectral peaks are tuned with the longitudinal periods of the building (~0.3 second for the first longitudinal mode and ~0.1 second for the second longitudinal mode). The FRS peaks associated with the fundamental period increased monotonically up the height of the building, achieving about 2 g at the roof during the service level tests (Figure 6.57) and as much as 8 g during the design event (EQ6) and MCE event (EQ7) (Figure 6.58). During the service level events (EQ1 – EQ3), the FRS peaks in the higher mode period region (~0.1 sec) were often lower than those associated with the fundamental mode (Figure 6.57). Different from the fundamental mode FRS peaks, the higher-mode FRS peaks at the building mid-height and upper floors (floor 5 to roof) were much smaller than those at the lower floors. In particular, the FRS of floor 5 was barely observed during the service level events, indicating that floor 5 represented the "node" location of the second mode. However, as a result of substantial damage to the building during the design event (EQ6) and MCE event (EQ7), the higher-mode FRS peaks at the building mid-height and upper floors (floor 5 to roof) increased pronouncedly and became larger than those at the lower floors (Figure 6.58).

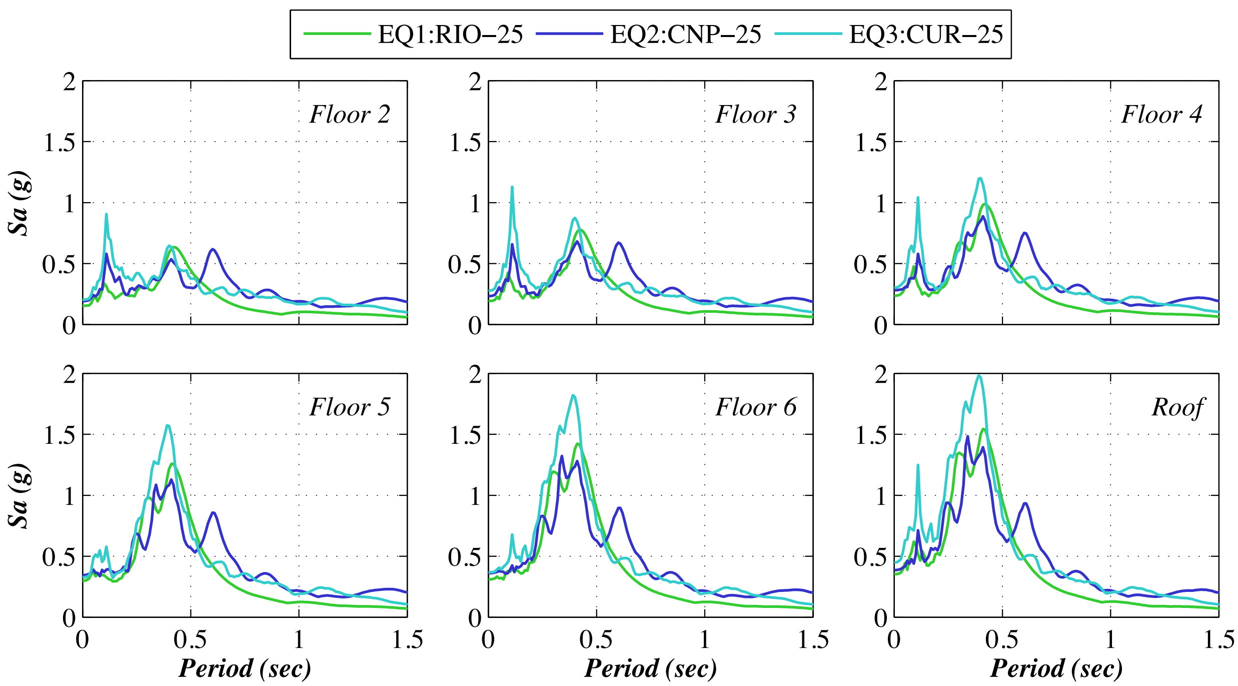

Figure 6.57. Floor response spectra (ξ=5%) – *<u>service level tests</u>*.

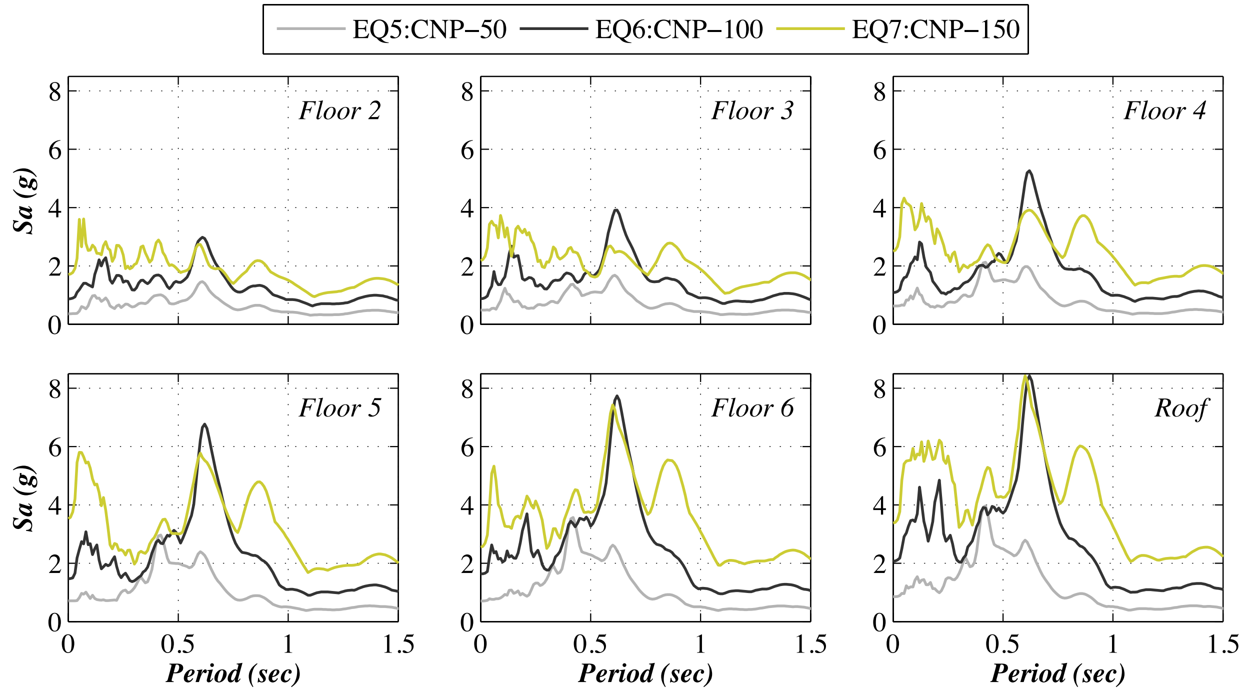

Figure 6.58. Floor response spectra (ξ=5%) – *above-the-service level tests*.

Figure 6.59 and Figure 6.60 illustrate the component amplification factors (a_p) for the pre-fire test motions. The component amplification factor is calculated as the ratio between the FRS and the PFA at the given floor (note that PFA represents the FRS value associated with a period of 0 second). The component amplification factors (a_p) is an important parameter that are widely used for characterizing the dynamic amplification effect of nonstructural systems in response to floor excitations. As shown in the figures, the amplification peaks associated with the fundamental mode ranged between 4 and 5 in all the pre-fire tests, which appeared less sensitive to the motion intensity compared with the FRS peaks. In comparison, the amplification effects of the higher mode peaks were smaller than those of the fundamental mode. While the higher mode amplification factors reached as much as 4 at the lower floors during the service level tests (Figure 6.59), the effect was significantly attenuated during the design event (EQ6) and MCE event (EQ7) when the building sustained extensive damage, since the higher mode amplification factors remained smaller than 3 during these two tests (Figure 6.60).

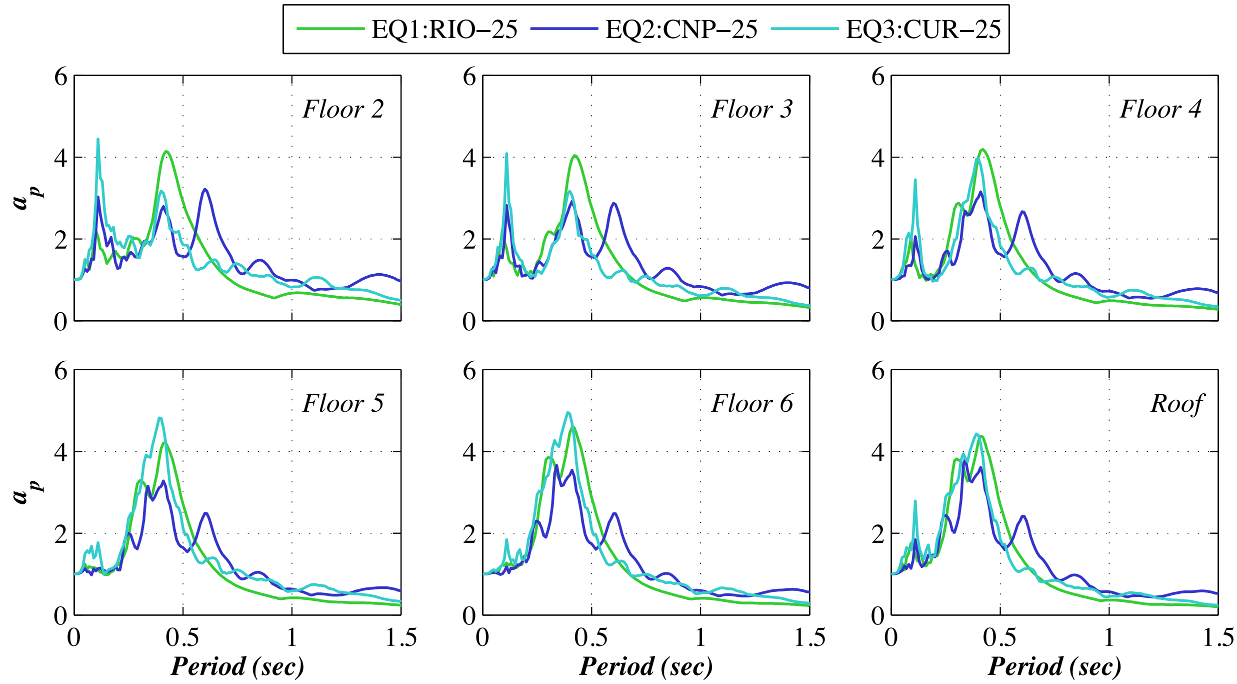

Figure 6.59. Component amplification factors a_p – *service level tests*.

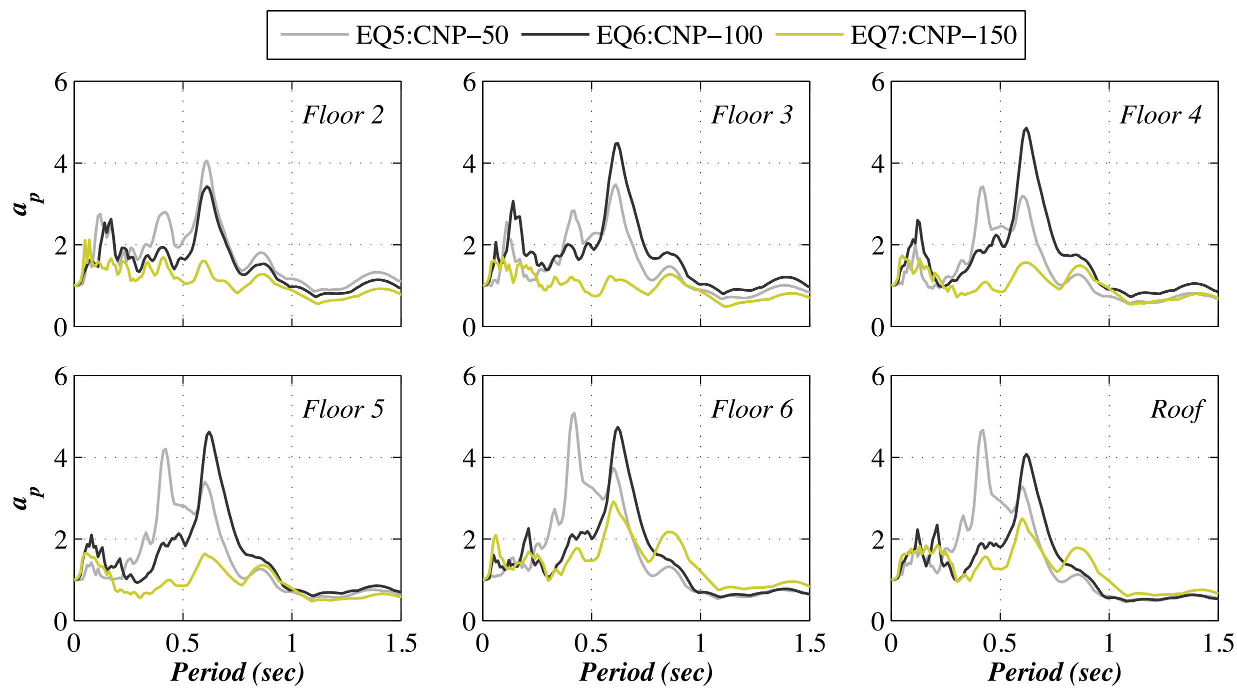

Figure 6.60. Component amplification factors a_p – *above-the-service level tests*.

6.3 Local Response

The test building consisted of a total of seventeen instrumented shear walls at three select levels, namely, level 1, 2, and 4. In addition, the deformations of the floor panel interface joists at the second floor were measured using linear potentiometers. The measured local shear wall and the floor joist deformations during the pre-fire earthquake test sequence (EQ1–EQ7) are discussed in this section.

6.3.1 Shear Wall Response

As shown in Figure 6.61, the lower two levels each included three corridor shear walls (denoted as *SW-c*, *SE-c* and *NW-c*) and three corner (exterior) shear walls (denoted as *SW-e*, *SE-e* and *NE-e*), while level 4 consisted of five instrumented walls as the northeast corner shear wall was not instrumented due to difficulties related to wall exterior accessibility. As shown in Figure 6.62, instrumentation installed on these shear walls involved: (1) displacement transducers (i.e., string potentiometers and linear potentiometers) on the shear wall panels, and (2) strain gages on the tie-down steel rods. Interested readers are referred to Appendix E for additional details of the shear wall instrumentation. Data recorded by these sensors provided local responses of individual shear walls in the following three categories:

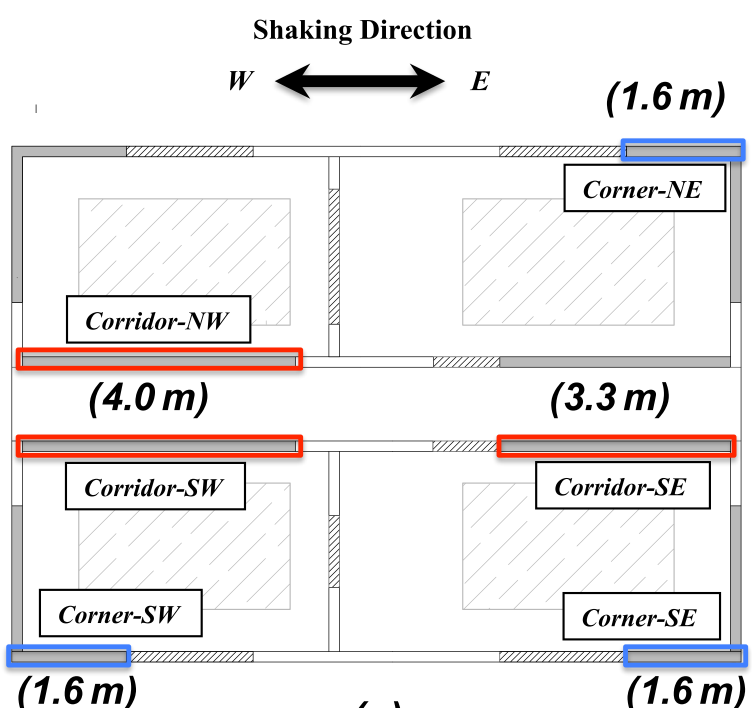

Figure 6.61. Plan layout of the instrumented shear walls.

- *Sheathing panel shear distortions:* measured using two diagonal and two vertically string potentiometers placed in a double-triangle configuration. Direct string potentiometer measurements were used to calculate the shear distortion (angle change of the triangles) of the shear wall structural panels. It is noted that the shape of the triangles varied as a result of the different shear wall dimensions (Figure 6.63).
- *Tie-down rod axial forces:* measured using a pair of collocated strain gages (or a single strain gage) on the tie-down rods. Since the tie-down rods all remained elastic during the earthquake tests (as discussed later), the axial force of the tie-down rod is calculated by multiplying the measured strain of the tie-down rod by its axial stiffness (product of sectional area and Young's modulus of steel). Table 6.4 summarizes the details of the instrumented tie-down rods.
- *Wall end vertical displacements:* measured directly using two vertically oriented linear potentiometers at the base of the wall (one sensor at each wall end).

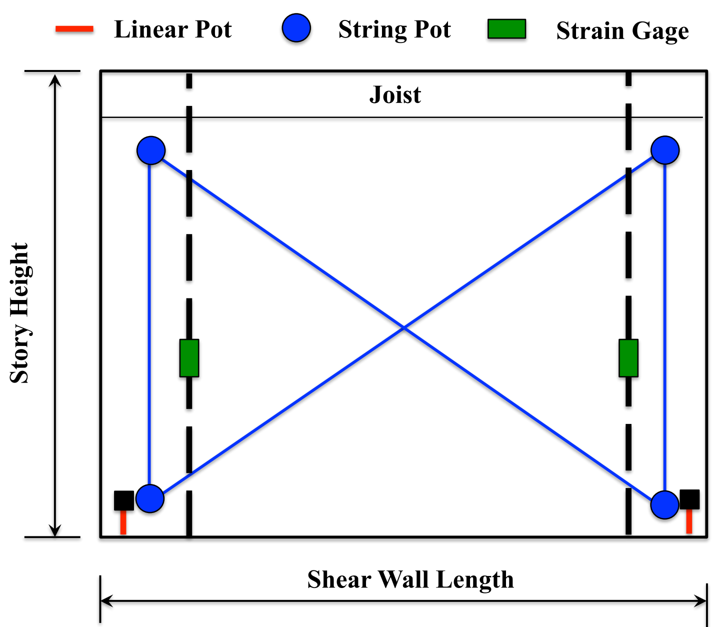

Wall	*L (cm)*	*H (cm)*	*θ (degree)*
Corridor (west)	345.4	243.8	35.2
Corridor (east)	284.5	236.8	39.8
Corner (exterior)	137.2	235.6	59.8

Figure 6.62. Schematic illustration of the instrumented shear wall and the string potentiometer triangle dimensions.

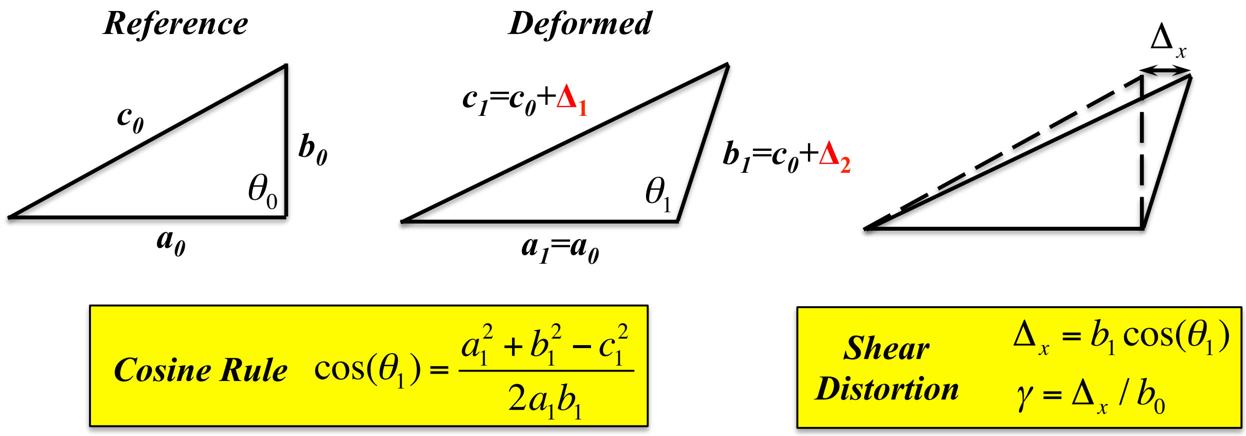

Figure 6.63. Illustration of sheathing panel shear distortion calculation.

Table 6.4. Detailed Specifications of the instrumented tie-down rods.

Level #	Corridor shear wall			Corner shear wall		
	Designation	*Diameter (mm)*	*f_u [f_y] (kN)*	*Designation*	*Diameter (mm)*	*f_u [f_y] (kN)*
1	ASTM A722 (Grade 150)	46	1779 [1423]	ASTM A722 (Grade 150)	46	1779 [1423]
2	ASTM A193 (Grade B7)	43	1337 [1070]	ASTM A36	29	265 [170]
4	ASTM A193 (Grade B7)	29	553 [442]	ASTM A36	19	118 [71]

Notes: f_u – ultimate tensile strength; f_y – yield strength; Young's modulus of all steel products taken as 200 GPa.

Local Response Histories

Data measured from the shear walls at the three levels of the test building allowed for investigating the local shear wall responses during the earthquake tests as well as comparing the seismic behavior different shear walls dependent on the variations of specific wall details (corridor vs corner) or vertical locations. The measured time history responses of level 2 shear walls during the design event (EQ6) are first presented. Subsequently, the peak local responses of all the instrumented shear walls are summarized. It is noted that even though the seismic drift demand of the test building achieved its largest value at level 4 during the pre-fire earthquake tests (PIDR attained ~0.9% at level 4 compared with ~0.6% at level 2 during the design event EQ6), the measured local shear wall responses (e.g., tie-down rod forces, wall end displacements) were larger at level 2 than those of the level 4 shear walls. Pre-processing of the measured local response involves a two-step procedure of the raw data recorded by individual sensors: (1) applying a low pass fourth-order Butterworth filter (with a corner frequency of 15 Hz) on the raw data, and (2) detrending the filtered results by subtracting the mean of the filtered data from the first two-second window. This procedure allows preserving the residuals of recorded by individual sensors while removing the high-frequency noise.

Figure 6.64 shows the measured local responses of the corridor shear wall pair (west and east segments on the south corridor wall line) at level 2 during the design event (EQ6). It is noted that the measured story drift at level 2 reached peak values of ~0.6% in both positive (eastward) and negative (westward) directions during this test (red circles represent the time instance when the story drift achieved the positive peak, whereas green circles correspond to that of the negative peak). With a peak story drift of ~0.6% at level 2, the peak shear distortion of the structural panels attained ~0.2% for the west wall segment and ~0.15% for east wall segment, accounting for 1/4 –1/3 of the peak story drift.

As the story drift reached the positive (eastward) peak (denoted in red circles), the wall end vertical displacements and the tie-down rod tensile forces of both the east and west wall segments achieved their peak values at the west ends of the individual segments. In contrast, these local responses remained very small at the east ends of the two wall segments, since the east ends of both wall segments were characterized by compression in the vertical direction when the shear walls were subjected to peak story drift in the eastward direction. Similarly, when the story drift reached the negative (westward) peak (denoted in green circles), the peak wall end vertical displacements and peak tie-down rod tensile forces of both the east and west wall segments occurred at the east ends of shear walls. In addition, the shear walls at the two sides of the corridor (east and west segments) achieved comparable peak local responses associated with occurrence of the peak story drift. This indicates that the east and west corridor shear walls performed as individual wall segments (referred to as Type I system per AISI code provisions (AISI, 2007)) in response to seismic lateral loads. In addition, the tie-down rods of both wall segments achieved peak tensile forces of ~200 kN associated with the positive (eastward) peak story drift and < 150 kN associated with the negative (westward) peak story drift. The peak tensile forces of the tie-down rods were well below (~15%) their yield strength of 1337 kN (see Table 1) during the design event (EQ6).

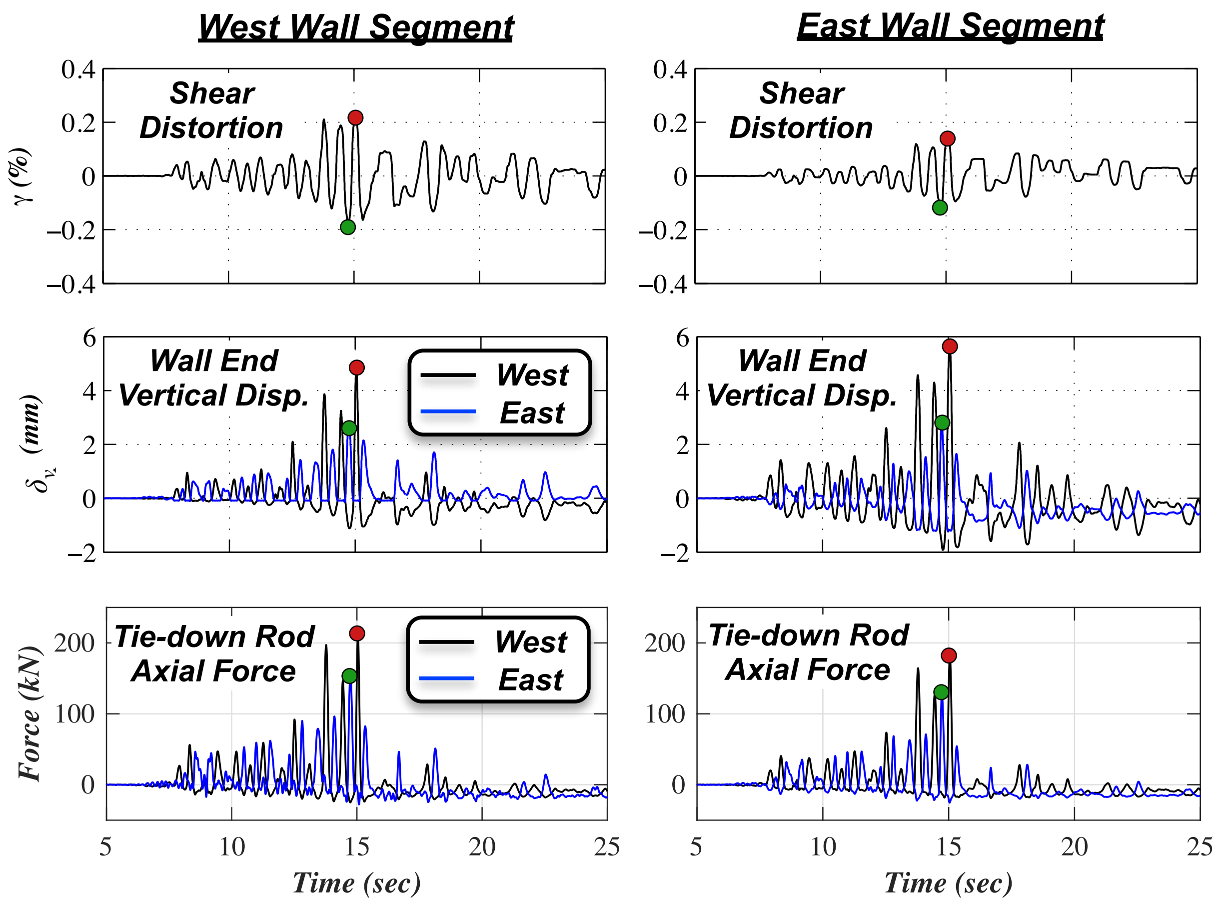

Figure 6.64. Local responses of the corridor shear wall pair at level 2 during the design earthquake test (EQ6): structural panel shear distortions (first row), wall-end vertical displacements (second row), and tie-rod tension forces (third row)

Figure 6.65 shows the measured responses of the longitudinal corner shear wall pair (southwest and southeast walls) at level 2 during the design event (EQ6). The shear force demands of the corner shear walls were much smaller than those of the corridor walls due to their much shorter length of the corner walls. As a result, the observed peak axial forces of the tie-down rods of the corner walls were substantially smaller than those of the corridor shear walls. The achieved peak wall end vertical displacements of the corner shear walls were only ~2 mm (compared to 5 mm for the corridor walls), whereas the peak tie-down rod axial forces were slightly larger than 60 kN (~40% their yield strength of 170 kN). In addition, the shear distortions of the corner shear walls were about 0.1%, which is smaller than those of the corridor shear walls (0.15% – 0.2 %). However, unlike the fact that the measured axial forces of the tie-down rods remained similar for the shear walls at the two ends of the corridor, the tie-down rod axial forces of the corner shear walls at the two sides of the building appeared less correlated.

This is partially due to the interaction between the tie-down rods of the longitudinal corner shear walls with those of the adjacent transverse shear walls.

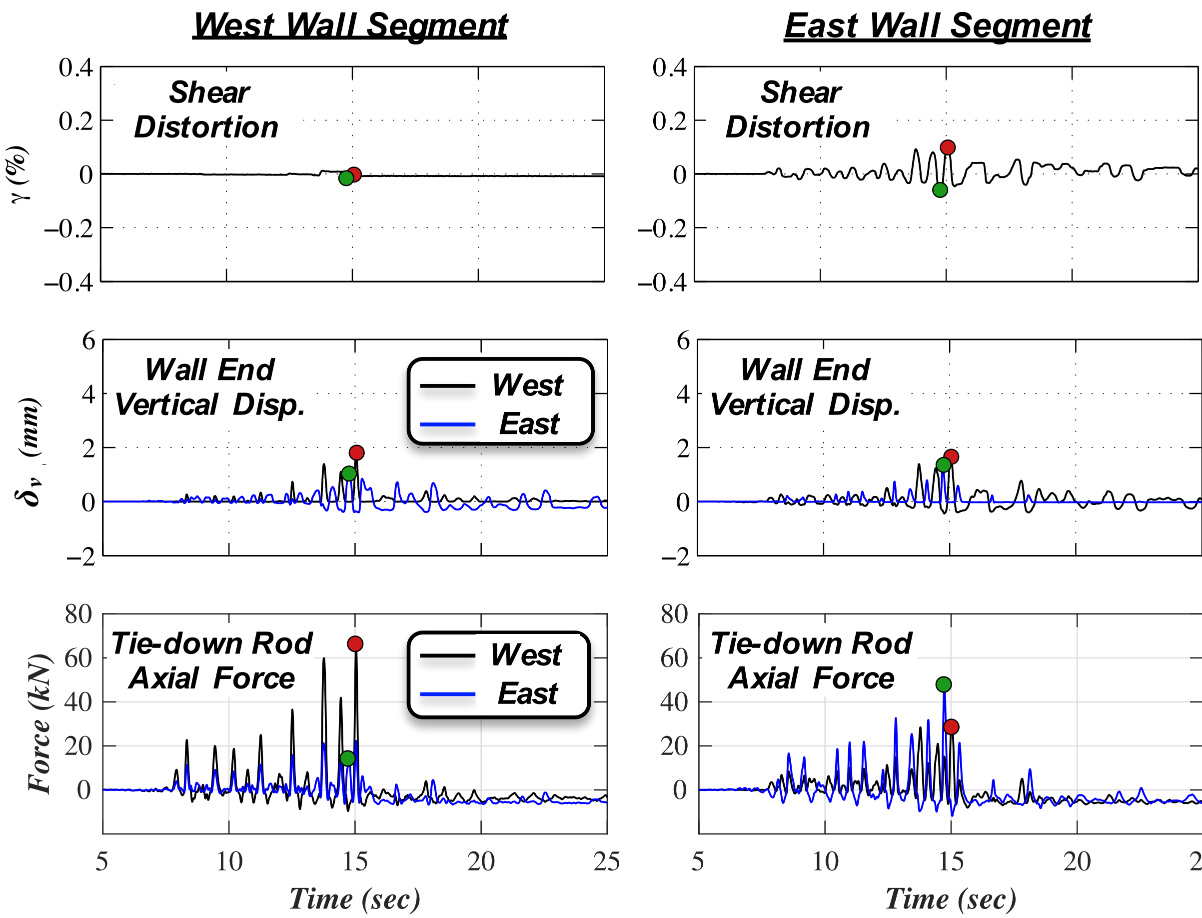

Figure 6.65. Local responses of the longitudinal corner shear wall pair at level 2 during the design earthquake test (EQ6): structural panel shear distortions (first row), wall-end vertical displacements (second row), and tie-rod tension forces (third row).

To demonstrate the interaction of the intersecting exterior corner shear walls, Figure 6.66 plots the tie-down rod axial force histories of the longitudinal and transverse walls at the southeast corner of level 2 during the design earthquake test (EQ6). Since both shear walls were located on the east side of the building, the peak tensile forces occurred when the story drift reached the negative (westward) peak (green circles). The peak forces of ~100 kN occurred on the two transverse wall tie-down rods (with comparable amplitude). It is also noted that the peak tensile force level remained lower than their nominal yield strength (~170 kN). The tie-down rods of the longitudinal walls also attained their peak tensile forces as the story drift reached the negative (eastward) peak (green circles), however their achieved tensile forces were smaller than those of the transverse wall tie-down rods. The tensile forces the transverse wall tie-down rods were larger than those of the longitudinal wall as they were located at the extreme edge. Therefore, the distance to the shear wall rocking center from the transverse wall tie-down rods was larger that from the longitudinal wall tie-down rods.

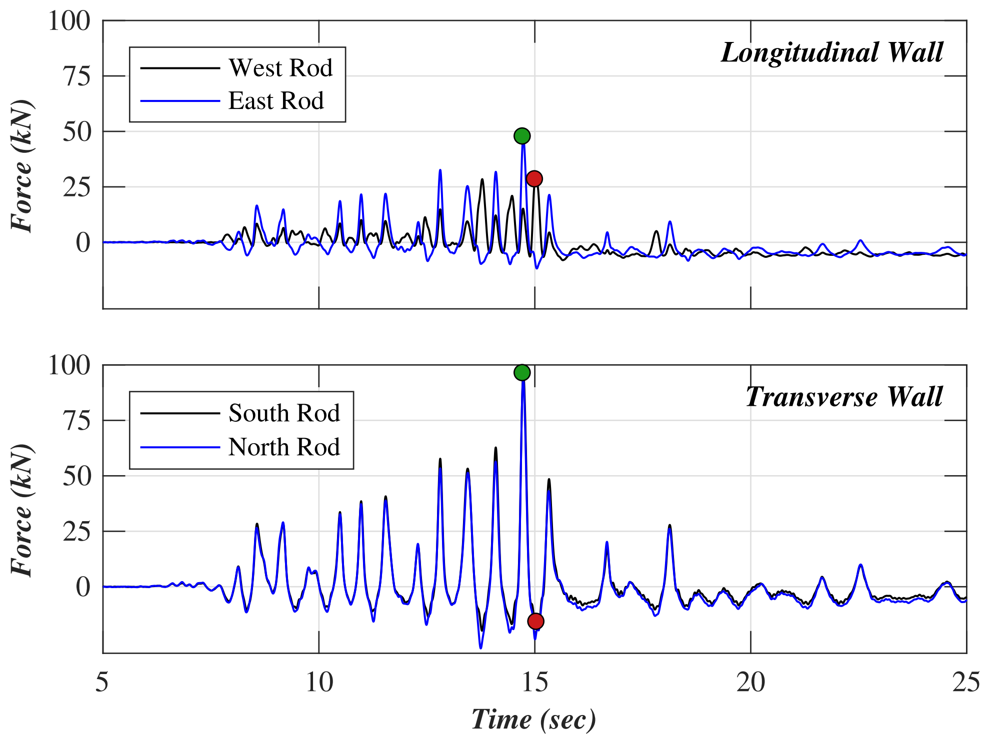

Figure 6.66. Tie-down rod axial force histories of the corner shear walls at level 2 during the design earthquake test (EQ6).

Peak Panel Shear Distortions

Figure 6.67 summarizes the peak (maximum and minimum) panel shear distortions of the instrumented corridor and corner shear walls with respect to the corresponding PIDRs. Each row of the figure contains two plots showing the peak shear distortions of the corridor walls on the left and those of the corner walls on the right (data points marked with different symbols represent the peaks of the different walls). As shown in the figure, the peak shear distortions increased almost in proportion with the drift demands. However, the corridor shear walls attained larger shear distortions compared to the corner shear walls at the same level. While the peak shear distortions of the corridor shear walls at the lower two levels reached about 0.6% under the largest drift demands, those of the corner shear walls were only about 0.2%. This is likely due to the distinctively different aspect ratios for the corridor and corner shear walls. In addition, the corner shear walls at level 4 attained much smaller shear distortions than the same type of the walls at the lower two levels.

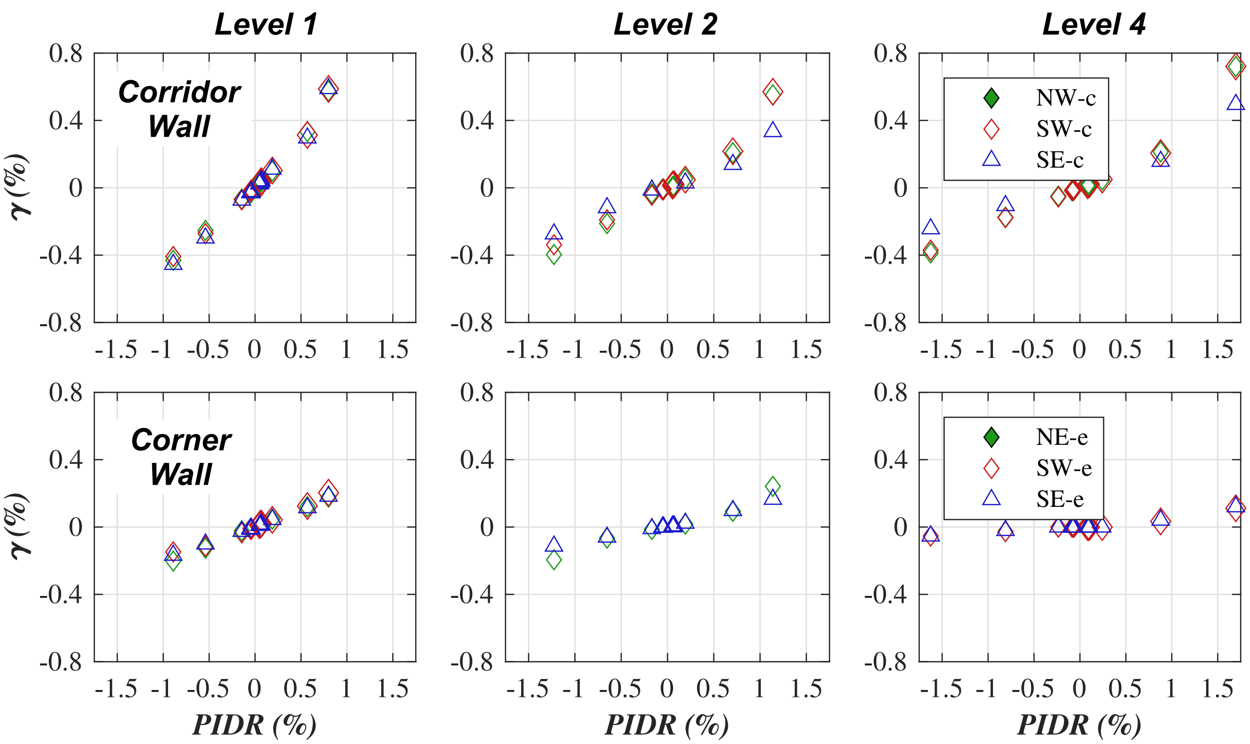

Figure 6.67. Peak panel shear distortions of the corridor (first row) and corner (second row) shear walls during the pre-fire earthquake test sequence.

Figure 6.68 summarizes the ratio of peak panel shear distortions and the corresponding PIDRs. As shown in the figure, the panel shear distortions of the level 1 corridor shear walls were typically 40%~60% of the drift demands, whereas those of the corner walls at the same level were only slightly larger than 20%. In addition, the shear distortion ratios of the shear walls were smaller at higher levels. For instance, the shear distortion ratios of the corridor shear walls reduced from 40%~60% at level 1 to 20%~40% at level 2 and around 20% at level 4. This is likely attributed to the effect of the tie rod systems, as the diameter of the tie rods of the level 4 was significantly smaller than those of the lower two levels.

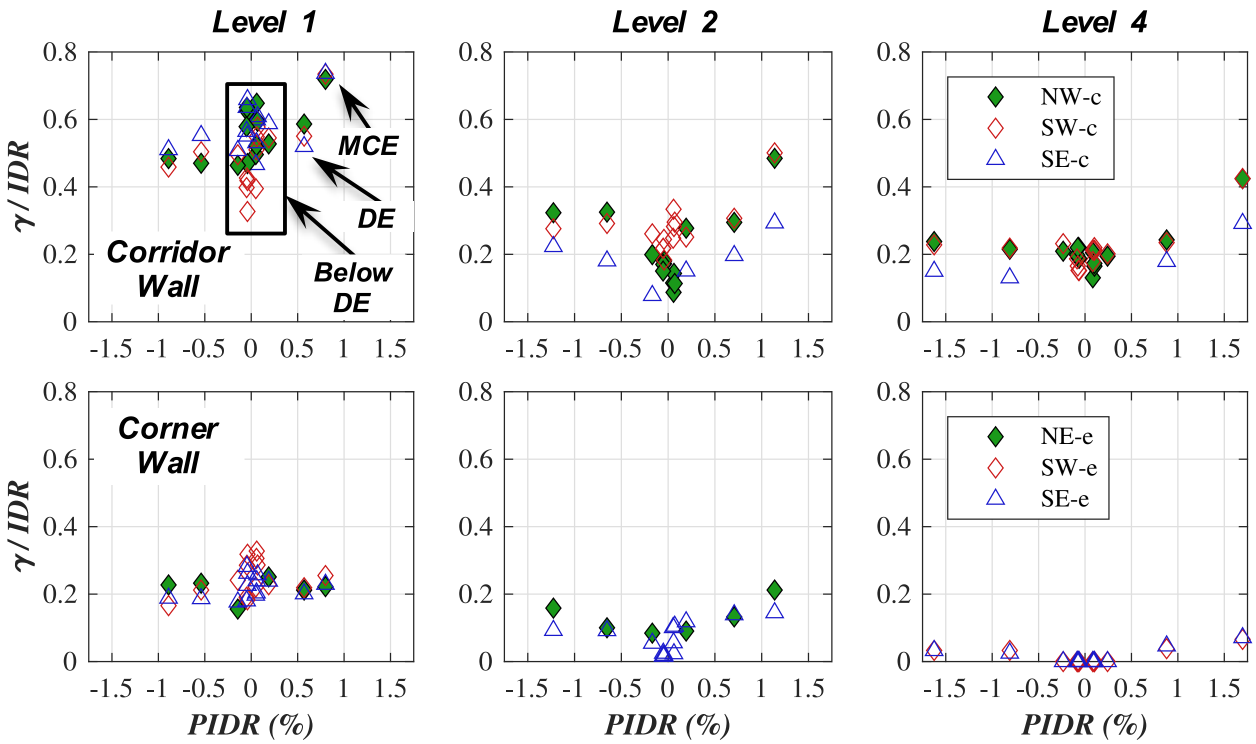

Figure 6.68. Normalized peak panel shear distortions of the corridor (first row) and corner (second row) shear walls during the pre-fire earthquake test sequence.

Peak Tie-down Rod Axial Forces

Figure 6.69 summarizes the measured peak tensile forces of the corridor and corner shear wall tie-down rods during the pre-fire earthquake test phase. It is noted that the tie-down rod axial forces of the northwest corridor shear walls were not measured since no strain gages were installed on these walls. Data points associated with the positive (eastward) PIDRs represent those of the measured peak tensile forces of the tie-down rods at the west ends of individual shear walls, whereas those associated with the negative (westward) PIDRs represent the peak tensile forces of the tie-down rods at the east ends of the shear walls.

As a result of larger lateral force demands at the lower two levels, the measured peak tensile forces of the shear wall tie-down rods at the lower levels were much larger than those of the level 4 shear walls. The axial forces of the corridor walls at the lower two levels achieved ~400 kN but only 200 kN at level 4. In addition, the peak tensile forces of the corridor shear wall tie-down rods were much larger than those of the corner shear walls at the same level. The achieved peak tensile forces remained comparable for the corridor shear wall pairs (east and west wall segments) at each of the three levels, while the forces differed apparently for the corner shear wall pairs. It is also important to note that the measured axial forces of all instrumented tie-down rods remained smaller than their respective yield strengths. During the pre-fire test phase, the tensile forces of the corridor shear wall tie-down rods reached only ~40% their respective yield strength, while those of the corner shear walls attained about 60% (refer to Table 6.4).

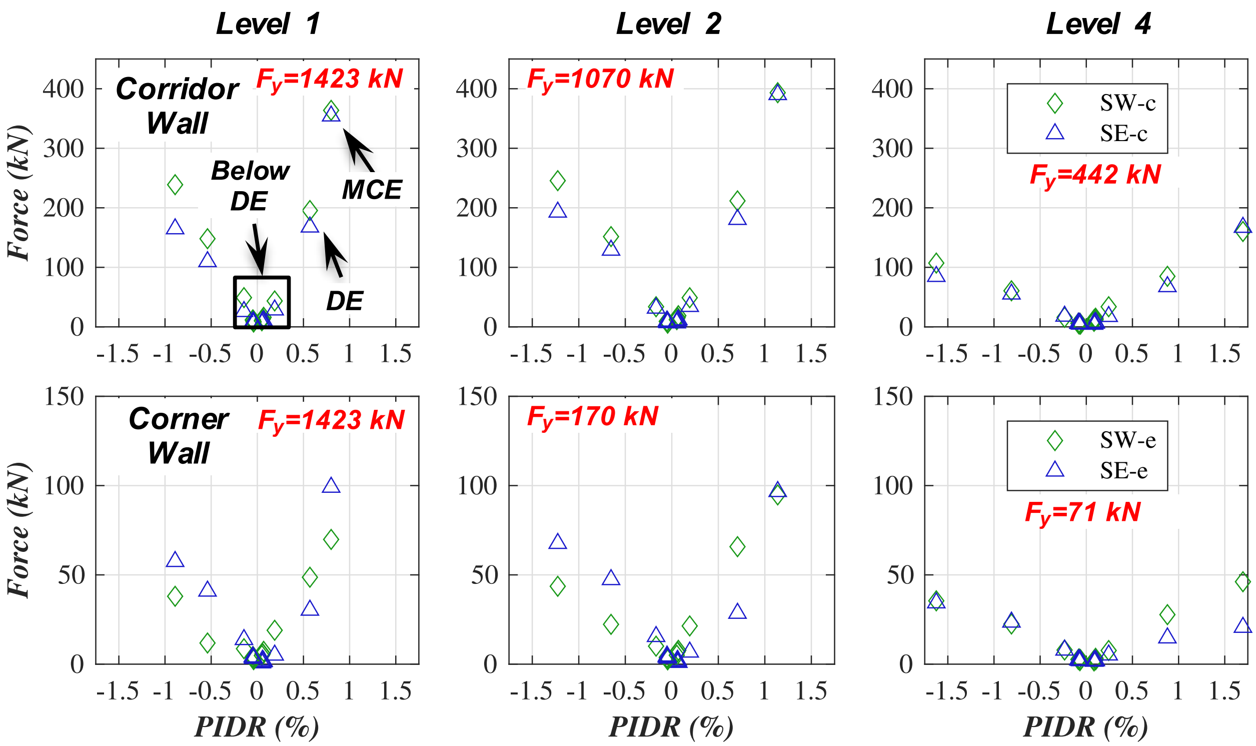

Figure 6.69. Peak tie-down rod tensile forces of the corridor (first row) and corner (second row) shear walls during the pre-fire earthquake test sequence.

Peak Wall End Vertical Displacements

Figure 6.70 summarizes the measured peak wall end vertical displacements of the corridor and corner shear walls during the pre-fire earthquake test phase. Data points associated with the positive (eastward) PIDRs represent the peak vertical displacements measured at the west ends of individual shear walls, whereas those associated with the negative (westward) PIDRs represent the peak vertical displacements measured at the east ends of the shear walls. As a result of larger tensile force demands of the tie-down rods at the lower two levels, the uplift displacements of the shear walls of these two levels appeared considerably larger than those at level 4. While only about 2 mm for the level 4 shear walls, the peak vertical displacements exceeded 10 mm at the lower two levels. In addition, the peak uplift displacements of the corridor shear walls were slightly larger than those of the corner shear walls at the same level, which is also attributed to the larger tensile force demands related to the corridor shear wall tie-down rods.

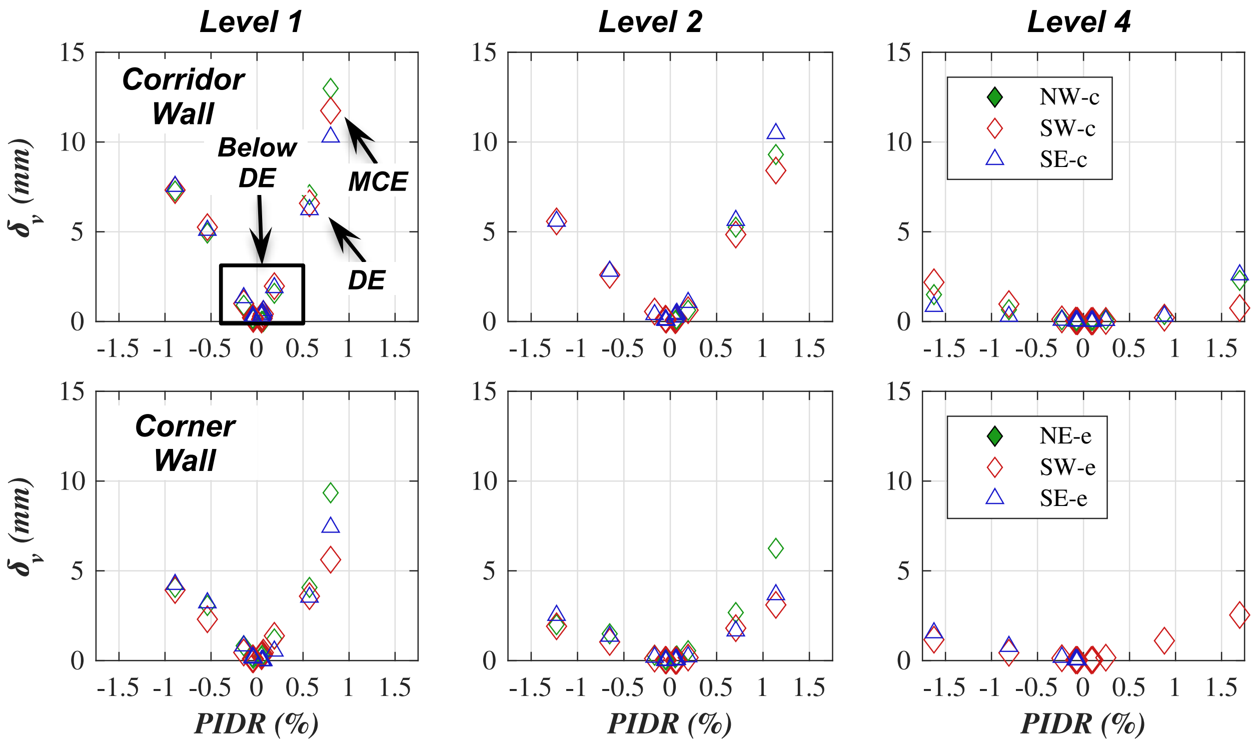

Figure 6.70. Peak wall end vertical displacements of the corridor (first row) and corner (second row) shear walls during the pre-fire earthquake test sequence.

6.3.2 Floor Joist Deformations

The floor panel interface joists at floor 2 were instrumented with four linear potentiometers (two each for the north and south span) at the underside of the joists to measure their longitudinal deformation (gap opening) between the panel interface joists. Figure 6.71 presents the joist deformation histories during three select earthquake tests, namely, EQ2:CNP-25 (service level event), EQ6:CNP-100 (design event), and EQ2:CNP-150 (MCE event). The color circles represent the time instances when the maximum (red) and minimum (green) interstory drift of level 1 were achieved. Although remained small during the pre-fire earthquake test sequence, the gap elongations (represented as positive) at the corridor ends were apparently larger than those at the exterior ends. This is likely due to the fact that the lateral force transferred from the diaphragm to the corridor walls are expected to be much larger than the force transferred to the exterior (gravity) wall. Furthermore, the occurrence of peak joist elongations coincided with the occurrences of the interstory drift of level 1 (as denoted by the red circles), indicating that joist deformations at the panel interface were correlated with the story drift demands.

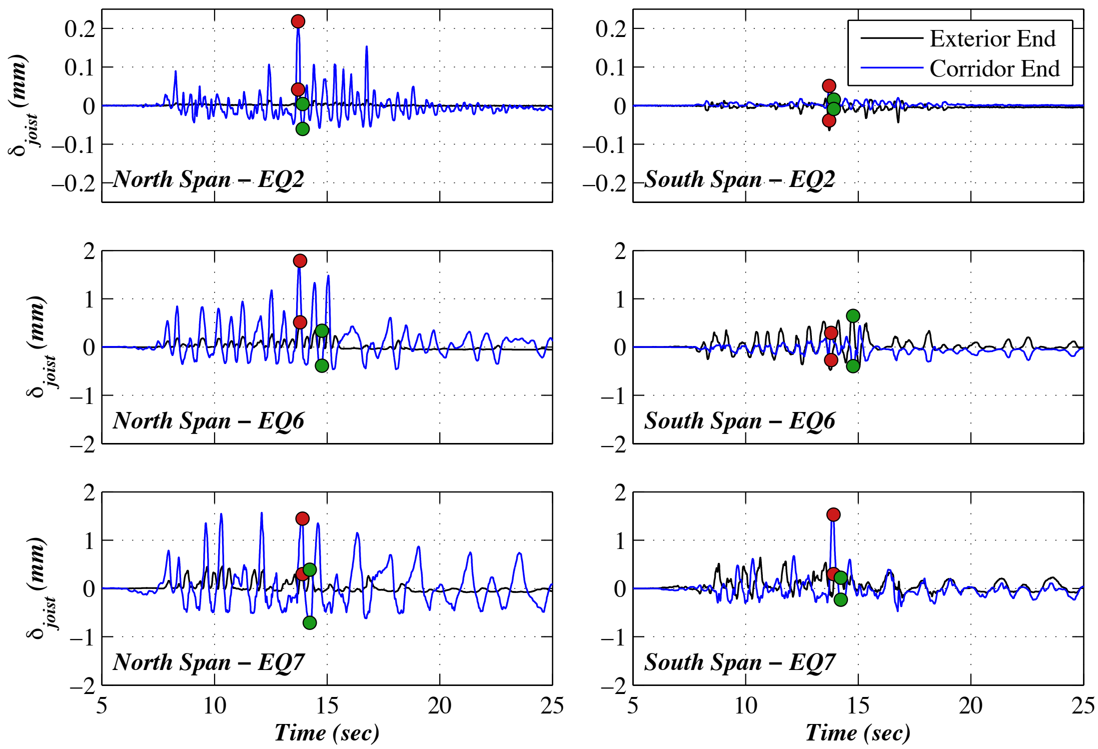

Figure 6.71. Joist deformation histories during EQ2:CNP-25, EQ6:CNP-100, and EQ7:CNP-150.

Table 6.5 summarizes the peak joist elongations and the normalized peak joist elongations (percentile ratio between the joist elongations and the story drift of level 1) during the pre-fire earthquake test sequence. The elongations of the panel interface joints attained only as low as 0.2 mm during the service level events (10% ~ 15% of the story drift) and about 2 mm during the design and MCE events (10% of the story drift for EQ6 and 5% for EQ7). Since the joist elongations remained very small, no visible damage to the interface joists was detected throughout the pre-fire test sequence.

Table 6.5. Peak joist deformations (elongation) during the pre-fire earthquake test phase.

Test Motion	*North span*		*South span*	
	δ_{joist}^{peak} *(mm)*	$\hat{\delta}_{joist}^{peak}$ *(%)*	δ_{joist}^{peak} *(mm)*	$\hat{\delta}_{joist}^{peak}$ *(%)*
EQ1:RIO-25	0.2	12.8	0.0	3.9
EQ2:CNP-25	0.2	12.1	0.1	3.5
EQ3:CUR-25	0.2	12.4	0.0	4.0

EQ4:CNP-25	0.3	14.6	0.1	3.5
EQ5:CNP-50	0.8	14.6	0.2	4.1
EQ6:CNP-100	1.8	10.3	0.6	3.7
EQ7:CNP-150	1.6	5.7	1.5	5.6

Notes: δ_{joist}^{peak} – peak deformation of the joists; $\hat{\delta}_{joist}^{peak}$ – peak deformation of the joist normalized by the interstory drift of level 1.

6.4 Physical Observation

Detailed physical inspection of the structural systems (i.e., walls, diaphragms) and its nonstructural components was conducted at four different stages throughout the pre-fire earthquake test phase: (1) pre-test inspection (associated with state S0), (2) post-SLE (associated with state S3), (2) post-DE (associated with state S6), and (3) post-MCE (associated with state S7). In addition, rapid inspections were conducted between the tests during the first two test days that involved multiple earthquake tests, although the primary purpose of these inspections was to examine the condition of critical structural components (e.g., mass plate anchorage, tie rod coupler connections).

Damage documentation relied upon visual inspections including physical marking of observed damage as well as detailed photographs, videos, and notes. The damage to building interior was marked using different colors and line types at different inspection stages: (a) *dashed blue* for pre-damage, (b) *solid blue* for damage occurred during the service level tests, (c) *solid black* for damage occurred during the design event, and (d) *solid red* for damage occurred during the MCE test.

6.4.1 Structural Systems

Inspection of the building interior focused primarily on the wall sheathing and diaphragm framing at each of the four inspection stages. In addition, the steel framing of the shear walls of the northwest compartment at level 4 was inspected following the end of pre-fire test sequence by removing the gypsum panels, since level 4 achieved the largest drift demands in the pre-fire test phase. No repairs were made to the structural components at any stages throughout the test program, and therefore the damage observed at each inspection stage represented the cumulative damage. Dependent on the severity of damage and their implications associated with the repair strategies, damage to the shear walls and gravity walls was classified into three damage states

(DSs), each associated with different damage modes. The damage states and description of the associated damage modes are summarized in Table 6.6. Damage to the floor diaphragm framing, however, is not classified using damage states due to the following two considerations: (1) observed damage of the floor diaphragm was not significant during these earthquake tests, and (2) research is needed to characterize the damage and failure mechanisms of the floor diaphragm systems.

Table 6.6. Damage states and the associated damage modes of the CFS wall systems.

Damage state[1]	*Damage mode description*
DS-1 (minor): primarily cosmetic damage — requires minimal repair to appear new	Incipient screw withdrawal (SC1), localized gypsum crushing or bulging (GYP1), gaps between gypsum panels (GP), joint tape cracking or flaking (TP)
DS-2 (moderate): localized damage — requires repair or partial replacement	Pervasive screw withdrawal along the panel boundary (SC2), sustained gypsum crushing or bulging on the boundary (GYP2), distorted or loosened gypsum panels (GYP3), punched opening in gypsum panel (OP), sheathing steel local buckling (SS)
DS-3 (severe): damage beyond repair —requires full replacement of wall	Buckled or distorted steel framing members, framing fastener connection failure

[1] Damage states apply to both shear walls and gravity walls.

Table 6.7 summarizes the observed damage of the interior wall sheathing and the associated damage states. It is noted, however, that wall finishes of the test building were not representative of common practice, and therefore the minor (cosmetic) damage (DS-1) observed in the tests may underestimate that of buildings with standard sheathing finishes. In addition, the wall systems did not sustained severe damage (DS-3) throughout the pre-fire test sequence, and therefore the damage states as summarized in the table include only the minor and moderate damage states (DS-1 and DS-2).

Table 6.7. Wall sheathing damage during the pre-fire earthquake test sequence.

Level	Type of Wall [1]	Inspection stage: Post-SLE DS	Post-SLE Damage mode [2]	Post-DE DS	Post-DE Damage mode [2]	Post-MCE (pre-fire) DS	Post-MCE (pre-fire) Damage mode [2]
1	SW-L (corridor)	DS-0	/	DS-2	SC1, GYP1, SS	DS-2	SC2, GYP2, SS
	GW-L (corridor and exterior)	DS-0	/	DS-1	SC1, GYP1	DS-2	SC2, GYP2
	SW-L (corner)	DS-0	/	DS-1	SC1, GYP1	DS-1	SC1, GYP1
	SW-T (corner)	DS-0	/	DS-1	SC1, GYP1	DS-1	SC1, GYP1
2	SW-L (corridor)	DS-0	/	DS-2	SC2, GYP2, TP	DS-2	SC2, GYP3, TP
	GW-L (corridor and exterior)	DS-0	/	DS-2	SC2, GYP2, TP	DS-2	SC2, GYP3, TP
	SW-L (corner)	DS-0	/	DS-1	TP	DS-1	SC1, GYP1, TP
	SW-T (corner)	DS-0	/	DS-1	TP	DS-1	SC1, GYP1, TP
3	SW-L (corridor)	DS-0*	SC1, GYP1	DS-2	SC2, GYP2	DS-2	SC2, GYP3
	GW-L (corridor and exterior)	DS-0*	SC1, GYP1	DS-2	SC2, GYP2,	DS-2	SC2, GYP3
	SW-L (corner)	DS-0	/	DS-1	SC1, GYP1	DS-1	SC1, GYP1
	SW-T (corner)	DS-0	/	DS-1	SC1, GYP1	DS-1	SC1, GYP1
4	SW-L (corridor)	DS-0*	SC1, GYP1	DS-2	SC2, GYP2	DS-2	SC2, GYP3
	GW-L (corridor and exterior)	DS-0*	SC1, GYP1	DS-2	SC2, GYP2	DS-2	SC2, GYP3
	SW-L (corner)	DS-0	/	DS-1	SC1, GYP1	DS-1	SC1, GYP1
	SW-T (corner)	DS-0	/	DS-1	SC1, GYP1	DS-1	SC1, GYP1
5	SW-L (corridor)	DS-0	/	DS-2	SC2, GYP2	DS-2	SC2, GYP3
	GW-L (corridor and exterior)	DS-0	/	DS-2	SC2, GYP2	DS-2	SC2, GYP3
	SW-L (corner)	DS-0	/	DS-1	SC1, GYP1	DS-1	SC1, GYP1
	SW-T (corner)	DS-0	/	DS-1	SC1, GYP1	DS-1	SC1, GYP1
6	SW-L (corridor)	DS-0	/	DS-2	SC1, GYP1, TP, OP	DS-2	SC2, GYP2, TP, OP
	GW-L (corridor and exterior)	DS-0	/	DS-1	SC1, GYP1, TP	DS-2	SC2, GYP2, TP
	SW-L (corner)	DS-0	/	DS-0	TP	DS-1	SC1, GCR1, TP
	SW-T (corner)	DS-0	/	DS-0	TP	DS-1	SC1, GCR1, TP

[1] SW-L – longitudinal shear wall, SW-T – transverse shear wall, GW-L – longitudinal gravity wall (including the openings); [2] refer to Table 6.6 for detailed description of the damage modes.
* Extant of sheathing damage inadequate to classify the walls into any damage states.

Post SLE Inspection

Due to the low seismic demands during the service level tests at all levels of the test building (PFA < 0.5 g, PIDR < 0.1%), interior sheathing sustained only a few instances of minor damage (DS-1) in the form of incipient screw withdrawal and localized gypsum crushing at bulging at level 3 and 4 (Figure 6.75), while no visible damage to interior sheathing occurred at all other levels. The extant of sheathing damage, however, was considered inadequate to classify the walls into any damage states.

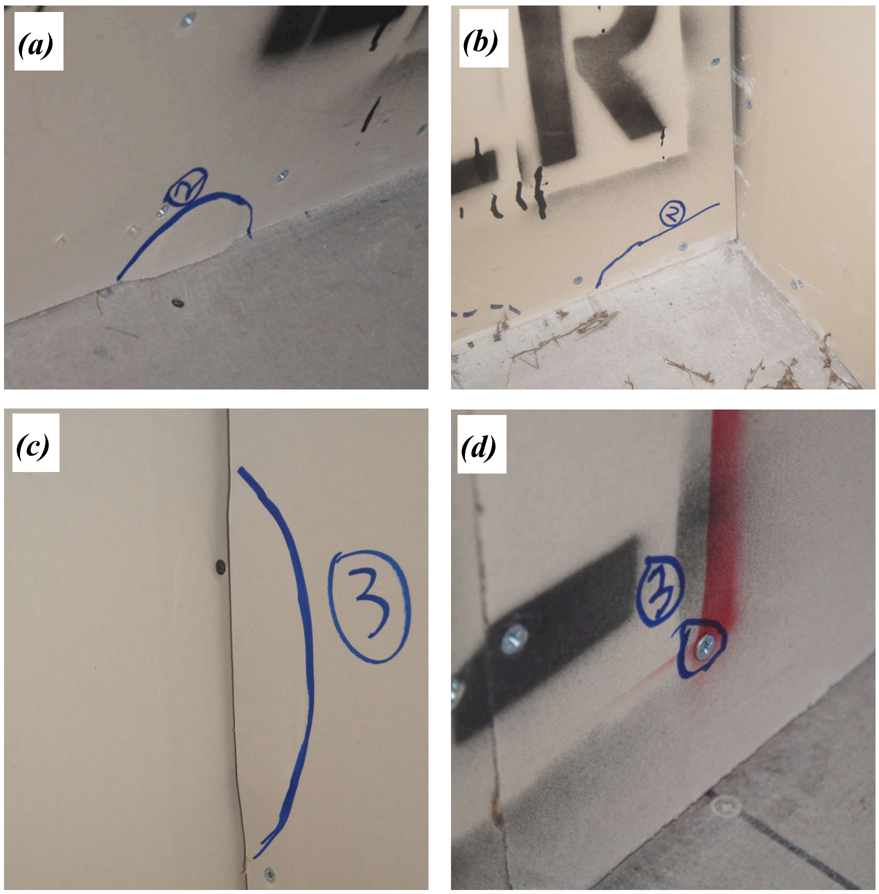

Figure 6.72. Interior sheathing damage during the service level earthquake tests: (a) bulged gypsum on the bottom edge (EQ2), (b) bulged gypsum at the bottom corner (EQ2), (c) bulged gypsum on the vertical edge (EQ3), and (d) incipient screw pull out (EQ3).

Post DE Inspection

Damage to interior sheathing continued to develop as the seismic drift demands increased during the 50% design event (EQ5) and design event (EQ6). Screw withdrawal and gypsum crushing of the corridor shear walls and gravity walls became more pervasive at all except the uppermost levels (Figure 6.73a-d). In particular, the vertical boundaries between the corridor shear walls and the gravity wall as well as the window and door openings sustained more extensive crushing damage. In contrast, damage to the corner shear walls remained minor, as they occurred only in the form of localized gypsum crushing at the corner and formation of gaps between gypsum panels. Since the interior gypsum was mudded and tapped at level 2 and 6, tape cracking or flaking along the panel joints was also observed at these levels. In addition, a punched opening was detected on the gypsum panels at the northeast room at level 6 due to the toppling of a water heater during EQ6 (Figure 6.73e).

Additionally, buckling of sheathing sheet steel (below the joist rim tracks) occurred in particular on the corridor shear walls at level 1 (Figure 6.74a) following the design event (EQ6). This type of damage was primarily due to the large unbraced gap height (> 4 cm) between the rim tracks and gypsum (Figure 6.74b), compared with the typical gap height of ~1.5 cm in common construction practice. This unintended effect was due to the inconsistency of the dimension of the in-situ installation of the wall framing height at level 1 and that of the prefabricated sheathing panels.

Post-MCE Inspection

As the seismic drift demands continued to increase during the MCE event (EQ7), physical damage to the building was characterized with continued damage to the wall sheathing as well as the initiation of the joist rim track localized buckling. While damage of corner shear wall sheathing remained minor (DS1) and did not differ pronouncedly from the previous test (EQ6), sheathing damage continued to develop around the corridor openings and the boundaries between the shear walls and the gravity walls in the form of loosened gypsum panels as well as severely crushed gypsum panels (Figure 6.75). Importantly, it was found that damage to the sheathing boundary at the south sides of the corridor walls at level 4 (Figure 6.76a and c) appeared much more severe than that at the north side (Figure 6.76b and d). Their performance distinction was likely due to the different gypsum panel edge conditions at the boundary (cut edge for the south-side gypsum panel vs wrapped edge on the north-side gypsum panel). It is recommended that further research be conducted to assess the effect of the panel edge conditions on their seismic behavior.

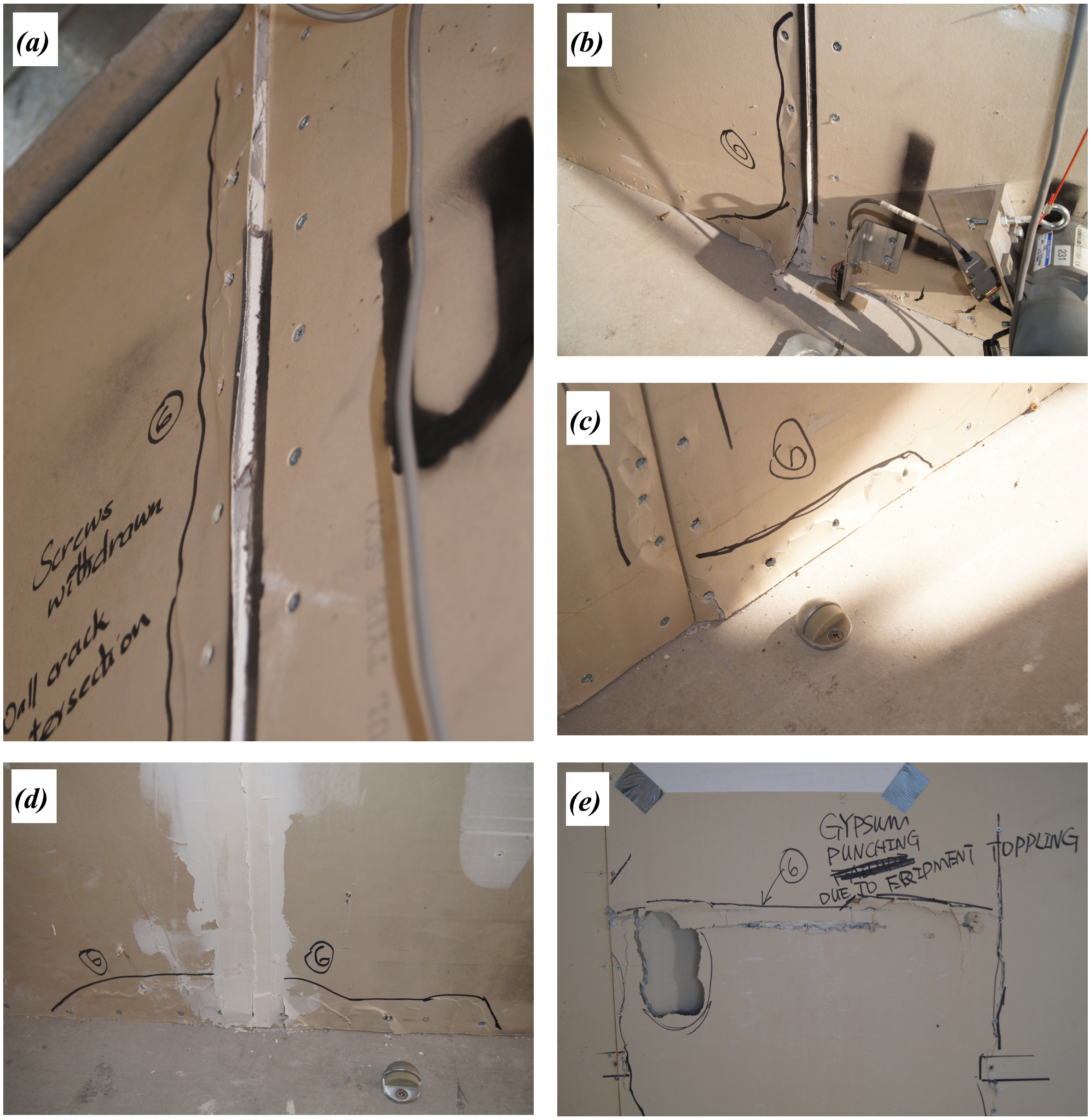

Figure 6.73. Sheathing damage following the design level test (EQ6): (a) corridor shear wall–gravity wall boundary at level 4 (upper), (b) (a) corridor shear wall–gravity wall boundary at level 4 (lower), (c) pervasive screw withdrawal and corner crushing of gravity wall at level 4, (d) corridor gravity wall boundary crushing at level 2, and (e) a punched opening on the gypsum panel at level 6.

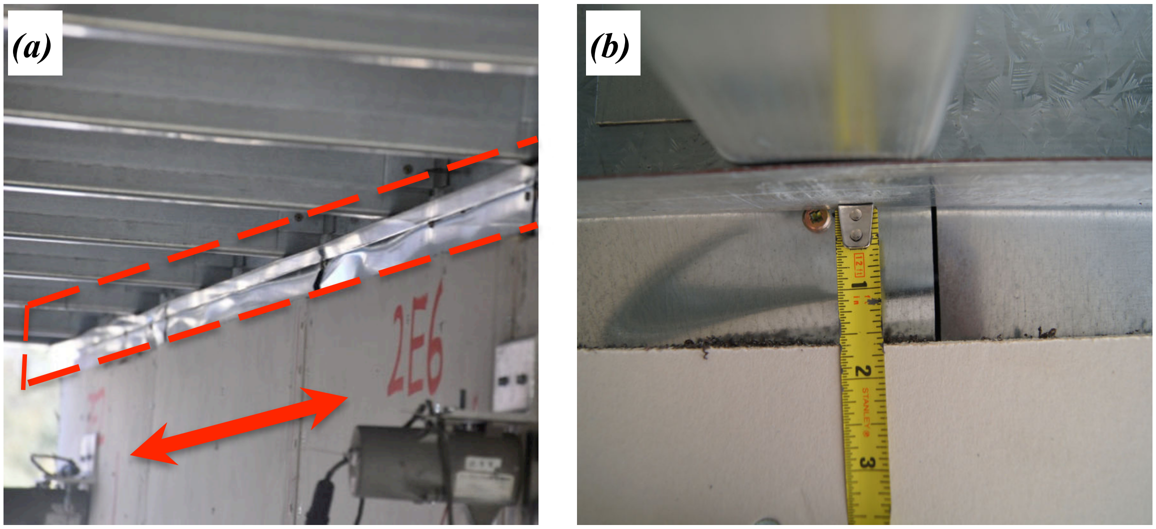

Figure 6.74. Buckled sheet steel of corridor shear wall structural panels at level 1 at the completion of the design level test (EQ6): (a) global view, and (b) close up view of gap.

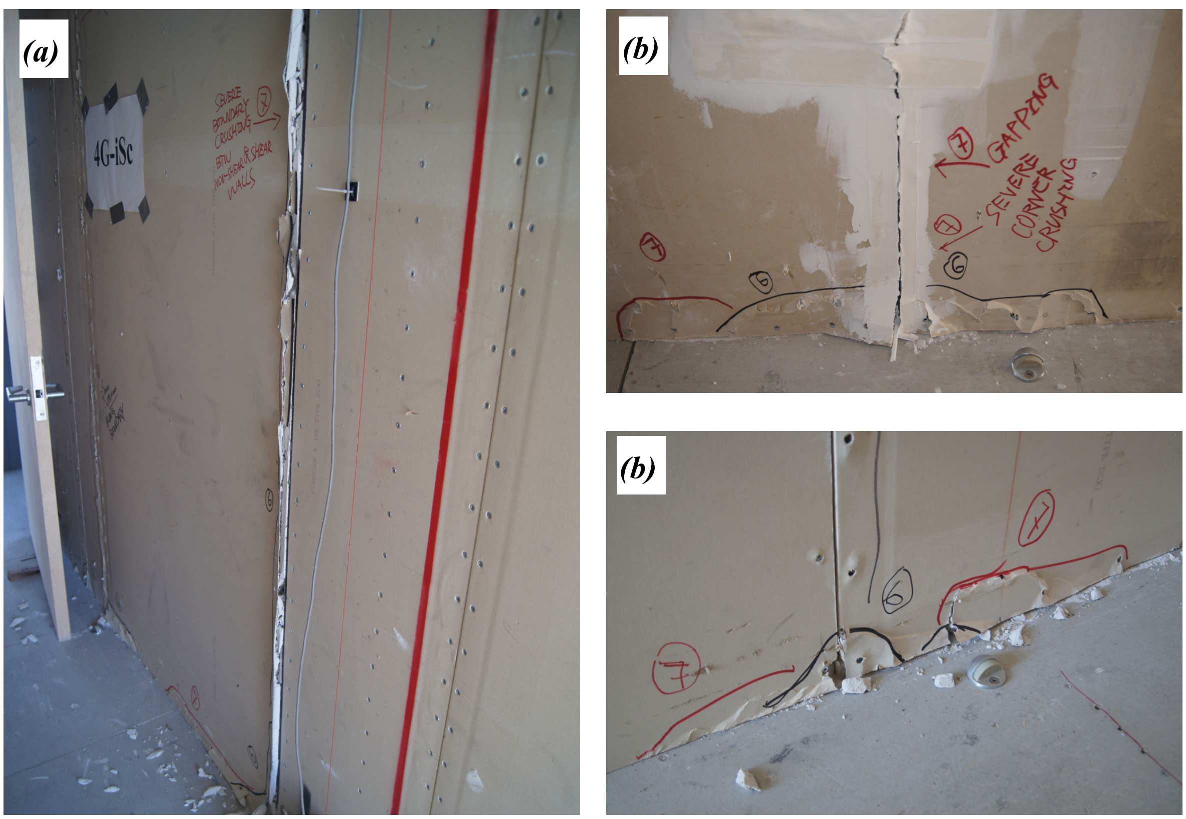

Figure 6.75. Interior sheathing damage at the completion of the MCE test (EQ7): (a) corridor shear wall–gravity wall boundary at level 4, (b) corridor shear wall–gravity wall boundary at level 2, and (c) continued corridor gravity wall boundary crushing at level 6.

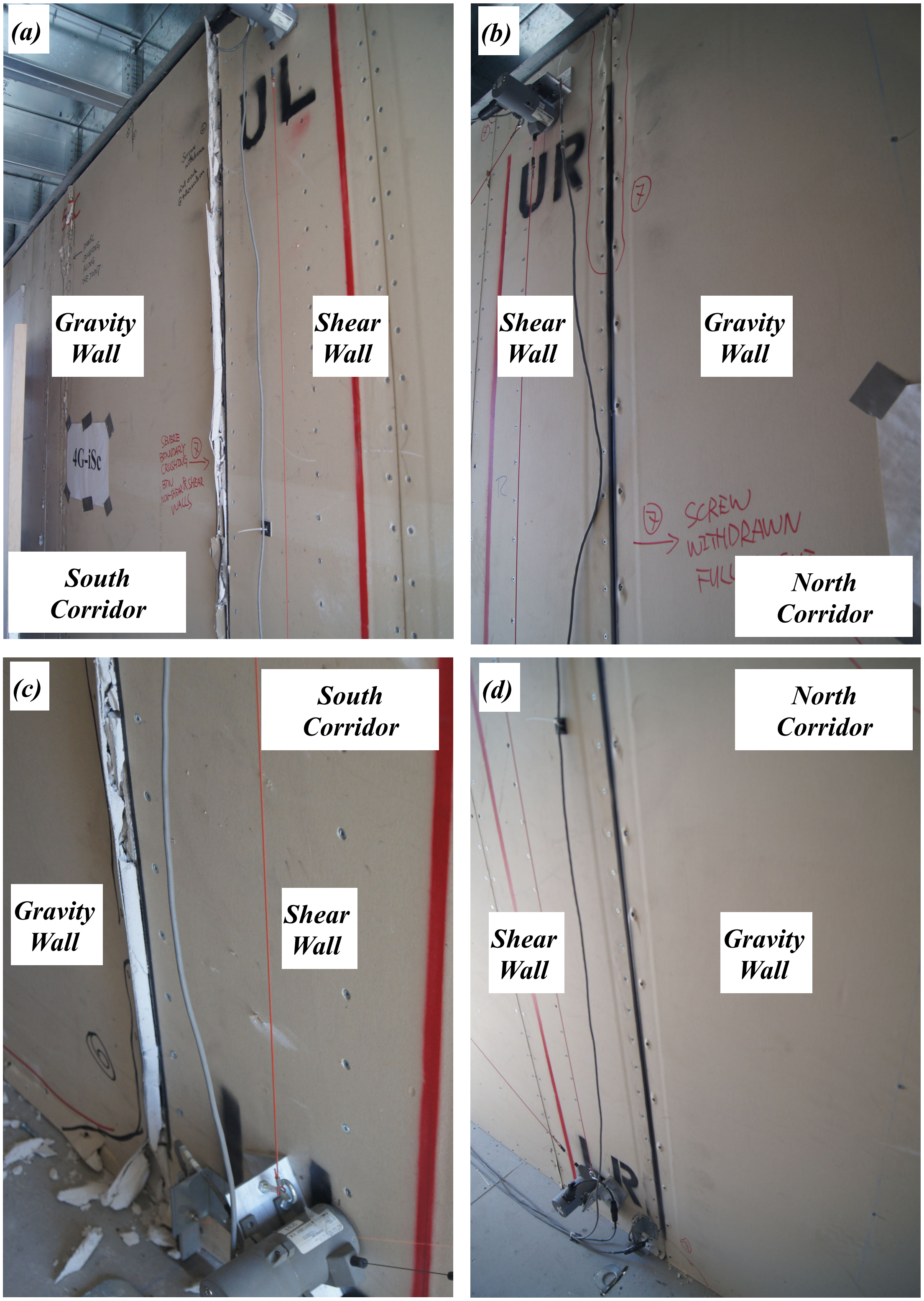

Figure 6.76. Comparison of corridor shear wall–gravity wall boundary sheathing damage following the MCE test (EQ7): (a) upper boundary – south corridor walls, (b) upper boundary – north corridor walls, (c) lower boundary – south corridor walls, and (d) lower boundary – north corridor walls.

Localized joist rim track buckling occurred at several locations at floor 4 through 6 (Figure 6.77). Damage of this kind was primarily located at the rim tracks above the corridor door openings or the exterior wall window openings. This localized damage mode is likely caused by the stiffness and strength discontinuities of the vertical structural elements.

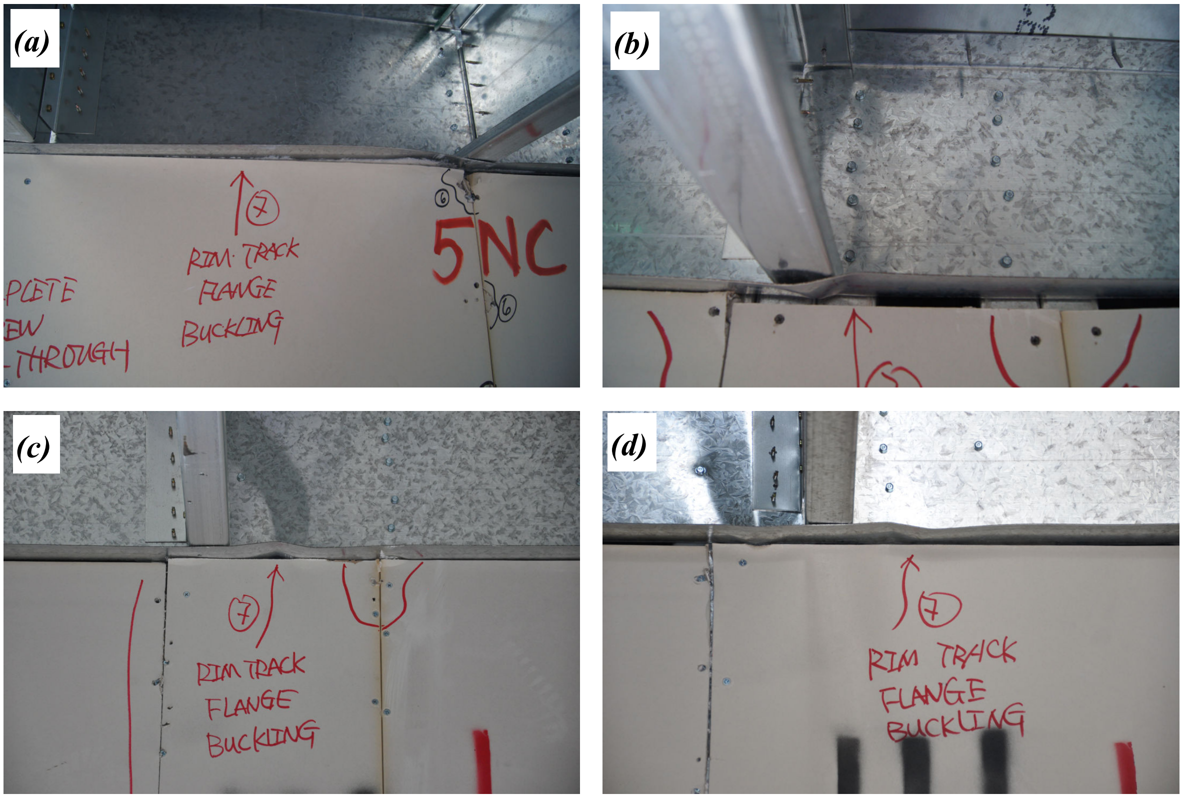

Figure 6.77. Damage to joist rim tracks following the pre-fire MCE test (EQ7): (a) buckled rim track flange above the level 4 corridor door opening, and (b) buckled rim track flange and web above the level 4 window opening, (c) buckled rim track flange and web above the level 5 corridor door opening, and (d) buckled rim track flange above the level 5 window opening.

Following the completion of the pre-fire earthquake test phase, the interior gypsum panels of the northwest compartment at level 4, which represented the level with the largest drift demands during the pre-fire test phase, were removed to allow for inspection of the shear wall framing and sheathing steel. As shown in Figure 6.78b-d, localized buckling of the sheathing steel was detected at the top of the corridor shear wall, while the framing studs and tracks did not sustained visible damage (Figure 6.78e). In addition, loosening of the bolts at the floor bearing connections was detected at the end of the pre-fire test sequence, resulting in very loose tie-down rods. In contrast, the wall framing and sheathing steel of the corner shear walls in the same compartment sustained no apparent damage (Figure 6.79).

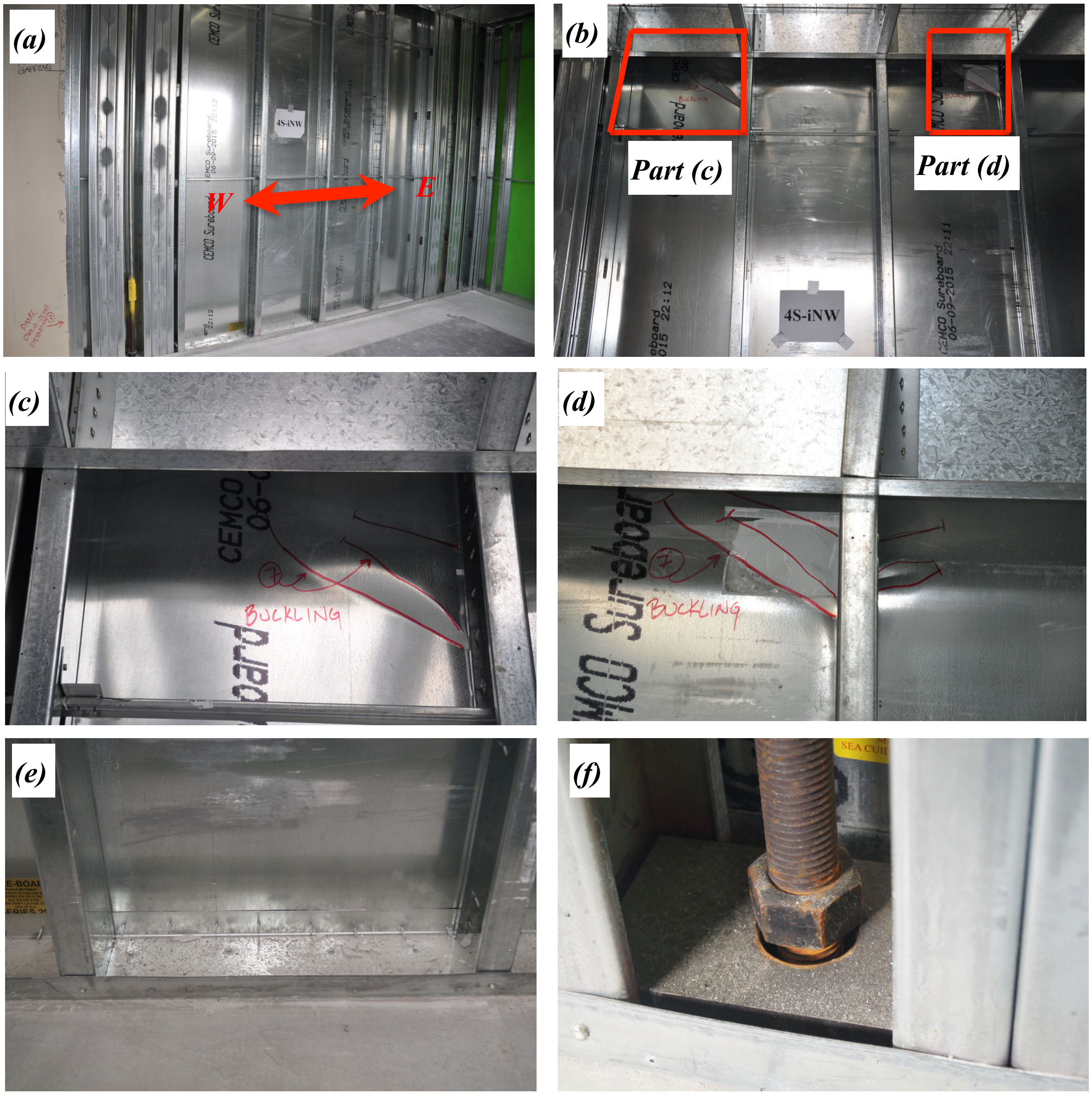

Figure 6.78. Longitudinal corridor shear wall framing following the pre-fire MCE test (EQ7): (a) wall framing, (b) localized buckling at the top of sheathing steel, (c) and (d) close-up of the localized buckling, (e) bottom track, and (f) loosened bolt of the tie-rod bearing connection.

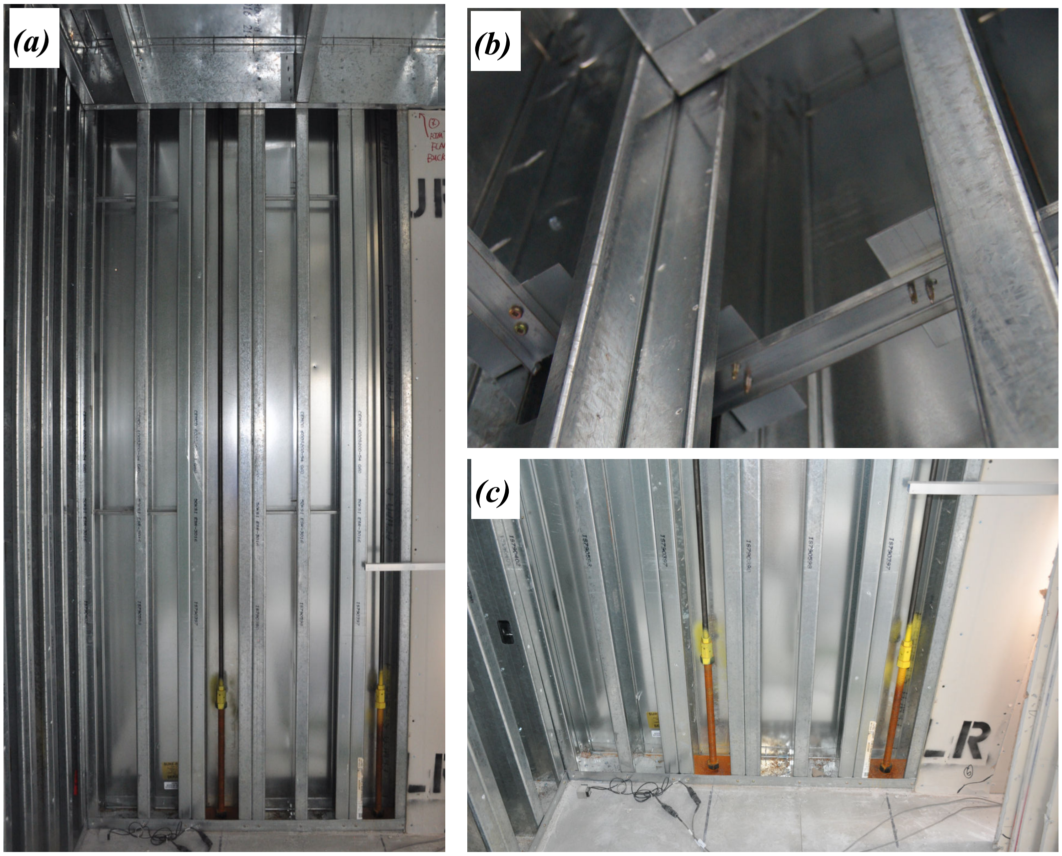

Figure 6.79. Longitudinal corner shear wall framing following the pre-fire MCE test (EQ7): (a) wall framing, (b) upper corner, and (c) bottom track and studs.

6.4.2 Exterior Wall Sheathing

Similar to the interior damage inspections, damage of the exterior sheathing was marked using different colors and line types to represent different inspection stages: (a) *blue solid* for pre-damage, (b) *orange solid* for damage occurred following the design event (EQ6), and (c) *red solid* for damage occurred following the MCE event (EQ7). Due to the time constraint of the test schedule, detailed photo documentation of building exterior was conducted only at two stages: (1) prior to the test sequence (pre-test), and (2) following the completion of pre-fire test phase (post-MCE).

No apparent damage to exterior sheathing was observed during the service level tests (EQ1-EQ3). Damage to exterior sheathing initiated following the design event (EQ6) and continued to propagate and became more pervasive during the MCE event (EQ7). Figure 6.80 illustrates the north and west faces of the building following the MCE event (EQ7). It is observed that the exterior sheathing damage was located primarily on the exterior gravity walls (between the window openings) and around the window openings (Figure 6.81a). In contrast, the corner shear walls (Figure 6.81b) and the east and west faces (Figure 6.80b) sustained very limited damage. Typical damage occurred in the form of gypsum crushing or bulging at the panel edges and corners as well as diagonal cracks around the window openings (Figure 6.81c-e).

Figure 6.80. Exterior sheathing following the pre-fire MCE event (EQ7): (a) north face, and (b) west face.

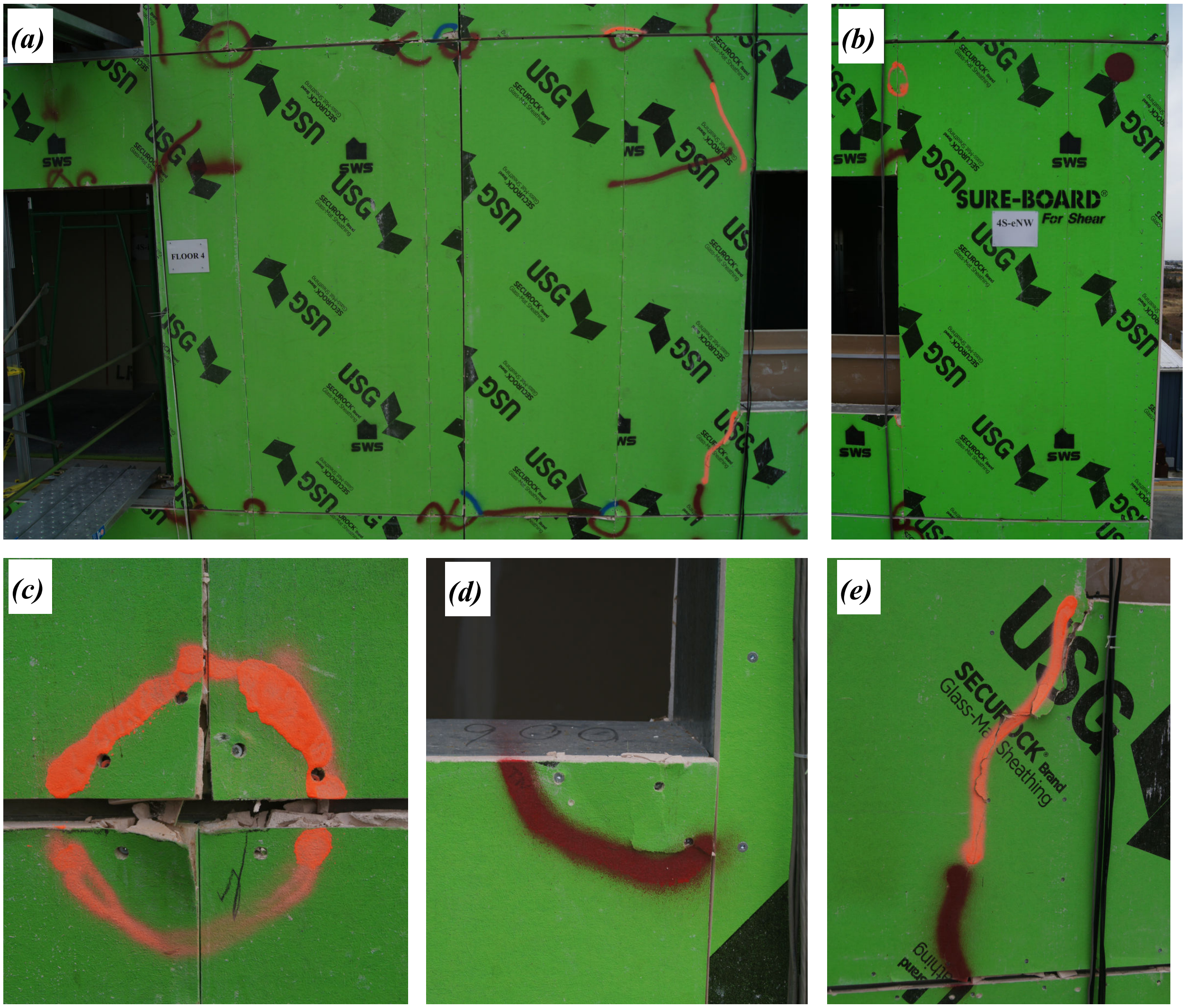

Figure 6.81. Exterior sheathing damage following the pre-fire MCE event (EQ7): (a) gravity wall and openings on the north face at level 4, (c) corner crushing, (c) corner bulging, and (e) diagonal cracks around the window opening.

6.4.3 Nonstructural Systems

Interior Partition Walls

Since the interior partition walls were oriented in the transverse direction and subjected to out-of-plane loading during the earthquake tests, only minor damage (DS-1) was observed on the partition walls during the pre-fire earthquake test phase. Typical damage occurred in the form of crushed gypsum corners and joint tape cracks at their intersections with the longitudinal structural walls.

Doors

Inspection of the physical damage to the doors was conducted at four inspection stages throughout the test program: post-EQ3, post-EQ6, post-EQ7 and post-EQ9. Dependent on the severity of damage and their implications related to functionality, the observed damage was categorized into three damage states (DSs). The damage states and associated physical damage modes are summarized in Table 6.8. The typical door damage modes observed during the earthquake tests are illustrated in Figure 6.82.

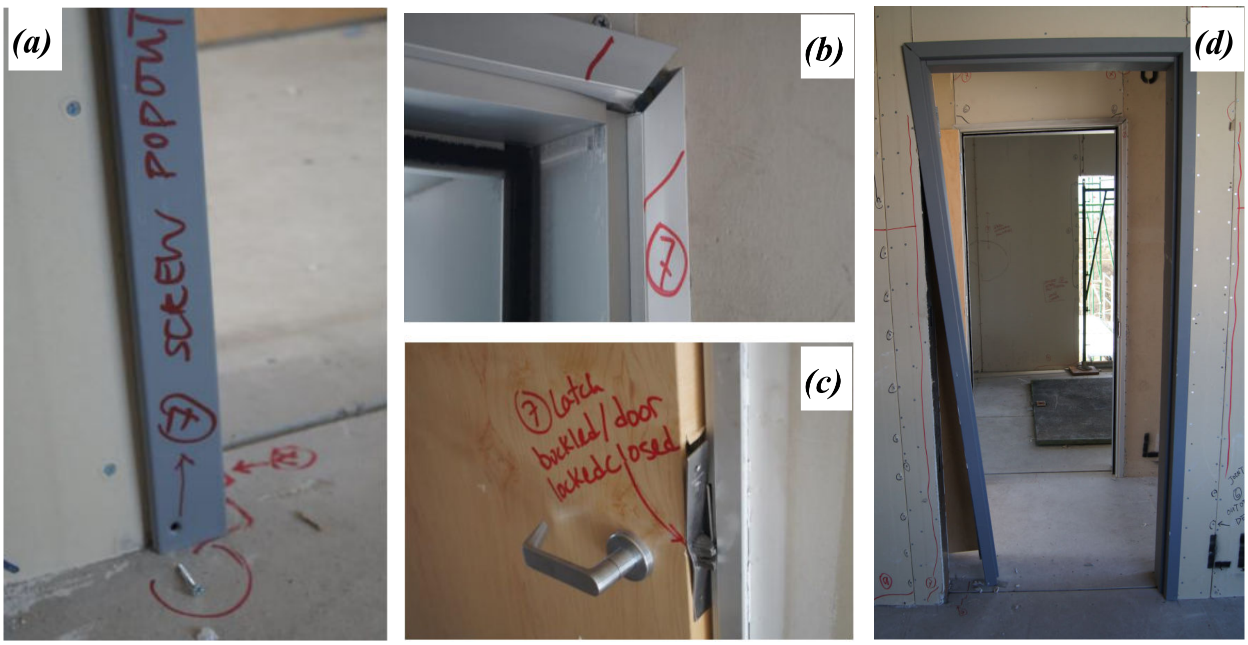

Figure 6.82. Examples of door damage: (a) door frame screw popping (DS-1), (b) door frame gapping (DS-2), (c) buckled door latch (DS-2), and (d) detached door frame (DS-3).

Table 6.8. Door damage states and the associated damage modes.

Damage state	*Physical damage mode*
DS-1 (minor)	Door frame gapping, screw withdrawal, door frame distortion, loose door frame, lock malfunction
DS-2 (moderate)	Door jam, door frame partial detachment, door latch failure
DS-3 (severe)	Door frame detachment

Table 6.9 summarizes the door damage states and the associated damage modes at the four inspection stages during the test sequence. It is noted that all the doors located in the fire compartments (four doors at level 2 and three doors at level 6) lost their functionality following the fire tests. The observed earthquake-induced door damage occurred exclusively on the corridor doors, since they were subjected to in-plane shear distortion throughout the earthquake

tests, while the doors on the partition walls sustained only limited damage. As the drift demands remained very low (PIDR < 0.1%) during the service level tests (EQ1-EQ3), the doors all functioned well with no apparent damage. Damage initiated on the corridor doors during the design event (EQ6, PIDR reached ~1.0%), which remained essentially minor (DS-1) (e.g., door frame screw popping (Figure 6.82a) and corner gapping (Figure 6.82b)). Damage continued to progress and became extensive during the MCE event (EQ7, PIDR > 1.5%). All the corridor doors expect those at level 1 suffered substantive damage in the form of latch plate failure (Figure 6.82c) as well as door frame distortion or even detachment (Figure 6.82d). Interested readers are referred to Appendix H for detailed photographic documentation of the physical door damage at different inspection stages.

Table 6.9. Summary of physical damage modes and damage states of the doors.

Level	*Short name*	*Inspection stage*							
		Post-EQ3		*Post-EQ6*		*Post-EQ7*		*Post-EQ9*	
		DS	*Mode*	*DS*	*Mode*	*DS*	*Mode*	*DS*	*Mode*
1	1-NC	DS-0		DS-0		DS-1	frame corner gapping	DS-1	
	1-SC	DS-0		DS-1	frame distortion (failed to lock)	DS-0		DS-1	frame distortion (failed to lock)
2	2-NR	DS-0		DS-0		DS-0		loss of functionality due to fire damage	
	2-NC	DS-0		DS-0		DS-2	buckled latch (failed to lock)		
	2-SC	DS-0		DS-1	frame distortion (failed to lock)	DS-1	frame distortion (failed to lock)		
	2-SR	DS-0		DS-0		DS-0			
3	3-NR	DS-0		DS-0		DS-0		DS-0	
	3-NC	DS-0		DS-1	lock malfunction	DS-2	frame corner gapping, latch failure, door jam	DS-2	door jam
	3-SC	DS-0		DS-1	lock malfunction	DS-2	loose frame, screw withdrawal	DS-2	door jam
	3-SR	DS-0		DS-0		DS-0		DS-0	
4	4-NR	DS-0		DS-0		DS-0		DS-0	
	4-NC	DS-0		DS-1	lock malfunction	DS-2	frame corner gapping, latch failure, door jam	DS-2	
	4-SC	DS-0		DS-0		DS-2	partially detached frame (failed to lock)	DS-3	detached frame
	4-SR	DS-0		DS-0		DS-0		DS-0	
5	5-NR	DS-0		DS-0		DS-0		DS-0	
	5-NC	DS-0		DS-0		DS-1	frame distortion (failed to lock)	DS-3	door jam
	5-SC	DS-0		DS-0		DS-1	frame distortion screw popping (failed to lock)	DS-3	detached frame
	5-SR	DS-0		DS-0		DS-0		DS-0	
6	6-NR	DS-0		DS-0		DS-0		DS-0	
	6-NC	DS-0		DS-1	frame corner gapping	DS-1		loss of functionality due to fire damage	
	6-SC	DS-0		DS-0		DS-2	partially detached frame (failed to lock)		
	6-SR	DS-0		DS-0		DS-0			

Appliances

This section summarizes the seismic performance of the appliances during the pre-fire earthquake tests. It is noted that all the appliances were removed from the building or properly stowed inside of the building prior to the fire tests, and therefore the discussion focuses on their seismic performance in the pre-fire earthquake test sequence. Physical inspections of the appliances were conducted at four different stages: post-EQ3 (following the service level motions), post-EQ5 (following the 50% design level motion), post-EQ6 (following the design level motion), and post-EQ7 (following the maximum considered earthquake motion). It is noted, however, that the post-EQ5 inspection of the appliances at level 6 was not performed due to unavailability of access. Since the wall-mounted television sets at level 1 suffered no damage to the appliance or mount throughout the earthquake tests, this section focuses on the seismic performance of the gas units, water heaters, and seismic gas shutoff valves during the pre-fire earthquake tests.

Table 6.10 summarizes the performance of the range units during the pre-fire earthquake test sequence. Regardless of the presence of restraints, none of the units observed any movement up to and including the 50% design level motion (however the drawer of a gas range unit at level 6 opened). During the design level motion (with a peak floor acceleration of ~0.7 g at the first floor and ~2.0 g at the sixth floor), one restrained unit at level 6 moved slightly due to restraint failure, while all the remaining three restrained units sustained no restraint failure and remained in position. In contrast, all the unrestrained units underwent substantive movement in the form of combined sliding and rotation (the observed displacement offsets reached as much as 8 cm for the units at level 1 and 50 cm for the units at level 6). During the maximum considered earthquake motions, the measured peak floor accelerations were >1.0 g at the first floor and ~3.0 g at the sixth floor. While no failure to the restraints occurred for the units at level 1, both restrained units at level 6 detached from their restraints and displaced (Figure 6.83). The unrestrained units at level 1 and level 6 observed significant movement (the displacement reached as much as 0.7 m for a unit at level 6). Although not observed during the tests, excessive sliding of a gas (or electric) range poses the potential risk of breaking the gas pipes and connections (or electrical cords and connectors) as a result of excessive pulling.

Table 6.10. Physical observations of the range units during the pre-fire earthquake tests.

Level	*Appliance unit*	*Physical observations*			
		Post-EQ3	*Post-EQ5*	*Post-EQ6*	*Post-EQ7*
1	Unrestrained gas range	No movement	No movement	slid ~5 cm, slight rotation (CCW)	slid ~0.6 cm, slight rotation (CCW)"
	Restrained gas range	No movement	No movement	No movement	No movement
	Restrained electric range	No movement	No movement	Restraint held; drawer opened	Restraint held; drawer opened
	Unrestrained electric range	Rotated (~2 cm)	No movement	slid ~8 cm, rotated (CCW)	slid 23 cm, rotated (CCW)
6	Restrained gas range	No movement	n/a	restraint failed, rotated (CCW)	Broke free from restraint and anti-tip over bracket, rotated (CW); top grate bounced off
	Unrestrained gas range	No movement, drawer openned	n/a	Slid 46 cm (8 cm to side)	Slid ~28 cm (~8 cm to side
	Unrestrained electric range	No movement	n/a	Slid 51 cm, rotated (CCW)	Slid ~71 cm, slight rotation (CCW); tether caught
	Restrained electric range	No movement	n/a	Restraint held; door and drawer opened	Broke free from restraint and anti-tip over bracket, rotated (CCW)

Figure 6.83. Performance of range units following MCE test (EQ7): (a) gas range units at level 6, (d) electric range units at level 6.

Table 6.11 summarizes the performance of the water heaters during the pre-fire earthquake test sequence. As discussed previously, the four braced water heaters each utilized a different bracing strategy to attach the unit to the adjacent wall framing (e.g., plumbers tape, off-the-shelf strap, and combined conduit and plumbers tape). During the service level motions, the water heaters observed no or only slight movement (< 2 cm) due to the relatively low floor acceleration demands (< 0.15 g at floor 1 and < 0.5 g at floor 6). As the floor acceleration demands increased significantly during the DE and MCE events, the water heaters performed poorly as a result of larger slenderness ratio and concentrated mass compared to the range units. The observed undesired effects included excessive movement (translation and rotation) (Figure 6.84a), bracing strap and fastener failure, and three instances of tipping over (the unbraced water heaters at level 1 and level 6, and the one at level 6 using off-the-shelf straps (Figure 6.84b)) with the ensuing water or gas leakage from the broken or disconnected pipes. The drywall screw disengaged and broke the plumber’s strap. The tipped-over water heater level 6 even punched into the adjacent gypsum boards and caused a ~0.5 m wide opening on the interior wall. From a fire safety perspective, damage of this kind may be considered as the loss of thermal barrier by directly exposing the CFS framing to fire hazards. In an event of post-earthquake fire, this may increase the risk of flame impingement and severely jeopardize the structural integrity of the light-gauge framing. From a structural perspective, this undesired performance (in spite of good-quality wall installation) necessitates further research to identify robust seismic bracing details for nonstructural components.

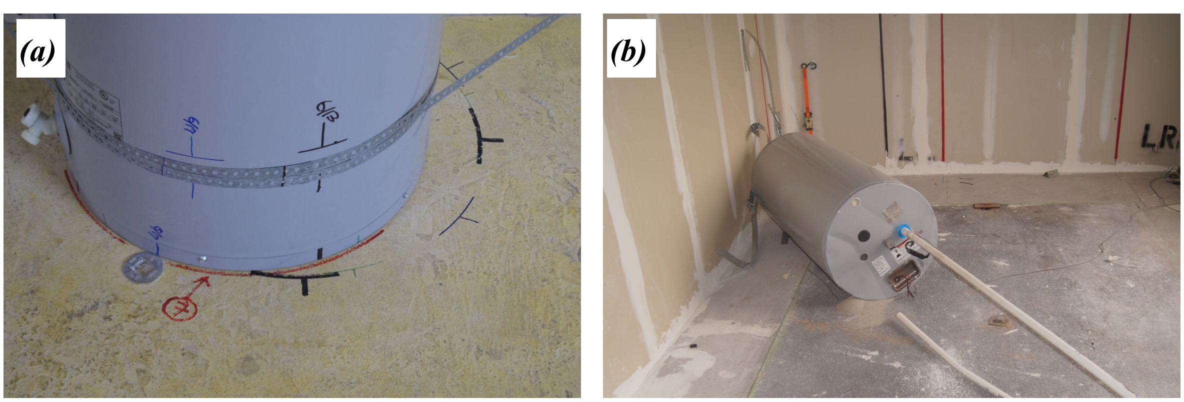

Figure 6.84. Performances of the water heaters: (a) base movement of the strapped water heater at level 1 following the MCE test (EQ7), and (b) toppling of the strapped water heater at level 6 following the DE test (EQ6).

Table 6.11. Physical observations of the water heaters during the pre-fire earthquake tests.

Level	*Restraint condition*	*Physical observations*			
		Post-EQ3	*Post-EQ5*	*Post-EQ6*	*Post-EQ7*
1	Unbraced	Rotated (<1 cm)	n/a	Tipped over*	n/a
	Single-wrap	No movement	n/a	Rotated, restraint held	Moved and rotated, restraint held
	Double-wrap	No movement	n/a	Moved (<1 cm), one strap fastener pullout	Moved and rotated, one strap broke
6	Unbraced	Moved towards mass plate	n/a	Tipper over (landed on mass plate)**	Moved and rotated, strap fastener pullout
	Off-the-shelf Strap	No movement	n/a	Tipped over*, strap broke	n/a
	Conduit and Plumbers tape	Moved (~1 cm northward)	n/a	Rotated	Broke free from restraint, remained standing

* equipment removed from the building following the inspection; ** equipment retrofitted using off-the-shelf bracing strap.

Table 6.12 summarizes the seismic performance of the seismic gas shutoff valves (SGSV) during the pre-fire earthquake test sequence (SGSV makes and models also specified in the table). It is noted that these off-the-shelf motion-activated SGSVs were mounted on the compressed air pipe assembly with visual activation indicators connected to the air tank outside of the test building. The inspection revealed that the shutoff valves performed satisfactorily in response to all the earthquake motions. The shutoff valves at level 1 were not triggered during the service level motions, which is due to the fact that the earthquake excitations were very low during these low-intensity motions (peak input accelerations < 0.1 g).

Table 6.12. Performance of the seismic gas shutoff valves during the pre-fire earthquake tests.

Level	*Unit*	*Performance*			
		Post-EQ3	*Post-EQ5*	*Post-EQ6*	*Post-EQ7*
1	California Valve (Model 300)	**GREEN** (active)	n/a	**RED** (shut off)	**RED** (shut off)
	Little Firefighter (Model AGV-75)	**GREEN** (active)	n/a	**RED** (shut off)	**RED** (shut off)
6	California Valve (Model 300)	**RED** (shut off)	n/a	**RED** (shut off)	**RED** (shut off)
	Little Firefighter (Model AGV-75)	**RED** (shut off)	n/a	**RED** (shut off)	**RED** (shut off)

7 FIRE TEST RESULTS

Following the first seven earthquake tests, live fire tests were conducted on the earthquake-damage building to evaluate the performance of fire protection systems and the impact of seismic damage of the building and the associated characteristics of the fires that ensued. In specific, the building was subjected to six compartment fire tests on three consecutive days, with the first four tests at level 2 and the last two at level 6. Detailed description of the fire test protocol is available in Section 3.3. As a result of different seismic drift demands, the severity of earthquake-induced damage differed significantly at the two levels. Damage to the level 2 gypsum panels occurred in the form of crushed and gapped panel joints as the drift demands exceeded 1% during the pre-fire earthquake tests, while level 6 sustained only minor damage (joint tape cracks and incipient corner crushing) due to much smaller drift demands. In this chapter, the fire compartment temperature responses during all the fire tests are presented first in Section 7.1. Subsequently, the flame and smoke propagation during the fire tests are analyzed in Section 7.2. Lastly, Section 7.3 summarizes the fire-induced physical damage of the structural systems and nonstructural components.

7.1 Temperature Responses

This section presents the temperature-time responses measured by the thermocouples (TCs) throughout all six live compartment fire tests. Temperature data were recorded in key locations that included the joint cracks, border-crushed joints, fire stops, stud cavities, joist cavities, door headers, and door frame gaps. Apart from these locations, temperatures at the center of the burn compartments were also measured using thermocouple (TC) trees with six different measurement locations along the height. The TCs were mounted to the ceiling using flanges and tie rods and insulated by a layer of ceramic blankets (25 mm thick) to provide proper heat protection to the TC trees.

7.1.1 Fire Test 1

Figure 7.1 shows the temperature responses of the southwest (burn) compartment at Level 2. A fully developed post-flashover fire condition was achieved in the compartment. The data indicates that a highly non-uniform temperature distribution over the height of the compartment.

The double peak behavior suggests the influence of wind affecting the compartment fire dynamics. The trends show the existence of a hot upper layer in the compartment. However, the first peak was obtained at a height of 966 mm (38 in.) off the ground shortly after the attainment of flashover, which changed with time. The second peak temperature was recorded at the thermocouples mounted at heights of 457 mm (18 in) and 762 mm (30 in) from the ceiling. The second peak was followed by the decay phase as a result of depletion of fuel in the burner pans.

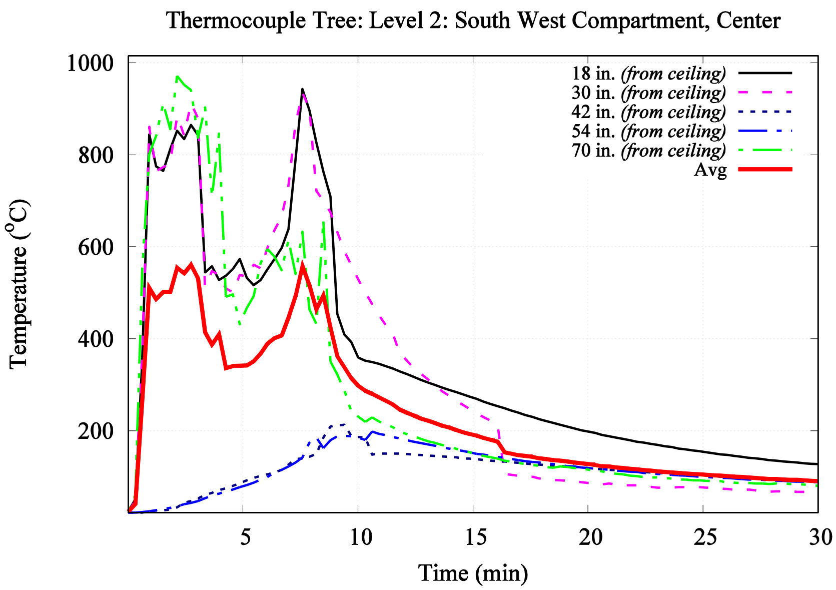

Figure 7.1. Temperatures of the southwest (burn) compartment (Fire Test 1).

Figure 7.2 shows the temperature responses of the exposed surface of the fire stop in the southwest (burn) compartment and on the unexposed side of the fire stop. It is observed from Figure 7.2a that the temperature on the surface of the fire stop track reached over 900 °C, thus confirming the presence of a hot upper layer (between 360 s and 420 s). At the same duration, the temperature recorded on the unexposed face of the fire stop was less than 50 °C. However, the temperature on the unexposed face reached a peak of over 72 °C when the temperature on the exposed side had decreased to about 100 °C. This is due to the conduction of heat through the metal track. In addition, smoke penetration through the fire stop material was observed at 218 seconds from the ignition. The temperature of fire stop on the unexposed face reached less than half the threshold value of 181 °C (325 °F), according to the qualifying T rating prescribed by ASTM E814 (UL 1479). In this regard, the fire stop material performed well in limiting the flames within the burn compartment. However, it should be noted that the burn was limited to 900 seconds.

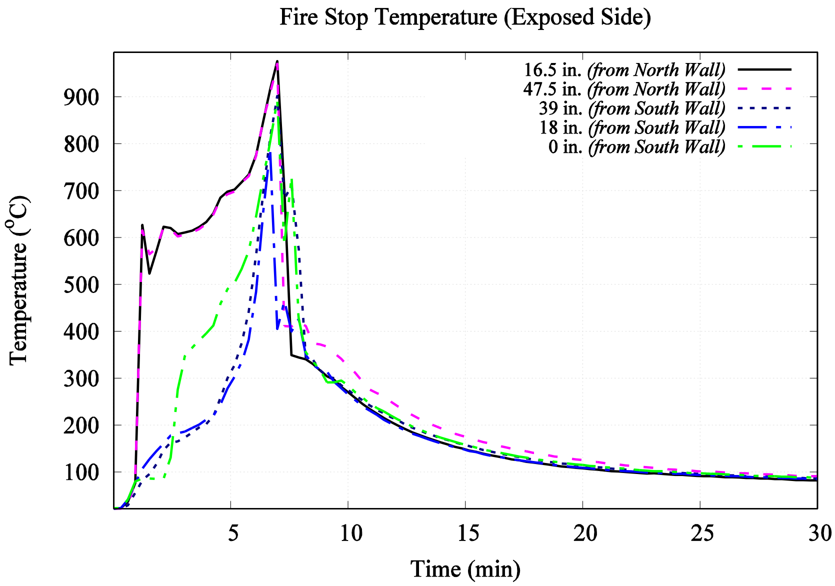

(a)

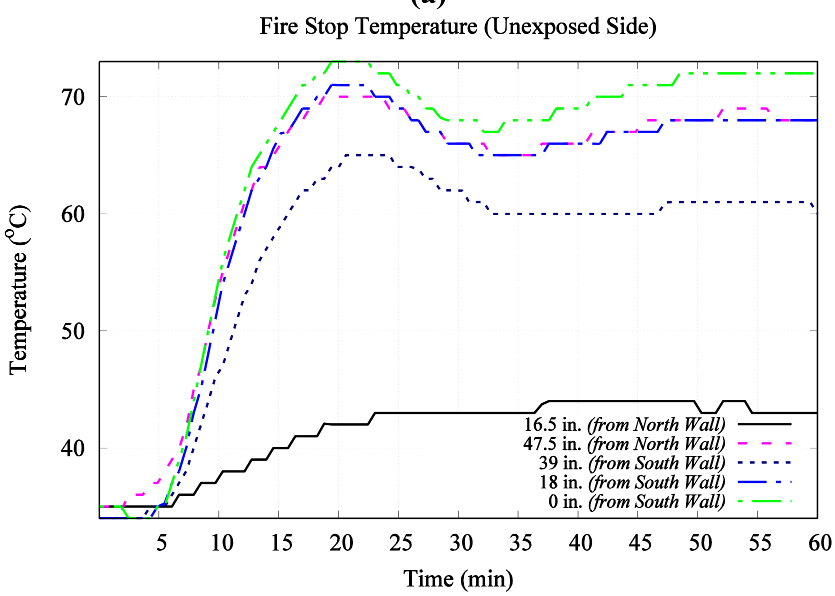

(b)

Figure 7.2. Temperatures of the fire and smoke track, a fire stop material: (a) exposed face (b) unexposed face (Fire Test 1).

Figure 7.3 shows the temperature responses of the stud and joist cavities. As shown in Figure 7.3a, the temperatures of the North wall was characterized by a double-peak behavior and reached a maximum value of over 950 °C (between 360 s and 420 s), which corresponds to the second peak of the upper layer compartment temperature. The peak temperatures of the stud cavities at the mid-height of the South wall were around 900 °C. However, the temperature of the cripple stud cavities below the window sill was as low as 150 °C and slightly over 100 °C at the stud-joist interface. This is attributed to the cooler lower layer and a high concentration of heat and flames extending from the window opening above the sill level. In addition, the temperature of the joist cavities remained consistently below 100 °C (Figure 7.3b), demonstrating a reasonable heat and fire separation zone between the floors. It should be noted that the joist cavity temperatures were measured by the TCs instrumented in the joist cavities from the floor above the burn compartment.

Figure 7.4 shows the temperature responses of the crack locations. The cracks were induced by the previous earthquake tests. Figure 7.4a shows the temperature in the cracks on the North wall of southwest (burn) compartment, whereas Figure 7.4b represents the temperatures measured in the southeast (adjacent) compartment, on the unexposed side of the partition wall, and the cracks on North and South walls that were formed closer to the partition wall. It is observed from Figure 7.4a that the crack temperatures in the mid-height of the compartment were as high as 750 °C. This is consistent with the peak cavity temperatures, which were also recorded at the mid-height of the North wall. However, the temperatures in the cracks on the upper layers remained within 350 and 400 °C. Lower temperatures were reported by the TCs embedded in the cracks near the ceiling. It should be noted that the temperatures were measured at different heights of the same crack that was formed between gypsum boards. However, the crack temperatures in the adjacent compartments did not increase significantly (Figure 7.4b). A peak temperature of around 60 °C was measured in the cracks, which may be attributed to the accumulation of smoke and heat in the southeast compartment.

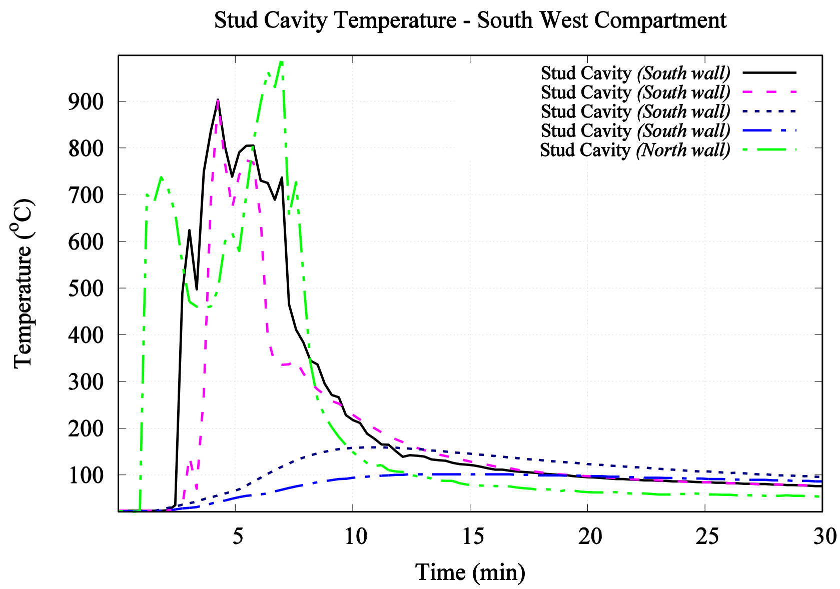

(a)

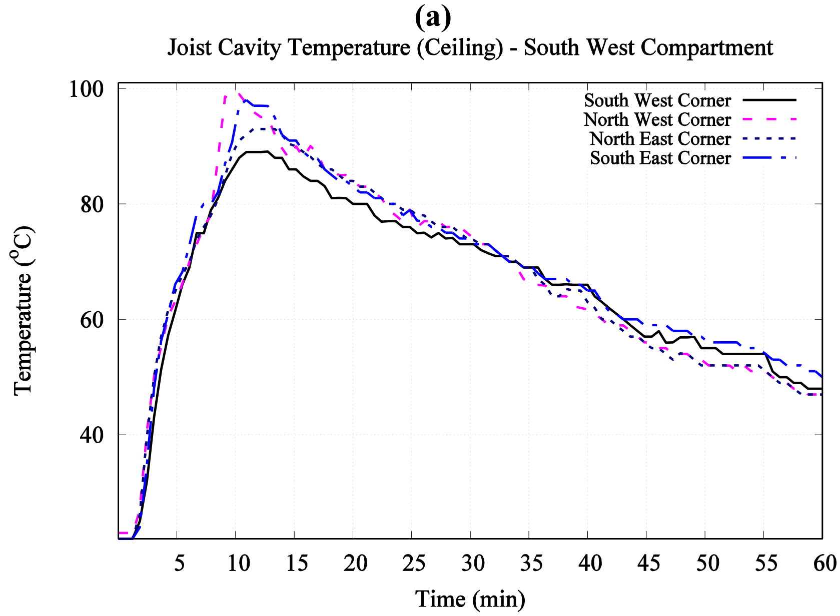

(b)

Figure 7.3. Cavity temperatures in the southwest (burn) compartment: (a) stud cavity, and (b) joist cavity (Fire Test 1).

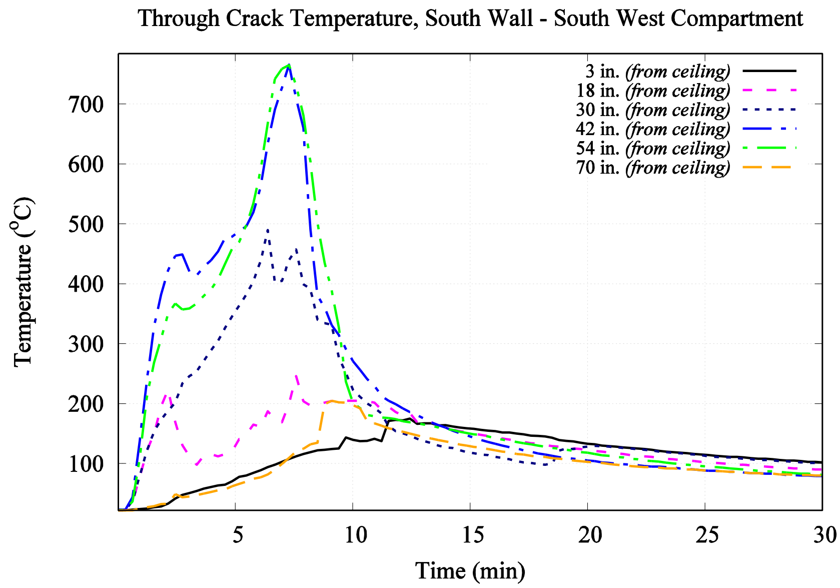

(a)

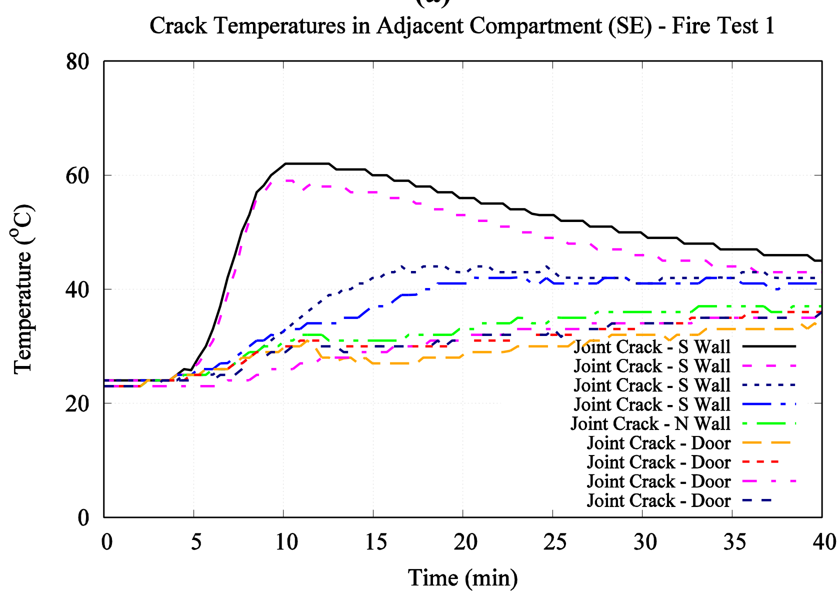

(b)

Figure 7.4. Crack temperatures: (a) southwest (burn) compartment (b) southwest (adjacent) compartment (Fire Test 1).

Figure 7.5 shows the temperature responses of the southeast compartment (adjacent to the southwest burn compartment). Smoke penetration was detected in the southeast compartment during the fire test conducted in the southeast compartment. As shown in Figure 7.5, the temperatures of the southeast compartment underwent only slight increase, which demonstrates no significant heat penetration in the adjacent compartment.

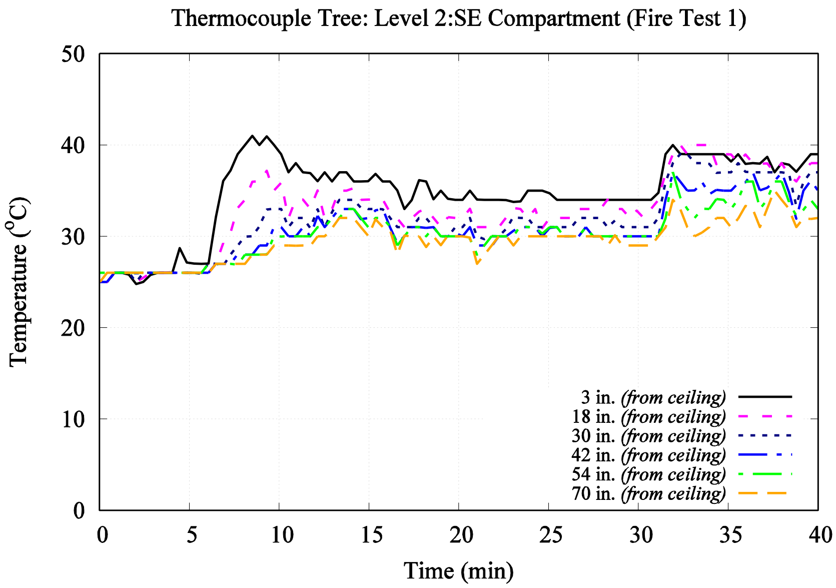

Figure 7.5. Temperatures of the southeast (adjacent) compartment (Fire Test 1).

7.1.2 Fire Test 2

Figure 7.6 shows the temperature responses of the southeast (burn) compartment at Level 2. Non-uniform compartment temperatures were observed with a multi-peak behavior indicating the influence of ventilation and wind flow through the compartment. During this test, the window opening of the burn compartment was partially closed, which resulted in the multi-peak response of temperature. Temperature degradation after the first peak (~50 seconds) was attributed to the incomplete combustion and the untimely termination of fire in the burn compartment. The second peak (~260 seconds) corresponded to a fully developed fire in the compartment. The third significant peak may be attributed to combustion of the doors that increased the compartment temperature before the total burn out. High temperatures were recorded in low- to mid-height of the compartment, which signifies a lower flame height within the compartment as a result of incomplete combustion.

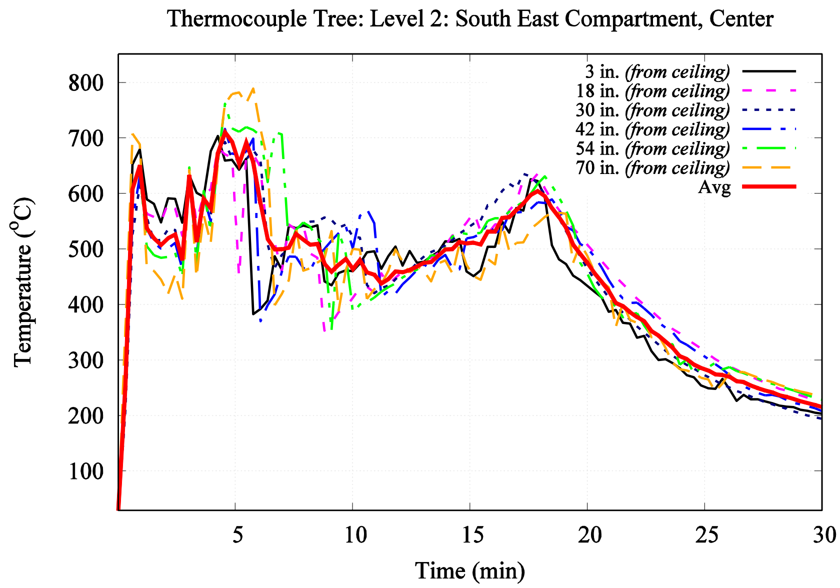

Figure 7.6. Temperatures of the southeast (burn) compartment (Fire Test 2).

Figure 7.7a presents the temperatures in the stud cavities in the southeast (burn) compartment, whereas Figure 7.7b presents the temperatures in the ceiling joist cavities within the floor diaphragm on Floor 3. The temperatures in the cavities of North and South walls show different trends. A peak temperature of ~500 °C was observed on the South wall of the compartment. The temperature in the stud cavities of the South wall did not change during the first 600 seconds from ignition. Thereafter, the temperature escalated for about 300 seconds before it dropped to under 100 °C and remained constant for the cooling cycle. This is attributed to the loss of thermal barrier (16 mm thick gypsum drywall) and heat propagation through the gypsum wallboards. Similar trends were observed on the North and East walls, indicating the failure of the gypsum wallboards. A peak temperature of 300 °C was recorded on the East wall. However, the stud cavities on the window header showed no significant temperature rise. Figure 7.7b indicates that the average joist cavity temperatures reached ~100 °C (similar to Fire Test 1) and a peak temperature of 120 °C in the stud cavity on the northeast corner.

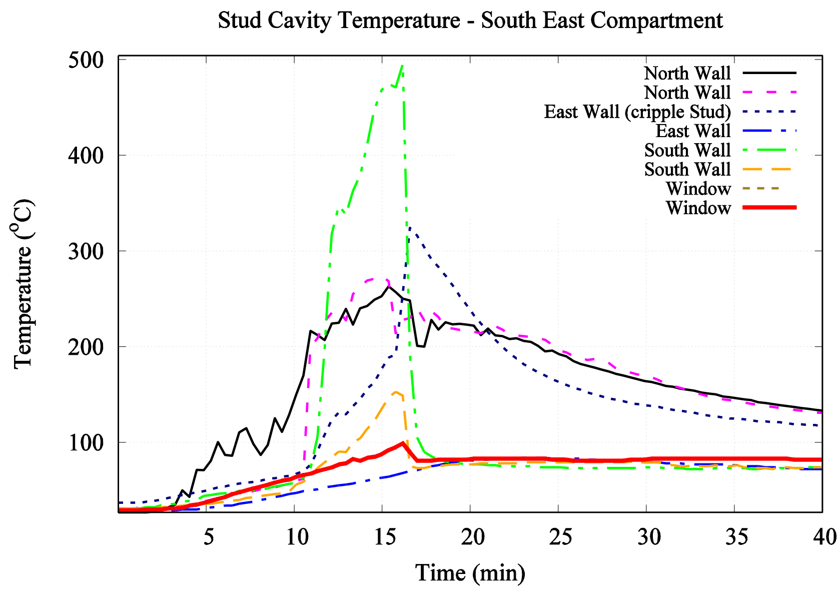

(a)

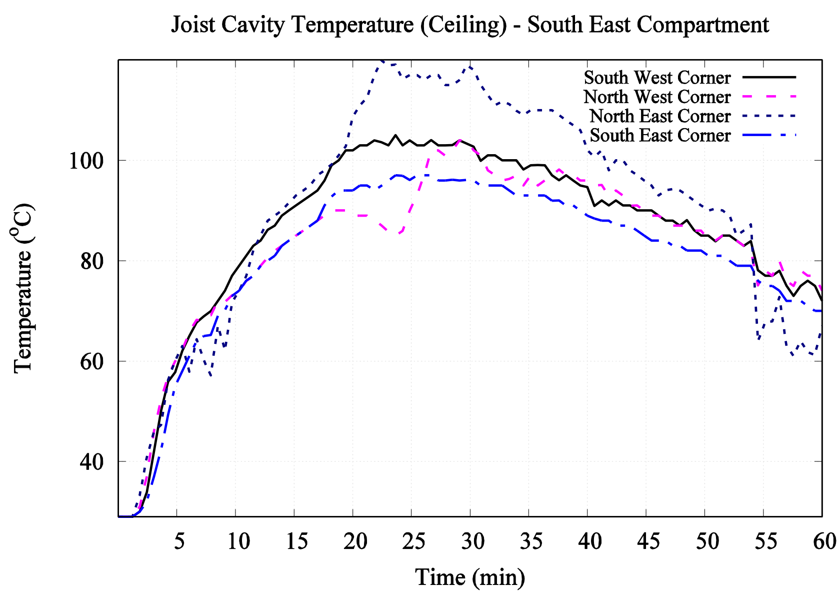

(b)

Figure 7.7.Cavity temperatures in the southeast (burn) compartment: (a) stud cavity, (b) joist cavity (Fire Test 2).

Figure 7.8 shows the temperature responses in the fire and smoke track, which is a fire stop material used for the top track on the partition walls. Similar to Fire Test 1, temperatures were obtained on both the exposed side in the southeast (burn) compartment (Figure 7.8a) and the unexposed side (Figure 7.8b). As shown in Figure 7.8a, the temperatures of the exposed face were highly non-uniform, which may be attributed to the sources that include unequal burning of fuel in the pans, ventilation conditions and compartment size, time to reach fully developed fire and compartment burn dynamics. However, a temperature over 650 °C was observed near the North wall. The temperature near the South wall was almost half of that on the North wall (300 °C). The temperatures at other measurement locations were ~100 °C, which may be due to the radiant heat in the compartment. The temperatures of the unexposed side ranged between 85 °C and 200 °C (Figure 7.8b), which is indicative of significant heat transfer through the fire stop track. It should be noted that the fire stop track of the unexposed side in Fire Test 2 was previously exposed to a fully developed fire in Fire Test 1.

Figure 7.9 shows the temperature responses of a through crack formed due to boundary crushing between the gypsum wallboards in the southeast (burn) compartment. The temperatures were measured by a TC tree mounted on the ceiling and the TC beads inserted into the crack at different heights. Note that TC embedded into the crack 762 mm (30 in.) from the ceiling malfunctioned during the test. The crack temperatures reached peak values at different time instances. The variation of the temperatures measured at different locations demonstrates the existence of a hot upper layer. Temperatures measured 457 mm (18 in.) from the ceiling reached a peak value of over 650 °C as the maximum temperature measured in the through crack. The TC located at 76 mm (3 in.) from the ceiling showed a double peak behavior, which was due to the circulation of cooler air within the compartment ceiling level. The time instance at which the first temperature drop coincided with the time when a cold draft of air was drawn in from the window opening. Since the burn continued for a longer duration with a lower intensity, the duration of the cooling (decay) phase was much longer than other compartment fire tests conducted on the second floor.

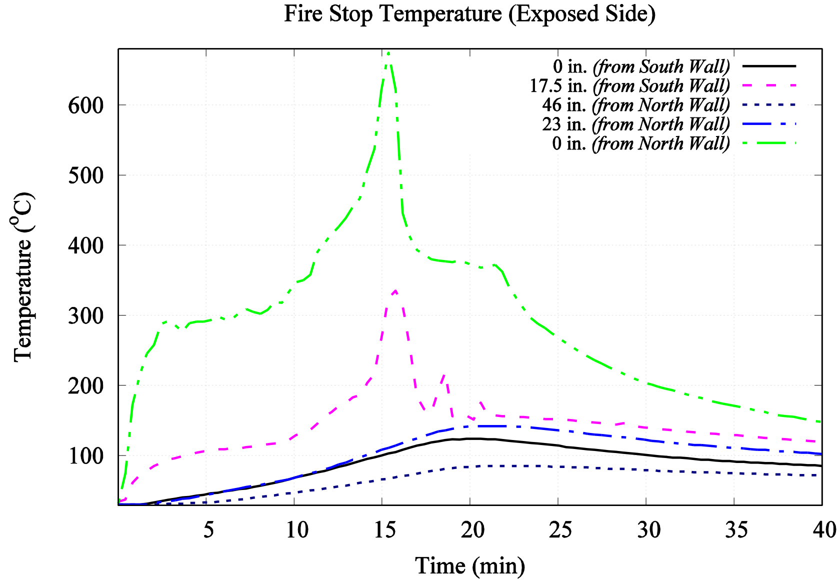

(a)

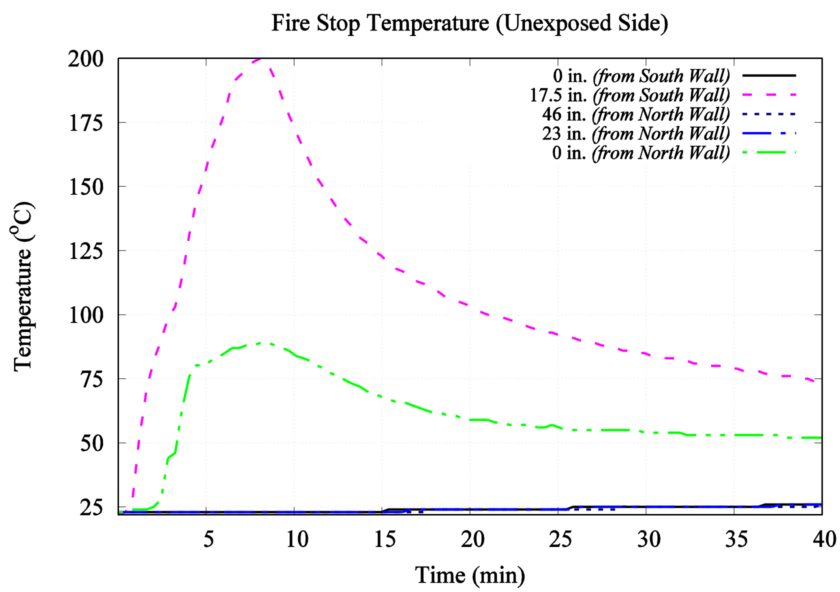

(b)

Figure 7.8.Temperatures of the fire and smoke track, a fire stop material: (a) exposed face (b) unexposed face (Fire Test 2).

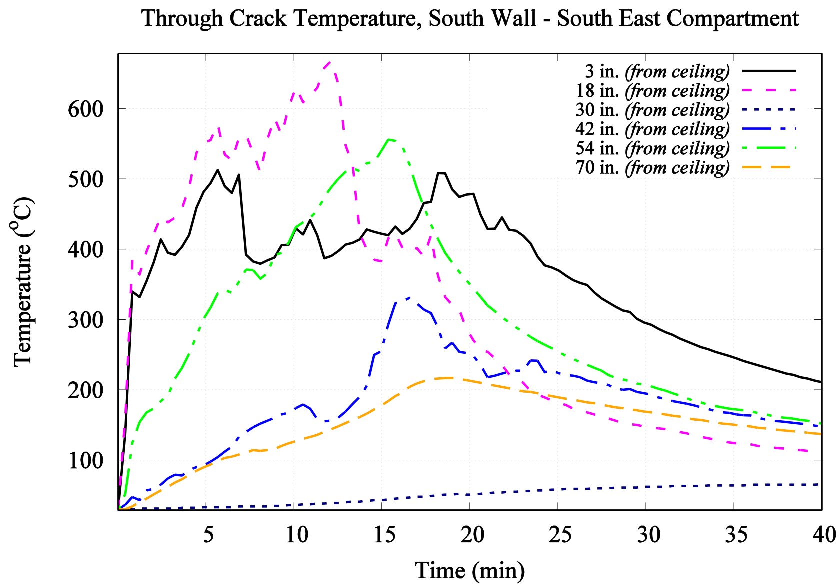

Figure 7.9. Crack temperatures of the southeast (burn) compartment (Fire Test 2).

Figure 7.10 shows the temperature responses of the southwest (adjacent) compartment. The intent of measuring the temperatures within the adjacent compartment was to observe the flow of heat through the burning door (or door frame) on the partition wall, which initiated the flame and smoke spread through the southwest compartment. The temperatures were measured at the different heights from the TC tree mounted at the center of the compartment. The trends show an average increment of 30 °C in the middle third measurement locations. This was further corroborated by the visually observed layer of smoke propagating from the southeast compartment to the southwest compartment before exiting from the window opening of the southwest compartment. The low temperatures in the southwest (adjacent) compartments may provide an environment with low discomfort level and benefit the evacuation and fire-fighting activities.

7.1.3 Fire Test 3

Figure 7.11 shows the temperature responses of the northwest (burn) compartment at Level 2. The temperature at 76 mm (3 in.) from the ceiling was lower than the temperatures at all other measurement locations. The temperature responses involved multiple peaks, indicating a non-uniform distribution of temperature in a fully developed fire at the various heights. In addition, the temperature trends of several locations appeared comparable.

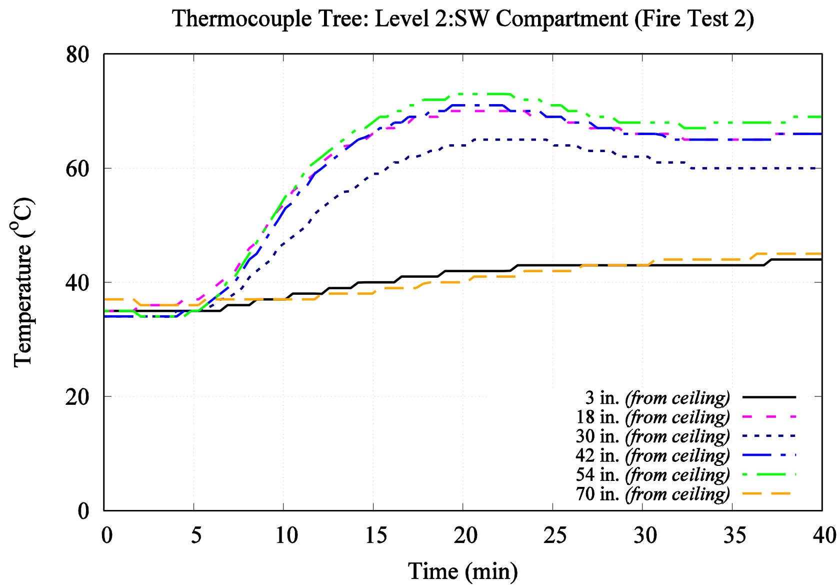

Figure 7.10.Temperatures of the southwest (adjacent) compartment (Fire Test 2).

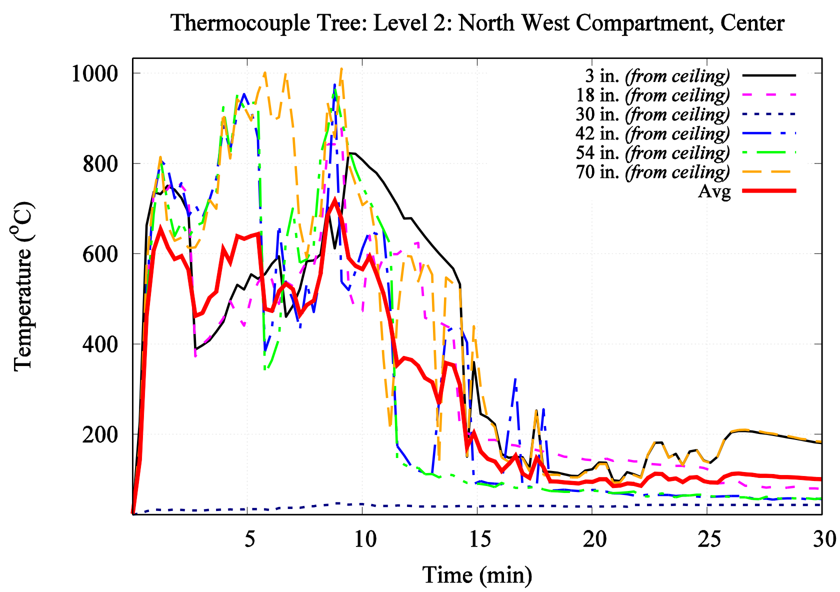

Figure 7.11. Temperatures of the northwest (burn) compartment (Fire Test 3)

Figure 7.12 shows the cavity temperature responses of the stud and joist cavities in the northwest (burn) compartment. Figure 7.12a shows the temperatures of the stud cavities on the North wall. It is observed that the stud cavity closer to the window opening reached temperatures over 400 °C and the adjacent cavity close to 200 °C (note that slight increase of the cripple stud cavity temperature may be due to TC malfunctioning). The trends indicate the loss of thermal barrier in the compartment at 300 seconds following the onset of ignition. Figure 7.12b shows the temperatures of the joist cavities within the floor diaphragm at Floor 3. An average temperature of 93 °C was recorded in the joist cavities, which suggests that the ceiling gypsum wallboards provided adequate thermal barrier to contain the heat penetration.

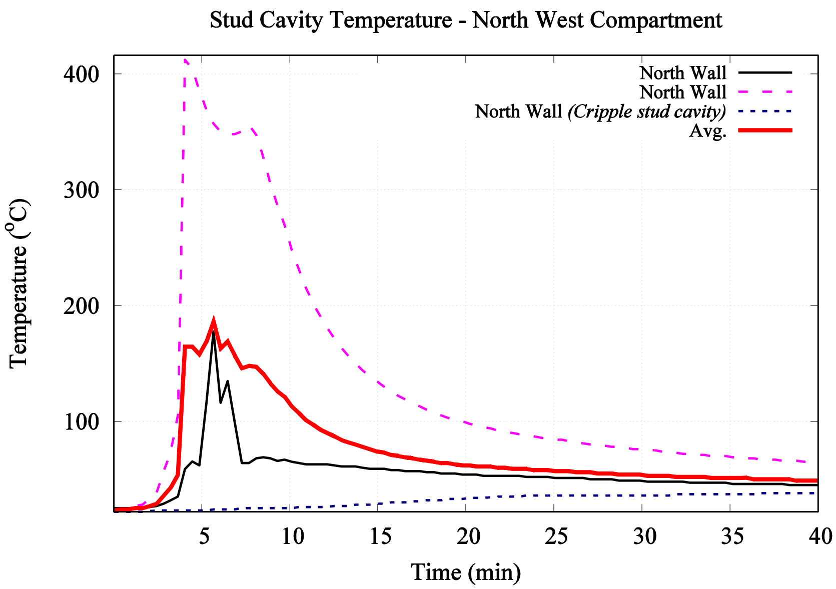

(a)

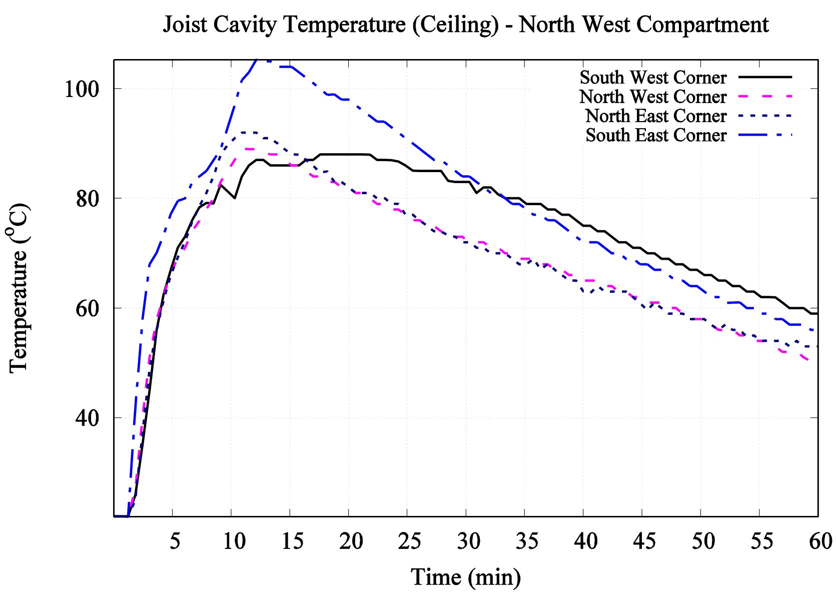

(b)

Figure 7.12. Cavity temperatures in the northwest (burn) compartment: (a) stud cavity, and (b) joist cavity (Fire Test 3).

Figure 7.13 shows the temperature responses of a through crack on the South wall formed due to boundary crushing between the gypsum wallboards in the northwest (burn) compartment. The TC beads were embedded at various depths dependent on the crack widths. The crack temperatures reached as high as 700 °C. The crack temperatures were higher near the ceiling than those at the bottom of the wall. This is consistent with the crack depths based on crude visual observation (accurate measurements of the crack depths were unavailable). It should be noted that the duration of the peak temperatures of the crack were consistent with the peak compartment temperatures.

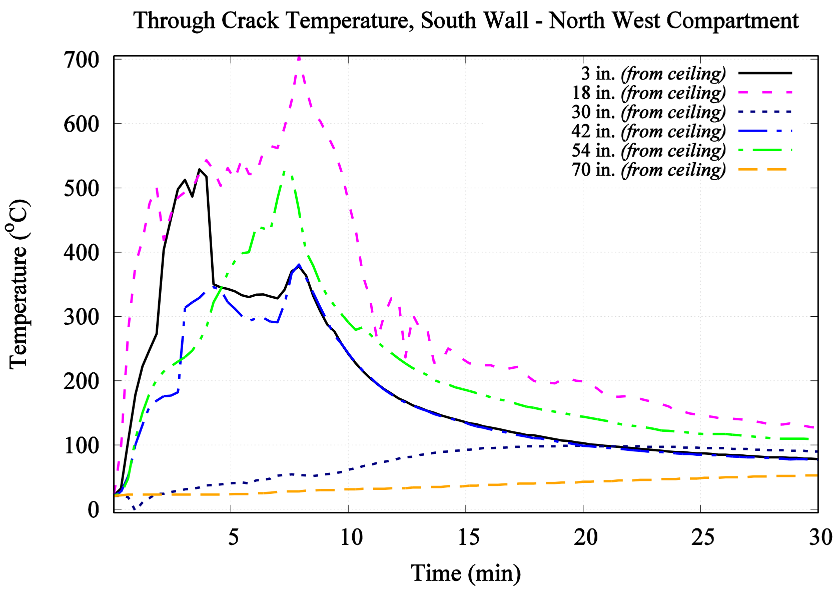

Figure 7.13. Crack temperatures of the northwest (burn) compartment (Fire Test 3).

7.1.4 Fire Test 4

Figure 7.14 shows the temperature responses of the East and West ends of the corridor (burn) compartment at Level 2. The temperatures of the East opening were much higher than those of the West opening, which was governed by the eastward wind direction. Visual observations indicated a large flame and smoke extension from the West opening of the corridor. All the thermocouples reported a similar trend during their growth phase. However, the temperatures at different heights within the compartment showed a non-uniform distribution after the full development of fire. Due to the geometry of the corridor (length much larger than width), the existence of a hot upper layer was not observed. The thermocouples closer to ceiling measured temperatures lower than those closer to the floor. The peak temperatures of the West opening reached over 800 °C, whereas the temperatures of the East opening were only slightly over 500 °C. Uniformly distributed temperatures over the height was observed at the West opening in the growth phase, while the temperature distributions were characterized with marked dissimilarities during the cooling phase.

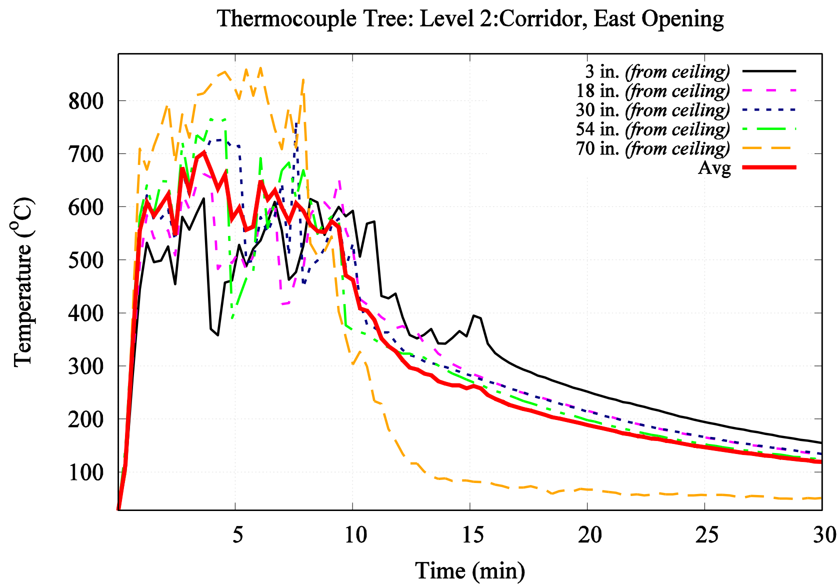

(a)

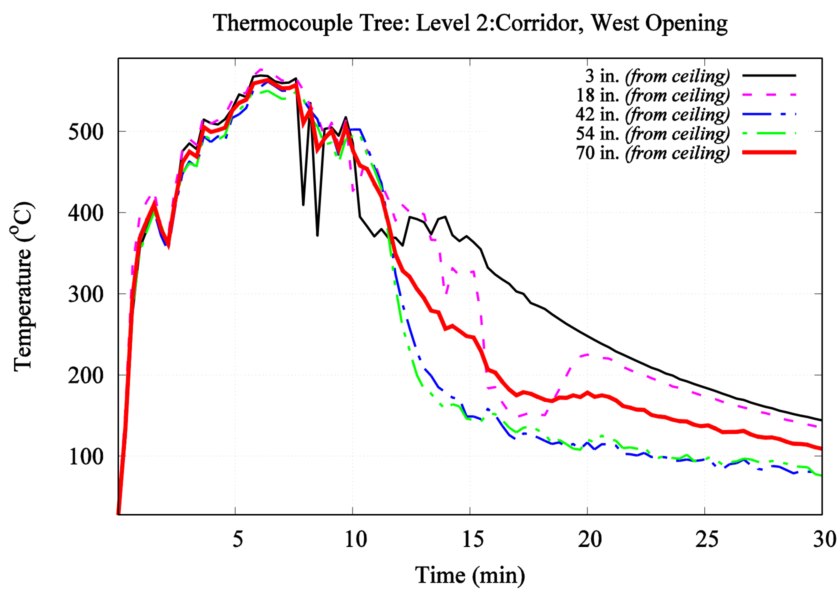

(b)

Figure 7.14. Temperatures of the corridor (burn) compartment: (a) east opening, and (b) west opening (Fire Test 4).

Figure 7.15 shows the temperature responses of the door frame and joist cavities in the corridor (burn) compartment. Since the pre-existing crack found on the corridor wall that would provide access to the stud cavities, the temperatures of stud cavities was not measured. However, the earthquake tests induced severe door frame distortion to the Level 2 corridor doors and created several gaps between the horizontal and vertical jambs. Figure 7.15a shows the temperatures of the cavities in the door jambs on both the North and South walls. The peak temperature attained over 850 °C for the door frame cavity of the North wall but ~450 °C for that of the South wall. This is attributed to the fact that the aluminum door casing on the North wall melted and exposed the TCs to direct flames, whereas the steel door frame on the South wall remained intact with minor deformation. Figure 7.15b shows the temperatures of the joist cavities within the floor diaphragm at Floor 3. Similar to those measured at other joist cavity locations, the temperatures of the joist cavity above the corridor were below 100 °C. This indicates a nominal heat transfer through the ceiling gypsum wallboards.

Figure 7.16 shows the temperature responses of the cracks in the corridor (burn) compartment. Figure 7.16a shows the temperatures measured in the crushed boundary gap on the North wall. It is observed that the peak temperature reached 475 °C at the ceiling height and 230 mm (9 in.) from the ceiling at a nearly identical time instance. The temperature responses were all characterized with multi-peak behavior that affirms the effect of wind on the compartment fire dynamics. Figure 7.16b shows the temperatures along the through crack on the South wall as measured by a TC tree. Similar to those of the North wall, the peak temperatures occurred near the ceiling (76 mm) and a depth of 460 mm from the ceiling. The peak temperatures attained ~ 650 °C.

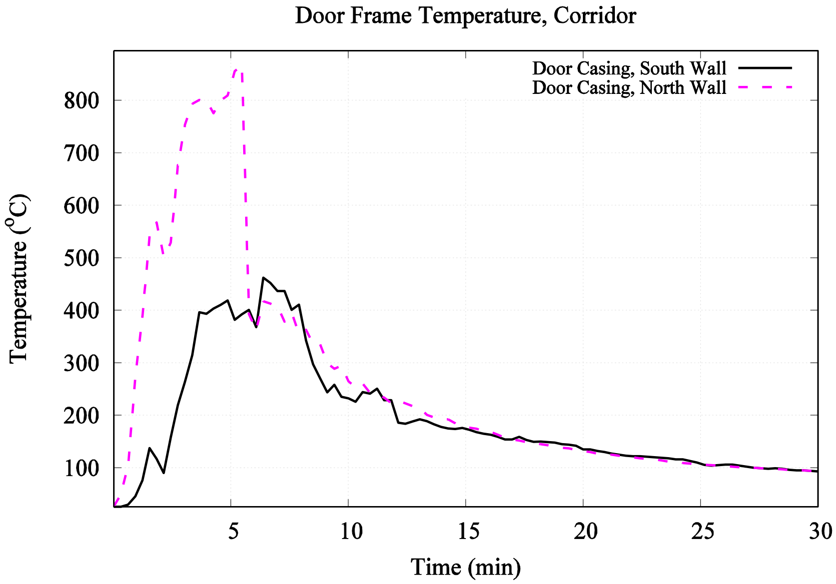

(a)

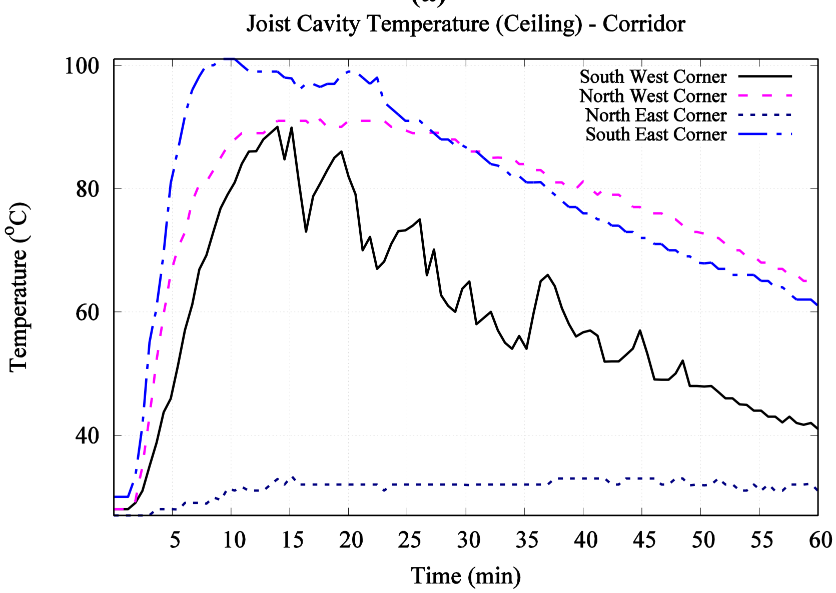

(b)

Figure 7.15. Cavity temperatures in the corridor (burn) compartment: (a) door frame cavity (b) joist cavity (Fire Test 4).

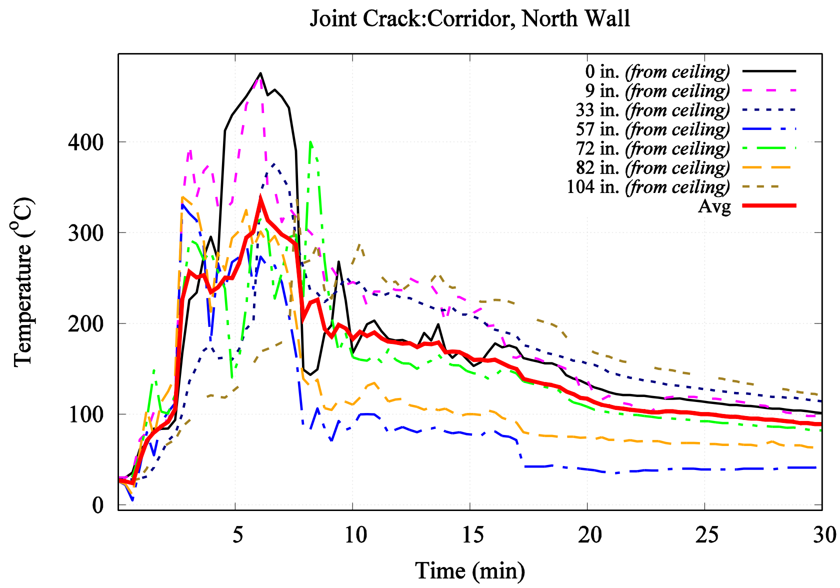

(a)

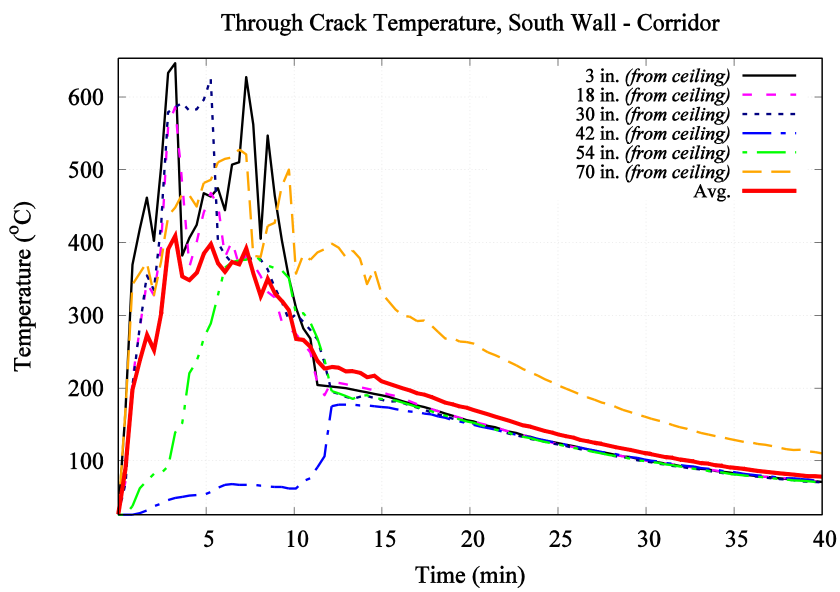

(b)

Figure 7.16. Crack temperatures in the corridor (burn) compartment: (a) joint crack (b) through crack (Fire Test 4).

7.1.5 Fire Test 5

The earthquake-induced damage to Level 6 was minimal damage, since the only observed damage of significance was the distortion of the door frame that resulted in wide gap on the door jamb. In this regard, the burn compartment was instrumented with only a limited amount of TCs to capture the compartment temperature responses, however no TCs were used to measure the temperature responses of the cracks or cavities.

Figure 7.17 shows the temperature responses of the East and West ends of the corridor (burn) compartment at Level 6. The temperatures measured near the West corridor opening were lower than those rest of the compartment since it was the only source of air inlet, which propagated through the narrowly confined corridor space towards the East corridor opening, which served as an exit for flame and smoke. This was consistent with the ambient West-to-East wind direction. Figure 7.17a shows the temperatures of the East corridor opening. A large flame and smoke extension was observed at the East corridor opening within a few seconds from the onset of ignition. The temperatures all contained double-peak behavior, which indicates the heat redistribution within the compartment. The first peak was lower than the second peak. This may be attributed to an enhanced rate of heat release within the corridor due to the burning door and frame. Peak temperatures reach 800 °C – 900 °C, which were significantly higher than the temperatures recorded at the West opening. The highest temperatures were observed at the mid-height of the compartment. Figure 7.17b shows the temperatures of the West corridor opening. The peak temperatures were slightly over 600 °C at the mid-height of the compartment. An abrupt drop of temperature near the ceiling around 300 seconds was attributed to the untimely fuel burn out in the eastward pans (as captured by the internal cameras). The TC located at 1372 mm (54 in.) from the ceiling malfunctioned. Only the bottommost thermocouple (1778 mm) on the TC tree showed a consistent data throughout the burn.

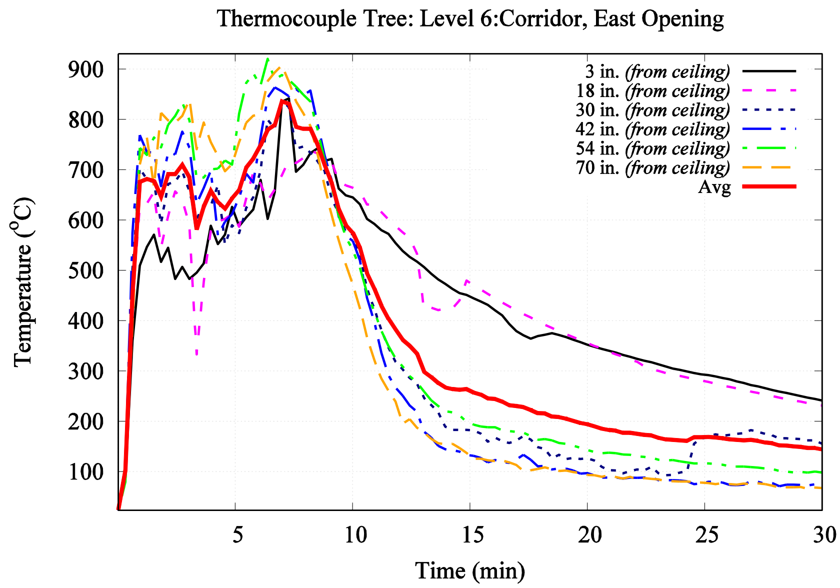

(a)

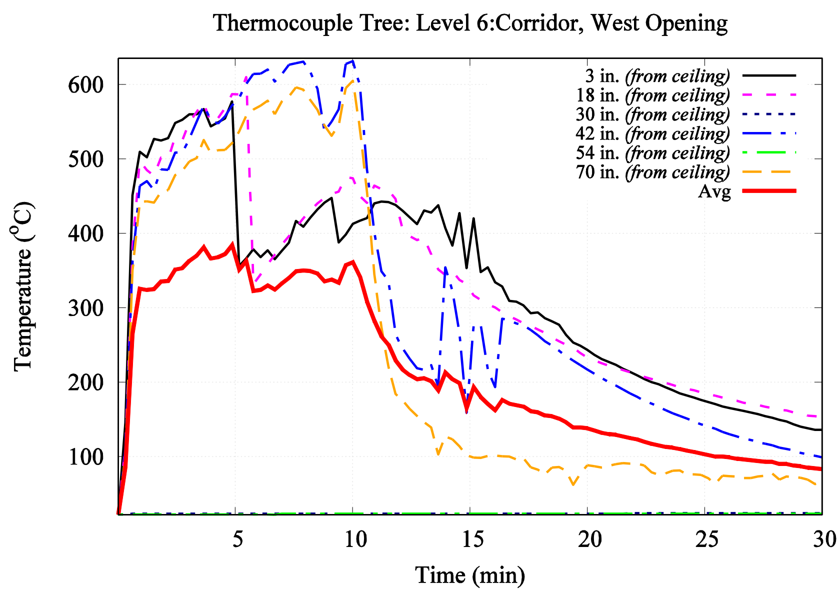

(b)

Figure 7.17. Temperatures of the corridor (burn) compartment: (a) east opening, and (b) west opening (Fire Test 5).

7.1.6 Fire Test 6

Figure 7.18 shows the temperature responses of the southwest (burn) compartment at Level 6. During this test, the post-flashover condition was reached rapidly and the temperatures attained as high as 1000 °C. Similar to those of the corridor fire tests (Fire Test 5), the temperatures in southwest compartment involved a double peak behavior which a higher second peak indicating the combustion of the door triggering a higher rate of heat release. The temperatures at different measurement locations were consistent (except the one at the height of 457 mm (18 in.) due to sensor malfunctioning). Higher wind velocity associated with a higher building height of Level 6 contributed to higher peak temperatures within the burn compartment.

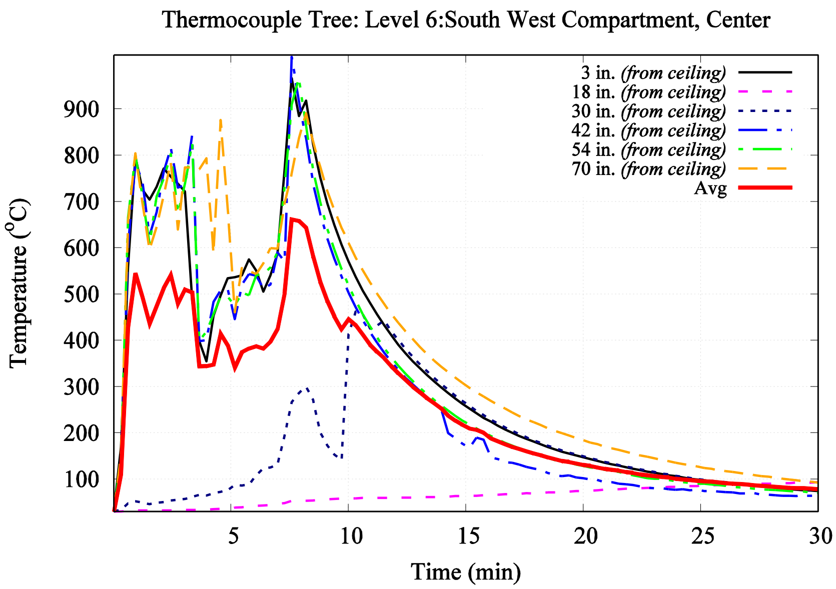

Figure 7.18. Temperatures of the southwest (burn) compartment (Fire Test 6).

7.2 Flame and Smoke Propagation in Fire Tests

In an event of fire, flame and smoke propagation of the building interior is very important as it affects the post-fire activities such as evacuation, fire-fighting and rescue operations. It also defines the capability of the compartments to contain the fire and the likelihood of the fire to travel throughout the burn floor and to other floors of the building. The flame and smoke spread throughout the burn floors of the test building and the exterior was studied using imagery data recorded by a network of internal surveillance cameras and external video cameras that captured the real-time fire tests. A minimum of three internal full HD coax surveillance cameras and one external video camera were used to record the internal flame penetration and smoke spread for each test, except the last test (Fire Test 6). In the absence of adequate internal cameras, hard hat mounted action cameras were used to record the observations. The cameras inside the burn compartments were considered as sacrificial, since they were likely to sustain damage or malfunction due to thermal radiations in the high temperature environments despite the attempt to protect them using insulated covering strategies. All the coax cable wiring for the cameras were run on the floor and were protected from direct flames by a 50 mm (2 in.) thick layer of ceramic blanket. Observations focused on flame penetration, flame propagation, flame extension, smoke penetration, smoke movement and smoke extensions, in addition to the flame spread on the fire-rated doors used in the burn compartments. The approximate flame heights reported herein are determined visually based on the extension of the flames on the exterior face of the building from the window openings and transoms. Table 7.1 summarizes the camera ID and their locations for recording the flame and smoke behavior during the fire tests. Real-time video monitoring was available during all the fire tests.

Table 7.1. Cameras used for recording flame and smoke behavior during the fire tests.

Test #	Camera IDs	Location
1	FT1-VC_01	South West Compartment
	FT1-VC_02	South East Compartment
	FT1-VC_03	Corridor
	FT1-VC_04	North East Compartment
	FT1-VC_G	External - South Elevation
2	FT2-VC_01	South East Compartment
	FT2-VC_02	Corridor
	FT2-VC_03	North East Compartment
	FT2-VC_G	Exterior - South Elevation
3	FT3-VC_01	North West Compartment
	FT3-VC_02	Corridor
	FT3-VC_03	North East Compartment
	FT3-VC_G	External - North Elevation
4	FT4-VC_01	Corridor
	FT4-VC_02	North East Compartment
	FT4-VC_G-1	External - West Elevation
	FT4-VC_G-2	Mobile (GoPro)
5	FT5-VC_01	Corridor
	FT5-VC_02	South East Compartment
	FT5-VC_03	North East Compartment
	FT5-VC_04	South West Compartment
6	FT6-VC_01	South West Compartment
	FT6-VC_02	South East Compartment
	FT6-VC_G	External - South Elevation

Table 7.2 and Table 7.3 summarize the conditions of the door and window openings located on the burn floor during the fire tests. The conditions of the openings influence the flame and smoke spread through the floor. It is noted that of the doors at the burn floor remained open

throughout the fire test except the ones of the burn compartment. All the window openings remained open in all the fire tests except Fire Test 2, during which the window opening was partially closed. In addition, the corridor end openings were partially closed with vertical drops installed to optimize the ventilation conditions of the corridor compartment fire tests.

Table 7.2. Conditions of the door openings on the burn floor for the live fire tests.

Test #	South Partition	Corridor-South	Corridor-North	North Partition
1	Closed	Open	Open	Closed
2	Closed	Closed	Open	Closed
3	Destroyed	Closed	Closed	Closed
4	Destroyed	Destroyed	Closed	Closed
5	Closed	Closed	Closed	Closed
6	Closed	Open	Open	Closed

Table 7.3. Conditions of the window and corridor end openings on the burn floor for the live fire tests.

Fire Test No.	Southwest Compartment	Southeast Compartment	Northwest Compartment	Northeast Compartment	Corridor
1	Part. Closed	Open	Open	Open	Part. Closed
2	Part. Closed	Open	Open	Open	Part. Closed
3	Open	Open	Open	Open	Part. Closed
4	Open	Open	Open	Open	Part. Closed
5	Open	Open	Open	Open	Part. Closed
6	Open	Open	Open	Open	Part. Closed

7.2.1 Fire Test 1

Figure 7.19 shows the camera layout for Fire Test 1. Camera FT1-VC_01 was mounted in the southwest (burn) compartment and it captured the ignition and fire grown before it malfunctioned after the flashover phase. Camera FT1-VC_02 was mounted with the view facing the fire rated wood door to monitor the flame penetration and smoke penetration from the burn compartment into the southeast compartment and to the rest of the floor space. Camera FT1-VC_03, which was floor-located at the west end of the corridor, captured the corridor smoke movement. The camera mounted on the North wall of the northeast compartment monitored the opened corridor doors of the southeast compartment and the smoke movement to the northern half of the floor space. In addition, an external video camera (FT1-VC-G) was used to capture the flame and smoke extension from the exterior window opening on the South façade.

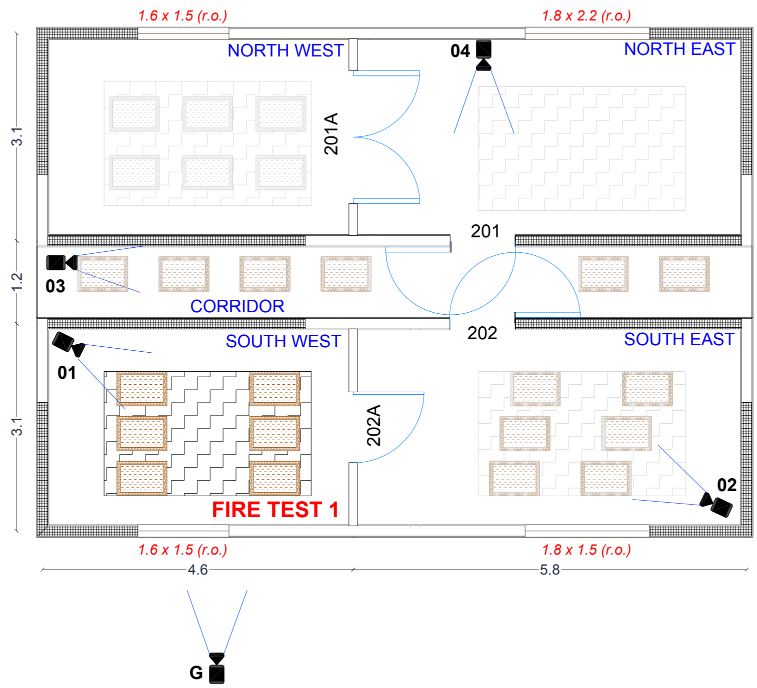

Figure 7.19. Camera layout: Fire Test 1.

The estimated travel distance of flame reached 2.43 m horizontally and 4.27 m vertically. Detailed observations from each camera and their timeline are summarized in Table 7.4. Fully developed fire was observed within 110 seconds from ignition. Smoke intrusion from the southwest (burn) compartment door was recorded by VC_02 within 50 seconds from ignition. An upper layer with a smoke depth of 0.76 m was recorded by VC_02 at 540 seconds after the ignition. No flame penetration was observed from the burn compartment door or the sides of the door frame. This is attributed to the fact that the door was located on the partition wall, which was perpendicular to the direction of earthquake shaking.

Table 7.4. Flame and smoke observations: Fire Test 1.

Observation	***Time (sec)***
Camera 1: FT1-VC_01	
Ignition of all burner pans	4
Internal camera malfunction - signal terminated	87
Camera 2: FT1-VC_02	
Smoke penetration into SE compartment through door frame gaps	50
Smoke penetration into SE compartment through fire stop track	218
Upper layer of SE compartment filled with smoke (depth = 0.762 m)	540
SE compartment filled with smoke - no visibility	585
Camera 3: FT1-VC_03/04	
Smoke movement into corridor via SE compartment	96
Smoke movement into NE compartment via SE compartment and corridor	532
Camera 4: FT1-VC_G	
Smoke extension from SW compartment window	8
Smoke movement to SE compartment through exterior window opening	85
Fully developed fire	110
Smoke plume formation near SE window opening due to wind in W-E direction	108
Smoke extension from SE compartment window	142
Smoke extension to south compartments on Level 1	480

Notes:
* No observed flame extension to SE compartment
* Exposed surface of wood door continued to smolder after total burnout
* Combustibles other than fuel included wood doors, paper tapes, and paper on gypsum wallboards

7.2.2 Fire Test 2

Figure 7.20 shows the camera layout for Fire Test 2. Camera FT2-VC_01 was the sacrificial camera mounted in the southeast compartment to capture the ignition and flame growth. It also captured the untimely burn out in several east burner pans, combustion of the fire rated doors and re-ignition of pans eventually leading to the occurrence of a fully developed fire. Untimely burnout of the fuel may be attributed to an incomplete burn of fuel in the burner pans due to insufficient ventilation conditions, while the re-ignition is attributed to the compartment fire dynamics. Re-radiation from the compartment walls along with sufficient oxygen supply from the partially closed window opening resulted in the re-ignition of pans and hence the fully-developed fire. Camera FT2-VC_02, which was floor-mounted at the west end of the corridor, captured the smoke movement through the corridor as well as the flame penetration from the door on the North wall of the burn compartment. The flame and smoke penetration occurred through the gap at the bottom of the corridor door and the door frame gaps, which were the result of earthquake damage. However, no flame or smoke passed through the joint gaps and cracks were given the short burn duration. The smoke depth on the upper layer of the corridor was estimated as 1.2 m from the ceiling. Camera FT2-VC_03 was mounted with its view facing the fire rated wood door to monitor flame penetration and smoke penetration through the door and frame gapping from the burn compartment into adjacent floor space (corridor and northeast compartment). Combustion of the unexposed surface of the wood door due to flame penetration was well captured by this camera. In addition, an external video camera (FT2-VC-G) was used to capture the flame and smoke extension from the exterior window opening on the South façade.

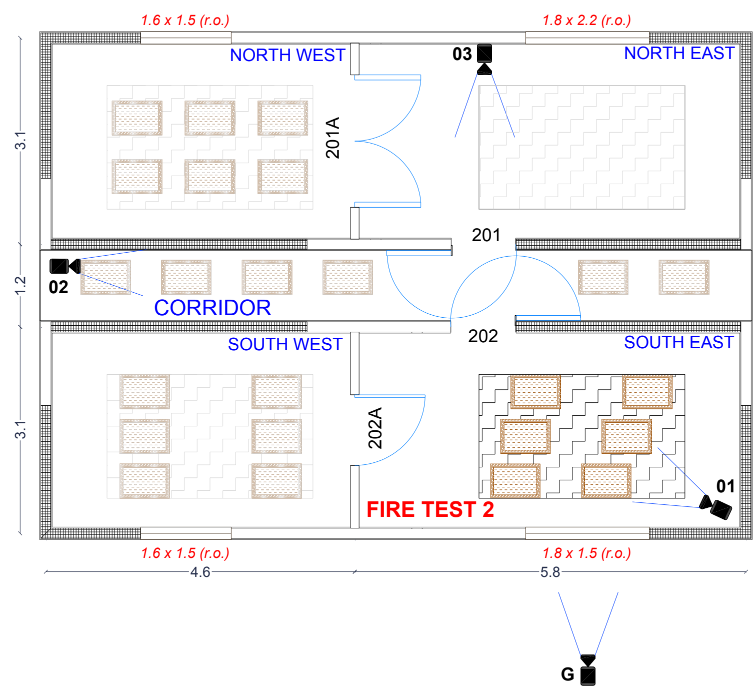

Figure 7.20. Camera layout: Fire Test 2

The estimated travel distance of flame reached 0.76 m horizontally and 3.05 m vertically. Detailed observations from each camera and their timeline are summarized in Table 7.5. Fully developed fire was observed after a delayed duration of 265 seconds from ignition. Smoke intrusion from the southeast (burn) compartment door occurred at 60 seconds from ignition (recorded by FT2-VC_02). Flame penetration was observed from the burn compartment door at 170 seconds from ignition. The exposed surface of the door continued to smolder until quenched using the water jet. The door lost its integrity and partially detached from the door frame.

Table 7.5. Flame and smoke observations: Fire Test 2.

Observation	Time (sec)
Camera 1: FT2-VC_01	
Fire put out in east pans due to incomplete combustion	52
Melting of door fixtures (handle and automatic door closer)	108
Combustion of wood doors *(on North and West wall)*	118
Re-ignition of east pans	172
Complete burn out of wood door on West wall	234
Internal camera malfunction - signal terminated	619
Camera 2: FT2-VC_02	
Smoke intrusion into the corridor through corridor's West opening	41
Smoke penetration into the corridor through door gapping	60
Complete fill-up of the corridor with smoke - No visibility	145
Rapid circulation of smoke through the corridor from W to E due to air draft	150
Flame penetration / spread through door gap at the bottom	170
Combustion of door due to flame leak on unexposed side	452
Flames on the door surface put off by blowing corridor wind	485
Upper layer of corridor filled with dense smoke *(depth from ceiling: 1.2 m)*	758
Large flames observed on unexposed face of corridor door	956
Camera 3: FT2-VC_03	
Smoke intrusion into NE compartment through corridor	131
Charring on unexposed door surface	560
Camera 4: FT2-VC_G	
Ignition of all burner pans	3
Smoke extension from SE compartment window opening	8
Smoke extension from SW compartment window opening	91
Smoke-filled SW compartment	180
Flame extension outside SE compartment window	257
Fully developed fire	265

Notes:

* Window partially covered w/ an opening dimensions: 0.762 m × 1.5 m.
* Vertical flame spread was limited due to W-E wind conditions.
* Flame and smoke extension were sporadic due to smaller size window opening.
* Door on west wall burned out completely since it was exposed to fire in FT1.
* Combustibles other than fuel included wood doors, paper tapes, and paper on gypsum wallboards
* Door gapping and frame distortion were caused by the earthquake motions
* Flame extension through door gap continued sporadically throughout the test
* Door continued to smolder until quenched by water jet

7.2.3 Fire Test 3

Figure 7.21 shows the camera layout for Fire Test 3. Camera FT3-VC_01 was the sacrificial camera mounted in the northwest (burn) compartment to captured the ignition, fire growth, flame penetration and combustion of the double-swing steel door on the exposed side. However, the double door occupied over 50% area of the wall and registered some distortion in earthquake tests unlike the door on the South partition wall in Fire Tests 1 and 2. Camera FT3-VC_02 was floor-mounted on the west end of the corridor to captured the smoke penetration through the closed door on the north corridor wall. Smoke penetration into the corridor was observed at 245 seconds from ignition through the gaps between the door frame and the distorted door. Apart from the door gaps, smoke intrusion was also observed through the west opening on the corridor due to the blowing wind. Camera FT3-VC03 was mounted on the North wall of the northeast compartment with its view facing the fire rated wood corridor door to capture the smoke penetration and flame extension through the distorted metal double door on the unexposed side. The northeast compartment was completely filled with thick smoke, resulting in complete loss of visibility inside the compartment. Combustion of the door frame and top right corners were noticed during the burn. The surface of the metal door continued to burn even after the total burn out of fire inside the compartment, which was later quenched by the water jet. Burning of door fixtures such as door closer was observed on the unexposed side of the fire rated metal doors. Unlike the wood doors, the metal doors remained attached to the door frame. In addition, an external video camera (FT3-VC-G) was used to capture the flame and smoke extension from the exterior window opening on the North façade. It captured extended smoke travel to the upper levels (Level 3 and Level 4) as a result of fast blowing wind as well as the formation of a fire whirl outside the window opening. The estimated travel distance of flame reached 1.83 m horizontally and 4.87 m vertically. Detailed observations from each camera and their timeline are summarized in Table 7.6.

Table 7.6. Flame and smoke bbservations: Fire Test 3.

Observation	Time (sec)
<u>Camera 1: FT3-VC_01</u>	
Ignition of all burner pans	3
Fully blown fire with thick smoke plume	42
Cameras unreliable due to suit and haze covering them	260
Flame penetration between distorted door frame and door gapping	424
Combustion of steel door frame	427
Haze formation on the camera lens - No visibility	512
<u>Camera 2: FT3-VC_02</u>	
Smoke flow into the corridor via NE compartment door (closed)	245
Smoke intrusion from corridor west opening	317
Corridor filled with dense smoke	332
Smoke flow into SE compartment via corridor	337
<u>Camera 3: FT3-VC_03</u>	
Smoke penetration through deformed door gaps and joints	50
Smoke-filled NE compartment - No visibility	180
Flame penetration from door gaps into NE compartment	249
Large flame extension on unexposed surface of metal door	400
Combustion of metal door frame and door closer	425
Dense layer of dark smoke in NE compartment *(layer depth: 0.76 m)*	530
Burning door quenched with the water jet	735
<u>Camera 4: FT3-VC_G</u>	
Smoke extension from NW compartment window opening	10
Smoke propagation into Level 3 and Level 4 NW compartments	33
Flame extension from NW compartment window opening	46
Smoke extension from NE compartment window opening	125
Smoke flow into Level 3 and Level 4 NE compartments	192

Notes:
* Combustibles other than fuel included wood doors, paper tapes and, paper on gypsum wallboards.
* Corridor door on NE compartment shut closed
* Door gapping and frame distortion caused by earthquake motions
* Smoldering of door continued until quenched by water jet
* Fire whirl formed outside the window
* Loss of visibility for FT3-VC_03 for an extend period of time
* Flames on metal door frame and door closer continued until quenched by water jet

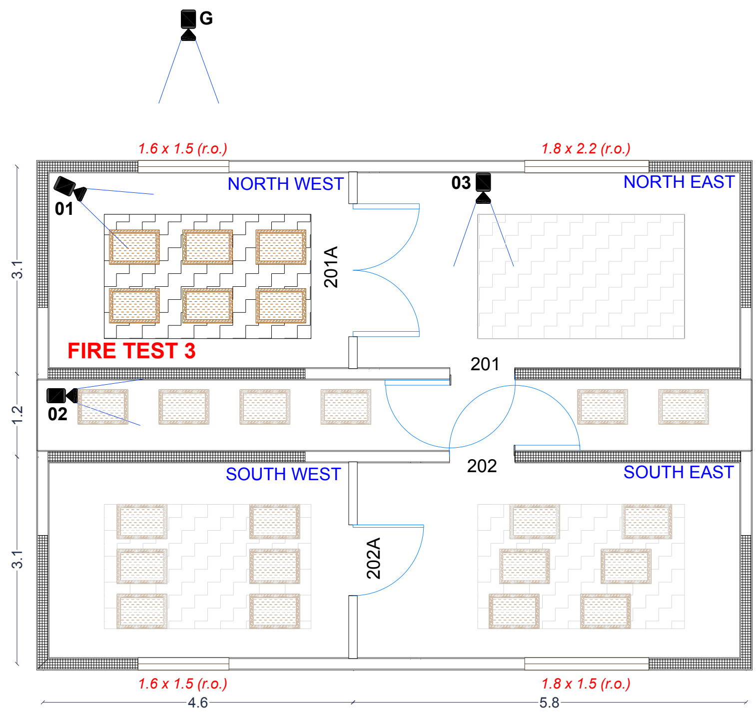

Figure 7.21. Camera layout: Fire Test 3.

7.2.4 Fire Test 4

Figure 7.22 shows the camera layout for Fire Test 4. It is noted that only two internal cameras were used for this test. Camera FT4-VC_01 was the sacrificial camera floor-mounted on the west end of the corridor. It captured the ignition of all burner pans strategically arranged and ignited in a narrowly confined space. It was observed that the corridor geometry created a tunnel effect, thus driving a current of air and heat along the West-to-East wind direction. During this test, fire was put off in two westmost burner pans, which eventually reignited after recreating an oxygen-rich environment. The camera malfunctioned upon the re-ignition of the burner pans continued burning until depletion of the fuel. The south corridor door that lost its integrity during the previous fire test was replaced by a piece of Type-X gypsum wallboard. The rapid burn out of the gypsum cover resulted in the smoke movement into the southern compartments. Camera FT4-VC_02 was mounted on the North wall of the northeast compartment to monitor the flame and smoke penetration through the corridor door frame gaps. In addition to the door frame smoke penetration, smoke leaked through the gap between the corridor walls and the ceiling. Combustion of the wood door on the exposed corridor side triggered the penetration of thick smoke through the earthquake-induced door frame gaps. This was followed by flame extension from the bottom door gap, which caused the combustion of the unexposed face of the door. The exterior cameras, namely, FT4-VC_G1 and FT4-VC_G2, were used to monitor the corridor openings. These cameras captured minimal smoke extension and rapid inlet of air draft at the east corridor opening, which created a post-flashover condition within the corridor. It also captured the smoke extensions from the window openings at all the compartments, indicating the failure of smoke barriers on the two door openings of the compartment. In addition, fire whirl was observed from the east corridor opening with a large horizontal stretch induced by the wind effect. The estimated travel distance of flame reached 2.44 m horizontally and 4.42 m vertically. Detailed observations from each camera and their timeline are summarized in Table 7.7.

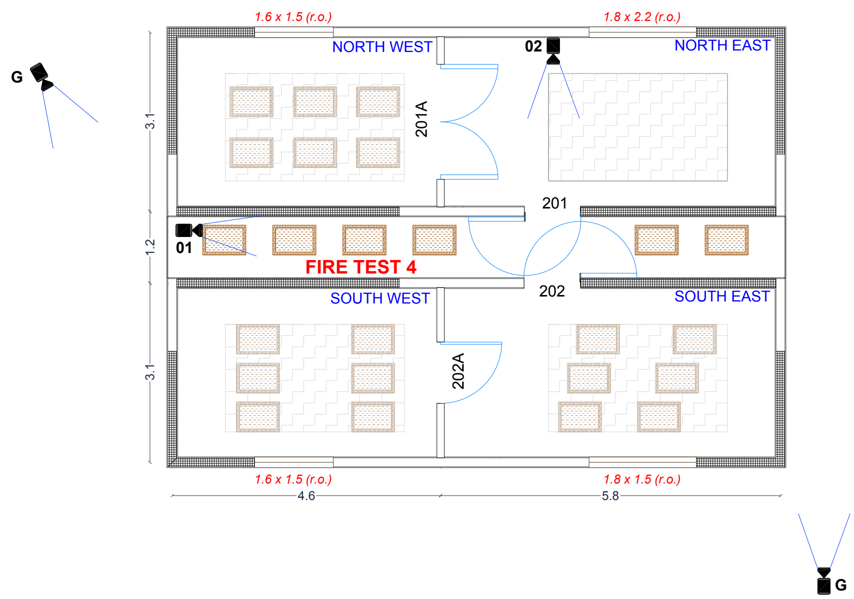

Figure 7.22. Camera layout: Fire Test 4.

Table 7.7. Flame and smoke observations: Fire Test 4.

Observation	Time (sec)
Camera 1: FT4-VC_01	
Ignition of all burner pans	11
Fire put out in west pans due to wind	108
Rapid inlet of air draft from West corridor opening	116
Re-ignition of pans on the east side	124
Internal camera malfunction - Signal terminated	510
Camera 2: FT4-VC_02	
Smoke penetration through gaps between wall and ceiling	33
Smoldering of wood door releasing dense smoke plume	40
Dense smoke from door frame gaps	59
Flame penetration through the gap between door and floor	74
Smoke filled NE compartment - No visibility	104
Flame extension through door frame gap	262
Camera 3: FT4-VC_G-1	
Smoke extension from West corridor opening	94
Smoke extension from NE and NW compartment window openings	189
Smoke penetration from corridor transom	237
Camera 4: FT4-VC_G-2	
Smoke extension from East corridor opening	28
Flame extension from the East corridor opening	40
Dense plume of black smoke through West corridor opening	222
Smoke spread through openings of all compartments (NE, NW, SE, SW)	328

Notes:
* Combustibles other than fuel included wood doors, paper tapes and, paper on gypsum wallboards.
* Fire whirl formation noticed outside the window
* Combustion of door on the unexposed side not observed
* Both the corridor doors failed and smoke and flame extension was observed in all the compartments

7.2.5 Fire Test 5

Figure 7.23 shows the camera layout for Fire Test 5. Camera FT5-VC_01 was the sacrificial camera floor-mounted at the west end of the corridor. It captured the ignition of all burner pans strategically arranged and ignited in a narrowly confined space as well as the smoke development in the corridor. A dense layer of smoke with a depth of 1.2 m from ceiling was observed. However, the camera failed to capture further information due to low visibility and lack of proximity from the corridor doors before the malfunctioning. Camera FT5-VC_02 was mounted on the East wall of the southeast compartment to monitor the door on the North wall of the compartment. It captured covered a large amount of fire-induced behavior in Fire Test 5. Smoke penetrated from the distorted door frame and the sides of the glazed portion in the southeast compartment within 64 seconds from ignition. This resulted in the upper layer smoke accumulation in the compartment. Thermal bowing was observed on the metal door, which resulted in snapping of the door closer, thus breaking it open. This resulted in excessive flame and smoke intrusion into the compartment. Furthermore, the glazed portion of the door cracked and completely ruptured, resulting in excessive flow of heat and smoke into the compartment. Camera FT5-VC_03 was mounted on the North wall of northeast compartment to capture the flame and smoke extension on the glazed metal door on the North wall of the corridor. It is noted that all the doors at Level 6 were 20-minute fire rating doors. Smoke penetrated through the glazed portion of the door and filled up the northeast compartment. Melting of door fixtures and charring of the door around the glazing were also captured in Camera FT5-VC_03. Camera FT5-VC_04 was located in the southwest compartment with the door closed throughout the test. Due to a series of events that triggered a high temperature environment in the southeast compartment, smoke and heat flow were repeatedly observed in the adjacent southwest compartment. The fact was evident from the burning paper on the gypsum board around the door frame. The estimated travel distance of flame reached 1.52 m horizontally and 3.65 m vertically. Detailed camera observations and their timeline are summarized in Table 7.8.

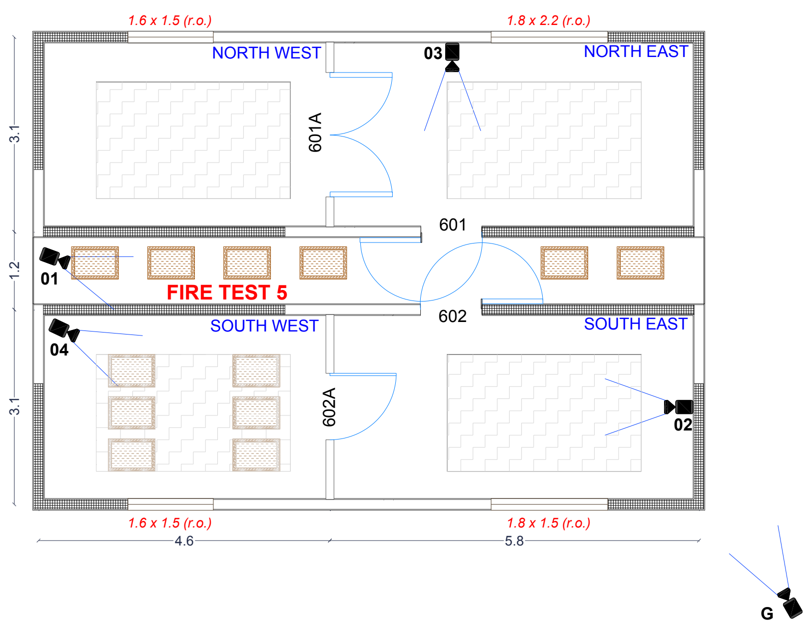

Figure 7.23. Camera layout: Fire Test 5.

Table 7.8. Flame and Smoke Observations: Fire Test 5.

Observation	Time (sec)
<u>Camera 1: FT5-VC_01</u>	
Dense upper layer of smoke accumulation in corridor *(layer depth: 1.22 m)*	60
Internal camera malfunction - Signal terminated	595
<u>Camera 2: FT5-VC_02</u>	
Smoke penetration from top and side door gaps	64
Dense upper layer of smoke accumulation in SE compartment	132
Flame extension into SE compartment from the metal door frame gaps	194
Thermal bowing of metal door and loss of door lock resulting in the rupture of door	211
Sudden flame and smoke intrusion from burning corridor into SE compartment	220
Combustion of unexposed face of metal door due to door rupture and fire growth	252
SE compartment completely filled with smoke and radiation	300
Cracking and rupture of the glazed portion of metal door on south corridor wall	467
Camera malfunctioning due to excessive radiation	498
<u>Camera 3: FT5-VC_03</u>	
Ignition of all burner pans	10
Smoke propagation into all NE and SE compartments	51
Smoke penetration from the door frame gaps	128
Smoke-filled NE compartment - No visibility	360
Melting of automatic door closer	540
Charring of the unexposed side of the door, especially around the glazing	600
<u>Camera 4: FT5-VC_04</u>	
Smoke penetration through distorted door frame and door gaps	237
Smoke intrusion from SW compartment window opening	254
Heat penetration through door frame gaps resulting in burning of gypsum board paper around the door frame	313

Notes:

** Combustibles (other than fuel) in the compartment limited to wood doors, paper tapes, and paper on gypsum wallboards.*

** Smoke penetration from the gap around the glazing on the door.*

** Flame penetration from ruptured door continued till complete burnout.*

** Door on partition wall to SW compartment remained closed throughout the test*

7.2.6 Fire Test 6

Figure 7.24 shows the camera layout for Fire Test 6. It is noted that only two internal cameras were used during this test. Camera FT6-VC_01 was mounted in the southwest (burn) compartment to capture the fire ignition and growth. The ignition of all burner pans up to the fully developed fire stage occurred at 38 seconds from ignition. Camera FT6-VC_02 was mounted on the East wall of the southeast compartment to monitor the flame and smoke penetration from the burn compartment into the southeast compartment and the rest of the floor. Smoke penetration due to burning metal door occurred within 44 seconds of ignition, just after the fully developed fire. Smoke flow through the window opening of the burn compartment flowed back into the southeast compartment from its window opening due to the wind. Smoke penetration was observed from the distorted door frame and the broken door handle. The estimated smoke depth in the southeast compartment was ~0.61 m from the ceiling. Smoke intensity increased in the compartment, which increased the thermal radiation. Flame penetration through the burning door was also observed, which resulted in charring of the door header. The exterior camera FT6-VC_03 captured the exterior flame and smoke extension on the South façade of the building. It captured a wind-induced fire whirl and a thick smoke plume outside the window. The estimated travel distance of flame reached 1.83 m horizontally and 3.65 m vertically. Detailed camera observations and their timeline are summarized in Table 7.9.

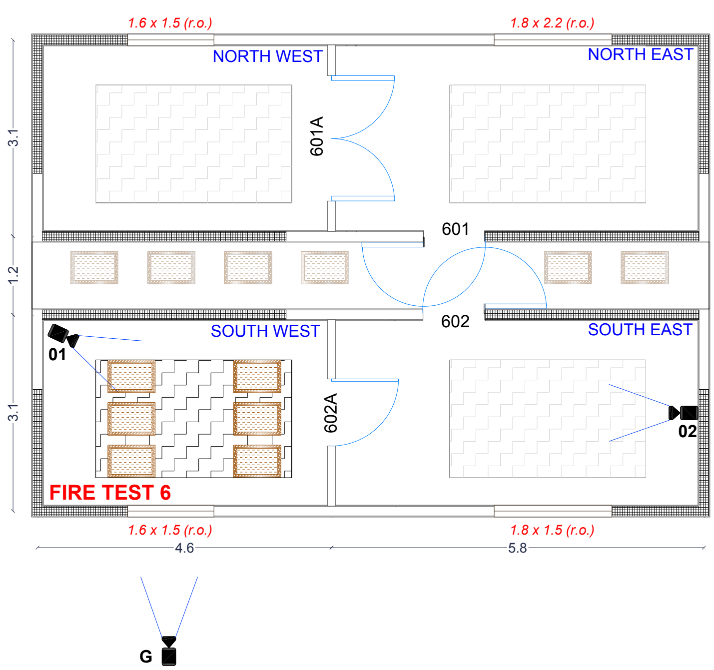

Figure 7.24. Camera layout: Fire Test 6.

Table 7.9. Flame and Smoke Observations: Fire Test 6.

Observation	Time (sec)
<u>Camera 1: FT6-VC_01</u>	
Ignition of all burner pans	6
Fully developed fire	38
Internal camera malfunctioning - signal terminated	104
<u>Camera 2: FT6-VC_02</u>	
Smoke penetration through metal door gap	44
Smoke intrusion from window opening of SE compartment	60
Smoldering of metal door and smoke penetration through door gaps	78
Smoke penetration though broken door handle	82
Dense upper layer of smoke accumulation in SE compartment *(depth: 0.61 m)*	127
Smoke-filled SE compartment - No visibility	159
Flame penetration though door head gap	355
Combustion of door framing *(head)*	528
Charring of door header	840
<u>Camera 3: FT6-VC_G</u>	
Smoke extension from SW compartment window opening	8
Flame extension from SW compartment window opening	51
Smoke plume formation outside SW compartment window opening	95
Smoke extension from SE compartment window opening	194

Notes:

* Combustibles other than fuel included wood doors, paper tapes, and paper on gypsum wallboards.

* Smoke penetration / leakage observed through roof

* Fire whirl formed outside the window

7.3 Fire-induced Physical Damage

7.3.1 Fire Test 1

Figure 7.25 shows the fire-induced damage to the southwest (burn) compartment at Level 2 as observed following the fire test. Figure 7.25a shows the view of the compartment floor with the empty burners and retention pans. The figure also shows the gypsum wall debris and ceiling on the floor. It is observed that the TC tree remained intact and the insulation protection was adequate. Figure 7.25b shows the partially detached gypsum from the ceiling joists, which indicates the loss of its integrity and failure of fasteners. Figure 7.25c shows the exposed side of the door with a completely charred layer. The door closer was damaged by fire and the automatic operation of the door was disrupted. Figure 7.25d shows the melted door handle on the exposed side after the fire test.

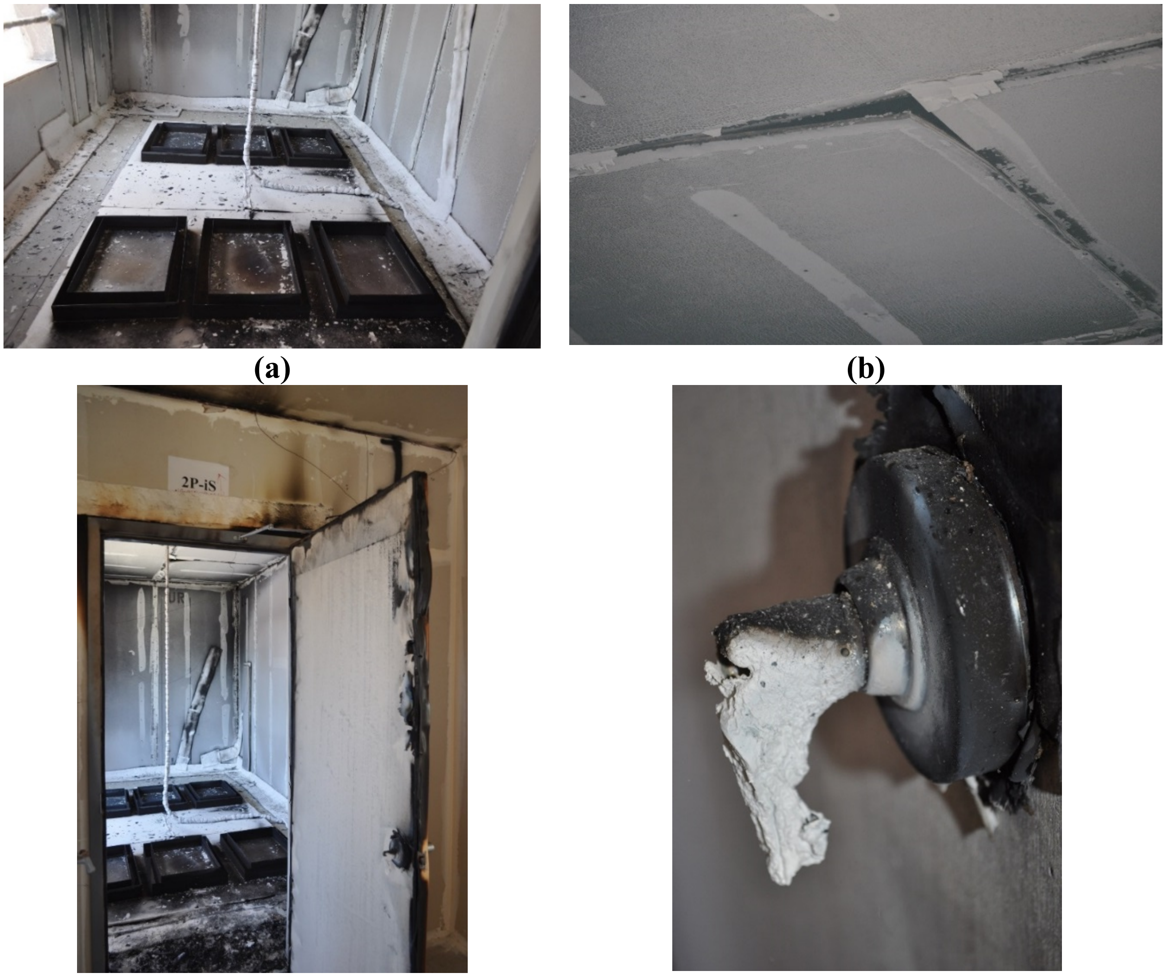

(a) (b)

(c) (d)

Figure 7.25. Damage to the burn compartment following Fire Test 1: (a) overall view of the damaged compartment, (b) ceiling damage, (c) exposed side of the fire rated door, and (d) melted door lock.

7.3.2 Fire Test 2

Figure 7.26 shows the fire-induced damage to the southeast (burn) compartment at Level 2. Figure 7.26a shows partially detached ceiling gypsum board with the detached fasteners (drywall screws). This was an effect of ceiling jet impingement on the soffit. Figure 7.26b shows the status of wood door on the partition wall. The door burned through completely in fire, however did not collapse. The door disintegrated when tried to open. Figure 7.26c shows the underside of the steel sheathed cement boards, which was used as the material for floor decking in the burn compartment. Sagging of the steel sheet was observed on the floor decking between the two floor joists. This is an indication of complete loss of rigidity of the floor decking, which was further affirmed by numerous cracks and a wobbly floor shown in Figure 7.26d.

(a) **(b)** **(c)** **(d)**

Figure 7.26. Damage to the burn compartment following Fire Test 2: (a) detached ceiling gypsum board, (b) disintegrated wood door following 2-side fire burns, (c) thermal bowing of floor sheathing board (underside), and (d) cracks on the fiber cement floor boards (upperside).

7.3.3 Fire Test 3

Figure 7.27 shows the fire-induced damage to the northwest (burn) compartment at Level 2. Figure 7.27a shows the post-test view of the burn compartment. Wide gaps were formed between the wall, ceiling, and floor gypsum boards as the paper tapes burned and the joint compound cracked and fell as debris all over the floor. As shown in Figure 7.27b, the gypsum boards developed numerous distinctive surface cracks. This is attributed to the dehydration of inherent moisture and chemically bonded water from gypsum. Figure 7.27c shows the buckling of the peripheral metal flat on the metal doors, and consequently resulted in the lose of operability due to door jam. Figure 7.27d shows the exposed surface of the metal door of the burn compartment.

(a) **(b)**

(c) **(d)**

Figure 7.27. Damage to the northwest (burn) compartment following Fire Test 3: (a) overall view of the burn compartment, (b) gypsum surface crack, (c) buckled door frame metal, and (d) overall view of the metal door.

7.3.4 Fire Test 4

Figure 7.28 shows the fire-induced damage to the corridor (burn) compartment at Level 2. Figure 7.28a shows the overall view of the east end of the corridor. It is observed that wall and ceiling gypsum boards cracked through the corridor and lost their integrity. Due to the concentration of flames on the east side of the corridor, more severe damage was observed on the walls to the east of the corridor doors. Figure 7.28b shows the surface cracks on the of the gypsum wall boards. Inside of the corridor, wider through cracks were formed along with the surface cracks, which were concentrated around the locations of the fasteners (drywall screws). Figure 7.28c shows the overall (westward) view of the corridor. It should be noted that the south corridor door opening was covered by a layer of 16 mm thick gypsum board. Charring of the edge of the north corridor door was observed. The misalignment of the north corridor door indicates that the door disconnected from the door frame. The aluminum door frame casing on the fire exposed side melted when exposed to fire. Figure 7.28d shows the close-up view of the charred door edge.

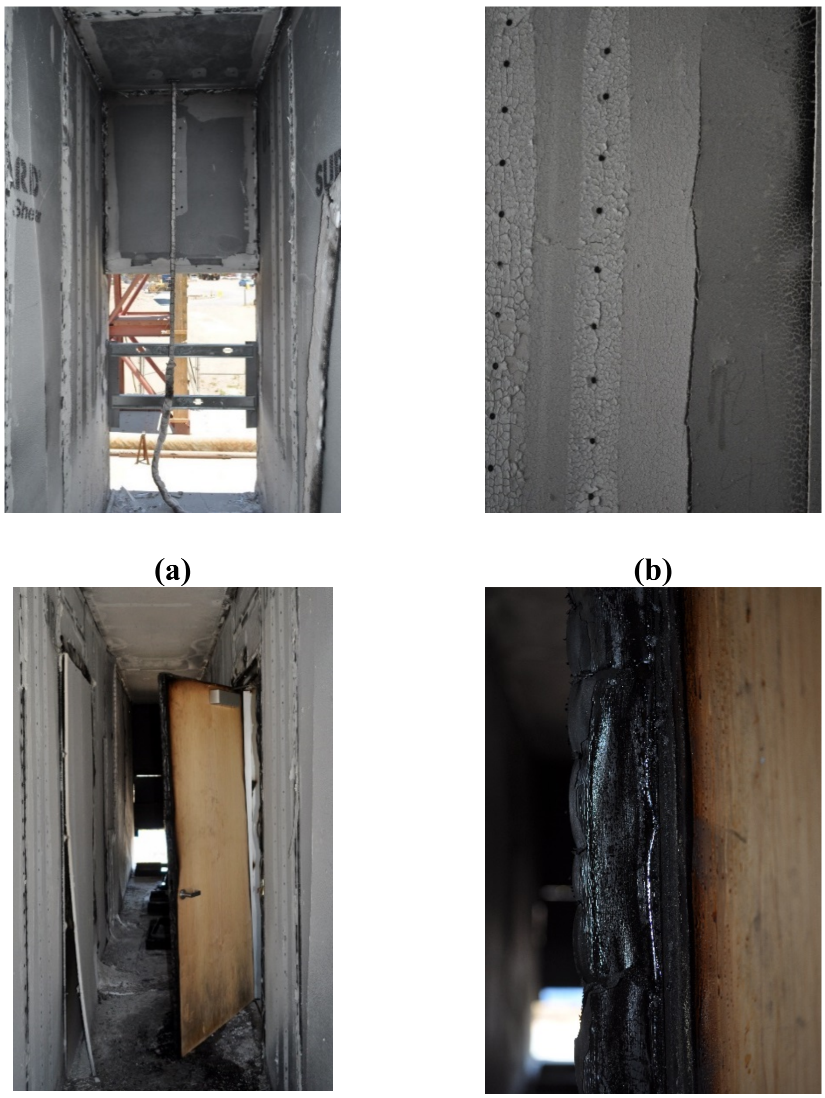

(a) (b)

(c) (d)

Figure 7.28. Damage to the burn compartment following Fire Test 4: (a) east end of the corridor, (b) gypsum board cracks, (c) north corridor door damage (facing west), (d) charring of corridor door.

7.3.5 Fire Test 5

Figure 7.29 shows the fire-induced damage to the corridor (burn) compartment at Level 6. Figure 7.29a shows the unexposed side of the south corridor door. The 20-minute fire rated door was glazed with a piece fire-proof glass on the top half. The door lost its functionality as the push bar was damaged by fire. The burn marks around the door frame at the top corners indicate the flame penetration from the earthquake-induced door gapping. The char around the glazing frame was consistent with the damage locations of the door frame. The figure also shows a melted door closer caused by the flame impingement through the door gaps. Figure 7.29b shows the rupture of the south corridor door. Rupture of the door was a result of thermal expansion of the metal door due to high temperature on the exposed side resulting in failure of the door latch. This damage mode was well captured by an internal camera mounted on the East wall of the southeast compartment. This was followed by a sudden inflow of smoke from the burning corridor. Figure 7.29c shows the flame extension from the ruptured door gap into the southeast compartment. As shown in Figure 7.29, the door glazing also ruptured during the tests, which is evident by the flame extension through the top of the door.

7.3.6 Fire Test 6

Damage photos for Fire Test 6 were not available. See the flame and smoke spread section for other details.

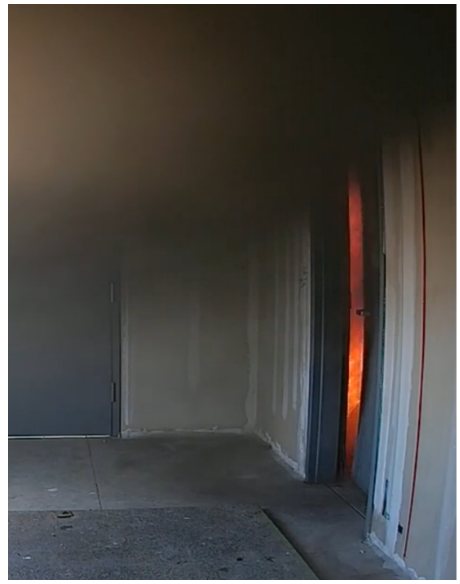

(a) (b)

(c) (d)

Figure 7.29. Damage to the burn compartment following Fire Test 5: (a) damage to the south corridor door (unexposed side), (b) rupture of the south corridor door, (c) flame penetration from the ruptured door frame gap, and (d) rupture of glazing of the south corridor door.

8 POST-FIRE EARTHQAUKE TEST RESULTS

This chapter presents the seismic response and observed physical damage of the test building during the post-fire earthquake test sequence, including a service-level aftershock event (EQ8:RIO-25) and a near-fault extreme event (EQ9:RRS-150). In this chapter, the global building responses (e.g., floor accelerations, interstory drifts, residual displacements, and etc.) are presented first as well as the local shear wall responses (e.g., tension rod forces, wall end vertical displacements). In particular, these responses are compared with those measured during the pre-fire earthquake tests to characterize the effect of prior earthquake-fire damage on the behavior of the test building. Lastly, the chapter provides a detailed summary of the physical damage of the test building at its final damage state.

8.1 Global Building Response

The global response presented in this section includes: (1) floor absolute accelerations, (2) floor relative displacements (with respect to the table platen), (3) interstory drift ratios (IDR), and (4) roof drift ratios (RDRs). While double integration method remains applicable for determining the floor displacement and IDR responses for test EQ8, it becomes ineffective for test EQ9 due to the presence of large residual displacements (as discussed previously in Chapter 6). In this regard, the floor displacements and IDRs for test EQ9 are determined using direct displacement measurements (see detailed discussions later in this section) instead of those from double integration. However, the base (story) shear forces of the test building during the post-fire earthquake tests are not presented due to the large uncertainty related to the calculation of floor inertial forces.

EQ8:RIO-25

The floor absolute acceleration, floor relative displacement, and IDR time histories during EQ8:RIO-25 are presented in Figure 8.1 through Figure 8.3. The procedures used for processing the building response in EQ8 remain identical to those used for the pre-fire earthquake tests. Each row of the figure contains three plots that correspond to the responses in the three directions (longitudinal, transverse, and torsional) associated with the centroid of a specific floor or level. It is noted that the units of the torsional responses (rad/sec^2 or rad) differ from that of the horizontal accelerations (g, cm, or %). The annotated text in each plot denotes the floor number and orientation of the time history response (e.g., *2-T* indicates the response at floor 2 in the transverse direction). The color circles represent the time instances when the maximum (red) and minimum (green) responses were achieved, with the purpose to facilitate correlating the measured responses of different floors or levels.

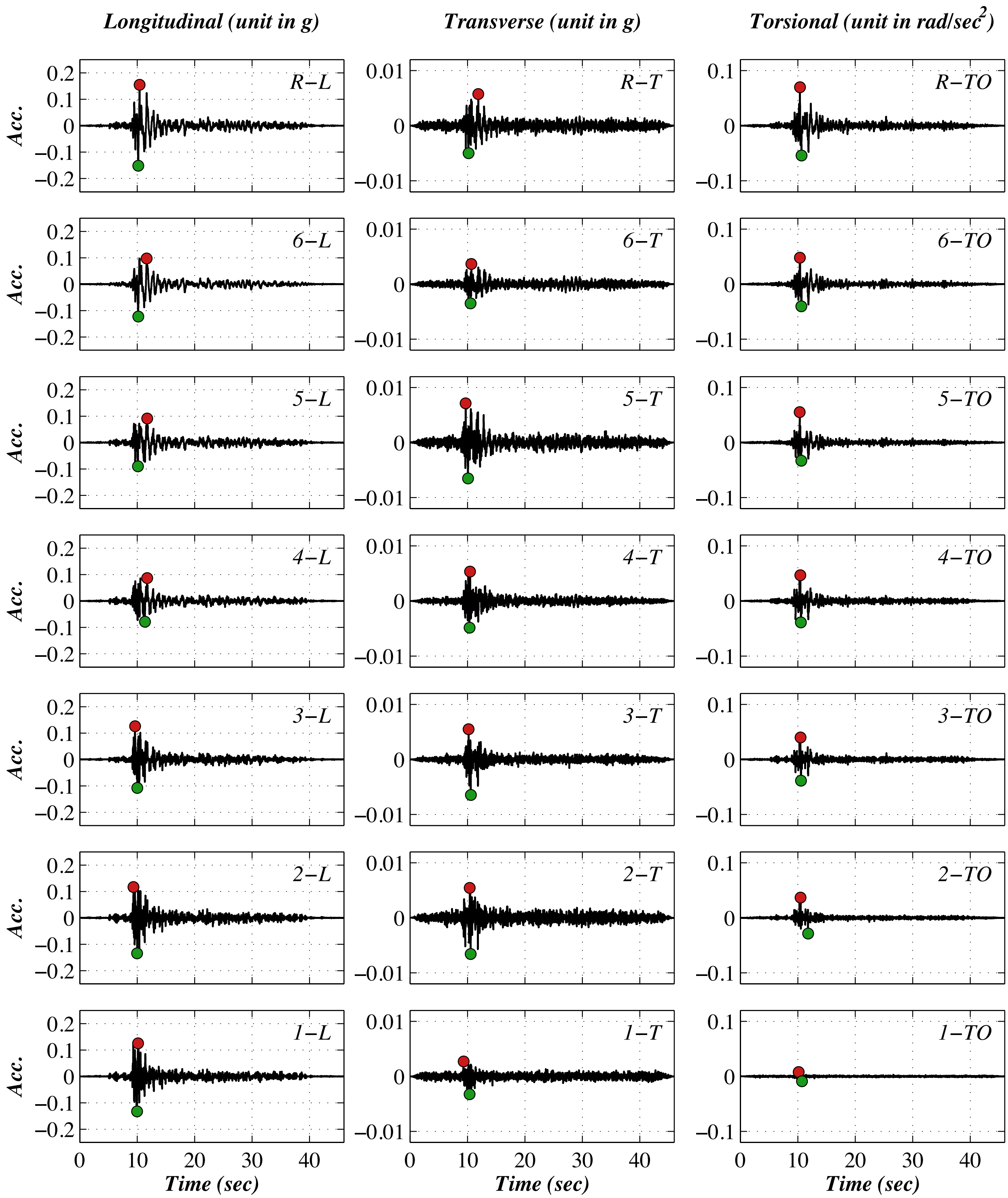

Figure 8.1. Measured floor absolute accelerations – EQ8:RIO-25.

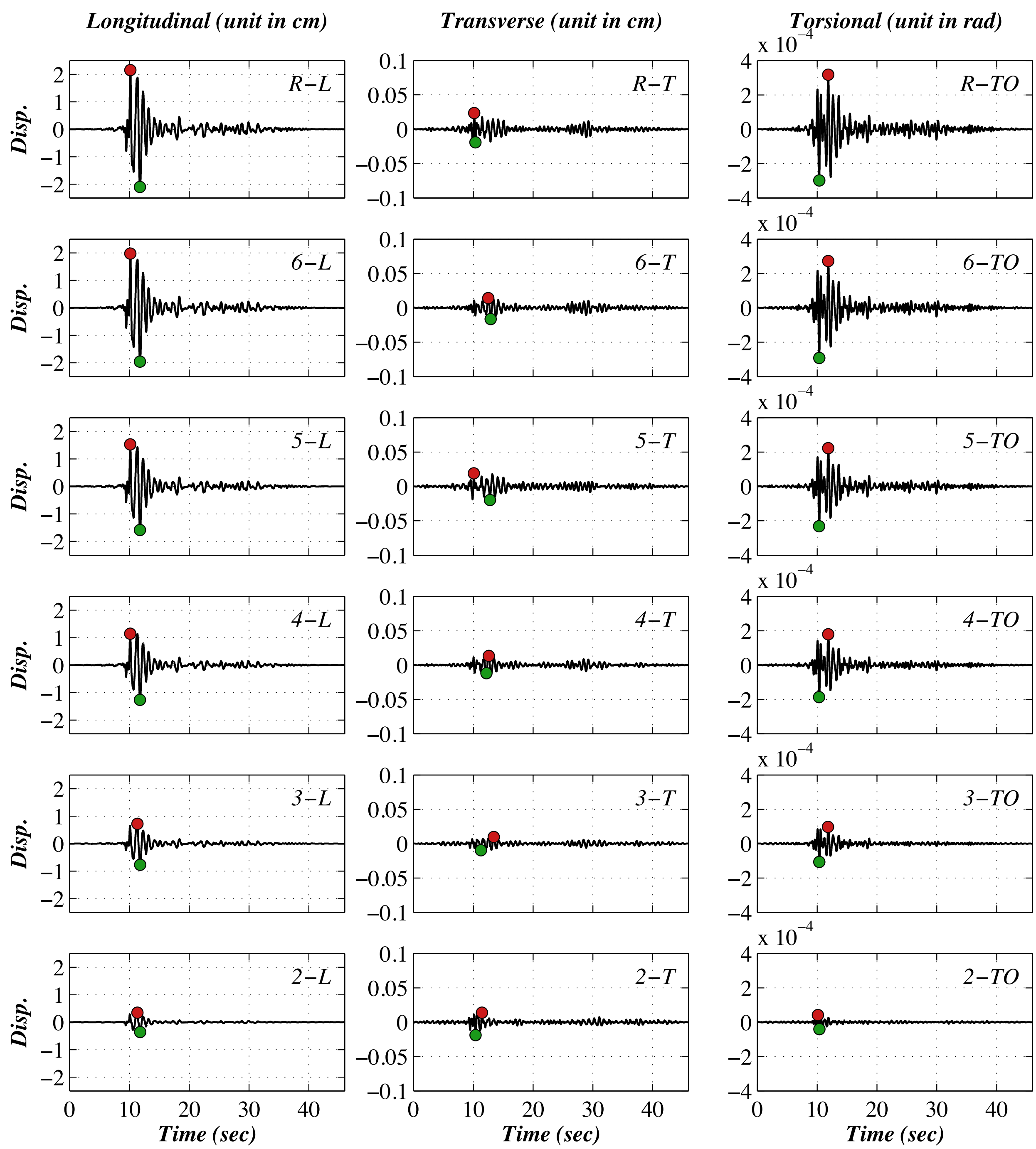

Figure 8.2. Measured floor relative displacements – EQ8:RIO-25.

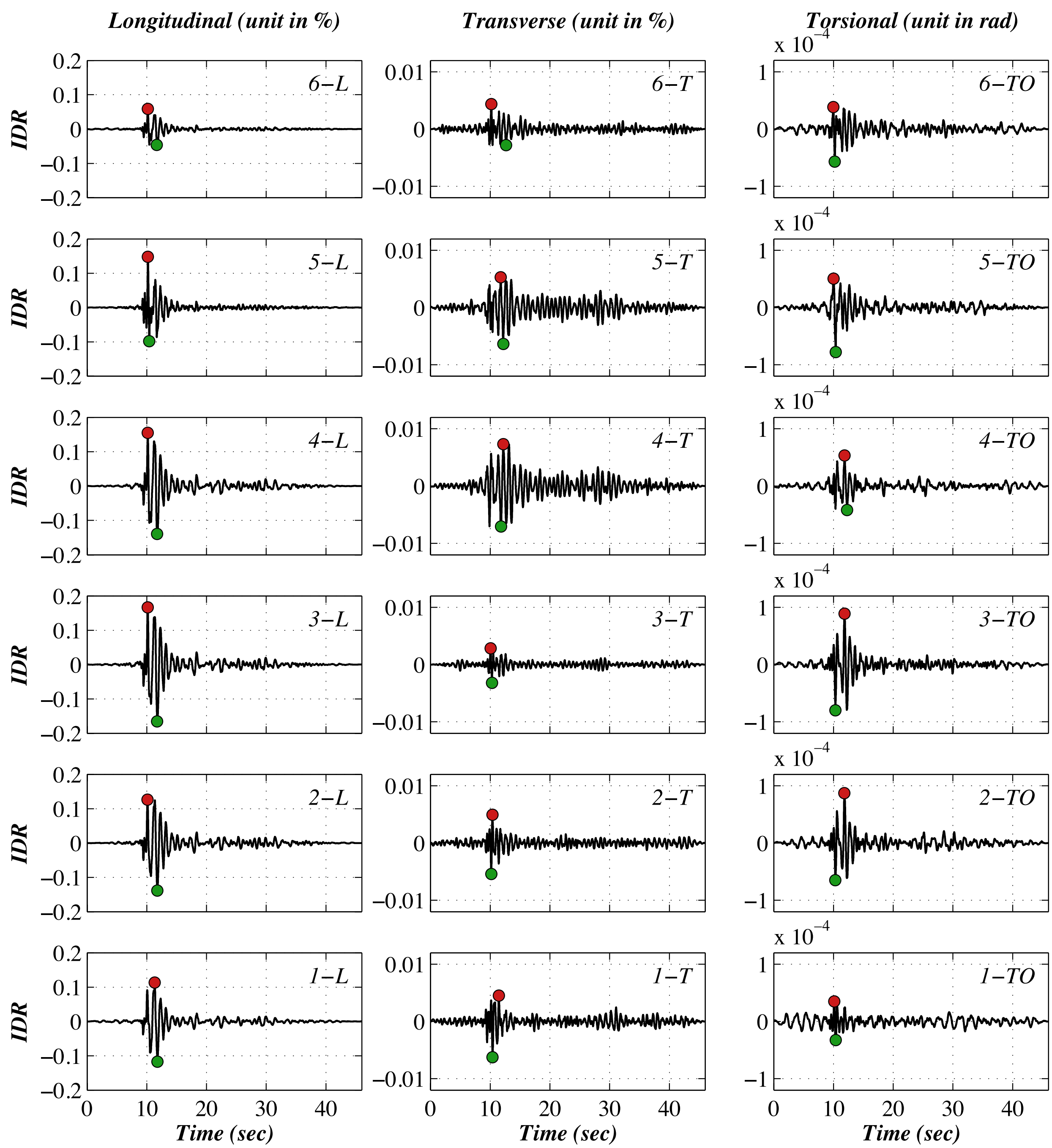

Figure 8.3. Measured interstory drift ratios – EQ8:RIO-25.

Figure 8.4 presents the longitudinal roof drift ratio (RDR) history during test EQ8:RIO-25. The RDR is determined using the displacements measured directly on the roof (measured with the GPS station at the roof center) and the table platen (measured with the string potentiometer). As shown in the figure, the PRDR reached about 0.1% with no apparent residual drift at the end of the test. However, since prior earthquake and fire tests induced substantial damage to the test building, the PRDR achieved during test EQ8 was twice as large as that attained during the pre-fire earthquake test using the same target input motion (EQ1:RIO-25), during which the test building achieved a PRDR of 0.05%.

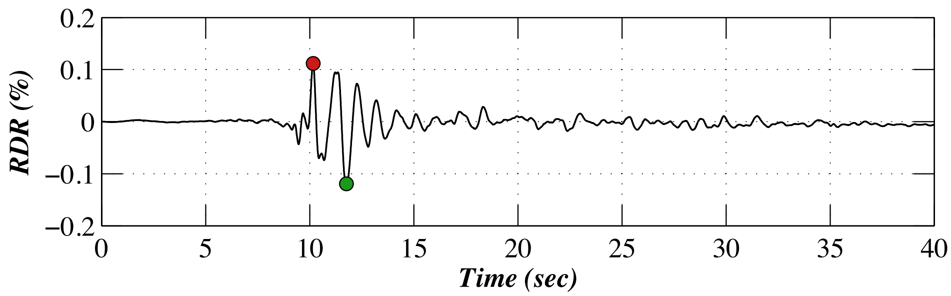

Figure 8.4. Measured roof drift ratio history – EQ8:RIO-25.

EQ9:RRS-150

Figure 8.5 presents the absolute floor accelerations in the three directions (longitudinal, transverse, and torsional) during test EQ9. The unit of torsional accelerations (in rad/sec^2) differs from that of the translational accelerations (g). The color circles represent the time instances when the maximum (red) and minimum (green) roof acceleration were achieved. Since the input motion represented a near-fault record containing large velocity pulses, the floor acceleration responses were dominated by the large impulse response, which occurred at ~8 seconds. Due to the formation of a soft-story mechanism at level 2, the acceleration responses at floor 3 through the roof were significantly larger than those of the lower two floors. The building achieved the largest translational accelerations at floor 5, exceeding 4 g in the longitudinal direction and reached 0.5 g in the transverse direction, while the peak torsional acceleration exceeded 2 rad/sec^2 at the roof.

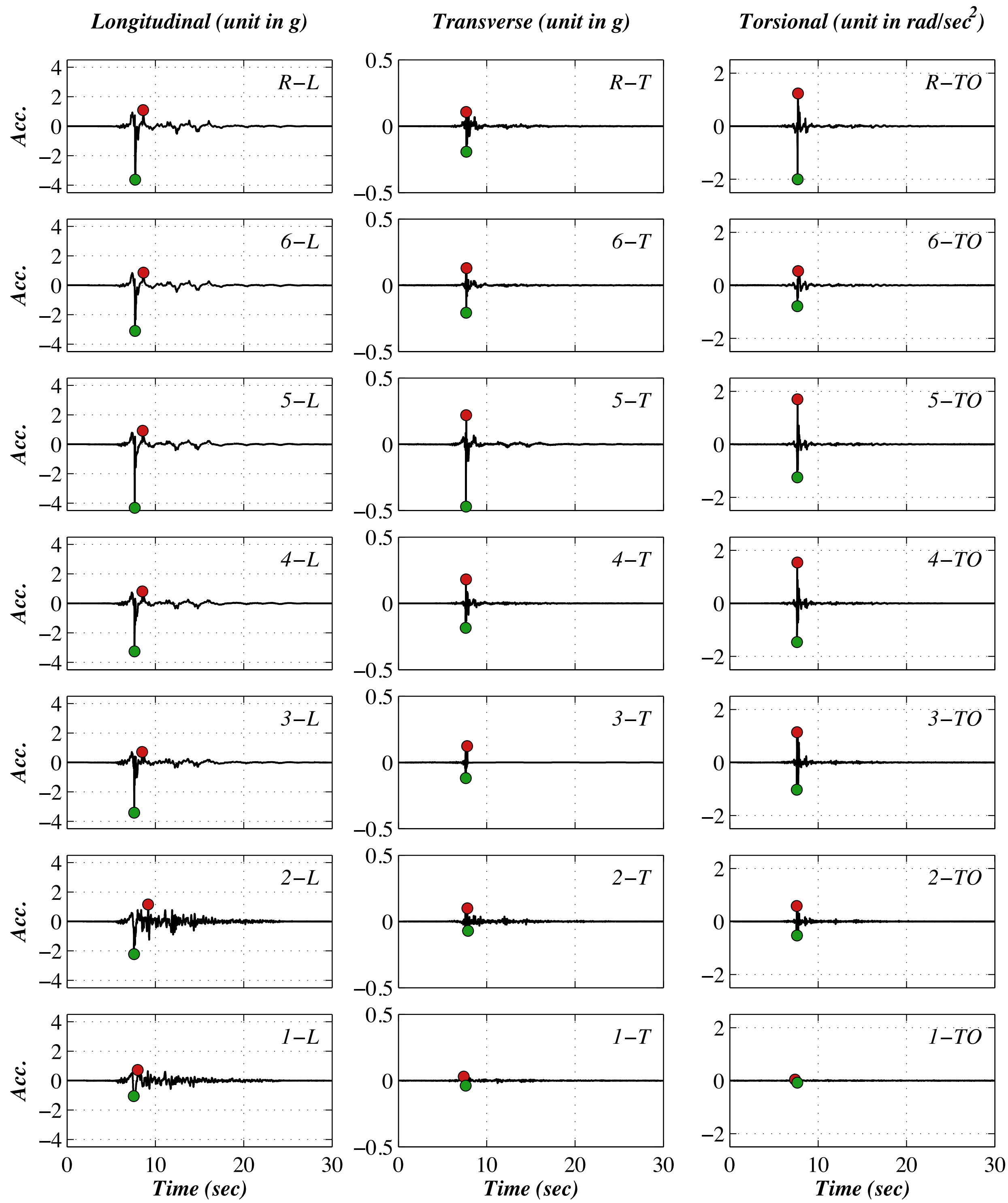

Figure 8.5. Measured floor absolute accelerations – EQ9:RRS-150.

The occurrence of large residual drifts following test EQ9 undermines the accuracy of the double integration method for capturing the baseline shift of the floor displacements. In this regard, the floor displacement and IDR response during test EQ9 were obtained using an incomplete set of direct displacement measurements: (1) the string potentiometers at the lower four floors, and (2) the GPS station at the center of the roof. Absent measurements at floor 5 and 6, the displacements of these two floors were interpolated using the displacements measured at floor 4 and roof. Since the displacement of floor 4 was measured using a string potentiometer with a sampling rate of 240 Hz, it was first decimated to 10 Hz (compatible with the GPS data) and then synchronized with the roof displacement. Subsequently, the displacements of floor 5 and 6 were obtained with the assumption that the differential displacement between floor 4 and the roof was distributed evenly over the upper three levels, since it is observed that the measured relative floor displacements were well in phase with each other (see Figure 8.6). Lastly, the interpolated floor displacements (with a sampling frequency of 10 Hz) are combined with the accelerometer measurements at the corresponding floor (with a sampling frequency of 240 Hz) using the Kalman filtering technique proposed by Bock et al. (2011) for estimating the final displacements of these two floors.

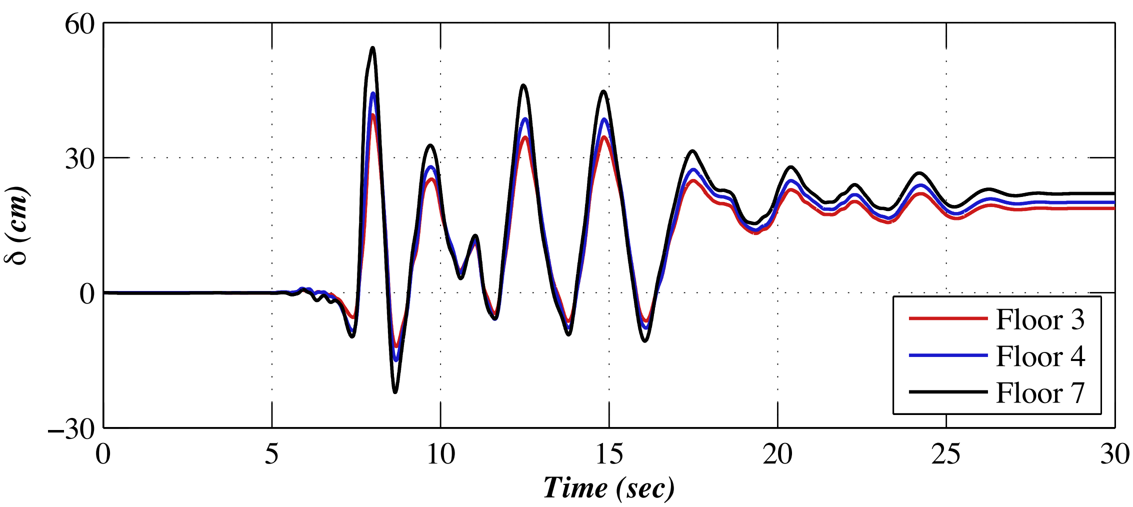

Figure 8.6. Measured longitudinal floor relative displacements at three select floors – EQ9:RRS-150.

Figure 8.7 shows the longitudinal absolute floor displacements and IDRs of the test building during test EQ9 (directly measured responses are denoted as black trace while the interpolated responses are denoted as blue traces). The figure also provides the residual floor displacements and IDRs, which are taken as the mean of the individual response at the end of the tests using a two-second window. The building underwent a residual displacement of ~22 cm at the roof, while more than 80% of the residual displacement was concentrated at level 2 (~18 cm). This is consistent with the residual IDR distribution that level 2 experienced a residual IDR of about 6% compared to only 0.4% for level 3 and 0.2% for level 1. Similarly, the transient IDR at level 2 were also significantly larger than those of the adjacent levels, attaining a peak value of ~12% in the positive (east) direction and > 4% in the negative (west) direction.

Figure 8.8 shows the longitudinal roof drift ratio (RDR) time history during test EQ9. The RDR is determined using the direct displacement measurements of the roof (measured with the GPS station at the center of the roof) and the table platen (measured with the string potentiometer). As shown in the figure, the roof drift achieved as much as 3% in the positive (east) direction and exceeded 1% in the negative (west) direction. The residual roof drift ratio reached about 1.2% (in the positive direction) at the completion of the test. As mentioned previously, more than 80% of the residual displacement was attributed to level 2 due to the formation of a soft-story mechanism.

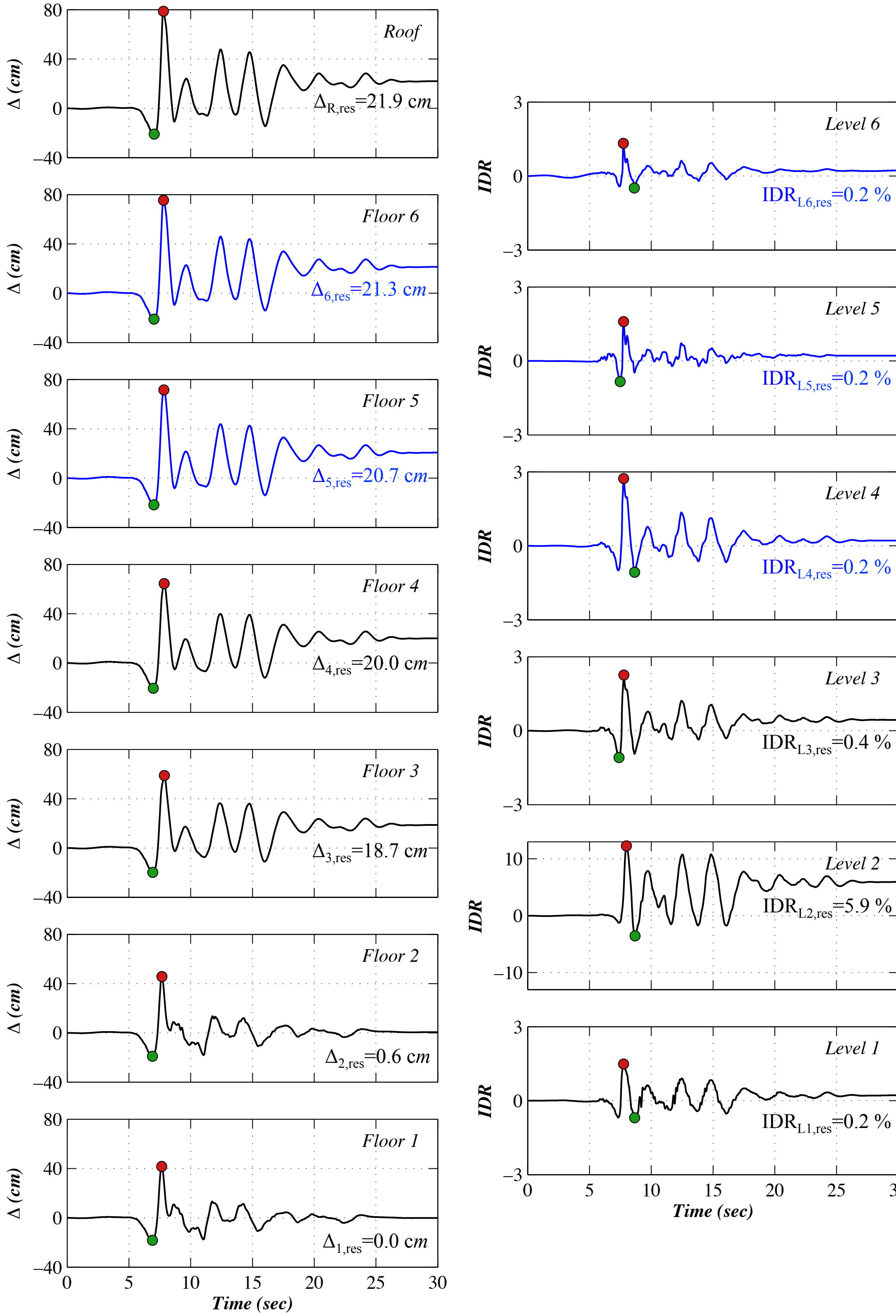

Figure 8.7. Measured and interpolated floor absolute displacements (left) and interstory drift ratios (right)– EQ9:RRS-150 (black traces indicates measured responses and blue traces indicate interpolated responses).

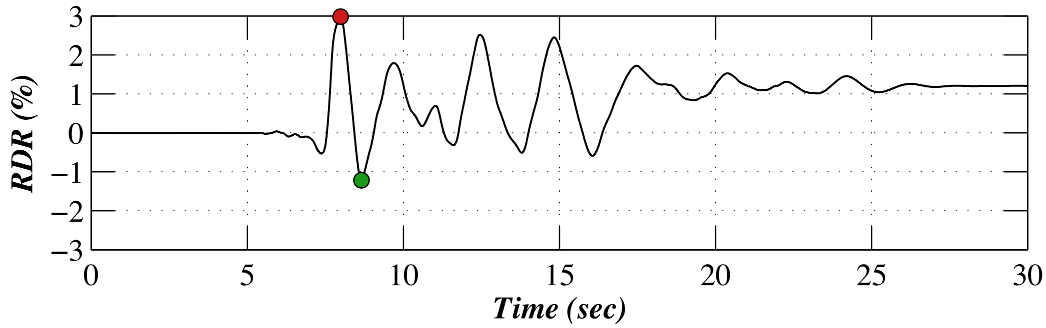

Figure 8.8. Measured roof drift ratio– EQ9:RRS-150.

To justify the use of linear interpolation for obtaining the floor displacements at levels 5 and 6, the residual displacement profile along the building height is analyzed using LiDAR point cloud datasets collected at the beginning and the end of the test program (Figure 8.9). The proposed point cloud analysis procedures involve two steps: (1) extract the building geometric information from point cloud data collected at various states of the test program, and (2) quantify the variations of building geometry (residual displacements) at two different states (beginning and end of the test program). In the first steps, the building facades are detected by fitting planes to the segmented point clouds using RANSAC algorithm. Subsequently, the vertical edges of as well as the corner points at the floor levels are determined in close form. In this second step, the iterative closest point (ICP) algorithm is used for aligning the point cloud data at the base of the building. Consequently, the residual building displacements are determined by quantifying the variations of the floor-level corner points between the two aligned point cloud datasets.

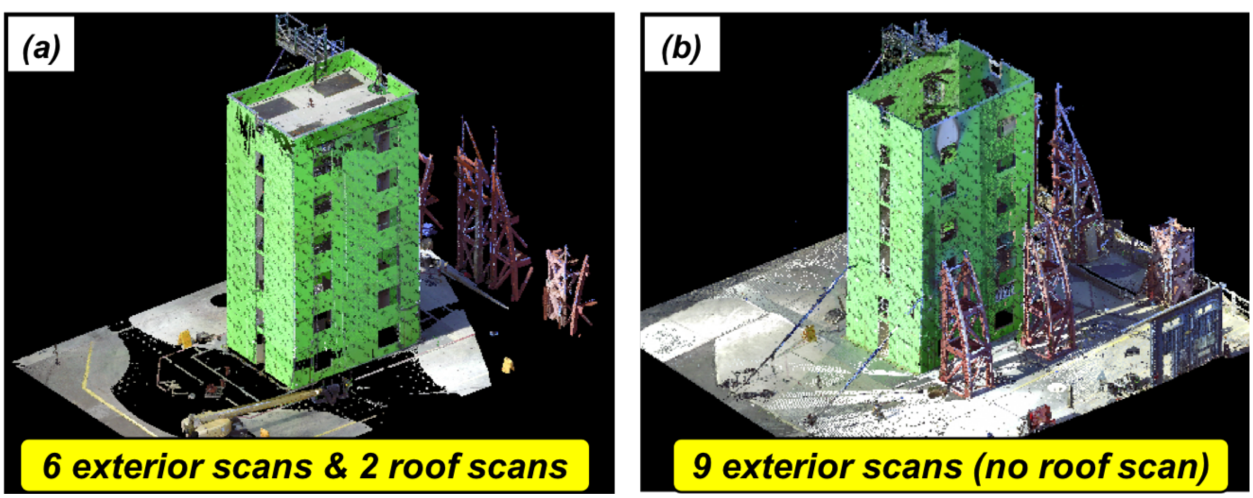

Figure 8.9. Point cloud models of the test building: (a) baseline condition (beginning of test program), and (b) final condition (end of test program).

Figure 8.10 compares the building residual displacement profile derived from the point cloud data with ground truth data. Ground truth measurements involved the roof residual displacement measured using GPS and the floor residual displacements at the lower four floors measured using string potentiometers. Agreement (~1 cm discrepancies) between the LiDAR-based results and ground truth measurements validates the effectiveness of the LiDAR sensing techniques for collecting accurate geometric information. In addition, the residual displacement profile followed a nearly linear trend from floor 4 through the roof. This validates the use of linear interpolation for obtaining the floor displacements at levels 5 and 6 where direct displacement measurements were not available.

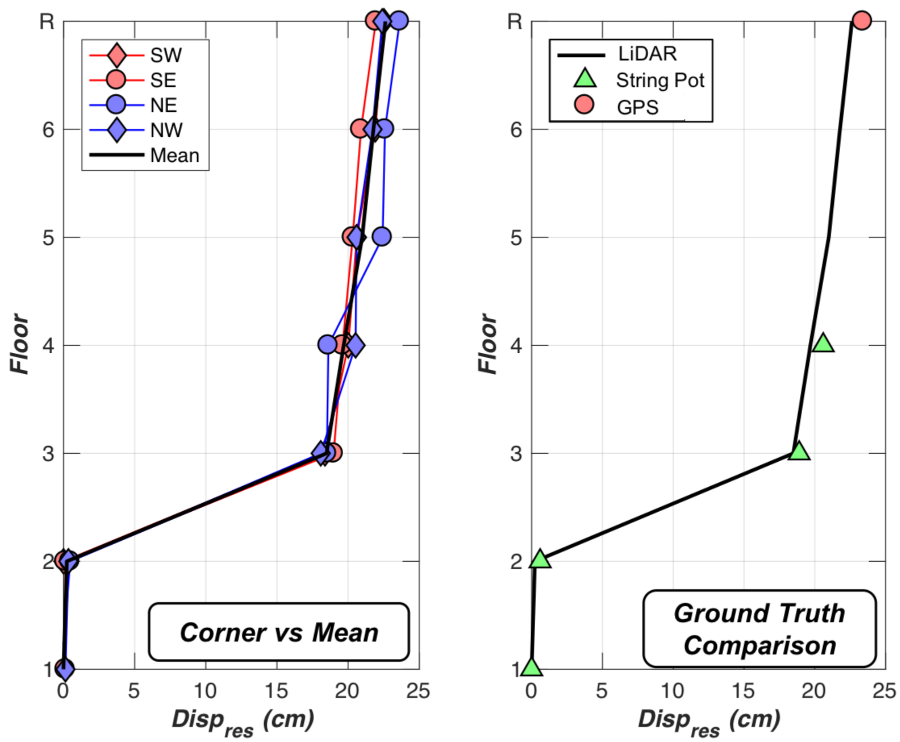

Figure 8.10. Comparison of LiDAR-based building residual displacements with ground truth measurements (GPS and string potentiometers).

8.1.1 Result Comparison and Discussion

To facilitate comparison of seismic behavior of the test building during the pre-fire and post-fire earthquake tests, the peak building responses, including peak floor accelerations (PFAs), peak inter-story drift ratios (PIDRs), peak roof drift ratios (PRDRs), and residual roof drift ratios (RDR_{res}), are summarized in Table 8.1. Detailed comparison and discussion of various responses are presented later in this section.

Table 8.1. Peak building responses during the earthquake tests

Test date	*Test Motion*	*PFA (g) (Floor #)*	*PIDR (%) (Level #)*	*PRDR (%)*	*RDR_{res} (%)*
June 13, 2016 (test day 1)	EQ1:RIO-25	0.35 (R)	0.08 (L4)	0.05	0.0
	EQ2:CNP-25	0.38 (R)	0.09 (L4)	0.07	0.0
	EQ3:CUR-25	0.45 (R)	0.10 (L4)	0.08	0.0
June 15, 2016 (test day 2)	EQ4:CNP-25	0.43 (R)	0.10 (L4)	0.09	0.0
	EQ5:CNP-50	0.85 (R)	0.24 (L3)	0.19	0.0
	EQ6:CNP-100	2.07 (R)	0.89 (L4)	0.70	0.0
June 17, 2016 (test day 3)	EQ7:CNP-150	3.77 (F5)	1.70 (L4)	1.49	0.1
Fire test phase (June 27 – 29, 2016)					
July 1, 2016 (test day 4)	EQ8:RIO-25	0.16 (R)	0.17 (L3)	0.12	0.0
	EQ9:RRS-150	4.43 (F5)	12.15 (L2)	2.84	1.2

PFA – peak floor acceleration; PIDR – peak interstory drift ratio; PRDR – peak roof drift ratio; RDR_{res} – residual roof drift ratio.

Peak Floor Accelerations and Peak Interstory Drift Ratios

Figure 8.11 compares the PFA and PIDR responses during the service level events (tests EQ1—EQ3 and EQ8). Although the seismic demands on the building were relatively low during these service-level earthquakes, the building observed apparent acceleration attenuations and larger interstory drifts during post-fire test EQ8. This is due to the fact that building sustained substantial stiffness deterioration due to damage accumulated during the prior earthquake and fire tests. As a result, the PIDRs achieved during the post-fire service level test (EQ8) were about twice as large as those attained during the pre-fire service level test sequence (EQ1—EQ3).

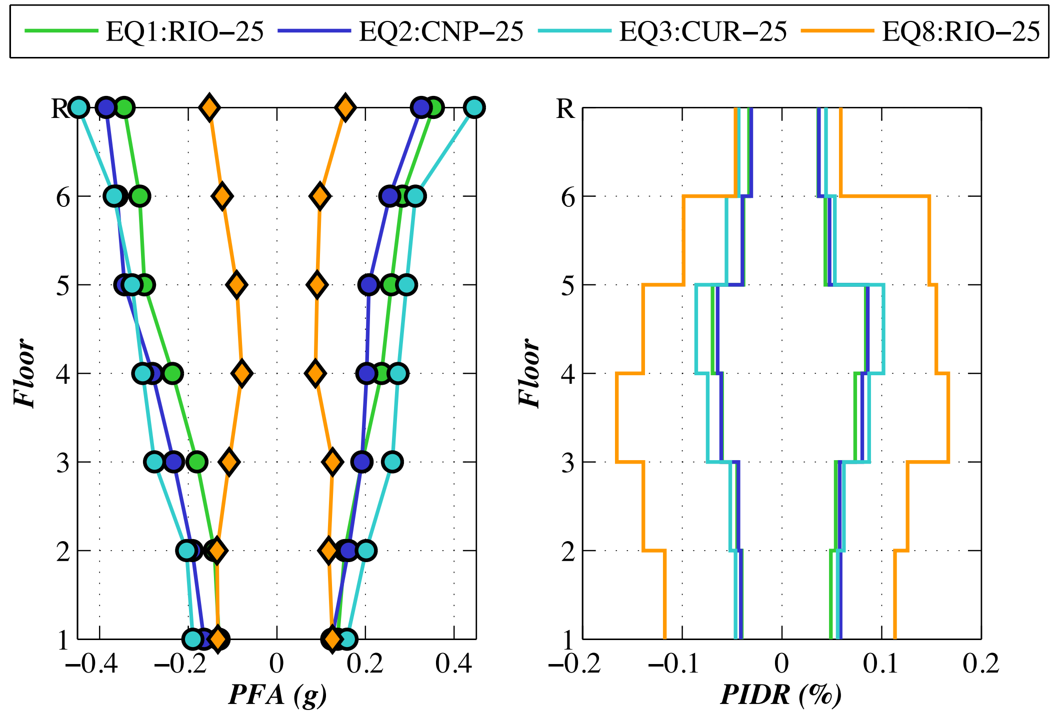

Figure 8.11. Building peak responses during the *service level* tests: (a) peak floor accelerations, and (b) peak interstory drift ratios.

Figure 8.12 presents the PFA and PIDR responses during the above-the-service-level events (i.e. EQ5—EQ7 and EQ9). As the motion intensity increased, the largest PIDR reached ~1.0% during the design event (EQ6) and above 1.5% during the MCE event (EQ7). It is also revealed that the largest PIDR occurred at the mid-height of building (level 3 and 4) throughout the pre-fire test sequence. These results are consistent with building physical observations as discussed in Section 6.4. In addition, the PFA increased almost monotonically up the height of the building during the pre-fire earthquake test sequence, indicating a fundamental-mode dominant structural response in these tests. The last earthquake test (near-fault MCE event EQ9) subjected the building to extremely large drift demands (an interstory drift ratio exceeding 12% at level 2) and resulted in a near-collapse condition of the specimen. It is also noted that the residual (permanent) RDR of building exceeded 1% following the test (see Table 8.1). This is attributed to the fire-induced damage to the gypsum sheathing at level 2, which significantly reduced the shear strength of the shear walls, helping facilitate formation of a soft-story mechanism during the final near-fault earthquake (EQ9).

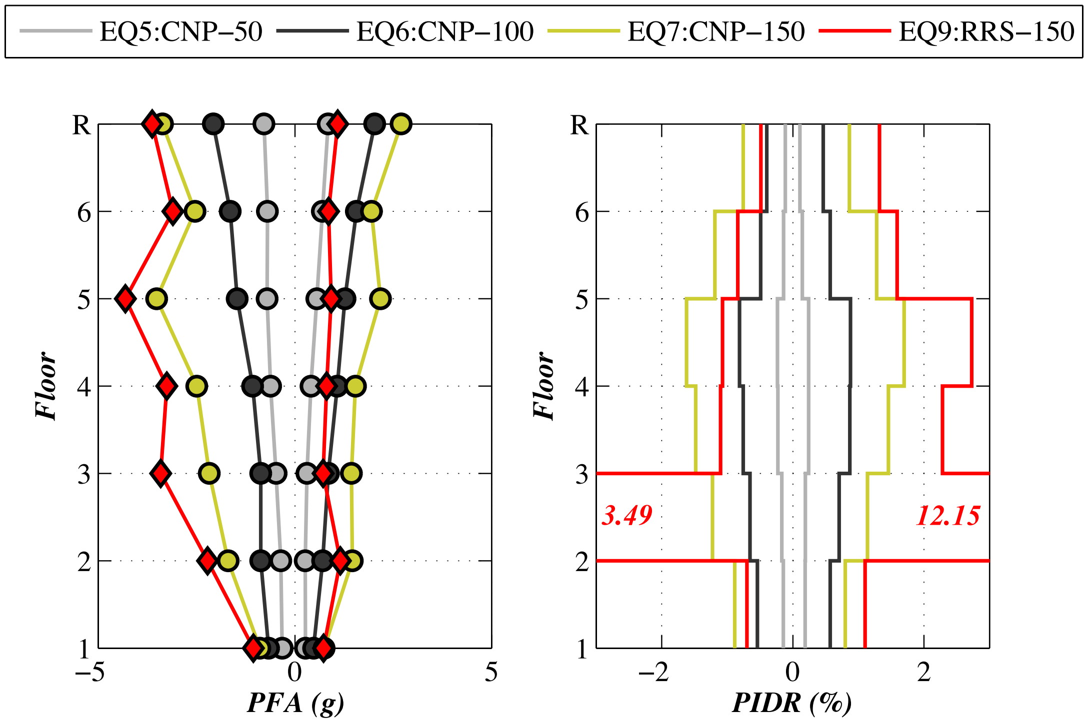

Figure 8.12. Building peak responses during the *above-service-level* tests: (a) peak floor accelerations, and (b) peak interstory drift ratios.

Residual IDRs and RDRs

Table 8.2 summarizes the residual IDR of the lower two (or three) levels achieved during the two MCE level earthquake tests (EQ7 and EQ9). The residual IDRs are determined using displacements measured directly using the string potentiometers located on the east side of the building, while the residual RDRs are determined using direct GPS measurements. As shown in the table, the building residual displacement remained very small at the completion of the pre-fire test sequence ($RDR_{res} < 0.1\%$), but increased abruptly following the post-fire MCE event (test EQ9). The distribution of the residual IDR shows that level 2 attained as much about 6% residual IDR compared to 0.4% for level 3 and 0.2% for level 1.

Table 8.2. Comparison of residual drift responses during the MCE level tests

Test	$IDR_{L1,res}$	$IDR_{L2,res}$	$IDR_{L3,res}$	RDR_{res}
EQ7:CNP-150	0.03	0.08	/	0.08
EQ9:RRS-150	0.21	5.93	0.44	1.20

Floor Acceleration Amplifications

Figure 8.13 compares the building acceleration amplification factor Ω. The acceleration amplification factor Ω is determined as the ratio between the peak acceleration achieved at each floor and the peak earthquake input acceleration. According to ASCE 7-10 (ASCE, 2010) code provisions, the amplification factor is empirically defined as 1+2z/h (z/h denotes the normalized building height), which represents a linear distribution along the building height from 1.0 at the base to 3.0 at the roof. During the pre-fire service level test sequence (EQ1-EQ3) (Figure 8.13a), the acceleration amplification factors increased monotonically up the height of the building with the largest values ranging between 2.0 and 2.5 at the roof, which was slightly lower than the code-specified value of 3.0 However, as the building sustained significant period elongation prior to the post-fire service level test EQ8, the floor accelerations were effectively attenuated (Ω close to 1.0). The amplification factors continued to increase during tests EQ5 and EQ6 as the motion intensity increased (Figure 8.13b). It is noted that the distribution of the amplification factors achieved during the design event (EQ6) matched well with the code-specified distribution along the building height. During the MCE events (EQ7 and EQ9), the observed floor amplification effects were significantly larger than the code-specified distribution at all floors (Figure 8.13b). This is due to the presence of impulse-like acceleration spikes during these tests.

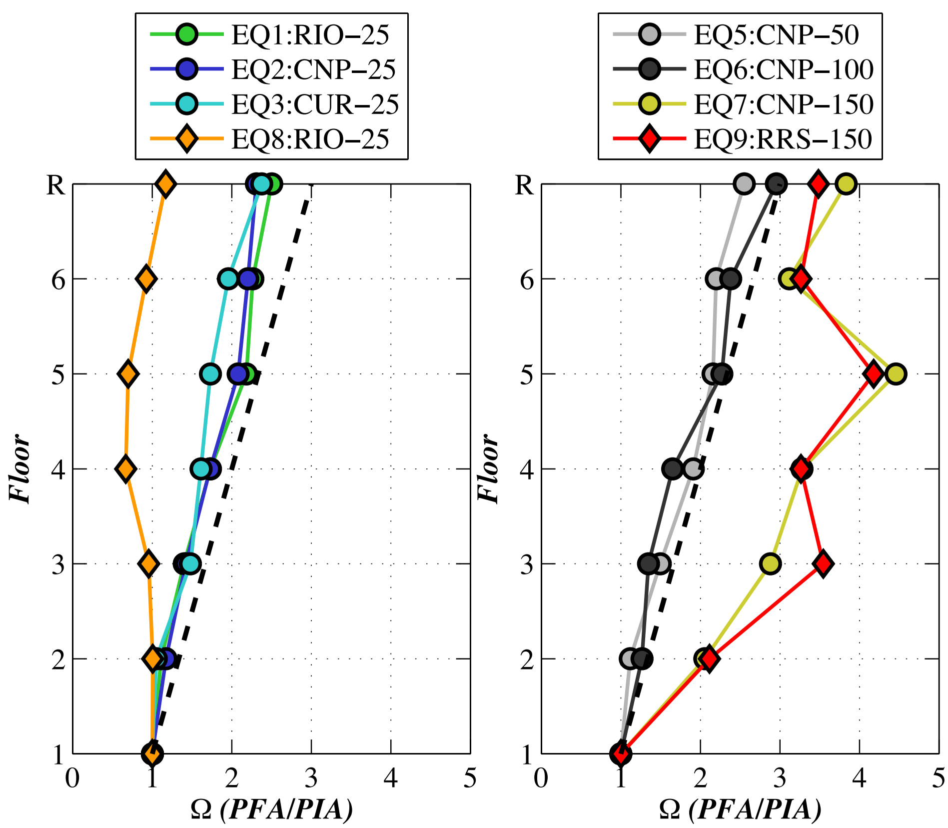

Figure 8.13. Acceleration amplification factor of the test building under: (a) *service level* tests, and (b) *above-service-level* tests.

Floor Response Spectra and Component Amplifications

Figure 8.14 and Figure 8.15 compare the floor response spectra (FRS) of the service level events (EQ1 and EQ8) and MCE earthquake events (EQ7 and EQ9) during the pre-fire and post-fire test phase, respectively. The FRS is defined as the 5% damped elastic pseudo-acceleration spectra for the achieved floor accelerations in the longitudinal direction. While EQ1 and EQ8 represented the same target input motion scaled to the service level intensity, EQ7 and EQ9 utilized different earthquake records scaled to the MCE level intensity. Therefore, the input motion spectra of EQ7 and EQ9 were equivalent only in an averaged sense at the period range of interest but involved large variations of their respective spectra shapes. Due to the lower accelerations of the building due to stiffness deterioration induced by the prior earthquake and fire tests, the FRS of the post-fire service level test (EQ8) were appreciably lower than those attained during the pre-fire test (EQ1) (Figure 8.14). On the other hand, the FRS of the post-fire MCE event (EQ9) were moderately higher than those achieved in the pre-fire MCE event (EQ7) within the short period region (< 0.3 sec). It is noted that the FRS at floor 3 contained a very sharp spectral peak at around 0.05 second, which is likely caused by the formation of the soft story at level 2. Due to the discrepancies of the spectral contents of the input motions, the FRS within 0.5 ~ 1.0 sec range contained two dominant peaks for test EQ7 while remained relatively flat for test EQ9.

Figure 8.16 and Figure 8.17 compare the component amplification factors (a_p) of the two service level events (EQ1 and EQ8) and two MCE earthquake events (EQ7 and EQ9), respectively. The component amplification factor, which is calculated as the ratio between the FRS and the PFA, characterizes the dynamic amplification effect of nonstructural systems in response to floor excitations. As shown in Figure 8.16, the component amplifications of the post-fire service level event (EQ8) at the lower floors (floor 2 through 5) was higher within the short period range (< 0.3 sec) compared with, despite of smaller floor accelerations compared to the pre-fire event (EQ1). In addition, the FRS of the upper floors (floor 4 through roof) observed a large spectral peak at around 1.2 second during the post-fire service level event (test EQ8), indicating the elongation of the building fundamental period compared to that of the corresponding pre-fire event (EQ1). For the two MCE level events (EQ7 and EQ9), the component amplifications remained comparable within the short period range (< 0.3 second) (Figure 8.17). Within this period range, the observed component amplification factors at all floors remained lower than 2.5 (the code-specified coefficient for flexible nonstructural components) as a result of the accumulated damage to the building.

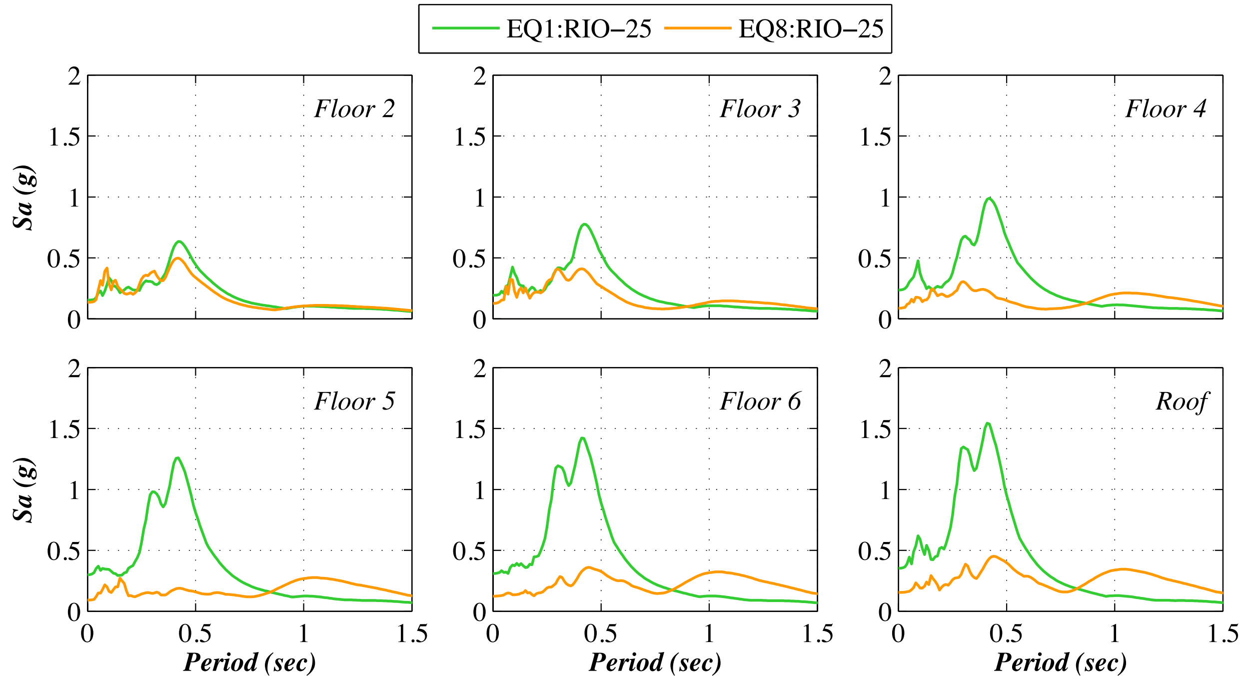

Figure 8.14. Floor response spectra (ξ=5%) – *service level* tests (EQ1 and EQ8).

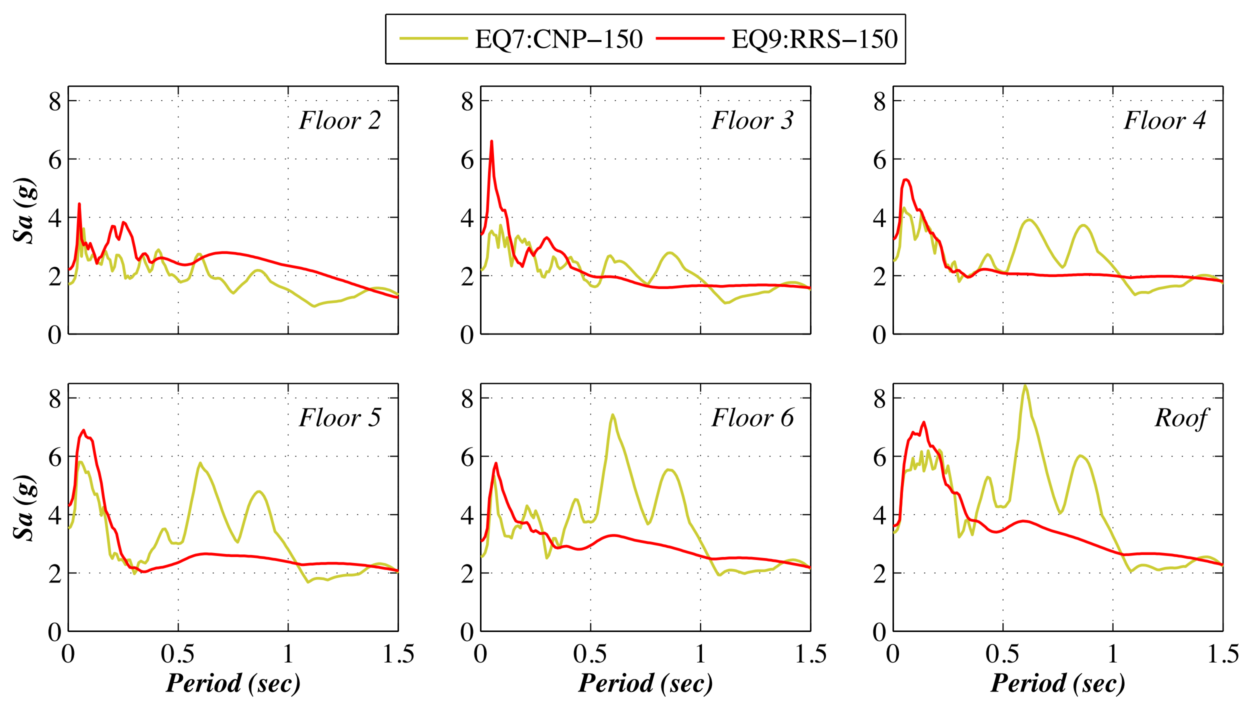

Figure 8.15. Floor response spectra (ξ=5%) – *MCE level* tests (EQ7 and EQ9).

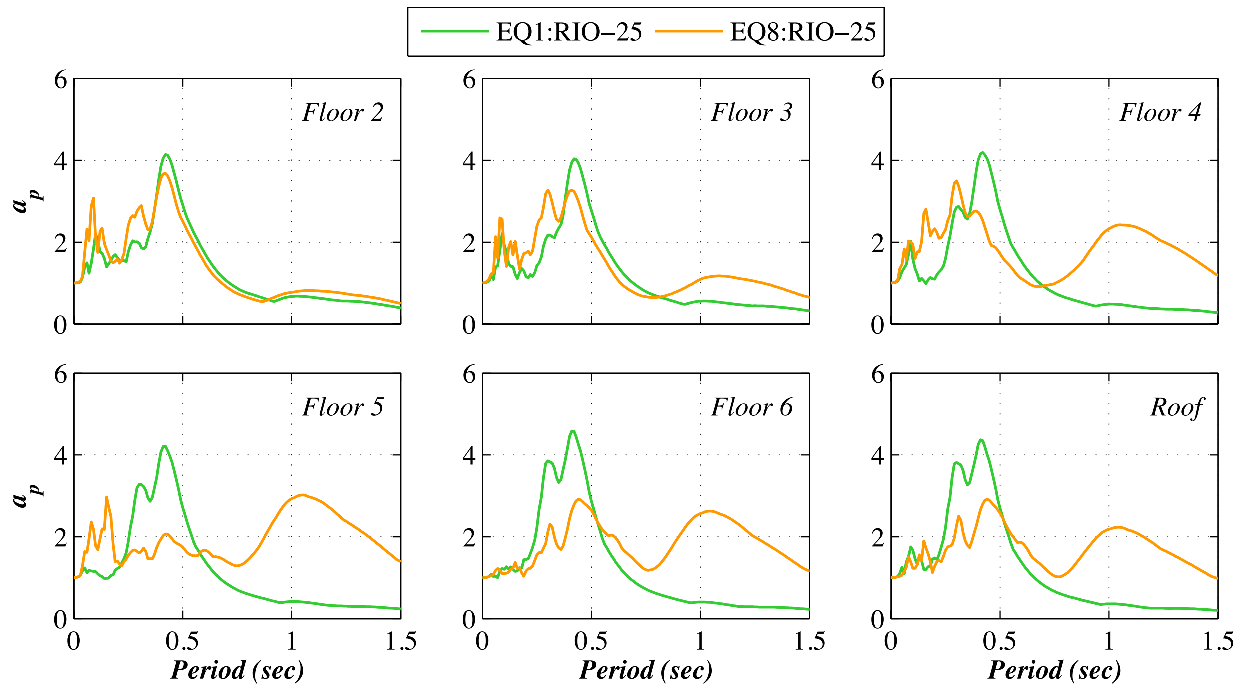

Figure 8.16. Component amplification factors – *service level* tests (EQ1 and EQ8).

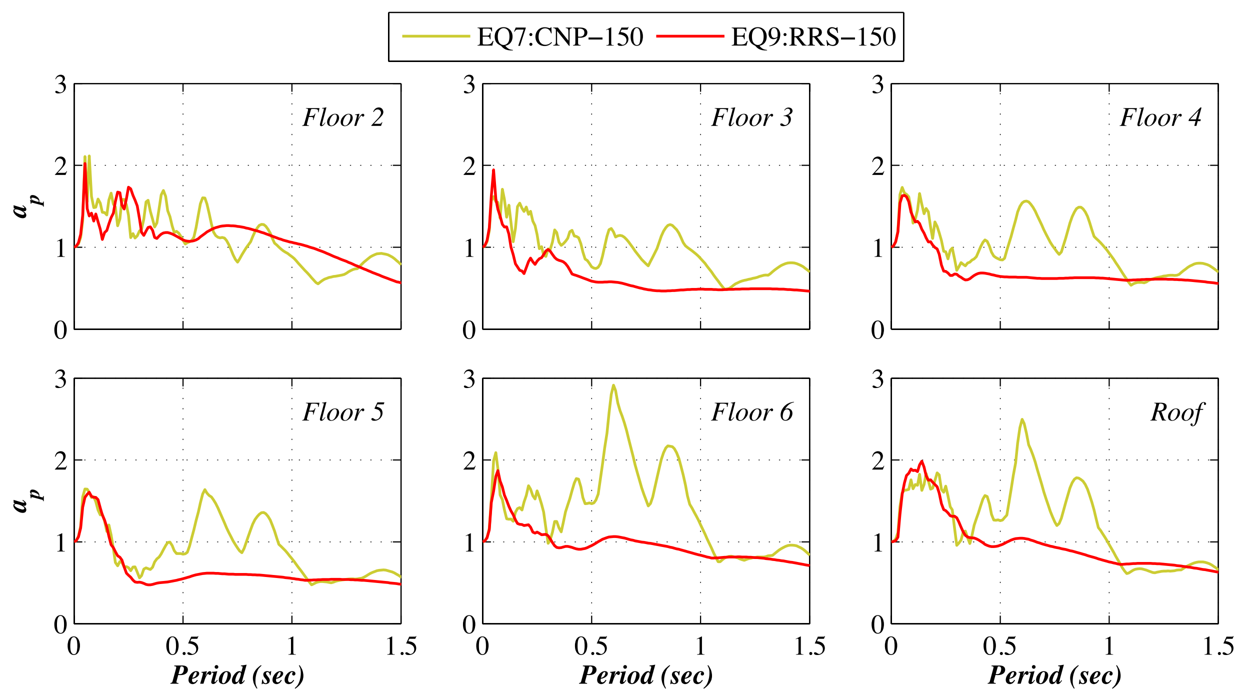

Figure 8.17. Component amplification factors – *MCE level* tests (EQ7 and EQ9).

8.2 Local Response

This section presents the shear wall responses during the post-fire earthquake test sequence. However, the measured local responses became less complete compared to those collected during the pre-fire test phase, since the shear wall sensors on the level 2 and level 4 exterior walls were removed prior to the fire test phase or damaged during the fire tests. Only the measured responses of level 1 corridor and corner shear walls and level 4 corridor shear walls remained consistent with those in the pre-fire test phase. In this regard, comparison and discussion of the pre-fire and post-fire shear wall local responses are limited to these shear walls.

Sheathing Panel Shear Distortions

Figure 8.18 plots the panel shear distortion histories of the corridor and corner shear wall pairs (southwest and southeast) at level 1 during EQ8:RIO-25 (service level event). Figure 8.19 presents the same results of the shear walls at level 1 during EQ9:RRS-150 (MCE event). The color circles represent the time instances when the maximum (red) and minimum (green) IDR were achieved. Similar to those observed during the pre-fire test sequence, the same type of the shear walls on the two sides of the building underwent comparable shear distortions. In addition, the panel shear distortions of the corridor walls (~0.7%) were much larger than those of the corner shear walls (~0.3%).

Figure 8.20 compares the peak panel shear distortions as well as the ratio of the peak panel shear distortions and corresponding PIDRs between the post-fire and pre-fire service level tests (EQ8 vs EQ1). Figure 8.21 presents the same set of results between the post-fire and pre-fire MCE level tests (EQ9 vs EQ7). The positive (or negative) peak panel shear distortions are correlated with the corresponding PIDR in the positive (or negative) directions. Since the drift demands of level 1 and level 4 during the post-fire tests (EQ8 and EQ9) were twice as much as those of the pre-fire counterparts (EQ1 and EQ7), the achieved peak panel shear distortions were also larger. It is observed that the panel shear distortion ratios of the level 4 corridor shear walls increased to about 60% during the post-fire service level test (EQ8) from ~20% for the pre-fire service level test (EQ1) (Figure 8.20), whereas the panel shear distortion ratios remained comparable between the pre-fire and post-fire MCE level tests (EQ7 and EQ9) (Figure 8.21).

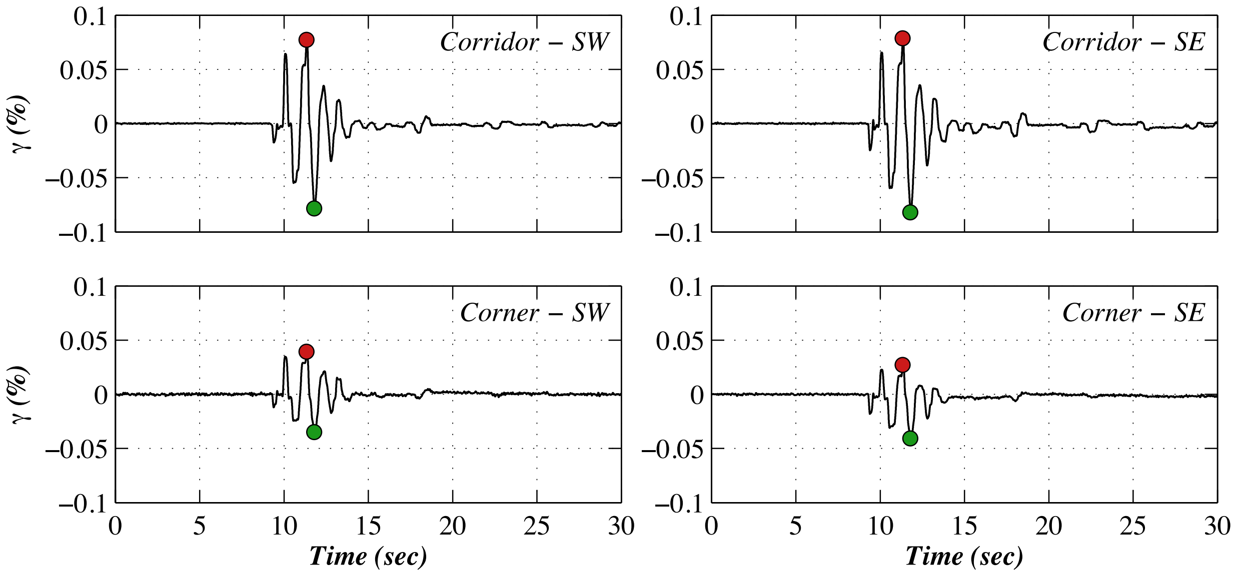

Figure 8.18. Sheathing panel shear distortion histories of the level 1 corridor and corner shear walls during test EQ8.

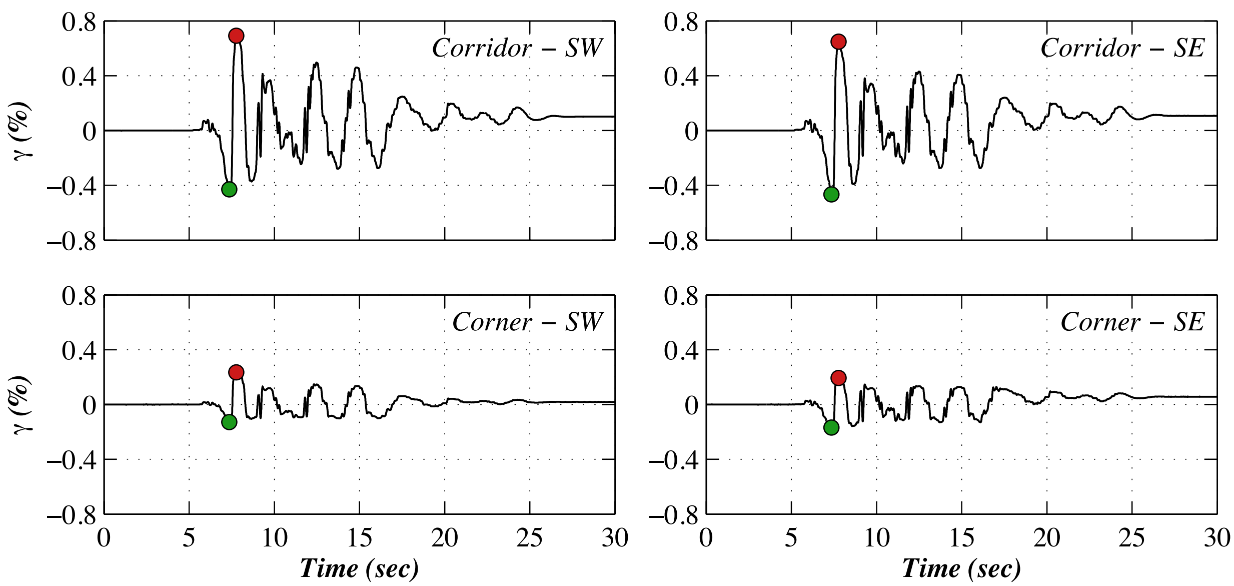

Figure 8.19. Sheathing panel shear distortion histories of the level 1 corridor and corner shear walls during test EQ9.

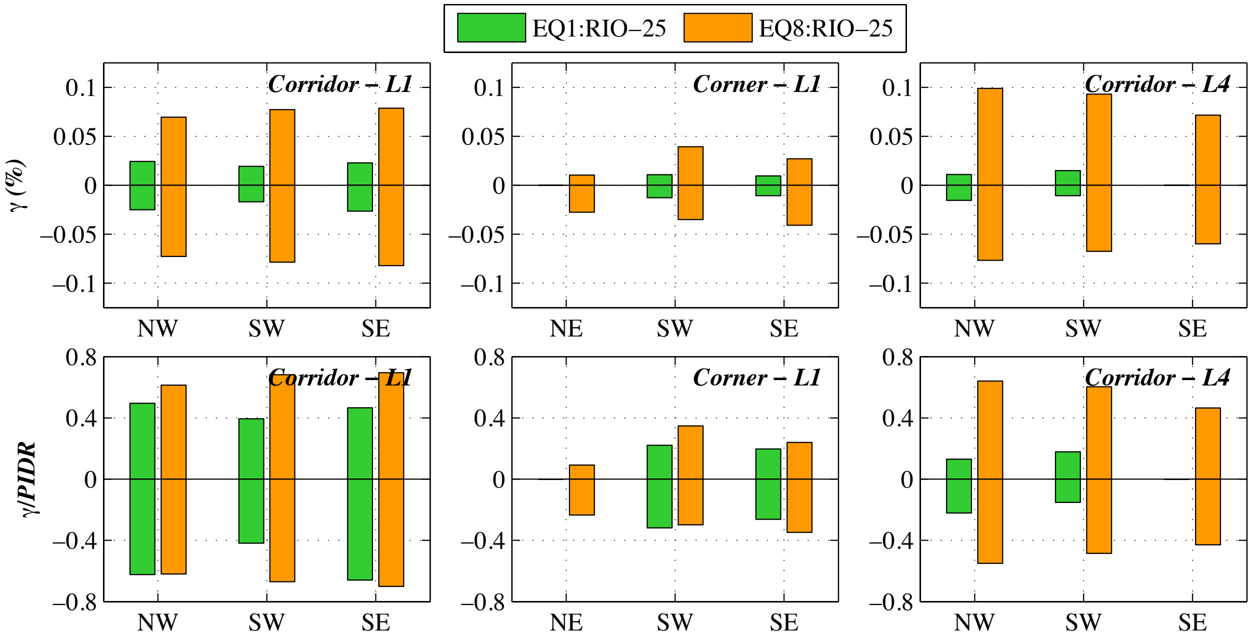

Figure 8.20. Comparison of peak panel shear distortions (first row) and peak panel shear distortion ratios (second row) of the shear walls during the *service level* tests (EQ1 and EQ8).

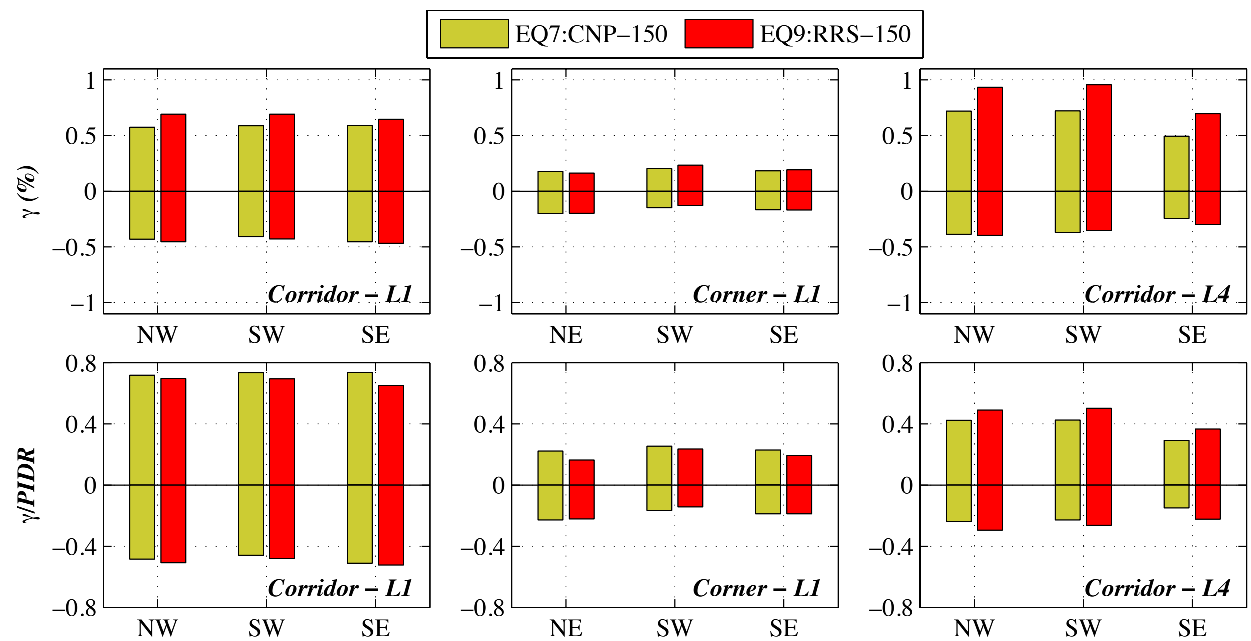

Figure 8.21. Comparison of peak panel shear distortions (first row) and peak panel shear distortion ratios (second row) of the shear walls during the *MCE level* tests (EQ7 and EQ9).

Tie-down Rod Axial Force

Figure 8.22 plots the tie-down rod axial force histories of the corridor shear wall pair (southwest and southeast) and the corridor shear wall pair (southwest and southeast) at level 1 during EQ8:RIO-25 (post-fire service level event). Figure 8.23 presents the same results of the level 1 corridor and corner shear walls during EQ9:RRS-150 (post-fire MCE event). The color circles represent the time instances when the maximum (red) and minimum (green) IDR were achieved. Due to the small seismic drift demands during the post-fire service level event (EQ8), the tensile forces of the level 1 shear wall tie-down rods were also very small (< 5 kN). During the post-fire MCE event (EQ9), the tie-down rod tensile forces increased significantly and exceeded 300 kN for the corridor shear wall tie-down rods and attained ~100 kN for the corner shear walls tie-down rods. It is noted that while the tie-down rod forces of the corridor shear wall pair at level 1 correlated well with each other in both amplitude and phase, the tie-down rod forces southeast corner shear wall were not consistent with those of the southwest corner shear wall. This is due to the fact that the continuous tie-down rod on the west end of the southeast corner walls sustained connection failure at level 2 (see Section 8.3 for details) during the post-fire MCE test (EQ9). This resulted in sudden loss of tensile capacity of the west wall end tie rods and redistribution of the axial forces to the adjacent rods, as it is clearly observed that the tensile force of the west end tie-down rod dropped abruptly following the attainment of PIDR and was no longer capable of resisting tensile loads afterwards.

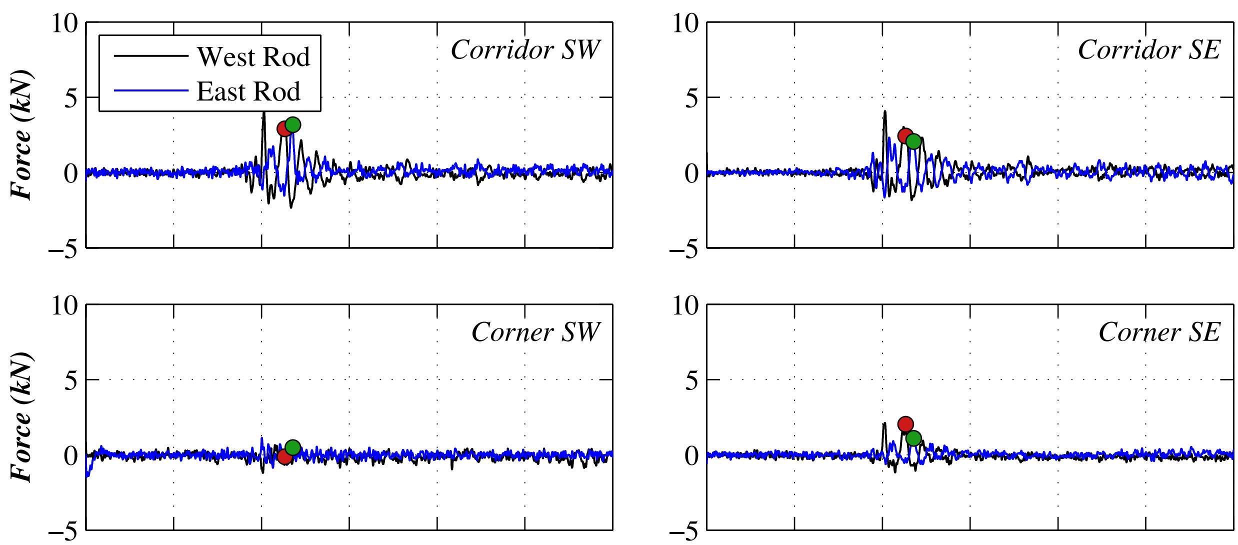

Figure 8.22. Tie-down rod axial force histories of the level 1 corridor and corner shear walls during test EQ8.

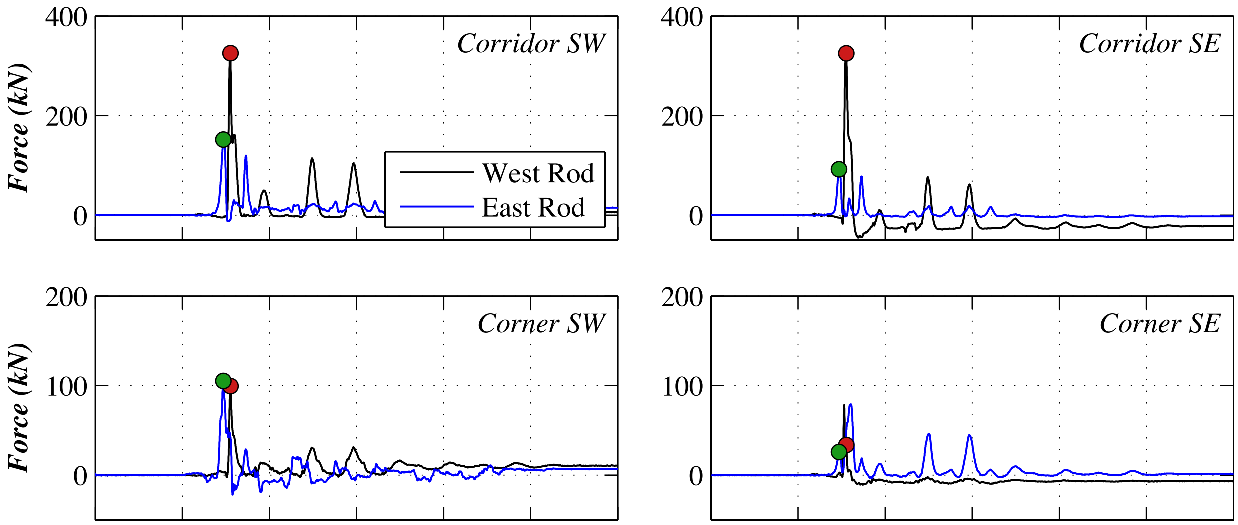

Figure 8.23. Tie-down rod axial force histories of the level 1 corridor and corner shear walls during test EQ9.

Figure 8.24 compares the tie-down rod axial force histories of the southeast corridor and corner shear walls at three different levels (e.g., level 1, 2, and 4) during the post-fire MCE test (EQ9:RRS-150). The color circles represent the time instances when the maximum (red) and minimum (green) RDR were achieved. The tie-down rod forces of the corridor shear walls at different levels correlate well with each other, since all the rods at the west wall ends achieved the peak forces when the maximum (eastward) interstory drift demands were attained, while those at the east ends achieved the peak forces when the minimum (westward) interstory drift demands were attained. As a result of larger force demands, the peak tensile forces of the corridor shear wall tie rods at the lower two levels were much larger than those at level 4. On the other hand, due to the rod connection failure on the west end of the southeast corner wall at level 2, the tensile axial forces of the west end tie-down rods of the corner walls at all three levels dropped almost simultaneously following the attainment of PIDR. Since the west end rods lost their tensile capacities, the east rods were subjected to substantiate tensile forces under positive interstory drift (building leaning eastward). Despite the extremely large seismic drift demands during the post-fire MCE event (EQ9), it is important to note that the peak tensile forces of the corridor shear wall tie-down rods at all three levels remained lower than their nominal yield strength (see Table 6.4 for details).

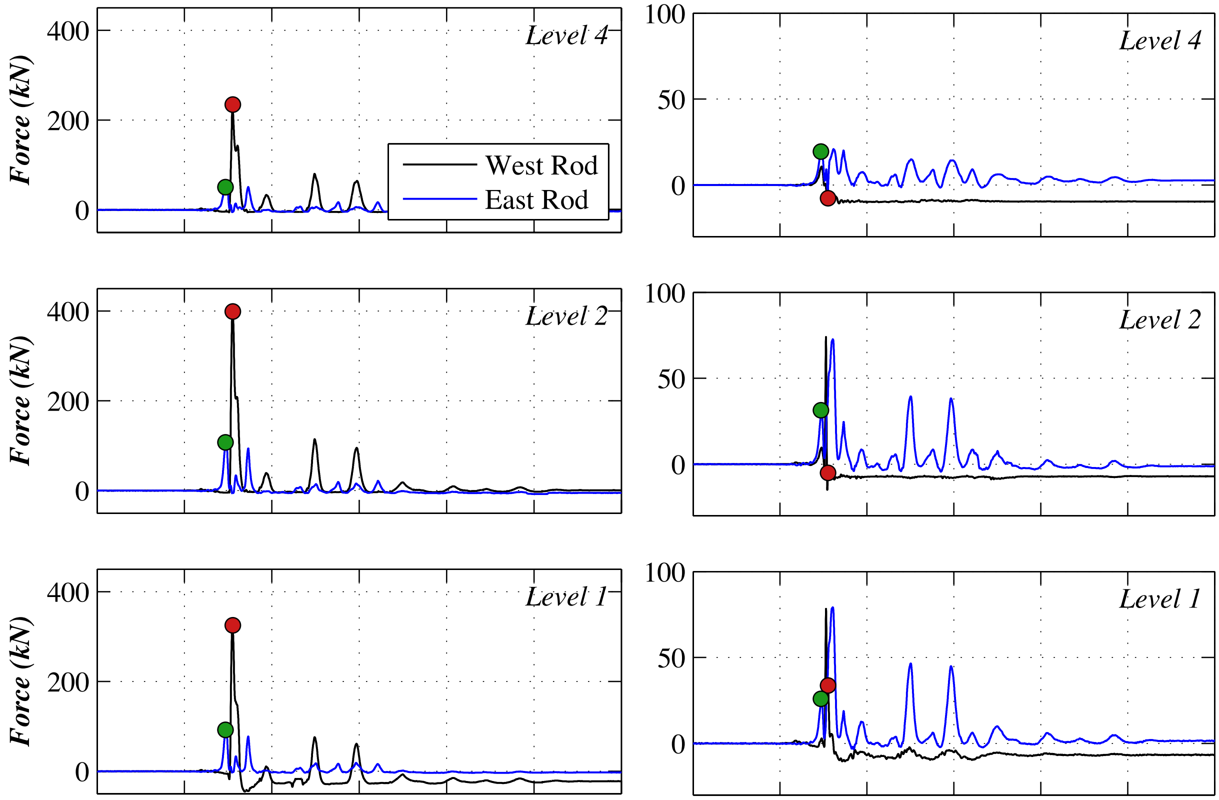

Figure 8.24. Tie-down rod axial force histories of the southeast corridor (left) and corner (right) shear walls at three different levels during test EQ9.

Figure 8.25 compares the peak tie-down rod tensile forces of the corridor and corner shear walls at the three different levels (i.e., level 1, 2, and 4) during the post-fire and pre-fire MCE tests (EQ9 vs EQ7). Each row contains the peak forces of the west end tie rods in the left plot (associated with positive interstory drift) and the east end tie rods in the right plot (associated with negative interstory drift). The result comparisons indicate that the peak tensile forces of the rods at the west end of the corridor walls remained similar, even though the drift demands were larger during the post-fire test (particularly at level 2). In comparison, the peak tensile forces of the east end rods were considerably smaller that those of the west end rods within the same shear walls, as a result of non-symmetric interstory drift (force) demands of the building in the positive (east) and negative (west) directions (see Figure 8.12b). For the shear walls at the southeast corner, the peak tensile forces of the rods at all three levels were consistently lower for the west end rods during the post-fire test and higher for the east rods when compared to the pre-fire test. This implies the redistribution of the tie-down rod axial forces due to the connection failure of the west tie-down rod at level 2.

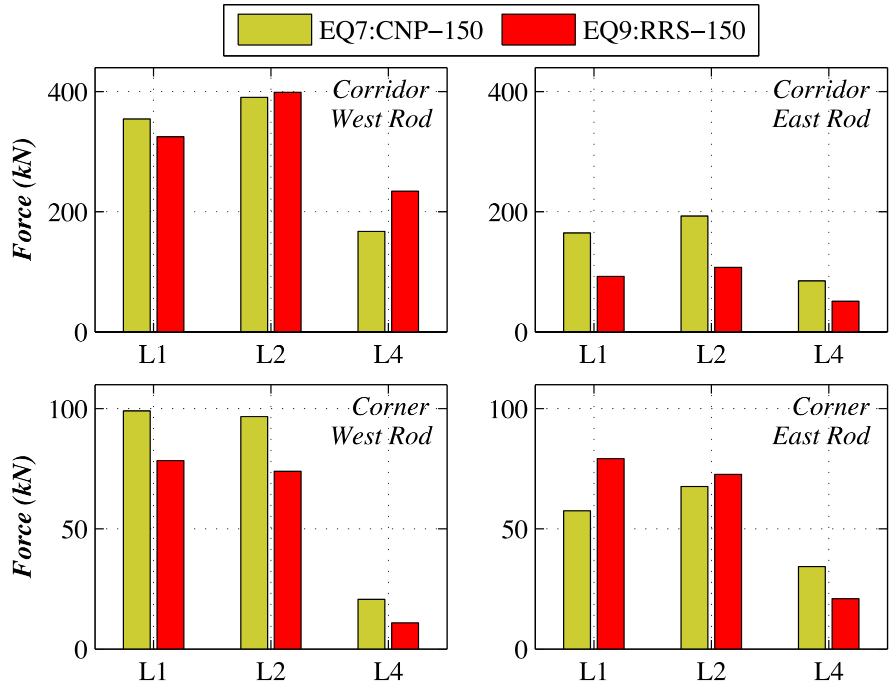

Figure 8.25. Comparison of peak tie-down rod tensile forces of the southeast corridor (first row) and southeast corner (second row) shear walls at three different levels between the *MCE level* tests (EQ7 and EQ9).

Wall End Vertical Displacements

Figure 8.26 plots the wall end vertical displacement histories of the corridor and corner shear wall pairs (southwest and southeast) at level 1 during EQ8:RIO-25 (service level event). Figure 8.27 presents the same results of the same shear walls for EQ9:RRS-150 (MCE event). The color circles represent the time instances when the maximum (red) and minimum (green) IDR were achieved. As indicated by the color circles, the peak vertical displacements at the west end of the wall always occurred in coincidence with the maximum (eastward) interstory drifts, whereas those at the east end of the wall in coincidence with the minimum (westward) interstory drift. The vertical (uplift) displacements of both the corridor and corner shear walls were very small (<1 mm) during the service level event (EQ8) but increased significantly (> 10 mm for the corridor walls) during the MCE event (EQ9). It is also observed that that the corridor shear walls underwent slightly larger uplift displacements than those of the corner shear walls.

Figure 8.28 compares the peak wall end vertical (uplift) displacements of the shear walls at level 1 and level 4 between the pre-fire and post-fire MCE tests (EQ7 vs EQ9). It is noted that the uplift displacements of the west wall end occurred in coincidence with the maximum (eastward) interstory drifts, whereas those of the east wall end occurred in coincidence with the minimum (westward) interstory drifts. Result comparison reveals that the uplift displacements of individual shear walls underwent comparable uplift displacements during the two MCE tests (EQ7 and EQ9). However, the uplift displacements of the level 1 corridor shear walls were substantially larger uplift displacements than those at level 4 as a result of larger tie-down rod axial force demands at level 1. In addition, the uplift displacements of the corridor shear walls at level 1 were also slightly larger than those of the corner shear walls at the same level.

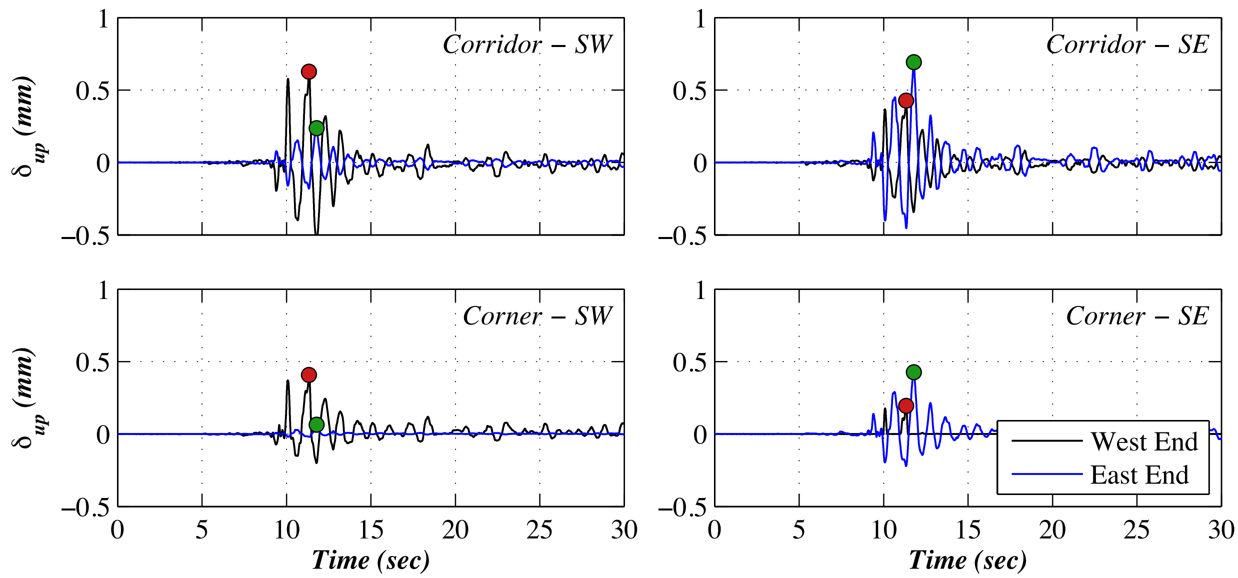

Figure 8.26. Wall end vertical displacement histories of level 1 corridor (first row) and corner (second row) shear walls during test EQ8.

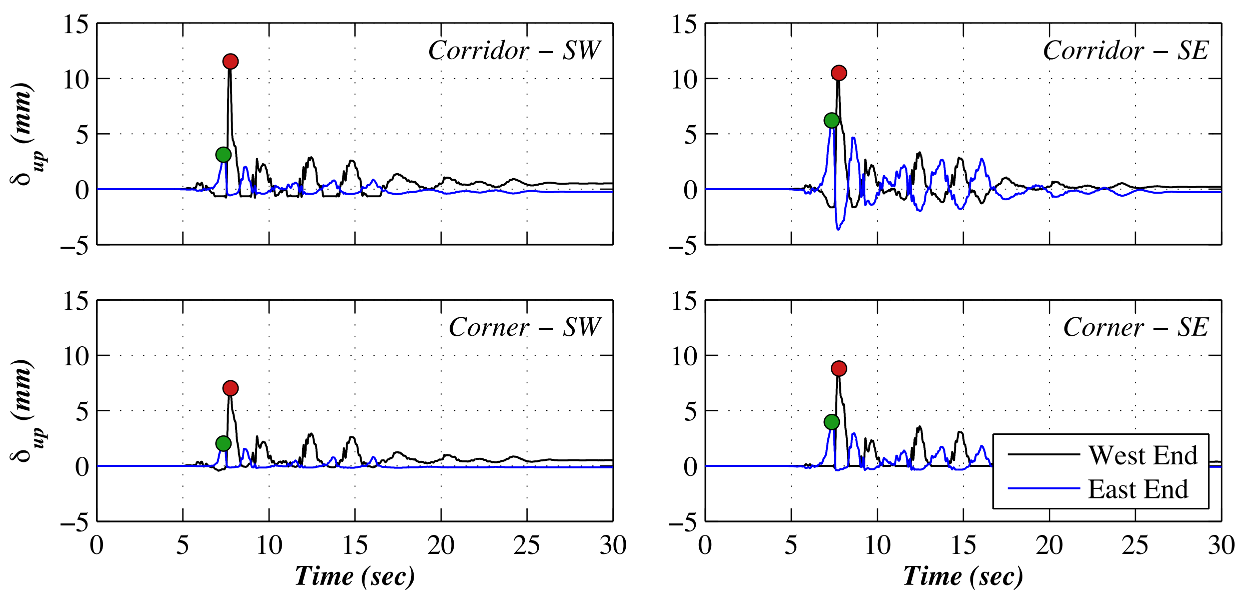

Figure 8.27. Wall end vertical displacement histories of level 1 corridor (first row) and corner (second row) shear walls during test EQ9.

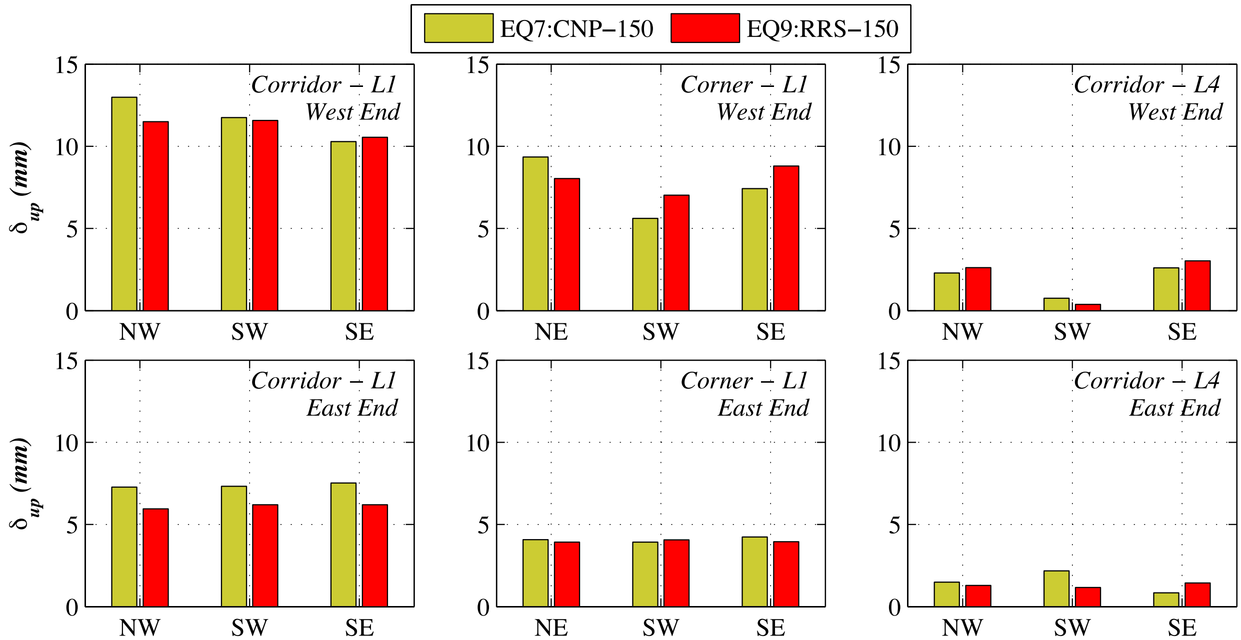

Figure 8.28. Comparison of peak wall end vertical (vertical) displacements of the level 1 and level 4 shear walls between the *MCE level* tests (EQ7 and EQ9).

8.3 Physical Observation

Rapid inspection was conducted following the service level aftershock event (EQ8) and confirmed no observed damage to the building due to its low seismic demands (PIDR < 0.2 % and PFA < 0.2 g). The final physical inspection of test building was conducted following the completion of the near-fault extreme earthquake event (EQ9). Since the appliances were not involved in the post-fire test sequence and the damage to the door system is presented in Chapter 6, this section focuses on physical damage of the structural components at its final state. To obtain a comprehensive knowledge of the final structural damage of the test building, inspection of the building interior involved the sheathing damage documentation and subsequently the wall framing and the sheathing steel of the structural panels by removing the compartment-side gypsum panels. Similar to pre-fire MCE inspection, damage occurred in the post-fire extreme MCE event was marked using solid red lines.

Due to the extremely large drift demands at level 2 of the building (transient PIDR exceeded 12% and residual IDR reached ~6%) during the final earthquake test (EA9), the building developed a soft-story mechanism at the completion of the test (Figure 8.29). The excessive interstory drift demands inflicted extremely severe damage on the structural components of level 2 and, importantly, revealed the ultimate damage mechanism of the lateral loading resisting system. The test building, however, resisted collapse largely due to redistribution of loads and the framing action of the continuous rod tie-down system. Damage to the remaining levels of the test building remained similar to those observed in the pre-fire test sequence, despite the continued increase of the interstory drift demands. In this regard, this section first summarizes the observed structural damage of level 2 and subsequently the structural damage of the remaining levels.

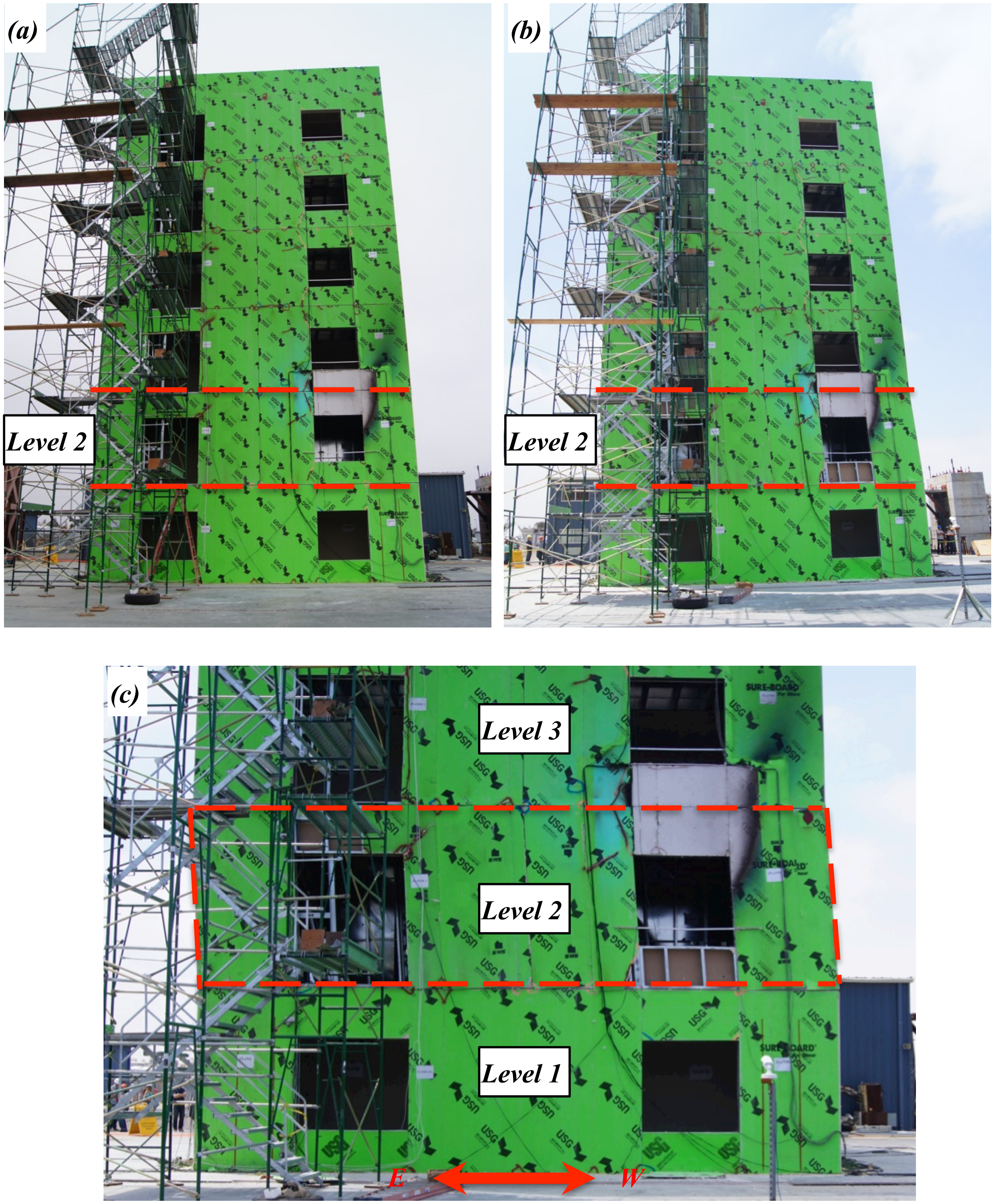

Figure 8.29. North elevation of the test building: (a) pre-EQ9 condition, and (b) post-EQ9 condition, and (c) post-EQ9 condition at the lower three levels.

8.3.1 Structural Damage: Level 2

Figure 8.30 through Figure 8.34 show the damage photos related to the sheathing damage of the wall system of level 2. It is noted that the structural panel steel sheathing of the corridor shear walls were located on the corridor side, while those of the corner walls were located on the exterior side. The building interior (compartment side) was sheathed with Type X gypsum panels of the four compartments. Except for the northeast compartment, the remaining three compartments of level 2 were the burn compartments that were directly exposed to live fire loads prior to the extreme MCE earthquake test (EQ9). The sheathing damage of the level 2 wall system is summarized in Table 8.3.

Table 8.3. Summary of sheathing damage of the level 2 wall system at the final state.

Type of wall	*Damage description*
Corridor shear wall	Corridor-side steel sheathed panels: completely detached panels, steel sheathing global buckling, and gypsum delamination (Figure 8.30a-d)
	Compartment-side gypsum panels: complete detached or fallen panels (Figure 8.31a, Figure 8.32c, Figure 8.33e, Figure 8.34c)
Corner shear wall (longitudinal)	Exterior-side steel sheathed panels: local buckling of steel sheathing at the bottom corner, panels remained attached (Figure 8.29c)
	Compartment-side gypsum panels: partially detached or fractured panels for the fire test compartments (Figure 8.31e, Figure 8.32d, Figure 8.33c), severely distorted panels for the non-fire test compartment (Figure 8.34e)
Corner shear wall (transverse)	Exterior-side steel sheathed panels: no occurrence of steel sheathing buckling, panels remained attached
	Compartment-side gypsum panels: loosely attached panels for the fire test compartments (Figure 8.31c, Figure 8.32a, Figure 8.33a), panels remained attached for the non-fire test compartment (Figure 8.34a)
Gravity wall	Exterior-side gypsum panels: corner crushing and fractures, fallen window sill panels (Figure 8.29c)
	Compartment-side gypsum panels: complete detached or fallen panels for the fire test compartments (Figure 8.32e), severely distorted panels for the non-fire test compartment (Figure 8.34d)
Partition wall	Partially detached or loosely attached panels on both sides of the walls (Figure 8.31b, Figure 8.32b, Figure 8.33b, Figure 8.34b)

Figure 8.30. Damage to corridor shear wall steel sheathing following the completion of the extreme MCE event (EQ9): (a) east corridor, (b) west corridor, (c) global buckling of steel sheathed panels, and (d) fastener pull-over failure.

Figure 8.31. Damage to the southwest compartment following the extreme MCE event (EQ9): (a) corridor shear wall, (b) interior partition wall, (c) transverse wall on the west side, (d) gravity wall, and (e) corner shear wall.

Figure 8.32. Damage to the southeast compartment following the extreme MCE event (EQ9): (a) transverse shear wall on the east side, (b) interior partition wall, (c) corridor shear wall, (d) corner shear wall, (e) gravity wall.

Figure 8.33. Damage to the northwest compartment following the extreme MCE event (EQ9): (a) transverse shear wall on the west side, (b) interior partition wall, (c) corner shear wall, (d) gravity wall, and (e) corridor shear wall.

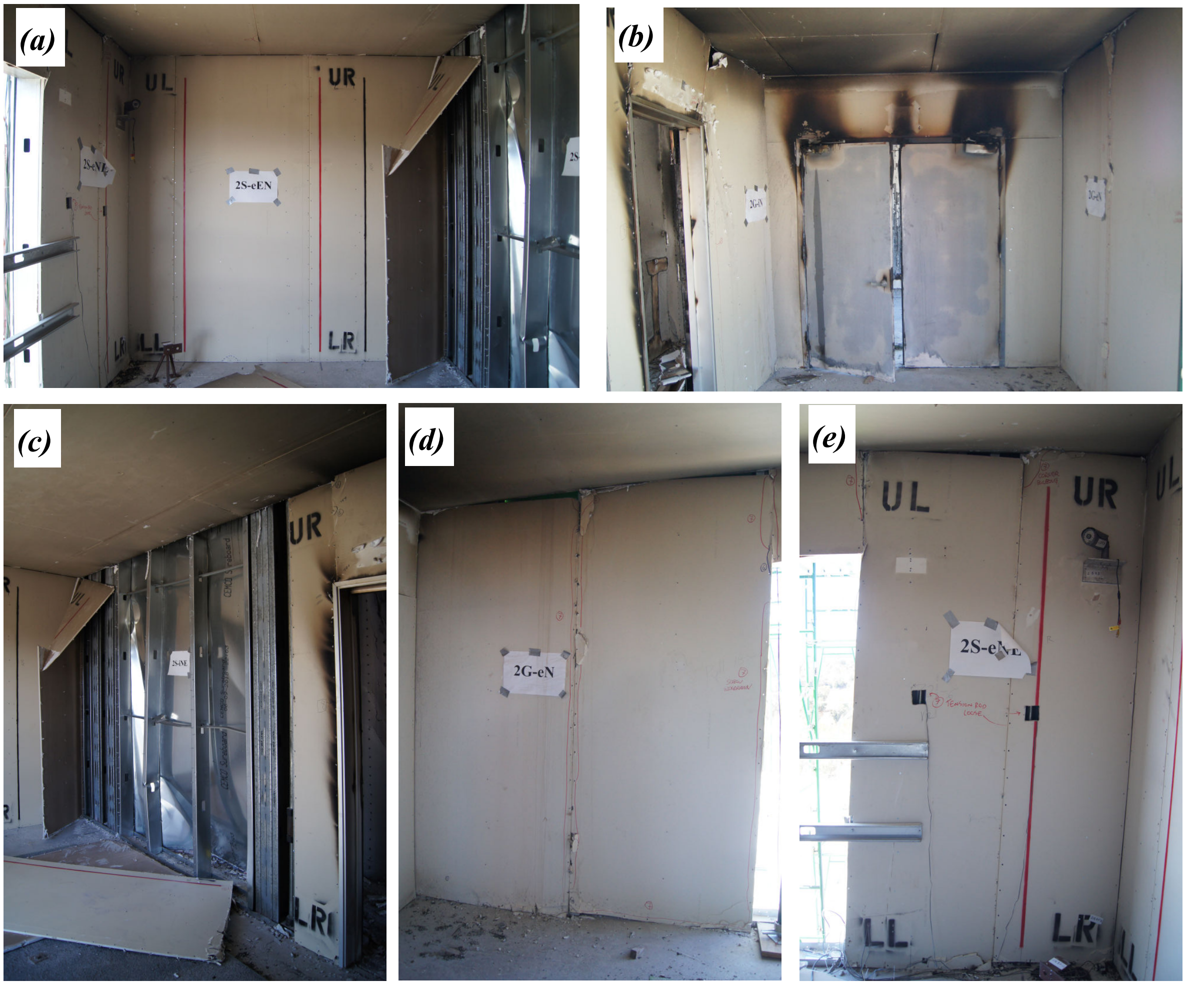

Figure 8.34. Damage to the northeast compartment following the extreme MCE event (EQ9): (a) transverse shear wall on the east side, (b) interior partition wall, (c) (b) corridor shear wall, (d) gravity wall, and (e) corner shear wall.

To document the physical damage of the steel framing and the continuous tie-down assemblies (including tie-down rods and compression posts), the compartment-side gypsum panels were removed to provide access for inspection. Figure 8.35 through Figure 8.38 show the damage photos related to the steel framing and tie-down assembly damage of the corridor shear walls. Figure 8.39 through Figure 8.42 show the damage photos related to the framing and tie-down assembly damage of the longitudinal corner shear walls. Figure 8.43 and Figure 8.44 show the damage photos related to the framing and tie-down assembly damage of the two transverse corner shear walls in the southwest and southeast compartment, while Figure 8.45 shows the damage photos of the exterior gravity wall framing (south side). Key characteristics regarding the damage to level 2 wall framing and tie-down assemblies are summarized as follows:

- *Corridor Shear Walls*: Due to the increase of unbraced length of the framing studs as a result of loss of sheathing panels on both sides of the wall, the vertical studs sustained extensive damage in the form of both global torsional buckling and local flange buckling (Figure 8.38c and e). In addition, local flange buckling of the bottom tracks also occurred at several locations. In contrast, the compression posts (stud packs) did not experience global buckling as a result of much larger strength and stiffness compared to the wall studs (spaced at 0.6 m), although a few instances of local flange buckling occurred at the base of the stud packs. All corridor shear wall tie-down rods performed well without connection failures.
- *Longitudinal Corner Shear Walls*: The (exterior side) structural panel steel sheathing remained attached to the framing to provide lateral stability to the framing. No global buckling or local buckling of the vertical studs and bottom tracks was detected (Figure 8.42a and b). In addition, the compression posts (stud packs) all performed well with no apparent damage. However, it is important to note that the west end tie-down rod in the southeast corner shear wall suffered the only instance of connection failure during the final test (Figure 8.40b and d), while all remaining tie-down rods performed well with no observed damage.
- *Transverse Corner Shear Walls*: Since the transverse corner shear walls were subjected to out-of-plane loading, the wall framing (studs and tracks) and the tie-down assemblies all performed well without apparent damage (Figure 8.43 and Figure 8.44).
- *Gravity Walls*: The (exterior-side) sheathing panels remained attached to the framing. No apparent damage to the vertical studs and bottom tracks was detected (Figure 8.45).

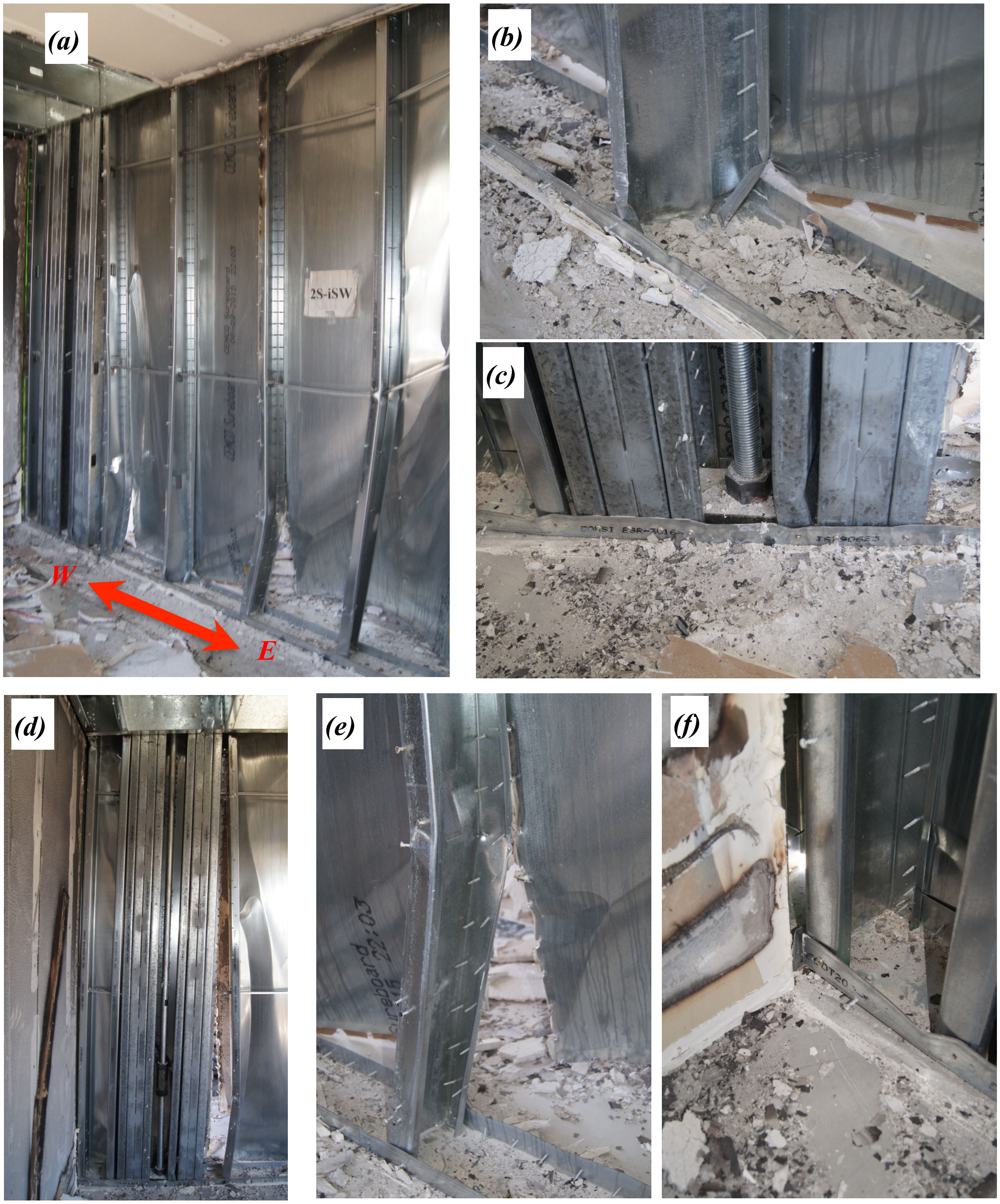

Figure 8.35. Southwest corridor shear wall at level 2 following of the extreme MCE event (EQ9): (a) wall framing, (b) stud local buckling at the base and stud-to-track connection failure, (c) compression post local buckling at the base, (d) tie-down assembly (west side), (e) stud global buckling, and (f) detached bottom track (west end of the wall).

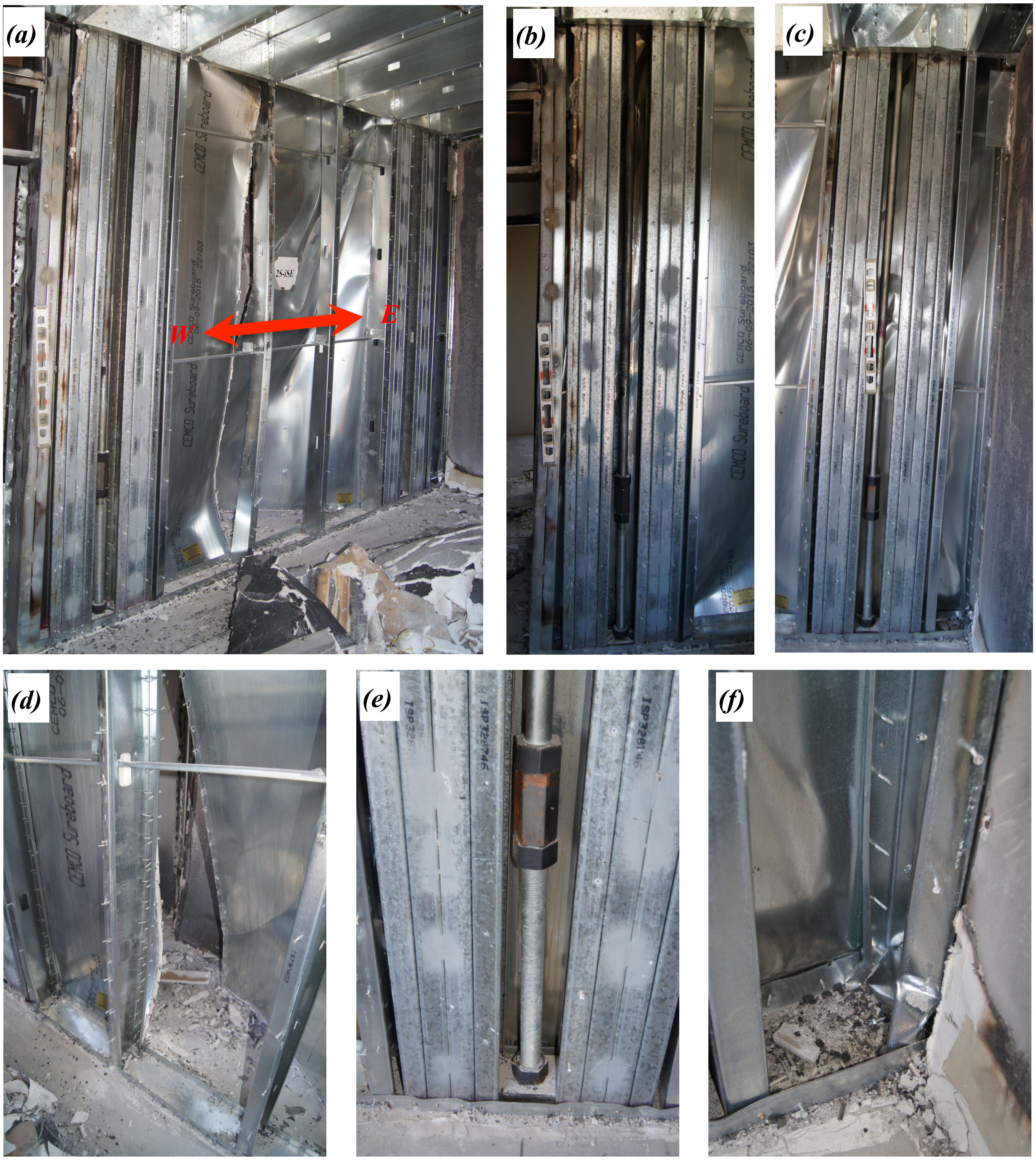

Figure 8.36. Southeast corridor shear wall at level 2 following the extreme MCE event (EQ9): (a) wall framing, (b) tie-down assembly (west side), (c) tie-down assembly (east side), (d) stud global buckling, (e) tie-down rod connection and bottom track flange buckling, and (f) crushed stud at the east end of the wall.

Figure 8.37. Northwest corridor shear wall at level 2 following the extreme MCE event (EQ9): (a) wall framing, (b) stud and track local buckling, (c) buckled and detached bottom track (west end of the wall), (d) tie-down assembly (east side), (e) crushed stud, and (f) stud global buckling.

Figure 8.38. Northeast corridor shear wall at level 2 following the extreme MCE event (EQ9): (a) CFS framing, (b) tie-down assembly (east side), (c) stud global buckling, (d) bottom track and tie rod bearing connection, and (e) vertical study and bottom track flange buckling.

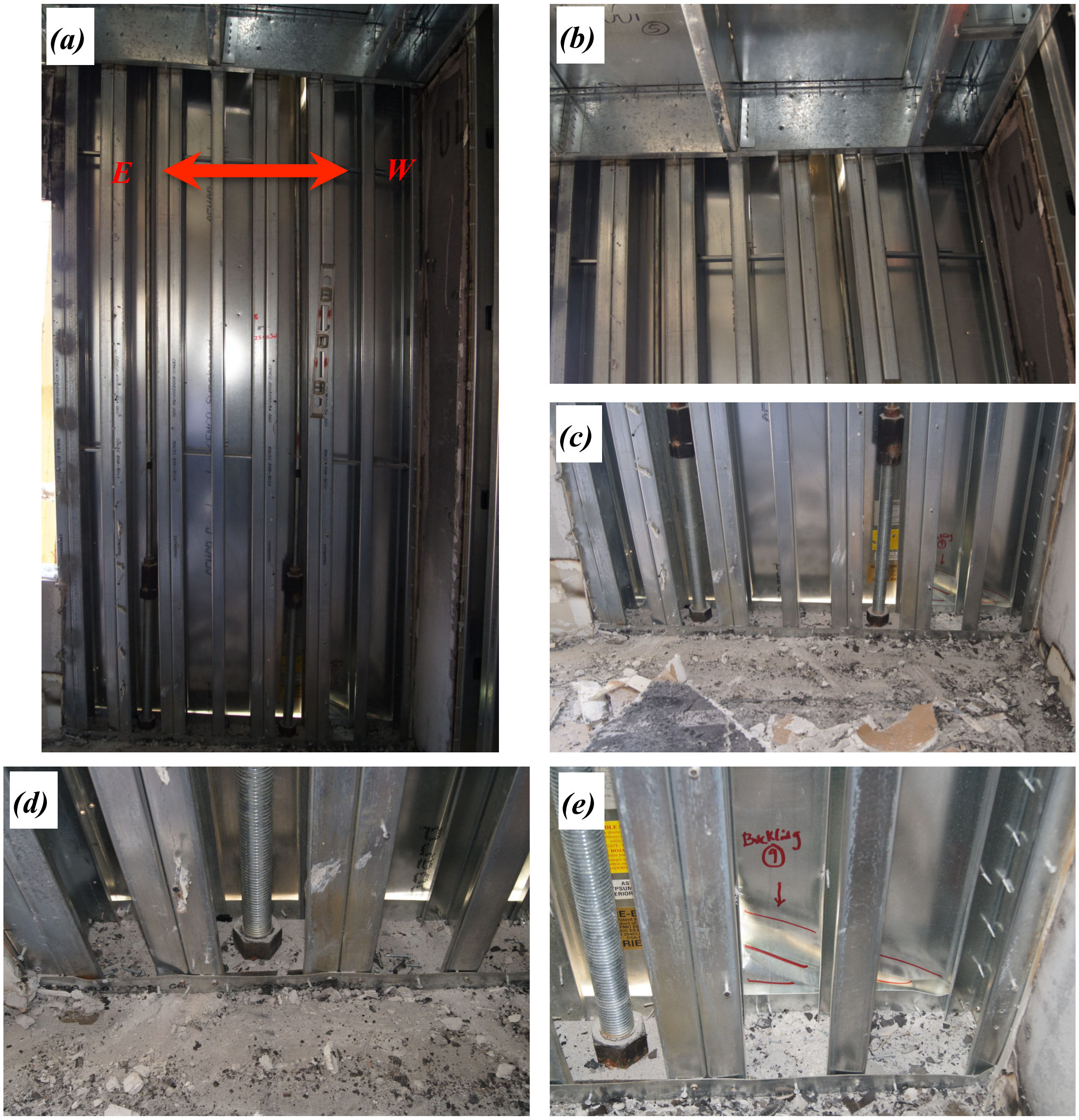

Figure 8.39. Southwest corner shear wall at level 2 following the completion of the extreme MCE event (EQ9): (a) wall framing, (b) upper framing and joist rim track, (c) lower framing and bottom track, (d) bottom track flange buckling, and (e) local buckling of exterior steel sheathing at the bottom corner and bottom track flange buckling.

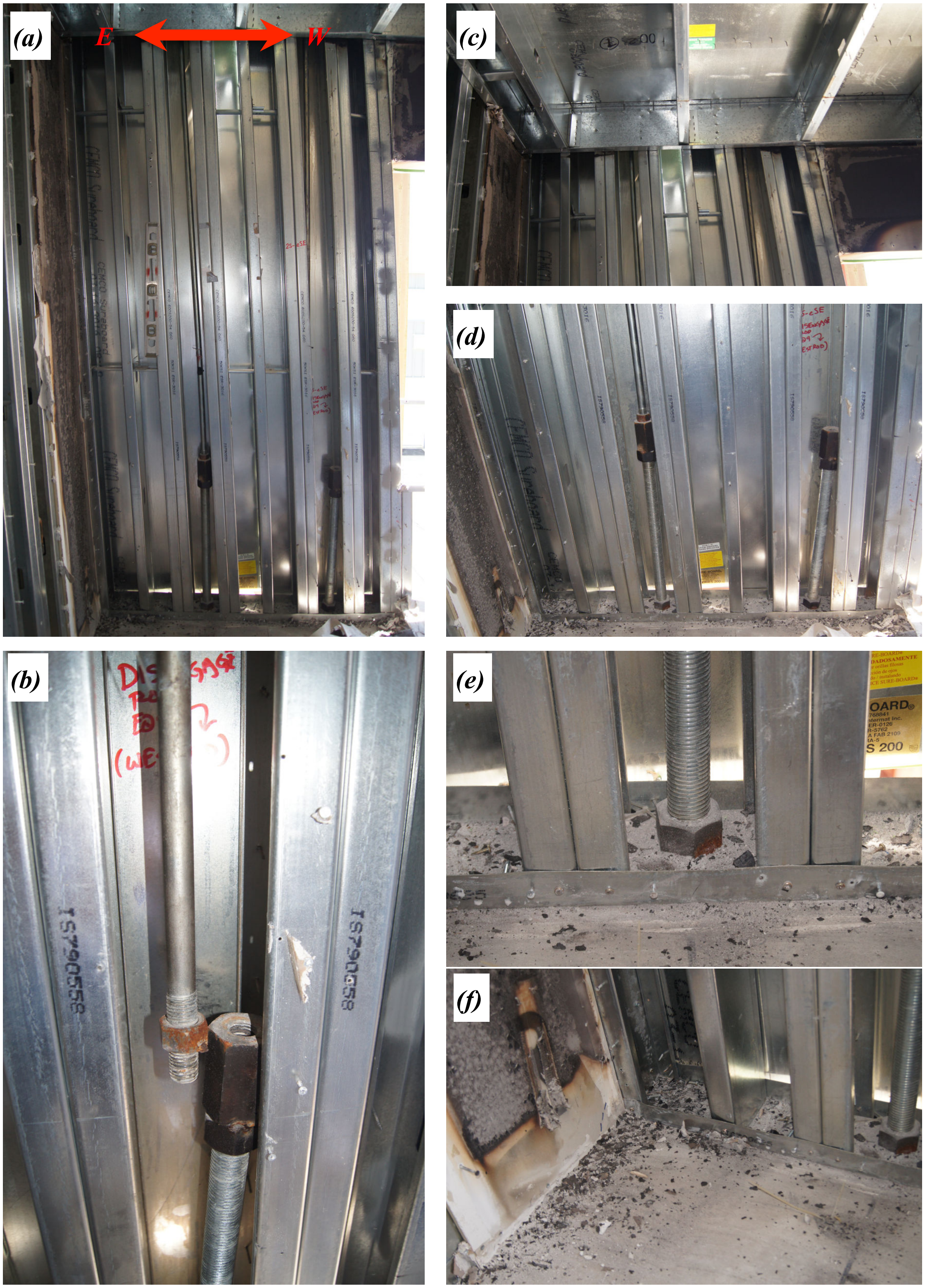

Figure 8.40. Southeast corner shear wall at level 2 following the extreme MCE event (EQ9): (a) wall framing, (b) close-up view of tie-down rod connection failure, (c) upper framing and joist rim track, (d) lower framing and tie-down rods, (e) bearing connection plate of west rod, and (f) bottom track (east end).

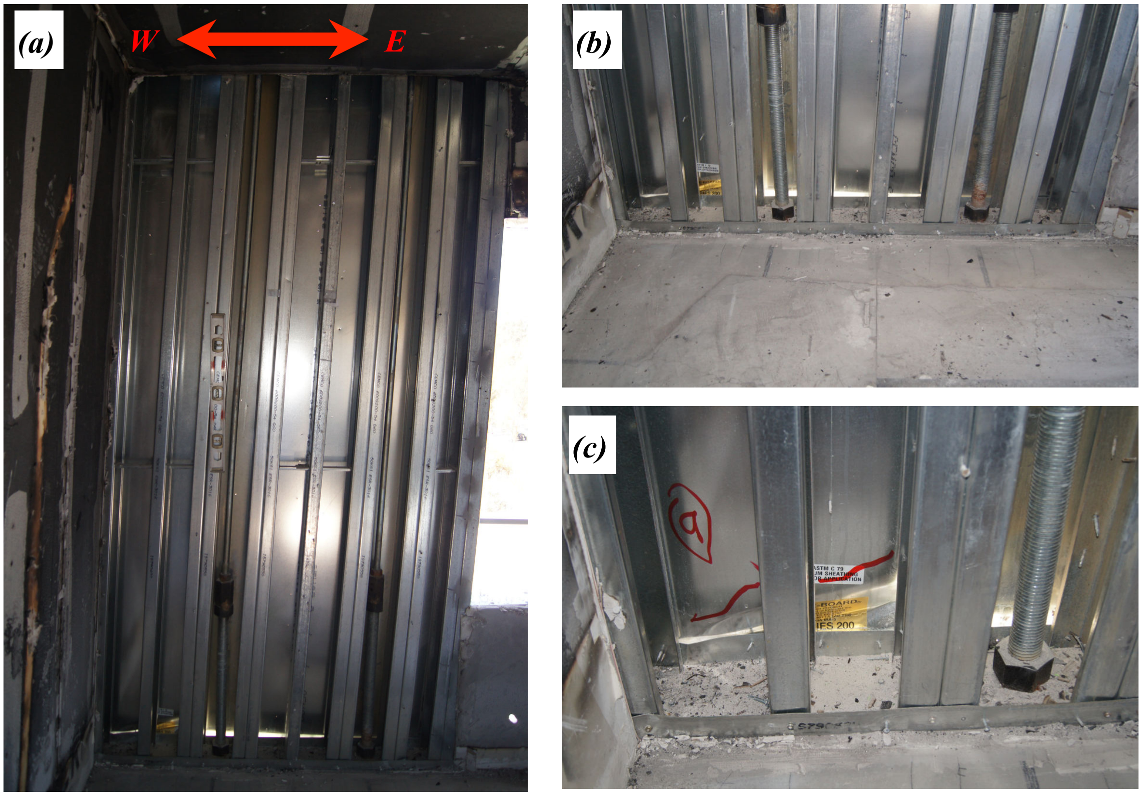

Figure 8.41. Northwest corner shear wall at level 2 following the extreme MCE event (EQ9): (a) wall framing, (b) lower framing and bottom track, and (c) local buckling of exterior steel sheathing at the bottom corner and bottom track flange buckling.

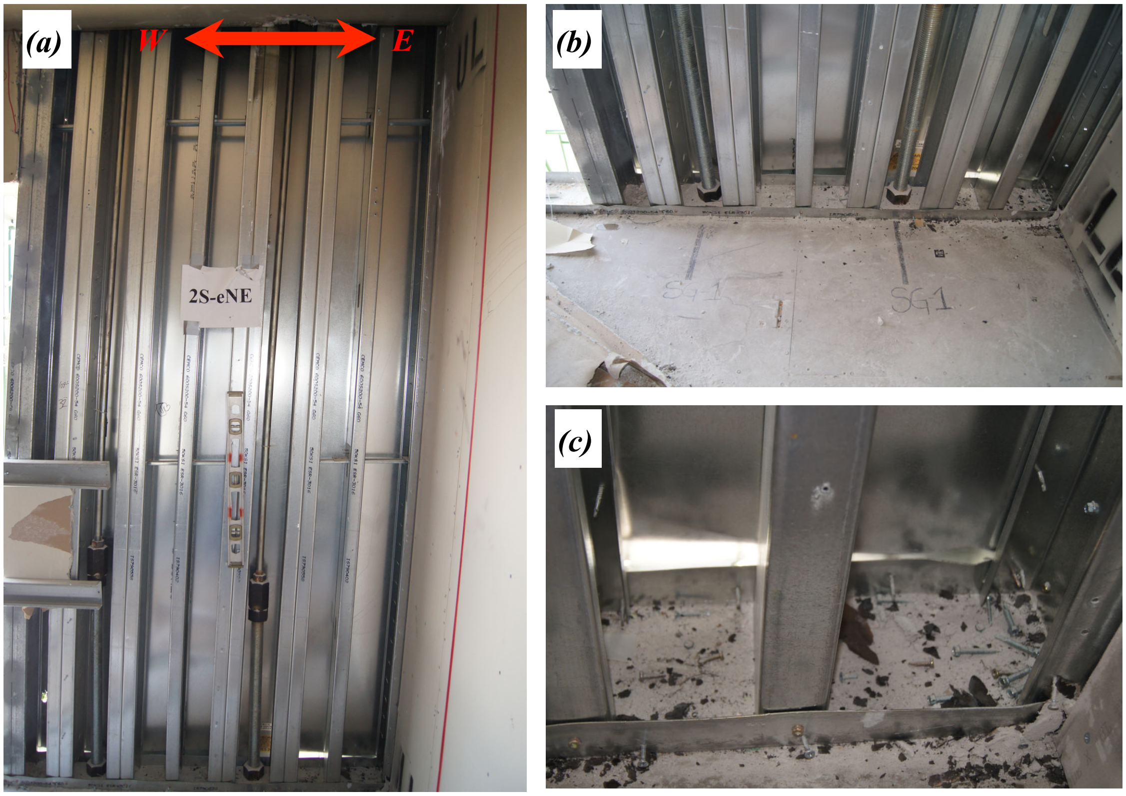

Figure 8.42. Northeast corner shear wall at level 2 following the extreme MCE event (EQ9): (a) wall framing, (b) lower framing and bottom track, and (c) sheathing connection failure.

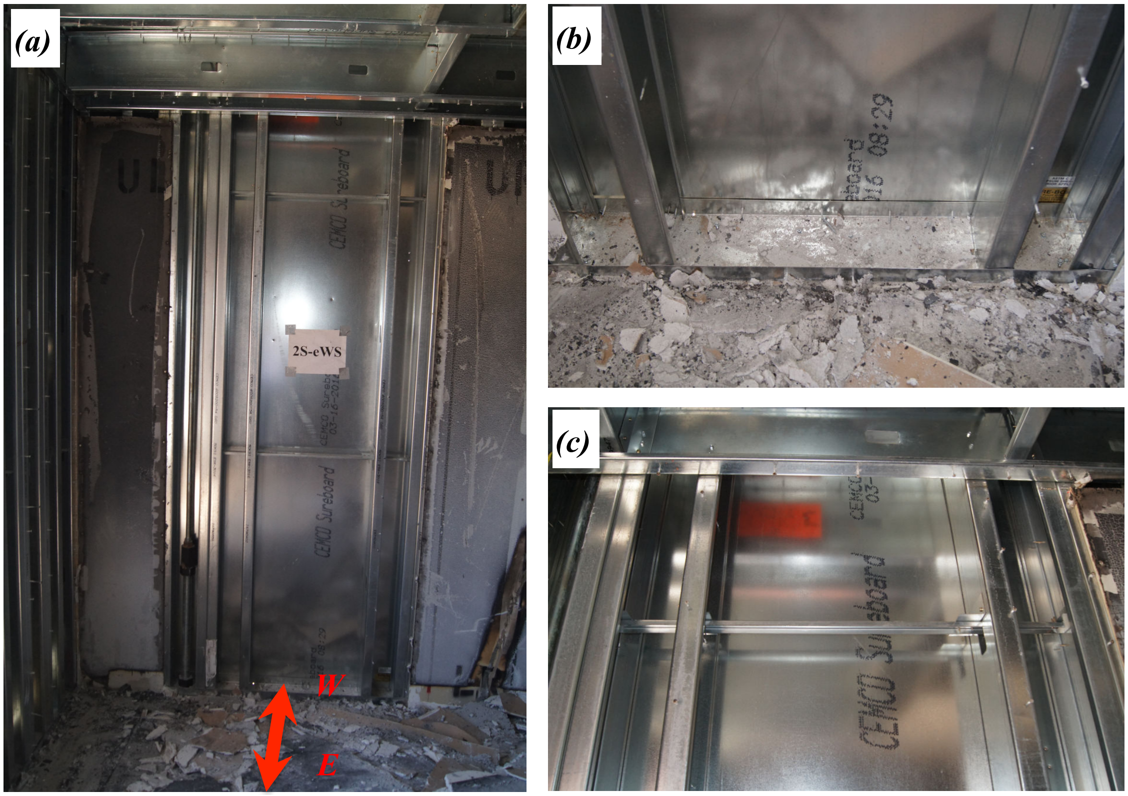

Figure 8.43. Southwest transverse corner shear wall at level 2 following the extreme MCE event (EQ9): (a) wall framing, (b) bottom track, and (c) exterior structural panel steel sheathing.

Figure 8.44. Southeast transverse corner shear wall at level 2 following the extreme MCE event (EQ9): (a) wall framing, (b) tie-down rod assembly, (c) bottom track, and (d) exterior structural panel steel sheathing.

Figure 8.45. Gravity wall (south side) at level 2 following the extreme MCE event (EQ9): (a) wall framing, (b) studs and bottom track (east), and (c) studs and bottom track (middle).

8.3.2 Structural Damage: All Levels Except Level 2

Although the PIDRs at all levels except level 2 achieved during the post-fire extreme MCE event (EQ9) were slightly larger than the corresponding PIDRs achieved during the pre-fire MCE test (EQ7), the observed damage modes of the structural components remained similar to those occurred during the pre-fire MCE event (EQ7). This section summarizes the observed structural damage to sheathing and joist rim tracks at the final inspection stage as well as damage observed following the removal of the compartment-side gypsum panels (i.e., wall framing, sheet sheathing, and tie-down assemblies).

Figure 8.46 through Figure 8.50 show the typical damage of the sheathing and joist rim tracks of all levels except level 2(on a floor-by-floor basis). Since damage to the different compartments at the same level appeared similar, the figures only show the damage of the northwest compartment. Sheathing and joist rim track damage continued to develop at all levels expect level 6 during the extreme MCE event (EQ9). In specific, the corridor wall sheathing panel damage appeared more severe compared to the gypsum panels on the other side of the walls. Typical damage occurred in the form of loosened or severe crushed panels, particularly at the boundaries between the shear walls and the gravity walls. Damage to the gypsum panels was most extensive around the window and door openings. Sheathing damage at level 3 and 4 appeared more severe as a result of higher drift demands (Figure 8.47c-d and Figure 8.48c-d). In addition, localized (flange or web) buckling of the rim tracks became pervasive at all levels except level 6. This type of damage occurred at the rim tracks above the shear wall-gravity wall boundaries or the wall-opening boundaries as a result of the discontinued vertical structural elements. The diaphragm joists and joist-to-rim track connections at all these levels performed well with no apparent damage. Damage of level 6 remained minimally for both non-fire-damaged sheathing (northwest compartment, Figure 8.50a-b) and the fire-damaged sheathing (southwest compartment, Figure 8.50c-d),

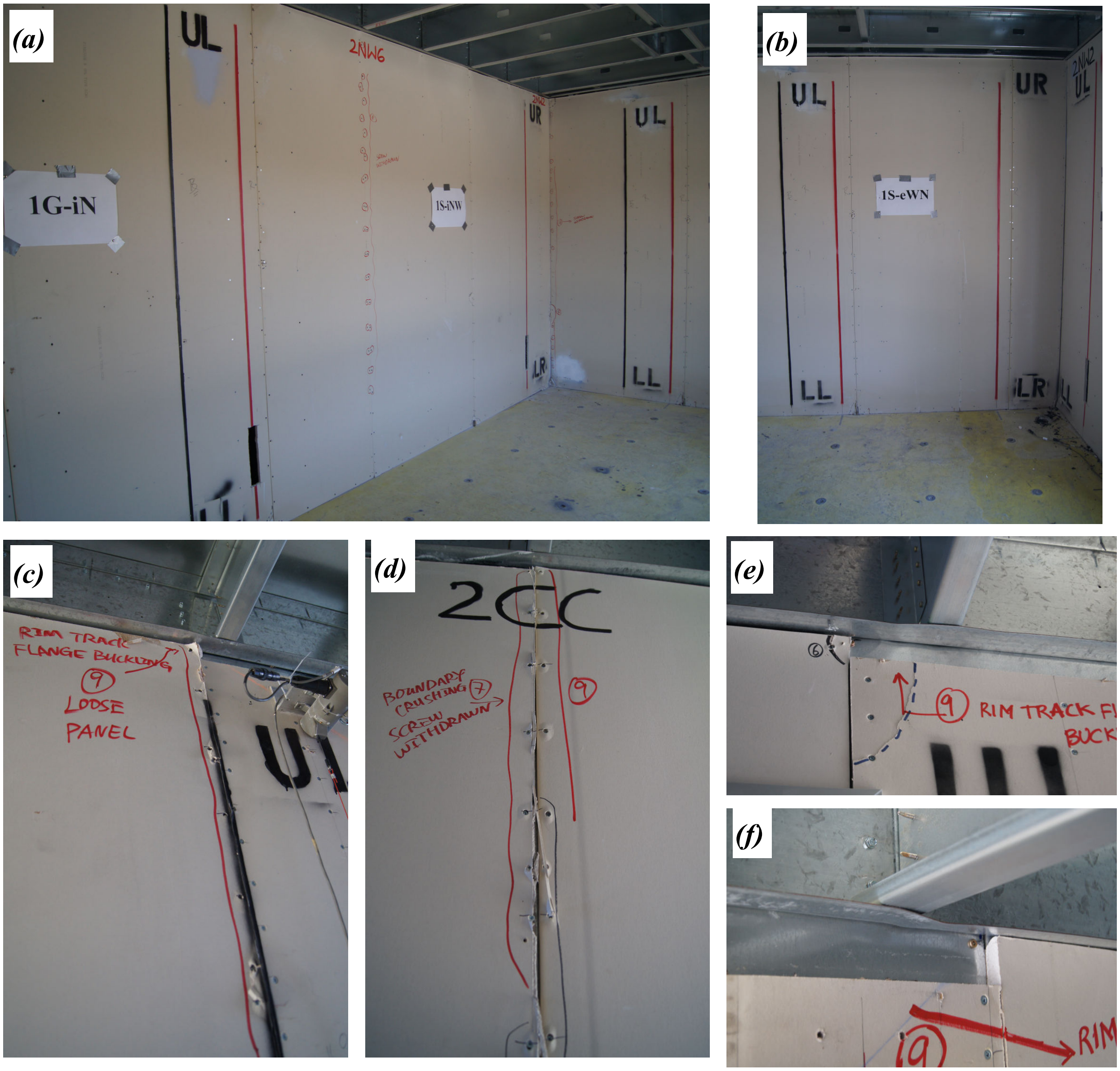

Figure 8.46. Damage to gypsum sheathing and joist rim tracks at level 1 following the extreme MCE event (EQ9).

Figure 8.47. Damage to gypsum sheathing and joist rim tracks at level 3 following the extreme MCE event (EQ9).

Figure 8.48. Damage to gypsum sheathing and joist rim tracks at level 4 following the extreme MCE event (EQ9).

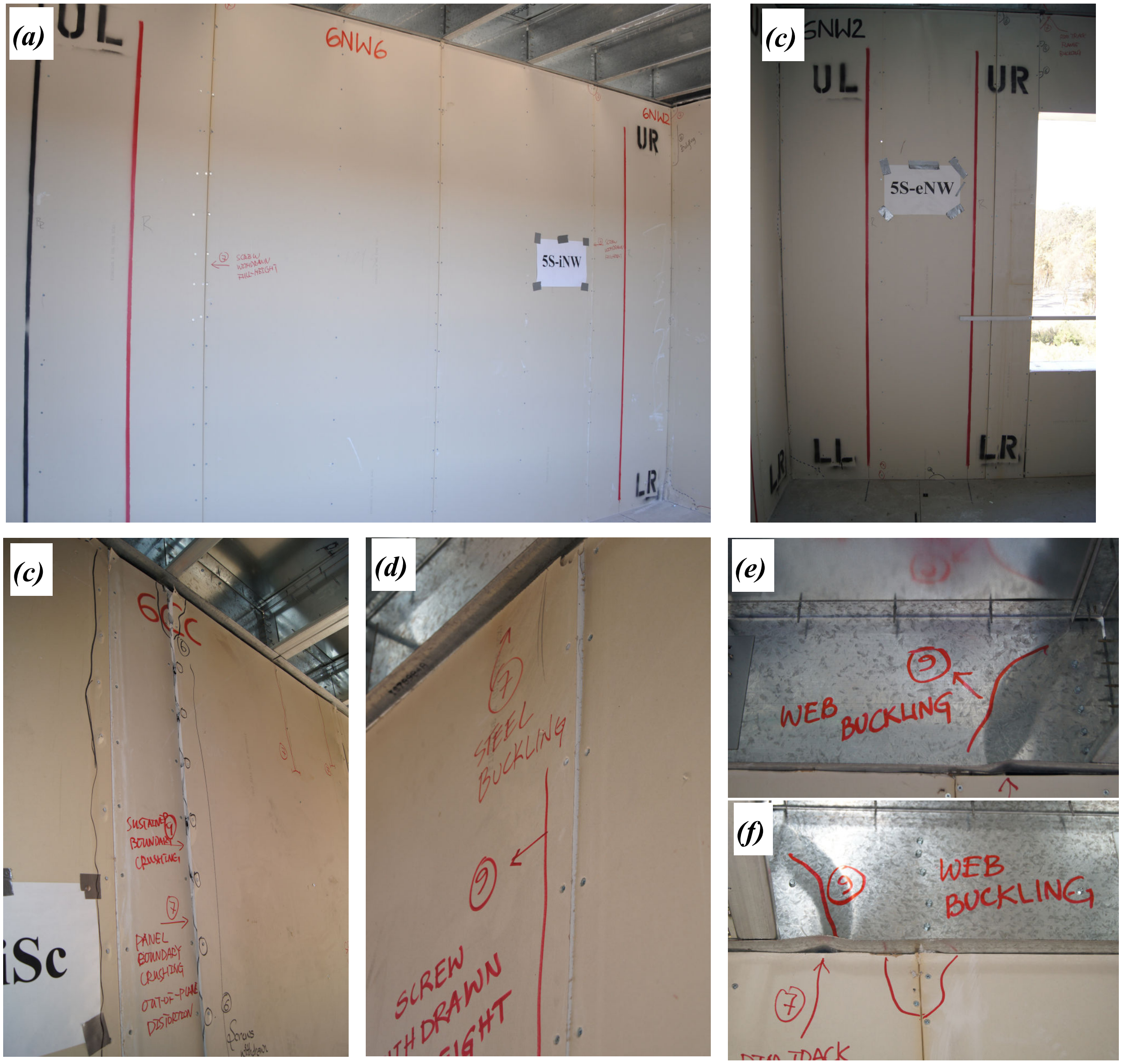

Figure 8.49. Damage to gypsum sheathing and joist rim tracks at level 5 following the extreme MCE event (EQ9).

Figure 8.50. Damage to gypsum sheathing and joist rim tracks at level 6 following the extreme MCE event (EQ9).

Figure 8.51 through Figure 8.55 show the damage photos related to the interior framing damage of the northwest corridor shear walls at the level 1, 3, 4, and 5 as well as the southwest corridor shear wall of level 6 (on a floor-by-floor basis). The corridor shear walls sustained sheathing steel local buckling at all levels except level 6. However, no visible damage to the corridor wall steel framing (studs and tracks) and the tie-down assemblies was detected following the extreme MCE event (EQ9). In addition, the longitudinal and transverse corner shear wall framing and the tie-down assemblies (except level 2) sustained no apparent damage, despite the large seismic drift demands (>2% at level 3 and 4) attained during the extreme MCE event (EQ9).

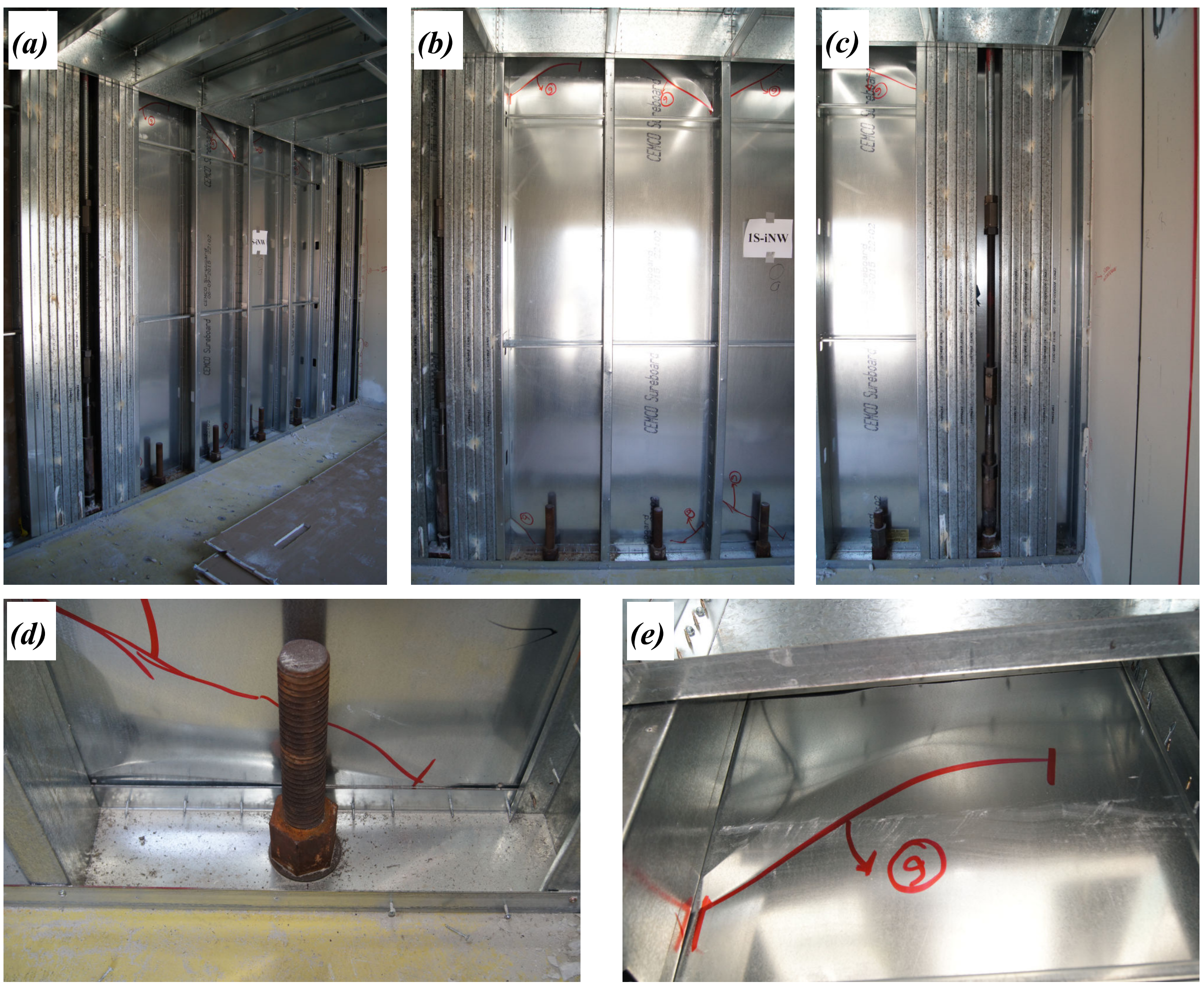

Figure 8.51. Northwest corridor shear wall at level 1 following the extreme MCE event (EQ9): (a) wall framing, (b) steel sheathing, (c) tie-down rod assembly (west side), (c) local buckling of steel sheathing at the bottom, and (e) local buckling of steel sheathing at the top.

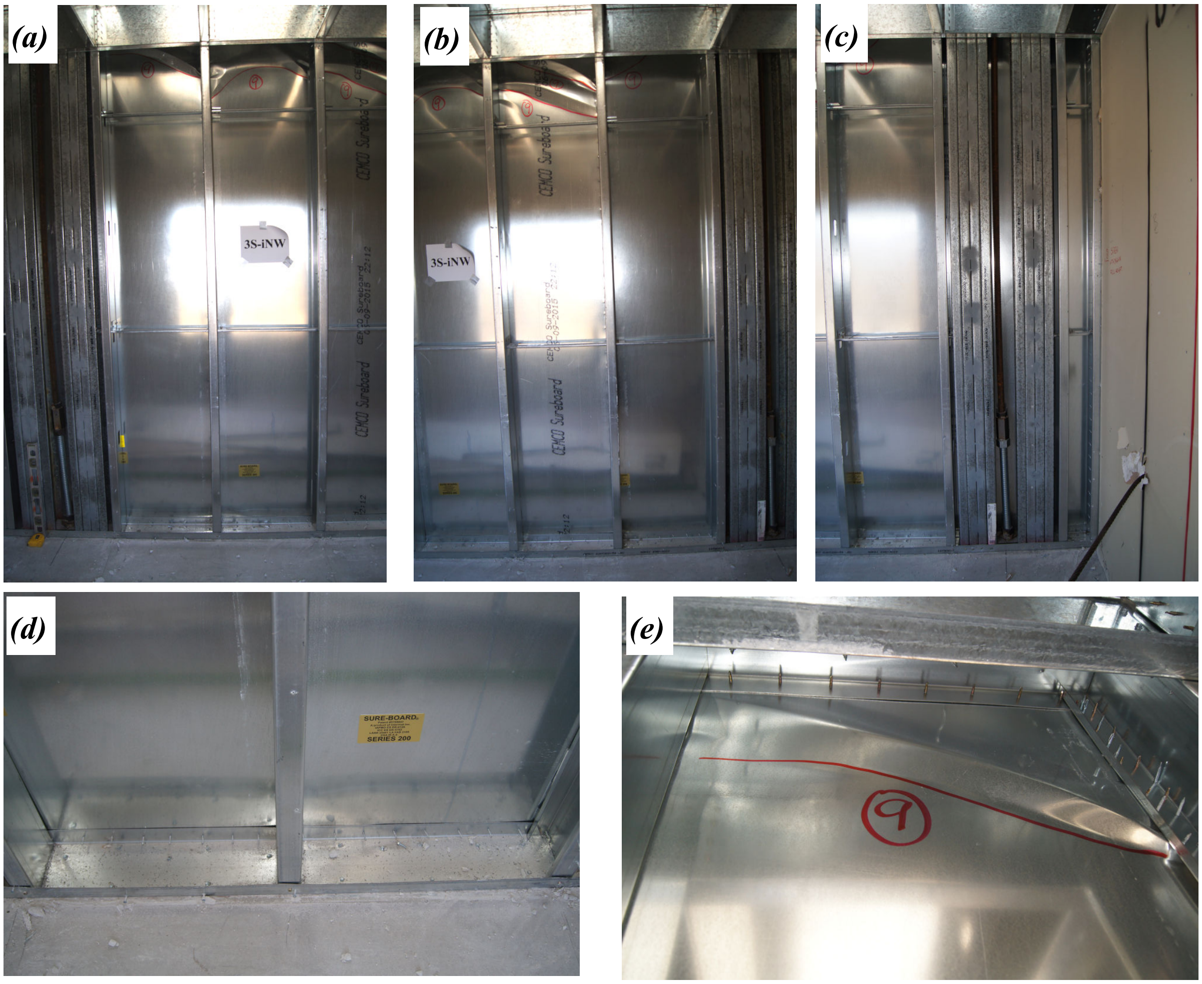

Figure 8.52. Northwest corridor shear wall at level 3 following the extreme MCE event (EQ9): (a) steel sheathing (east side), (b) steel sheathing (west side), (c) tie-down rod assembly (west side), (d) bottom track and lower sheathing, and (e) local buckling of steel sheathing at the top.

Figure 8.53. Northwest corridor shear wall at level 4 following the extreme MCE event (EQ9): (a) wall framing, (b) steel sheathing, (c) bottom track and lower sheathing, and (d) local buckling of steel sheathing at the top.

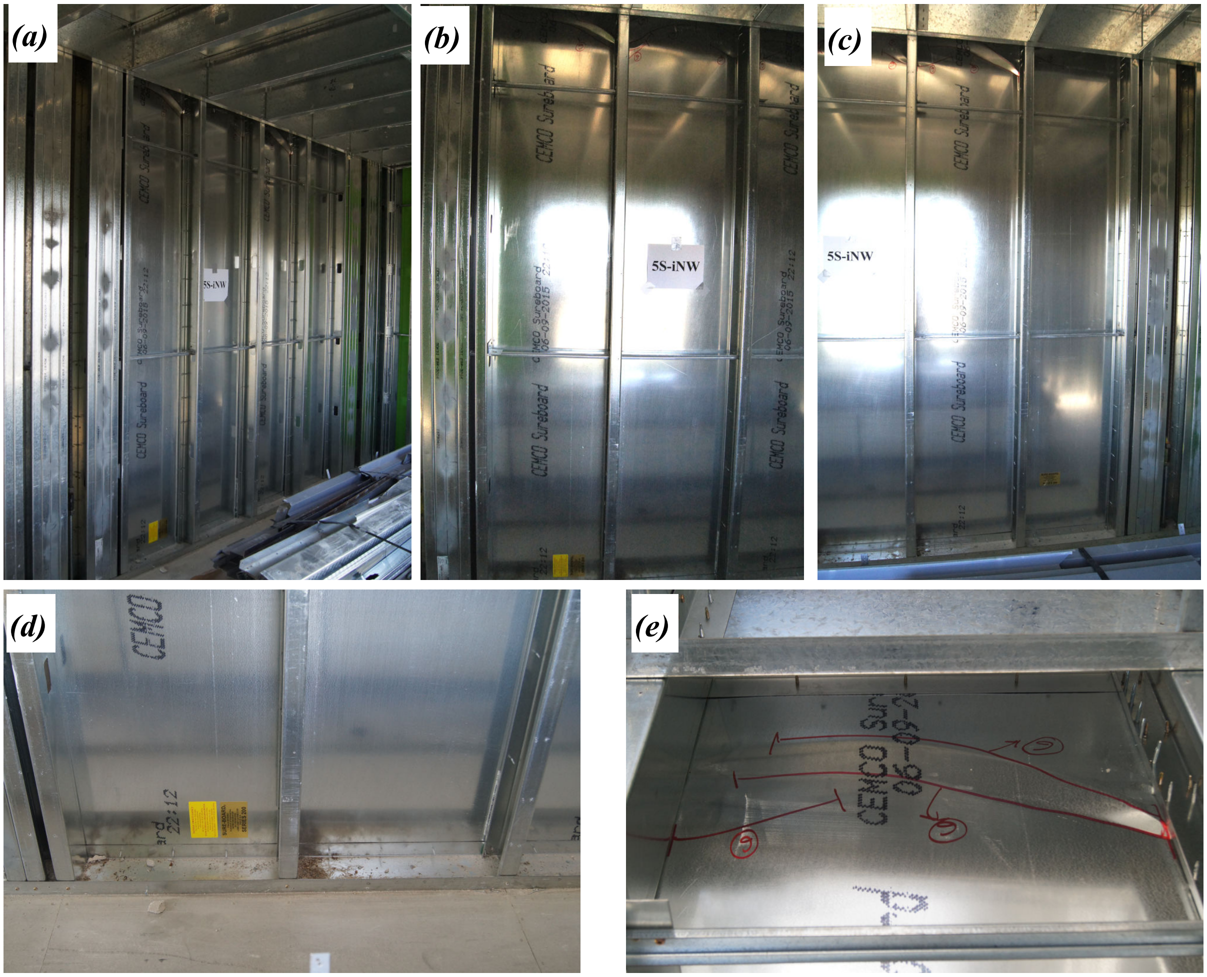

Figure 8.54. Northwest corridor shear wall at level 5 following the extreme MCE event (EQ9): (a) wall framing, (b) steel sheathing (east side), (c) steel sheathing (west side), (d) bottom track and lower sheathing, and (e) local buckling of steel sheathing at the top.

Figure 8.55. Southwest corridor shear wall at level 6 following the extreme MCE event (EQ9): (a) wall framing, (b) steel sheathing and tie-down assembly (west side), (c) steel sheathing and tie-down assembly (east side).

9 CONCLUSIONS

9.1 Motivations and Scope

A substantial growth in the use of cold-formed steel (CFS) framed construction has recently been observed, notably in high seismic regions in the western United States. Structural systems of this kind consist of light-gauge framing members (e.g., studs, tracks, joists) attached with sheathing materials (e.g., wood, sheet steel). CFS-framed structures can offer lower installation and maintenance costs than other structural types, particularly when erected with prefabricated assemblies. They are also durable, formed of an inherently ductile material of consistent behavior, lightweight, and manufactured from recycled materials. Compared to other lightweight framing solutions, CFS is non-combustible, an important basic characteristic to minimize fire spread. While these lightweight systems provide the potential to support the need for resilient and sustainable housing, the state of understanding regarding their structural behavior in response to extreme events, in particular earthquakes and ensuing hazards, remains relatively limited.

To advance knowledge regarding the multi-hazard performance of mid-rise CFS construction, a full-scale six-story cold-formed steel building was constructed and tested on the UCSD Large High Performance Outdoor Shake Table test facility between April and July 2016. Within the three-week test program, the test building was first subjected to a suite of seven earthquake motions with progressively increasing motion intensity (from service to MCE level). Following the first seven earthquake tests, live fire tests were conducted on the earthquake-damage building in six strategically selected rooms to evaluate the performance of fire protection systems and the impact of seismic damage of the building and the associated characteristics of the fires that ensued. Finally, for the first time, the test building was subjected two post-fire earthquake tests, including a low-amplitude 'aftershock' and an extreme near-fault target MCE-scaled motion. In addition, low-amplitude white noise and ambient vibration data were collected during construction and test phases to support identification of the dynamic characteristics of the test building throughout the test program.

A rich set of data has emerged from this test program that enables systematic studies of the dynamic characteristics, the seismic and fire response of the building, and the observed physical damage of the test building during the earthquake and fire tests. Test results from this experimental research project will be important to the practitioners in several aspects: (i) evaluating the seismic and post-earthquake fire performance, (ii) supporting advancement of engineering models for use in current design practice, (iii) contributing to next- generation design codes, and (iv) improving construction and design practices.

9.2 Major Findings

This report presents a comprehensive study of the system-level performance of the full-scale CFS building under a unique simulated multi-hazard scenario (earthquake and post-earthquake fire tests). The global and local responses of the test building during the earthquake tests as well as the compartment temperature response of the building during the fire tests are discussed in detailed. The physical damage of the structural systems and nonstructural components of the test building at various stages throughout the test program is summarized and associated with the demands of the building during the extreme loading scenarios. In addition, the low-amplitude vibration data collected from the experimental program allowed for a comprehensive system identification study to understand the evolution of the modal parameters (i.e., natural frequencies, damping ratios, and mode shapes). Key findings from this unique test program are summarized as follows:

1. ***Pre-fire Earthquake Tests***: The test building suffered minimal damage during the service level earthquake tests and remained largely in the quasi-linear range, with very low drift demands imposed on the specimen (interstory drift $< 0.2\%$). During the design level earthquake test, the corridor shear and gravity walls at level 3 and 4 suffered damage in the form of gypsum panel crushing and fastener withdrawal when the interstory drifts at these two levels reached about 1.0%. This is corroborated by the fact that the building fundamental period increased by more than 50%. Damage continued to progress as the interstory drift exceeded 1.5% during the maximum considered earthquake (MCE) test, however observed damage to the building remained readily repairable, with the structural shearwalls at the lower floors (those that could be inspected) developing their intended local steel sheathing buckling mechanism near attachment points along framing member perimeters. The building structural components performed satisfactorily throughout the pre-fire earthquake test sequence. The most significant damage to the structural system, as noted, occurred in the form of buckled sheet steel on the corridor shear

walls composite panels. The pre-fire earthquake test sequence however do highlight the potential risk of fuel and fire ignition following the earthquakes, as the various appliances placed in the building were prone to large movements, bracing or restraint failure, and tipping in some cases.

2. ***Fire Tests***: Post-flashover conditions were achieved in all six compartment fire tests at the given ventilation conditions, with the corresponding maximum compartment temperatures ranging between 800 °C and 1100 °C (four out of six tests exceeding 1000 °C). The elevated temperature caused significant degradation of interior fire rated gypsum wallboards on sheet steel and plain fire rated gypsum wallboards sans sheet steel, leading to loss of structural strength. Loss of rigidity in floor sheathing due to degradation of cement board on top of the sheet steel caused significant floor deflections (about 1.5 cm). Thermal bowing of floor diaphragm systems were observed after the fire tests, which is indicative of significant flow of heat from the floor system under consideration. The dehydrated and detached ceiling panel may cause potential overhead hazards in the case of an aftershock event, and the extended flames through the building exterior openings also emphasize the high likelihood of travelling fire hazards. It is recommended that further investigation be conducted to assess the fire performance of light-gauge buildings with realistic architectural features (glazed windows, exterior and interior wall finishes) and appliances.

3. ***Post-fire Earthquake Tests***: The low-amplitude aftershock (EQ8) significantly attenuated seismic acceleration demands in the building as a result of the elongated period caused by the pre-fire earthquake sequence. No further damage to the building occurred as a result of the relatively low seismic drift demands (PIDR <0.2%). The extreme near-fault earthquake test scaled to a target MCE level (EQ9) induced excessively large drift demands (PIDR exceeded 12% and residual drift reached ~6% at level 2) to the building and resulted in the formation of a soft story mechanism at level 2. Damage to the structural systems at this level occurred in the form of complete detachment of wall sheathing panels as well as global and local buckling of the framing members (studs and tracks), while the structural damage to the remaining levels remained similar to those observed during the pre-fire earthquake test phase. The extremely severe damage to the wall systems at level 2 caused complete loss of structural integrity of corridor and exterior longitudinal shear walls. Despite the excessive damage to level 2, the test

building resisted collapse due to redistribution of loads and framing action of the building rod tie-down system.

4. ***Low-amplitude Vibration Tests***: Using test data recorded from the low-amplitude vibration tests during the construction and test phases, the modal properties of the test building are analyzed using four state-of-the-art time-domain system identification methods, including two input-output and two output-only methods. It is observed that installation of interior gypsum panels on the CFS wall framing increased the natural frequencies of the test building by about 10% as a result of the stiffness contribution of the gypsum-to-framing fasteners, while the damping ratios of the building remained consistent at the various stages throughout the construction phase. During the earthquake and fire test phase, the progression of building damage resulted in reduced natural frequencies and increased damping ratios. The frequency losses remained sufficiently small (<10%) during the serviceability level earthquake test sequence but increased substantially following the design level test (as much as 40%) and the MCE level test (exceeded 50%) due to much larger seismic drift demands. However, the fire tests induced no substantial change in frequency to the earthquake-damaged building. The evolution of the identified modal parameters correlates well with the progression of damage observed during the test program, demonstrating the effectiveness of the system identification methods for structural damage assessment and health monitoring.

REFERENCES

AISI (American Iron and Steel Institute) (2007). *North American Standard for Cold-formed Steel Farming—Lateral Design*. AISI S213, Washington DC.

AISI (American Iron and Steel Institute) (2012a). *North American Specification for the Design of Cold-formed Steel Structural Members.* AISI S100, Washington DC.

Allemang, R.J., and Brown, D. L. (1982). "A correlation coefficient for modal vector analysis." *Proc., 1st International Modal Analysis Conference*, Orlando, FL.

ASCE (American Society of Civil Engineers) (2010). *Minimum Design Loads for Buildings and Other Structures*. ASCE 7, Reston, VA

Astroza, R., Ebrahimian, H., Conte, J. P., Restrepo, J. I., and Hutchinson, T.C. (2016). "System identification of a full-scale five-story reinforced concrete building tested on the NEES‐UCSD shake table." *Structural Control and Health Monitoring*, 23(3), 535-559.

Balh, N., DaBreo, J., Ong-Tone, C., El-Saloussy, K., Yu, C. , and Rogers, C. A. (2014). "Design of steel sheathed cold-formed steel framed shear walls." *Thin-Walled Struct.* , 75, 76–86.

Branston, A., Chen, Y. C. , Boudreault, F. A. , and Rogers, C. A. (2006). "Testing of light-gauge steel-frame—Wood structural panel shear walls." *Can. J. Civ. Eng.*, 33(5), 561–572.

Bock, Y., Melgar, D., and Crowell, B.W. (2011). "Real-time strong-motion broadband displacements from collocated GPS and accelerometers." *Bull. Seismol. Soc. Am.,* 101(6), 2904-2925.

Goldberg, D., and Bock, Y. (2016). *Shake Table Experiments GPS Deployments: June-July, 2016*. Scripps Orbit and Permanent Array Center, La Jolla, CA

Della Corte, G., Fiorino, L., and Landolfo, R. (2006). "Seismic Behavior of Sheathed Cold-Formed Structures: Numerical Study." *ASCE J. Struct. Eng.*, 132(4), 558-569.

Dubina, D. (2008). "Behavior and performance of cold-formed steel-framed houses under seismic action." *J. Constr. Steel Res.*, 64 (7–8), 896–913.

Fiorino, L., Della Corte, G. , and Landolfo, R. (2007). "Experimental tests on typical screw connections for cold-formed steel housing." *Eng. Struct.*, 29(8), 1761–1773.

Fiorino, L.A., Iuorio, O., and Landolfo, R. (2009). "Sheathed cold-formed steel housing: A seismic design procedure." *Thin-Walled Struct.*, 47(8), 919–930.

Fülöp, L. A., and Dubina, D. (2004a). "Performance of wall-stud cold-formed shear panels under monotonic and cyclic loading. Part I: Experimental research." *Thin-Walled Struct.* , 42 (2), 321–338.

Fülöp, L. A., and Dubina, D. (2004b). "Performance of wall-stud cold-formed shear panels under monotonic and cyclic loading. Part II: Numerical modelling and performance analysis." *Thin-Walled Struct.* , 42 (2), 339–349.

Fülöp, L. A., and Dubina, D. (2006). "Design criteria for seam and sheeting-to-framing connections of cold-formed steel shear panels." *ASCE J. Struct. Eng.*, 132(4), 582–590.

Heylen, W., Lammens, S., and Sas, P. (1995). *Modal analysis testing and theory*. PMA-KU Leuven, Belgium.

Hoehler, M., and Smith, C. (2016). Influence of Fire on the Lateral Load Capacity of Steel-sheathed Cold-Formed Steel Shear Walls – Report of Test. *NISTIR 8160*, National Institute of Standards and Technology, Gaithersburg, MD.

Imregun M, and Ewins D. (1993). "Realization of complex mode shapes." *Proc., 11th International Modal Analysis Conference,* Kissimmee, FL.

James, G.H., Carne, T.G., and Lauffer, J.P. (1995). "The natural excitation technique (NExT) for modal parameter extraction from operating structures." *International Journal of Analytical and Experimental Modal Analysis*, 10(4), 260.

Juang, J.N., and Pappa, R. S. (1985). "An eigensystem realization algorithm for modal parameter identification and model reduction." *Journal of Guidance, Control, and Dynamics*, 8(5), 620-627.

Juang, J.N., Phan, M., Horta, L.G., and Longman, R.W. (1993). "Identification of observer/Kalman filter Markov parameters-Theory and experiments." *Journal of Guidance, Control, and Dynamics,* 16(2), 320-329.

Landolfo, R., Fiorino, L., and Della Corte, G. (2006). "Seismic behavior of sheathed cold-formed structures: Physical tests." *ASCE J. Struct. Eng.,* 132(4), 570–581.

Liu, P., Peterman, K.D., and Schafer, B.W. (2014). "Impact of construction details on OSB-sheathed cold-formed steel framed shear walls." *J. Constr. Steel Res.*, 101, 114–123.

Luco, J.E., Ozcelik, O., and Conte, J.P. (2009). "Acceleration tracking performance of the UCSD-NEES shake table." ." *ASCE J. Struct. Eng.*, 136(5), 481-490.

Moaveni B, He X, Conte J.P., Restrepo J.I., and Panagiotou M. (2011). "System identification study of a seven-story full-scale building slice tested on the UCSD-NEES shake table." *ASCE J. Struct. Eng.,* 137(6),705–717.

NFPA (National Fire Protection Association) (2013). *Standard for Fire Doors and Other Opening Protectives*. NFPA 80, Quincy MA.

Peeters, B., and De Roeck, G. (2001). "Stochastic system identification for operational modal analysis: a review." *Journal of Dynamic Systems, Measurement, and Control*, 123(4), 659-667.

Peterman, K.D., Stehman, M.J., Madsen, R.L., Buonopane, S.G., Nakata, N., and Schafer, B.W. (2016a). "Experimental seismic response of a full-scale cold-formed steel-framed building. I: System-level response." *ASCE J. Struct. Eng.*, 04016127.

Peterman, K.D., Stehman, M.J., Madsen, R.L., Buonopane, S.G., Nakata, N., and Schafer, B.W. (2016b). "Experimental seismic response of a full-scale cold-formed steel-framed building. II: Subsystem-level response." *ASCE J. Struct. Eng.*, 04016128.

Richardson, M.H., and Formenti, D.L. (1982). "Parameter estimation from frequency response measurements using rational fraction polynomials." *Proc., 1st IMAC Conference*, Orlando, FL.

Serrette, R., Encalada, J., Juadines, M. , and Nguyen, H. (1997). “Static racking behavior of plywood, OSB, gypsum, and fiberboard walls with metal framing.” *ASCE J. Struct. Eng.,* 123(8), 1079–1086.

Shamim, I., Dabreo, J., and Rogers, C.A. (2013). “Dynamic testing of single- and double-story steel-sheathed cold-formed steel-framed shear walls.” *ASCE J. Struct. Eng.*, 139(5), 807–817.

Shamim, I., and Rogers, C.A. (2013). "Steel sheathed/CFS framed shear walls under dynamic loading: Numerical modelling and calibration." *Thin-Walled Struct.*, 71, 57–71.

Shamim, I., and Rogers, C.A. (2015). " Numerical evaluation: AISI S400 steel-sheathed CFS framed shear wall seismic design method." *Thin-Walled Struct.*, 95, 48–59.

Skolnik, D.A. and Wallace, J.W. (2010). “Critical assessment of interstory drift measurements.” *ASCE Journal of Structural Engineering*, 136(12), 1574–1584.

Van Overschee, P. and De Moor, B. (1996). *Subspace Identification for Linear systems: Theory, Implementation, Applications.* Kluwer academic publishers, Boston, MA.

Welch, P. (1967). “The use of fast Fourier transform for the estimation of power spectra: a method based on time averaging over short, modified periodograms.” *IEEE Transactions on Audio and Electroacoustics*, 15(2), 70-73.

Yu, C. (2010). “Shear resistance of cold-formed steel framed shear walls with 0.686 mm, 0.762 mm, and 0.838 mm steel sheet sheathing.” *Eng. Struct.*, 32 (6), 1522–1529.

Zhang, W., Mahdavian, M., Li, Y., and Yu, C. (2016). “Experiments and Simulations of Cold-Formed Steel Wall Assemblies Using Corrugated Steel Sheathing Subjected to Shear and Gravity Loads.” *J. Struct. Eng.*, 143(3), 04016193.

APPENDIX A – PROJECT PARTICIPANTS

Table A.1. Project academic team

Name	*Title*	*Affiliation*
Tara Hutchinson	Professor (PI)	University of California, San Diego
Gilbert Hegemier	Professor (co-PI)	University of California, San Diego
Brian Meacham	Associate Professor	Worcester Polytechnic Institute
Xiang Wang	Postdoctoral Researcher	University of California, San Diego
Praveen Kamath	Postdoctoral Researcher	Worcester Polytechnic Institute
Srikar Gunisetty	Graduate Researcher	University of California, San Diego
Daniel Arthur	Research Assistant	Worcester Polytechnic Institute

Table A.2. Government and institutional sponsors

List of Sponsors
Department of Housing and Urban Development
California Seismic Safety Commission
Jacobs School of Engineering, University of California, San Diego
Department of Fire Protection Engineering, Worcester Polytechnic Institute

Table A.3. Industrial sponsors

Company Name	***Primary Contact***
Allegion	Tim Weller
CEMCO Steel	Fernando Sesma
DCI Engineers	Harry Jones
DPR Construction	Steve Helland
Insurance Institute for Business & Home Safety	Tim Reinhold
MiTek Structural Connectors	Jesse Karns
Rivante	Douglas Antuma
Society of Fire Protection Engineers (SFPE) Foundation	Maggie McGray
Southwest Carpenters Union	Thomas Rooney
State Farm Insurance	Pat Boyer, Jack Jordan, Larry Stevig
Suffolk Construction	Andrew Carniff
Sure-Board	Kelly Holcomb
SWS Panel	Diego Rivera
USG Building Materials	
United Scaffold, Inc.	Greg Leonard
Walters & Wolf	Rick Calhoun

APPENDIX B – SHAKE TABLE SPECIFICATIONS

The UCSD Large High Performance Outdoor Shake Table (LHPOST) is the largest outdoor shake table in the world and the largest shake table of its kind in the United States (Figure B.1). This experimental facility is currently operated within the Natural Hazards Engineering Research Infrastructure (NHERI) equipment inventory. Uniquely, it enables seismic testing of large scale and/or full-scale structural or geotechnical systems with realistic earthquake loading, extensive instrumentation and data archiving. This testing site is essential for capturing system responses of the full-scale tests that cannot be achieved at smaller scales.

Figure B.1. UCSD Large High Performance Outdoor Shake Table (LHPOST).

As shown in Figure B.2, the LHPOST test facility is composed of several essential components:

- A moving steel platen with it dimension of 7.6m x 12.2m and a weight of ~1700 kN.
- A reinforced concrete reaction mass block
- Two servo-controlled dynamic horizontal actuators equipped with high flow servo-valves to power the shake table
- A platen sliding system consisting of six vertical actuators to react against all vertical forces with very low friction allowing the table to operate at a high stroke and velocity capacity
- Two nitrogen-filled hold down struts to resist overturning moments
- A yaw restraint system consisting of two pairs of slaved hydrostatic pressure-balanced bearings

With the velocity, stroke capabilities, and the frequency bandwidth as summarized in Table B.1, the shake table is capable of accurately reproducing severe near-fault earthquake ground motions even for very large structural systems (nheri.ucsd.edu).

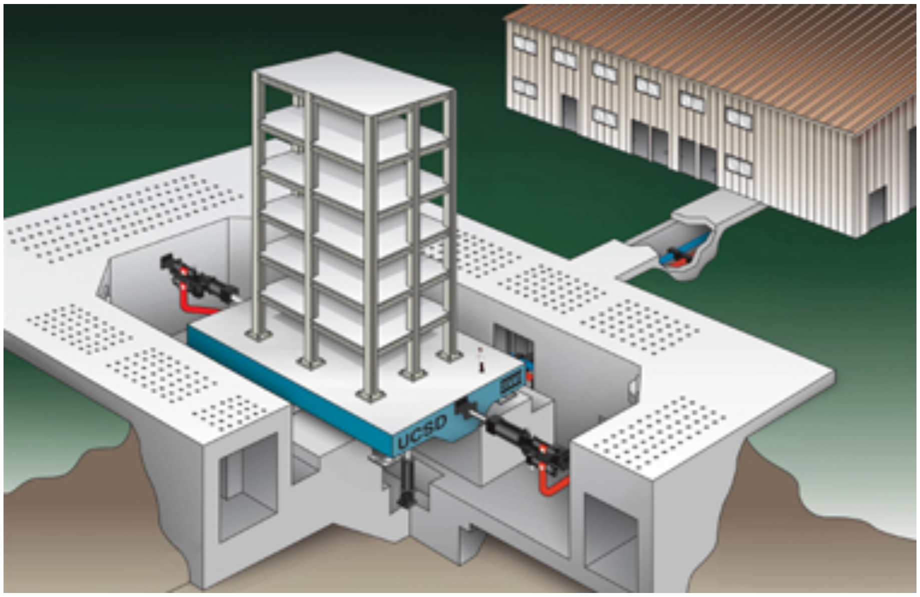

Figure B.2. Schematic view of the LHPOST test facility (nheri.ucsd.edu).

Table B.1. Shake table performance specifications

Dimension	7.6 m x 12.2 m
Peak acceleration: bare table (400 ton payload)	4.2 g (1.2 g)
Peak velocity	1.8 m/s
Displacement stroke	±0.75 m
Maximum (vertical) payload	20 MN
Force capacity of actuators	6.8 MN
Maximum overturning moment: bare table (400 ton payload)	35 MN-m (50 MN-m)
Frequency bandwidth	0-33 Hz

APPENDIX C – TEST PROTOCOL

Construction Phase – Day 1 (05/05/2016)

No.	Type of test	Sampling rate (Hz)
1	0.08 g pulse	240
2	1.5% g RMS white noise (4 min)	240
3	0.08 g pulse	240
4	3.0% g RMS white noise (4 min)	240
5	0.08 g pulse	240
6	5.0% g RMS white noise (4 min)	240
7	0.08 g pulse	240

Description: mass configuration 1 – unanchored interior gypsum with partial transversal partition wall installation.
Sensor list: 25 accelerometers (MEMS), 12 strain gauges, 1 linear potentiometer.
Notes: 20 min ambient vibration before and after the tests.

Construction Phase – Day 2 (05/16/2016)

No.	Type of test	Sampling rate (Hz)
1	shock (tire) test – location 1	240
2	shock (tire) test – location 2	240
3	shock (tire) test – location 3	240
4	0.08 g pulse	240
5	1.5% g RMS white noise (3 min)	240
6	0.08 g pulse	240
7	3.0% g RMS white noise (3 min)	240
8	0.08 g pulse	240
9	shock (tire) test – location 1	240
10	shock (tire) test – location 2	240
11	shock (tire) test – location 3	240

Description: mass configuration 2 – unanchored interior gypsum with partition wall & door installation completed.

Sensor list: 53 accelerometers (MEMS), 12 strain gauges, 1 linear potentiometer.

Construction Phase – Day 2 (05/16/2016)

No.	Type of test	Sampling rate (Hz)
1	shock (tire) test – location 1	240
2	shock (tire) test – location 2	240
3	shock (tire) test – location 3	240
4	0.08 g pulse	240
5	1.5% g RMS white noise (3 min)	240
6	0.08 g pulse	240
7	3.0% g RMS white noise (3 min)	240
8	0.08 g pulse	240
9	ambient vibration (20 min)	240

Description: mass configuration 3 (baseline) – unanchored interior gypsum with partition wall & door installation completed.
Sensor list: 53 accelerometers (MEMS), 12 strain gauges, 1 linear potentiometer.

Construction Phase – Day 3 (06/09/2016)

No.	Type of test	Sampling rate (Hz)
1	0.08 g pulse	240
2	1.5% g RMS white noise (3 min)	240
3	0.08 g pulse	240
4	3.0% g RMS white noise (3 min)	240
5	0.08 g pulse	240

Description: mass configuration 3 (baseline). Interior gypsum & partition wall fully anchored. Door installation completed. All doors open.
Sensor list: 63 accelerometers (MEMS), 12 accelerometers (Kinemetric), 67 strain gauges, 68 string potentiometers, 35 linear potentiometers.

No.	Type of test	Sampling rate (Hz)
1	0.08 g pulse	240
2	1.5% g RMS white noise (3 min)	240
3	0.08 g pulse	240
4	3.0% g RMS white noise (3 min)	240
5	0.08 g pulse	240

Description: mass configuration 3 (baseline). Interior gypsum & partition wall fully anchored. Door installation completed. All doors closed.
Sensor list: 63 accelerometers (MEMS), 12 accelerometers (Kinemetric), 67 strain gauges, 68 string potentiometers, 35 linear potentiometers.

Testing Phase – Day 1 (06/13/2016)

No.	Type of test	Sampling rate (Hz)	Starting time (PST) – Duration (sec)
1	1.5% g RMS white noise for building warm up and sensor engagement (1 min)	240	
2	0.08 g pulse	240	
3	1.5% g RMS white noise (3 min)	240	
4	3.0% g RMS white noise (3 min)	240	
5	**25% RIO360 – service level (EQ1)**	240	11:11:00 – 60
6	1.5% g RMS white noise (3 min)	240	
7	**25% CNP196 – service level (EQ2)**	240	11:36:54 – 60
8	1.5% g RMS white noise (3 min)	240	
building inspection & quick data check (table down)			
9	1.5% g RMS white noise for building warm up and sensor engagement (1 min)	240	
10	**25% CUREW – service level (EQ3)**	240	14:19:53 – 200
11	0.08 g pulse	240	
12	1.5% g RMS white noise (3 min)	240	
13	3.0% g RMS white noise (3 min)	240	

Testing Phase – Day 2 (06/15/2016)

No.	Type of test	Sampling rate (Hz)	Starting time (PST) – Duration (sec)
1	1.5% g RMS white noise for building warm up and sensor engagement (1 min)	240	
2	0.08 g pulse	240	
3	1.5% g RMS white noise (3 min)	240	
4	3.0% g RMS white noise (3 min)	240	
5	**25% CNP196 – service level (EQ4)**	240	10:05:51 – 60
6	0.08 g pulse	240	
7	1.5% g RMS white noise (3 min)	240	
8	3.0% g RMS white noise (3 min)	240	
building inspection & quick data check (table down)			
9	1.5% g RMS white noise for building warm up and sensor engagement (1 min)	240	
10	**50% CNP196 – 50% design level (EQ5)**	240	12:35:06 – 60
11	1.5% g RMS white noise (3 min)	240	
12	3.0% g RMS white noise (3 min)	240	
13	**100% CNP196 – design level (EQ6)**	240	13:00:51 – 60
14	0.08 g pulse	240	
15	1.5% g RMS white noise (3 min)	240	
16	3.0% g RMS white noise (3 min)	240	

Testing Phase – Day 3 (06/17/2016)

No.	Type of test	Sampling rate (Hz)	Starting time (PST) – Duration (sec)
1	1.5% g RMS white noise for building warm up and sensor engagement (1 min)	240	
2	0.08 g pulse	240	
3	1.5% g RMS white noise (3 min)	240	
4	3.0% g RMS white noise (3 min)	240	
5	**150% CNP196 – MCE level (EQ7)**	240	11:35:04 – 60
6	0.08 g pulse	240	
7	1.5% g RMS white noise (3 min)	240	
8	3.0% g RMS white noise (3 min)	240	

Testing Phase – Day 4 (07/01/2016)

No.	Type of test	Sampling rate (Hz)	Starting time (PST) – Duration (sec)
1	1.5% g RMS white noise (3 min)	240	
2	3.0% g RMS white noise (3 min)	240	
3	**25% RIO360 – service level “aftershock” (EQ8)**	240	09:41:52 – 60
4	1.5% g RMS white noise (3 min)	240	
5	3.0% g RMS white noise (3 min)	240	
building inspection & quick data check (table down)			
6	1.5% g RMS white noise for building warm up and sensor engagement (1 min)	240	
7	**150% RRS228 – near-fault MCE level (EQ9)**	240	11:25:13 – 60

Ambient Vibration Tests -- Construction Phase (05/04/2016 -- 05/31/2016)

Date	#	Test name	Starting time (PST) – duration (min)	DAQ (channel #)	Stairs condition
05/04/16	1	AMB-1A	07:59 – 60	MEMS (24)	Attached
	2	AMB-1B	12:56 – 60		
05/05/16	3	AMB-2A	08:04 - 20	MEMS (24)	Unattached
	4	AMB-2B	09:59 - 20		
	5	AMB-2C	13:42 - 20		
	6	AMB-2D	15:35 - 20		
05/06/16	7	AMB-3A	09:58 - 20	MEMS (24)	Unattached
	8	AMB-3B	13:58 - 20		
05/09/16	9	AMB-4A	10:19 - 20	MEMS (24)	Attached
	10	AMB-4B	14:22 - 20		
05/10/16	11	AMB-5A	10:08 - 20	MEMS (24)	Attached
	12	AMB-5B	14:01 - 20		
05/11/16	13	AMB-6A	09:59 - 20	MEMS (24)	Attached
	14	AMB-6B	13:53 - 20		
05/12/16	15	AMB-7A	10:00 - 20	MEMS (24)	Attached
	16	AMB-7B	14:04 - 20		
05/13/16	17	AMB-8A	09:54 - 20	MEMS (24)	Attached
	18	AMB-8B	15:01 - 20	MEMS (57)	
05/16/16	19	AMB-9A	08:10 - 20	MEMS (57)	Unattached
05/18/16	20	AMB-10A	10:09 - 20	MEMS (57)	Attached
	21	AMB-10B	14:08 - 20	MEMS (57)	
05/19/16	22	AMB-11A	09:56 - 20	MEMS (57)	Attached
	23	AMB-11B	13:59 - 20	MEMS (57)	
05/20/16	24	AMB-12A	10:04 - 20	MEMS (57)	Attached
	25	AMB-12B	14:30 - 20	MEMS (57)	
05/27/16	26	AMB-13A	14:04 - 20	MEMS (57)	Attached
05/31/16	27	AMB-14A	10:14 - 20	MEMS (57)	Attached
	28	AMB-14B	14:17 - 20	MEMS (57)	

Ambient Vibration Tests – Testing Phase (06/09/2016 -- 07/01/2016)

Date	#	Test name	Starting time (PST) – duration (min)	DAQ (channel #)	Stairs condition
06/09/16	29	AMB-E0	09:14 - 10	KIN (11)	Unattached
Pre-fire earthquake test phase (06/13/2016 -- 06/17/2016)					
06/17/16	30	AMB-E1	21:54 - 10	KIN (10)	Unattached
Fire test phase (06/27/2016 -- 06/29/2016)					
06/30/16	34	AMB-E2	12:58 - 12	MEMS (57)	Attached
Post-fire earthquake test phase (07/01/2016)					
07/01/16	35	AMB-E3	12:30 - 10	MEMS (57)	Unattached
Completion of test program					

Notes: bold-faced date indicates date of shake table testing

APPENDIX D – INPUT EARTHQUAKE MOTIONS

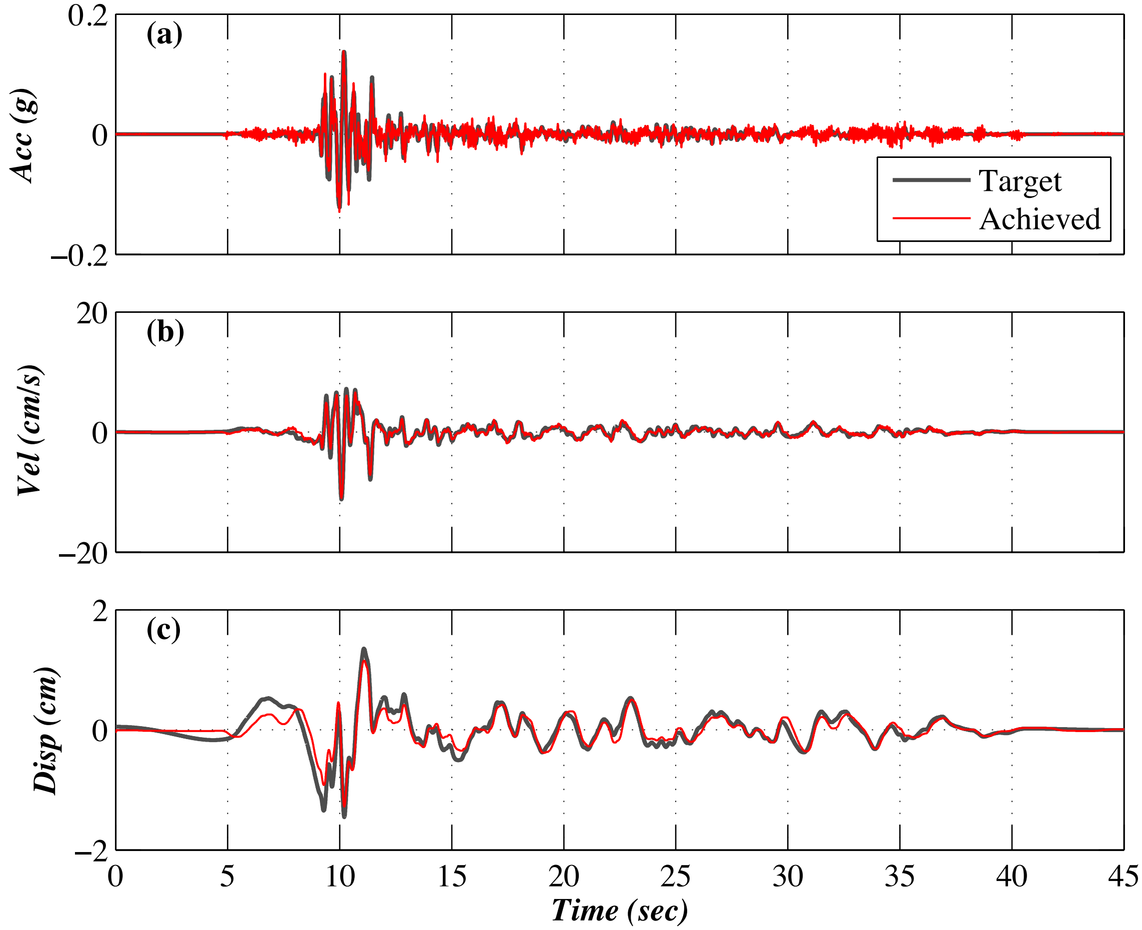

Figure D.1. Target and achieved table input motion EQ1:RIO-25: (a) input accelerations, (b) input velocities, and (c) input displacements.

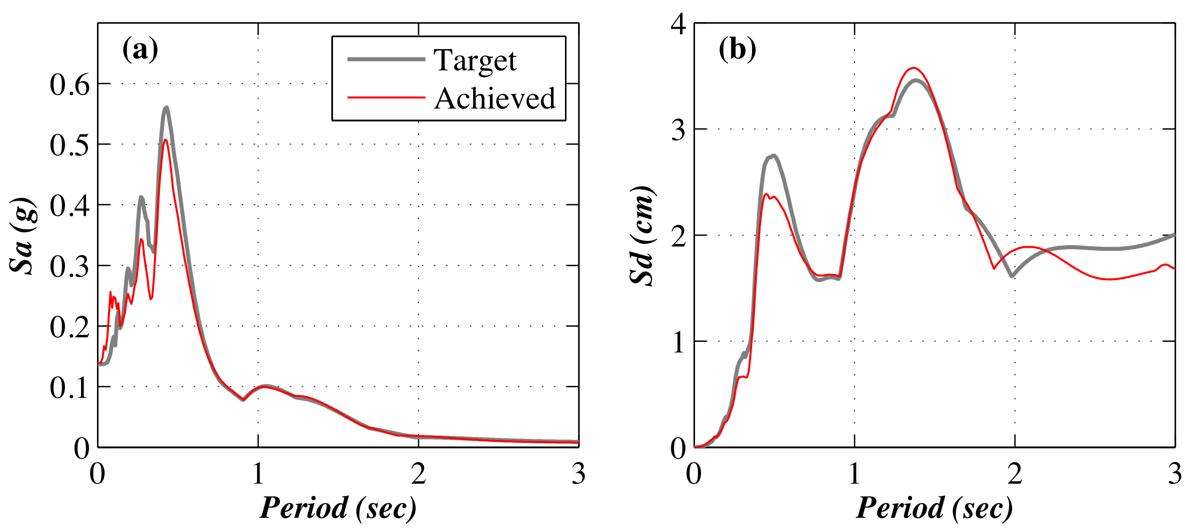

Figure D.2. Target and achieved spectra of table input motion EQ1:RIO-25: (a) acceleration spectra, and (b) displacement spectra.

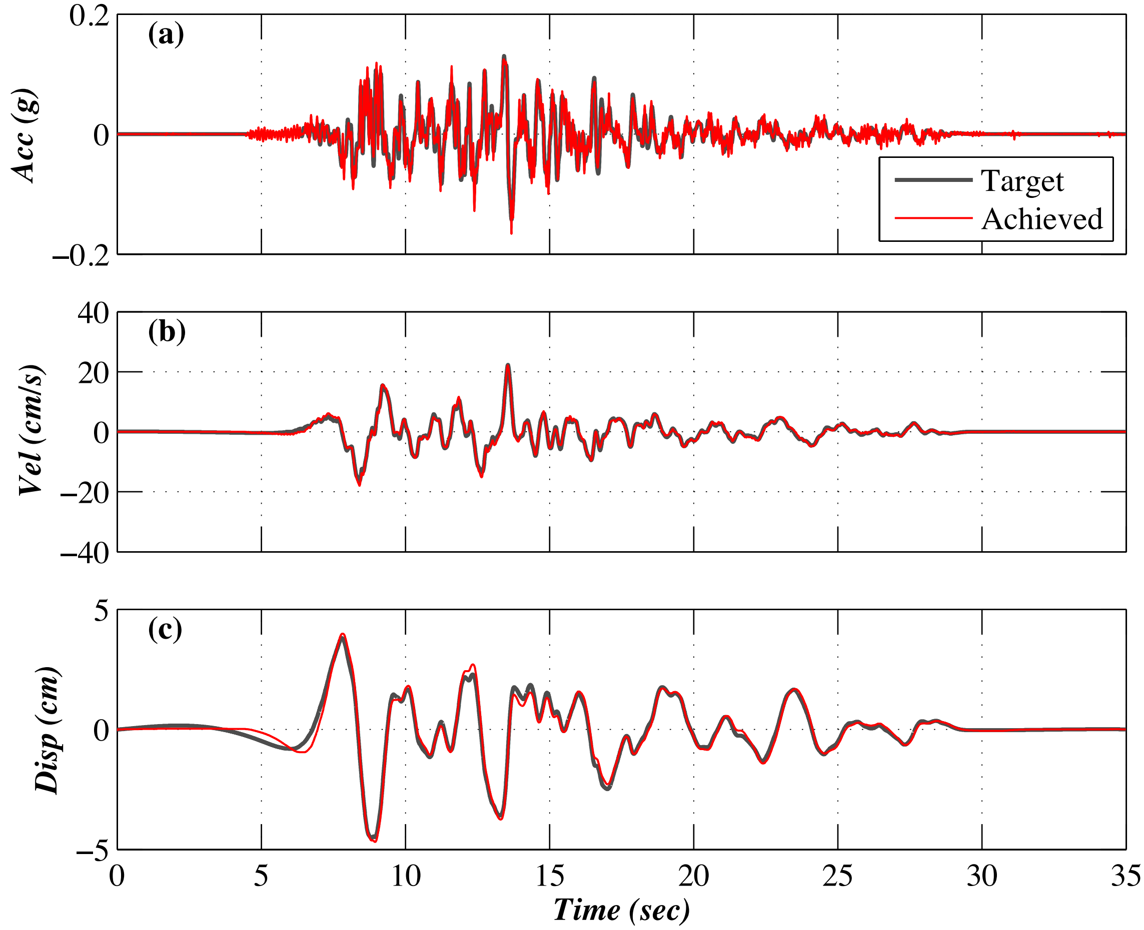

Figure D.1. Target and achieved table input motion EQ2:CNP-025: (a) input accelerations, (b) input velocities, and (c) input displacements.

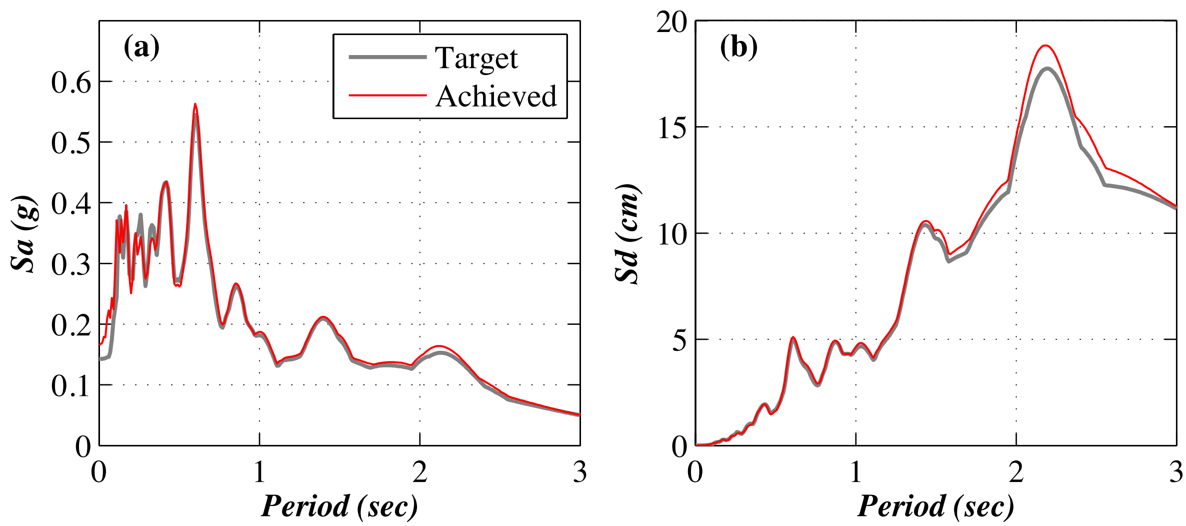

Figure D.4. Target and achieved spectra of table input motion EQ2:CNP-025: (a) acceleration spectra, and (b) displacement spectra.

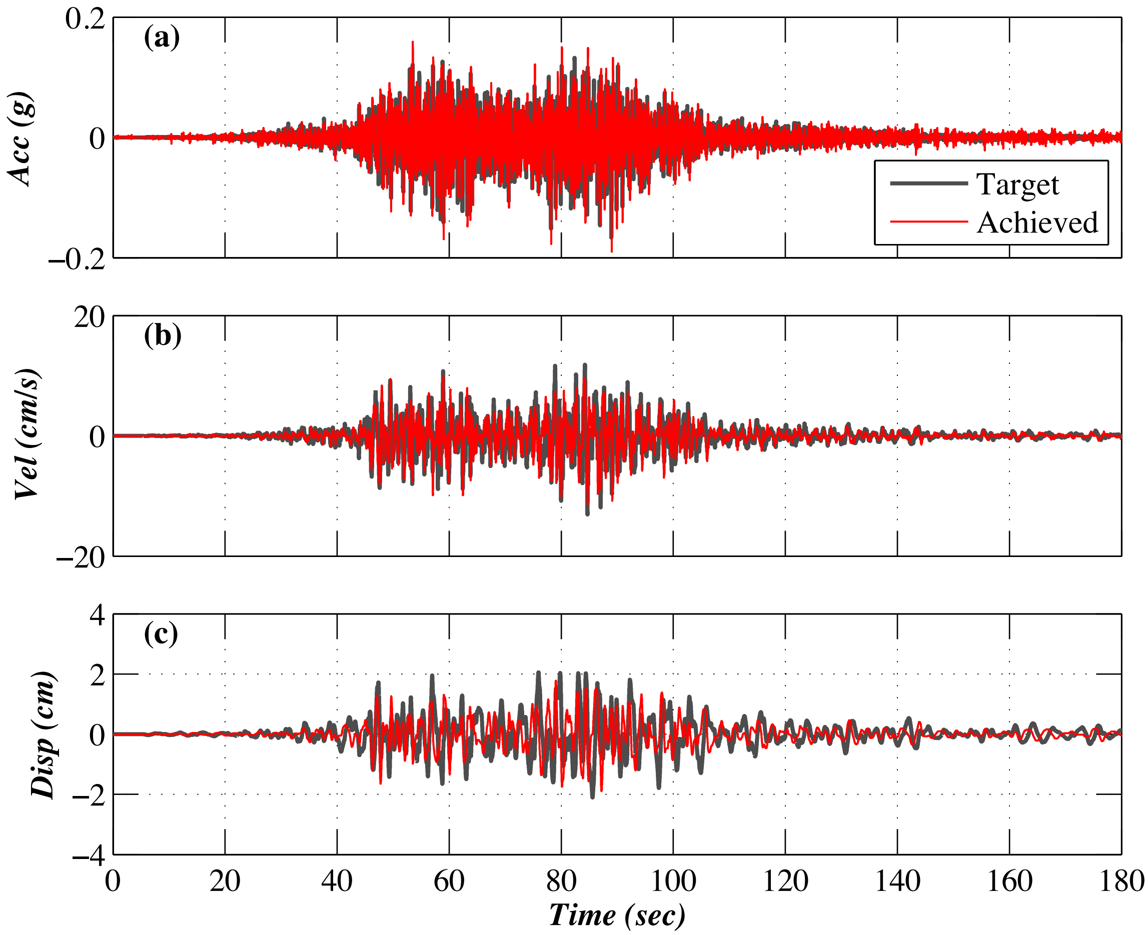

Figure D.5. Target and achieved table input motion EQ3:CUR-025: (a) input accelerations, (b) input velocities, and (c) input displacements.

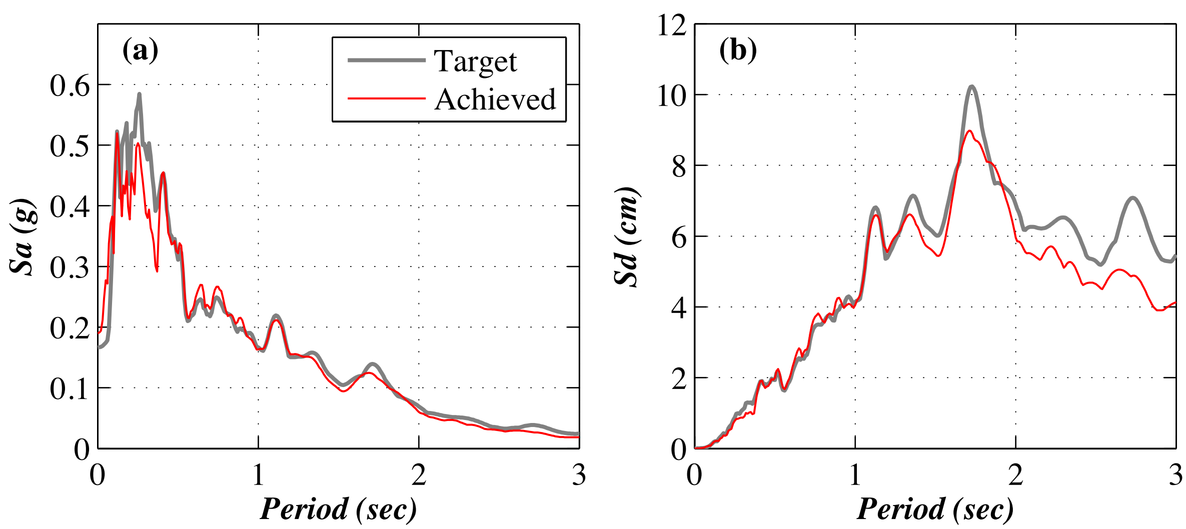

Figure D.6. Target and achieved spectra of table input motion EQ3:CUR-025: (a) acceleration spectra, and (b) displacement spectra.

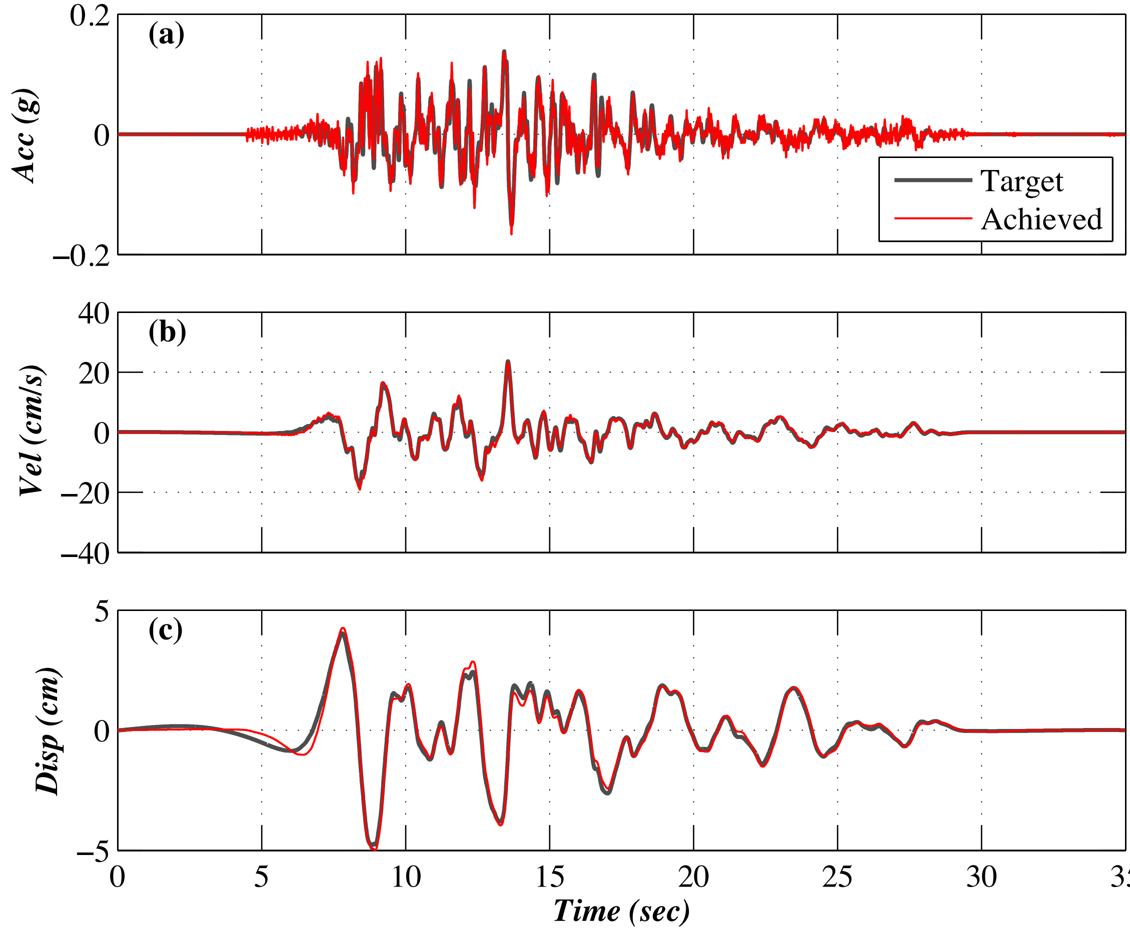

Figure D.7. Target and achieved table input motion EQ4:CNP-025: (a) input accelerations, (b) input velocities, and (c) input displacements.

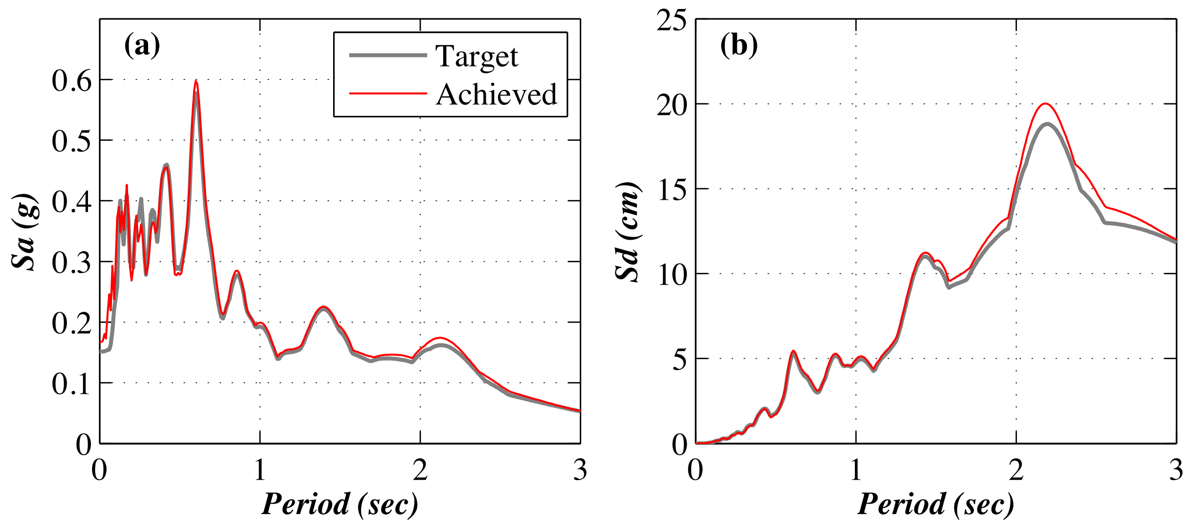

Figure D.8. Target and achieved spectra of table input motion EQ4:CNP-025: (a) acceleration spectra, and (b) displacement spectra.

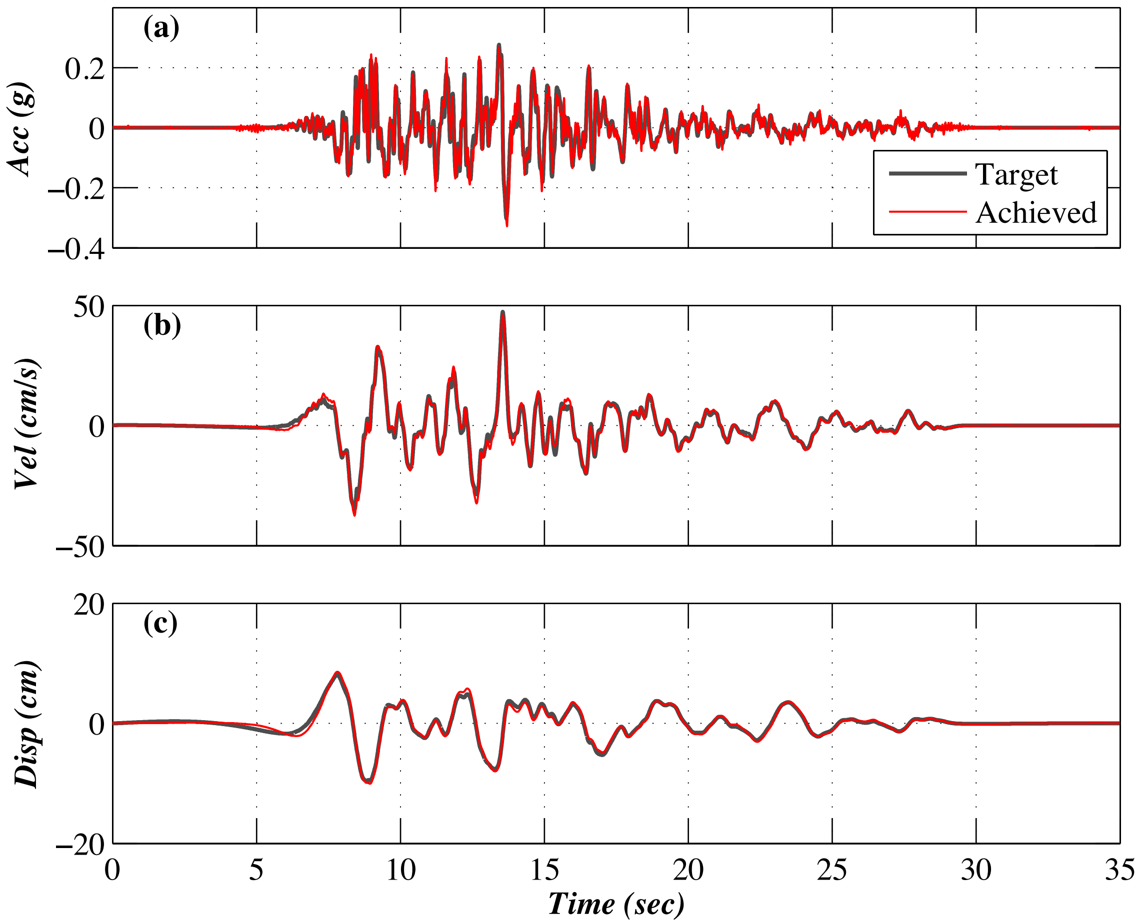

Figure D.9. Target and achieved input motion EQ5:CNP-050: (a) input accelerations, (b) input velocities, and (c) input displacements.

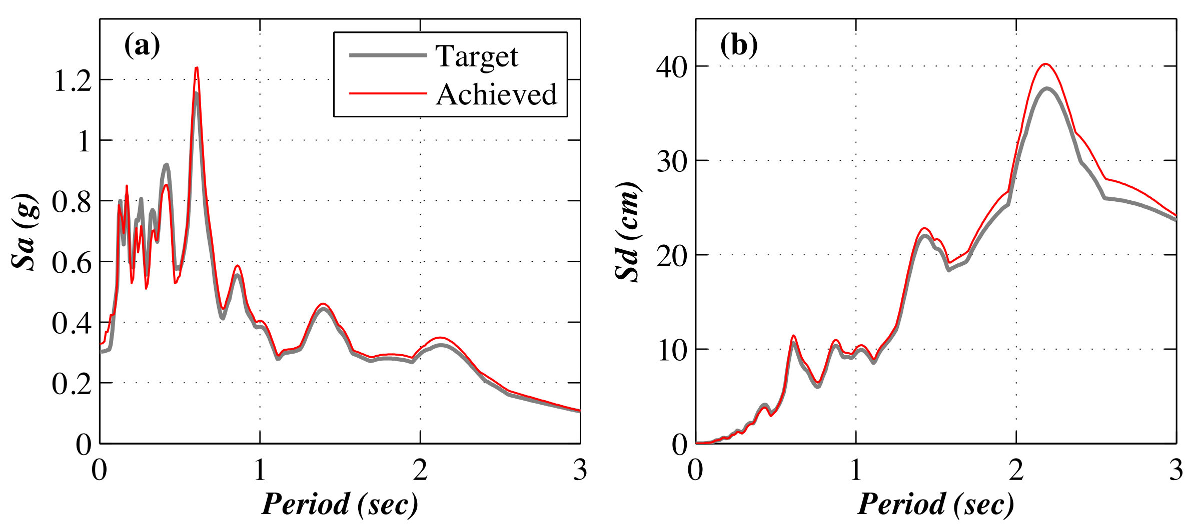

Figure D.10. Target and achieved spectra of input motion EQ5:CNP-50: (a) acceleration spectra, and (b) displacement spectra.

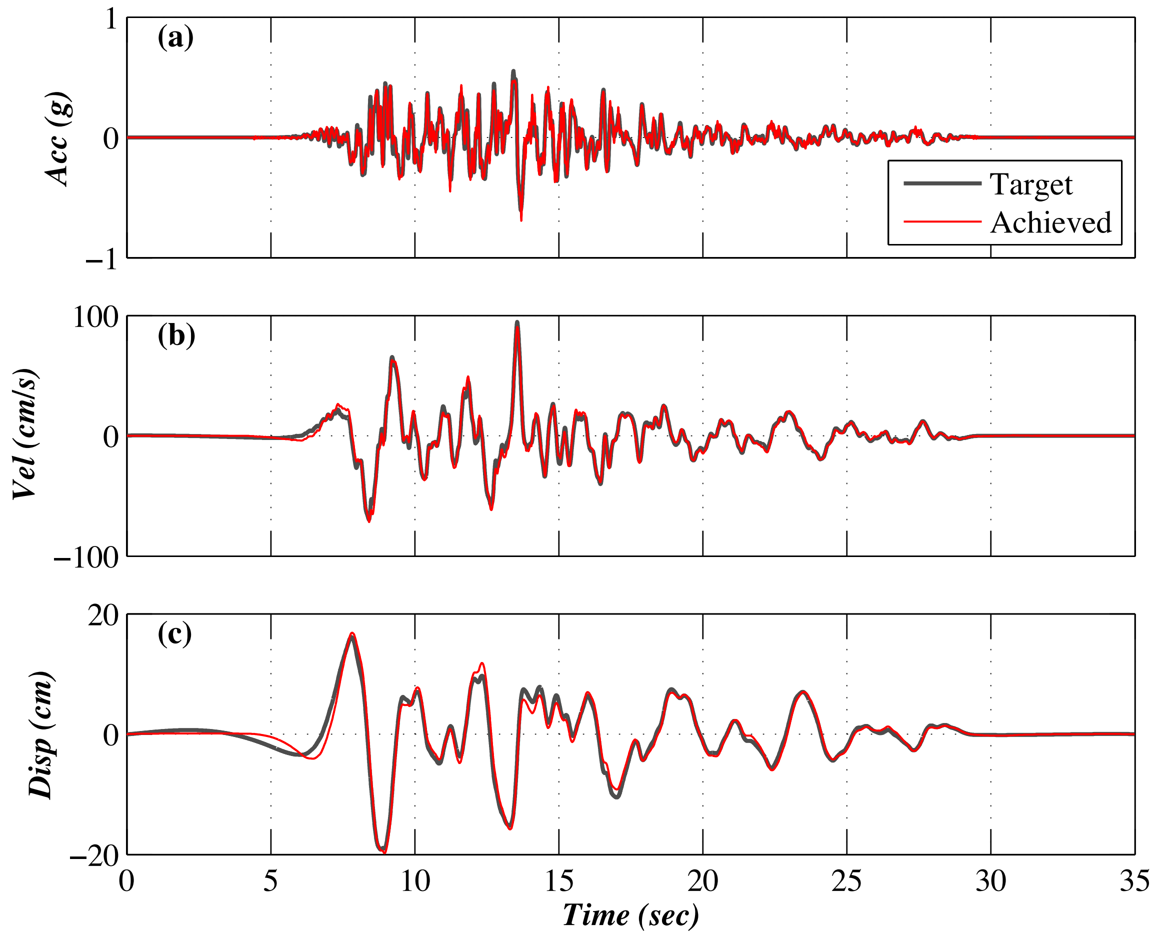

Figure D.11. Target and achieved input motion EQ6:CNP-100: (a) input accelerations, (b) input velocities, and (c) input displacements.

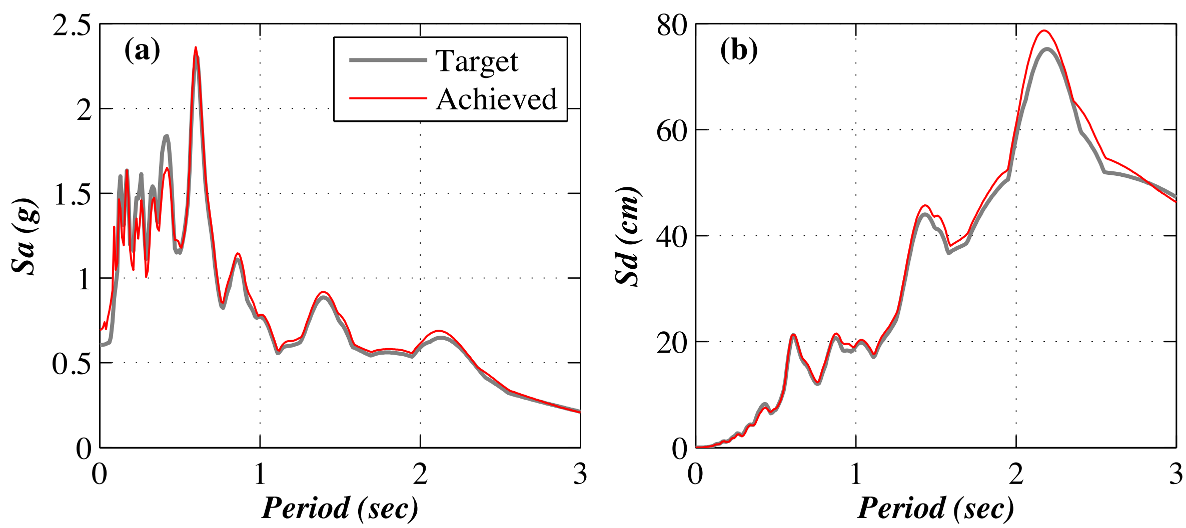

Figure D.12. Target and achieved spectra of input motion EQ6:CNP-100: (a) acceleration spectra, and (b) displacement spectra.

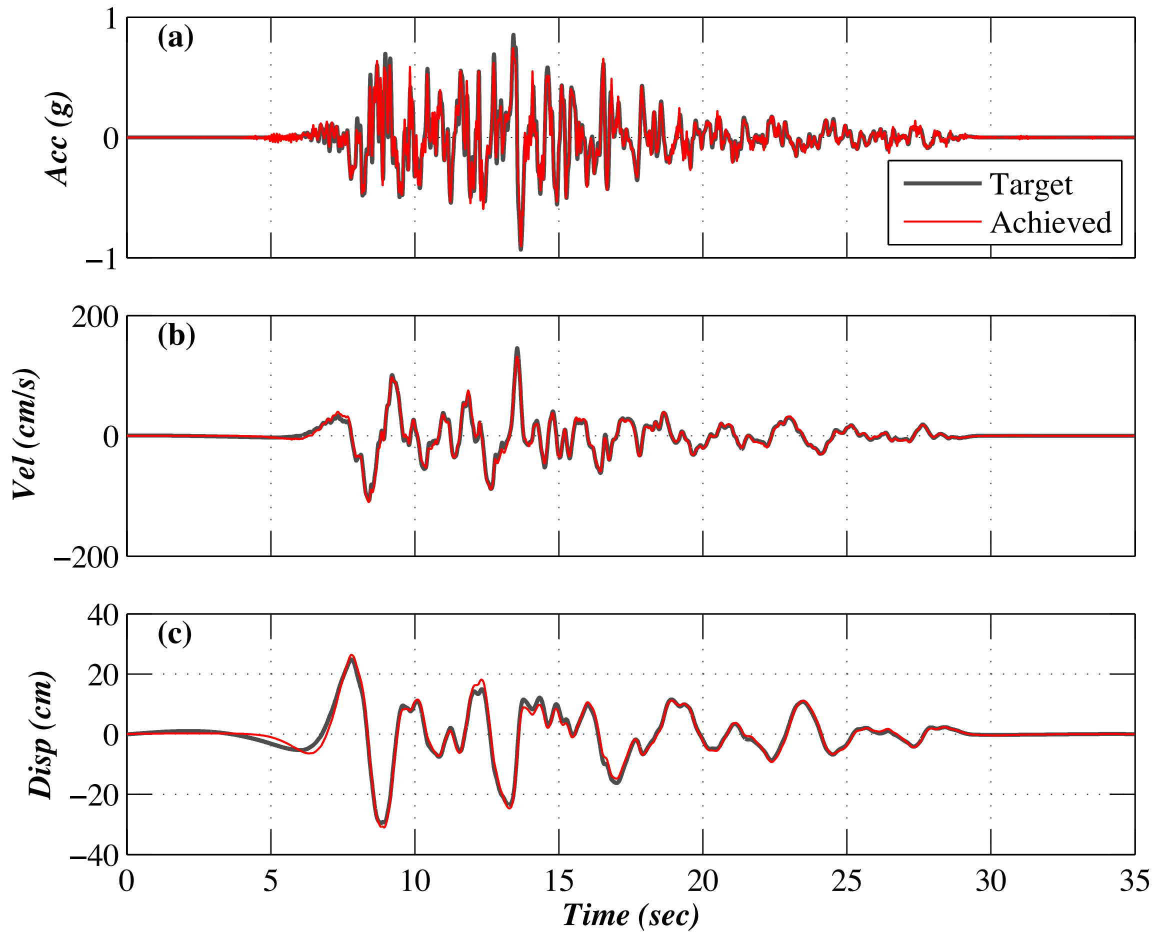

Figure D.13. Target and achieved input motion EQ7:CNP-150: (a) input accelerations, (b) input velocities, and (c) input displacements.

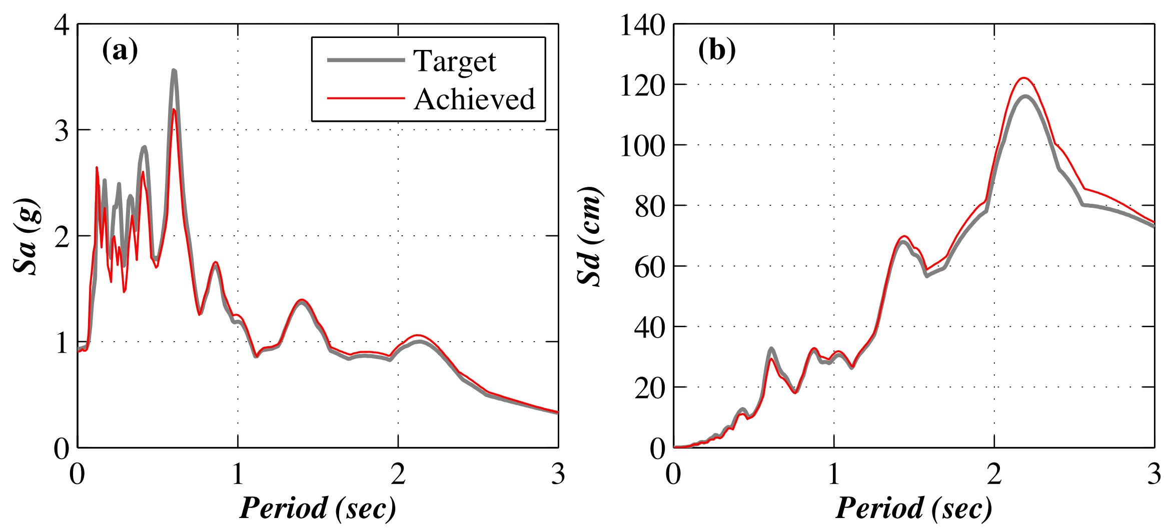

Figure D.14. Target and achieved spectra of input motion EQ7:CNP-150: (a) acceleration spectra, and (b) displacement spectra.

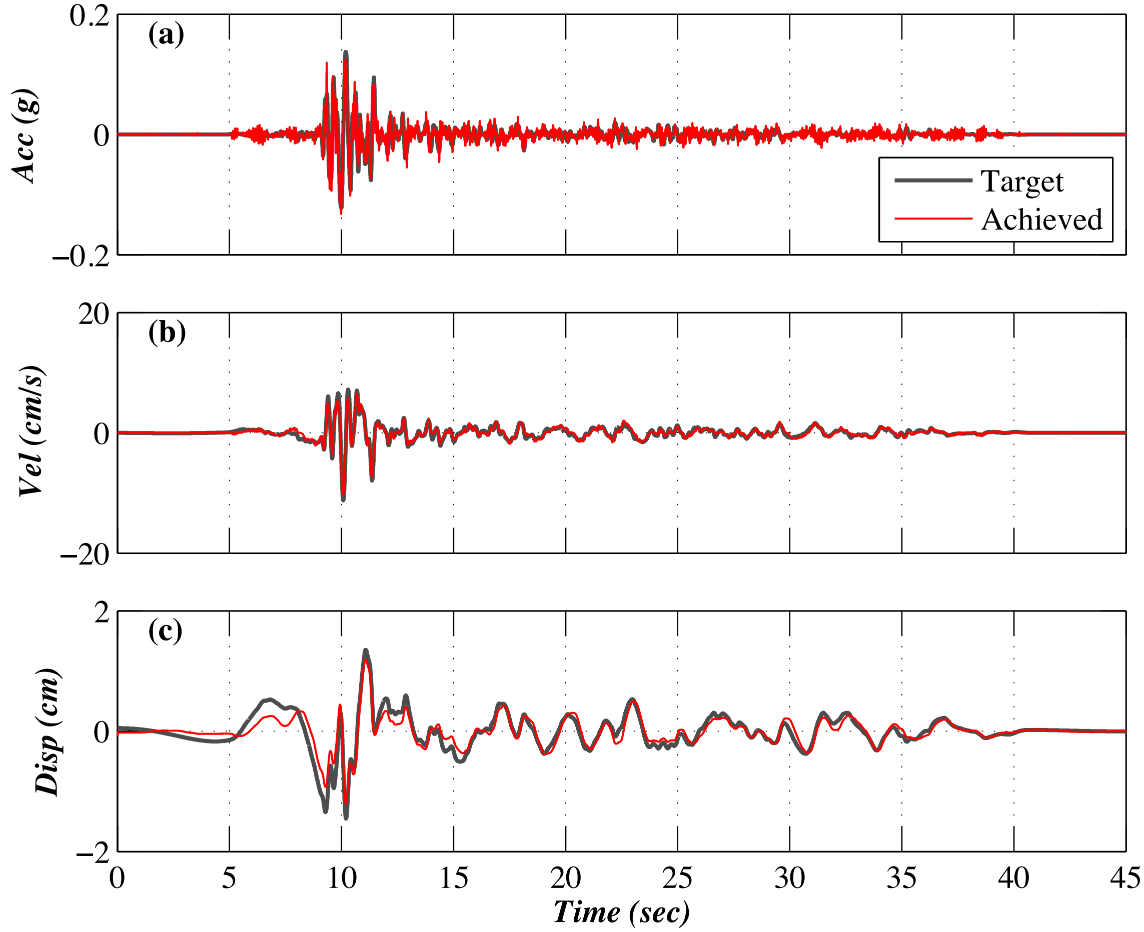

Figure D.15. Target and achieved table input motion EQ8:RIO-25: (a) input accelerations, (b) input velocities, and (c) input displacements.

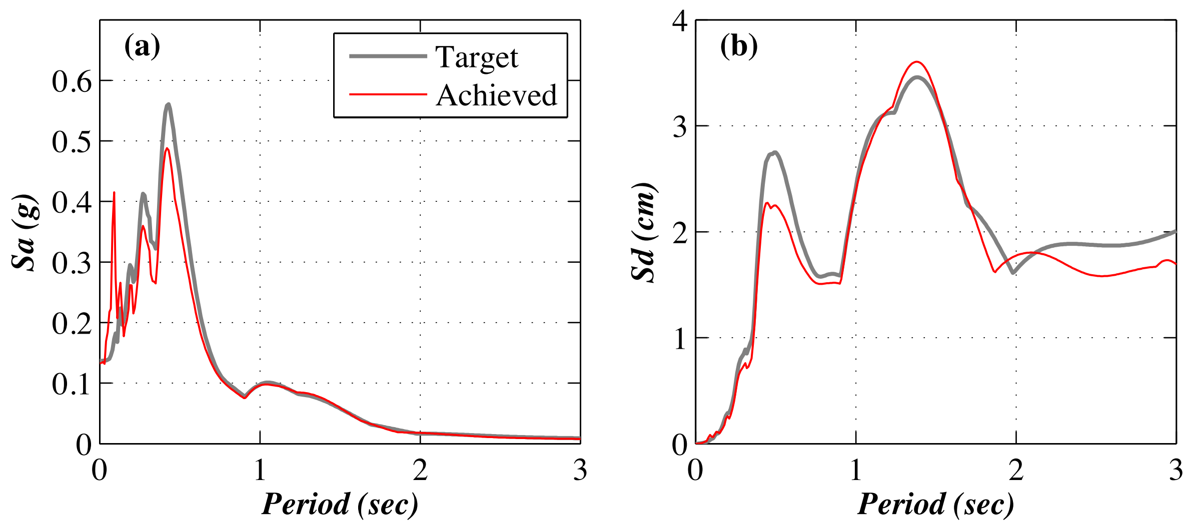

Figure D.16. Target and achieved spectra of table input motion EQ8:RIO-25: (a) acceleration spectra, and (b) displacement spectra.

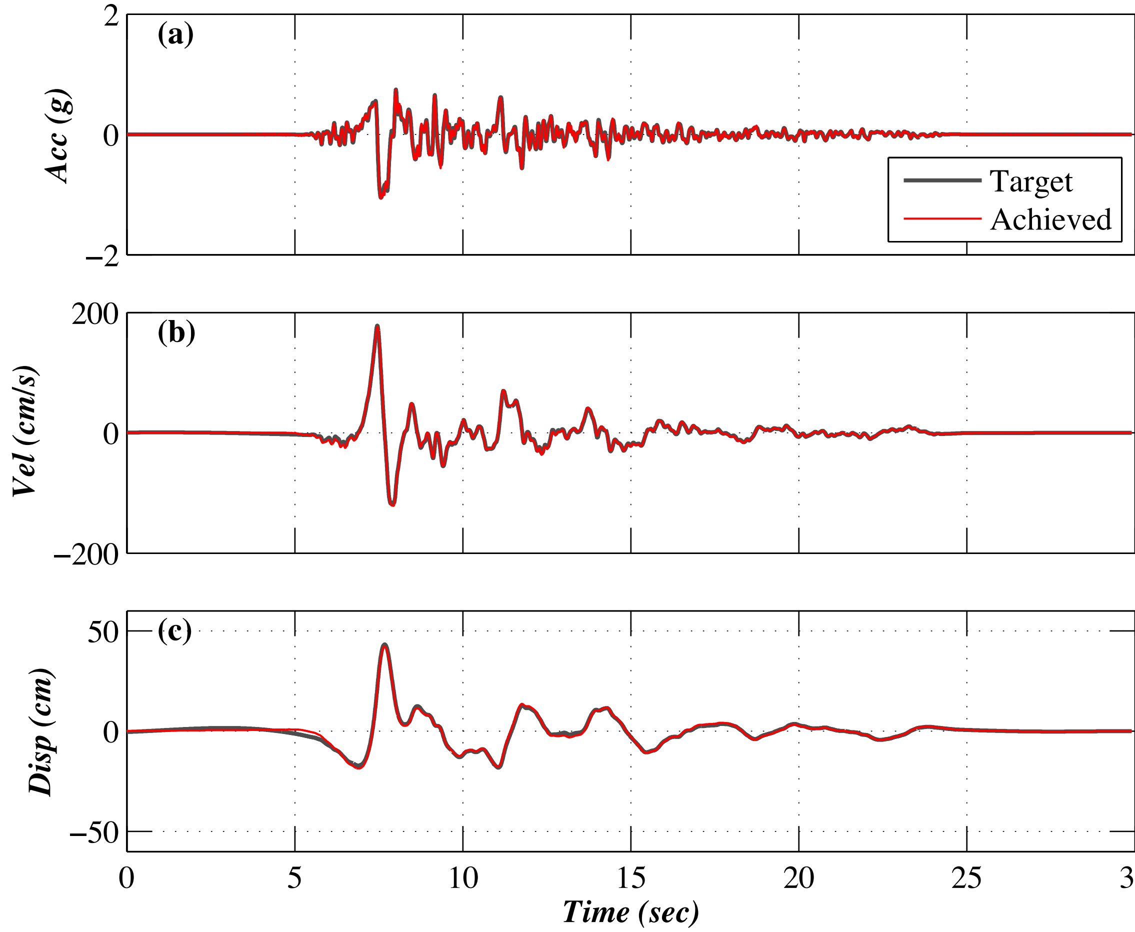

Figure D.17. Target and achieved input motion EQ9:RRS-150: (a) input accelerations, (b) input velocities, and (c) input displacements.

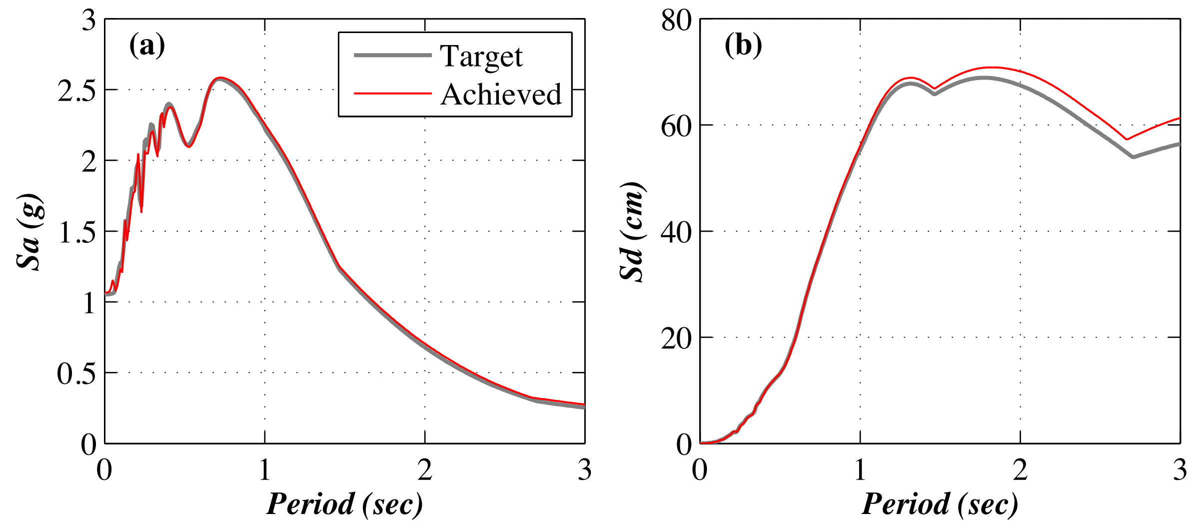

Figure D.18. Target and achieved spectra of input motion EQ9:RRS-150: (a) acceleration spectra, and (b) displacement spectra.

APPENDIX E – INSTRUMENTATION PLAN OF ANALOG SENSORS

This appendix documents the detailed instrumentation plan of the analog sensors installed on the test building during the earthquake test phase. The analog sensor system consisted of five different types of sensors: (1) MEMS accelerometers, (2) Kinemetric accelerometers, (3) string potentiometers, (4) linear potentiometers, and (5) strain gages.

The analog sensors were installed progressively during the construction stage and modified during the test phase. In this regard, a total of four configurations (two for construction phase and two for test phase) were employed during the test program (Table E.1). Detailed information of the analog sensor instrumentation for all four configurations is documented in the following sections (one configuration for each section). Each section contains the sensor number count and floor-by-floor sensor layouts of a specific configuration.

Table E.1. Analog sensor instrumentation configurations.

Configuration	Type of sensor					Total
	Accel. (MEMS)	Accel. (Kinemetrics)	String pot.	Linear pot.	Strain gage	
C1 – construction phase (May 5 – 15, 2016)	25	0	0	1	12	38
C2 – construction phase (May 15 – June 9, 2016)	57	0	0	1	12	70
E1 – pre-fire test phase (June 10 – 17, 2016)	68	12	71	39	67	257
E2 – post-fire test phase (July 1, 2016)	59	0	52	22	59	192

Analog Sensor Instrumentation – Configuration C1

Table E.2. Analog sensor count – Configuration C1.

Floor #	Type of sensor				
	Accel. (MEMS)	Accel. (Kinemetrics)	String pot.	Linear pot.	Strain gage
1	3	0	0	0	8
2	3	0	0	0	4
3	3	0	0	0	0
4	3	0	0	0	0
5	3	0	0	0	0
6	5	0	0	0	0
Roof	5	0	0	1	0
Total	25	0	0	1	12

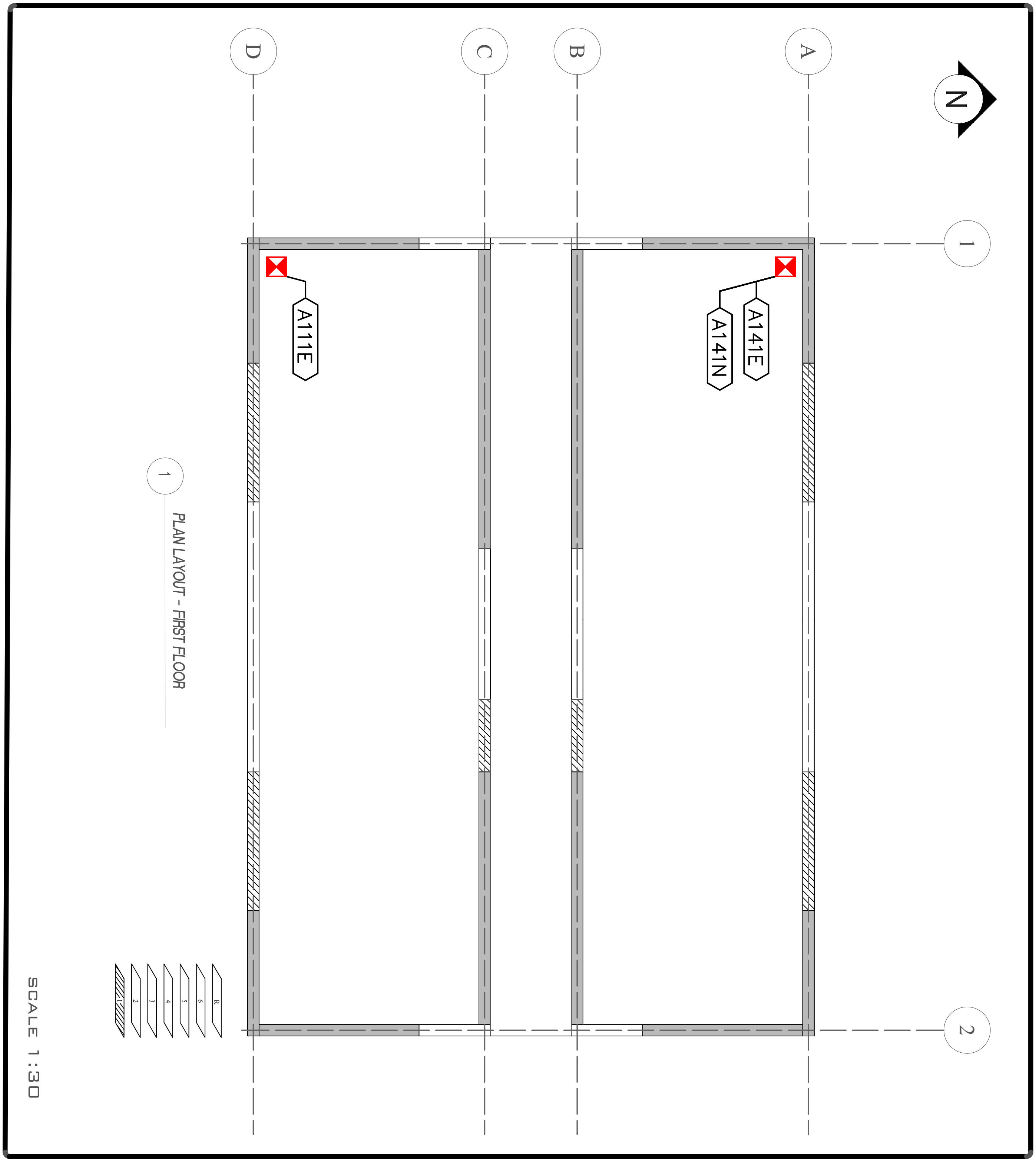

UCSD

UNIVERSITY OF CALIFORNIA, SAN DIEGO
DEPARTMENT OF STRUCTURAL ENGINEERING
LA JOLLA - CALIFORNIA 92093-0085

PROJECT NO. DATE:

NO.	DATE	REVISIONS

CFS Shake Table Test Project
Accelerometers (MEMS) - Floor 1
Configuration C1

SRIKAR GUNISETTY
Graduate Student Researcher
XIANG WANG
Post-doctoral Researcher

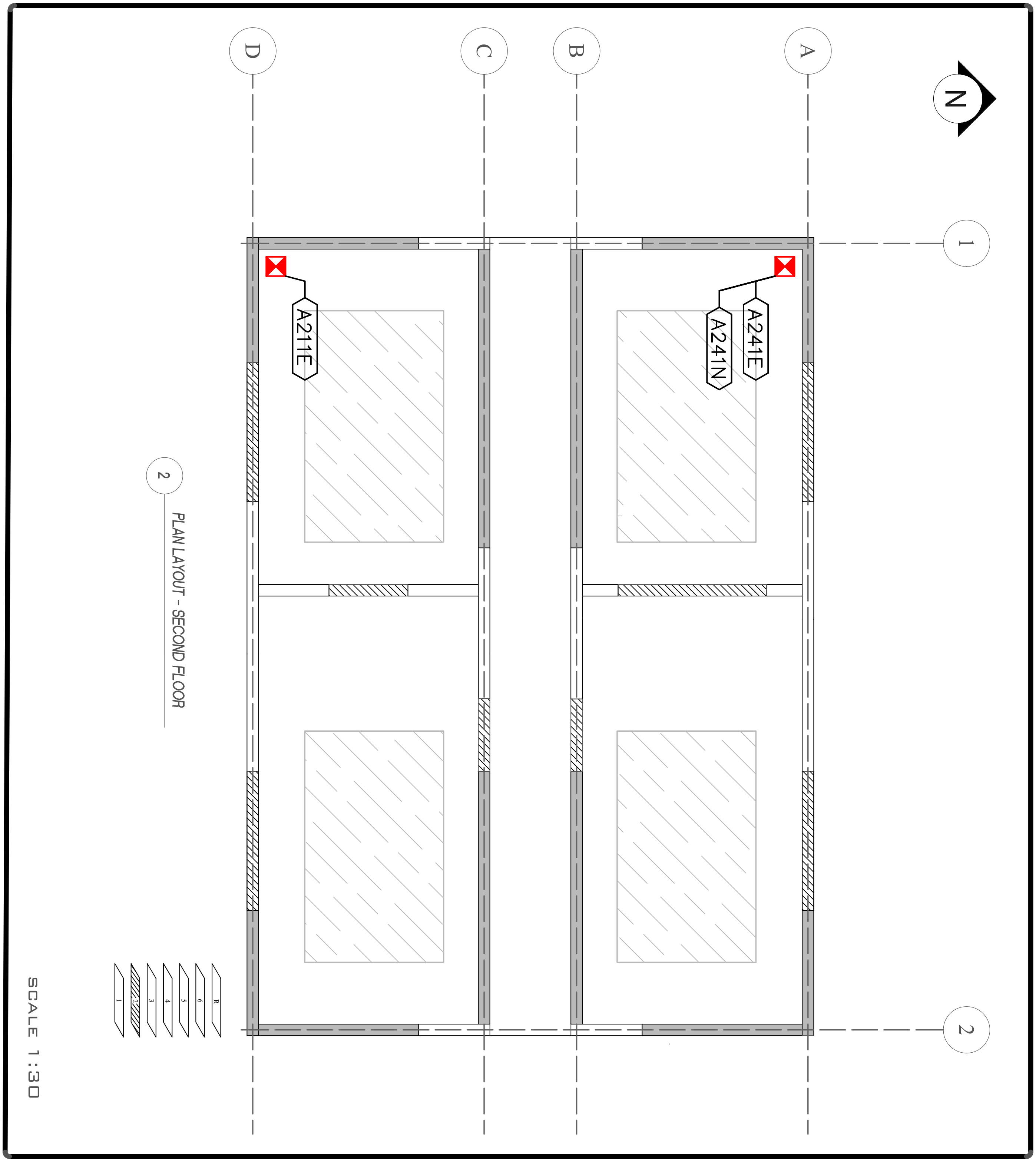

UCSD

UNIVERSITY OF CALIFORNIA, SAN DIEGO
DEPARTMENT OF STRUCTURAL ENGINEERING
LA JOLLA - CALIFORNIA 92093-0085

PROJECT NO. DATE:

NO.	DATE	REVISIONS

CFS Shake Table Test Project
Accelerometers (MEMS) - Floor 2
Configuration C1

SRIKAR GUNISETTY
Graduate Student Researcher
XIANG WANG
Post-doctoral Researcher

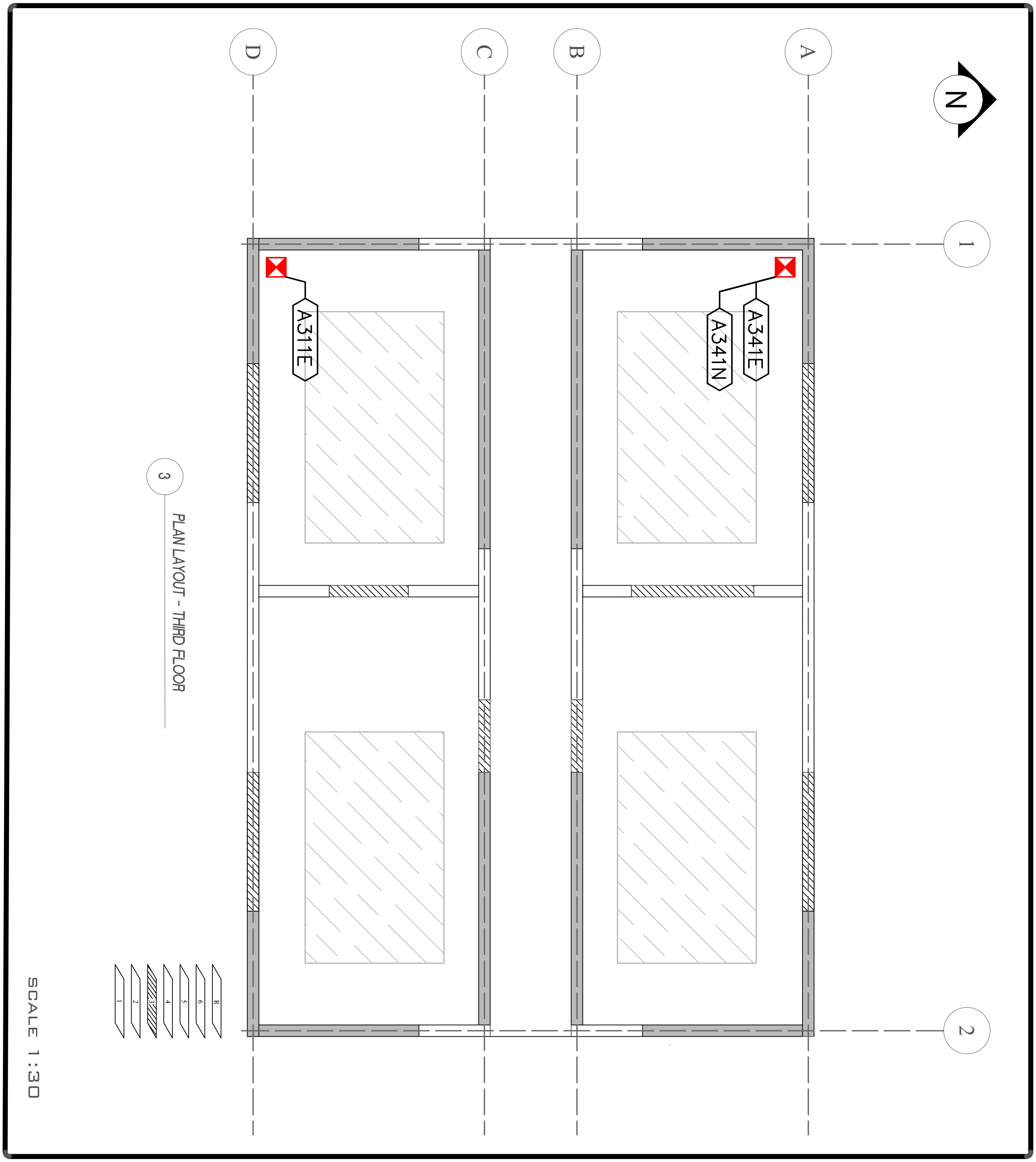

UCSD
UNIVERSITY OF CALIFORNIA, SAN DIEGO
DEPARTMENT OF STRUCTURAL ENGINEERING
LA JOLLA - CALIFORNIA 92093-0085

PROJECT NO. DATE:

NO.	DATE	REVISIONS

CFS Shake Table Test Project
Accelerometers (MEMS) - Floor 3
Configuration C1

SRIKAR GUNISETTY
Graduate Student Researcher
XIANG WANG
Post-doctoral Researcher

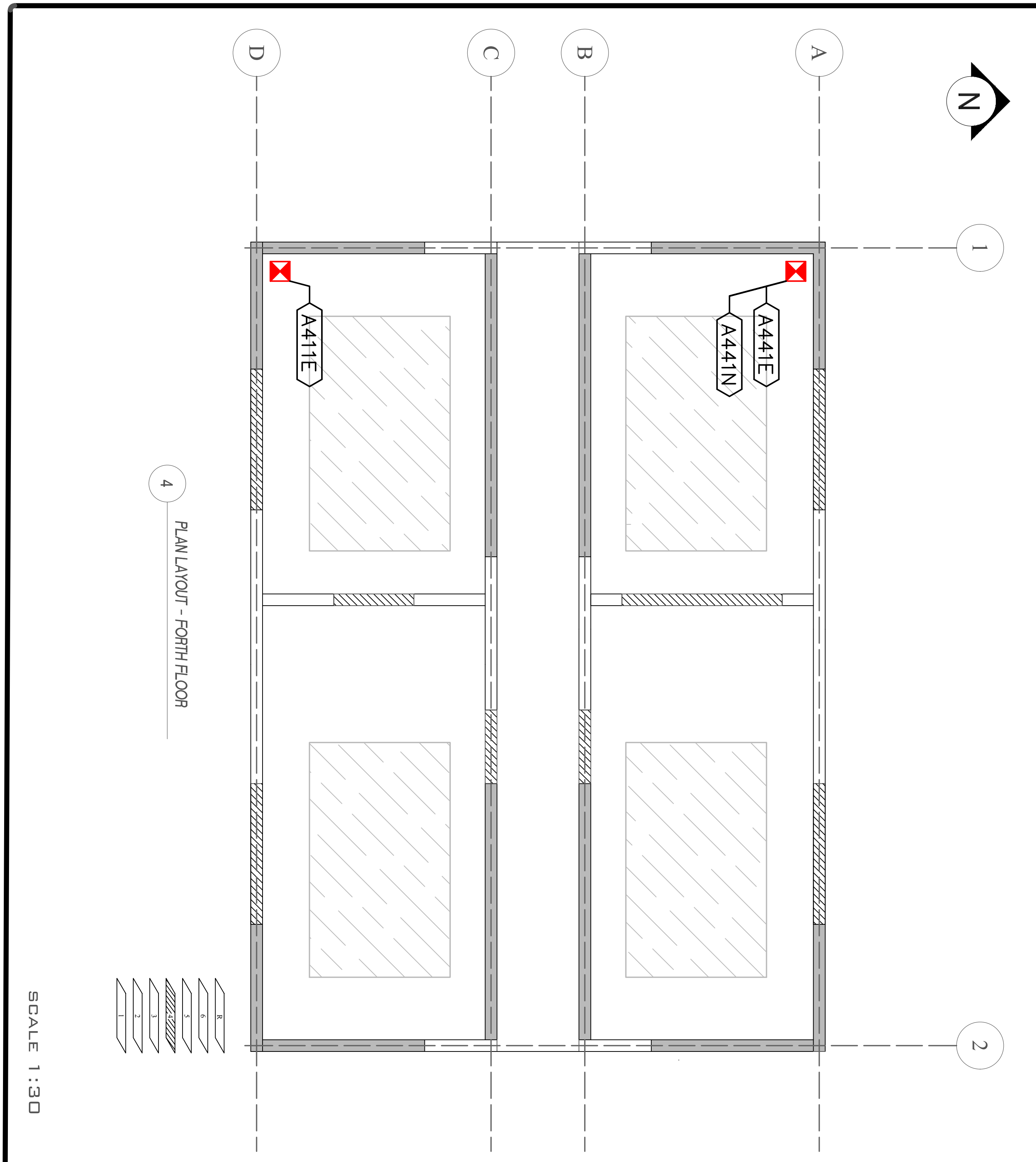

UCSD

UNIVERSITY OF CALIFORNIA, SAN DIEGO
DEPARTMENT OF STRUCTURAL ENGINEERING
LA JOLLA - CALIFORNIA 92093-0085

PROJECT NO. DATE:

NO.	DATE	REVISIONS

CFS Shake Table Test Project
Accelerometers (MEMS) - Floor 4
Configuration C1

SRIKAR GUNISETTY
Graduate Student Researcher
XIANG WANG
Post-doctoral Researcher

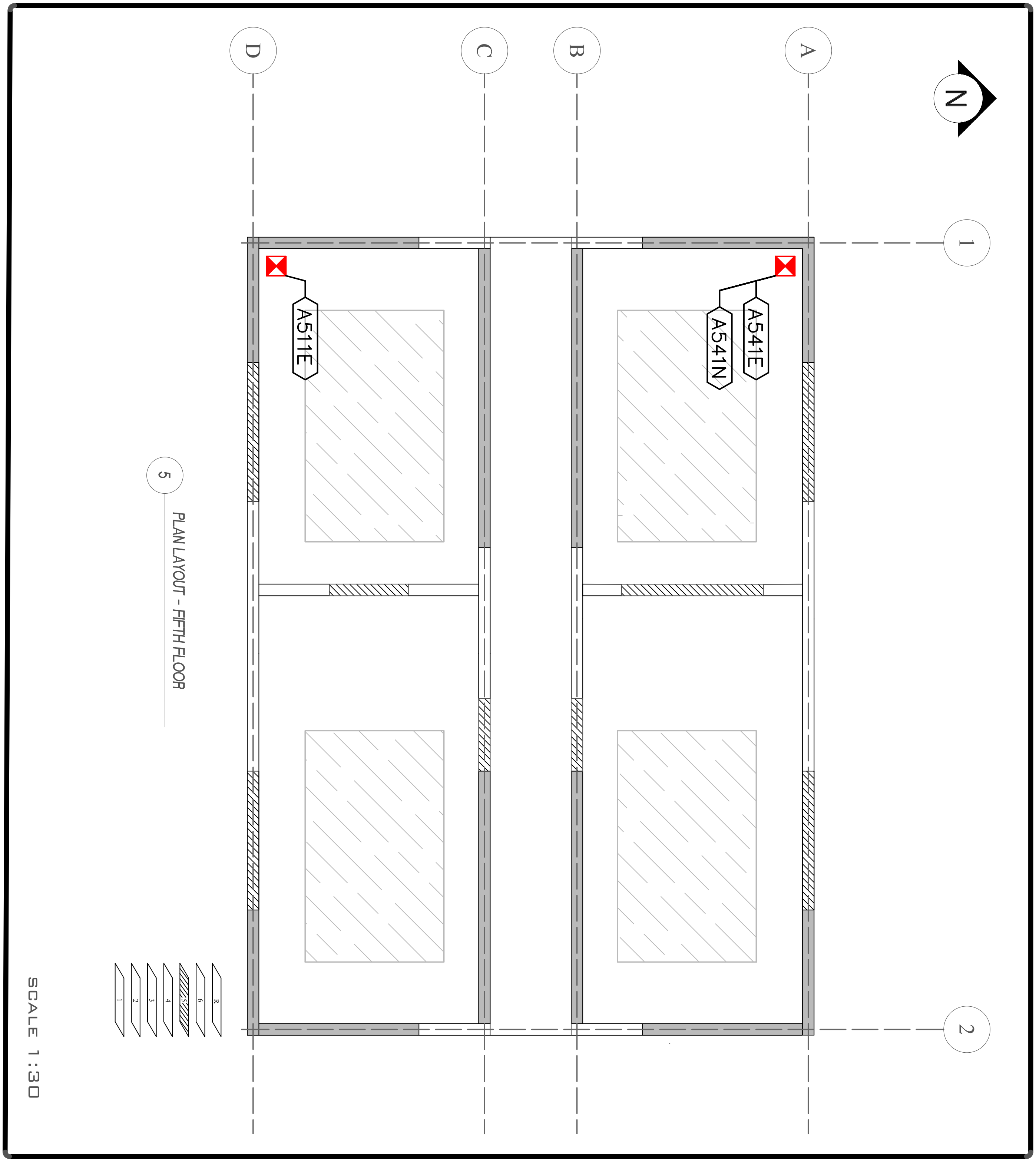

UCSD
UNIVERSITY OF CALIFORNIA, SAN DIEGO
DEPARTMENT OF STRUCTURAL ENGINEERING
LA JOLLA - CALIFORNIA 92093-0085

PROJECT NO. DATE:

NO.	DATE	REVISIONS

CFS Shake Table Test Project
Accelerometers (MEMS) - Floor 5
Configuration C1

SRIKAR GUNISETTY
Graduate Student Researcher
XIANG WANG
Post-doctoral Researcher

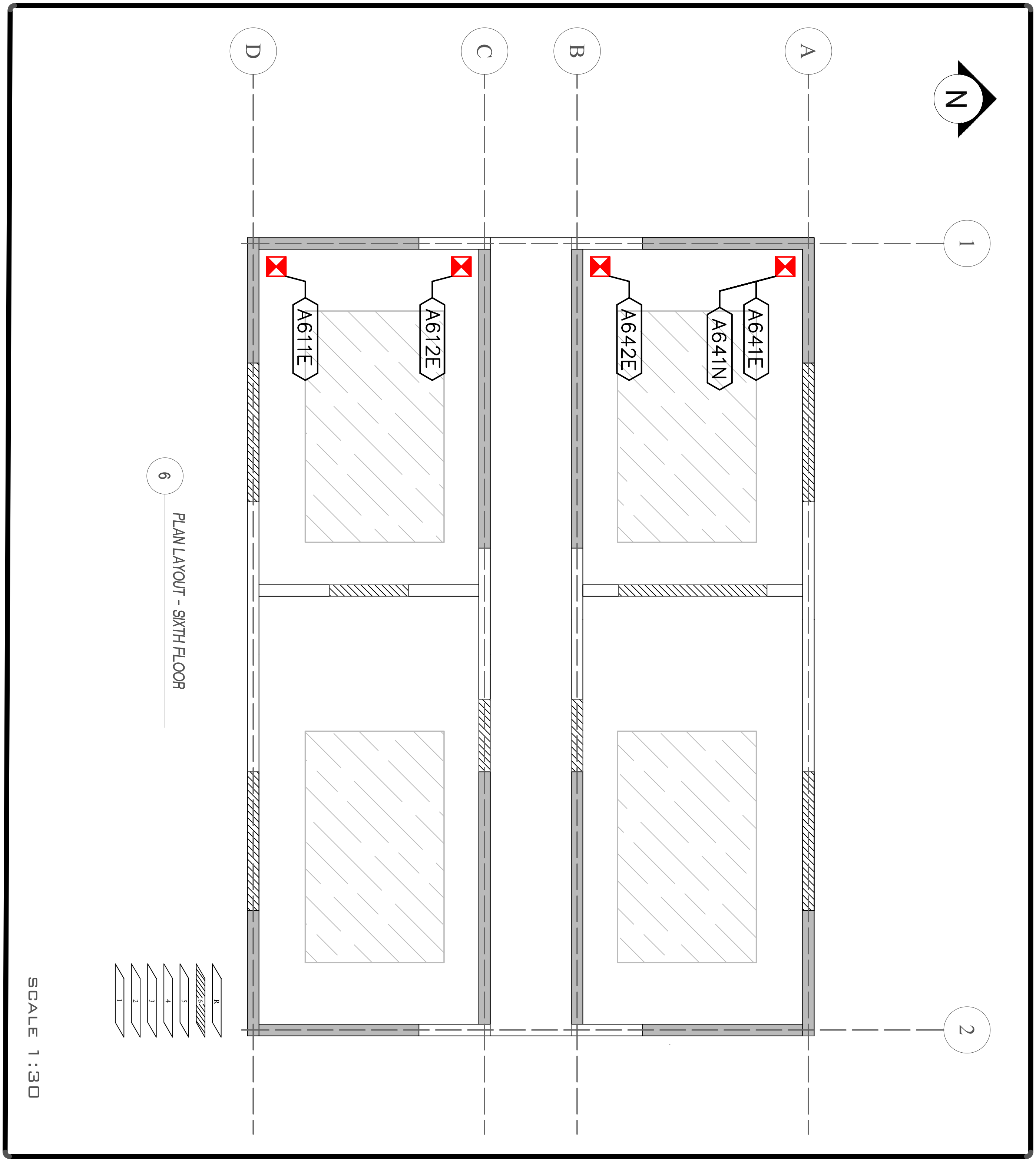

UCSD UNIVERSITY OF CALIFORNIA, SAN DIEGO DEPARTMENT OF STRUCTURAL ENGINEERING LA JOLLA - CALIFORNIA 92093-0085 PROJECT NO. DATE:	NO.	DATE	REVISIONS	CFS Shake Table Test Project Accelerometers (MEMS) - Floor 6 Configuration C1	SRIKAR GUNISETTY Graduate Student Researcher XIANG WANG Post-doctoral Researcher

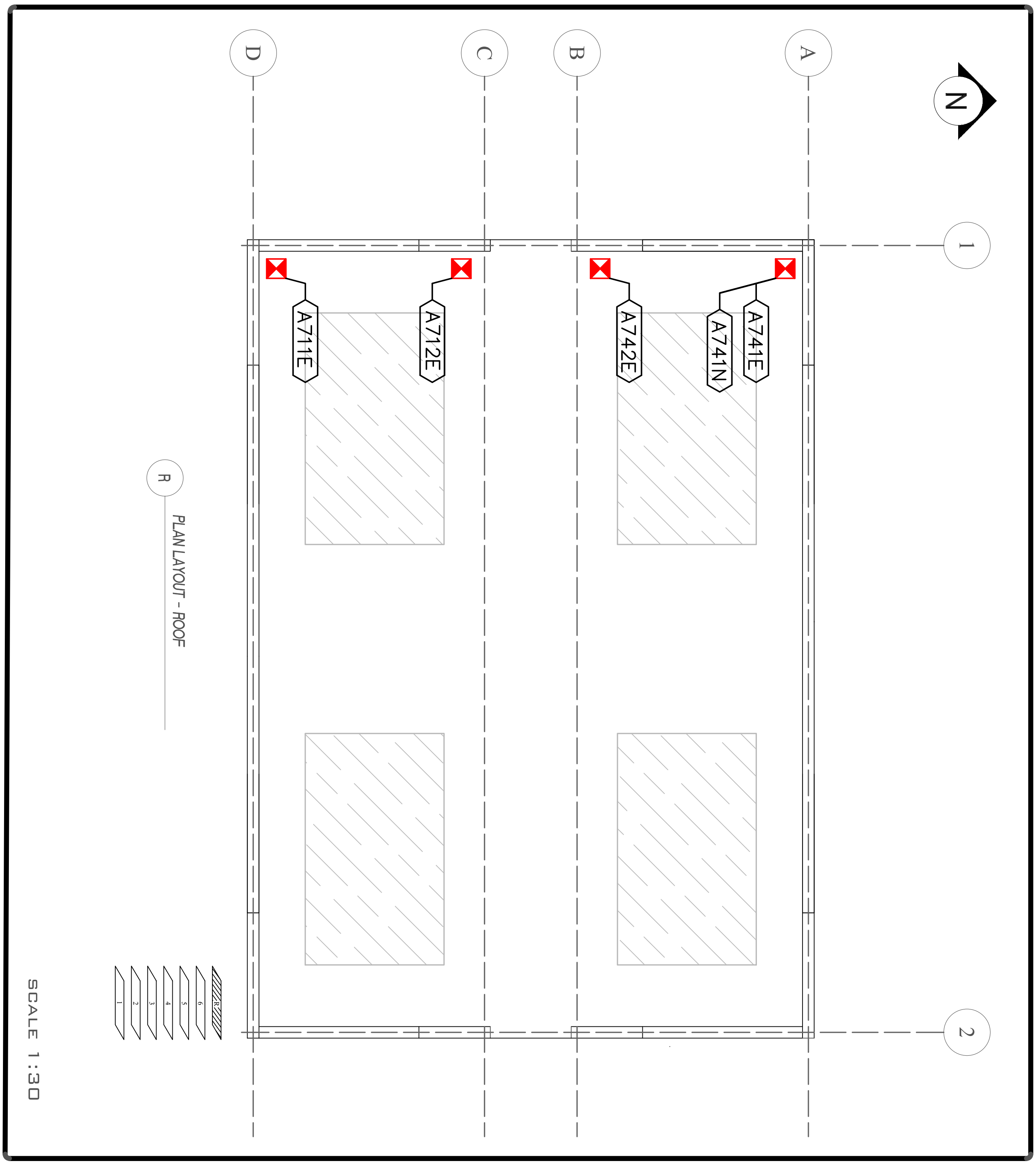

UCSD UNIVERSITY OF CALIFORNIA, SAN DIEGO DEPARTMENT OF STRUCTURAL ENGINEERING LA JOLLA - CALIFORNIA 92093-0085 PROJECT NO. DATE:	NO. DATE REVISIONS	CFS Shake Table Test Project Accelerometers (MEMS) - Roof Configuration C1	SRIKAR GUNISETTY Graduate Student Researcher XIANG WANG Post-doctoral Researcher

Analog Sensor Instrumentation – Configuration C2

Table E.3. Analog sensor count – Configuration C2.

Floor #	Type of sensor				
	Accel. (MEMS)	Accel. (Kinemetrics)	String pot.	Linear pot.	Strain gage
1	3	0	0	0	8
2	10	0	0	0	4
3	10	0	0	0	0
4	8	0	0	0	0
5	8	0	0	0	0
6	8	0	0	0	0
Roof	10	0	0	1	0
Total	57	0	0	1	12

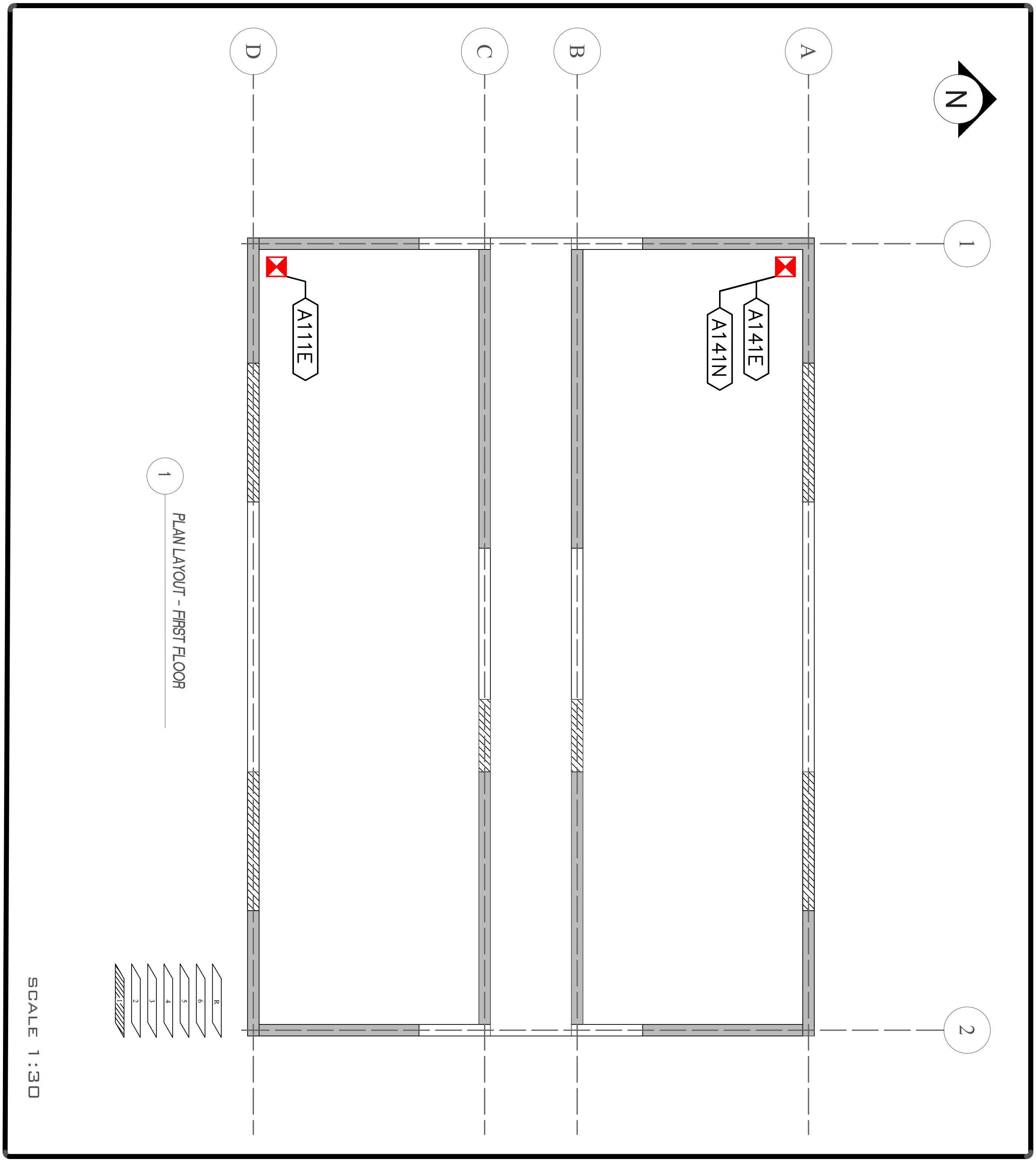

UCSD

UNIVERSITY OF CALIFORNIA, SAN DIEGO
DEPARTMENT OF STRUCTURAL ENGINEERING
LA JOLLA - CALIFORNIA 92093-0085

PROJECT NO. DATE:

NO.	DATE	REVISIONS

CFS Shake Table Test Project
Accelerometers (MEMS) - Floor 1
Configuration C2

SRIKAR GUNISETTY
Graduate Student Researcher
XIANG WANG
Post-doctoral Researcher

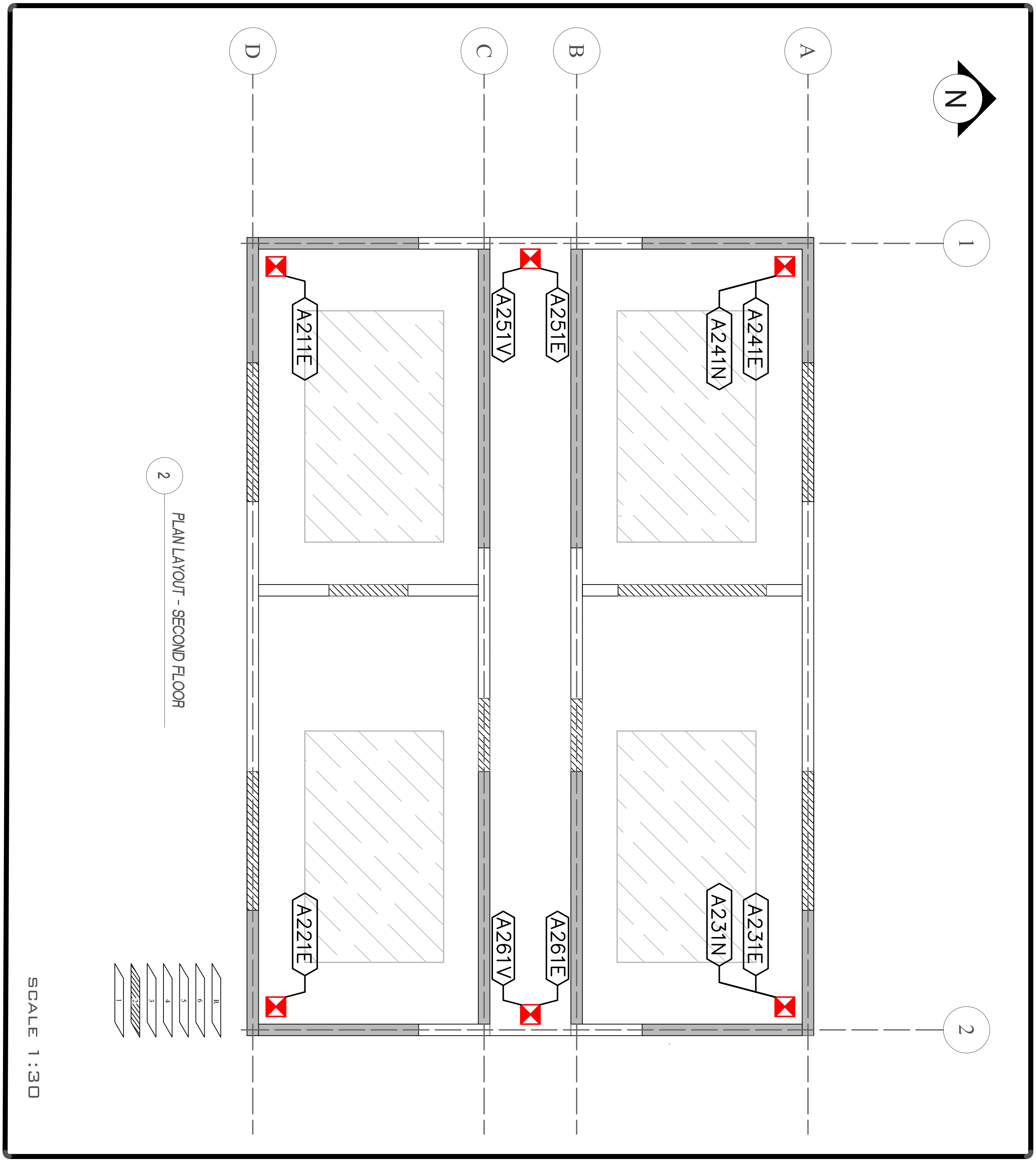

UCSD
UNIVERSITY OF CALIFORNIA, SAN DIEGO
DEPARTMENT OF STRUCTURAL ENGINEERING
LA JOLLA - CALIFORNIA 92093-0085
PROJECT NO. DATE:

NO.	DATE	REVISIONS

CFS Shake Table Test Project
Accelerometers (MEMS) - Floor 2
Configuration C2

SRIKAR GUNISETTY
Graduate Student Researcher
XIANG WANG
Post-doctoral Researcher

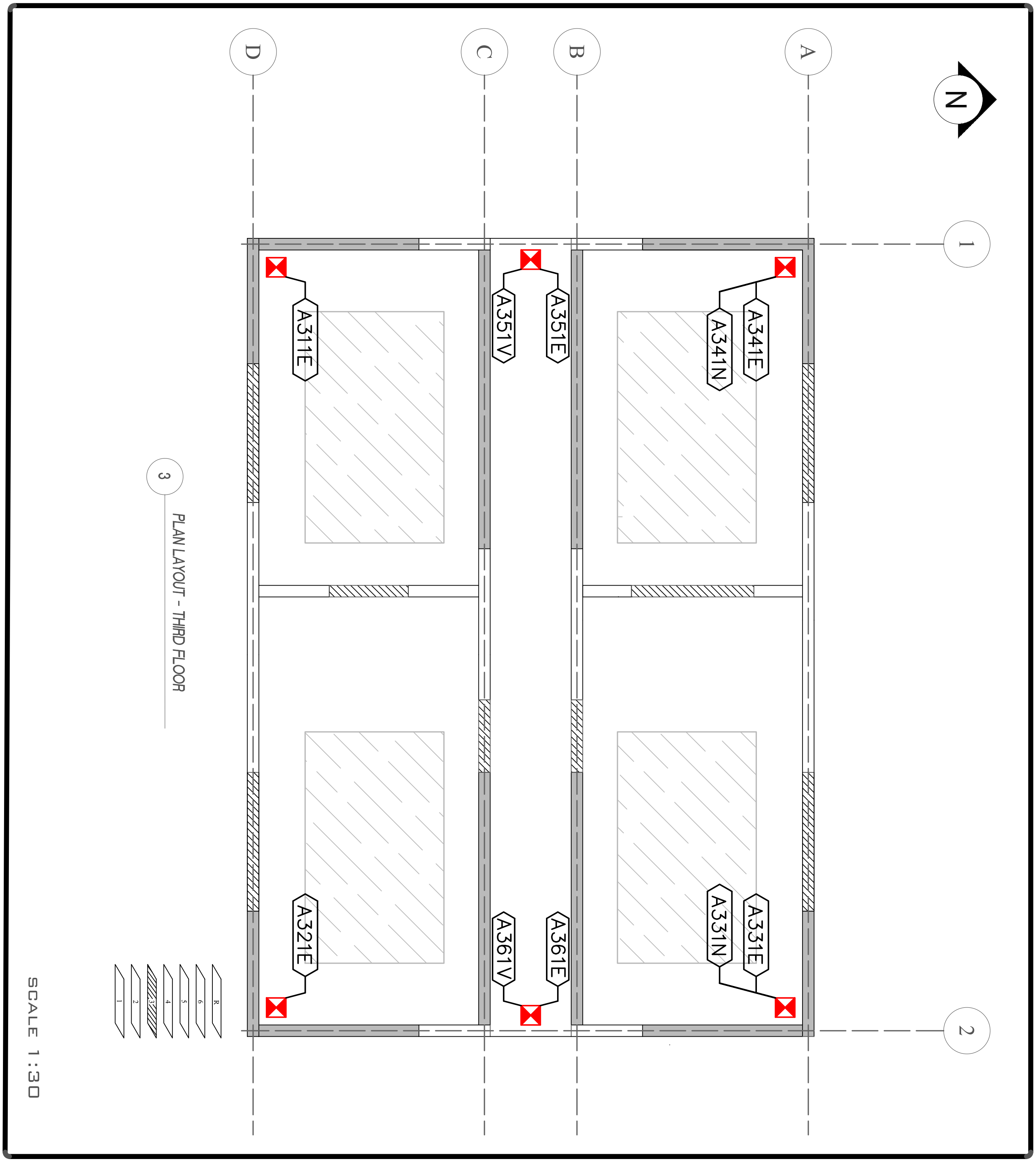

UCSD

UNIVERSITY OF CALIFORNIA, SAN DIEGO
DEPARTMENT OF STRUCTURAL ENGINEERING
LA JOLLA - CALIFORNIA 92093-0085

PROJECT NO. DATE:

NO.	DATE	REVISIONS

CFS Shake Table Test Project
Accelerometers (MEMS) - Floor 3
Configuration C2

SRIKAR GUNISETTY
Graduate Student Researcher
XIANG WANG
Post-doctoral Researcher

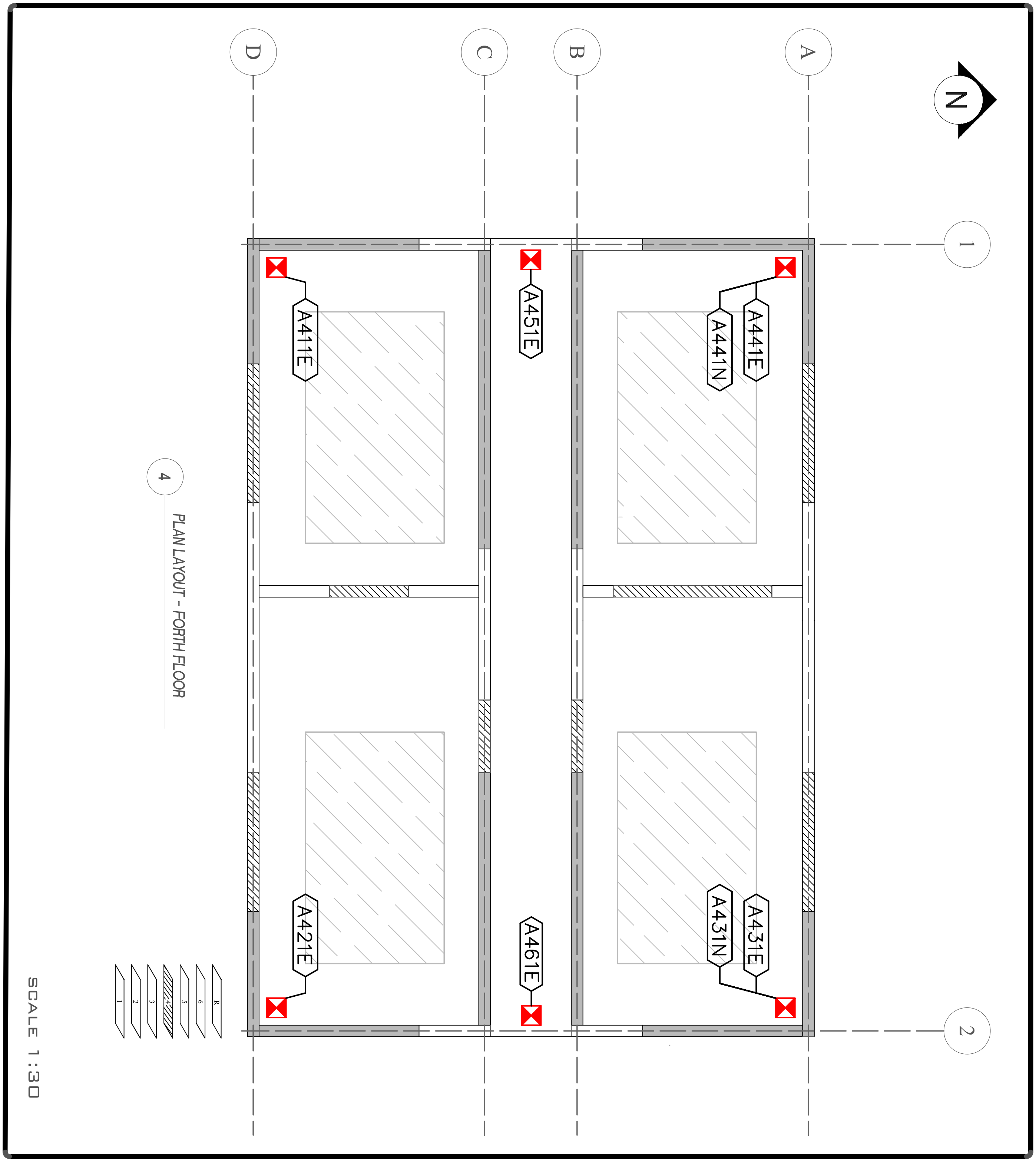

UCSD

UNIVERSITY OF CALIFORNIA, SAN DIEGO
DEPARTMENT OF STRUCTURAL ENGINEERING
LA JOLLA - CALIFORNIA 92093-0085

PROJECT NO. DATE:

NO.	DATE	REVISIONS

CFS Shake Table Test Project
Accelerometers (MEMS) - Floor 4
Configuration C2

SRIKAR GUNISETTY
Graduate Student Researcher
XIANG WANG
Post-doctoral Researcher

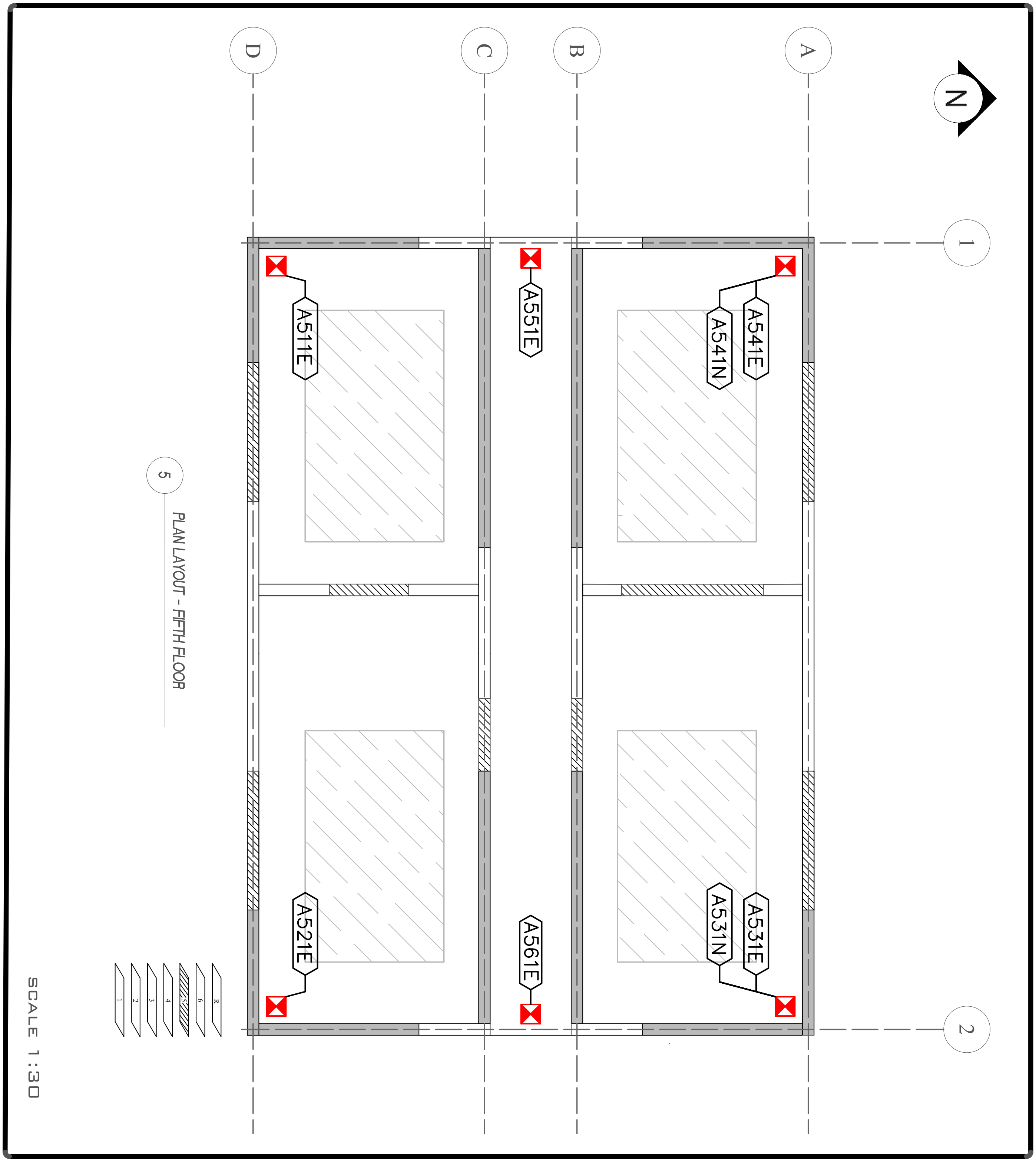

UCSD

UNIVERSITY OF CALIFORNIA, SAN DIEGO
DEPARTMENT OF STRUCTURAL ENGINEERING
LA JOLLA - CALIFORNIA 92093-0085

PROJECT NO. DATE:

NO.	DATE	REVISIONS

CFS Shake Table Test Project
Accelerometers (MEMS) - Floor 5
Configuration C2

SRIKAR GUNISETTY
Graduate Student Researcher
XIANG WANG
Post-doctoral Researcher

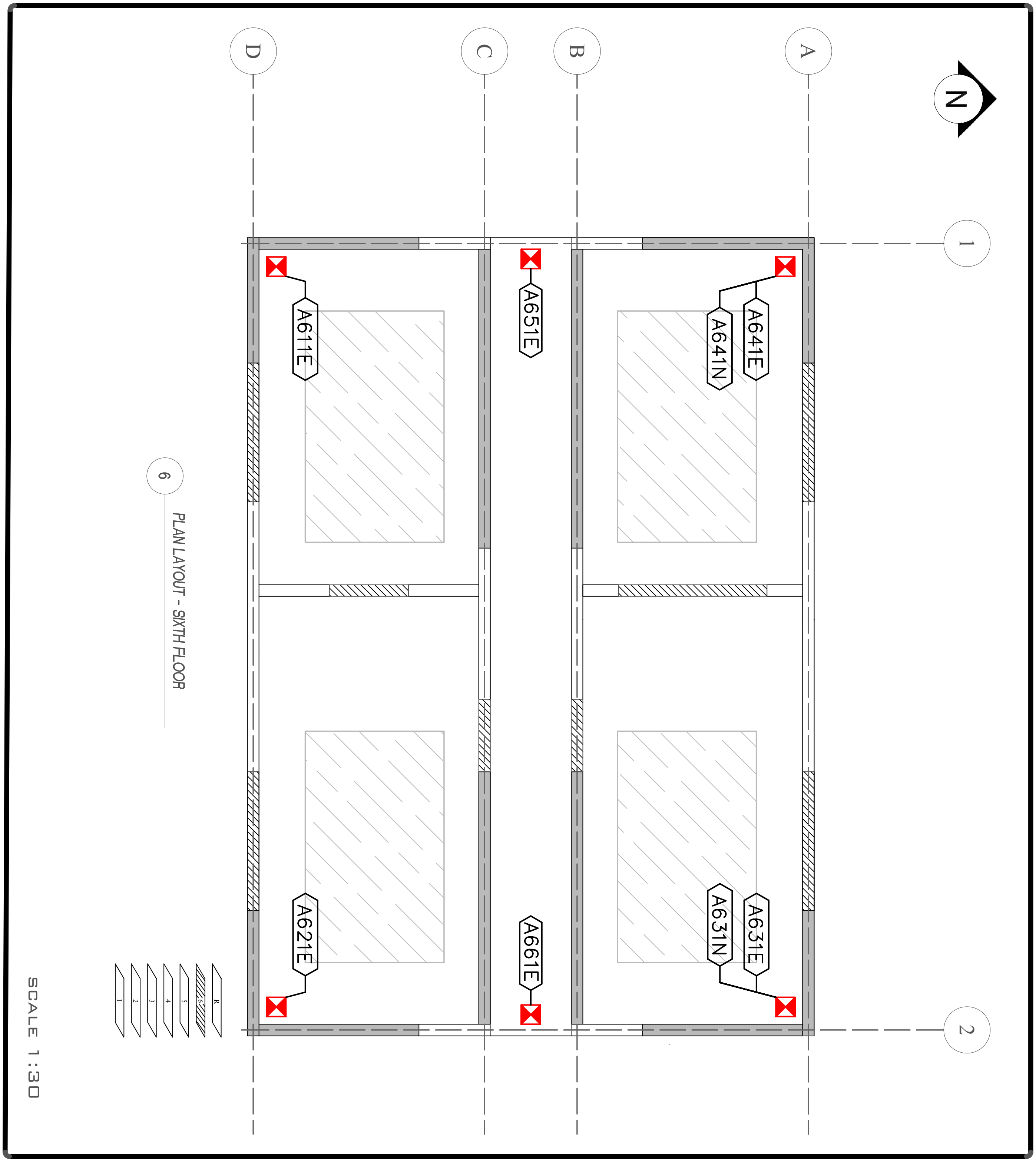

UCSD

UNIVERSITY OF CALIFORNIA, SAN DIEGO
DEPARTMENT OF STRUCTURAL ENGINEERING
LA JOLLA - CALIFORNIA 92093-0085

PROJECT NO. DATE:

NO.	DATE	REVISIONS

CFS Shake Table Test Project
Accelerometers (MEMS) - Floor 6
Configuration C2

SRIKAR GUNISETTY
Graduate Student Researcher
XIANG WANG
Post-doctoral Researcher

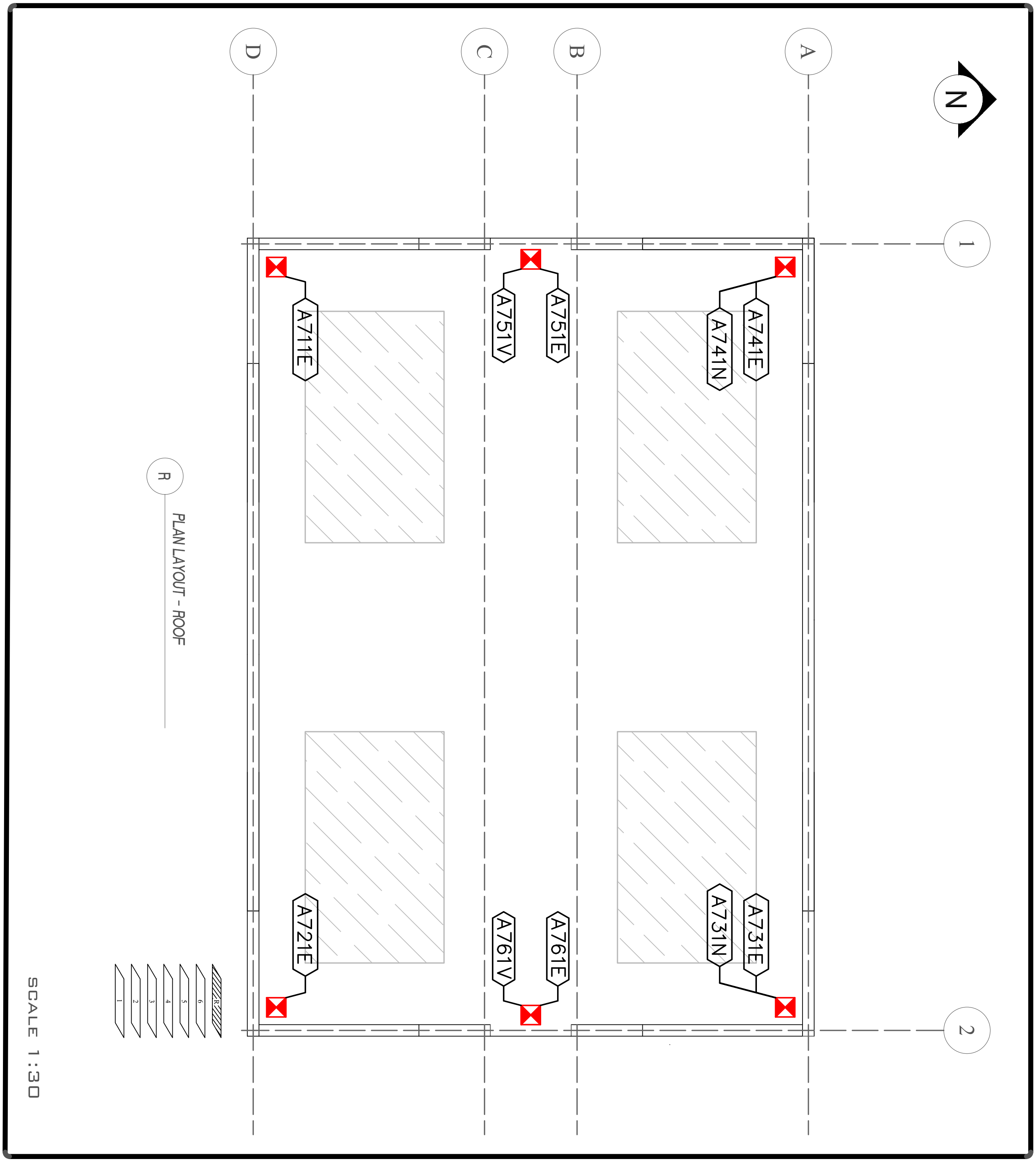

UCSD

UNIVERSITY OF CALIFORNIA, SAN DIEGO
DEPARTMENT OF STRUCTURAL ENGINEERING
LA JOLLA - CALIFORNIA 92093-0085

PROJECT NO. DATE:

NO.	DATE	REVISIONS

CFS Shake Table Test Project
Accelerometers (MEMS) - Roof
Configuration C2

SRIKAR GUNISETTY
Graduate Student Researcher
XIANG WANG
Post-doctoral Researcher

Analog Sensor Instrumentation – Configuration E1

Table E.4. Analog sensor number count – Configuration E1.

Floor #	Type of sensor				
	Accel. (MEMS)	Accel. (Kinemetrics)	String pot.	Linear pot.	Strain gage
1	4	0	25	12	31
2	12	3	25	16	20
3	12	0	1	0	0
4	8	3	20	10	16
5	8	0	0	0	0
6	11	3	0	0	0
Roof	13	3	0	1	0
Total	68	12	71	39	67

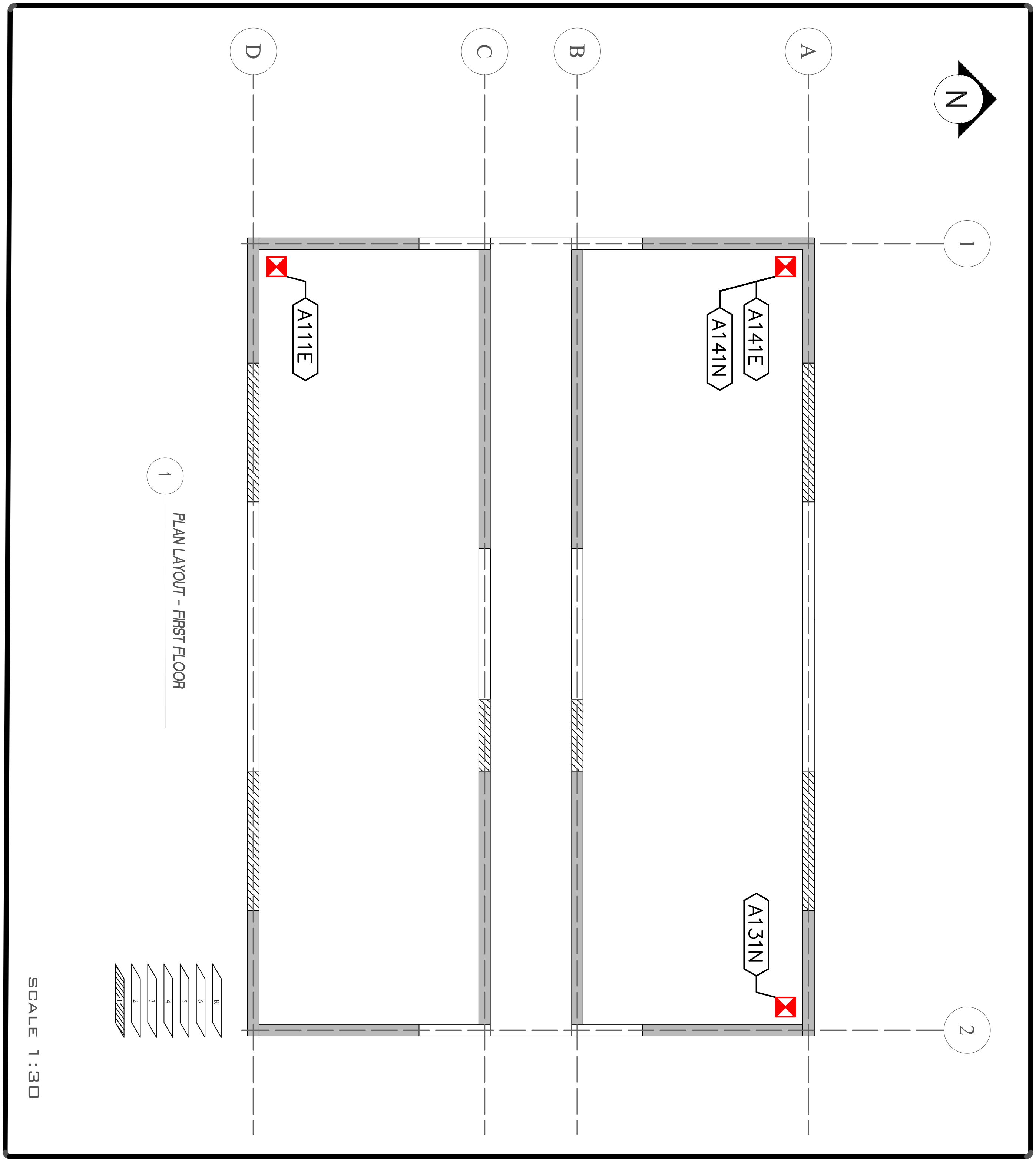

UCSD

UNIVERSITY OF CALIFORNIA, SAN DIEGO
DEPARTMENT OF STRUCTURAL ENGINEERING
LA JOLLA - CALIFORNIA 92093-0085

PROJECT NO. DATE:

NO.	DATE	REVISIONS

CFS Shake Table Test Project
Accelerometers (MEMS) - Floor 1
Configuration E1 (pre-fire)

SRIKAR GUNISETTY
Graduate Student Researcher
XIANG WANG
Post-doctoral Researcher

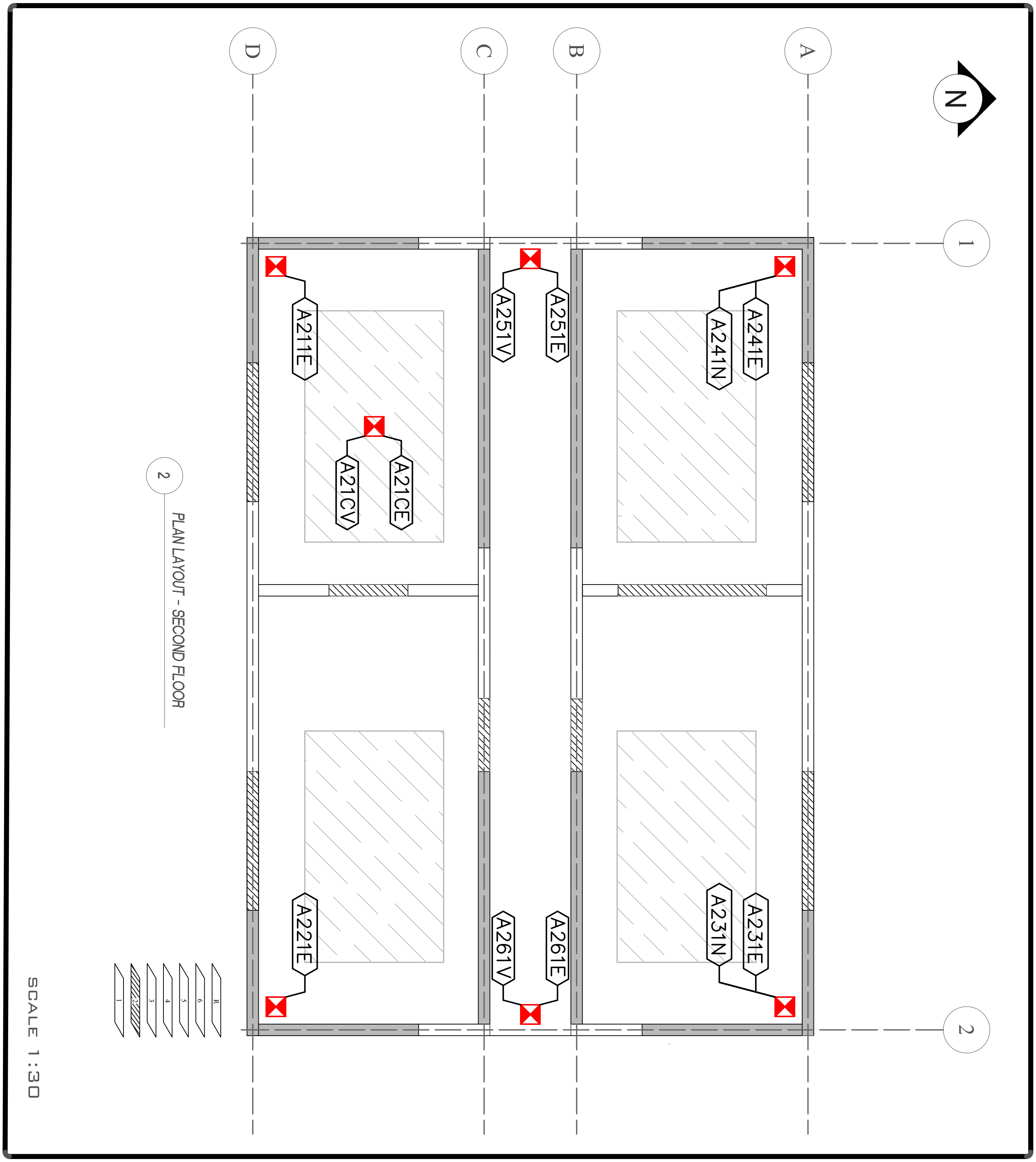

UCSD

UNIVERSITY OF CALIFORNIA, SAN DIEGO
DEPARTMENT OF STRUCTURAL ENGINEERING
LA JOLLA - CALIFORNIA 92093-0085

PROJECT NO. DATE:

NO.	DATE	REVISIONS

CFS Shake Table Test Project
Accelerometers (MEMS) - Floor 2
Configuration E1 (pre-fire)

SRIKAR GUNISETTY
Graduate Student Researcher
XIANG WANG
Post-doctoral Researcher

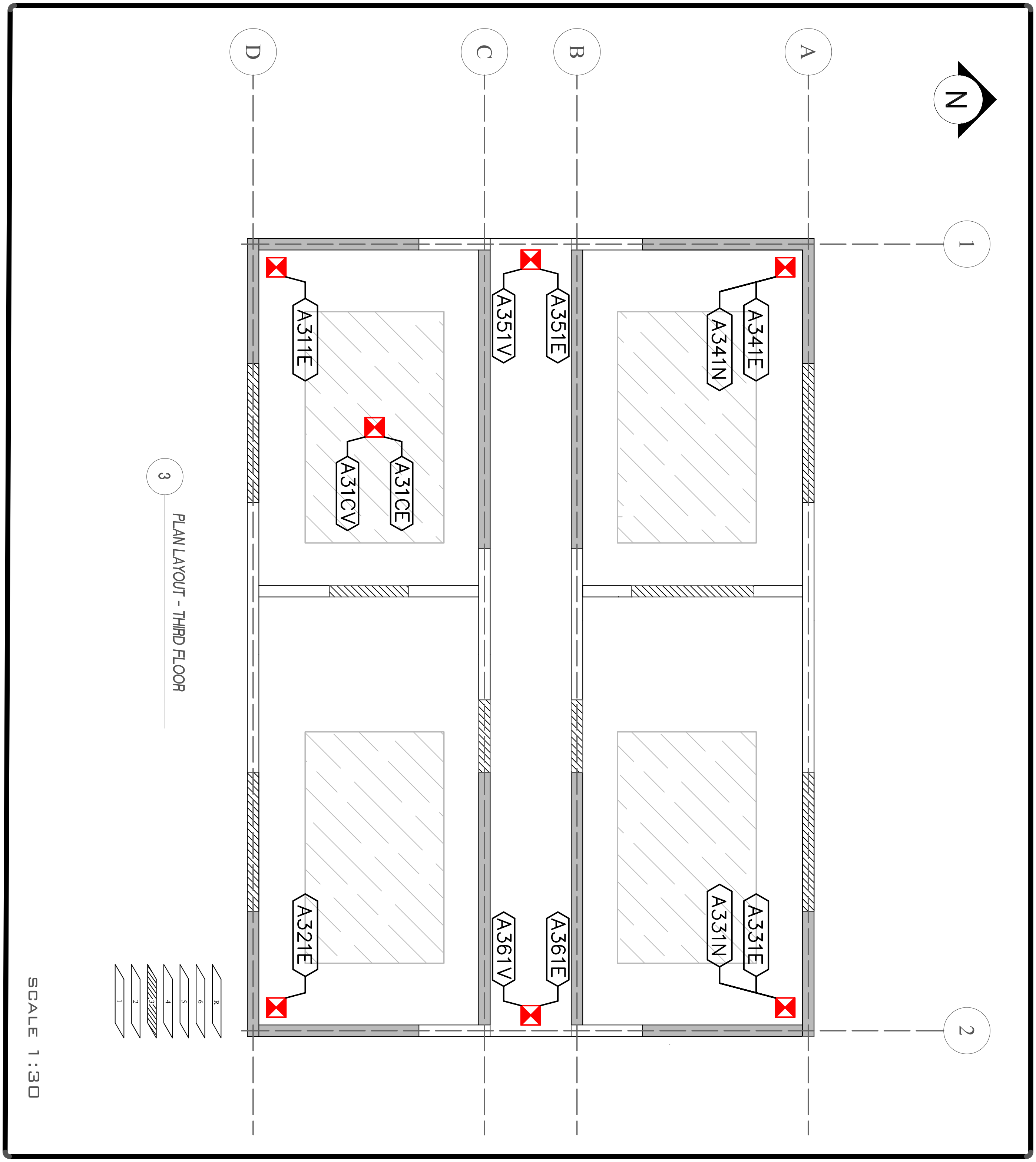

UCSD

UNIVERSITY OF CALIFORNIA, SAN DIEGO
DEPARTMENT OF STRUCTURAL ENGINEERING
LA JOLLA - CALIFORNIA 92093-0085

PROJECT NO. DATE:

NO.	DATE	REVISIONS

CFS Shake Table Test Project
Accelerometers (MEMS) - Floor 3
Configuration E1 (pre-fire)

SRIKAR GUNISETTY
Graduate Student Researcher
XIANG WANG
Post-doctoral Researcher

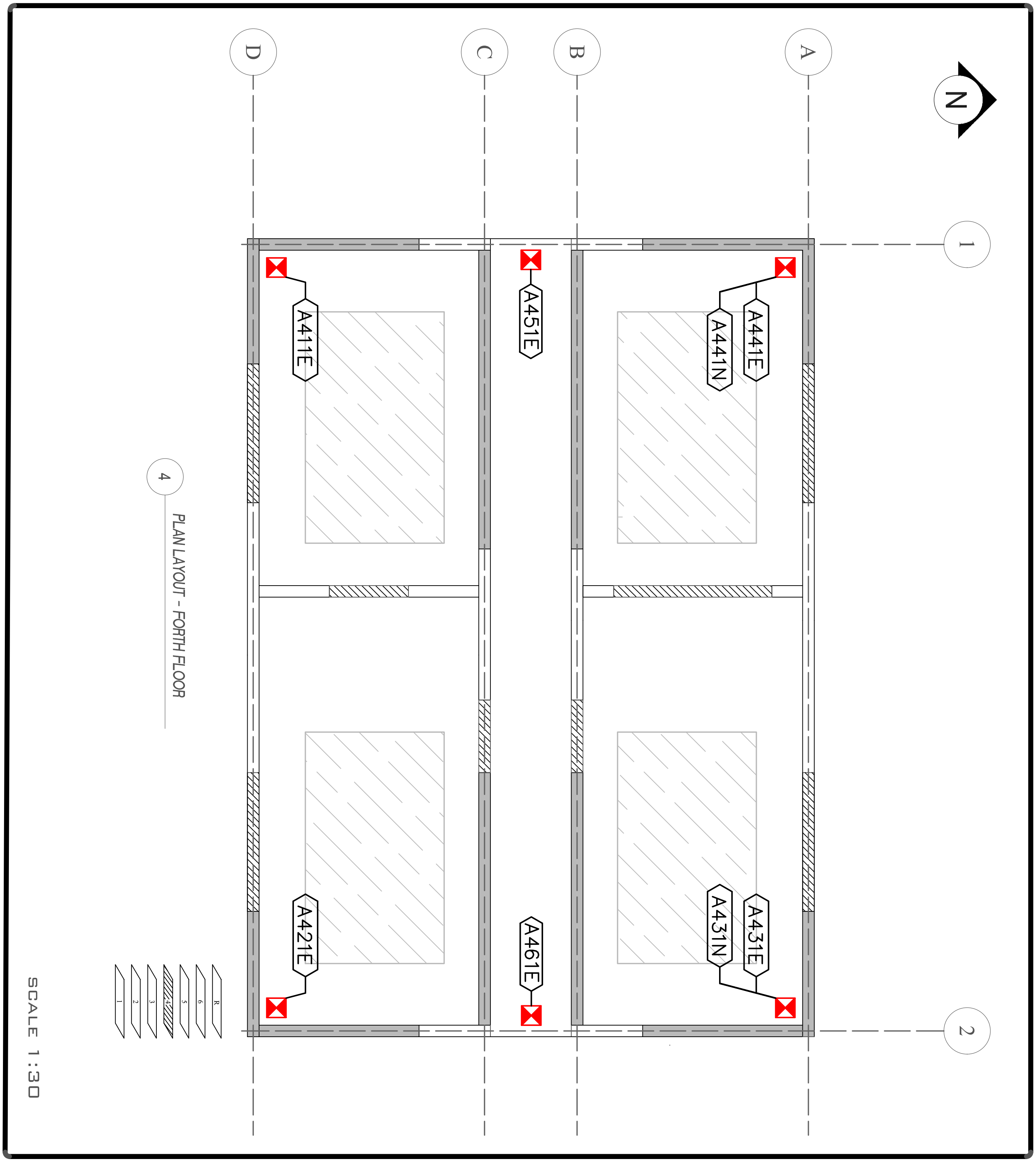

UCSD

UNIVERSITY OF CALIFORNIA, SAN DIEGO
DEPARTMENT OF STRUCTURAL ENGINEERING
LA JOLLA - CALIFORNIA 92093-0085

PROJECT NO. DATE:

NO.	DATE	REVISIONS

CFS Shake Table Test Project
Accelerometers (MEMS) - Floor 4
Configuration E1 (pre-fire)

SRIKAR GUNISETTY
Graduate Student Researcher
XIANG WANG
Post-doctoral Researcher

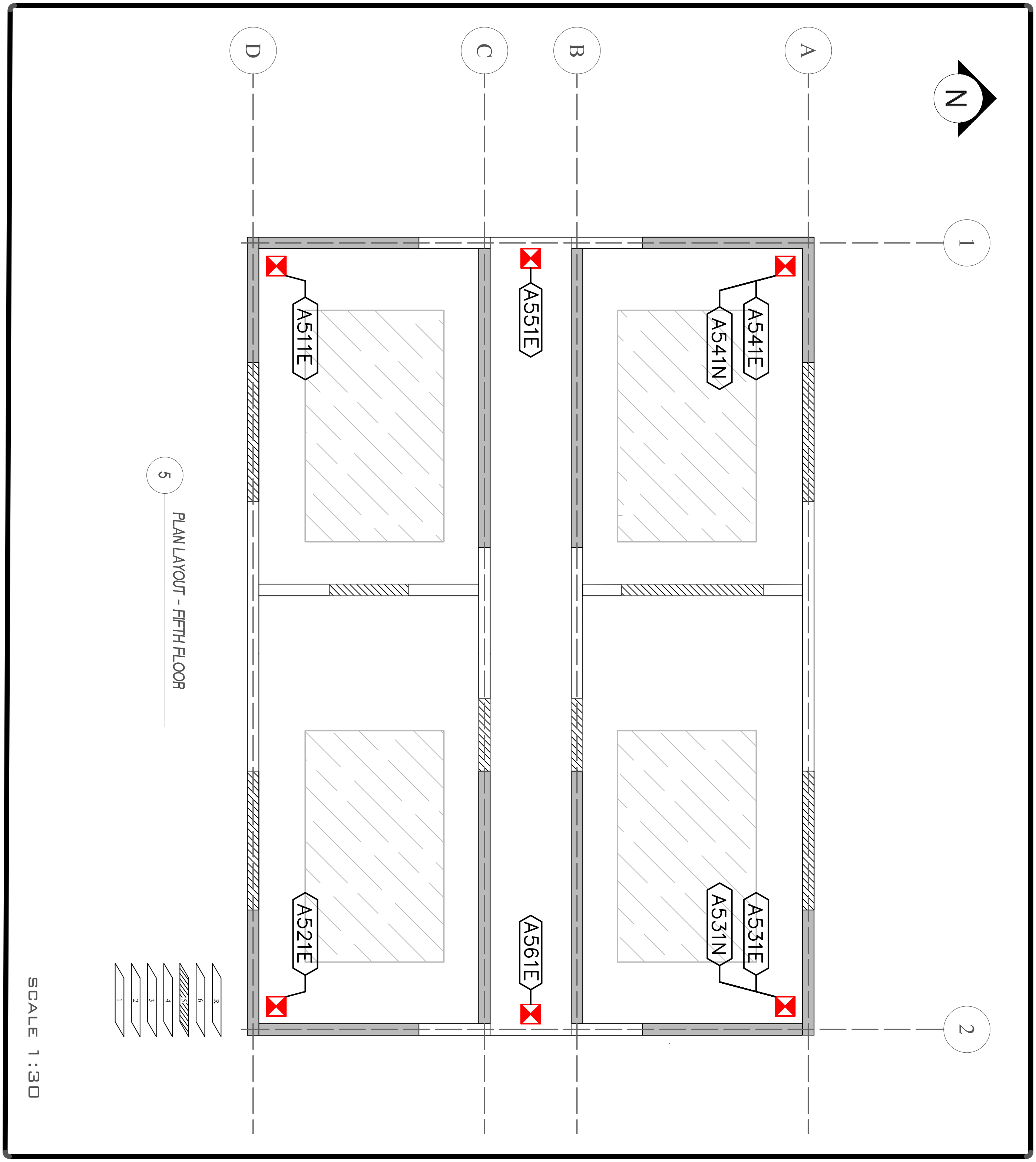

UCSD UNIVERSITY OF CALIFORNIA, SAN DIEGO DEPARTMENT OF STRUCTURAL ENGINEERING LA JOLLA - CALIFORNIA 92093-0085 PROJECT NO. DATE:	NO. DATE REVISIONS	CFS Shake Table Test Project Accelerometers (MEMS) - Floor 5 Configuration E1 (pre-fire)

SRIKAR GUNISETTY
Graduate Student Researcher
XIANG WANG
Post-doctoral Researcher

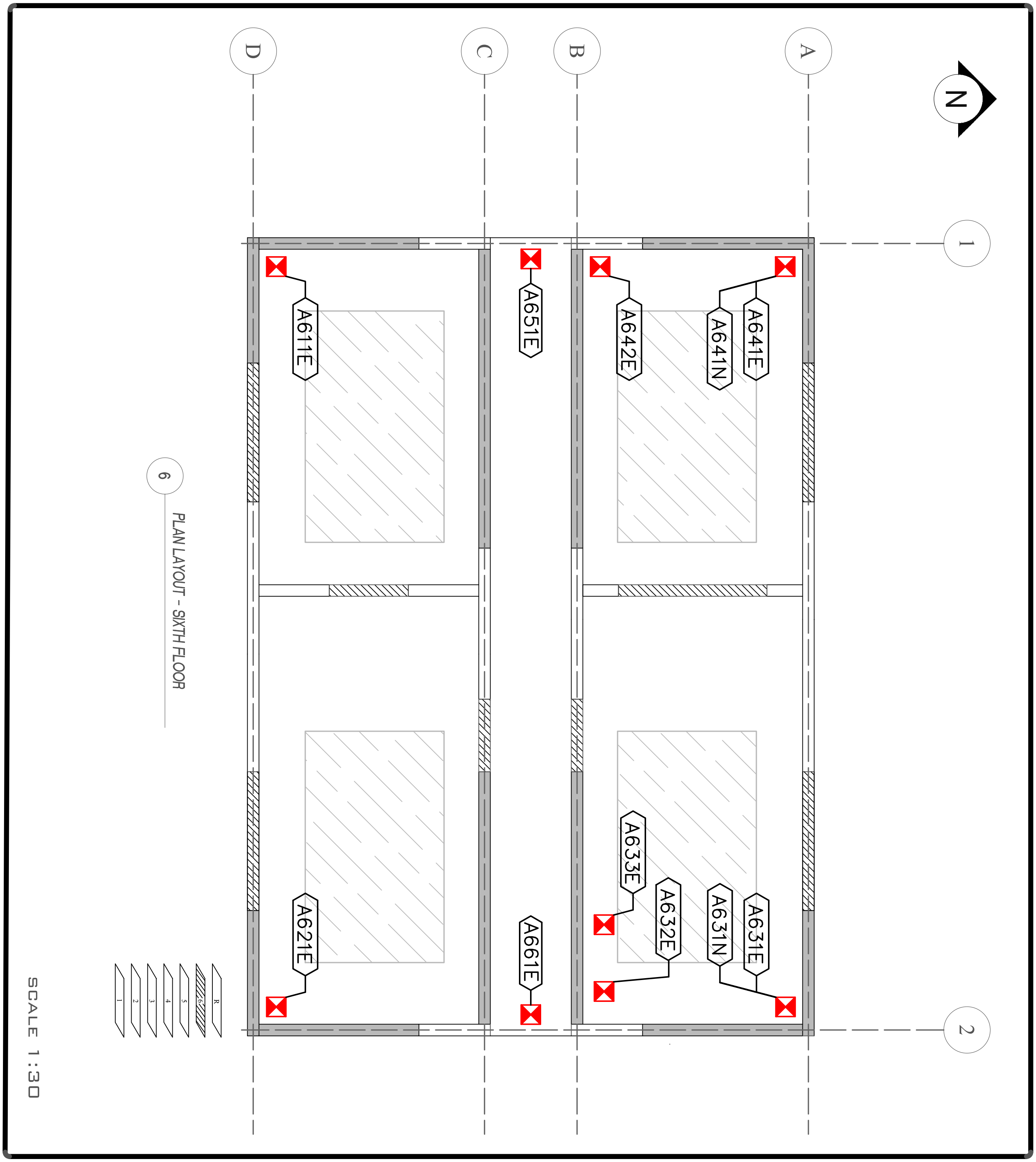

UCSD

UNIVERSITY OF CALIFORNIA, SAN DIEGO
DEPARTMENT OF STRUCTURAL ENGINEERING
LA JOLLA - CALIFORNIA 92093-0085

PROJECT NO. DATE:

NO.	DATE	REVISIONS

CFS Shake Table Test Project
Accelerometers (MEMS) - Floor 6
Configuration E1 (pre-fire)

SRIKAR GUNISETTY
Graduate Student Researcher
XIANG WANG
Post-doctoral Researcher

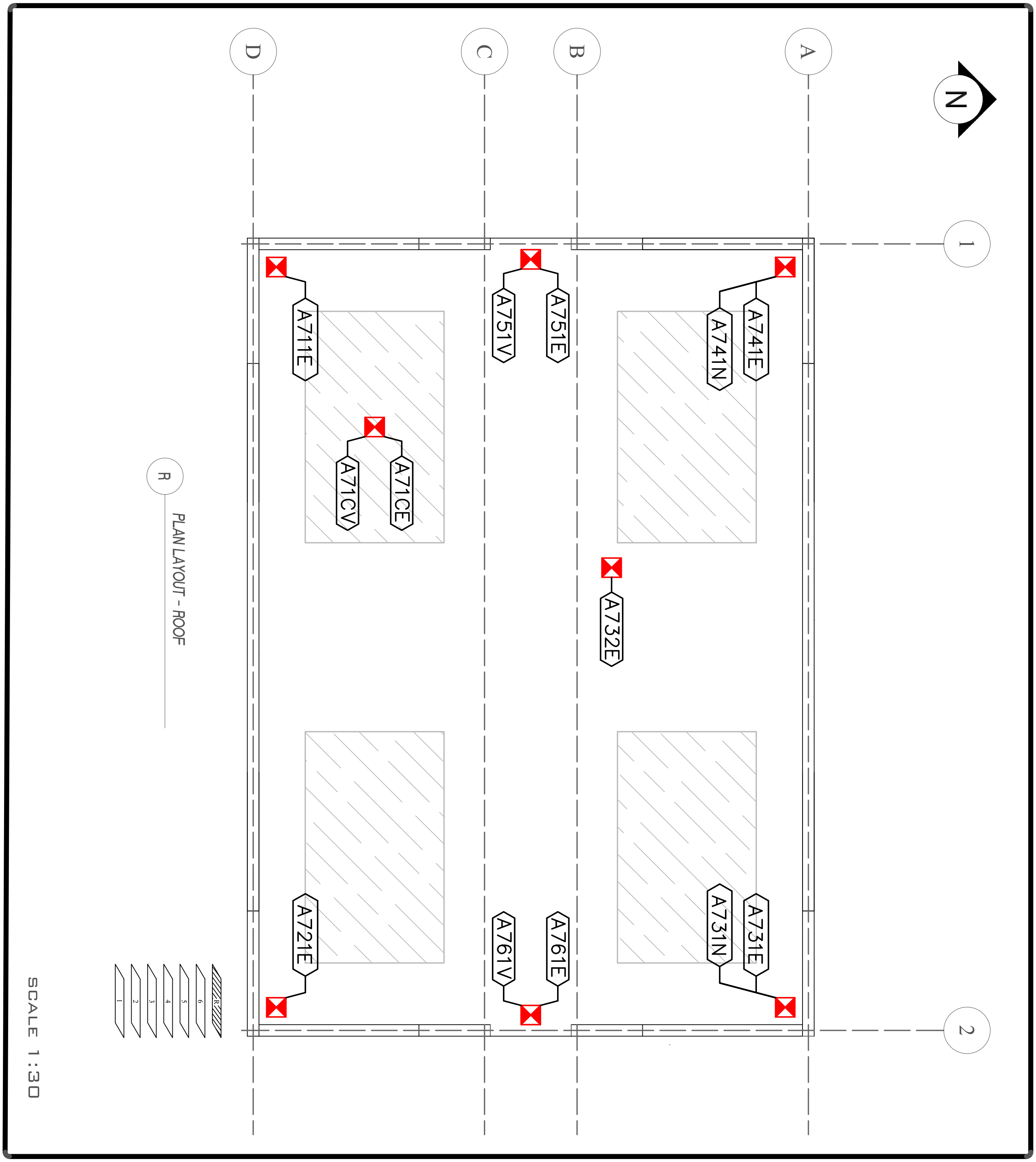

UCSD

UNIVERSITY OF CALIFORNIA, SAN DIEGO
DEPARTMENT OF STRUCTURAL ENGINEERING
LA JOLLA - CALIFORNIA 92093-0085

PROJECT NO. DATE:

NO.	DATE	REVISIONS

CFS Shake Table Test Project
Accelerometers (MEMS) - Roof
Configuration E1 (pre-fire)

SRIKAR GUNISETTY
Graduate Student Researcher
XIANG WANG
Post-doctoral Researcher

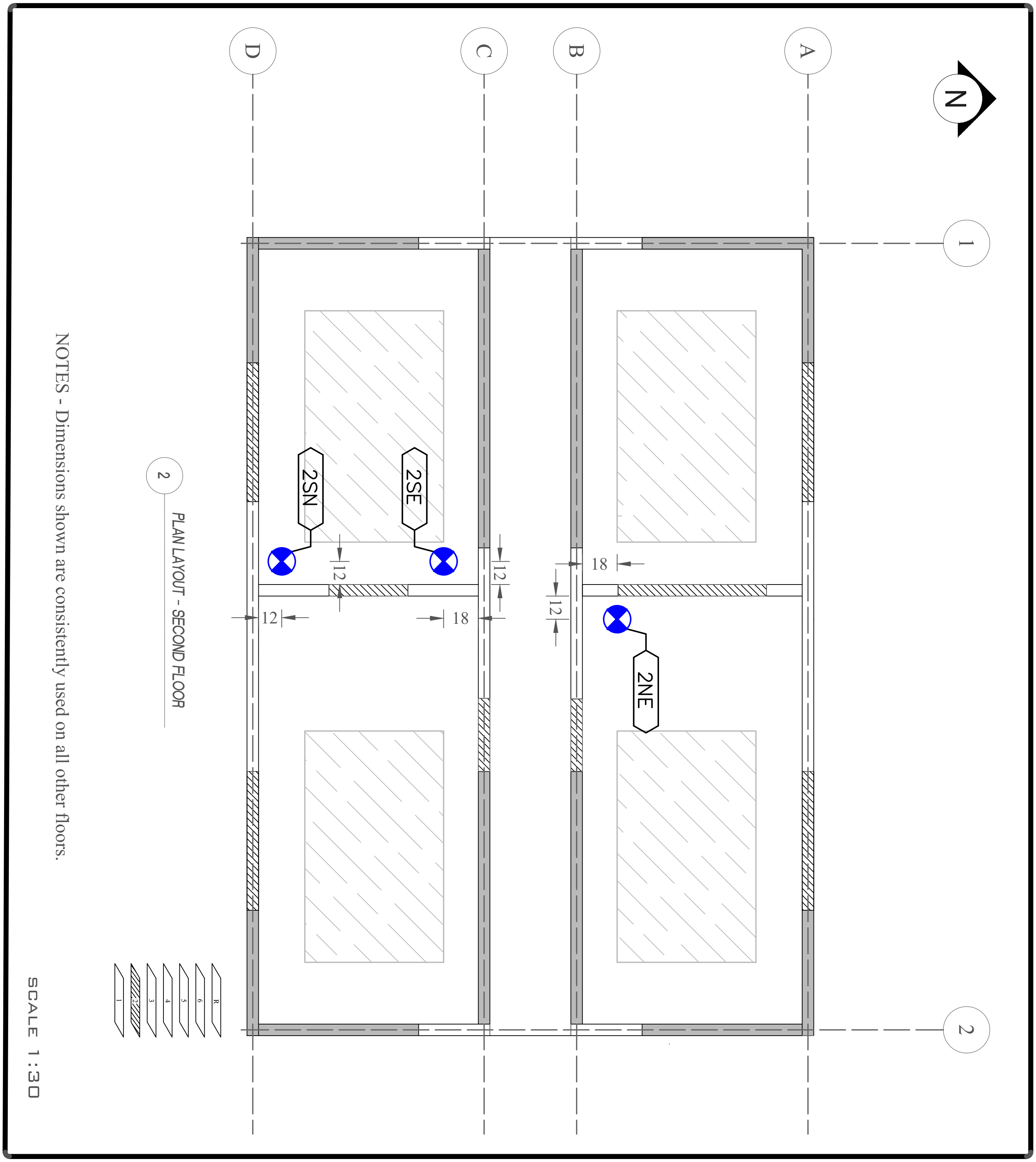

UCSD

UNIVERSITY OF CALIFORNIA, SAN DIEGO
DEPARTMENT OF STRUCTURAL ENGINEERING
LA JOLLA - CALIFORNIA 92093-0085

PROJECT NO. DATE:

NO.	DATE	REVISIONS

CFS Shake Table Test Project
Accelerometers (Kinemetrics) - Floor 2
Configuration E1

SRIKAR GUNISETTY
Graduate Student Researcher
XIANG WANG
Post-doctoral Researcher

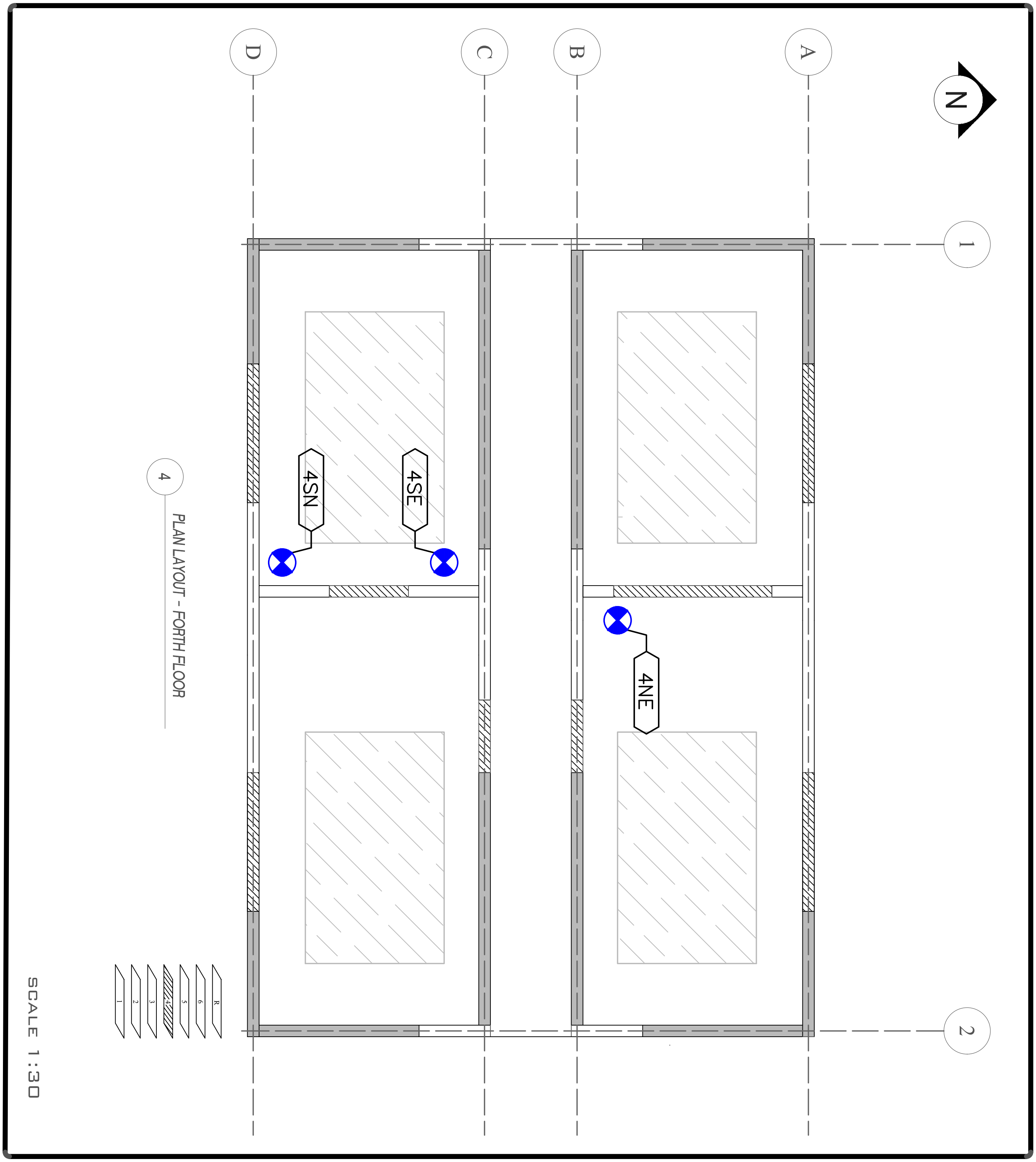

UCSD UNIVERSITY OF CALIFORNIA, SAN DIEGO DEPARTMENT OF STRUCTURAL ENGINEERING LA JOLLA - CALIFORNIA 92093-0085 PROJECT NO. DATE:	NO. DATE REVISIONS	CFS Shake Table Test Project Accelerometers (Kinemetrics) - Floor 4 Configuration E1	SRIKAR GUNISETTY Graduate Student Researcher XIANG WANG Post-doctoral Researcher

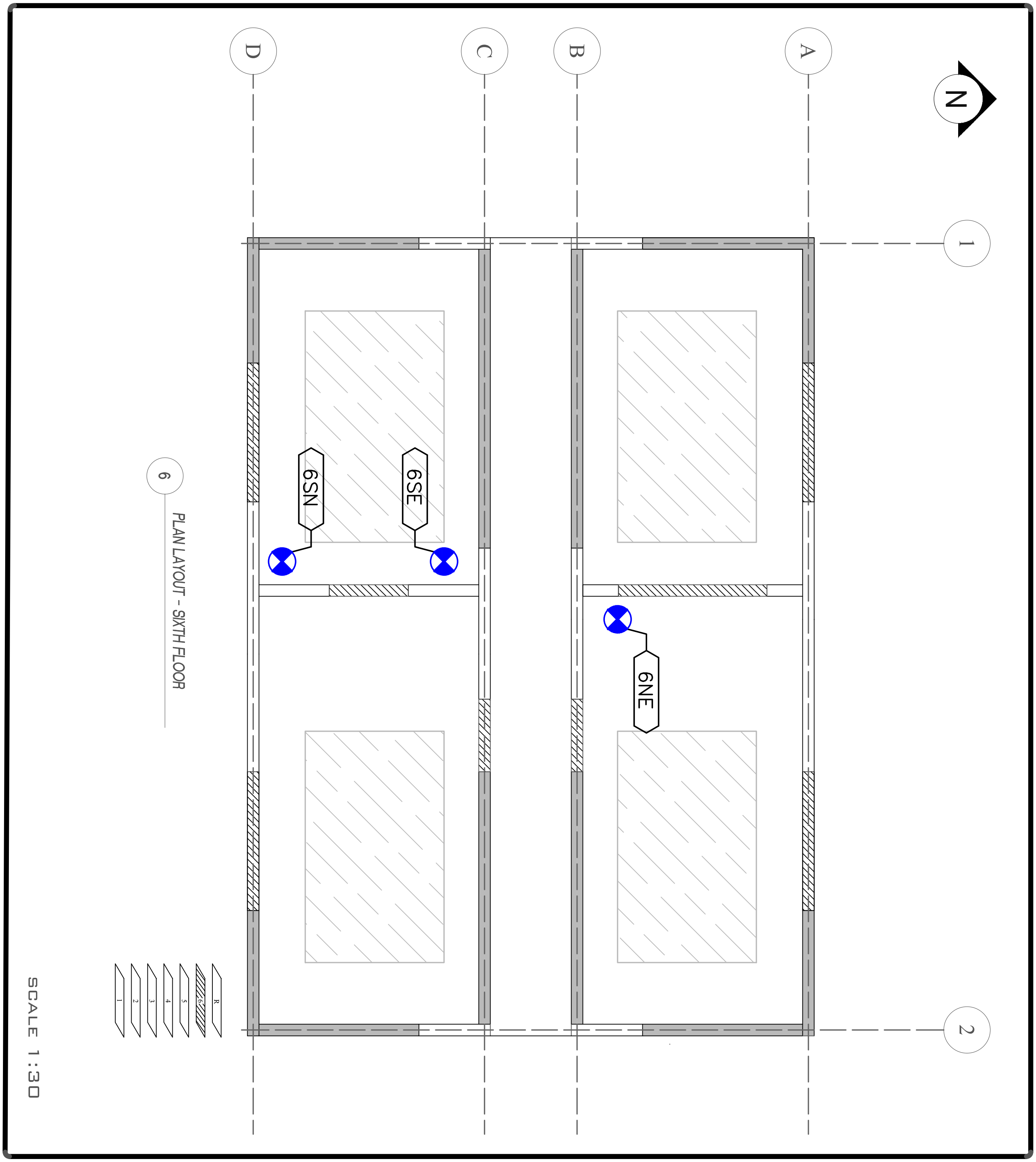

UCSD
UNIVERSITY OF CALIFORNIA, SAN DIEGO
DEPARTMENT OF STRUCTURAL ENGINEERING
LA JOLLA - CALIFORNIA 92093-0085

PROJECT NO. DATE:

NO.	DATE	REVISIONS

CFS Shake Table Test Project
Accelerometers (Kinemetrics) - Floor 6
Configuration E1

SRIKAR GUNISETTY
Graduate Student Researcher
XIANG WANG
Post-doctoral Researcher

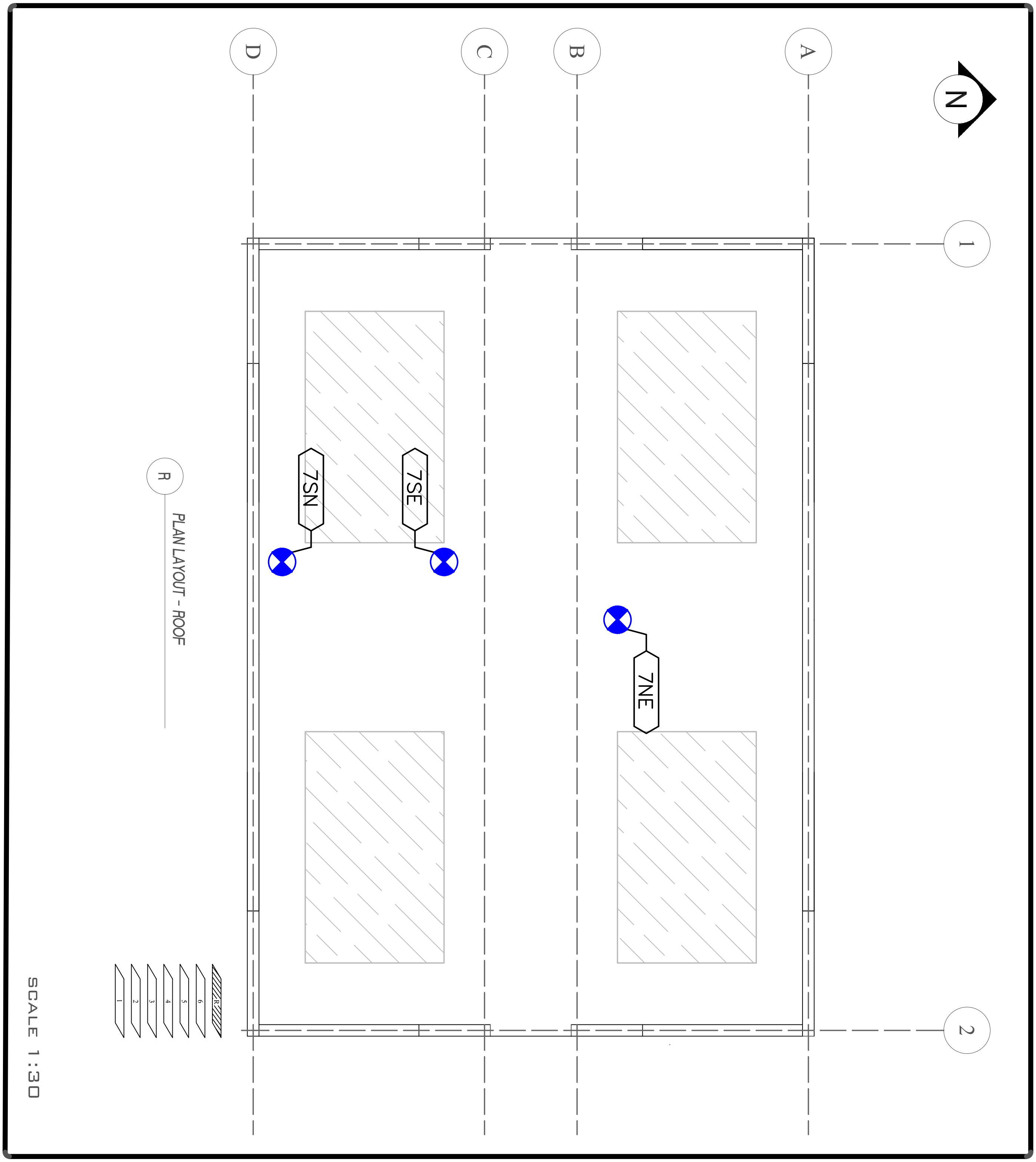

UCSD	NO. DATE REVISIONS		
UNIVERSITY OF CALIFORNIA, SAN DIEGO DEPARTMENT OF STRUCTURAL ENGINEERING LA JOLLA - CALIFORNIA 92093-0085 PROJECT NO. DATE:		CFS Shake Table Test Project Accelerometers (Kinemetrics) - Roof Configuration E1	SRIKAR GUNISETTY Graduate Student Researcher XIANG WANG Post-doctoral Researcher

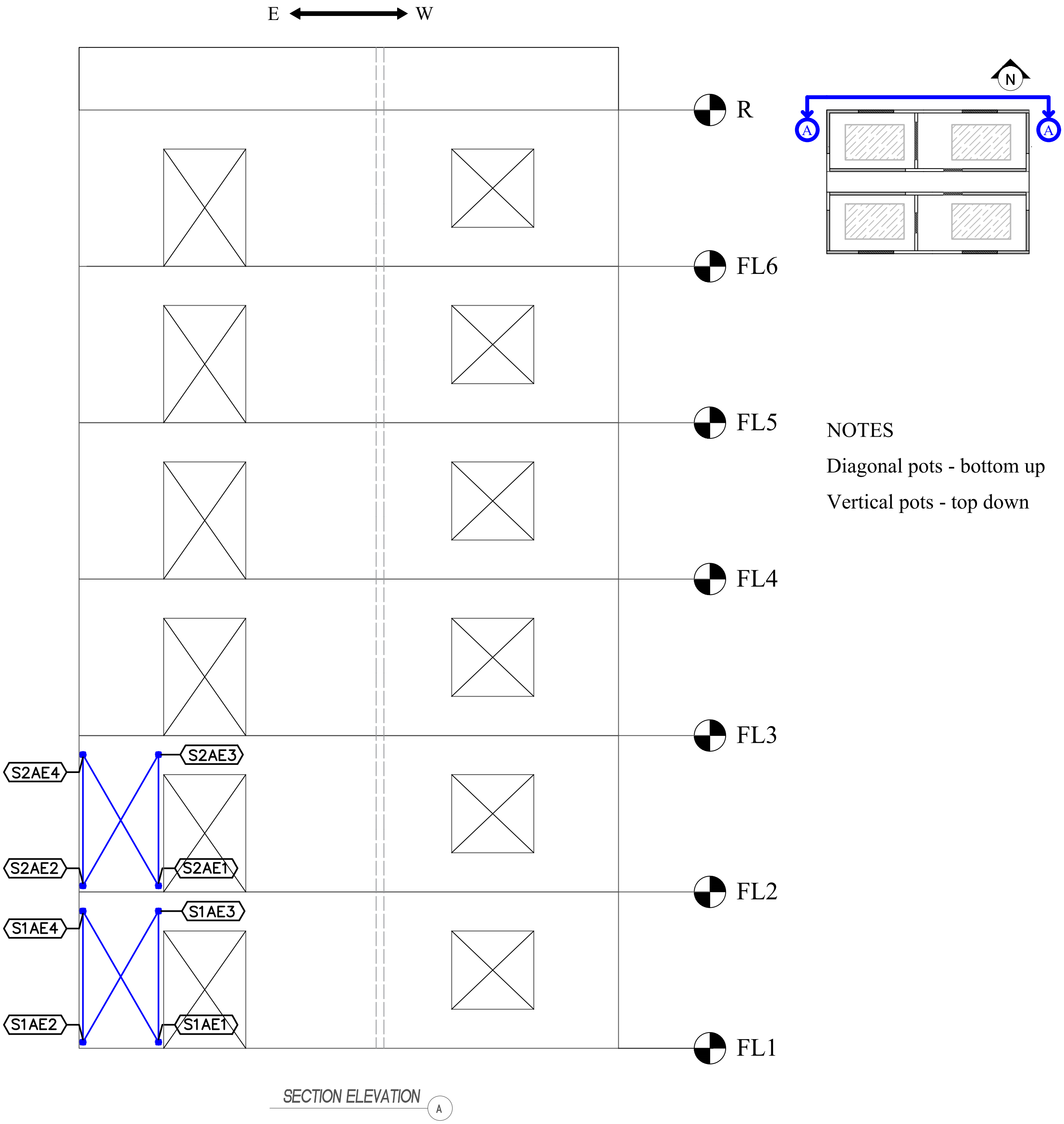

NOTES
Diagonal pots - bottom up
Vertical pots - top down

NOTES - String potentiometers on the exterior side on wall line A

SCALE 1:30

UCSD UNIVERSITY OF CALIFORNIA, SAN DIEGO DEPARTMENT OF STRUCTURAL ENGINEERING LA JOLLA - CALIFORNIA 92093-0085 PROJECT NO. DATE:	NO. DATE REVISIONS	CFS Shake Table Test Project String Potentiometers - Wall line A Configuration - E1

SRIKAR GUNISETTY
Graduate Student Researcher
XIANG WANG
Post-doctoral Researcher

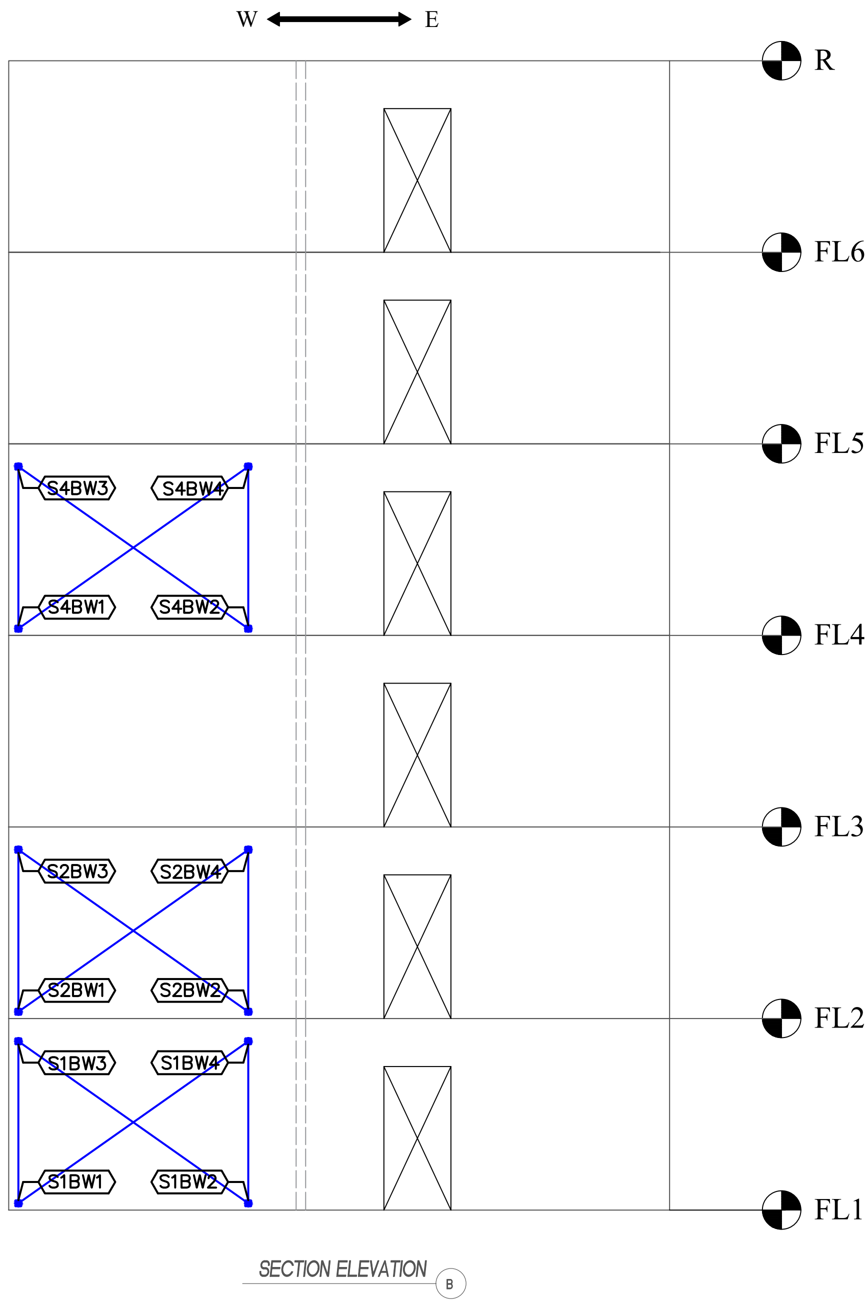

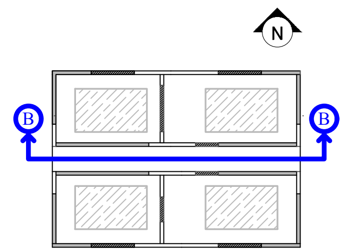

NOTES

Diagonal pots - bottom up

Vertical pots - top down

NOTES - String potentiometers on the corridor side on wall line B

SCALE 1:30

UCSD UNIVERSITY OF CALIFORNIA, SAN DIEGO DEPARTMENT OF STRUCTURAL ENGINEERING LA JOLLA - CALIFORNIA 92093-0085 PROJECT NO. DATE:	NO.	DATE	REVISIONS	CFS Shake Table Test Project String Potentiometers - Wall line B Configuration - E1	SRIKAR GUNISETTY Graduate Student Researcher XIANG WANG Post-doctoral Researcher

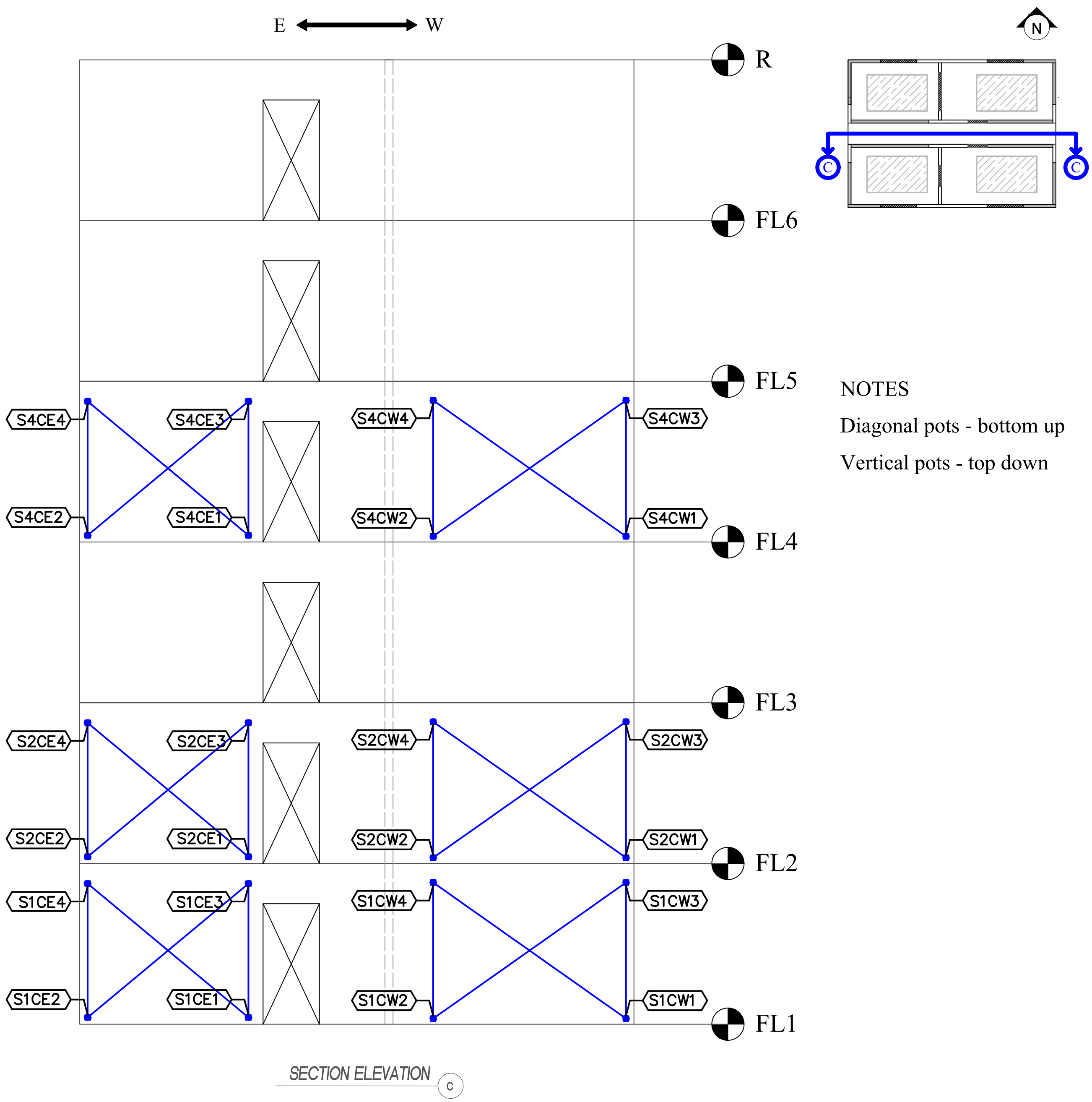

NOTES

Diagonal pots - bottom up

Vertical pots - top down

NOTES - String potentiometers on the corridor side on wall line C

SCALE 1:30

UCSD

UNIVERSITY OF CALIFORNIA, SAN DIEGO
DEPARTMENT OF STRUCTURAL ENGINEERING
LA JOLLA - CALIFORNIA 92093-0085

PROJECT NO. DATE:

NO.	DATE	REVISIONS

CFS Shake Table Test Project
String Potentiometers - Wall line C
Configuration - E1

SRIKAR GUNISETTY
Graduate Student Researcher
XIANG WANG
Post-doctoral Researcher

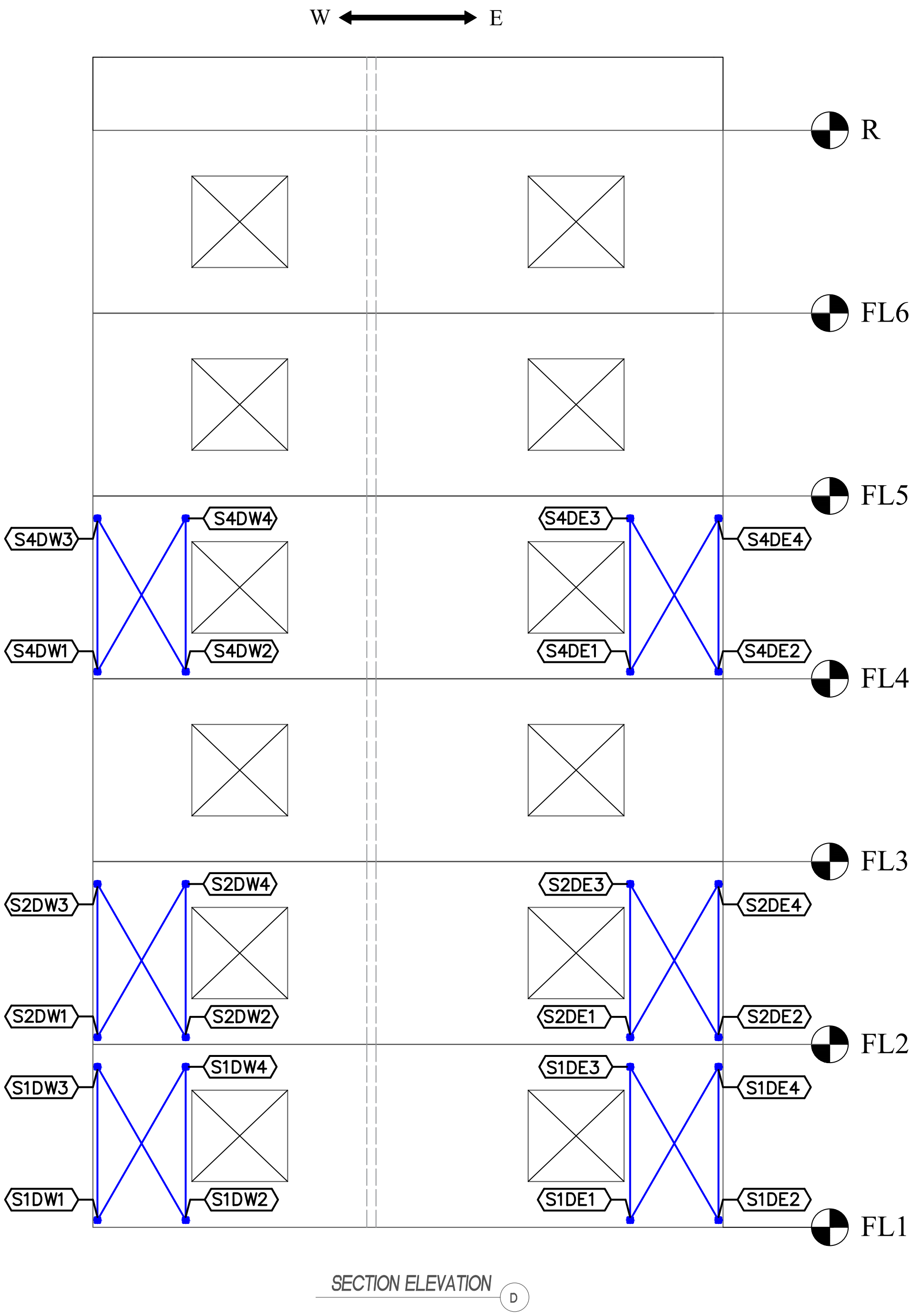

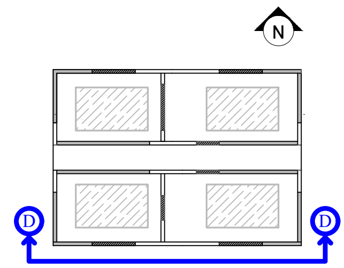

NOTES

Diagonal pots - bottom up

Vertical pots - top down

NOTES - String potentiometers on the exterior side on wall line D

SCALE 1:30

UCSD UNIVERSITY OF CALIFORNIA, SAN DIEGO DEPARTMENT OF STRUCTURAL ENGINEERING LA JOLLA - CALIFORNIA 92093-0085 PROJECT NO. DATE:	CFS Shake Table Test Project String Potentiometers - Wall line D Configuration - E1	SRIKAR GUNISETTY Graduate Student Researcher XIANG WANG Post-doctoral Researcher

NO. DATE REVISIONS

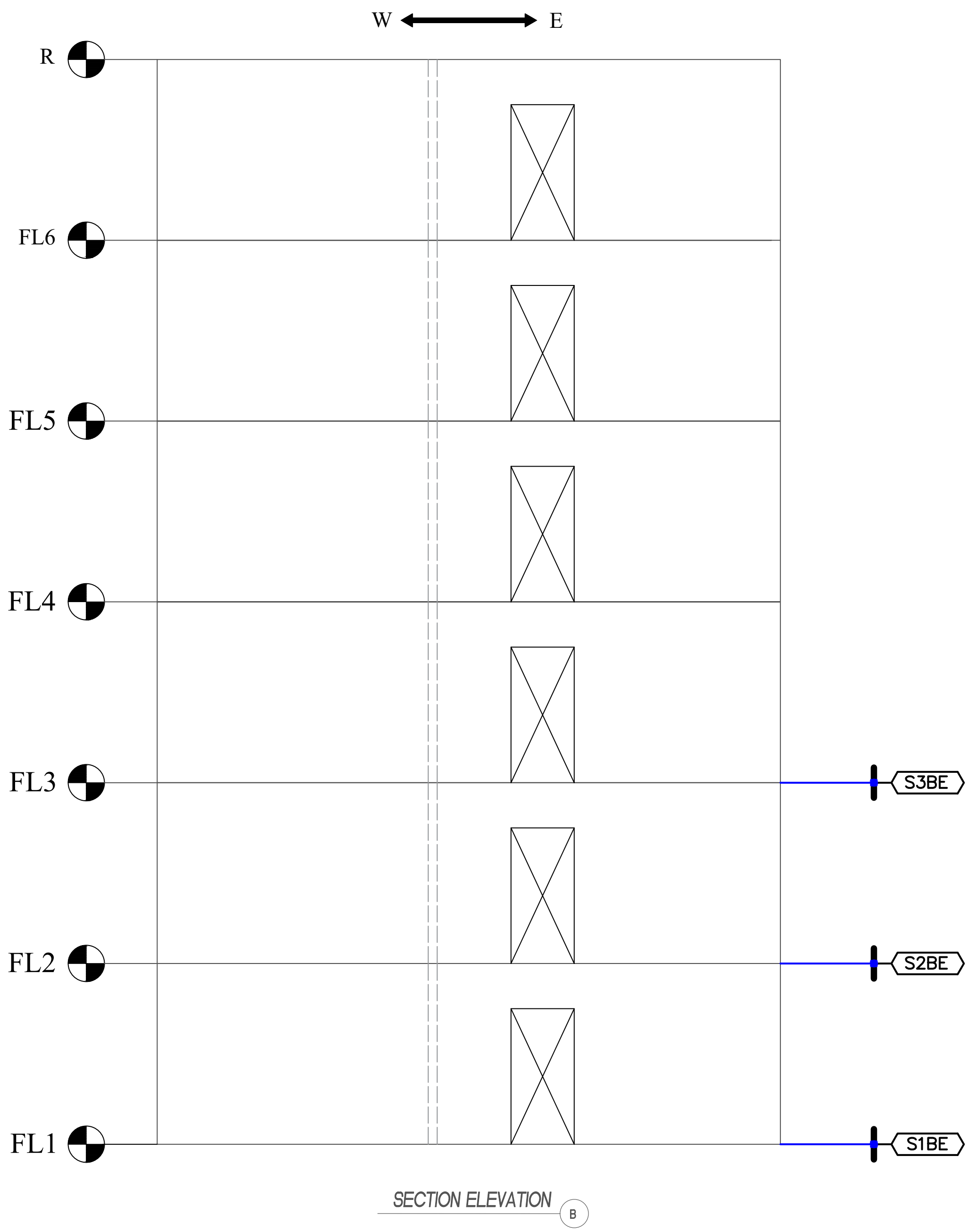

NOTES - String potentiometers on the exterior east side on wall line B

SCALE 1:30

UCSD UNIVERSITY OF CALIFORNIA, SAN DIEGO DEPARTMENT OF STRUCTURAL ENGINEERING LA JOLLA - CALIFORNIA 92093-0085 PROJECT NO. DATE:	NO. DATE REVISIONS	CFS Shake Table Test Project String Potentiometers - Fixture Configuration - E1	SRIKAR GUNISETTY Graduate Student Researcher XIANG WANG Post-doctoral Researcher

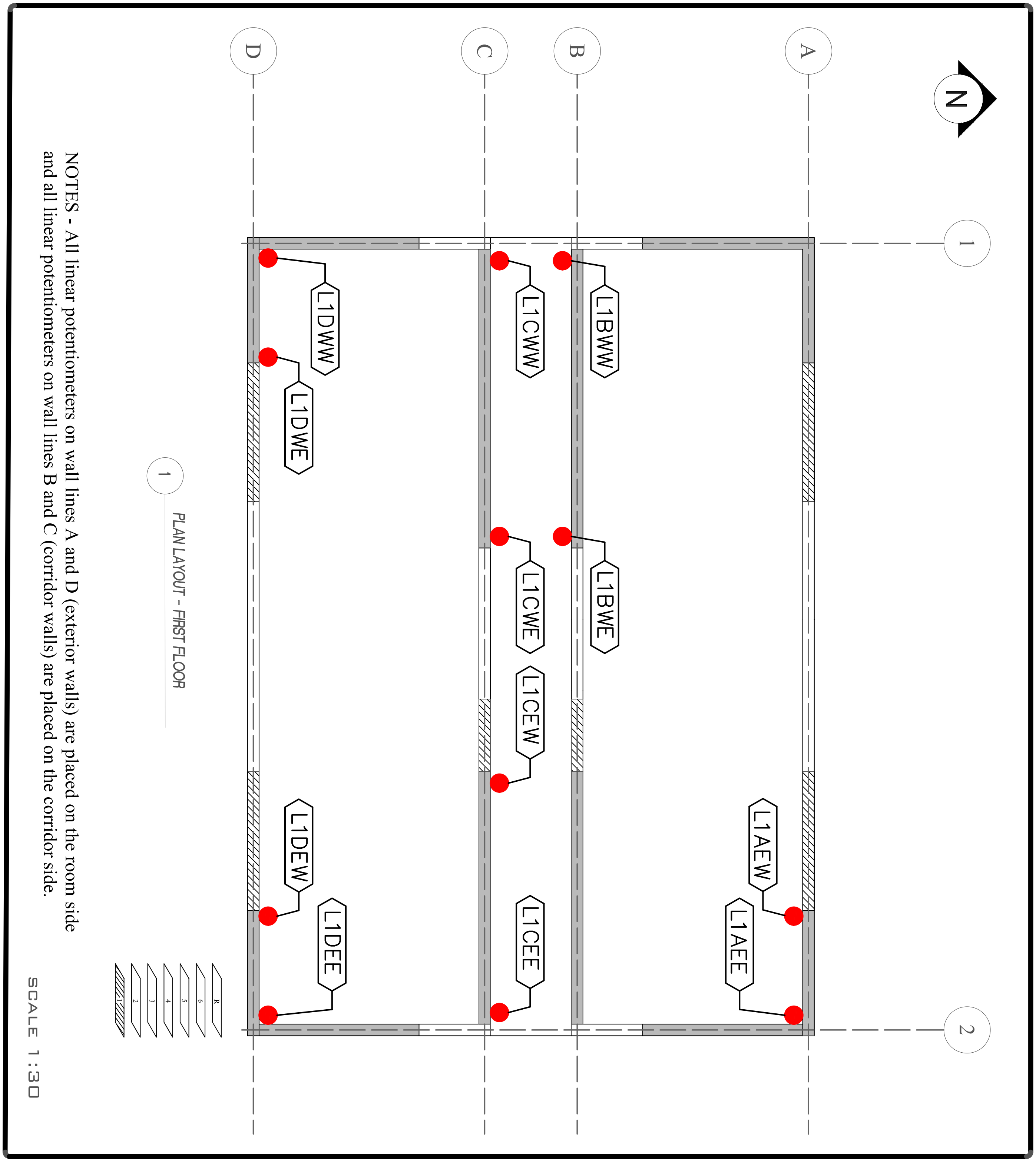

UCSD UNIVERSITY OF CALIFORNIA, SAN DIEGO DEPARTMENT OF STRUCTURAL ENGINEERING LA JOLLA - CALIFORNIA 92093-0085 PROJECT NO. DATE:	NO. DATE REVISIONS	CFS Shake Table Test Project Linear Potentiometers - Floor 1 Configuration E1	SRIKAR GUNISETTY Graduate Student Researcher XIANG WANG Post-doctoral Researcher

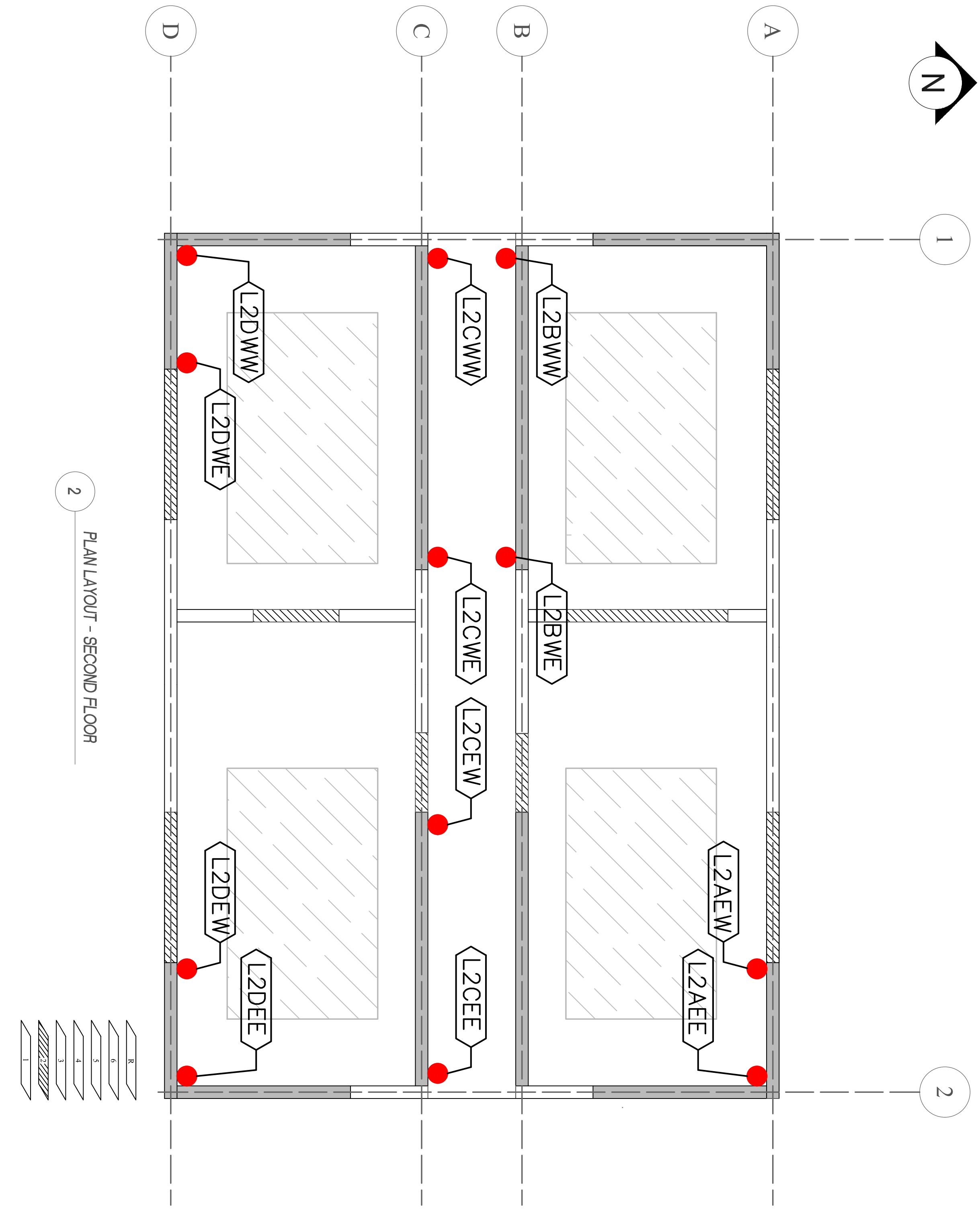

NOTES - All linear potentiometers on wall lines A and D (exterior walls) are placed on the room side and all linear potentiometers on wall lines B and C (corridor walls) are placed on the corridor side.

SCALE 1:30

UCSD	NO. / DATE / REVISIONS		
UNIVERSITY OF CALIFORNIA, SAN DIEGO DEPARTMENT OF STRUCTURAL ENGINEERING LA JOLLA - CALIFORNIA 92093-0085 PROJECT NO. DATE:		CFS Shake Table Test Project Linear Potentiometers - Floor 2 Configuration E1	SRIKAR GUNISETTY Graduate Student Researcher XIANG WANG Post-doctoral Researcher

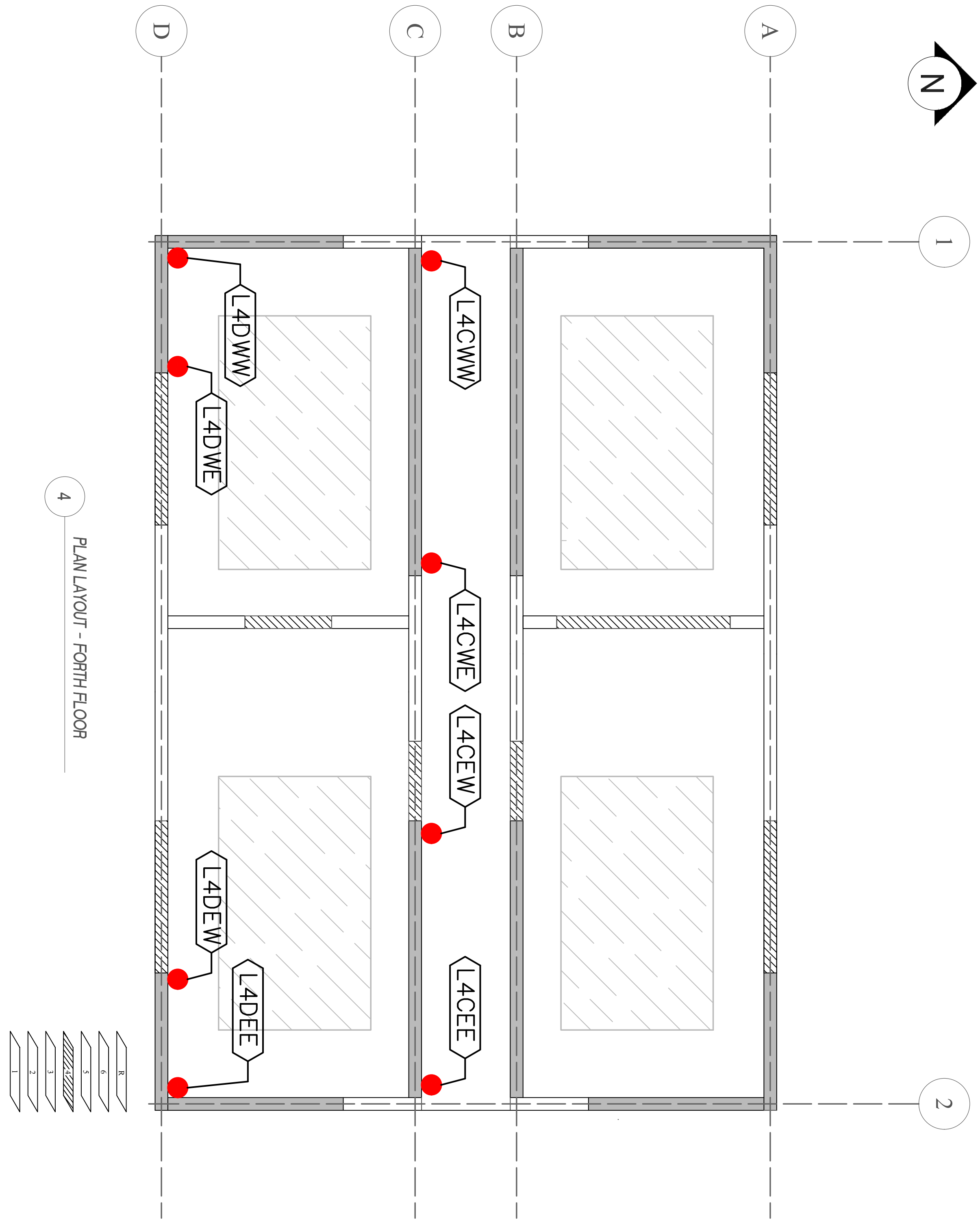

NOTES - All linear potentiometers on wall line D (exterior wall) are placed on the room side and all linear potentiometers on wall line C (corridor walls) are placed on the corridor side.

SCALE 1:30

UCSD UNIVERSITY OF CALIFORNIA, SAN DIEGO DEPARTMENT OF STRUCTURAL ENGINEERING LA JOLLA - CALIFORNIA 92093-0085 PROJECT NO. DATE:	NO. DATE REVISIONS	CFS Shake Table Test Project Linear Potentiometers - Floor 4 Configuration E1	SRIKAR GUNISETTY Graduate Student Researcher XIANG WANG Post-doctoral Researcher

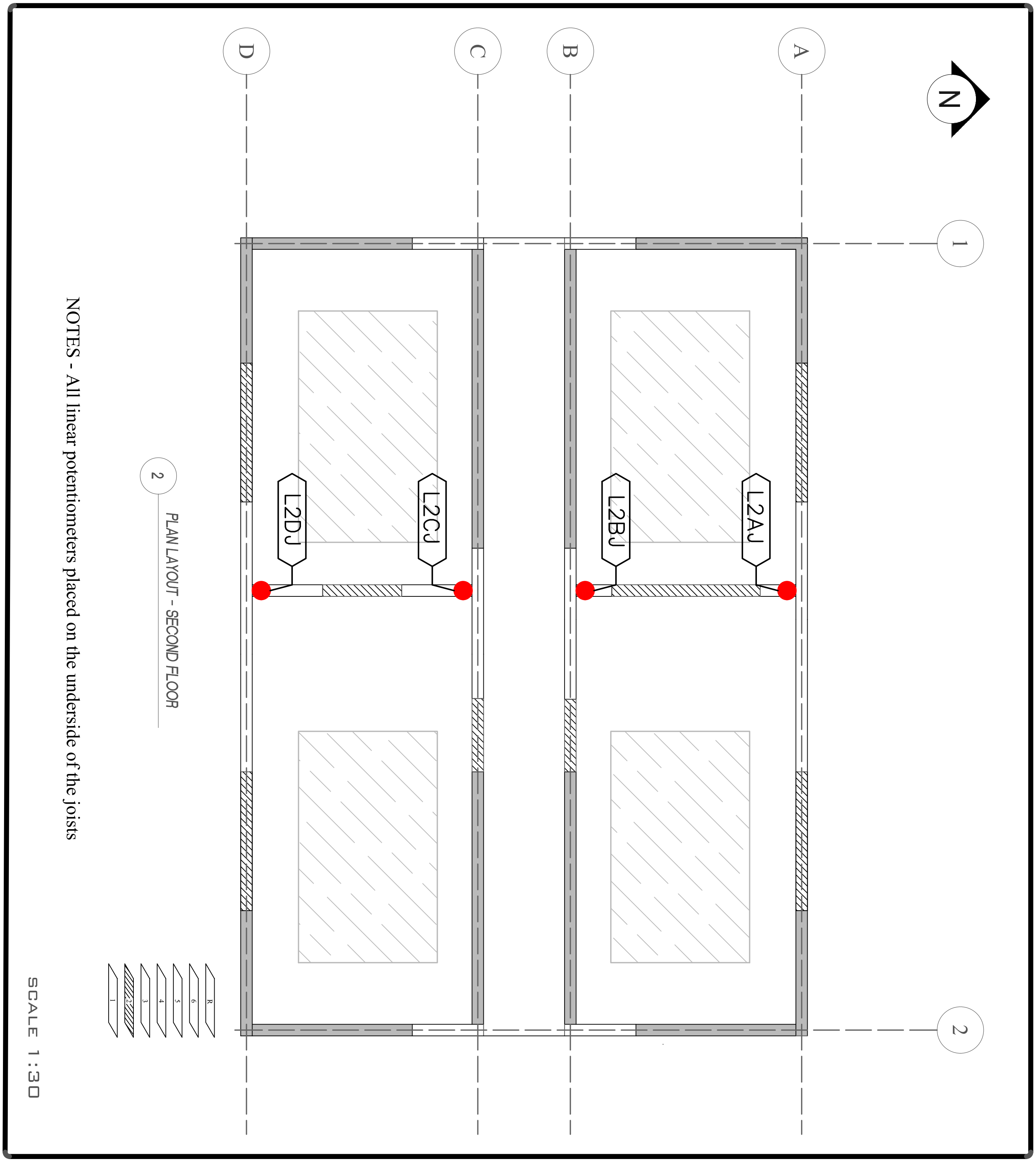

UCSD

UNIVERSITY OF CALIFORNIA, SAN DIEGO
DEPARTMENT OF STRUCTURAL ENGINEERING
LA JOLLA - CALIFORNIA 92093-0085

PROJECT NO. DATE:

NO.	DATE	REVISIONS

CFS Shake Table Test Project
Linear Potentiometers - Floor 1 ceiling
Configuration E1

SRIKAR GUNISETTY
Graduate Student Researcher
XIANG WANG
Post-doctoral Researcher

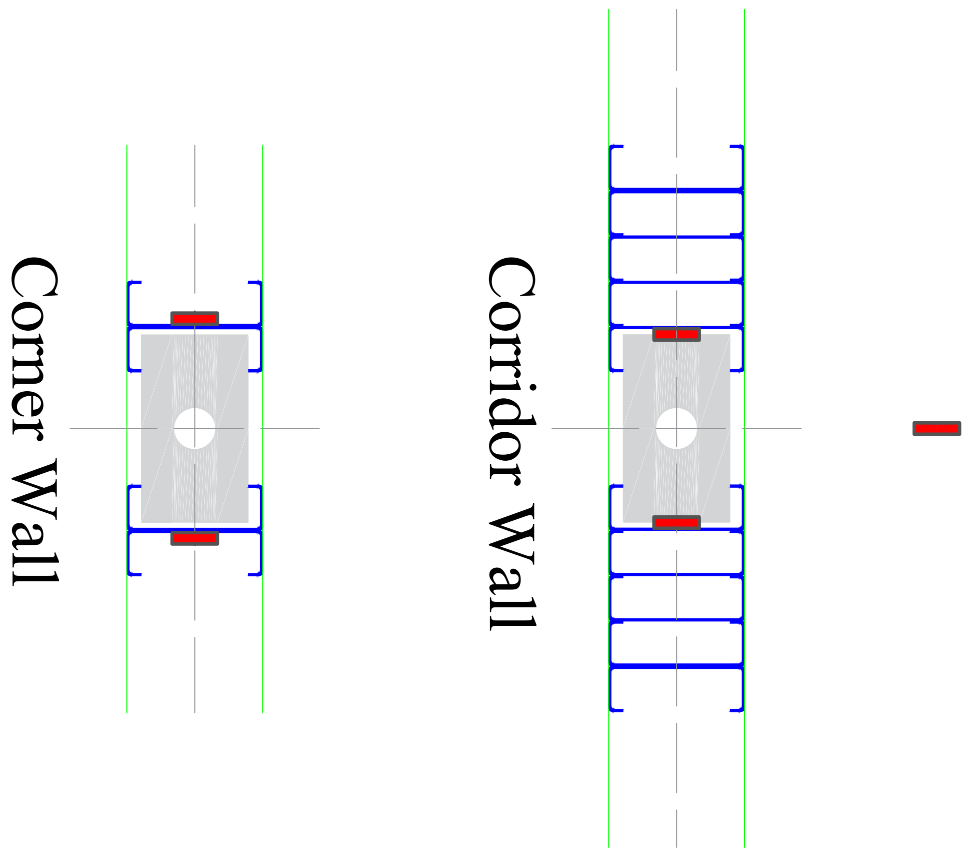

SCALE 1:30

UCSD
UNIVERSITY OF CALIFORNIA, SAN DIEGO
DEPARTMENT OF STRUCTURAL ENGINEERING
LA JOLLA - CALIFORNIA 92093-0085

PROJECT NO. DATE:

NO.	DATE	REVISIONS

CFS Shake Table Test Project
Strain Gauges - Compression Post Details
Configuration - E1

SRIKAR GUNISETTY
Graduate Student Researcher
XIANG WANG
Post-doctoral Researcher

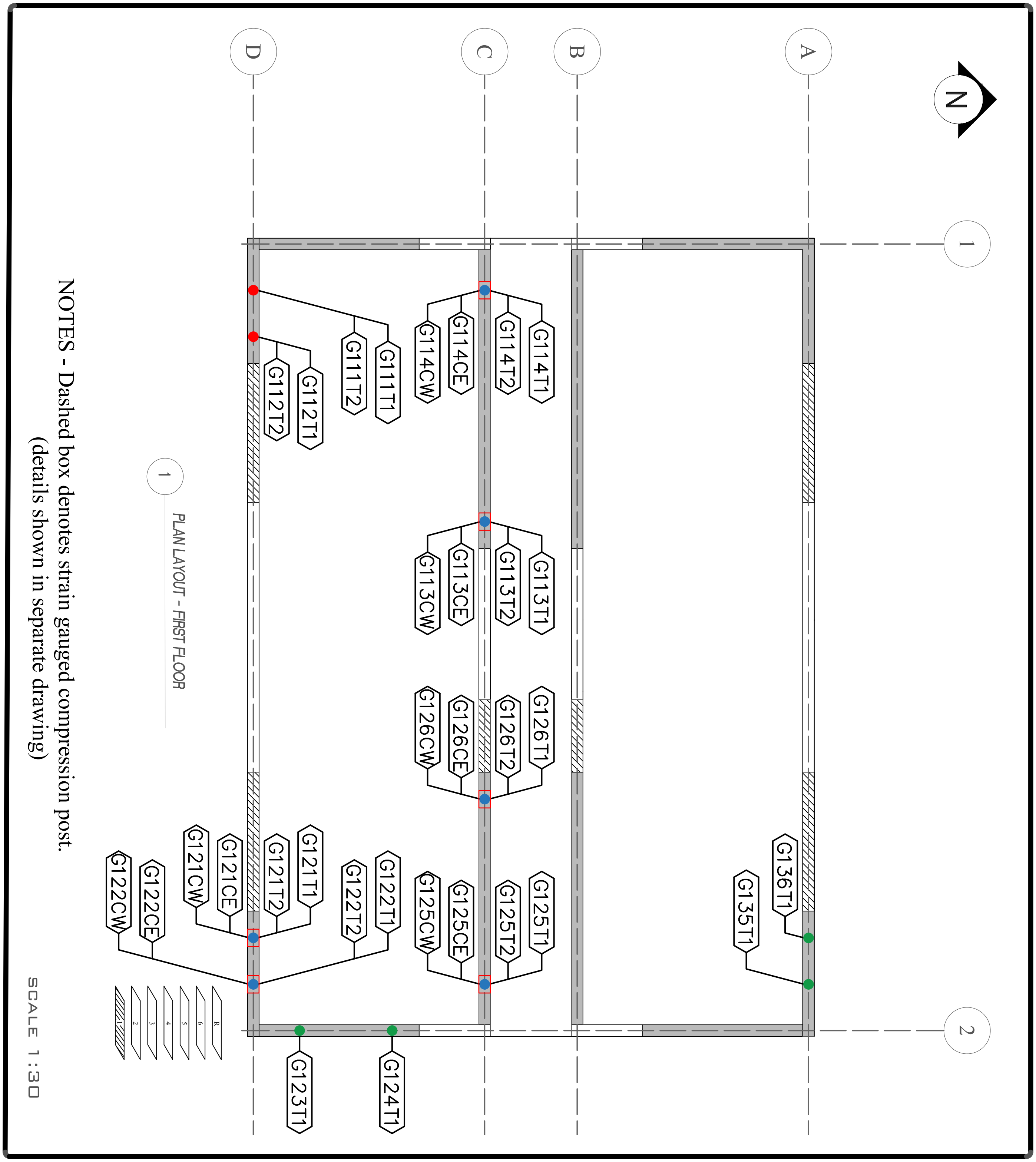

UCSD
UNIVERSITY OF CALIFORNIA, SAN DIEGO
DEPARTMENT OF STRUCTURAL ENGINEERING
LA JOLLA - CALIFORNIA 92093-0085

PROJECT NO. DATE:

NO.	DATE	REVISIONS

CFS Shake Table Test Project
Strain gauges - Floor 1
Configuration - E1

SRIKAR GUNISETTY
Graduate Student Researcher
XIANG WANG
Post-doctoral Researcher

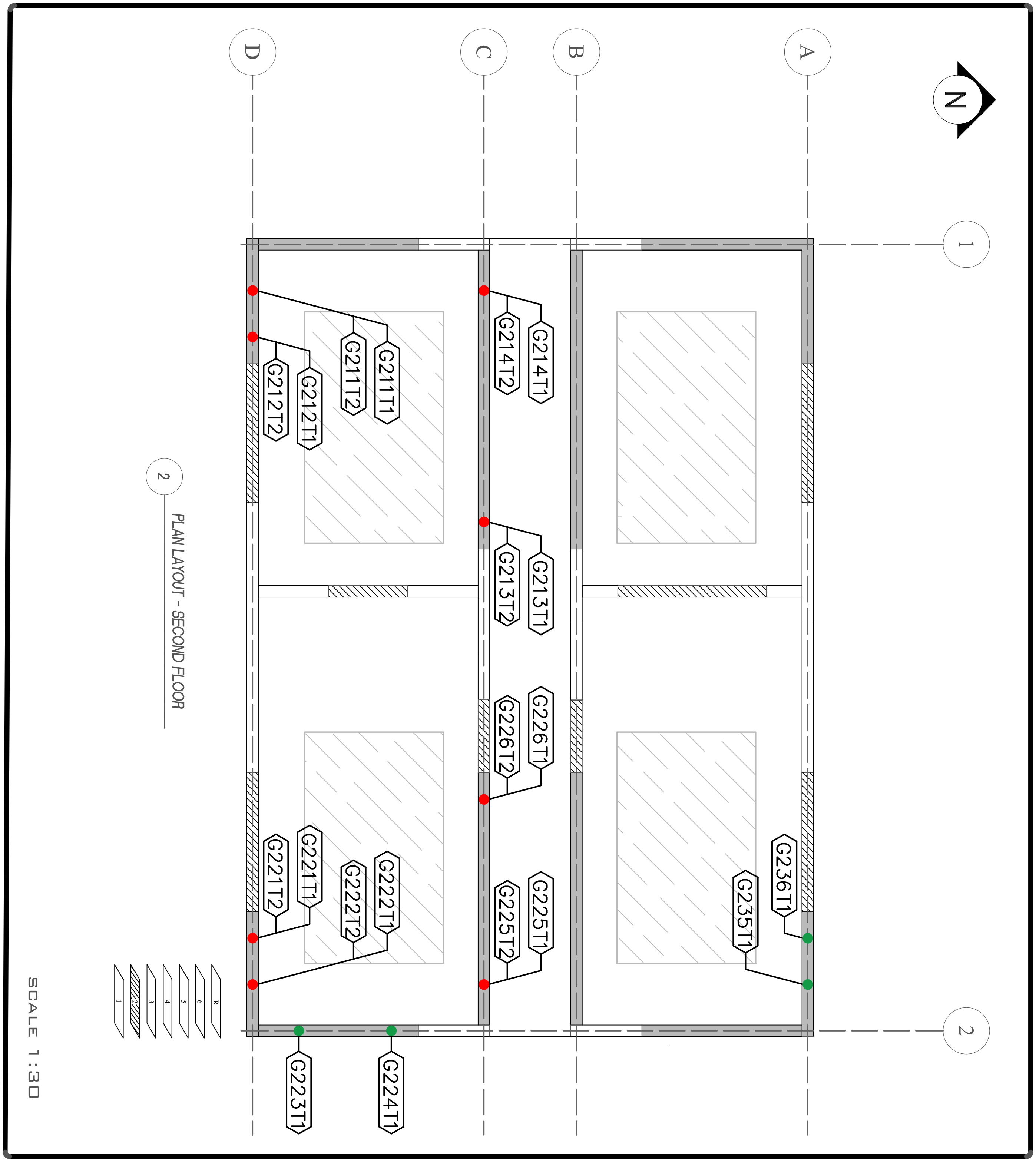

UCSD UNIVERSITY OF CALIFORNIA, SAN DIEGO DEPARTMENT OF STRUCTURAL ENGINEERING LA JOLLA - CALIFORNIA 92093-0085 PROJECT NO. DATE:	NO. DATE REVISIONS	CFS Shake Table Test Project Strain gauges - Floor 2 Configuration - E1

SRIKAR GUNISETTY
Graduate Student Researcher
XIANG WANG
Post-doctoral Researcher

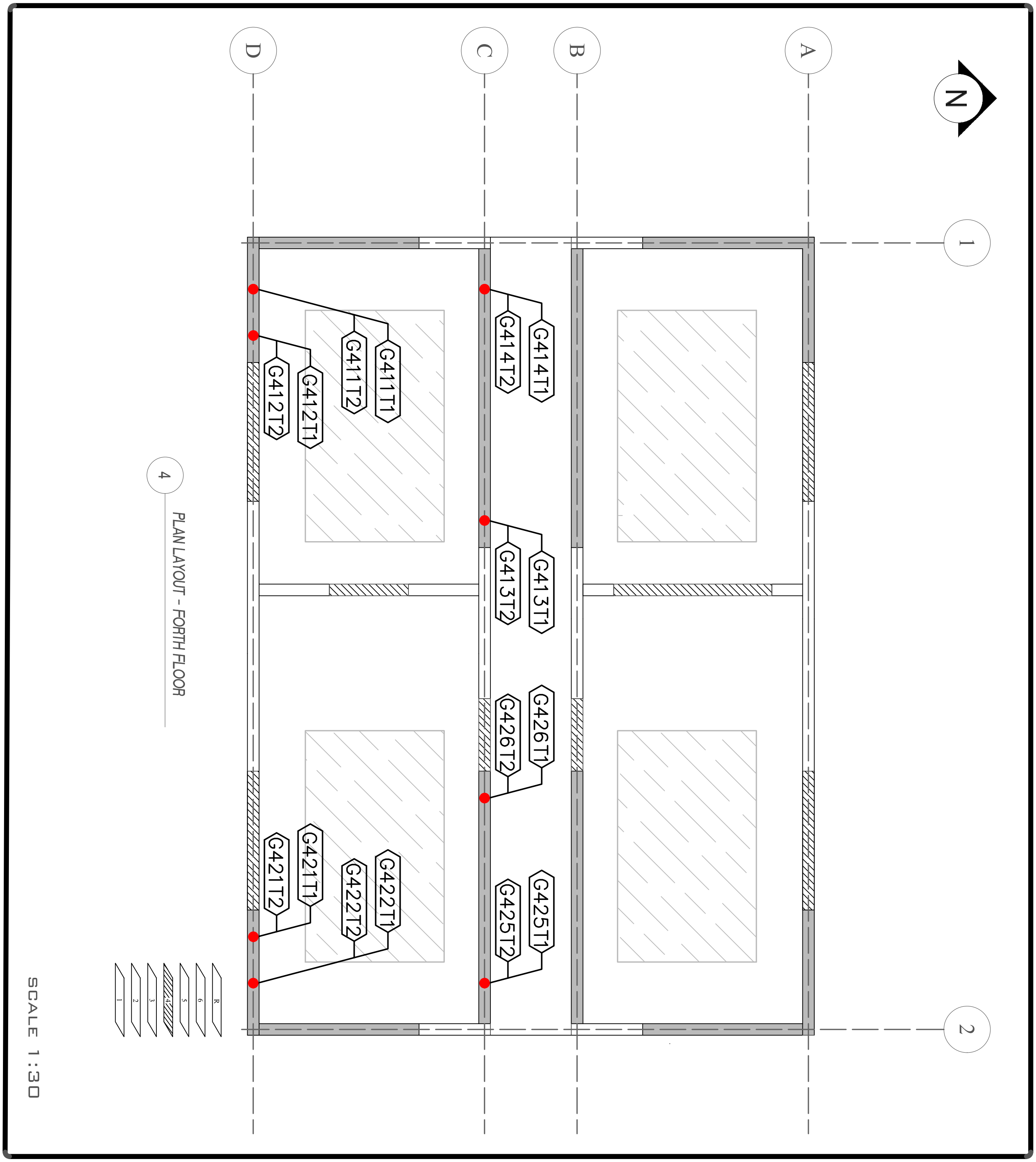

UCSD

UNIVERSITY OF CALIFORNIA, SAN DIEGO
DEPARTMENT OF STRUCTURAL ENGINEERING
LA JOLLA - CALIFORNIA 92093-0085

PROJECT NO. DATE:

NO.	DATE	REVISIONS

CFS Shake Table Test Project
Strain gauges - Floor 4
Configuration - E1

SRIKAR GUNISETTY
Graduate Student Researcher
XIANG WANG
Post-doctoral Researcher

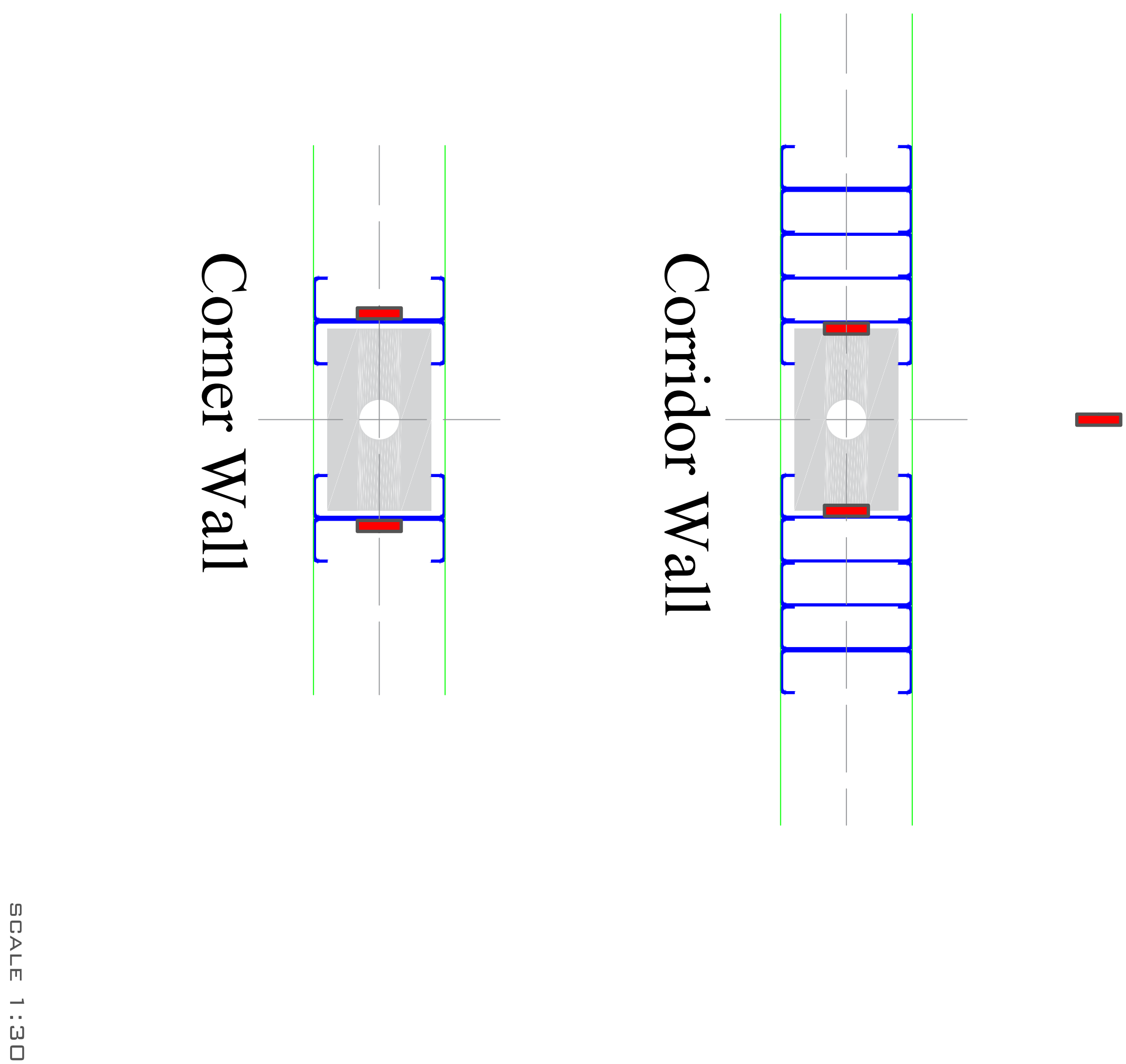

UCSD UNIVERSITY OF CALIFORNIA, SAN DIEGO DEPARTMENT OF STRUCTURAL ENGINEERING LA JOLLA - CALIFORNIA 92093-0085 PROJECT NO. DATE:	NO. DATE REVISIONS	CFS Shake Table Test Project Strain Gauges - Compression Post Details Configuration - E1

SRIKAR GUNISETTY
Graduate Student Researcher
XIANG WANG
Post-doctoral Researcher

Analog Sensor Instrumentation – Configuration E2

Table E.5. Analog sensor count – Configuration E2.

Floor #	Type of sensor				
	Accel. (MEMS)	Accel. (Kinemetrics)	String pot.	Linear pot.	Strain gage
1	4	0	25	12	31
2	10	0	9	4	20
3	10	0	1	0	0
4	8	0	17	6	8
5	8	0	0	0	0
6	8	0	0	0	0
Roof	11	0	0	0	0
Total	59	0	52	22	59

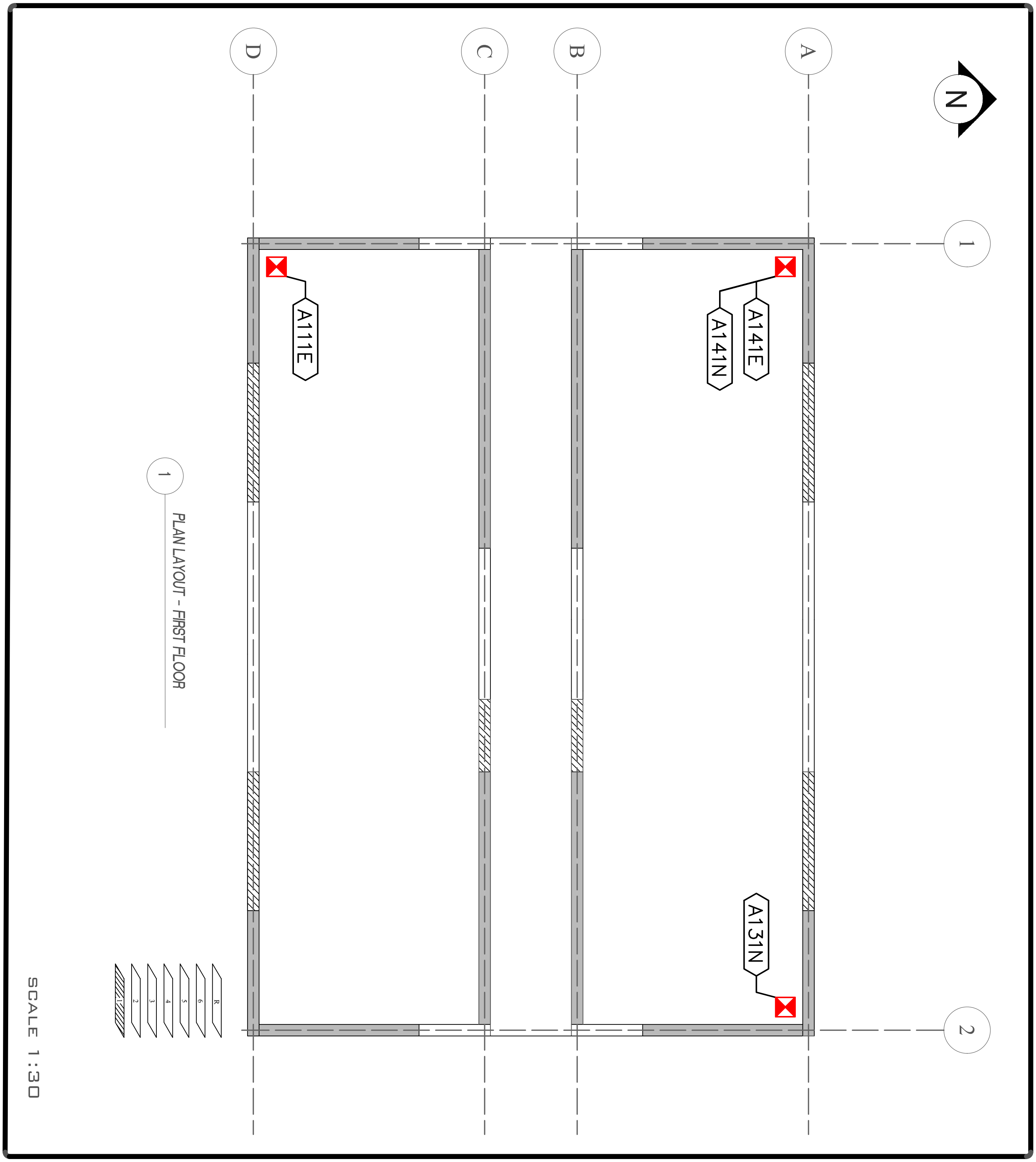

UCSD

UNIVERSITY OF CALIFORNIA, SAN DIEGO
DEPARTMENT OF STRUCTURAL ENGINEERING
LA JOLLA - CALIFORNIA 92093-0085

PROJECT NO. DATE:

NO.	DATE	REVISIONS

CFS Shake Table Test Project
Accelerometers (MEMS) - Floor 1
Configuration E2 (post-fire)

SRIKAR GUNISETTY
Graduate Student Researcher
XIANG WANG
Post-doctoral Researcher

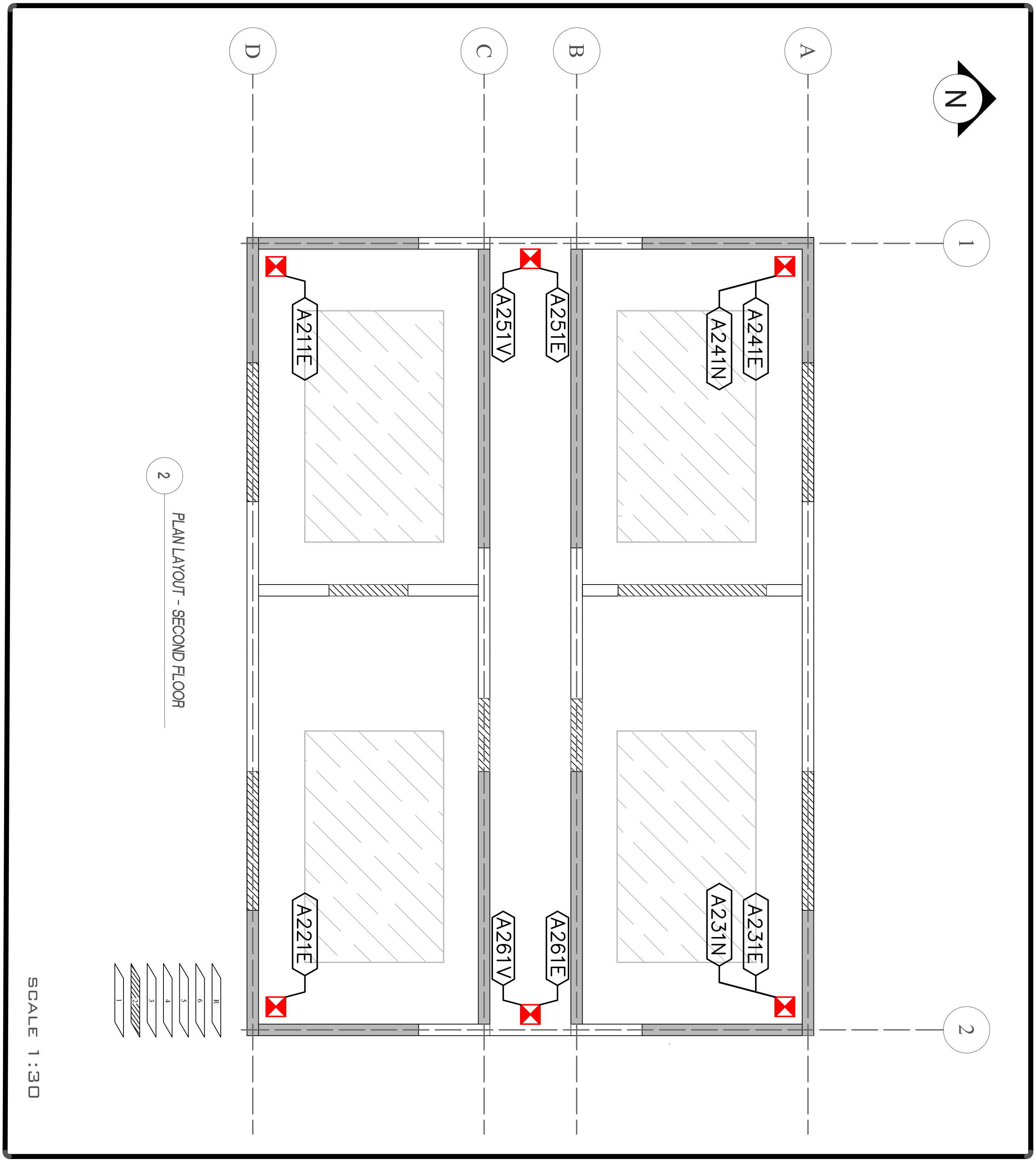

UCSD
UNIVERSITY OF CALIFORNIA, SAN DIEGO
DEPARTMENT OF STRUCTURAL ENGINEERING
LA JOLLA - CALIFORNIA 92093-0085
PROJECT NO. DATE:

NO.	DATE	REVISIONS

CFS Shake Table Test Project
Accelerometers (MEMS) - Floor 2
Configuration E2 (post-fire)

SRIKAR GUNISETTY
Graduate Student Researcher
XIANG WANG
Post-doctoral Researcher

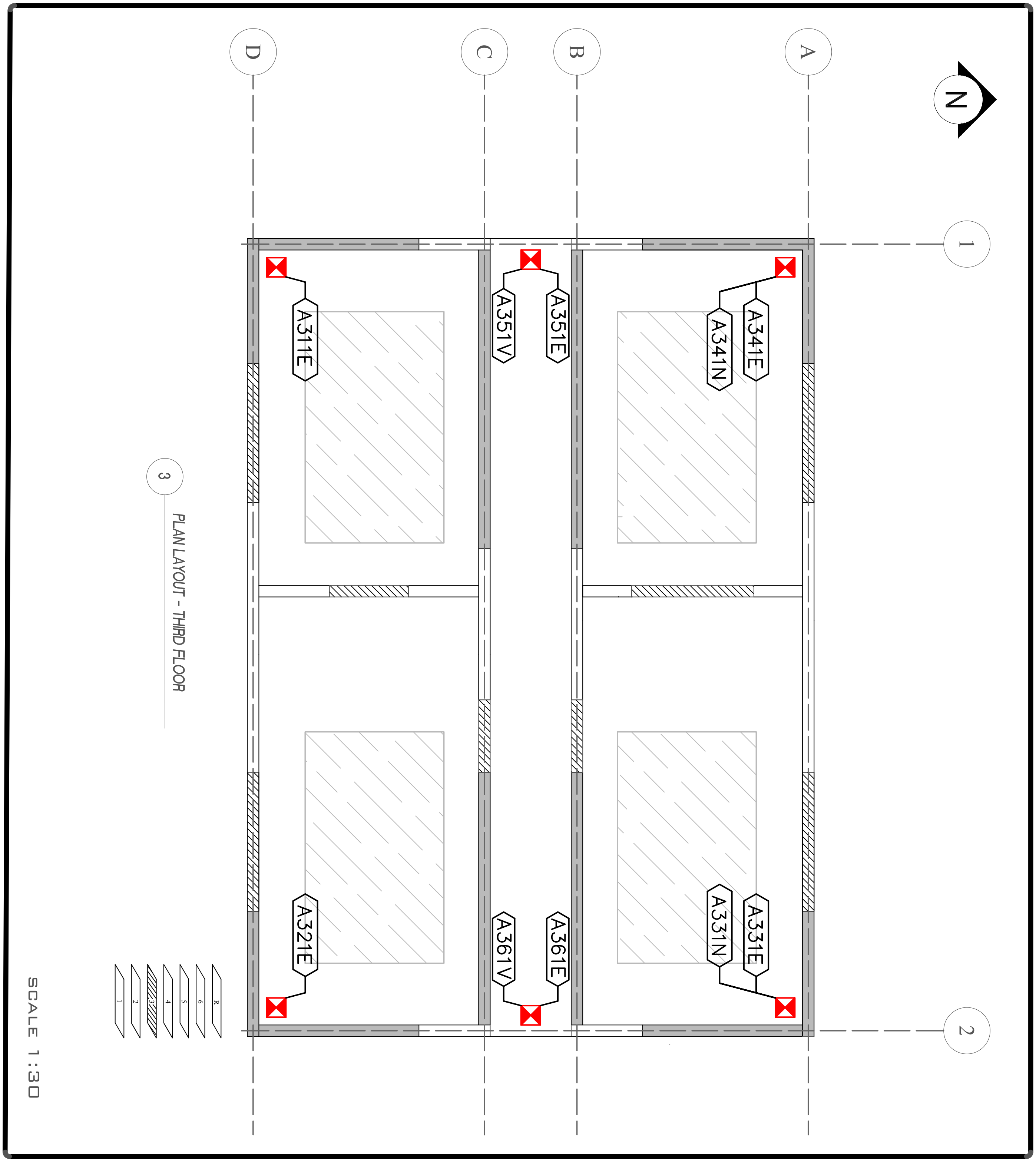

UCSD UNIVERSITY OF CALIFORNIA, SAN DIEGO DEPARTMENT OF STRUCTURAL ENGINEERING LA JOLLA - CALIFORNIA 92093-0085 PROJECT NO. DATE:	NO. DATE REVISIONS	CFS Shake Table Test Project Accelerometers (MEMS) - Floor 3 Configuration E2 (post-fire)	SRIKAR GUNISETTY Graduate Student Researcher XIANG WANG Post-doctoral Researcher

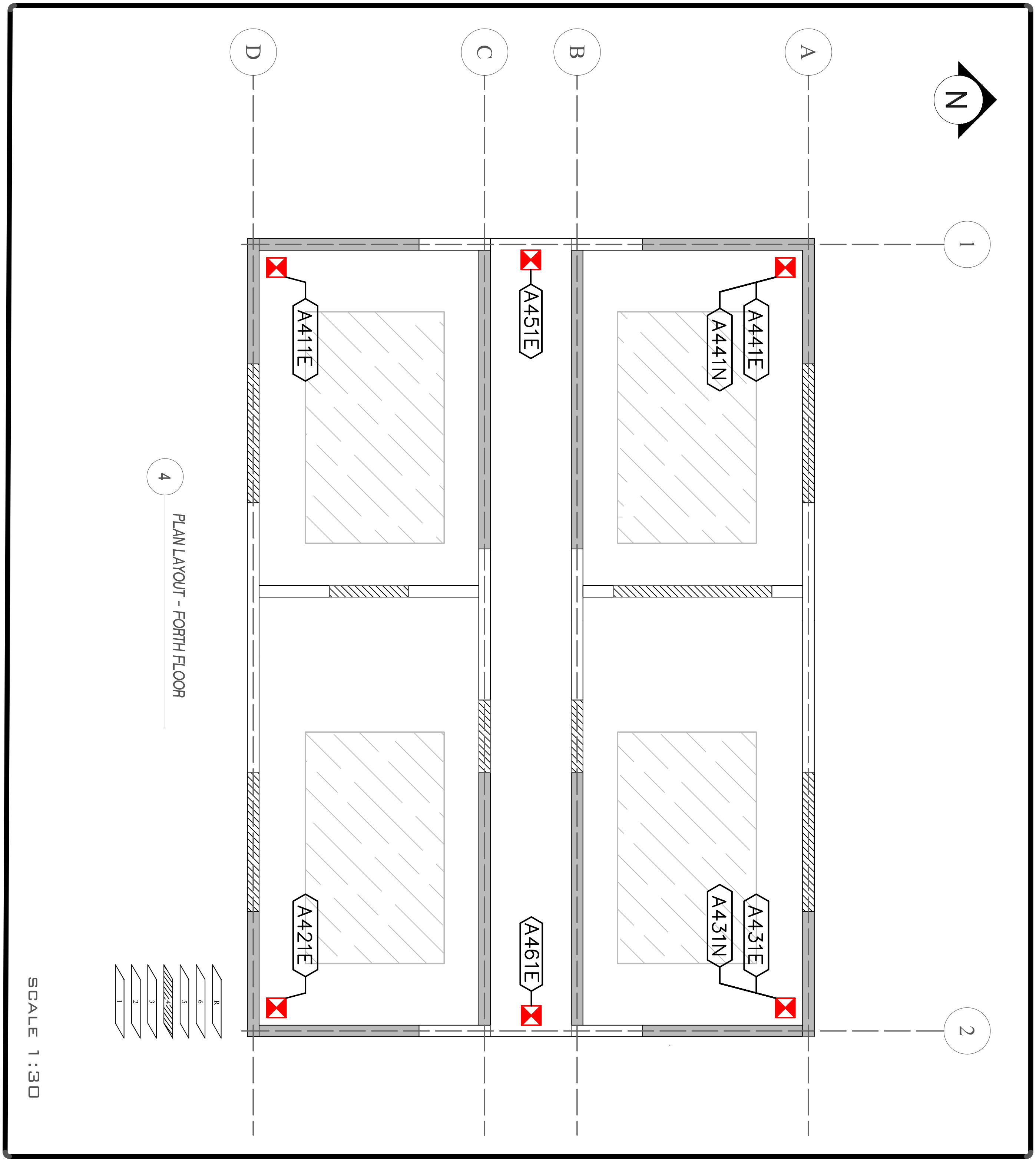

UCSD

UNIVERSITY OF CALIFORNIA, SAN DIEGO
DEPARTMENT OF STRUCTURAL ENGINEERING
LA JOLLA - CALIFORNIA 92093-0085

PROJECT NO. DATE:

NO.	DATE	REVISIONS

CFS Shake Table Test Project
Accelerometers (MEMS) - Floor 4
Configuration E2 (post-fire)

SRIKAR GUNISETTY
Graduate Student Researcher
XIANG WANG
Post-doctoral Researcher

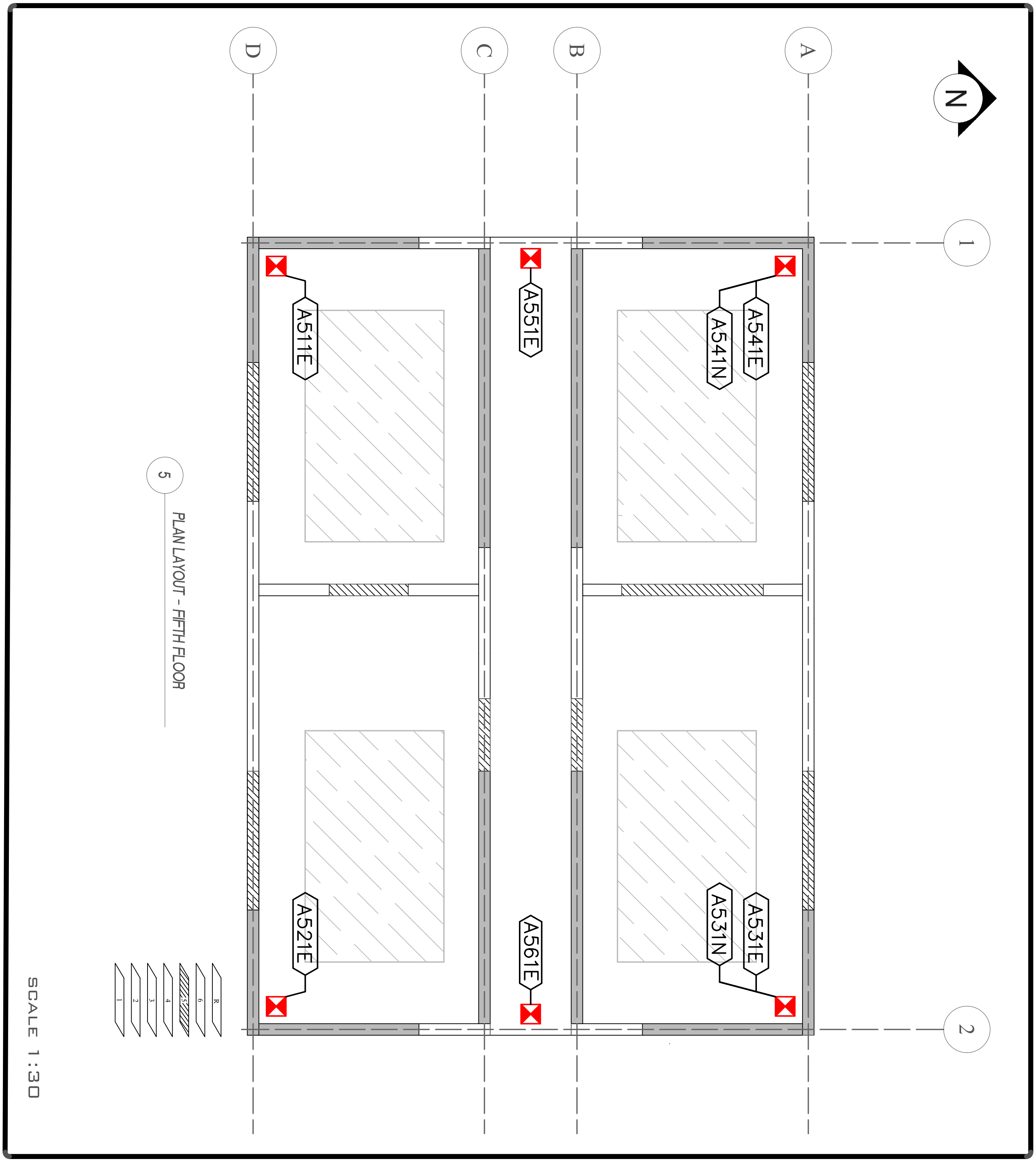

UCSD	NO.	DATE	REVISIONS		
UNIVERSITY OF CALIFORNIA, SAN DIEGO DEPARTMENT OF STRUCTURAL ENGINEERING LA JOLLA - CALIFORNIA 92093-0085 PROJECT NO. DATE:				CFS Shake Table Test Project Accelerometers (MEMS) - Floor 5 Configuration E2 (post-fire)	SRIKAR GUNISETTY Graduate Student Researcher XIANG WANG Post-doctoral Researcher

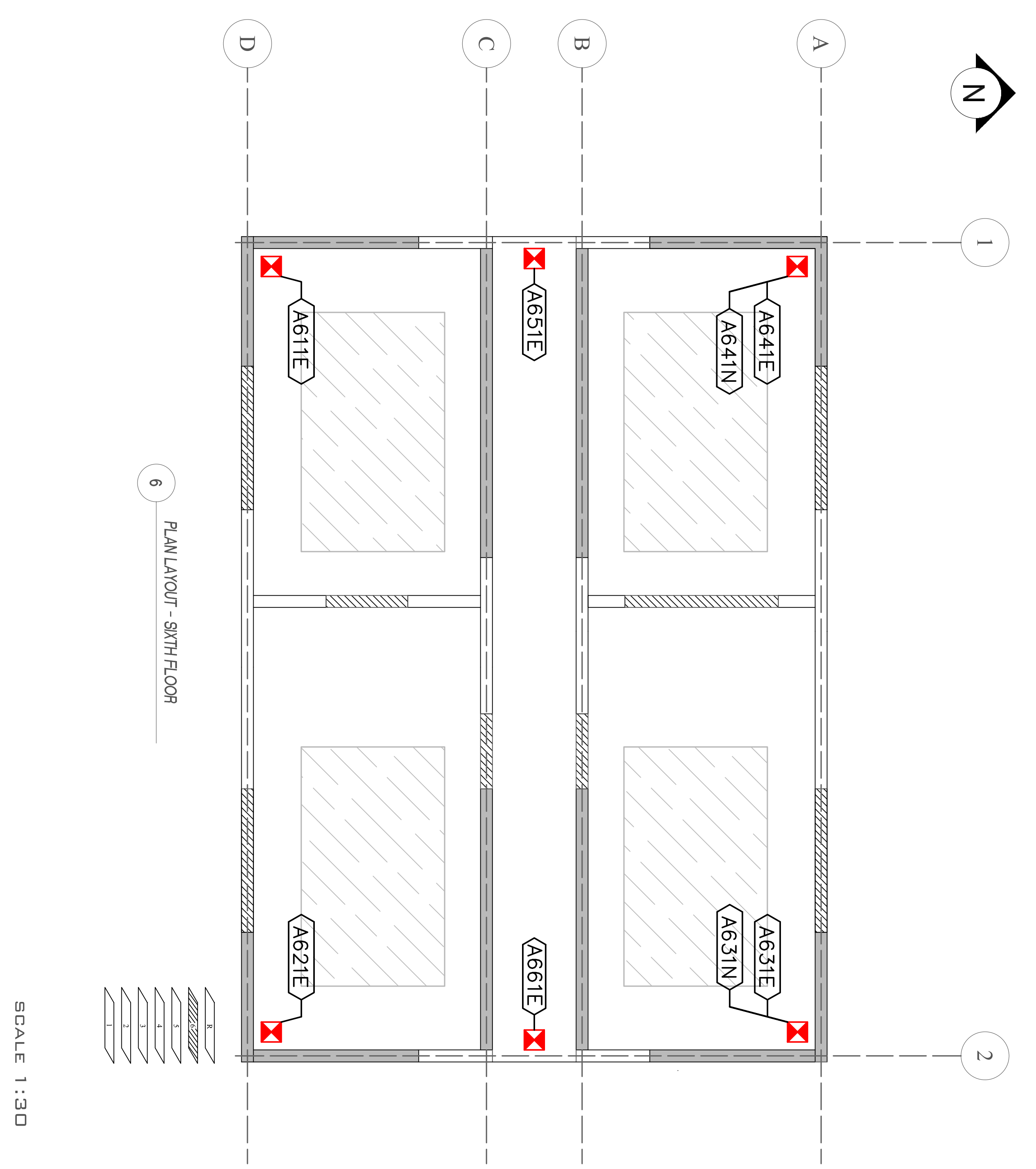

UCSD

UNIVERSITY OF CALIFORNIA, SAN DIEGO
DEPARTMENT OF STRUCTURAL ENGINEERING
LA JOLLA - CALIFORNIA 92093-0085

PROJECT NO. DATE:

NO.	DATE	REVISIONS

CFS Shake Table Test Project
Accelerometers (MEMS) - Floor 6
Configuration E2 (post-fire)

SRIKAR GUNISETTY
Graduate Student Researcher
XIANG WANG
Post-doctoral Researcher

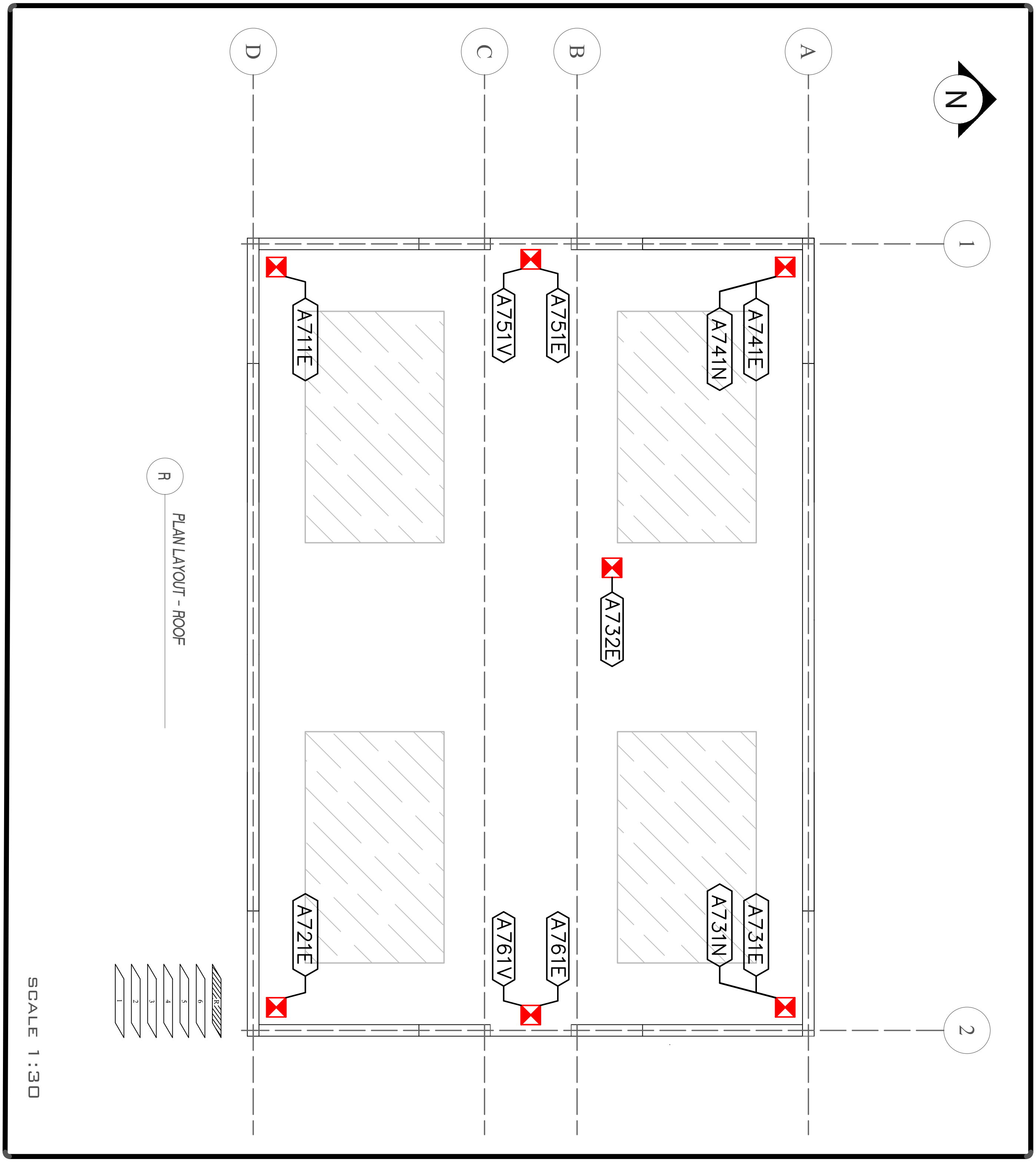

UCSD

UNIVERSITY OF CALIFORNIA, SAN DIEGO
DEPARTMENT OF STRUCTURAL ENGINEERING
LA JOLLA - CALIFORNIA 92093-0085

PROJECT NO. DATE:

NO.	DATE	REVISIONS

CFS Shake Table Test Project
Accelerometers (MEMS) - Roof
Configuration E2 (post-fire)

SRIKAR GUNISETTY
Graduate Student Researcher
XIANG WANG
Post-doctoral Researcher

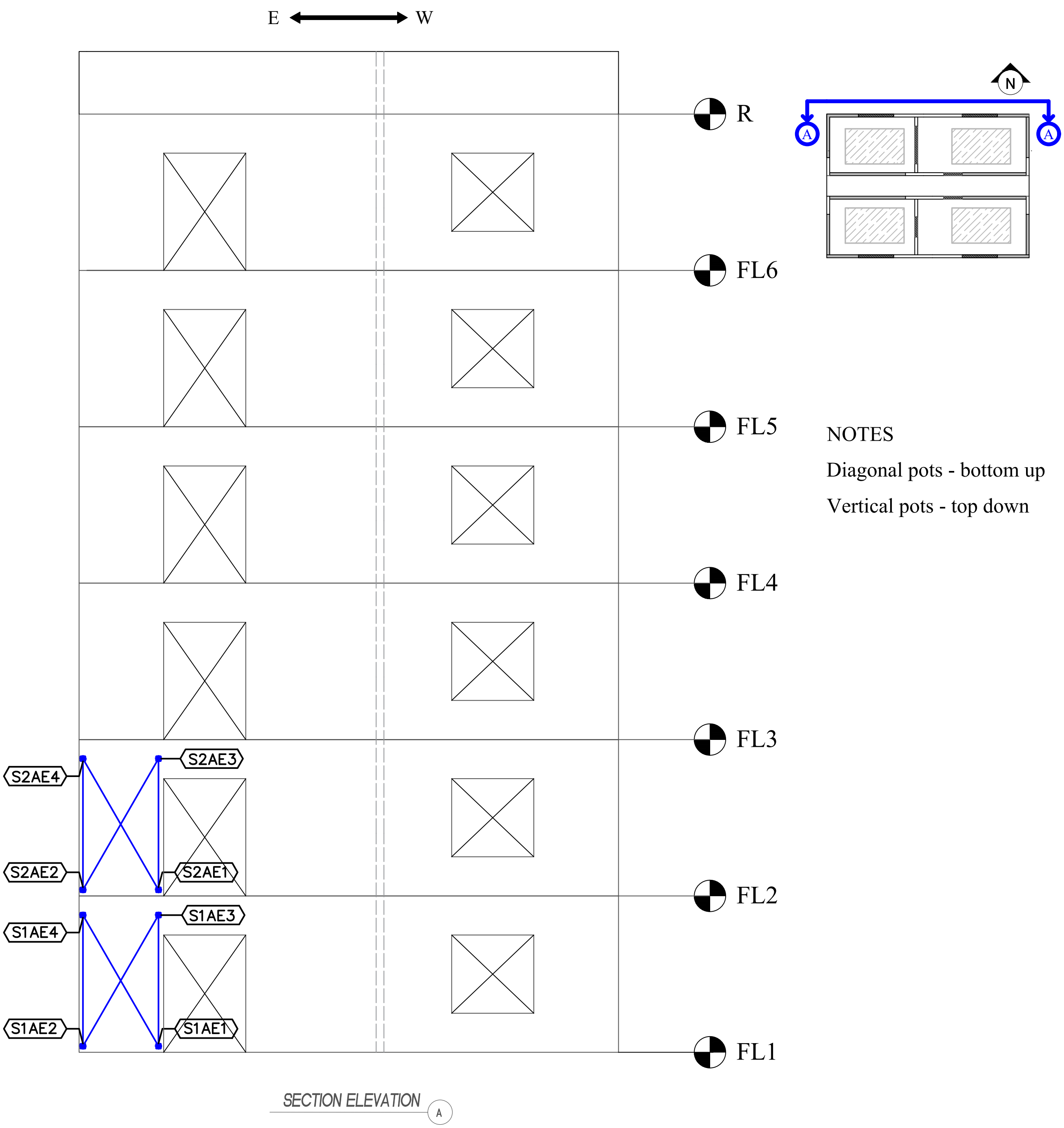

NOTES
Diagonal pots - bottom up
Vertical pots - top down

NOTES - String potentiometers on the exterior side on wall line A

SCALE 1:30

UCSD
UNIVERSITY OF CALIFORNIA, SAN DIEGO
DEPARTMENT OF STRUCTURAL ENGINEERING
LA JOLLA - CALIFORNIA 92093-0085
PROJECT NO. DATE:

NO.	DATE	REVISIONS

CFS Shake Table Test Project
String Potentiometers - Wall line A
Configuration - E2

SRIKAR GUNISETTY
Graduate Student Researcher
XIANG WANG
Post-doctoral Researcher

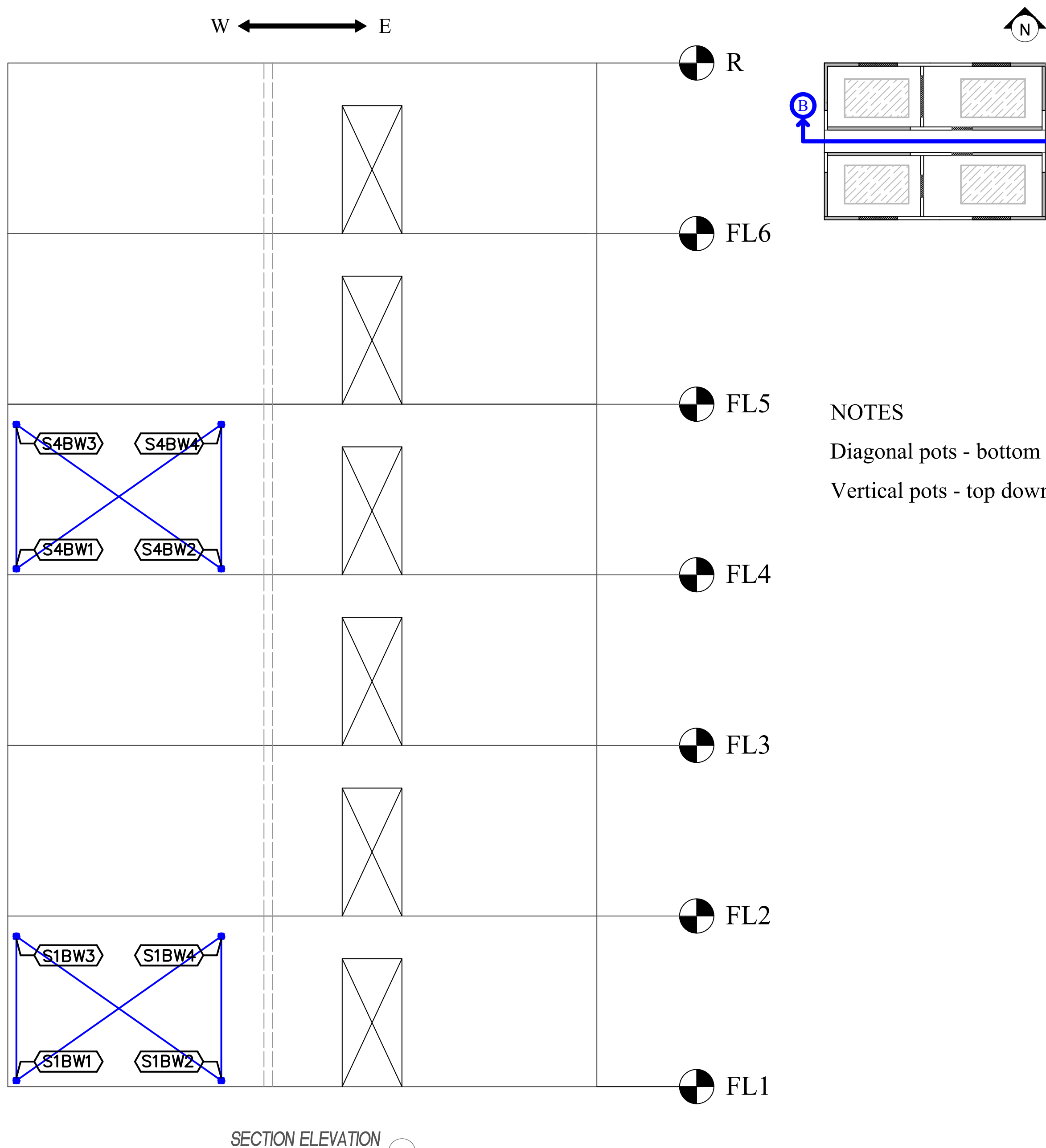

NOTES
Diagonal pots - bottom up
Vertical pots - top down

NOTES - String potentiometers on the corridor side on wall line B

SCALE 1:30

UCSD UNIVERSITY OF CALIFORNIA, SAN DIEGO DEPARTMENT OF STRUCTURAL ENGINEERING LA JOLLA - CALIFORNIA 92093-0085 PROJECT NO. DATE:	NO. DATE REVISIONS	CFS Shake Table Test Project String Potentiometers - Wall line B Configuration - E2	SRIKAR GUNISETTY Graduate Student Researcher XIANG WANG Post-doctoral Researcher

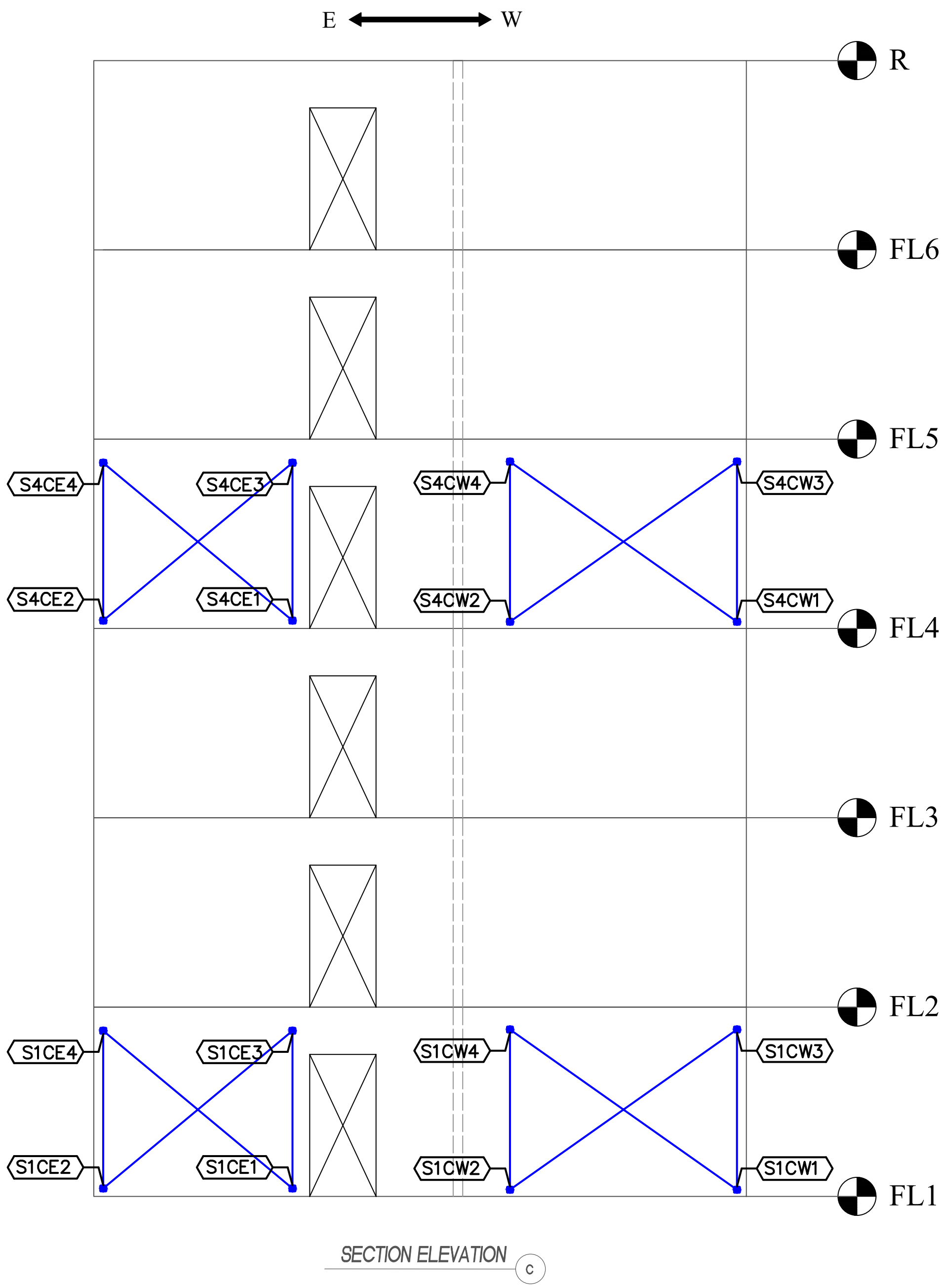

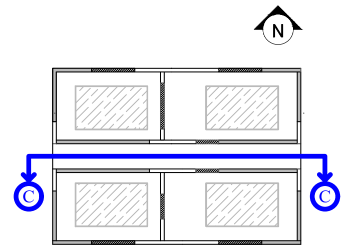

NOTES

Diagonal pots - bottom up

Vertical pots - top down

NOTES - String potentiometers on the corridor side on wall line C

SCALE 1:30

UCSD UNIVERSITY OF CALIFORNIA, SAN DIEGO DEPARTMENT OF STRUCTURAL ENGINEERING LA JOLLA - CALIFORNIA 92093-0085 PROJECT NO. DATE:	NO. DATE REVISIONS	CFS Shake Table Test Project String Potentiometers - Wall line C Configuration - E2	SRIKAR GUNISETTY Graduate Student Researcher XIANG WANG Post-doctoral Researcher

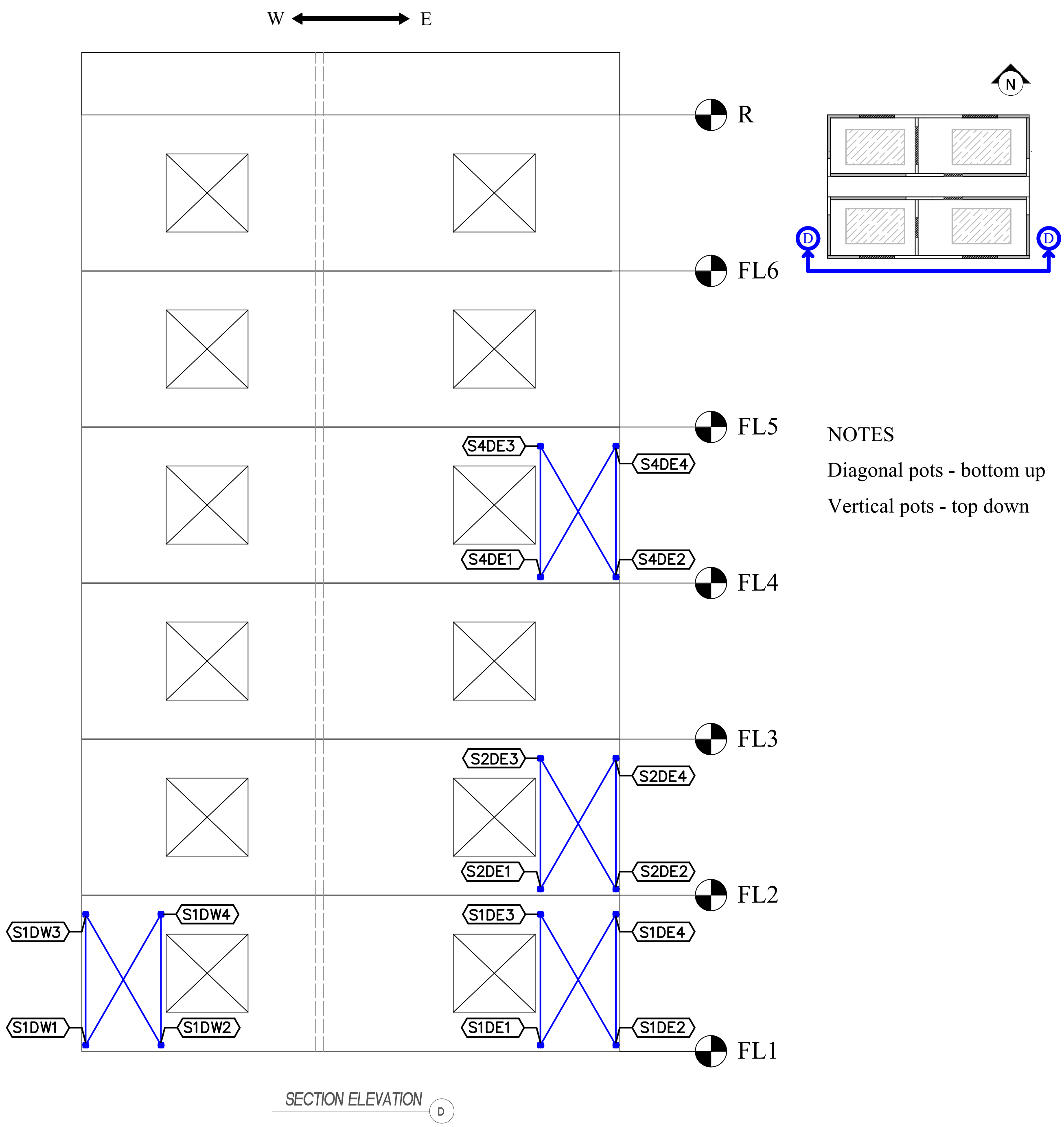

NOTES - String potentiometers on the exterior side on wall line D

SCALE 1:30

UCSD UNIVERSITY OF CALIFORNIA, SAN DIEGO DEPARTMENT OF STRUCTURAL ENGINEERING LA JOLLA - CALIFORNIA 92093-0085 PROJECT NO. DATE:	NO. DATE REVISIONS	CFS Shake Table Test Project String Potentiometers - Wall line D Configuration - E2	SRIKAR GUNISETTY Graduate Student Researcher XIANG WANG Post-doctoral Researcher

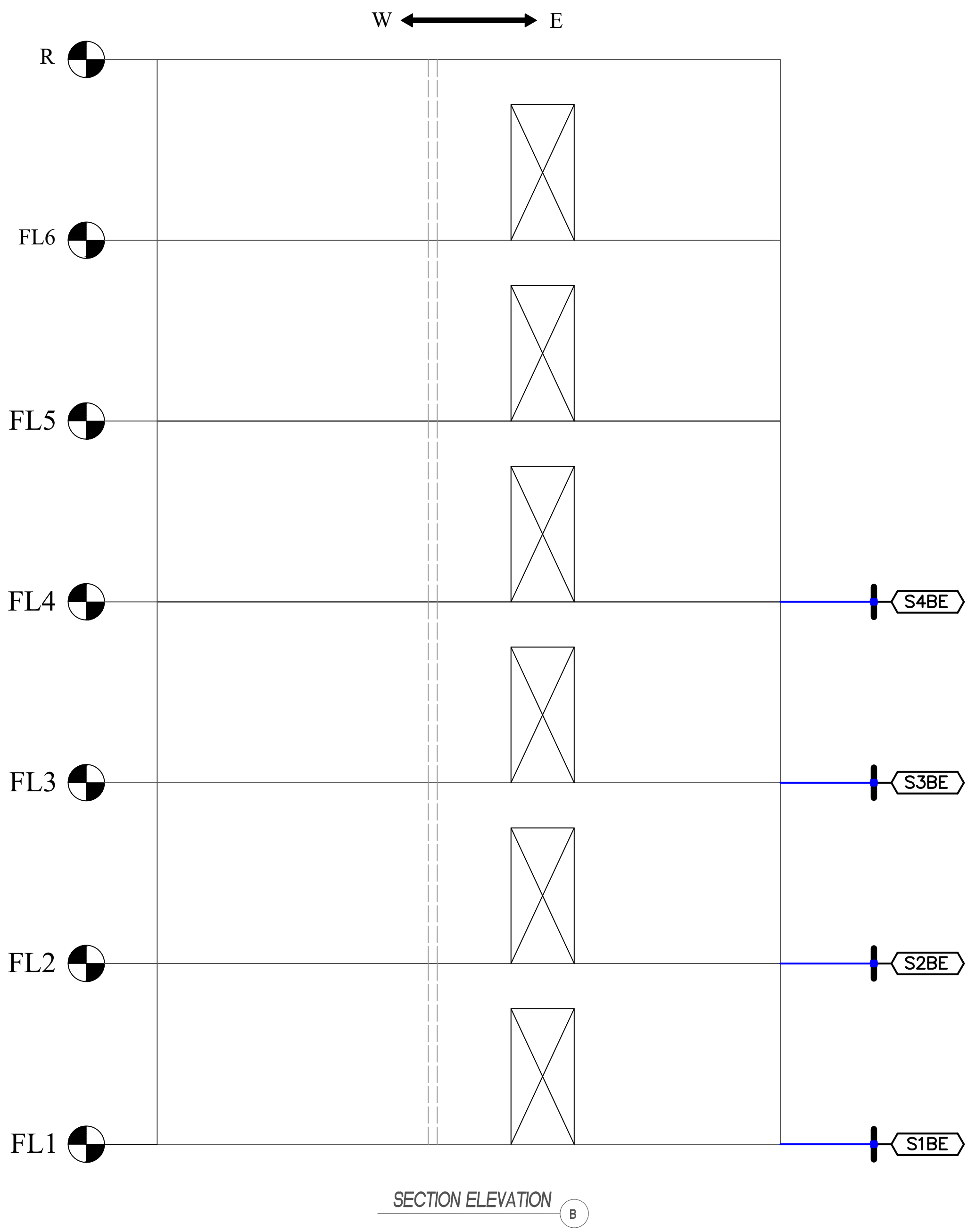

NOTES - String potentiometers on the exterior east side on wall line B

SCALE 1:30

UCSD UNIVERSITY OF CALIFORNIA, SAN DIEGO DEPARTMENT OF STRUCTURAL ENGINEERING LA JOLLA - CALIFORNIA 92093-0085 PROJECT NO. DATE:	NO.	DATE	REVISIONS	CFS Shake Table Test Project String Potentiometers - Fixture Configuration - E2	SRIKAR GUNISETTY Graduate Student Researcher XIANG WANG Post-doctoral Researcher

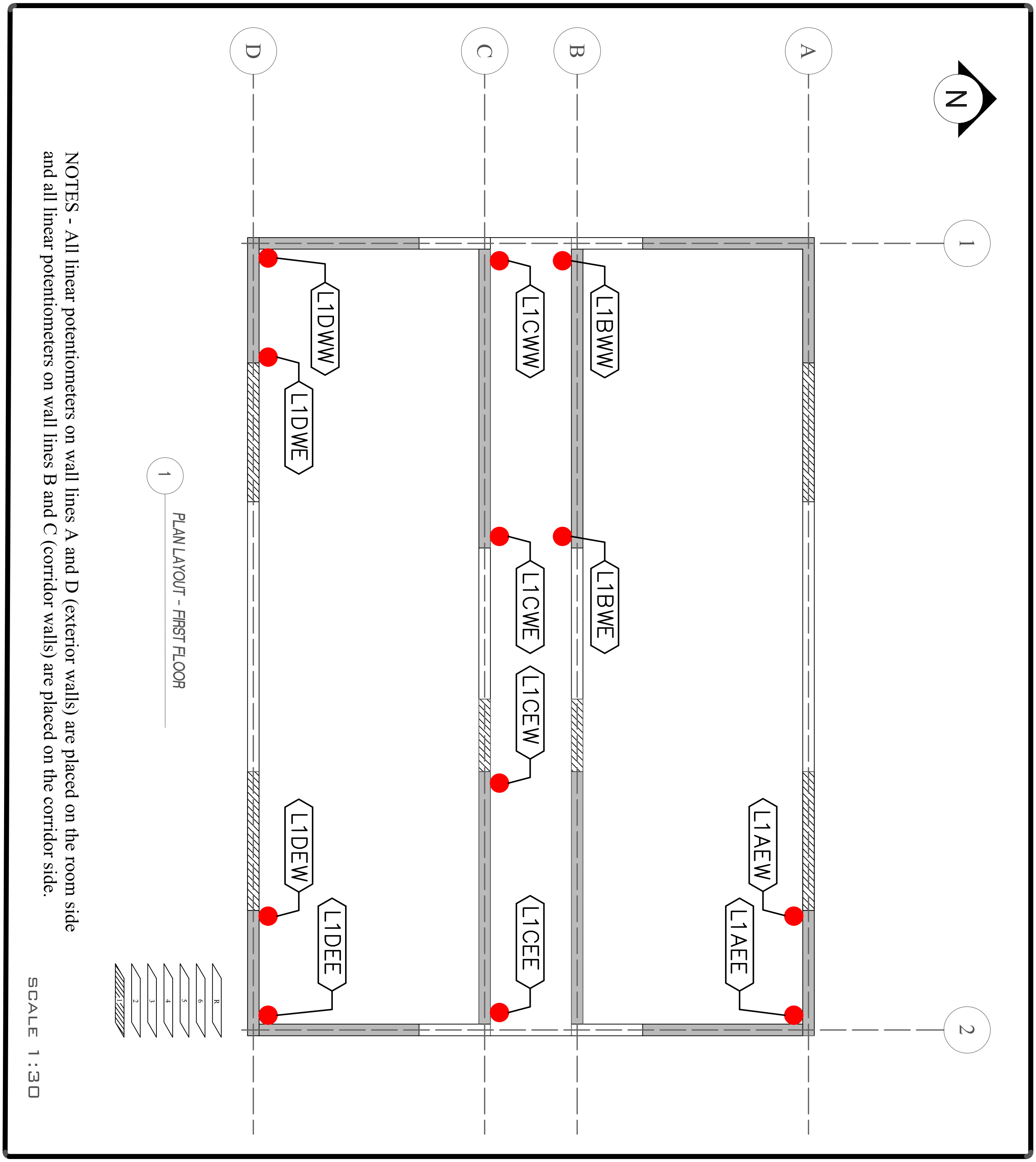

UCSD UNIVERSITY OF CALIFORNIA, SAN DIEGO DEPARTMENT OF STRUCTURAL ENGINEERING LA JOLLA - CALIFORNIA 92093-0085 PROJECT NO. DATE:	NO. DATE REVISIONS	CFS Shake Table Test Project Linear Potentiometers - Floor 1 Configuration E2

SRIKAR GUNISETTY
Graduate Student Researcher
XIANG WANG
Post-doctoral Researcher

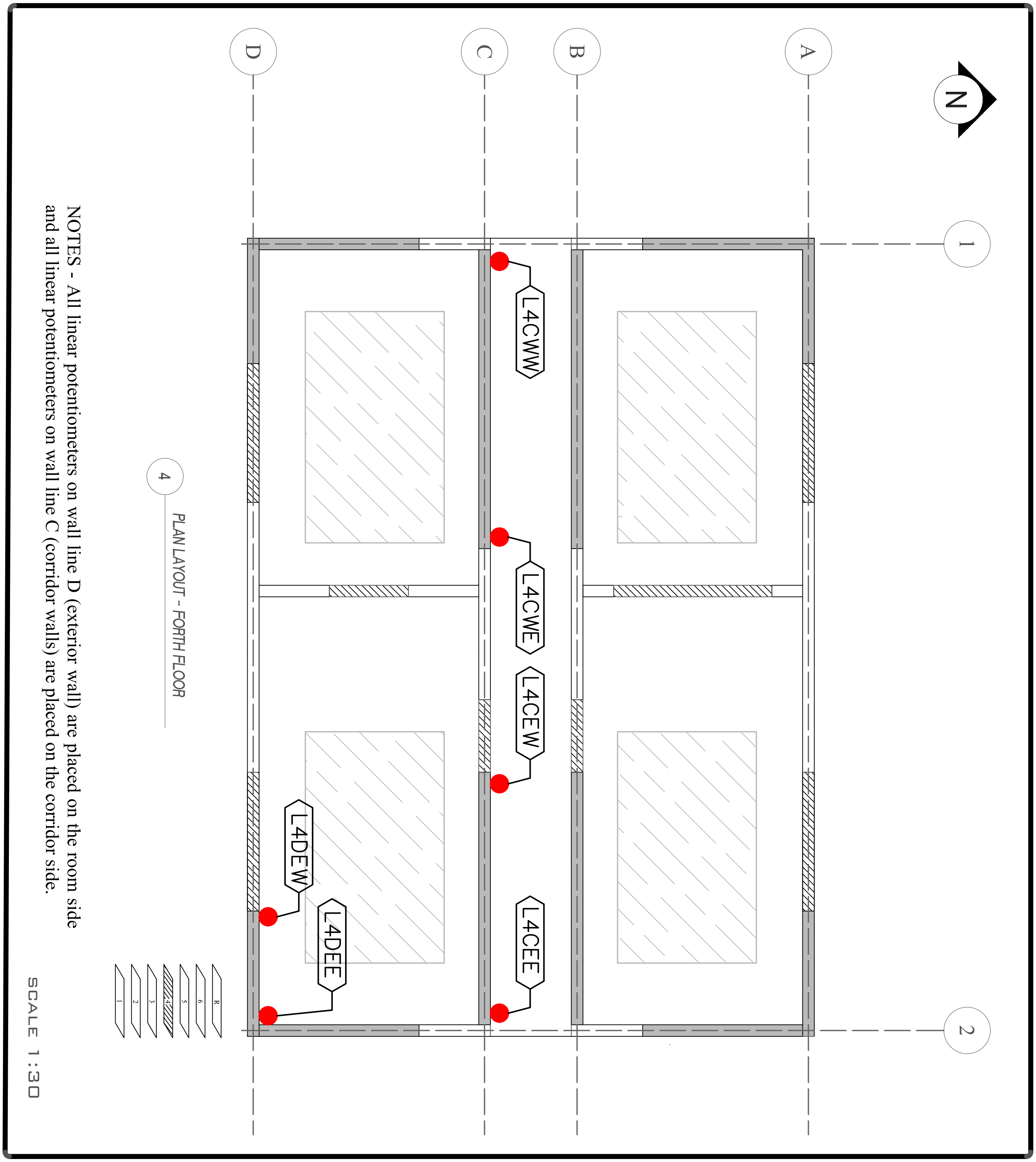

UCSD
UNIVERSITY OF CALIFORNIA, SAN DIEGO
DEPARTMENT OF STRUCTURAL ENGINEERING
LA JOLLA · CALIFORNIA 92093-0085

PROJECT NO. DATE:

NO.	DATE	REVISIONS

CFS Shake Table Test Project
Linear Potentiometers - Floor 4
Configuration E2

SRIKAR GUNISETTY
Graduate Student Researcher
XIANG WANG
Post-doctoral Researcher

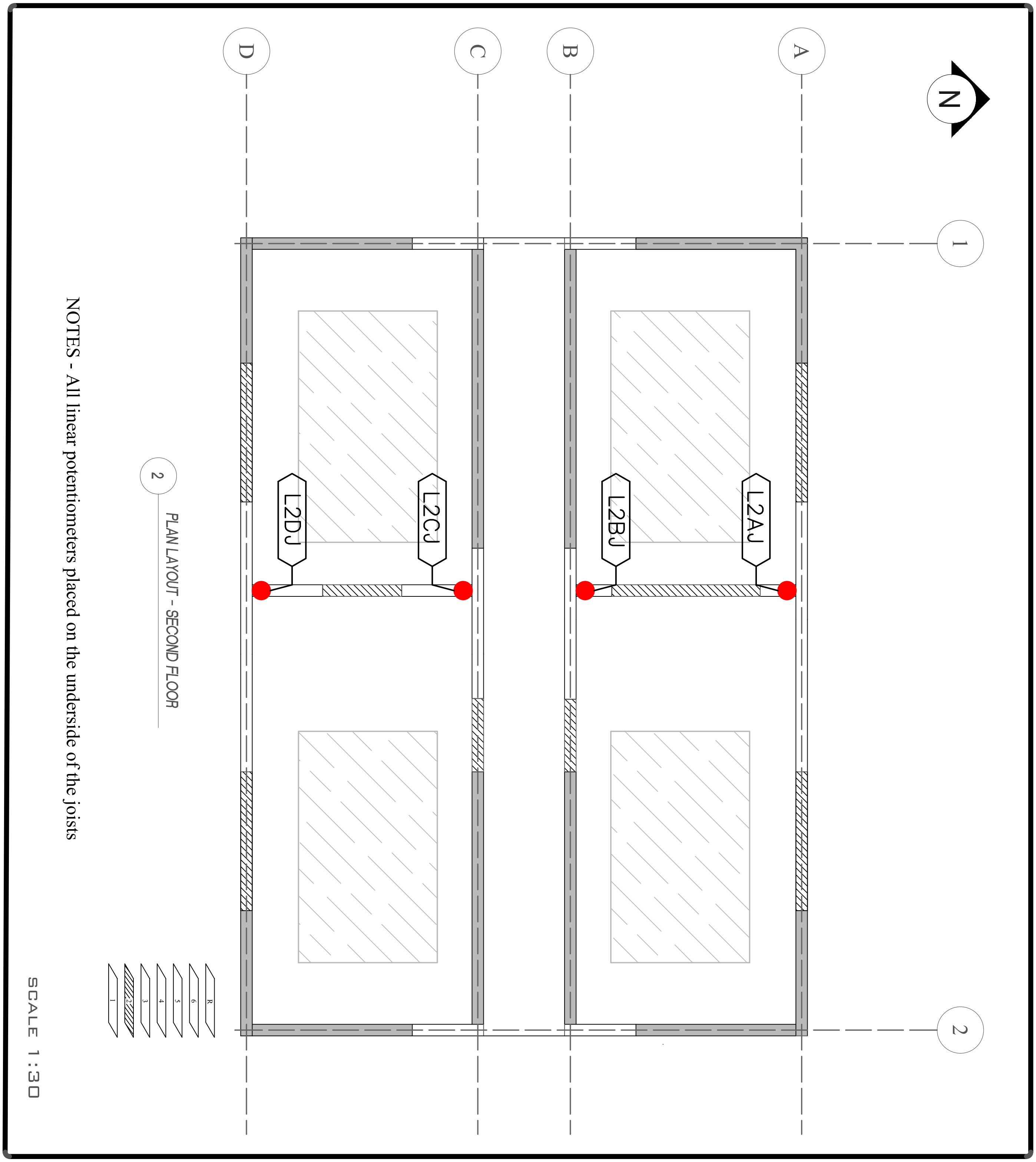

UCSD

UNIVERSITY OF CALIFORNIA, SAN DIEGO
DEPARTMENT OF STRUCTURAL ENGINEERING
LA JOLLA - CALIFORNIA 92093-0085

PROJECT NO. DATE:

NO.	DATE	REVISIONS

CFS Shake Table Test Project
Linear Potentiometers - Floor 1 ceiling
Configuration E2

SRIKAR GUNISETTY
Graduate Student Researcher
XIANG WANG
Post-doctoral Researcher

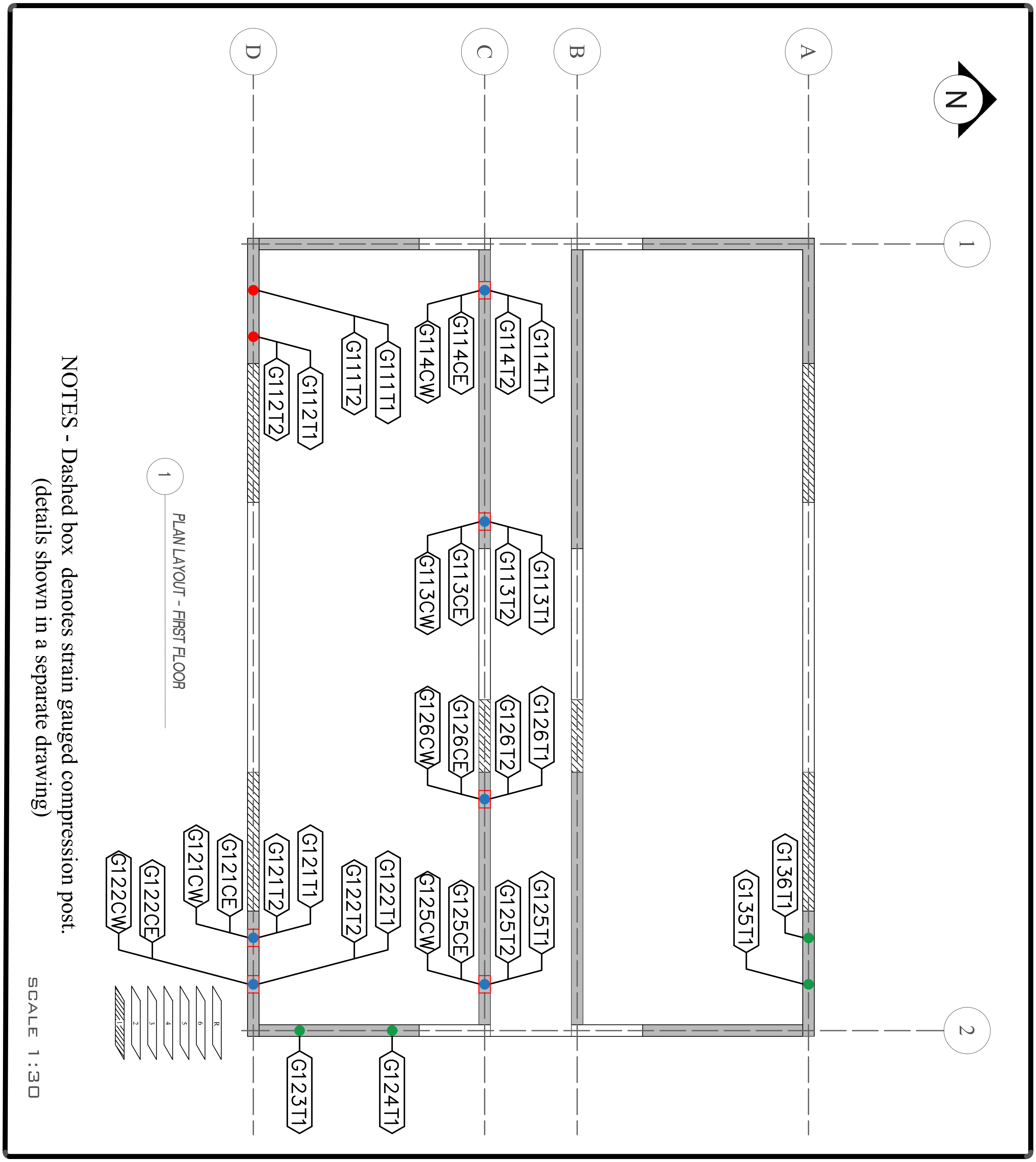

UCSD UNIVERSITY OF CALIFORNIA, SAN DIEGO DEPARTMENT OF STRUCTURAL ENGINEERING LA JOLLA - CALIFORNIA 92093-0085 PROJECT NO. DATE:	NO. DATE REVISIONS	CFS Shake Table Test Project Strain gauges - Floor 1 Configuration - E2

SRIKAR GUNISETTY
Graduate Student Researcher
XIANG WANG
Post-doctoral Researcher

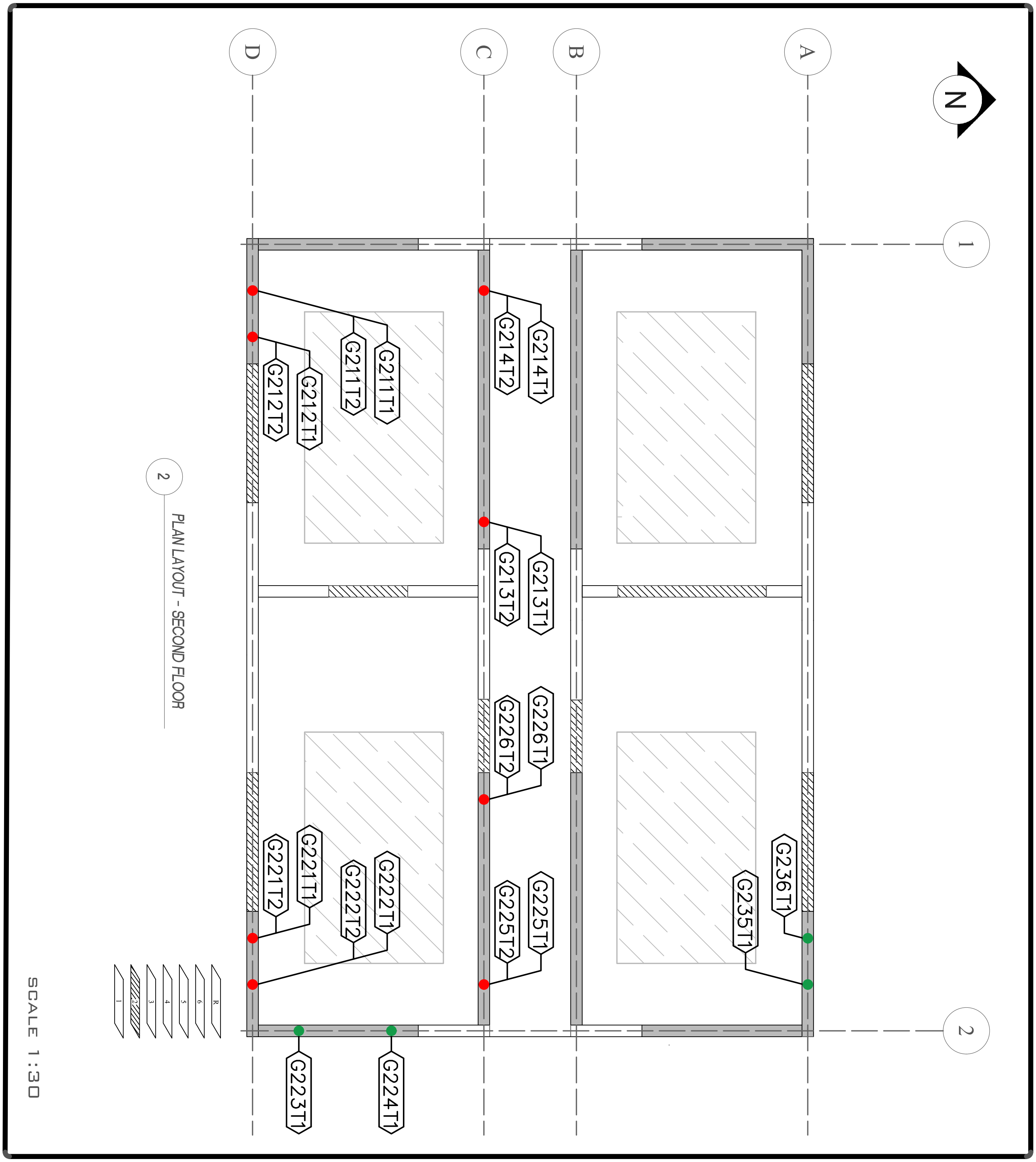

UCSD	NO.	DATE	REVISIONS	CFS Shake Table Test Project	SRIKAR GUNISETTY
UNIVERSITY OF CALIFORNIA, SAN DIEGO DEPARTMENT OF STRUCTURAL ENGINEERING LA JOLLA - CALIFORNIA 92093-0085				Strain gauges - Floor 2	Graduate Student Researcher XIANG WANG
PROJECT NO. DATE:				Configuration - E2	Post-doctoral Researcher

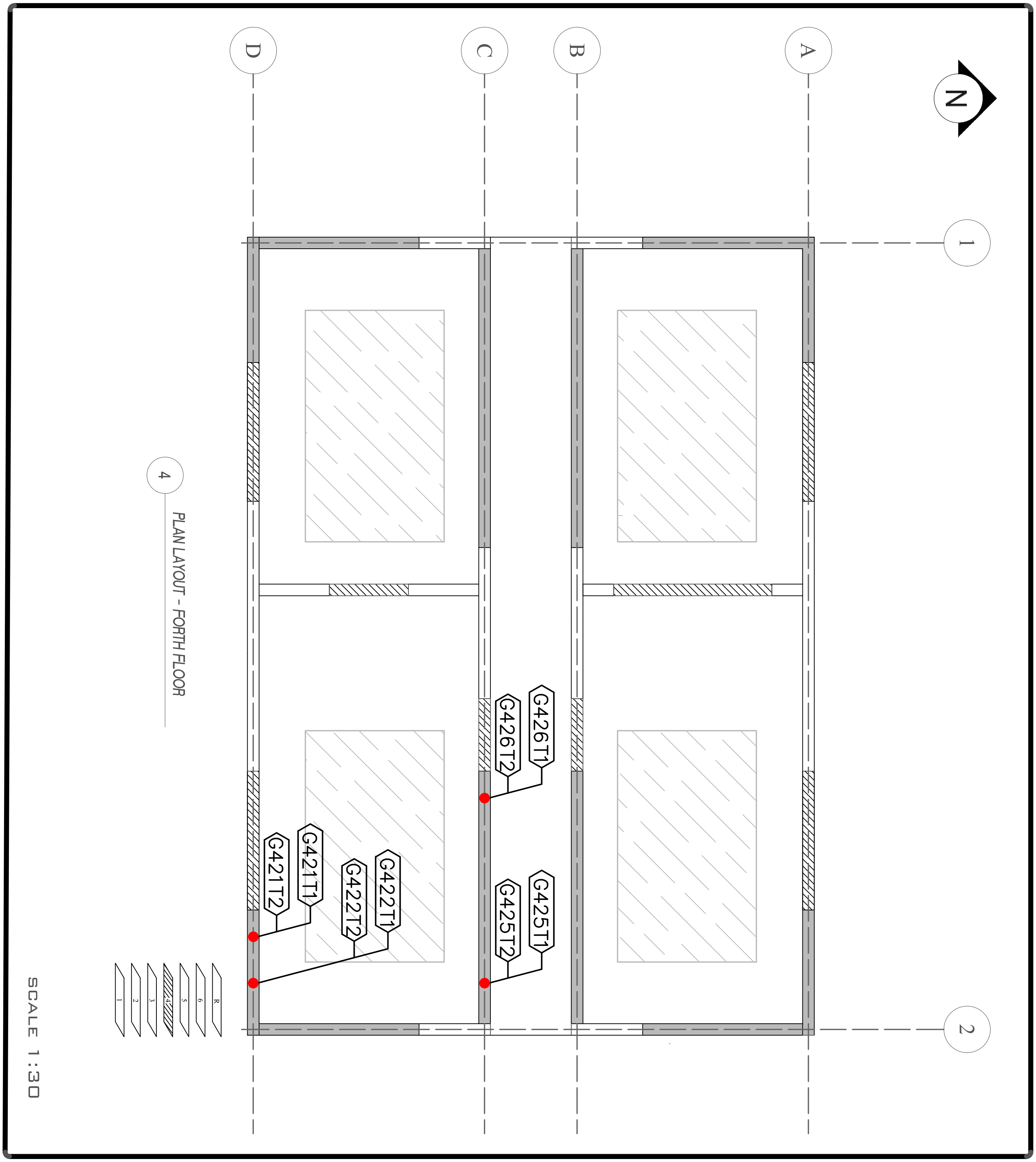

UCSD

UNIVERSITY OF CALIFORNIA, SAN DIEGO
DEPARTMENT OF STRUCTURAL ENGINEERING
LA JOLLA - CALIFORNIA 92093-0085

PROJECT NO. DATE:

NO.	DATE	REVISIONS

CFS Shake Table Test Project
Strain gauges - Floor 4
Configuration - E2

SRIKAR GUNISETTY
Graduate Student Researcher
XIANG WANG
Post-doctoral Researcher

APPENDIX F – INSTRUMENTATION PLAN OF VIDEO CAMERAS

This appendix documents the detailed instrumentation plan of the video camera system for the earthquake test phase. The camera system consisted of four different types of cameras, namely, GoPro cameras, coax cameras, IP cameras, and high definition (HD) camcorders. The camera layouts were modified at several different stages during the test phase, resulting in a total of four configurations as summarized in Table F.1. The plan layouts of the video camera system at all four configurations are documented in the following sections (one configuration in a separate section). Each section contains the camera count, floor-by-floor camera layouts, and the associated camera views regarding an individual configuration. It is noted that each camera is assigned with a unique five-digit name (using a combination of numeric and alphabetical characters), which are incorporated within the floor-by-floor camera layouts. Table F.2 provides a complete list of the camera names and the associated camera views.

Table F.1. Video camera system configurations.

Configuration	Camera type				Total
	GoPro	Coax	HD Camcorder	IP camera	
Configuration 1 (EQ 1-3)	12	22	4	/	38
Configuration 2 (EQ 4-5)	14	28	3	/	45
Configuration 3 (EQ 6-7)	/	28	4	2	34
Configuration 4 (EQ 8-9)	12	9	3	2	26

Table F.2. Summary of camera name and the associated views.

Level #	*Camera name*	*Location*	*Camera view*
1	1G1W1	South wall of quadrant 1	Corridor shear wall
1	1G1A2	South wall of quadrant 1	appliances on the west side
1	1G1F3	North west corner of quadrant 1	floor components (rim track, joist, clip configuration).
1	1G2A4	South wall of quadrant 2	appliances on the east side.
1	1G2F5	Floor of quadrant 2	ceiling joists.
1	1G3F6	North east corner of quadrant 3	corner formed by longitudinal wall, transverse wall, shake

			table
1	1G4W7	North wall of quadrant 4	corridor shear wall
1	1G4R8	North wall of quadrant 4	appliances on the east side
1	1G4F9	North west corner of quadrant 4	floor components (rim track, joist, clip configuration)
1	1G5F10	North wall of quadrant 5	corridor ceiling joists
1	1G6F11	North wall of quadrant 6	intersection of shear and non-shear wall boundary.
1	1I1R1	West wall of quadrant 1	full room
2	2G3F12	North east corner of quadrant 3	corner formed by longitudinal wall, transverse wall, first floor.
2	2C1W1	South wall of quadrant 1	corridor shear wall
2	2C2R2	South east corner of quadrant 2	full room
2	2C3R3	North east corner of quadrant 3	full room
2	2C4R4	North east corner of quadrant 4	full room
3	3C1W5	South wall of quadrant 1	corridor shear wall
3	3C1F6	North west corner of quadrant 1	floor components (rim track, joist, clip configuration)
3	3C2F7	East wall of quadrant 2	ceiling joists
3	3C3R8	North east corner of quadrant 3	full room
3	3C4R9	North east corner of quadrant 4	full room
3	3C5F10	North wall of quadrant 5	corridor ceiling joists
3	3C6F11	North wall of quadrant 6	intersection of shear and non-shear wall boundary.
4	4C1W12	South wall of quadrant 1	corridor shear wall
4	4C2F13	East wall of quadrant 2	ceiling joists
4	4C3R14	North east corner of quadrant 3	full room
4	4C4R15	North east corner of quadrant 4	full room
5	5C1W16	South wall of quadrant 1	corridor shear wall
5	5C1F17	North west corner of quadrant 1	floor components (rim track, joist, clip configuration)
5	5C2F18	East wall of quadrant 2	ceiling joists.
5	5C3R19	North east corner of quadrant 3	full room.
5	5C4R20	North east corner of quadrant 4	full room.

5	5C5F21	North wall of quadrant 5	corridor ceiling joists.
6	6C1A22	East wall of quadrant 1	appliances on the west.
6	6C2A23	W wall of quadrant 2	appliances on the east.
6	6C3A24	North west corner of quadrant 3	full room.
6	6C4A25	North east corner of quadrant 4	full room.
7	7C1A26	South west corner of parapet wall	SW corner.
7	7C2A27	South east corner of parapet wall	SE corner.
7	7C3A28	North east corner of the parapet wall	full roof.
E	EIE	East exterior of the test building	first floor corridor
E	EHN	North exterior of the test building	north elevation
E	EHS	South exterior of the test building	south elevation
E	EHSW	South-west exterior of the test building	isometric view
E	EGE	East exterior of the test building	first floor corridor
E	EGW	West exterior of the building	first floor corridor

Video Camera Layout – Configuration 1

Table F.3. Video cameras counts – Configuration 1

Location	Type of camera				Total
	GoPro	Coax	HD Camcorder	IP camera	
Level-1	11	-	/	/	11
Level-2	1	2	/	/	3
Level-3	/	7	/	/	7
Level-4	/	4	/	/	4
Level-5	/	6	/	/	6
Level-6	/	2	/	/	2
Roof	/	1	/	/	1
Exterior	/	/	4	/	4
Total	12	22	4	0	**38**

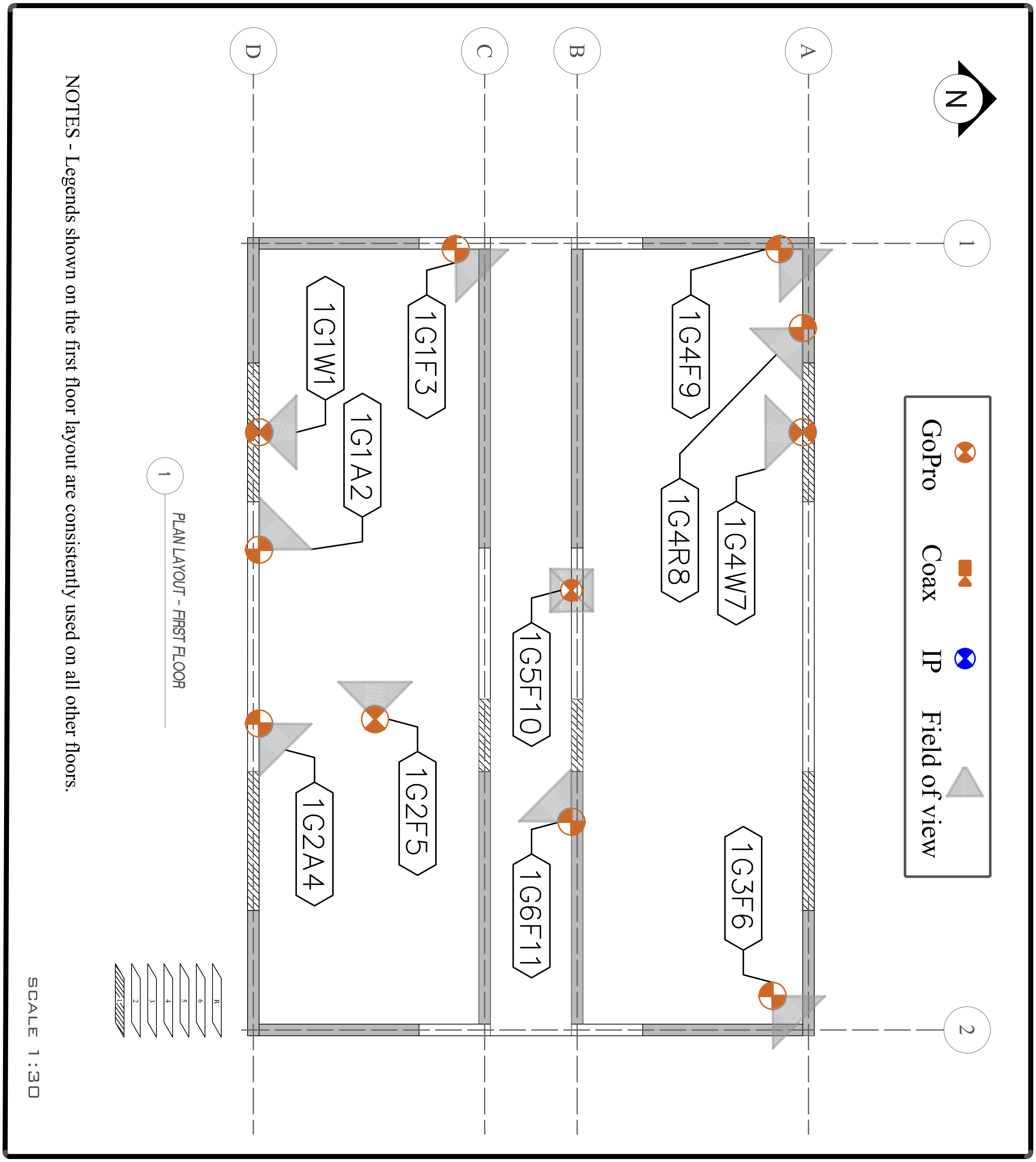

UCSD UNIVERSITY OF CALIFORNIA, SAN DIEGO DEPARTMENT OF STRUCTURAL ENGINEERING LA JOLLA - CALIFORNIA 92093-0085 PROJECT NO. DATE:	CFS Shake Table Test Project Cameras - Floor 1. Configuration 1	SRIKAR GUNISETTY Graduate Student Researcher XIANG WANG Post-doctoral Researcher

NO.	DATE	REVISIONS

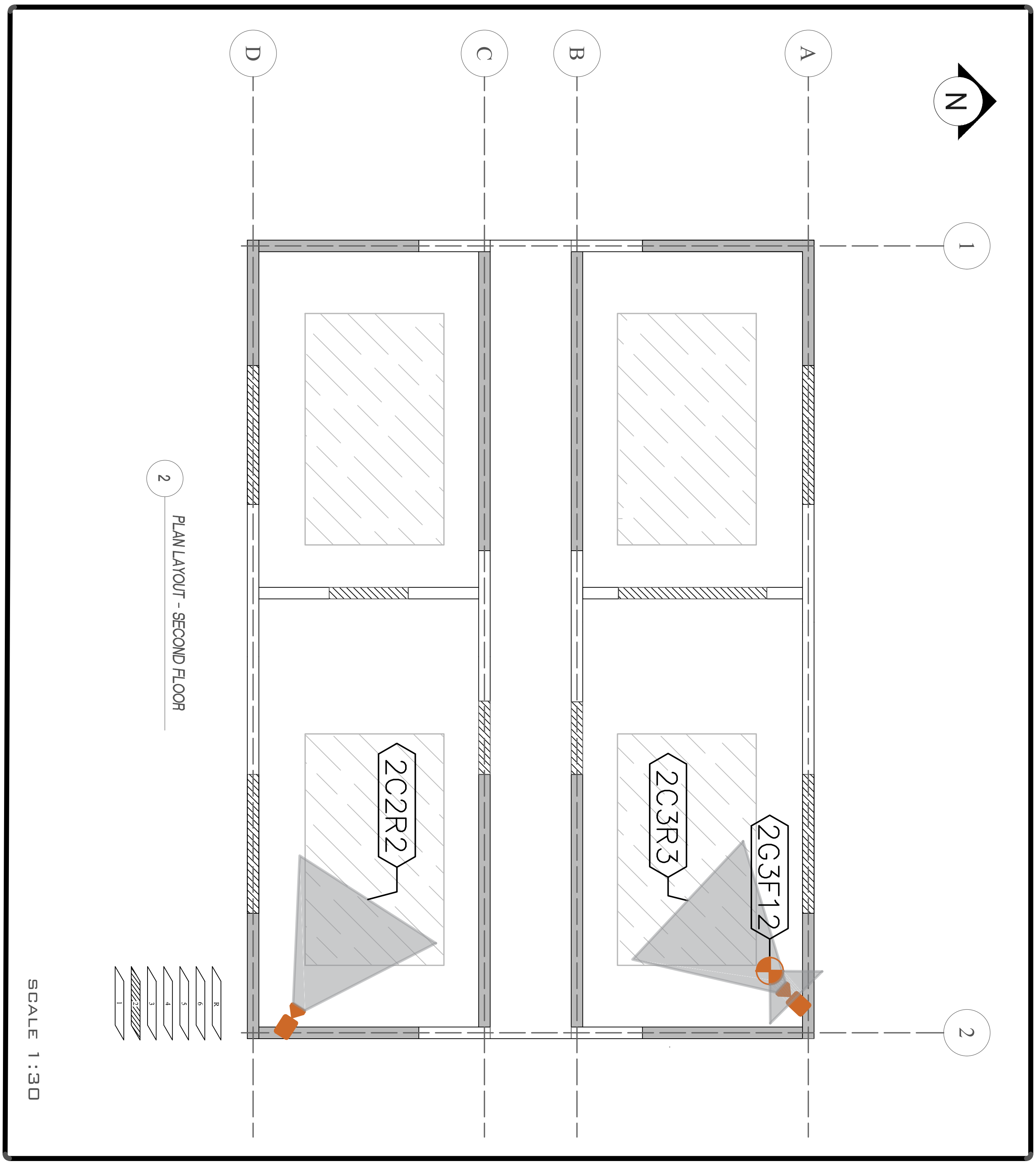

UCSD

UNIVERSITY OF CALIFORNIA, SAN DIEGO
DEPARTMENT OF STRUCTURAL ENGINEERING
LA JOLLA - CALIFORNIA 92093-0085

PROJECT NO. DATE:

NO.	DATE	REVISIONS

CFS Shake Table Test Project
Cameras - Floor 2.
Configuration 1

SRIKAR GUNISETTY
Graduate Student Researcher
XIANG WANG
Post-doctoral Researcher

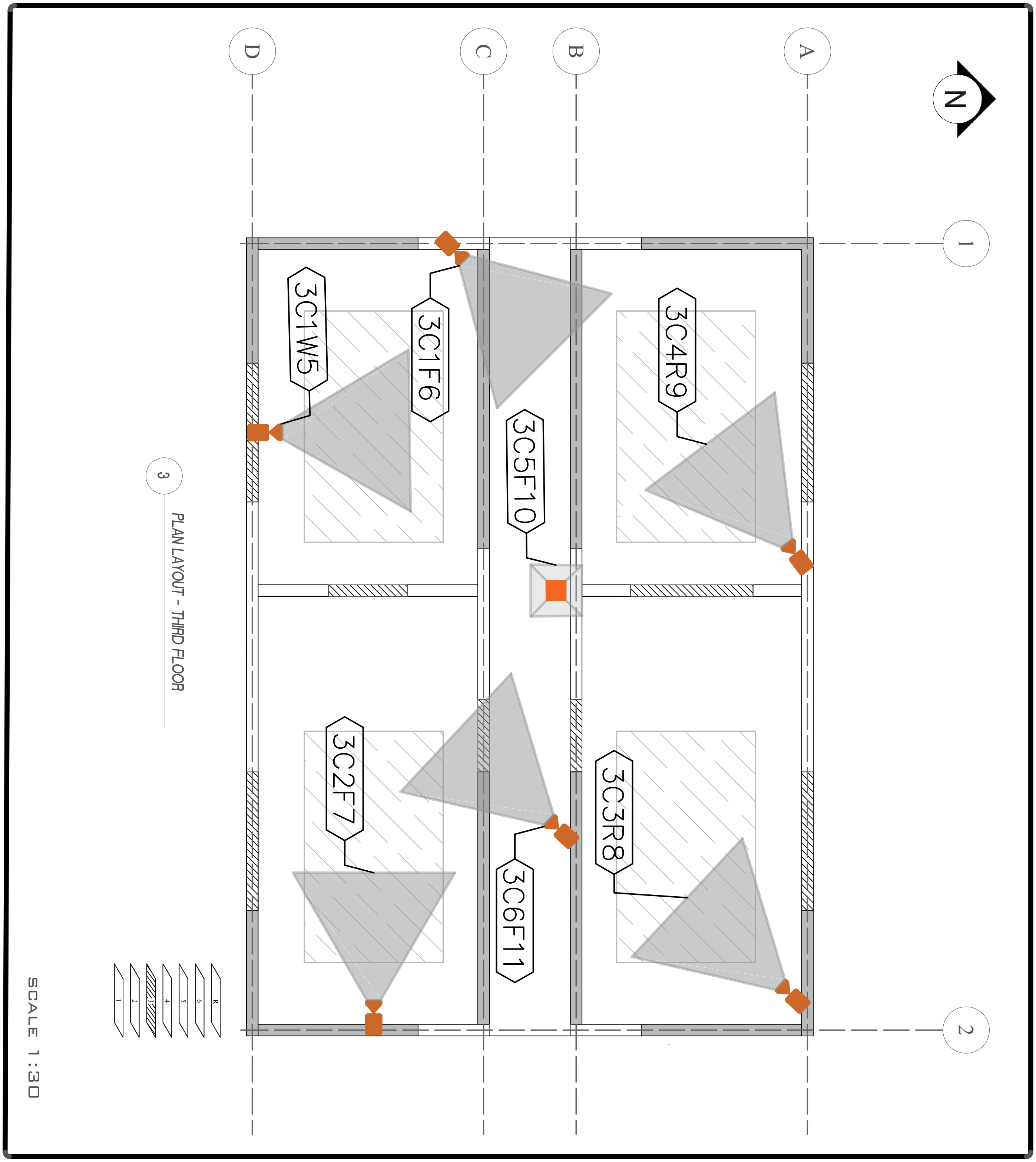

UCSD
UNIVERSITY OF CALIFORNIA, SAN DIEGO
DEPARTMENT OF STRUCTURAL ENGINEERING
LA JOLLA - CALIFORNIA 92093-0085

PROJECT NO. DATE:

NO.	DATE	REVISIONS

CFS Shake Table Test Project
Cameras - Floor 3.
Configuration 1

SRIKAR GUNISETTY
Graduate Student Researcher
XIANG WANG
Post-doctoral Researcher

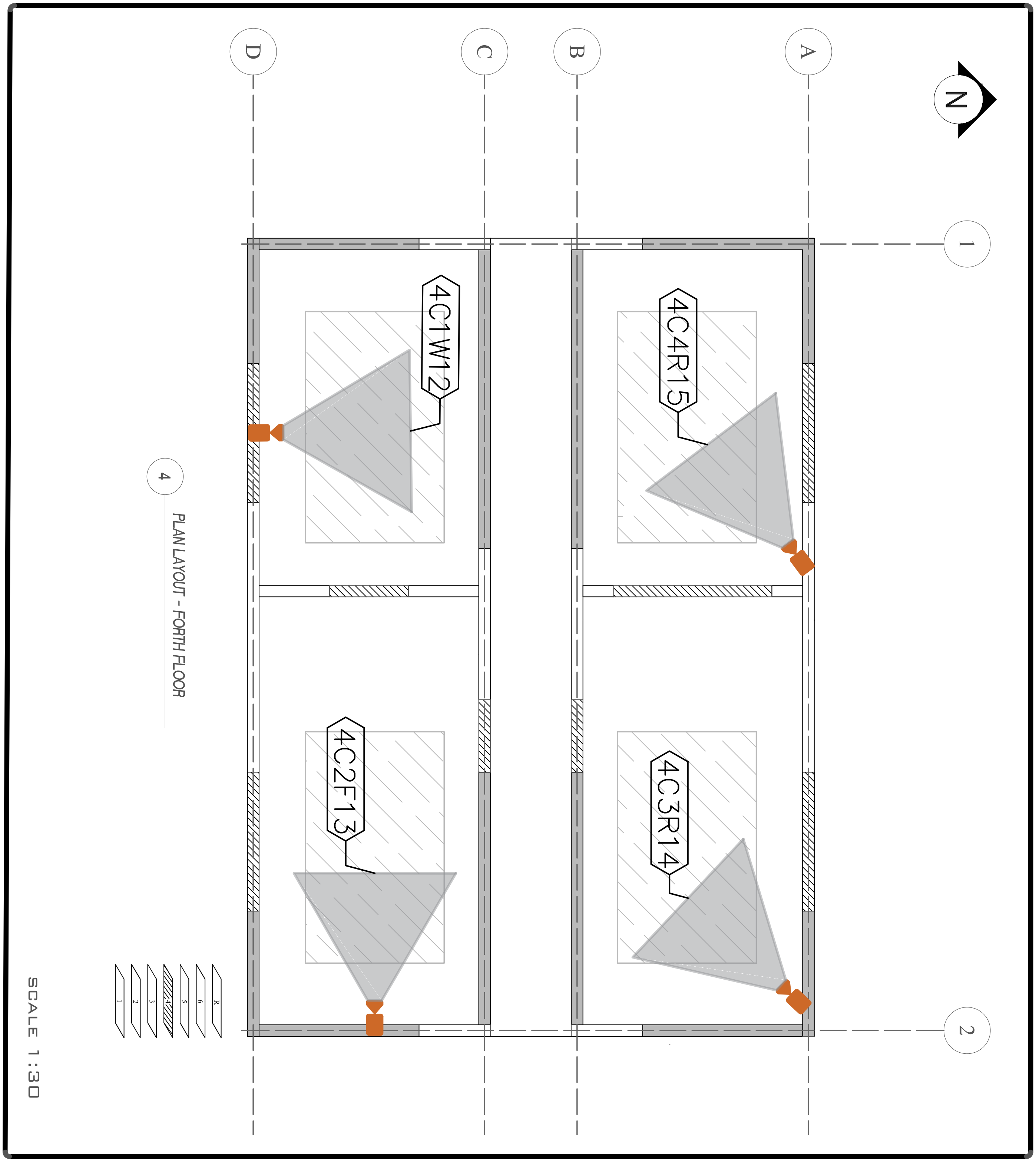

UCSD

UNIVERSITY OF CALIFORNIA, SAN DIEGO
DEPARTMENT OF STRUCTURAL ENGINEERING
LA JOLLA - CALIFORNIA 92093-0085

PROJECT NO. DATE:

NO.	DATE	REVISIONS

CFS Shake Table Test Project
Cameras - Floor 4.
Configuration 1

SRIKAR GUNISETTY
Graduate Student Researcher
XIANG WANG
Post-doctoral Researcher

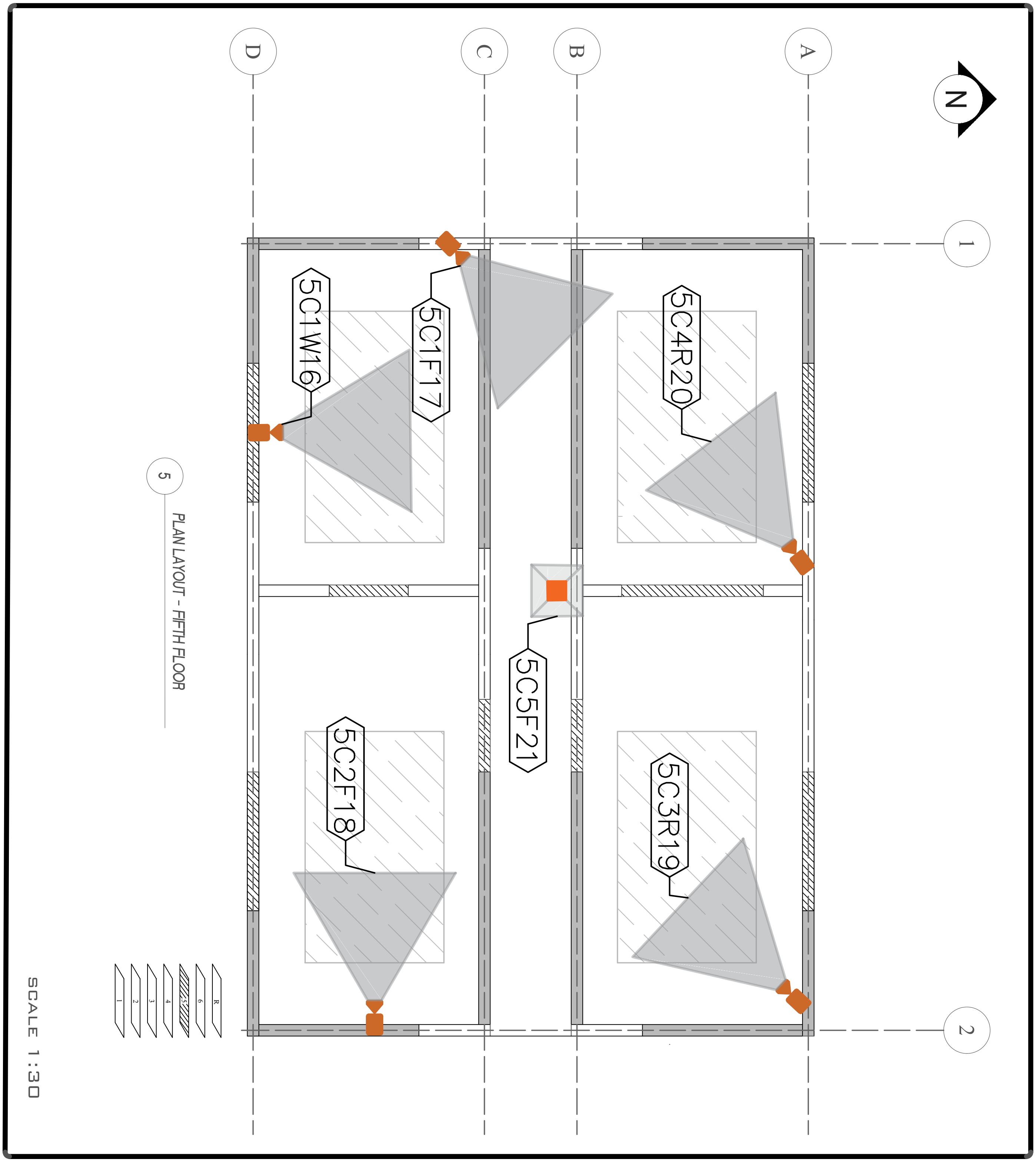

UCSD

UNIVERSITY OF CALIFORNIA, SAN DIEGO
DEPARTMENT OF STRUCTURAL ENGINEERING
LA JOLLA - CALIFORNIA 92093-0085

PROJECT NO. DATE:

NO.	DATE	REVISIONS

CFS Shake Table Test Project
Cameras - Floor 5.
Configuration 1

SRIKAR GUNISETTY
Graduate Student Researcher
XIANG WANG
Post-doctoral Researcher

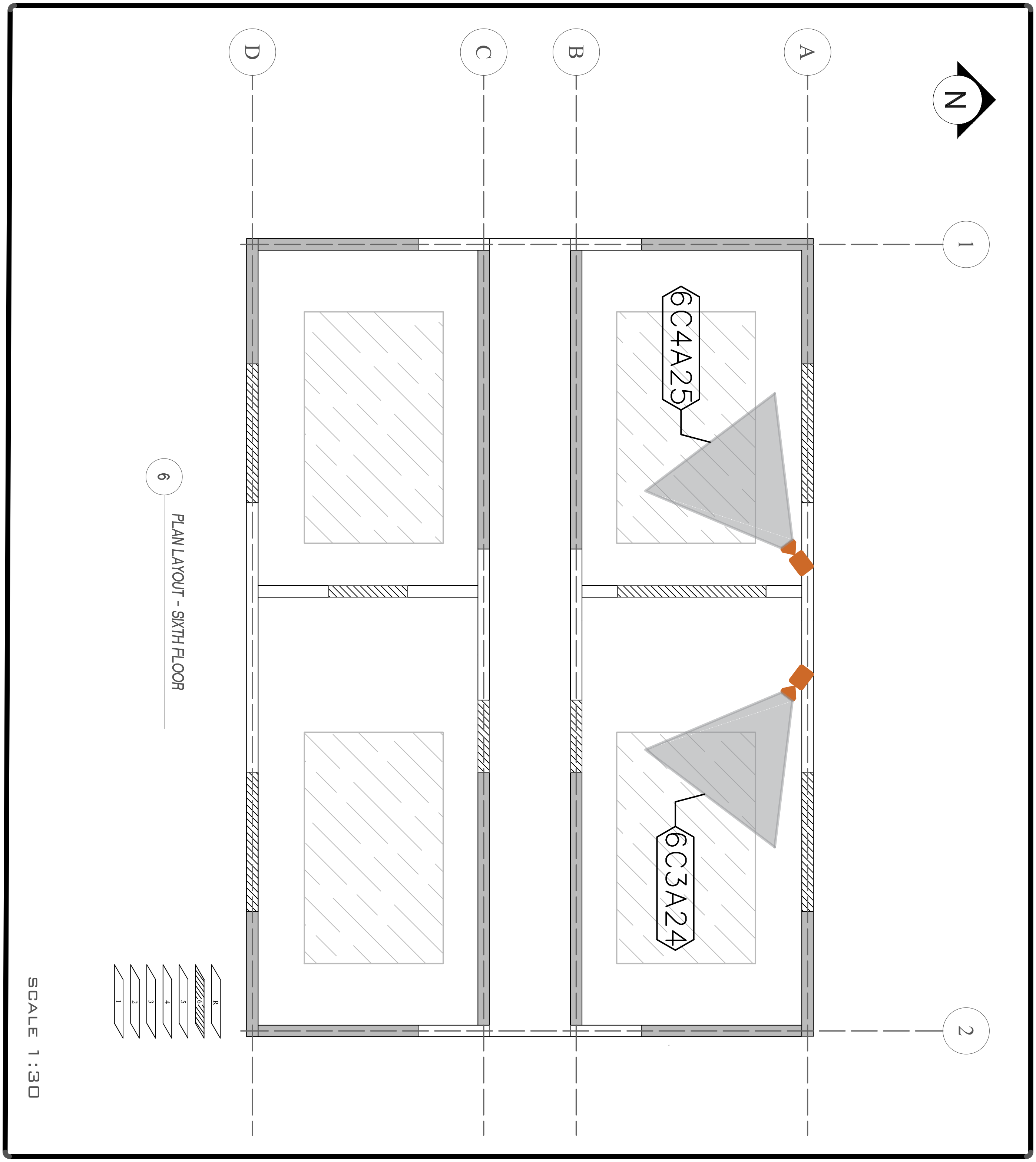

UCSD UNIVERSITY OF CALIFORNIA, SAN DIEGO DEPARTMENT OF STRUCTURAL ENGINEERING LA JOLLA - CALIFORNIA 92093-0085 PROJECT NO. DATE:	NO. DATE REVISIONS	CFS Shake Table Test Project Cameras - Floor 6. Configuration 1

SRIKAR GUNISETTY
Graduate Student Researcher
XIANG WANG
Post-doctoral Researcher

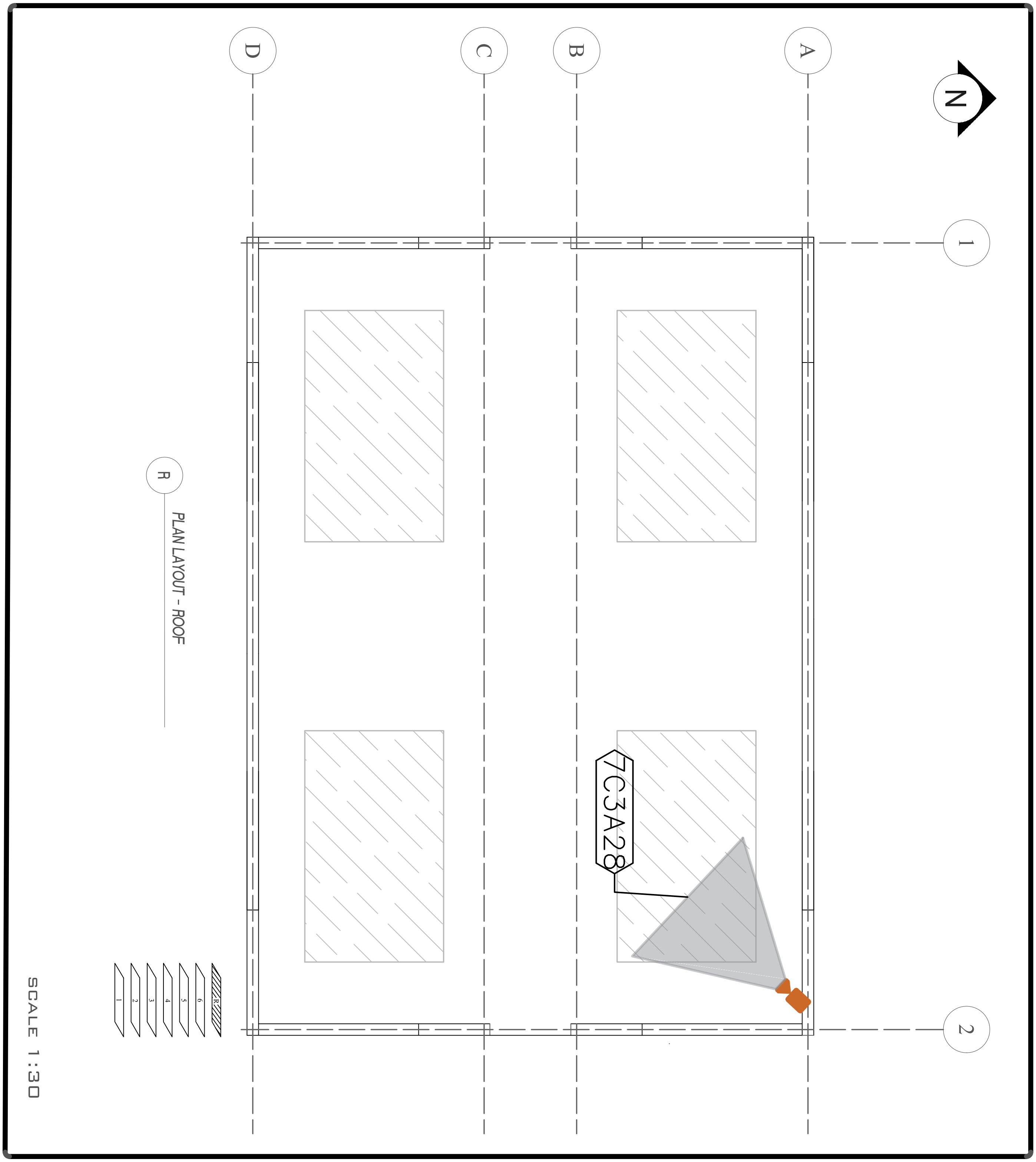

UCSD
UNIVERSITY OF CALIFORNIA, SAN DIEGO
DEPARTMENT OF STRUCTURAL ENGINEERING
LA JOLLA - CALIFORNIA 92093-0085

PROJECT NO. DATE:

NO.	DATE	REVISIONS

CFS Shake Table Test Project
Cameras - Roof.
Configuration 1

SRIKAR GUNISETTY
Graduate Student Researcher
XIANG WANG
Post-doctoral Researcher

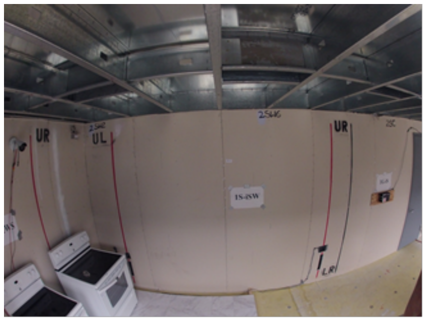

1G1W1

1G1A2

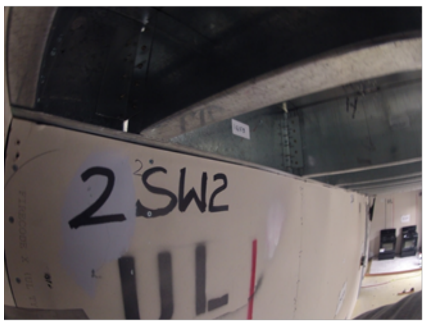

1G1F3

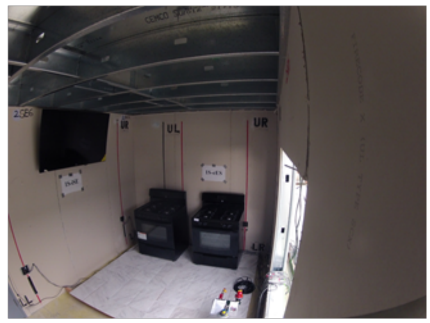

1G2A4

1G2F5

1G3F6

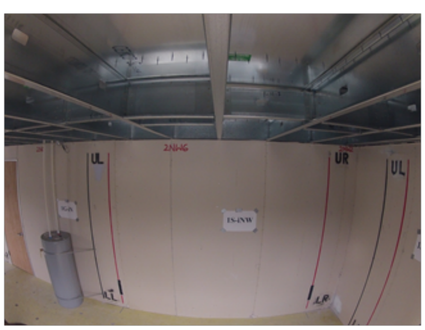

1G4W7

1G4R8

1G4F9

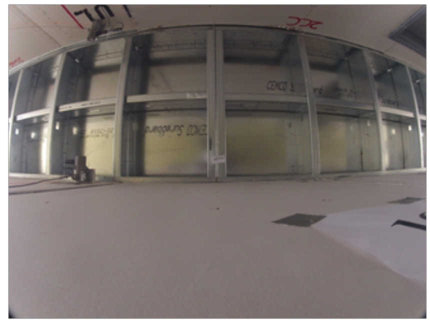

1G5F10

1G6F11

2G3F12

2C2R2

2C3R3

3C1W5

3C1F6

3C2F7

3C3R8

3C4R9

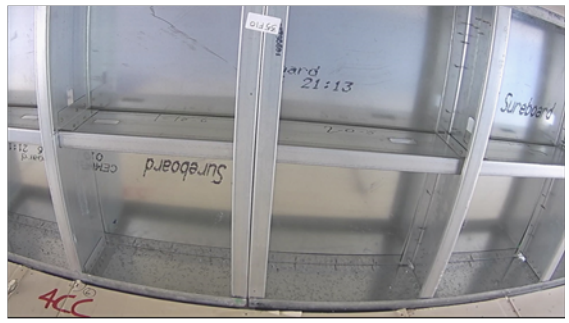

3C5F10

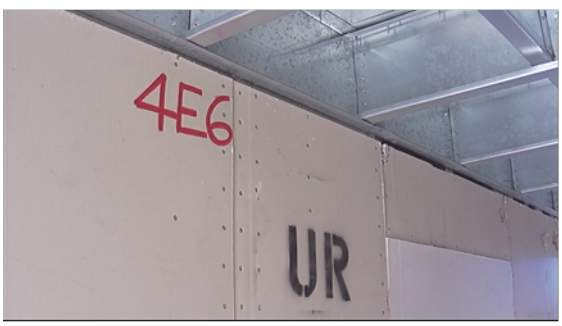

3C6F11

4C1W12

4C2F13

4C3R14

4C4R15

5C1W16

5C1F17

5C2F18

5C3R19

5C4R20

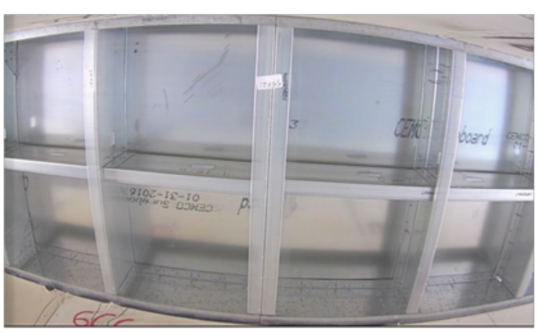

5C5F21

6C3A24

6C4A25

7C3A28

EHS

EHNW

EHSW

Video Camera Layout – Configuration 2

Table F.4. Video cameras counts – Configuration 2

Location	Type of camera				Total
	GoPro	Coax	HD Camcorder	IP camera	
Level-1	11	/	/	/	11
Level-2	1	4	/	/	5
Level-3	/	7	/	/	7
Level-4	/	4	/	/	4
Level-5	/	6	/	/	6
Level-6	/	4	/	/	4
Roof	/	3	/	/	3
Exterior	2	/	3	/	5
Total	14	28	3	0	**45**

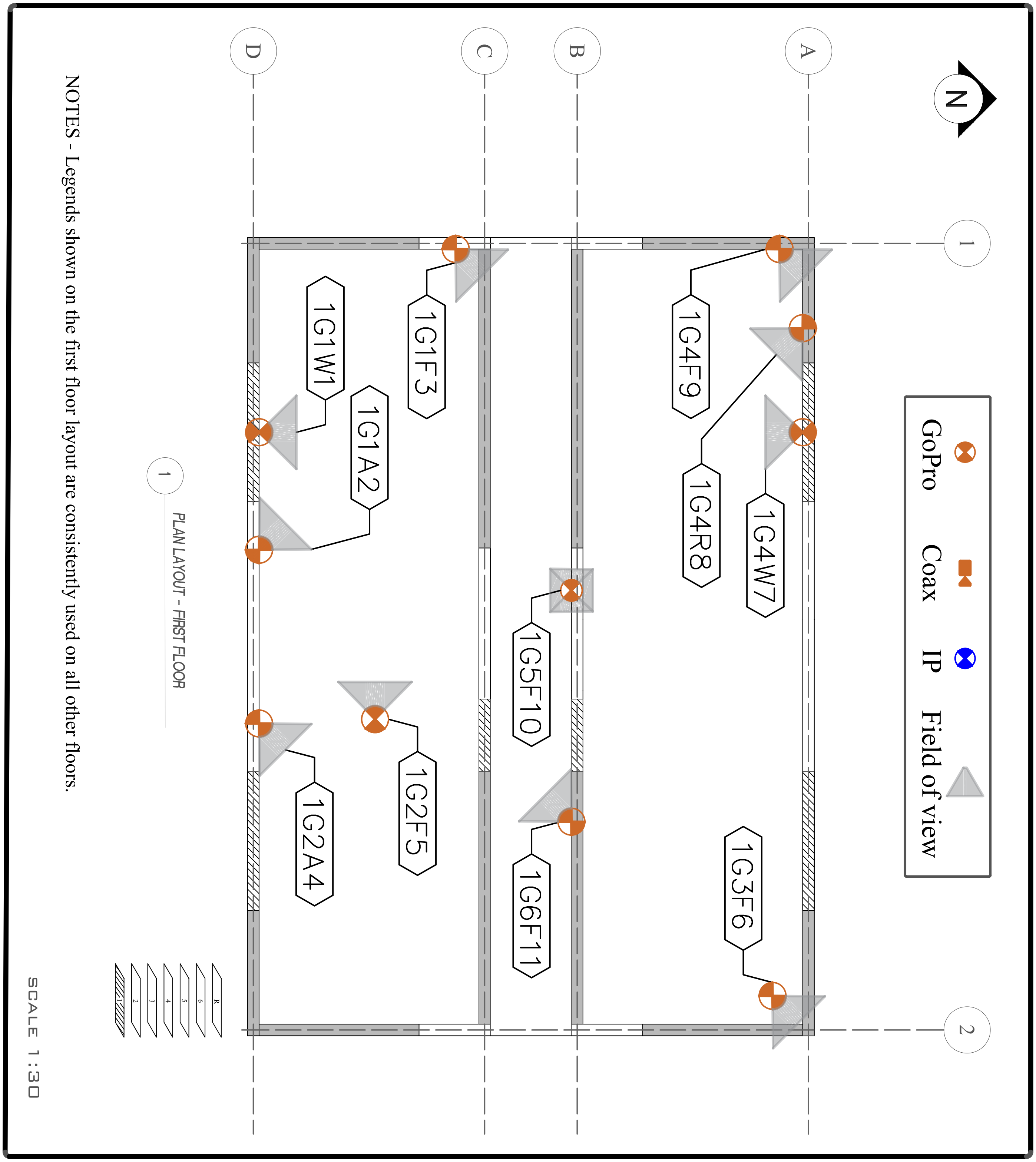

UCSD

UNIVERSITY OF CALIFORNIA, SAN DIEGO
DEPARTMENT OF STRUCTURAL ENGINEERING
LA JOLLA - CALIFORNIA 92093-0085

PROJECT NO. DATE:

NO.	DATE	REVISIONS

CFS Shake Table Test Project
Cameras - Floor 1.
Configuration 2

SRIKAR GUNISETTY
Graduate Student Researcher
XIANG WANG
Post-doctoral Researcher

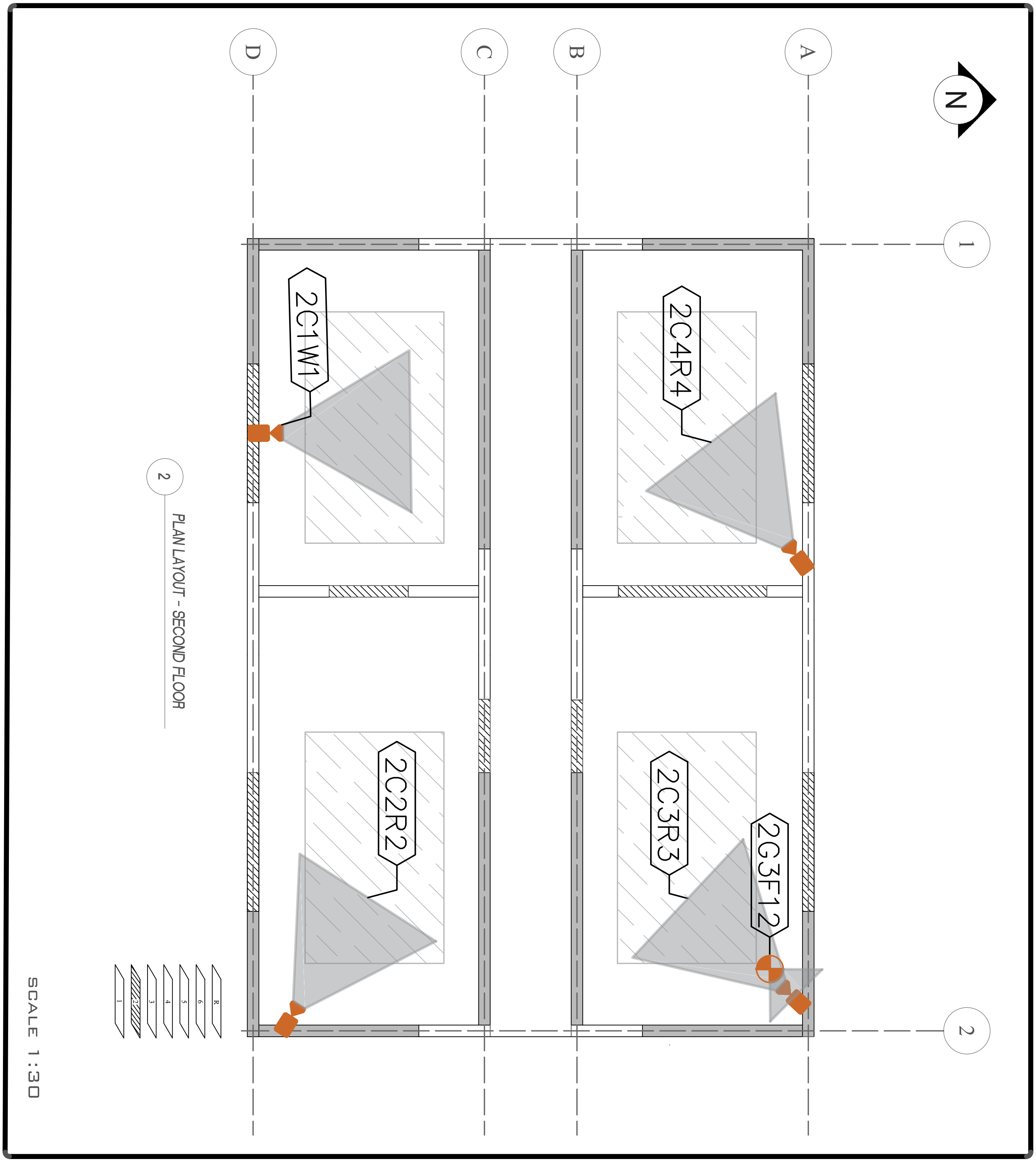

UCSD

UNIVERSITY OF CALIFORNIA, SAN DIEGO
DEPARTMENT OF STRUCTURAL ENGINEERING
LA JOLLA - CALIFORNIA 92093-0085

PROJECT NO. DATE:

NO.	DATE	REVISIONS

CFS Shake Table Test Project
Cameras - Floor 2.
Configuration 2

SRIKAR GUNISETTY
Graduate Student Researcher
XIANG WANG
Post-doctoral Researcher

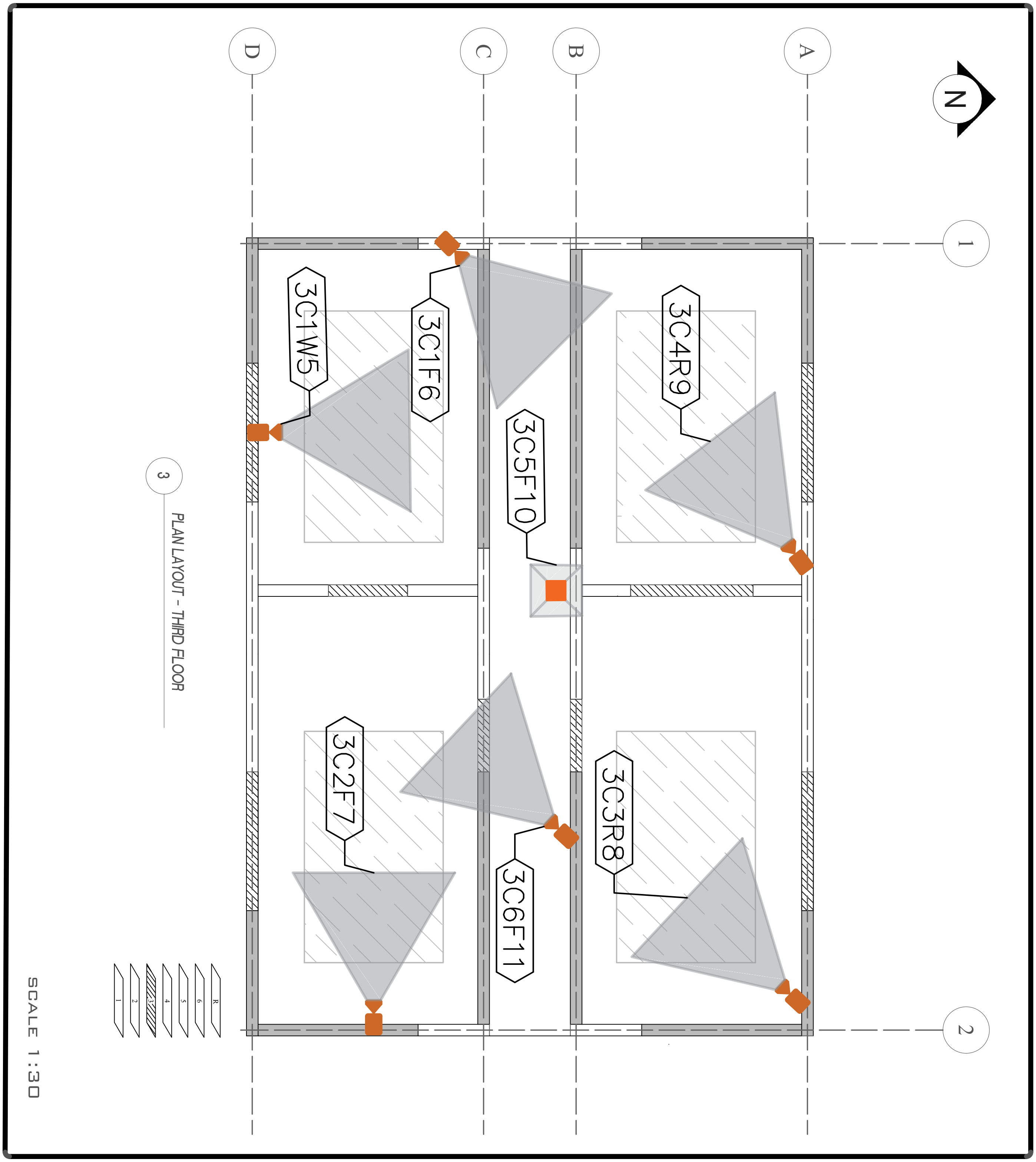

UCSD

UNIVERSITY OF CALIFORNIA, SAN DIEGO
DEPARTMENT OF STRUCTURAL ENGINEERING
LA JOLLA - CALIFORNIA 92093-0085

PROJECT NO. DATE:

NO.	DATE	REVISIONS

CFS Shake Table Test Project
Cameras - Floor 3.
Configuration 2

SRIKAR GUNISETTY
Graduate Student Researcher
XIANG WANG
Post-doctoral Researcher

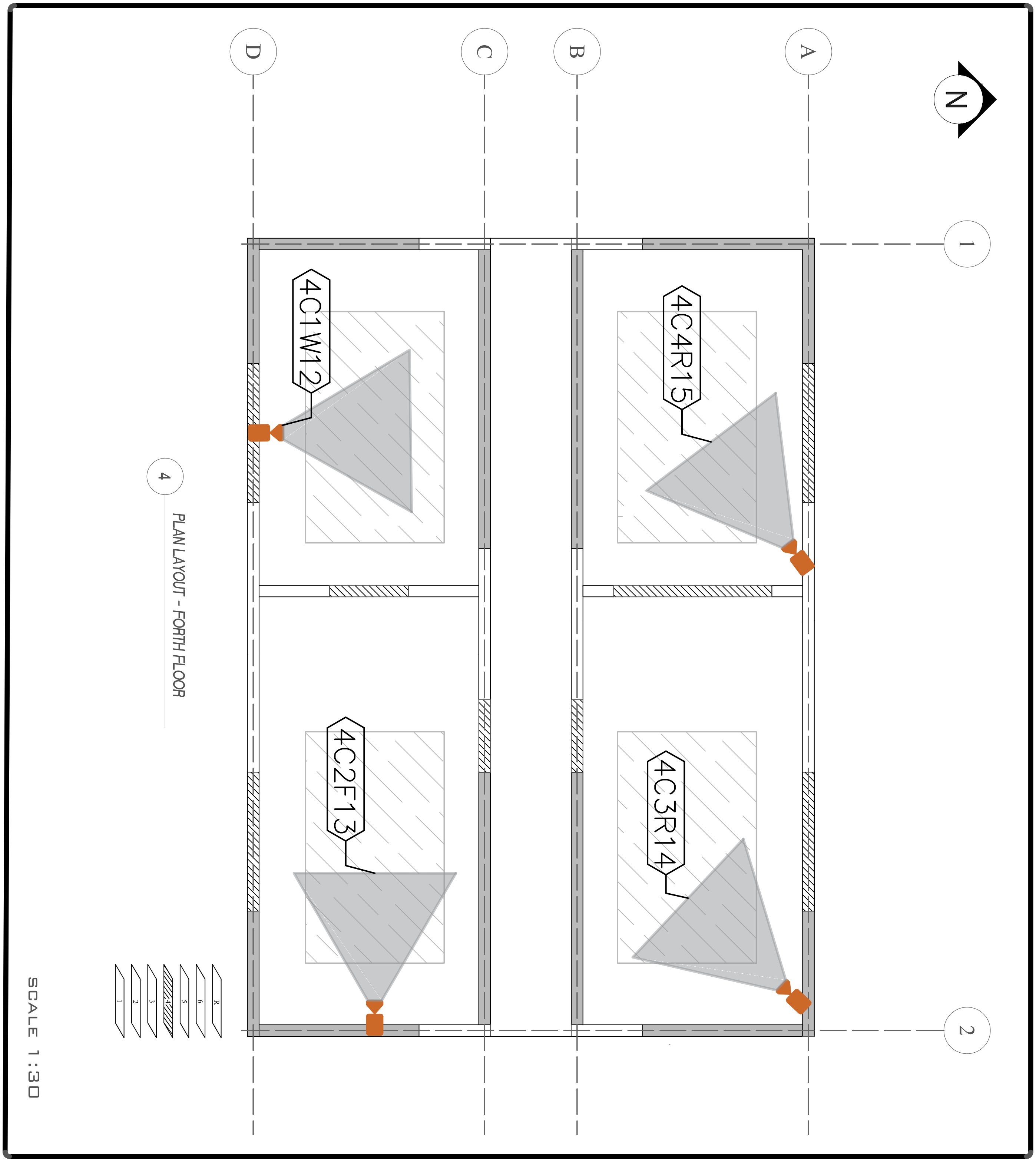

UCSD

UNIVERSITY OF CALIFORNIA, SAN DIEGO
DEPARTMENT OF STRUCTURAL ENGINEERING
LA JOLLA - CALIFORNIA 92093-0085

PROJECT NO. DATE:

NO.	DATE	REVISIONS

CFS Shake Table Test Project
Cameras - Floor 4.
Configuration 2

SRIKAR GUNISETTY
Graduate Student Researcher
XIANG WANG
Post-doctoral Researcher

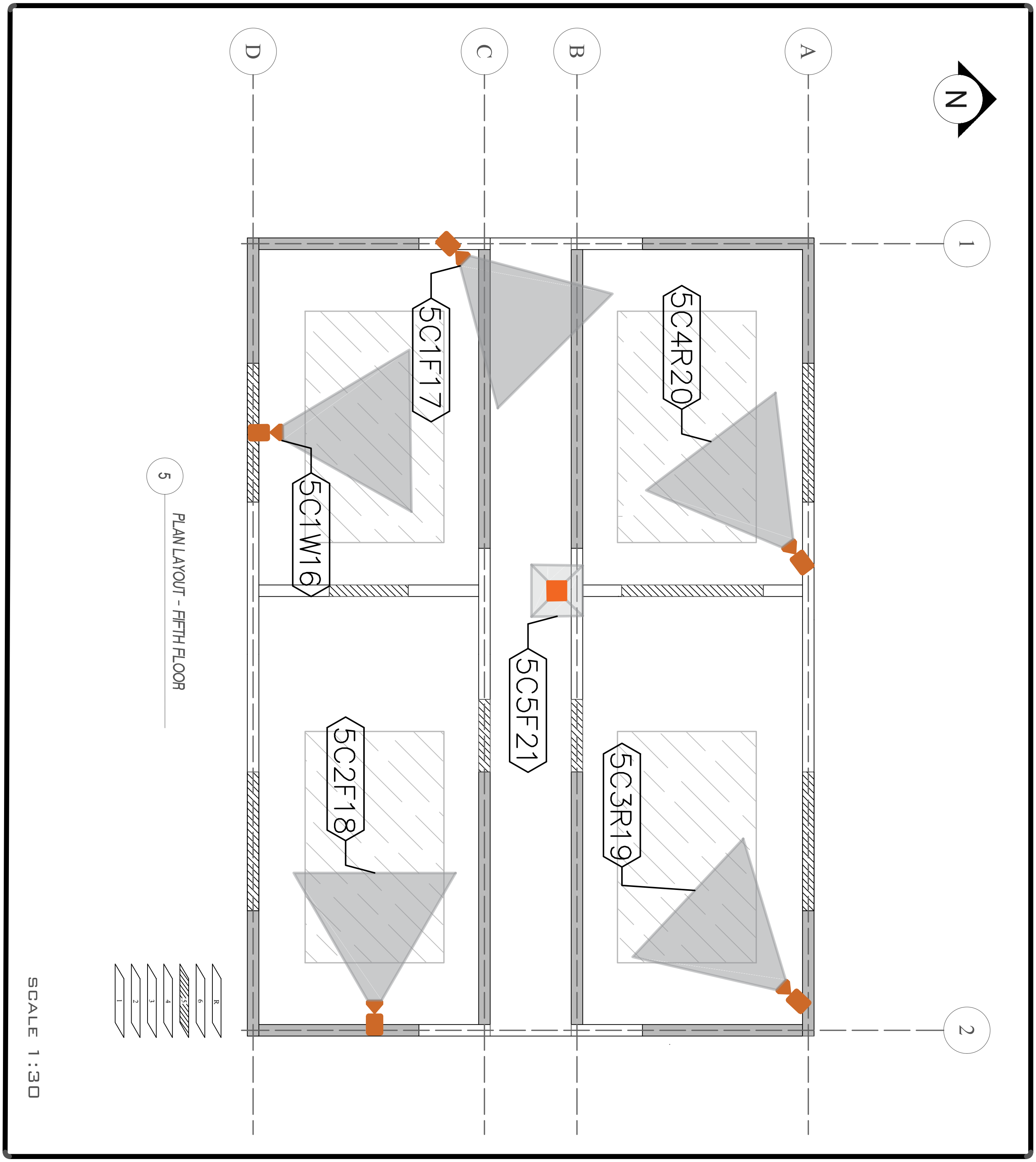

UCSD	NO.	DATE	REVISIONS	CFS Shake Table Test Project	SRIKAR GUNISETTY
UNIVERSITY OF CALIFORNIA, SAN DIEGO DEPARTMENT OF STRUCTURAL ENGINEERING LA JOLLA - CALIFORNIA 92093-0085				Cameras - Floor 5.	Graduate Student Researcher
PROJECT NO. DATE:				Configuration 2	XIANG WANG Post-doctoral Researcher

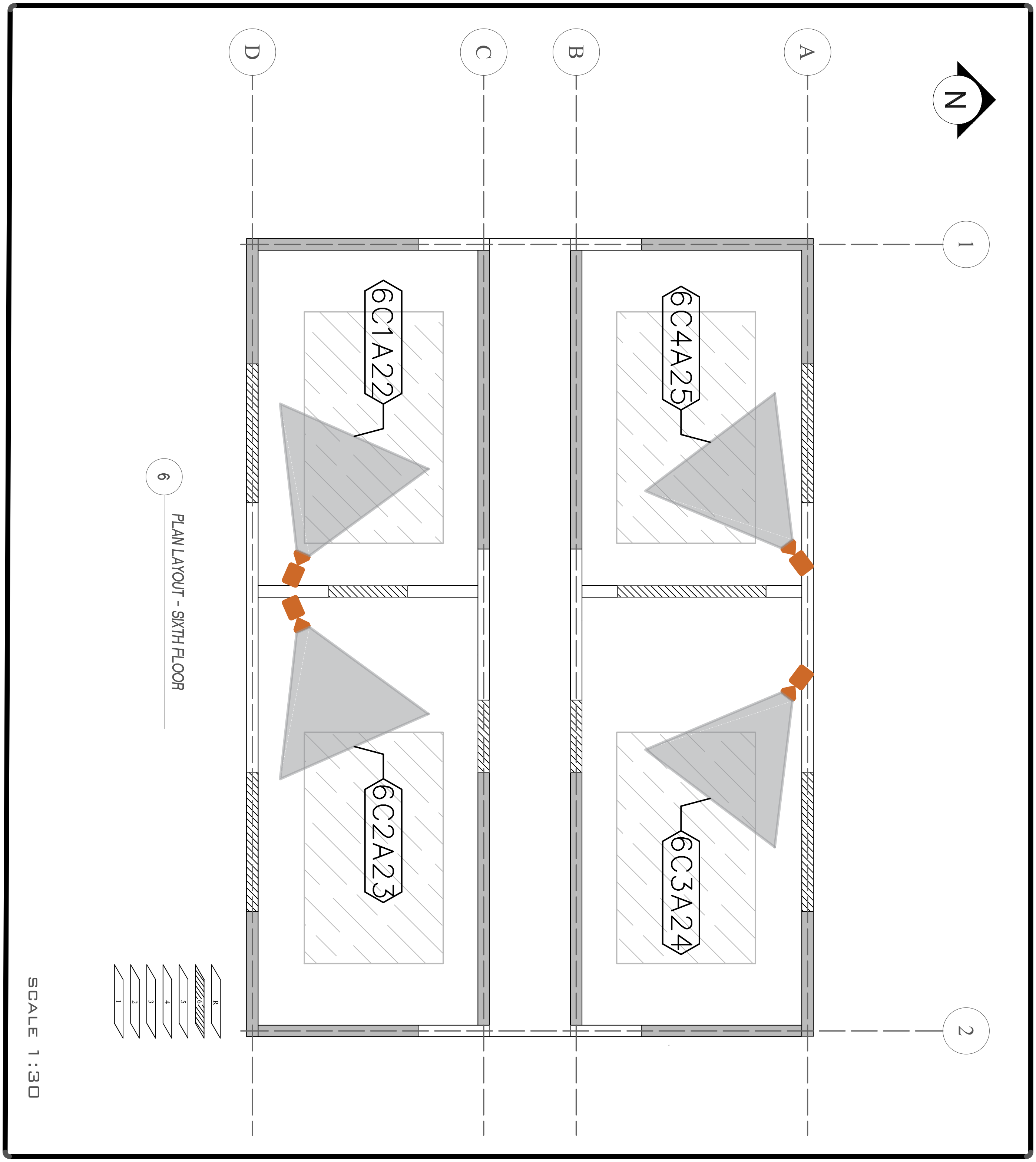

UCSD
UNIVERSITY OF CALIFORNIA, SAN DIEGO
DEPARTMENT OF STRUCTURAL ENGINEERING
LA JOLLA - CALIFORNIA 92093-0085
PROJECT NO. DATE:

NO.	DATE	REVISIONS

CFS Shake Table Test Project
Cameras - Floor 6.
Configuration 2

SRIKAR GUNISETTY
Graduate Student Researcher
XIANG WANG
Post-doctoral Researcher

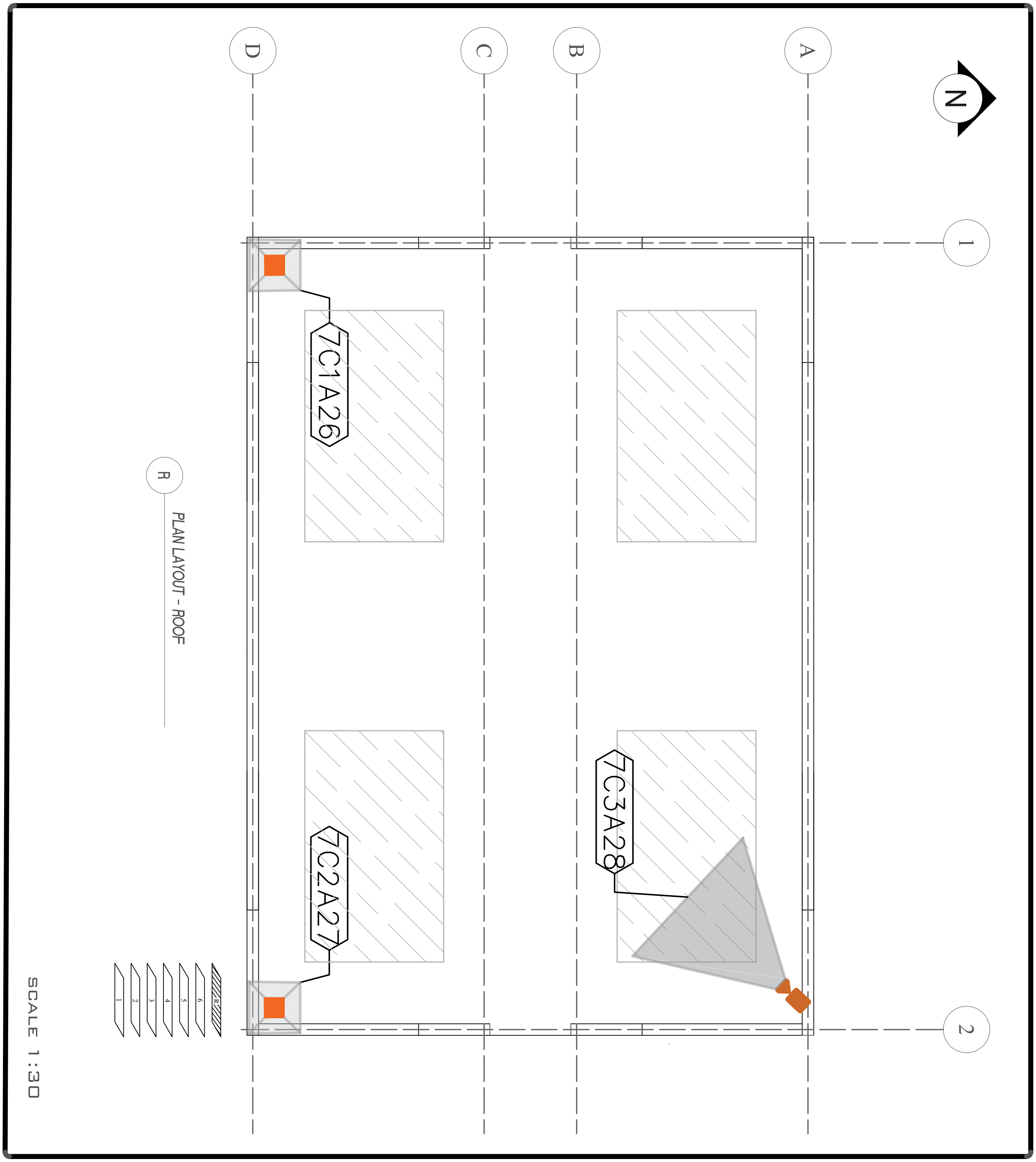

UCSD UNIVERSITY OF CALIFORNIA, SAN DIEGO DEPARTMENT OF STRUCTURAL ENGINEERING LA JOLLA - CALIFORNIA 92093-0085 PROJECT NO. DATE:	NO. DATE REVISIONS	CFS Shake Table Test Project Cameras - Roof. Configuration 2	SRIKAR GUNISETTY Graduate Student Researcher XIANG WANG Post-doctoral Researcher

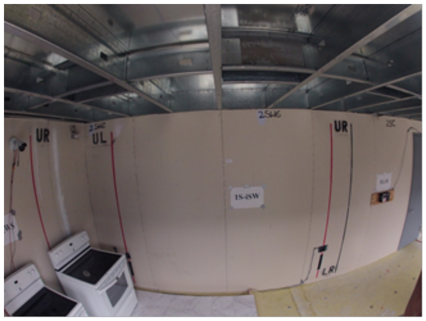

1G1W1

1G1A2

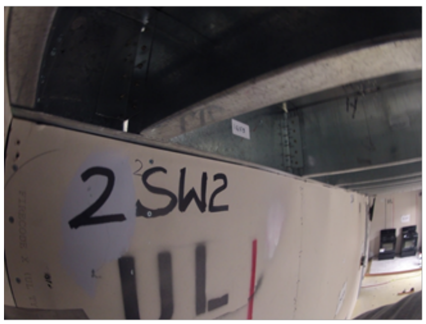

1G1F3

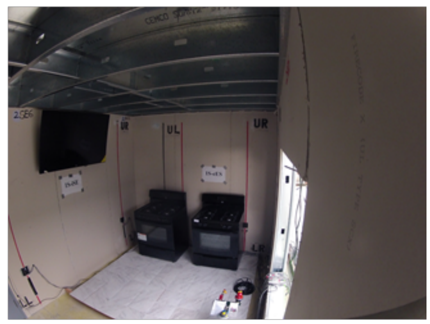

1G2A4

1G2F5

1G3F6

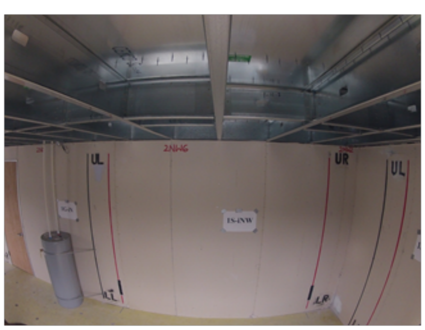

1G4W7

1G4R8

1G4F9

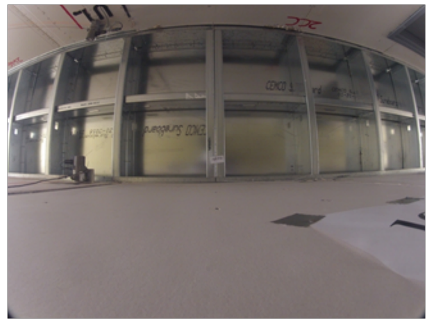

1G5F10

1G6F11

2G3F12

2C1W1

2C2R2

2C3R3

2C4R4

3C1W5

3C1F6

3C2F7

3C3R8

3C4R9

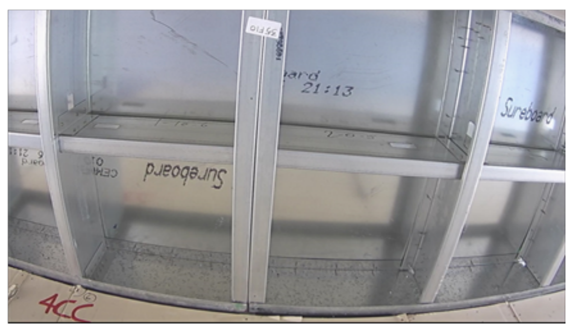

3C5F10

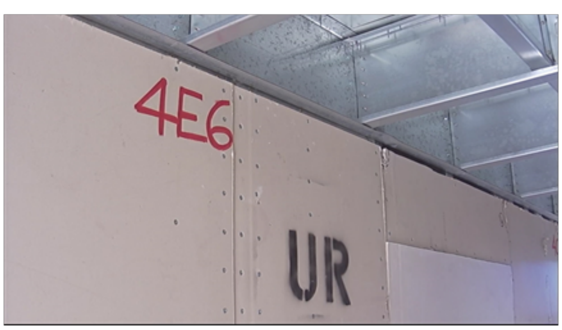

3C6F11

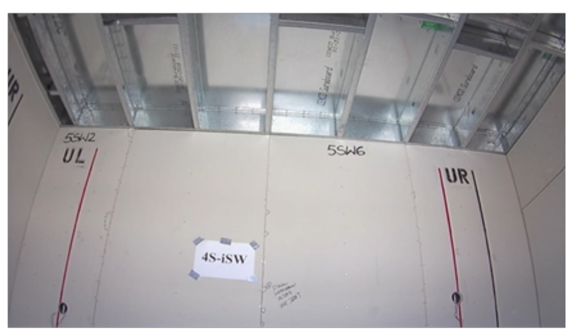

4C1W12

4C2F13

4C3R14

4C4R15

5C1W16

5C1F17

5C2F18

5C3R19

5C4R20

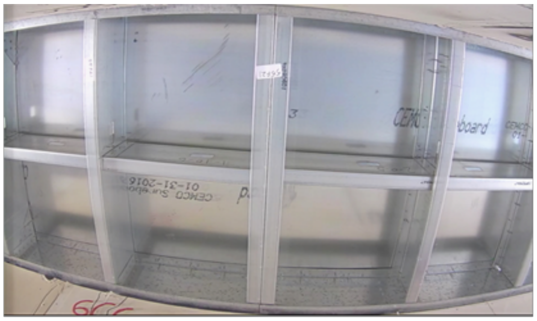

5C5F21

6C1A22

6C2A23

6C3A24

6C4A25

7C1A26

7C2A27

7C3A28

EHS

EHNW

EHSW

EGE

EGW

Video Camera Layout – Configuration 3

Table F.5. Video cameras counts – Configuration 3

Location	Type of camera				Total
	GoPro	Coax	HD Camcorder	IP camera	
Level-1	/	/	/	1	1
Level-2	/	4	/	/	4
Level-3	/	7	/	/	7
Level-4	/	4	/	/	4
Level-5	/	6	/	/	6
Level-6	/	4	/	/	4
Roof	/	3	/	/	3
Exterior	/	/	4	1	5
Total	0	28	4	2	**34**

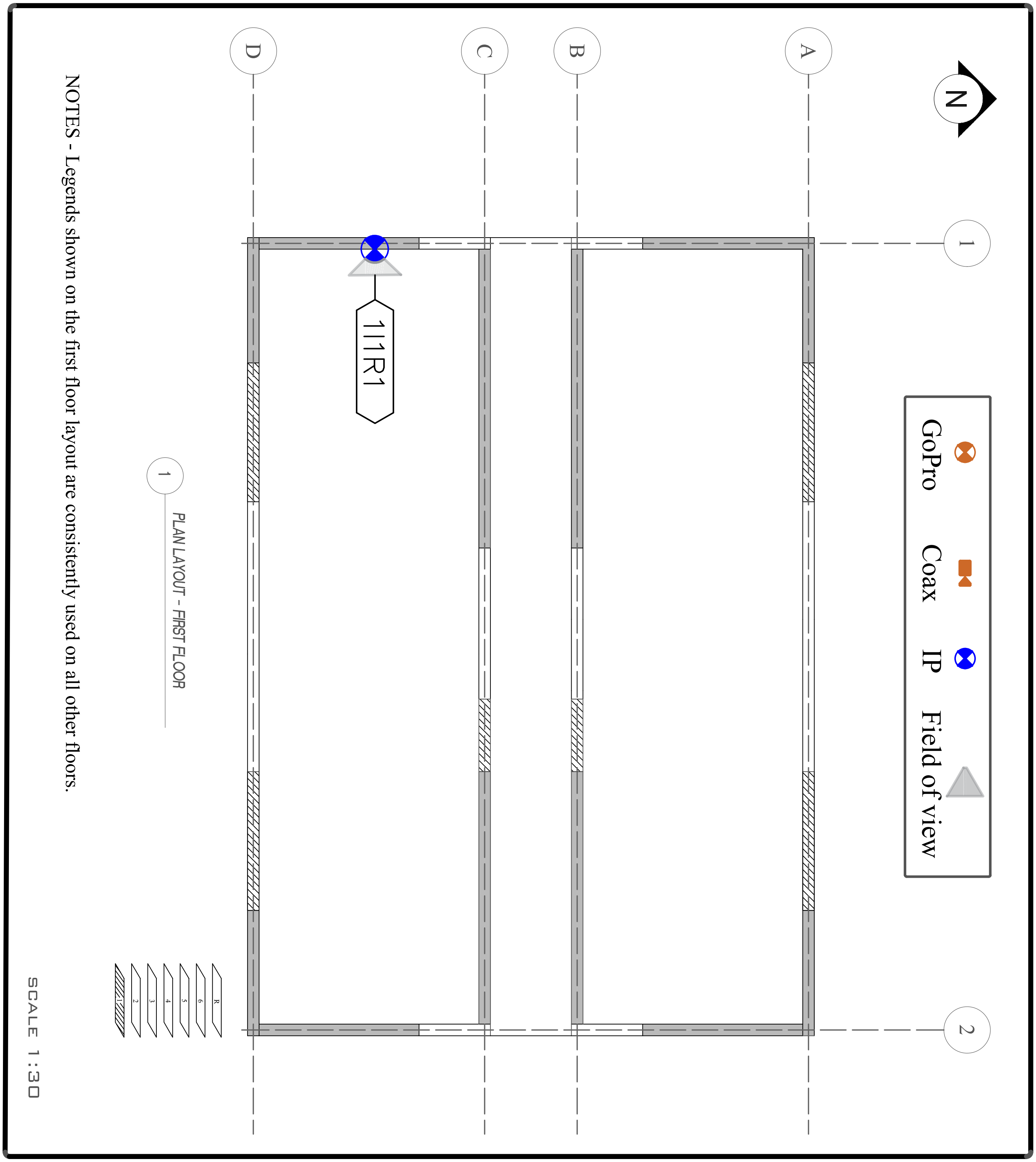

UCSD

UNIVERSITY OF CALIFORNIA, SAN DIEGO
DEPARTMENT OF STRUCTURAL ENGINEERING
LA JOLLA - CALIFORNIA 92093-0085

PROJECT NO. DATE:

NO.	DATE	REVISIONS

CFS Shake Table Test Project
Cameras - Floor 1.
Configuration 3

SRIKAR GUNISETTY
Graduate Student Researcher
XIANG WANG
Post-doctoral Researcher

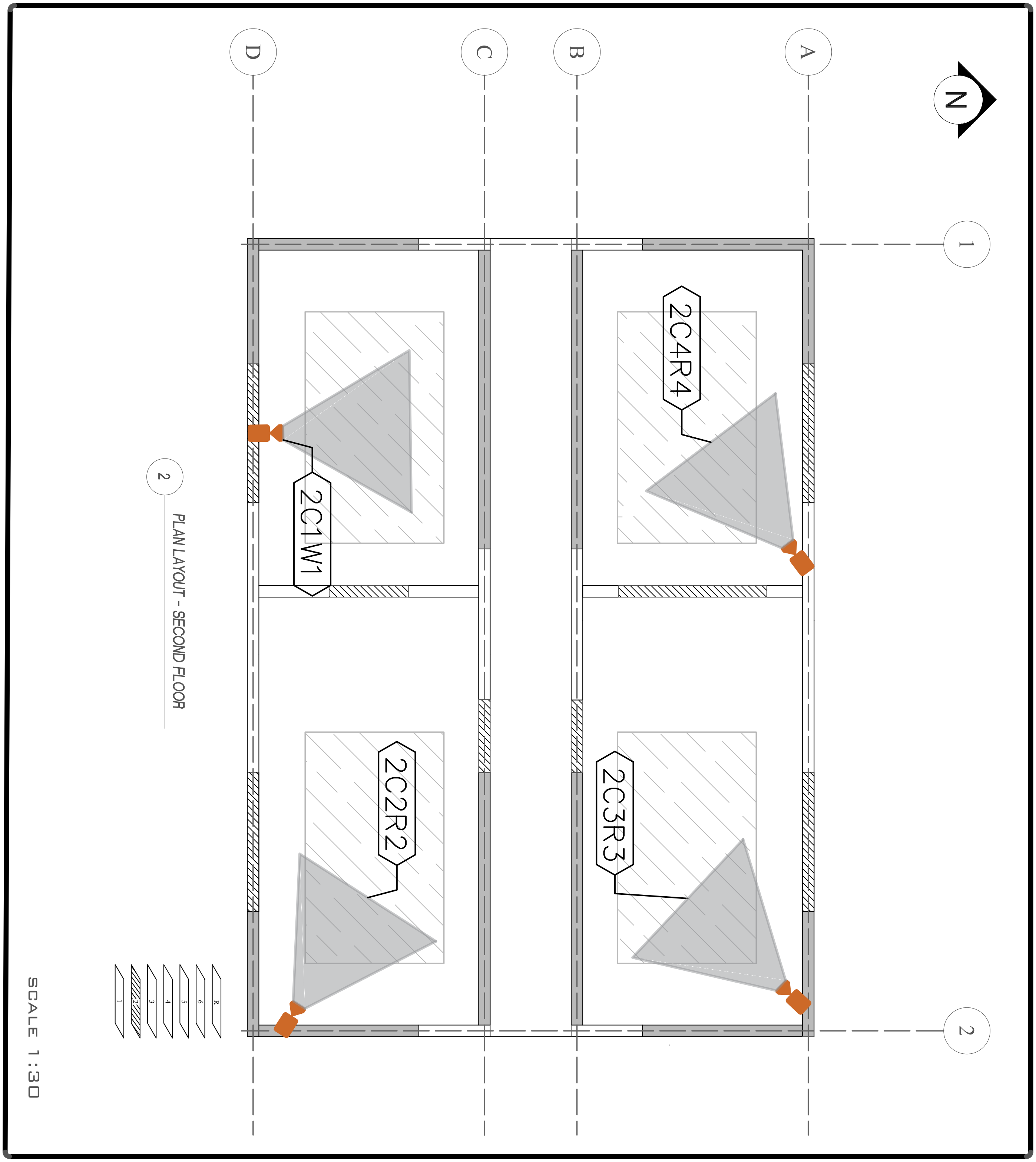

UCSD

UNIVERSITY OF CALIFORNIA, SAN DIEGO
DEPARTMENT OF STRUCTURAL ENGINEERING
LA JOLLA - CALIFORNIA 92093-0085

PROJECT NO. DATE:

NO.	DATE	REVISIONS

CFS Shake Table Test Project
Cameras - Floor 2.
Configuration 3

SRIKAR GUNISETTY
Graduate Student Researcher
XIANG WANG
Post-doctoral Researcher

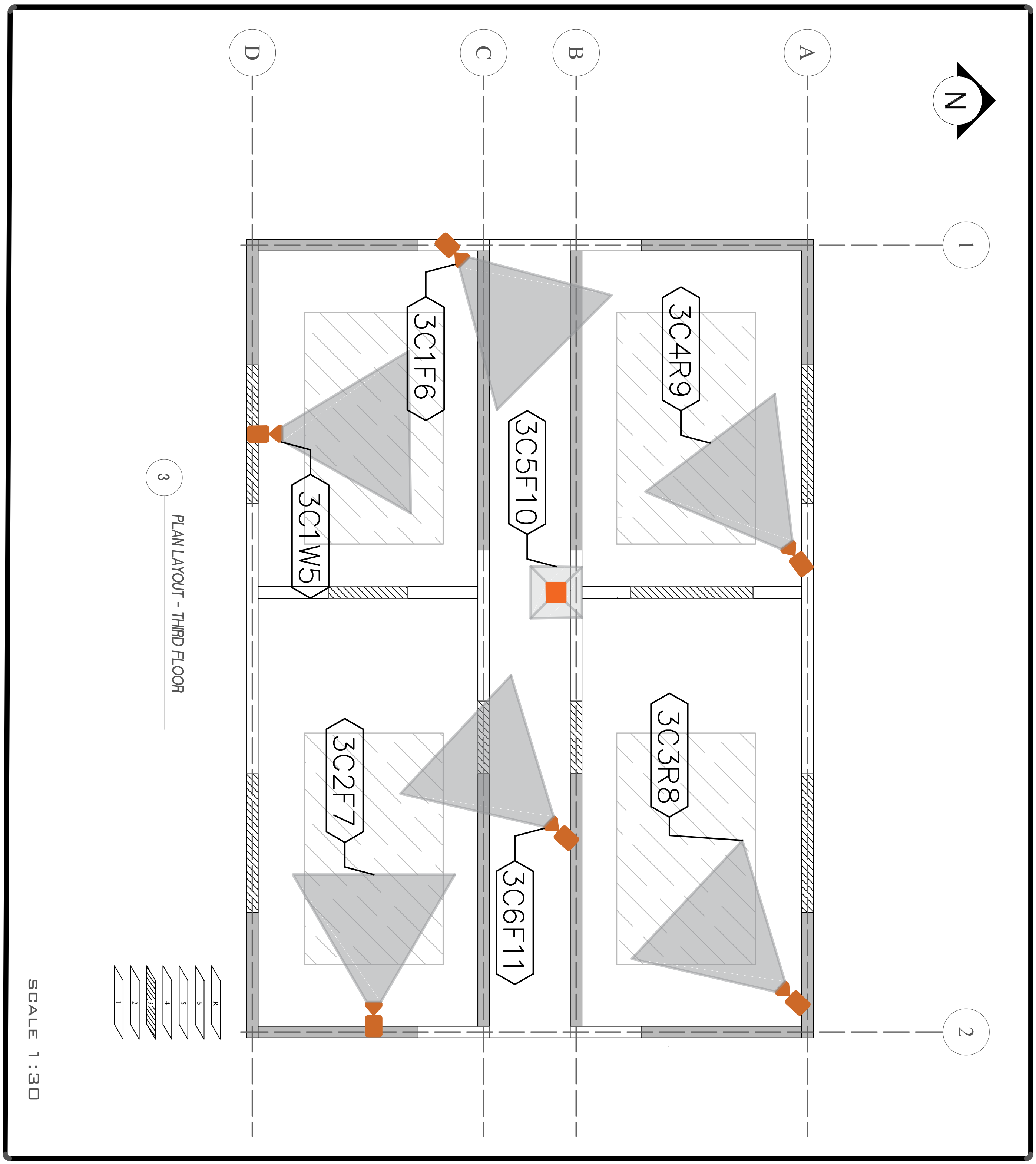

UCSD

UNIVERSITY OF CALIFORNIA, SAN DIEGO
DEPARTMENT OF STRUCTURAL ENGINEERING
LA JOLLA - CALIFORNIA 92093-0085

PROJECT NO. DATE:

NO.	DATE	REVISIONS

CFS Shake Table Test Project
Cameras - Floor 3.
Configuration 3

SRIKAR GUNISETTY
Graduate Student Researcher
XIANG WANG
Post-doctoral Researcher

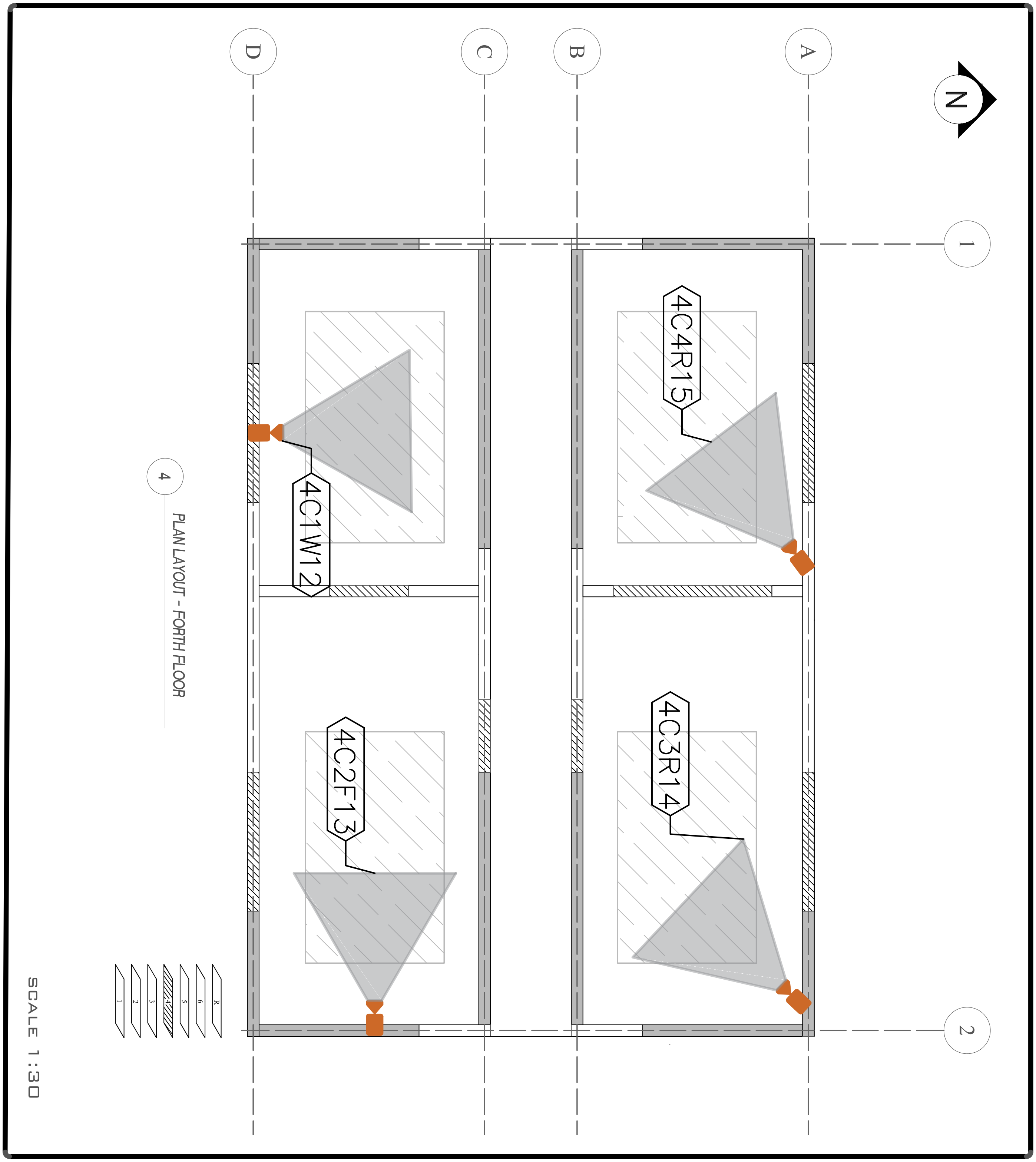

UCSD

UNIVERSITY OF CALIFORNIA, SAN DIEGO
DEPARTMENT OF STRUCTURAL ENGINEERING
LA JOLLA - CALIFORNIA 92093-0085

PROJECT NO. DATE:

NO.	DATE	REVISIONS

CFS Shake Table Test Project
Cameras - Floor 4.
Configuration 3

SRIKAR GUNISETTY
Graduate Student Researcher
XIANG WANG
Post-doctoral Researcher

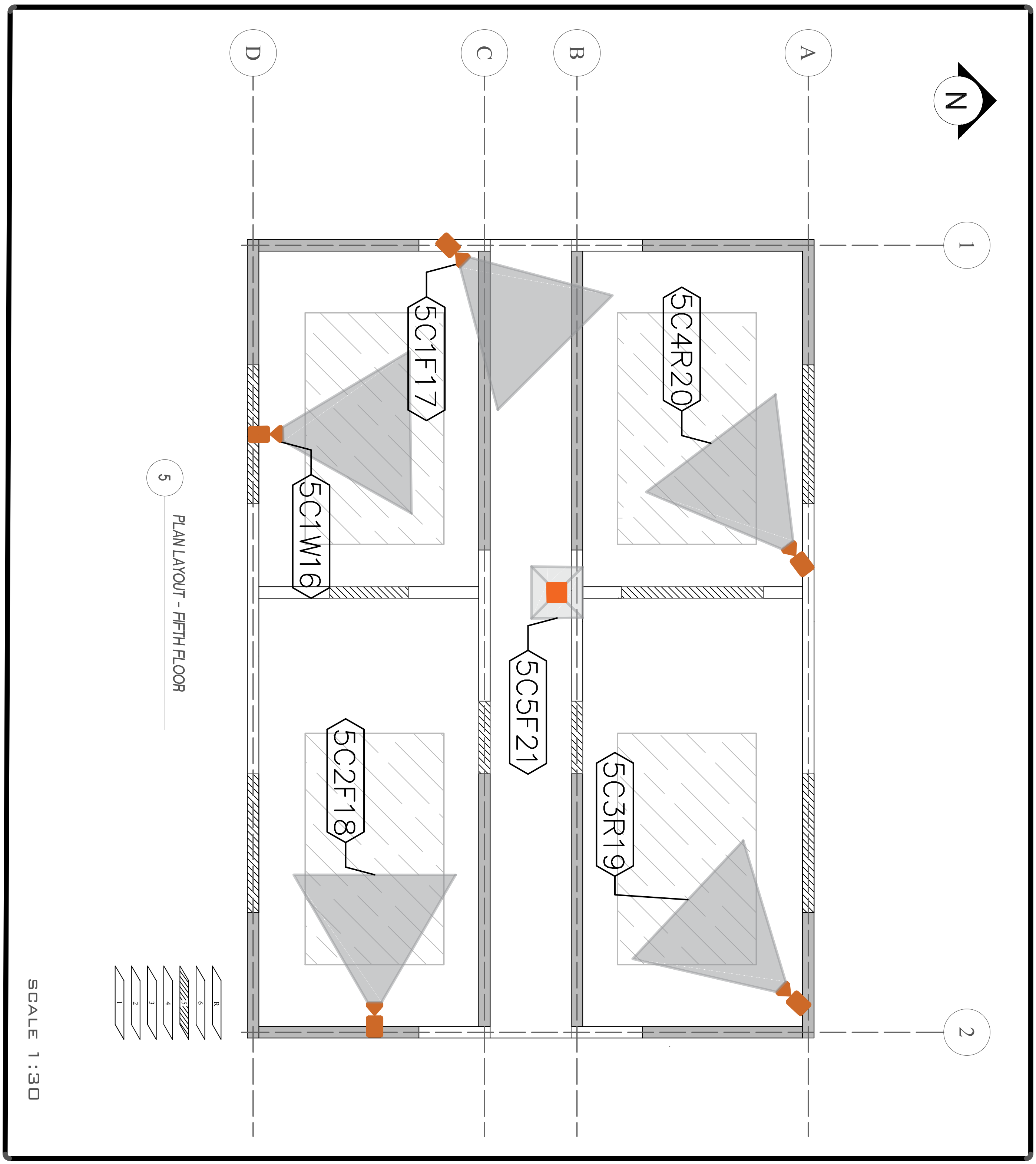

UCSD UNIVERSITY OF CALIFORNIA, SAN DIEGO DEPARTMENT OF STRUCTURAL ENGINEERING LA JOLLA - CALIFORNIA 92093-0085 PROJECT NO. DATE:	NO. DATE REVISIONS	CFS Shake Table Test Project Cameras - Floor 5. Configuration 3

SRIKAR GUNISETTY
Graduate Student Researcher
XIANG WANG
Post-doctoral Researcher

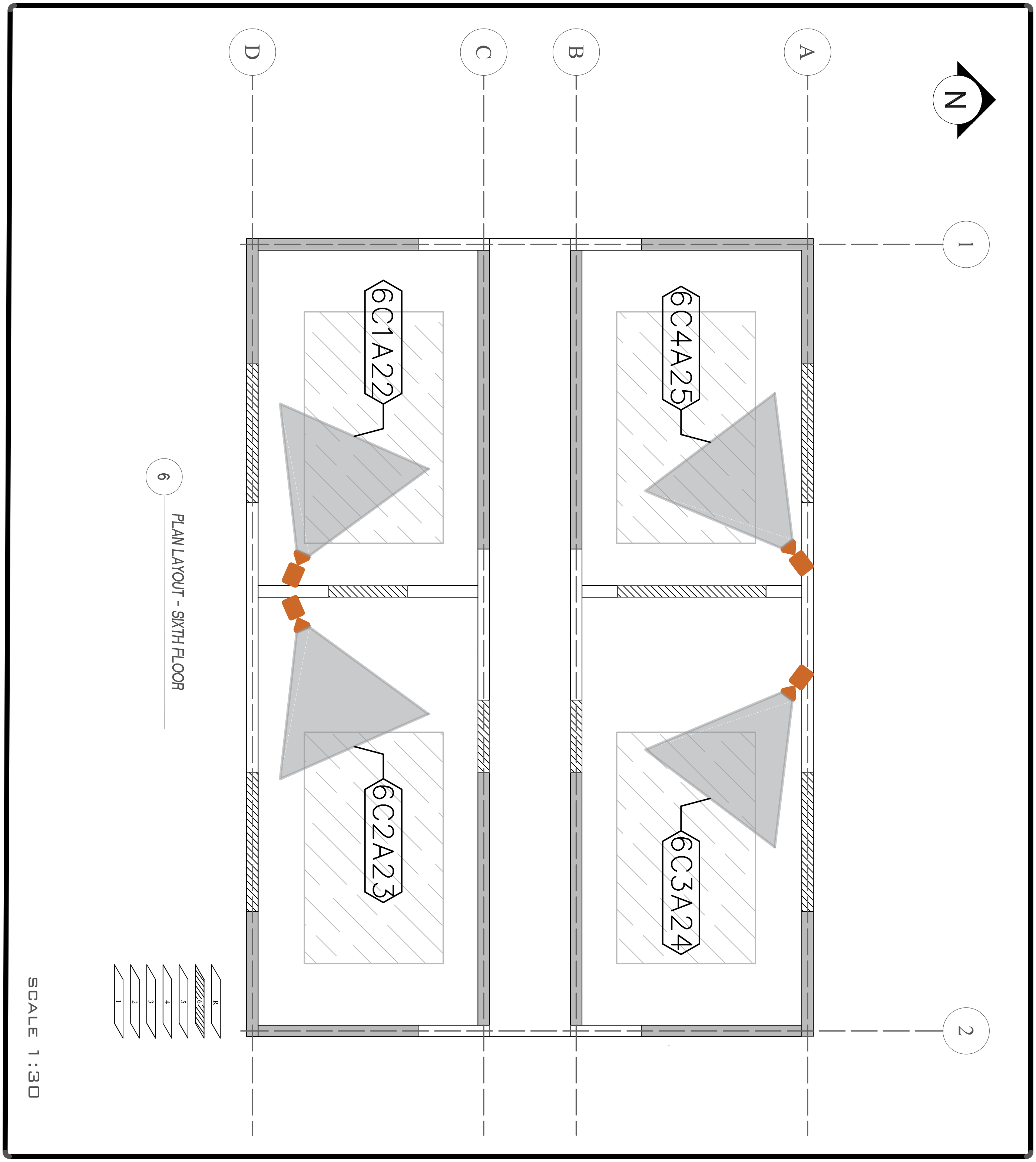

UCSD

UNIVERSITY OF CALIFORNIA, SAN DIEGO
DEPARTMENT OF STRUCTURAL ENGINEERING
LA JOLLA - CALIFORNIA 92093-0085

PROJECT NO. DATE:

NO.	DATE	REVISIONS

CFS Shake Table Test Project
Cameras - Floor 6.
Configuration 3

SRIKAR GUNISETTY
Graduate Student Researcher
XIANG WANG
Post-doctoral Researcher

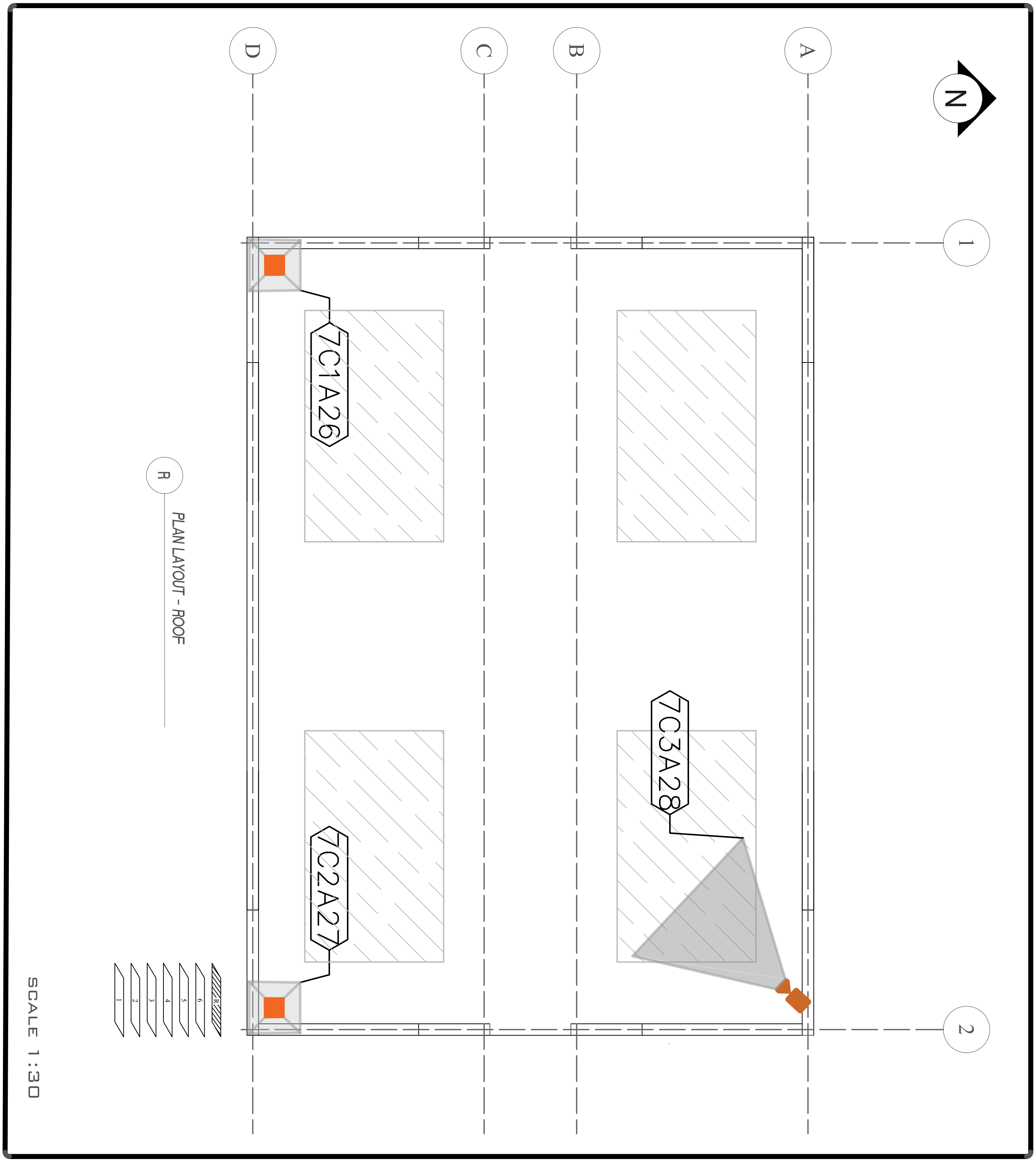

UCSD	NO.	DATE	REVISIONS	CFS Shake Table Test Project	SRIKAR GUNISETTY
UNIVERSITY OF CALIFORNIA, SAN DIEGO DEPARTMENT OF STRUCTURAL ENGINEERING LA JOLLA - CALIFORNIA 92093-0085				Cameras - Roof.	Graduate Student Researcher
PROJECT NO. DATE:				Configuration 3	XIANG WANG Post-doctoral Researcher

1I1R1

2C1W1

2C2R2

2C3R3

2C4R4

3C1W5

3C1F6

3C2F7

3C3R8

3C4R9

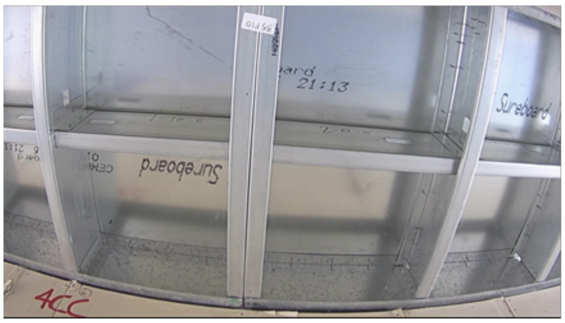

3C5F10

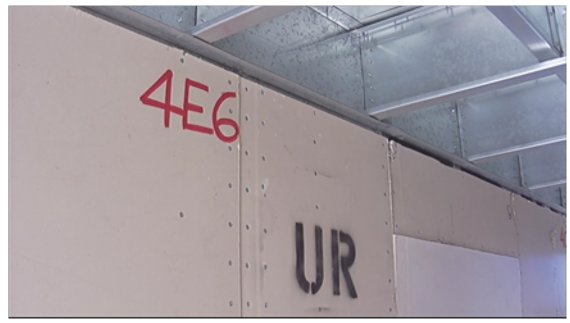

3C6F11

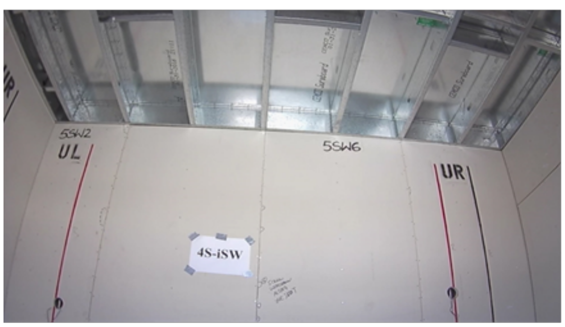

4C1W12

4C2F13

4C3R14

4C4R15

5C1W16

5C1F17

5C2F18

5C3R19

5C4R20

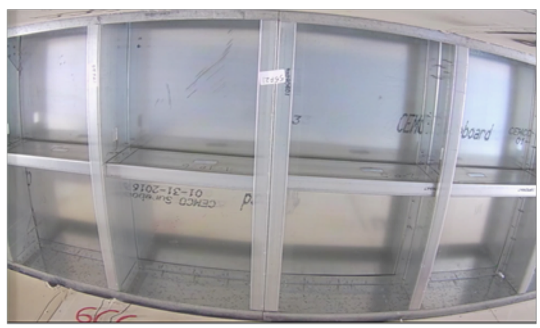

5C5F21

6C1A22

6C2A23

6C3A24

6C4A25

7C1A26

7C2A27

7C3A28

EIE

EHN

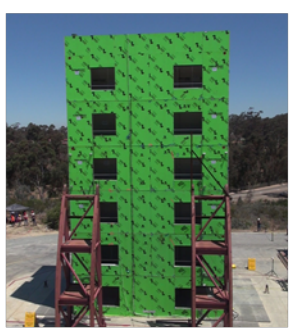

EHS

EHNW

EHSW

Video Camera Layout – Configuration 4

Table F.6. Video cameras counts – Configuration 3

Location	Type of camera				Total
	GoPro	Coax	HD Camcorder	IP camera	
Level-1	4	/	/	/	4
Level-2	8	/	/	/	8
Level-3	/	2	/	/	2
Level-4	/	2	/	/	2
Level-5	/	2	/	/	2
Level-6	/	2	/	/	2
Roof	/	1	/	/	1
Exterior	/	/	3	2	5
Total	12	9	3	2	**26**

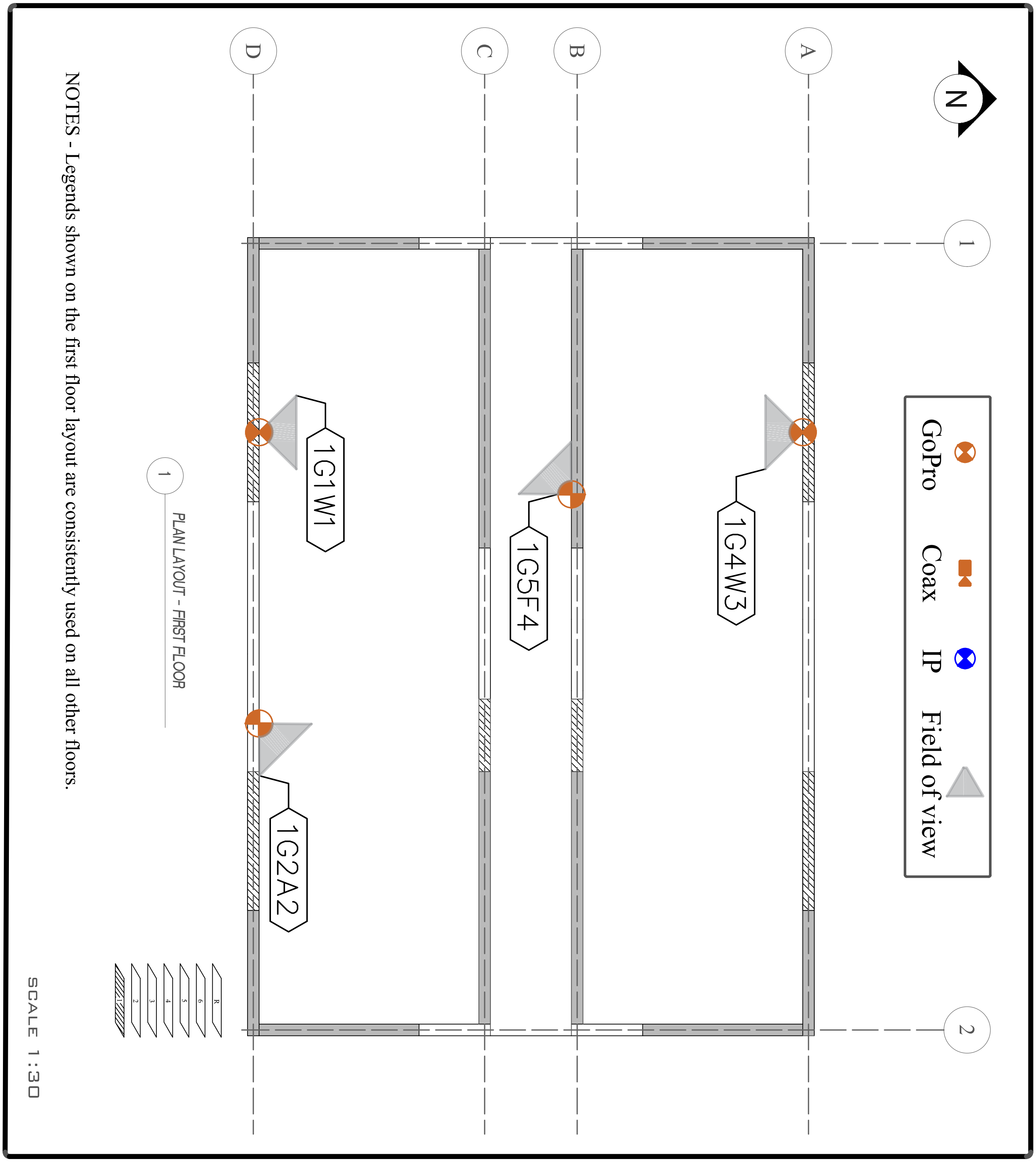

UCSD UNIVERSITY OF CALIFORNIA, SAN DIEGO DEPARTMENT OF STRUCTURAL ENGINEERING LA JOLLA - CALIFORNIA 92093-0085 PROJECT NO. DATE:	NO.	DATE	REVISIONS	CFS Shake Table Test Project Cameras - Floor 1 Configuration 4	SRIKAR GUNISETTY Graduate Student Researcher XIANG WANG Post-doctoral Researcher

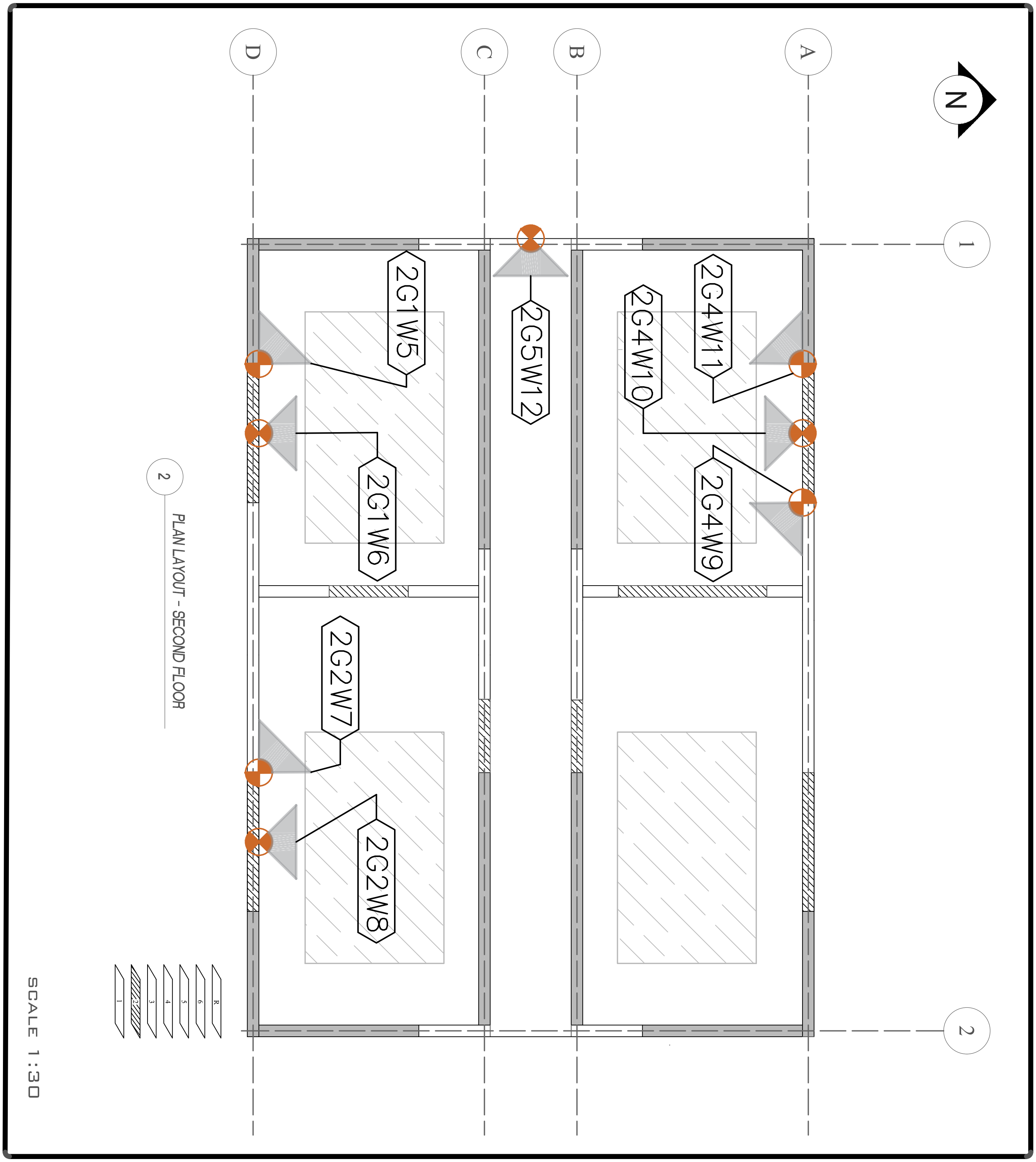

UCSD

UNIVERSITY OF CALIFORNIA, SAN DIEGO
DEPARTMENT OF STRUCTURAL ENGINEERING
LA JOLLA - CALIFORNIA 92093-0085

PROJECT NO. DATE:

NO.	DATE	REVISIONS

CFS Shake Table Test Project
Cameras - Floor 2
Configuration 4

SRIKAR GUNISETTY
Graduate Student Researcher
XIANG WANG
Post-doctoral Researcher

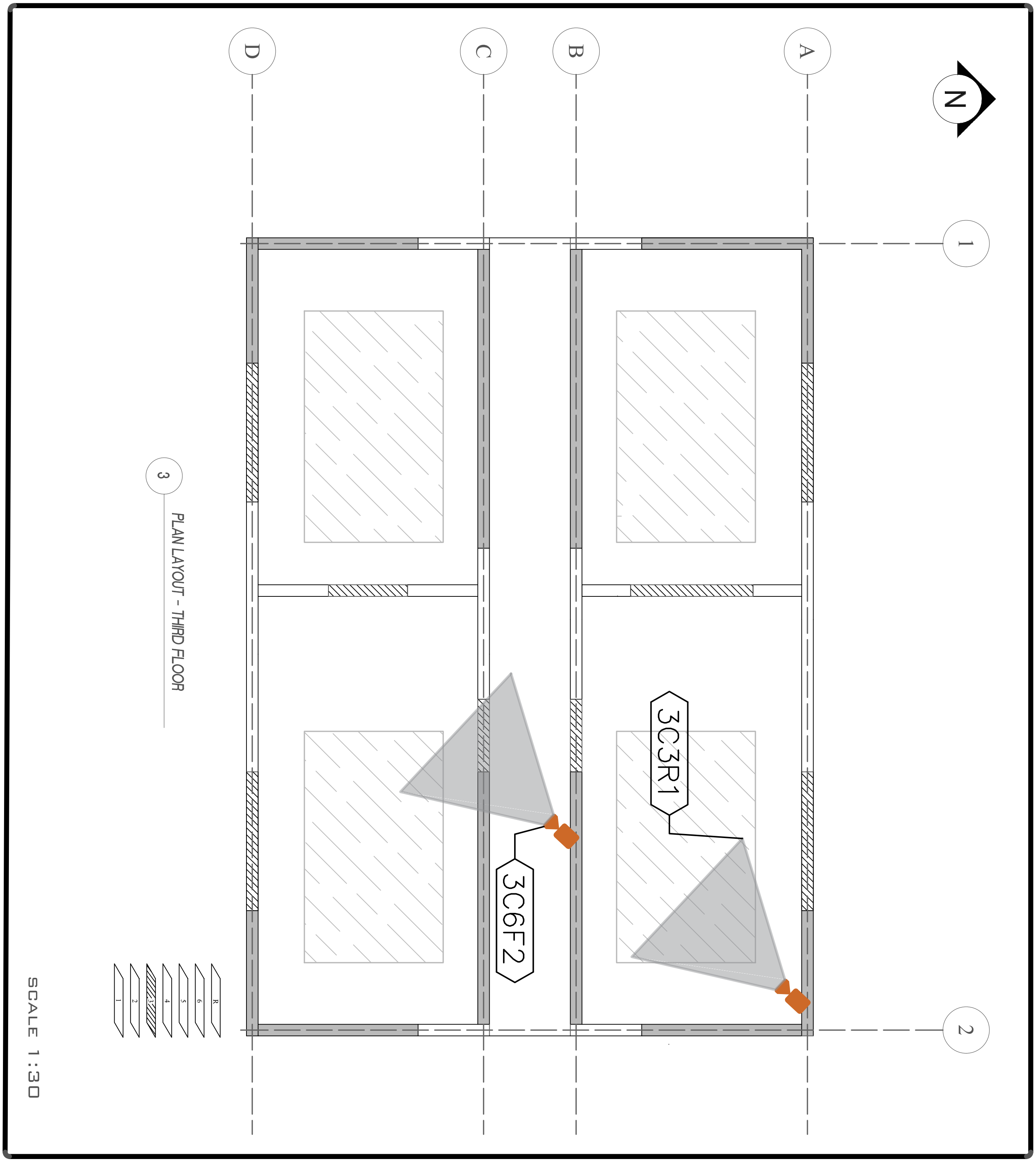

UCSD

UNIVERSITY OF CALIFORNIA, SAN DIEGO
DEPARTMENT OF STRUCTURAL ENGINEERING
LA JOLLA - CALIFORNIA 92093-0085

PROJECT NO. DATE:

NO.	DATE	REVISIONS

CFS Shake Table Test Project
Cameras - Floor 3
Configuration 4

SRIKAR GUNISETTY
Graduate Student Researcher
XIANG WANG
Post-doctoral Researcher

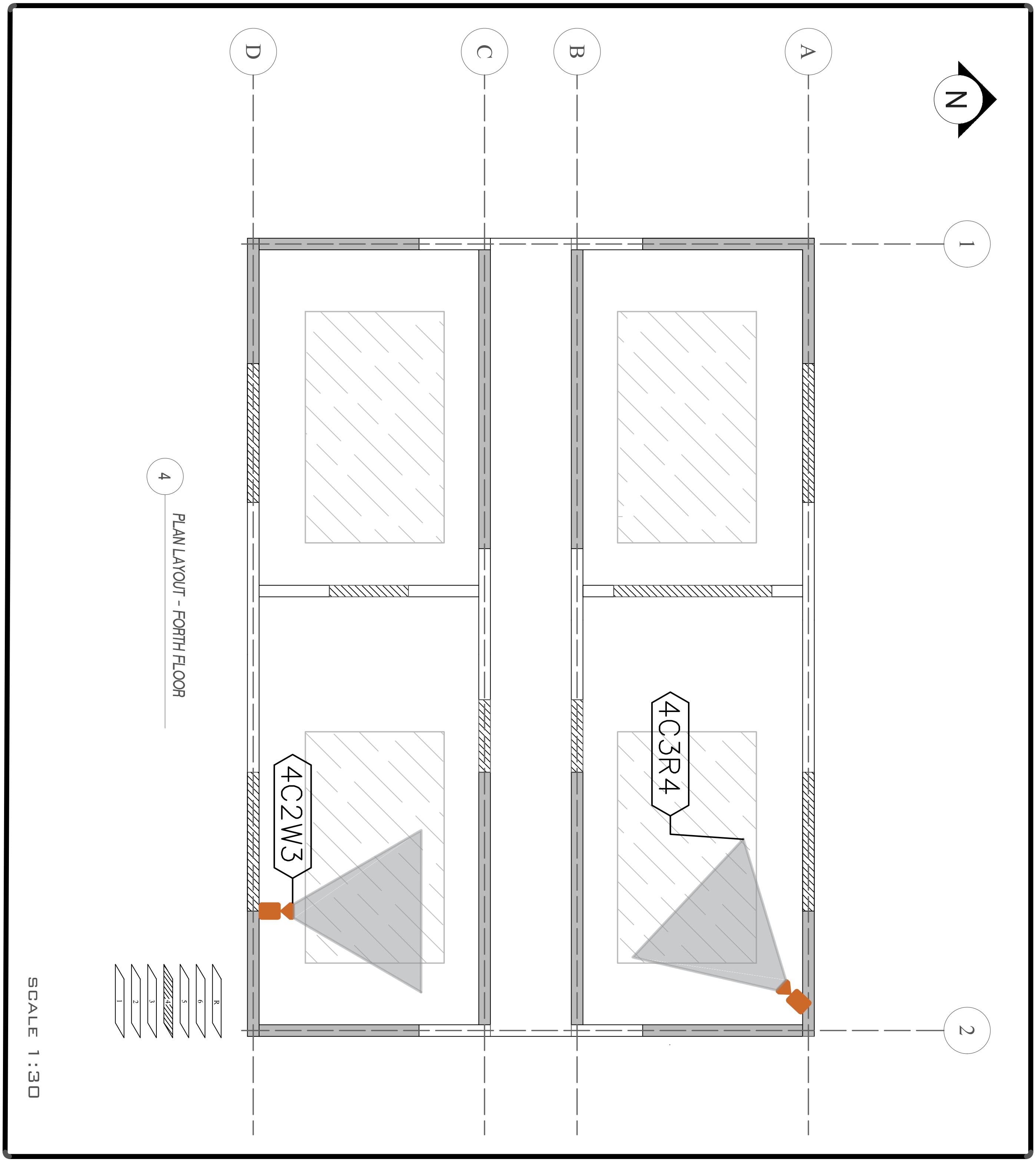

UCSD

UNIVERSITY OF CALIFORNIA, SAN DIEGO
DEPARTMENT OF STRUCTURAL ENGINEERING
LA JOLLA - CALIFORNIA 92093-0085

PROJECT NO. DATE:

NO.	DATE	REVISIONS

CFS Shake Table Test Project
Cameras - Floor 4
Configuration 4

SRIKAR GUNISETTY
Graduate Student Researcher
XIANG WANG
Post-doctoral Researcher

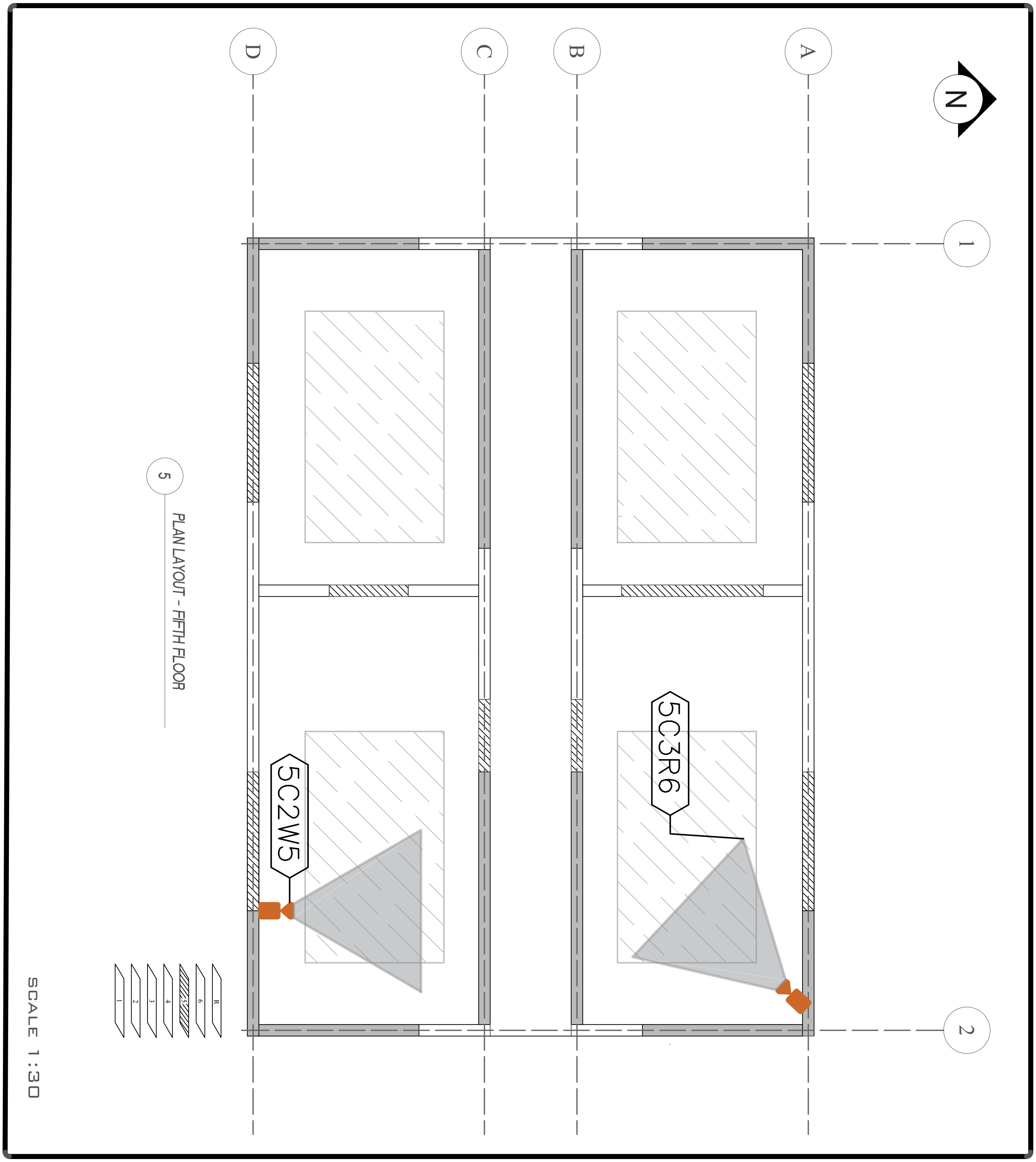

UCSD

UNIVERSITY OF CALIFORNIA, SAN DIEGO
DEPARTMENT OF STRUCTURAL ENGINEERING
LA JOLLA - CALIFORNIA 92093-0085

PROJECT NO. DATE:

NO.	DATE	REVISIONS

CFS Shake Table Test Project
Cameras - Floor 5
Configuration 4

SRIKAR GUNISETTY
Graduate Student Researcher
XIANG WANG
Post-doctoral Researcher

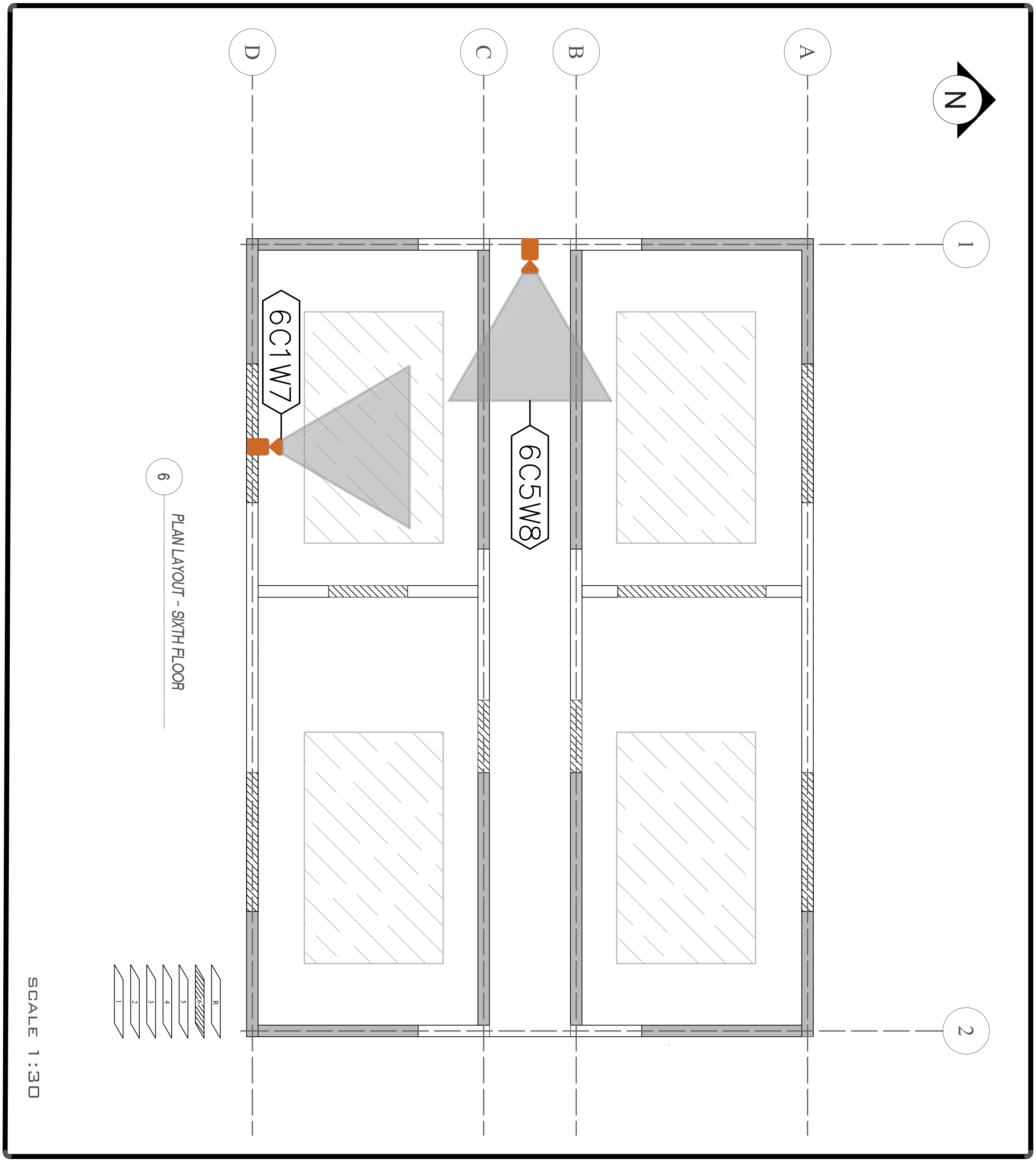

UCSD

UNIVERSITY OF CALIFORNIA, SAN DIEGO
DEPARTMENT OF STRUCTURAL ENGINEERING
LA JOLLA - CALIFORNIA 92093-0085

PROJECT NO. DATE:

NO.	DATE	REVISIONS

CFS Shake Table Test Project
Cameras - Floor 6
Configuration 4

SRIKAR GUNISETTY
Graduate Student Researcher
XIANG WANG
Post-doctoral Researcher

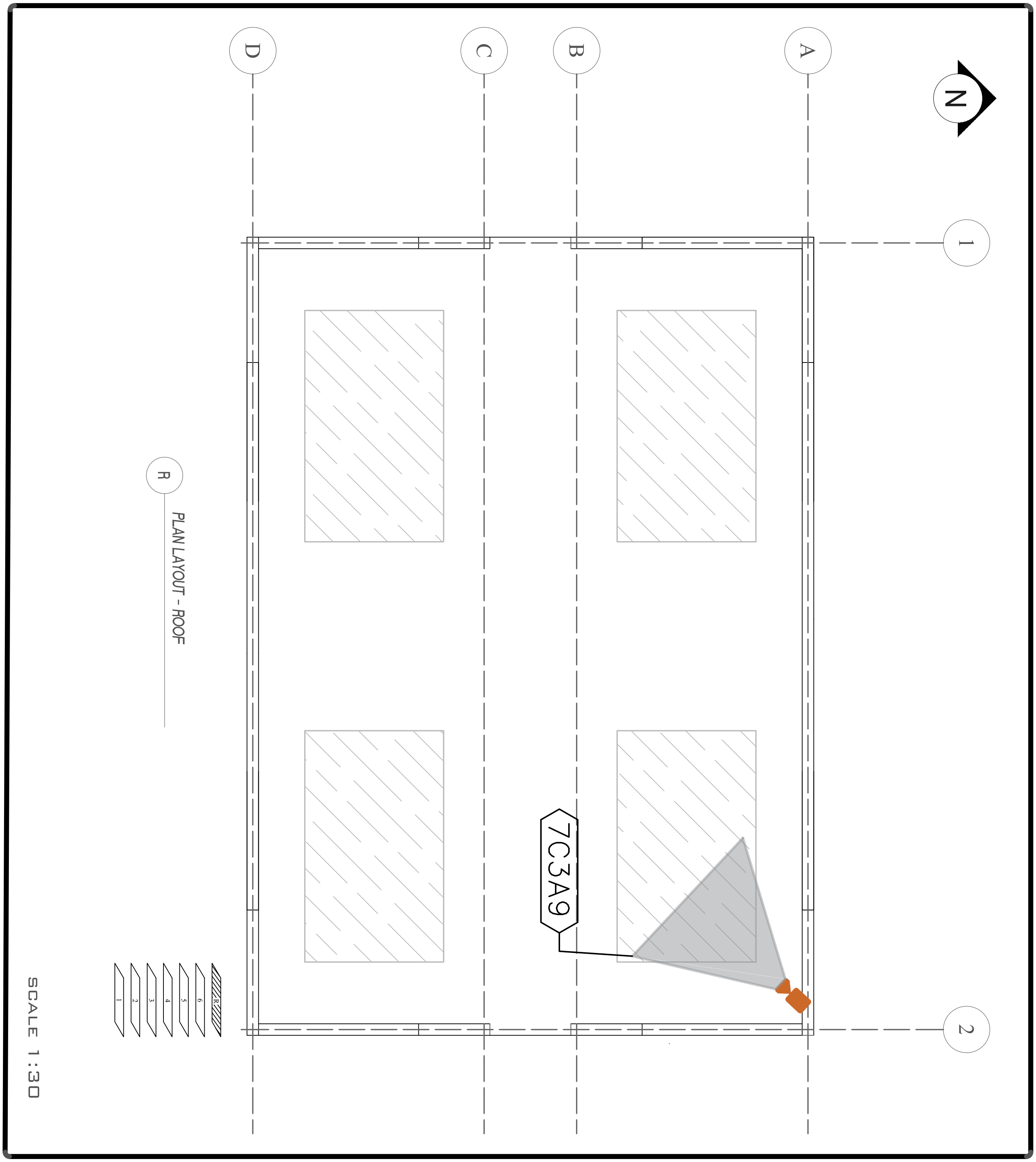

UCSD UNIVERSITY OF CALIFORNIA, SAN DIEGO DEPARTMENT OF STRUCTURAL ENGINEERING LA JOLLA - CALIFORNIA 92093-0085 PROJECT NO. DATE:	NO. DATE REVISIONS	CFS Shake Table Test Project Cameras - Roof Configuration 4

SRIKAR GUNISETTY
Graduate Student Researcher
XIANG WANG
Post-doctoral Researcher

1G1W1

1G2A2

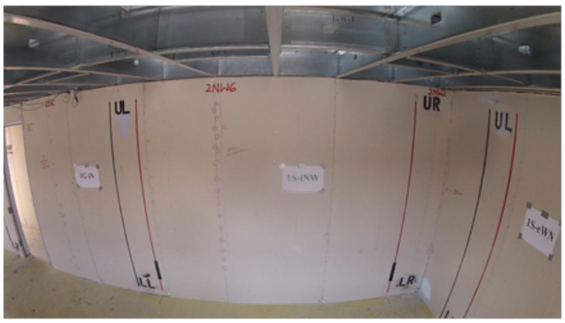

1G4W3

1G5F4

2G1W5

2G1W6

2G2W7

2G2W8

2G4W9

2G4W10

2G4W11

2G5W12

3C3R1

3C6F2

4C2W3

4C3R4

5C2W5

5C3R6

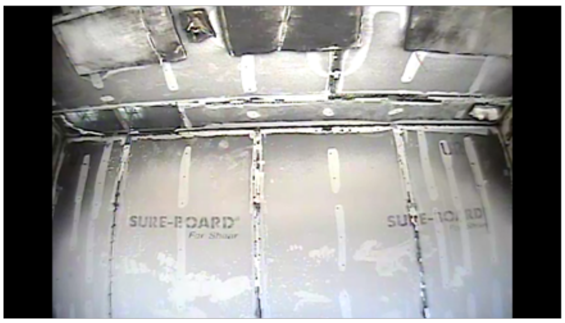

6C1W7

6C5W8

7C3A9

EHN

EHS

EHSW

APPENDIX G – ACCELERATION DOUBLE INTEGRATION PROCEDURES

G.1 Procedures

A simple and effective double integration procedure is proposed to provide consistent criteria for obtaining the building global response (e.g., floor accelerations, floor displacements, and interstory drifts) the accelerations measured at the four corners. The proposed procedures are described as follows:

Step 1: Obtain the acceleration time history from raw data and detrend the constant-value shift

Step 2: Taper the first and last second of acceleration time history with half-cosine function

Step 3: Pad five seconds of zeros to the beginning and the end of the acceleration time history

Step 4: Filter the zero-padded acceleration time history using the 4th-order, 0.15-30 Hz band-pass Butterworth filter (filter applied in time domain)

Step 5: Obtain the velocity time history by integrating the filtered acceleration time history using the 4th-order Runge-Kutta method

Step 6: Correct the linear-trend baseline shift and filter the velocity time history using the 4th-order 0.15-30 Hz band-pass Butterworth filter (filter applied in the time domain).

Step 7: Obtain the displacement time history by integrating the filtered velocity time history using the 4th-order Runge-Kutta method

Step 8: Correct the linear-trend baseline shift and filter the displacement time history using the 4th-order 0.15-30 Hz band-pass Butterworth filter (filter applied in the time domain)

Step 9 (Final Step): Truncate the first and last 5 seconds of data from the obtained acceleration, velocity, and displacement time histories to match the original duration of the time histories

Plots are provided at each steps using the measured acceleration time history of motion FB-2:LAC100 at the southeast corner of foundation level to facilitate the understanding of entire proposed procedure.

G.2 Results Validation

The proposed procedure is validated by comparing the displacement time histories by double integrating the measured acceleration time history at the southeast corner of foundation level with the one measured by the string potentiometer attached to the same location during all test motions.

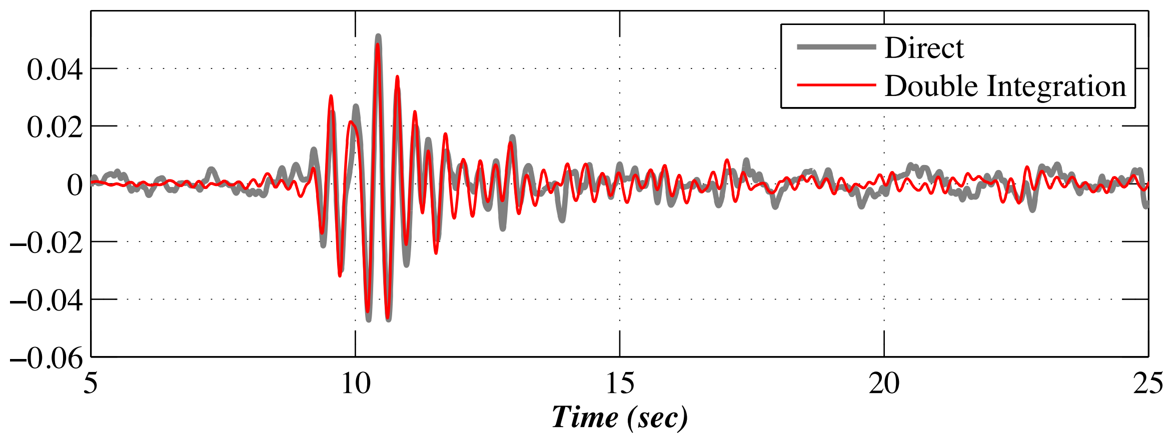

Figure G.1. Comparison of interstory drift response at level 2 – EQ1:RIO-25.

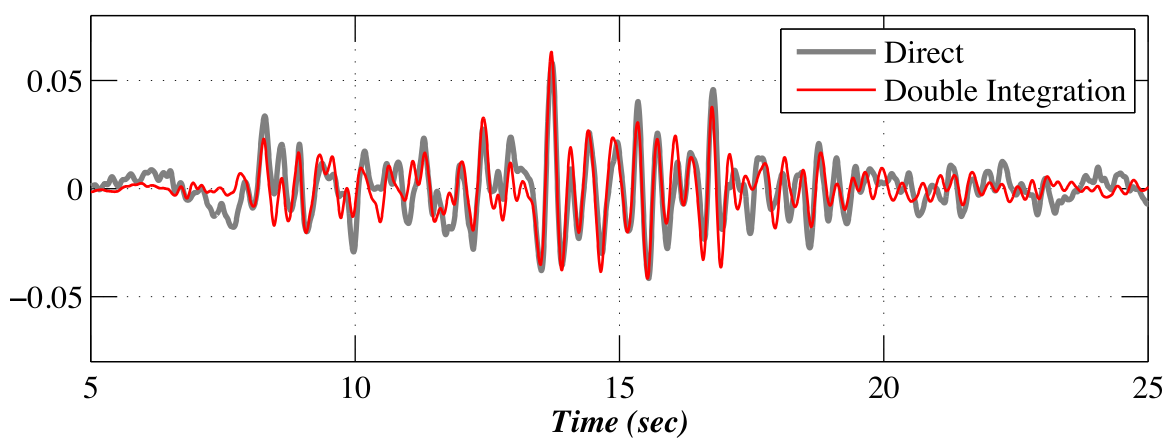

Figure G.2. Comparison of interstory drift response at level 2 – EQ2:CNP-25.

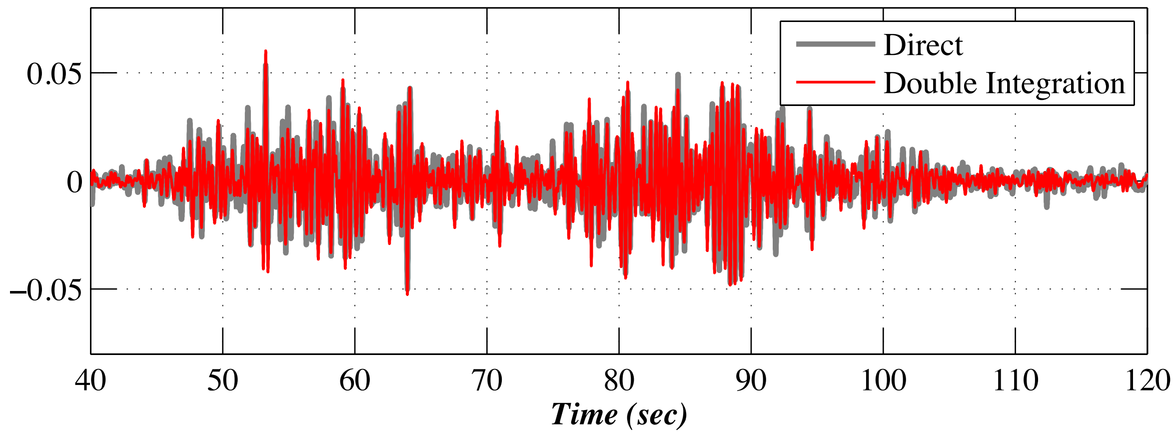

Figure G.3. Comparison of interstory drift response at level 2 – EQ3:CUR-25.

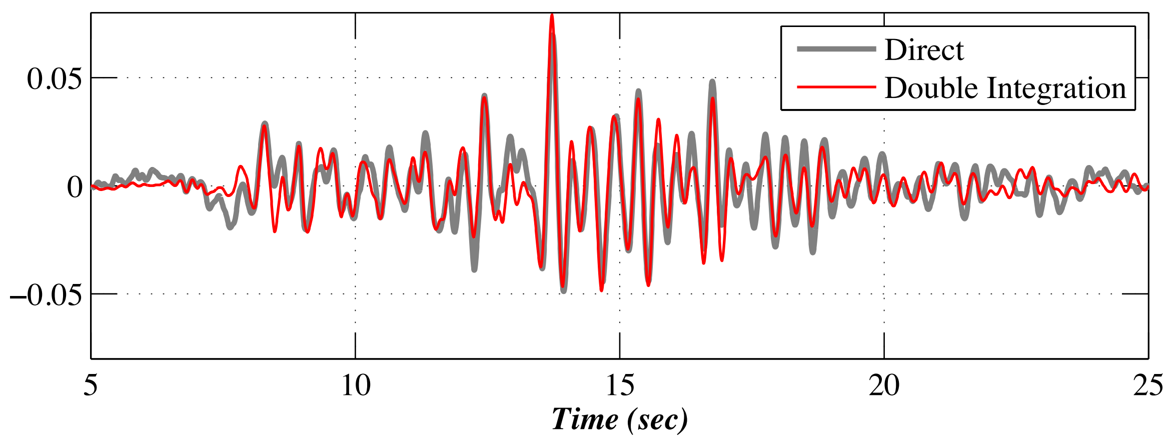

Figure G.4. Comparison of interstory drift response at level 2 – EQ4:CNP-25.

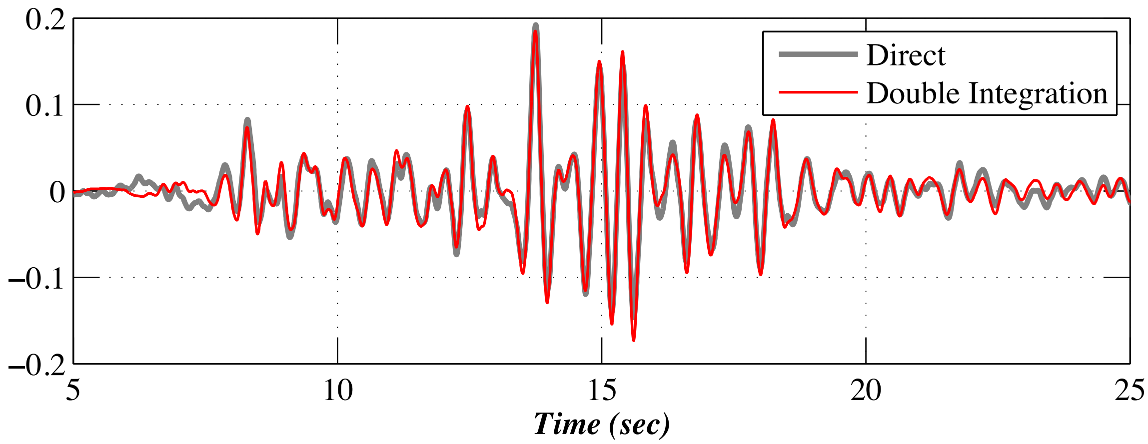

Figure G.5. Comparison of interstory drift response at level 2 – EQ5:CNP-50.

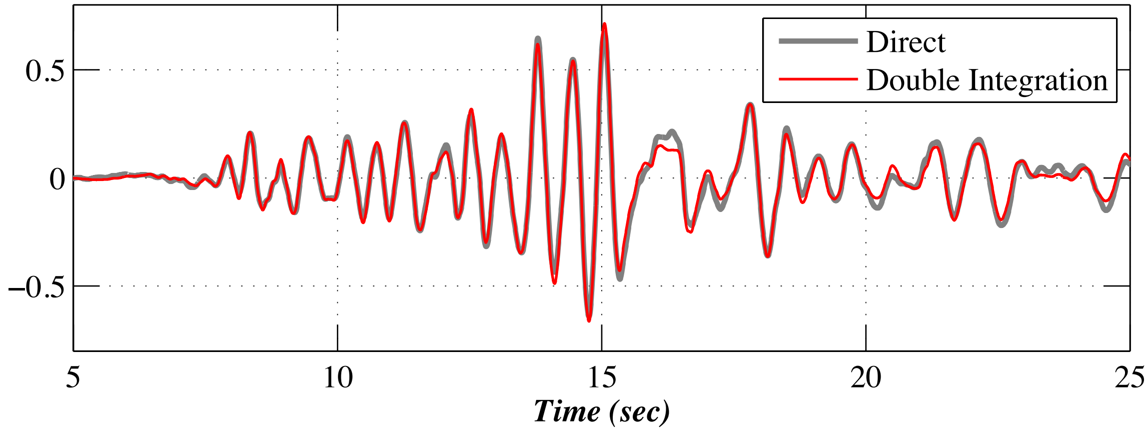

Figure G.6. Comparison of interstory drift response at level 2 – EQ6:CNP-100.

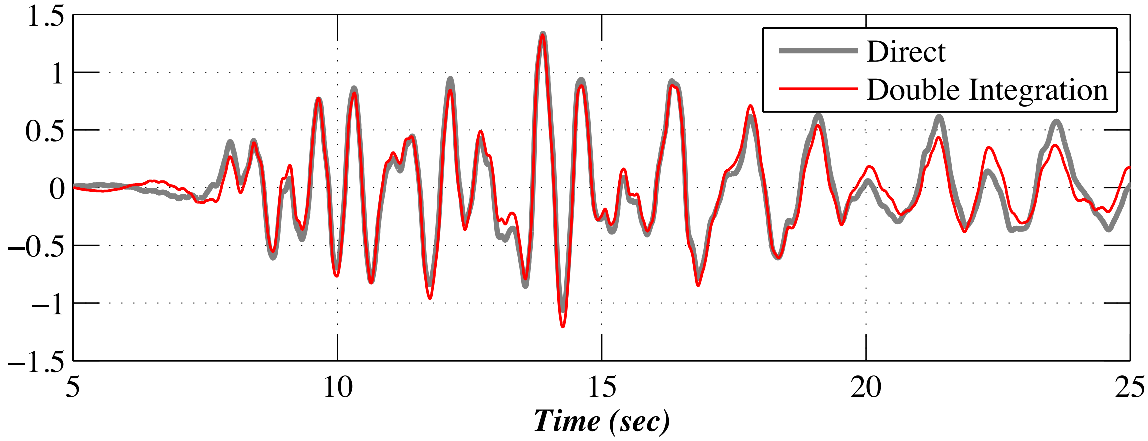

Figure G.7. Comparison of interstory drift response at level 2 – EQ7:CNP-150.

APPENDIX H DOOR INSTALLATION AND DAMAGE PHOTOS

H.1 Doors (As-installed Condition)

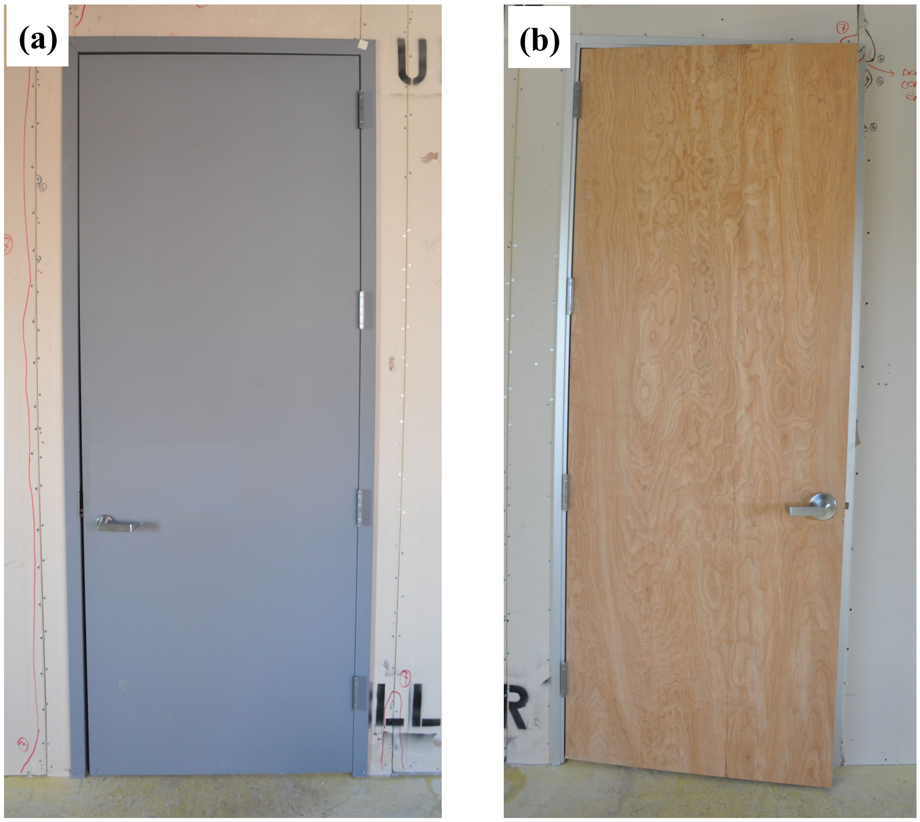

Figure H.1. Doors at level 1: (a) 1-SC, (b) 1-NC.

Figure H.2. Doors at level 2: (a) 2-SC, (b) 2-NC, (c) 2-SR, and (d) 2-NR.

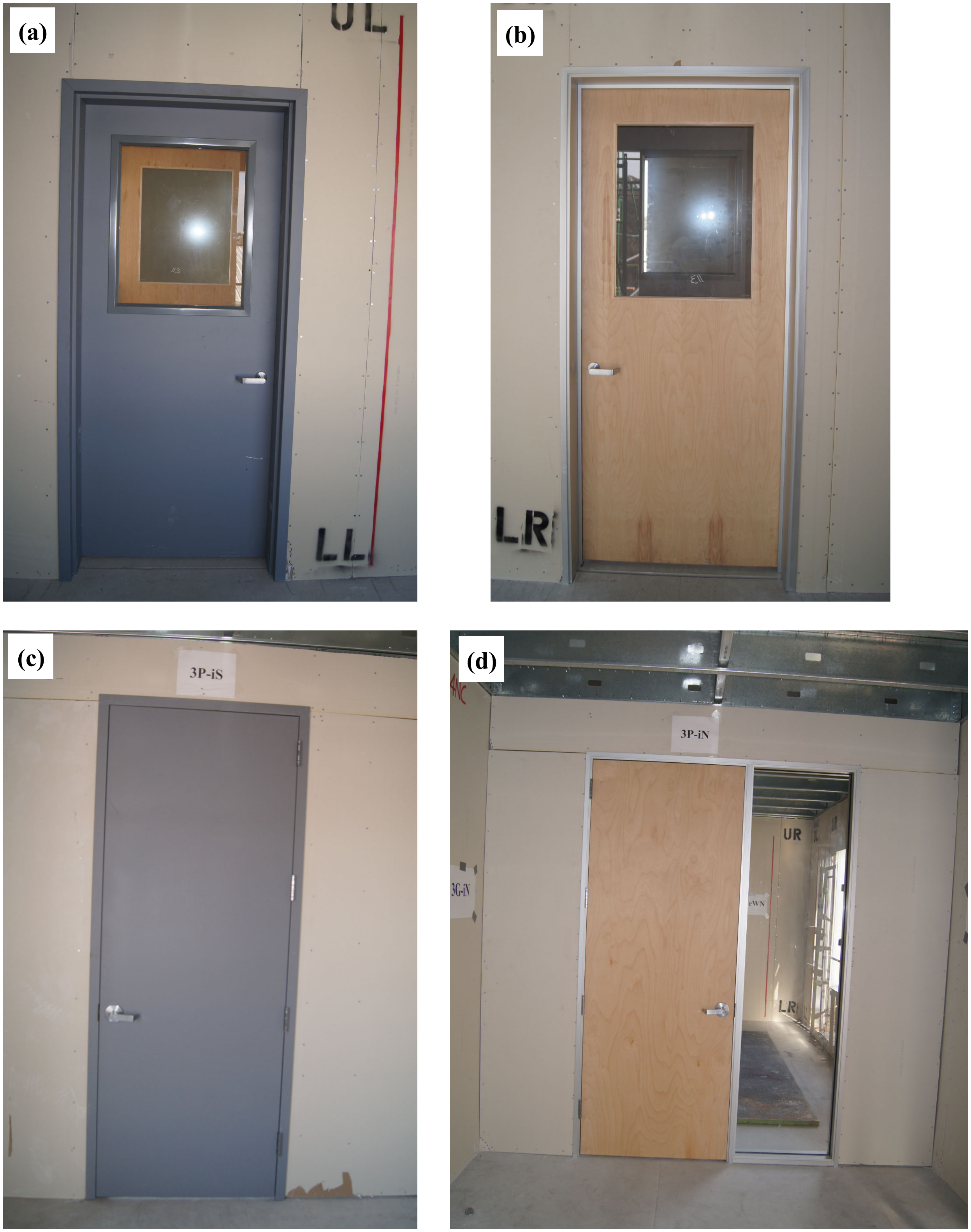

Figure H.3. Doors at level 3: (a) 3-SC, (b) 3-NC, (c) 3-SR, and (d) 3-NR.

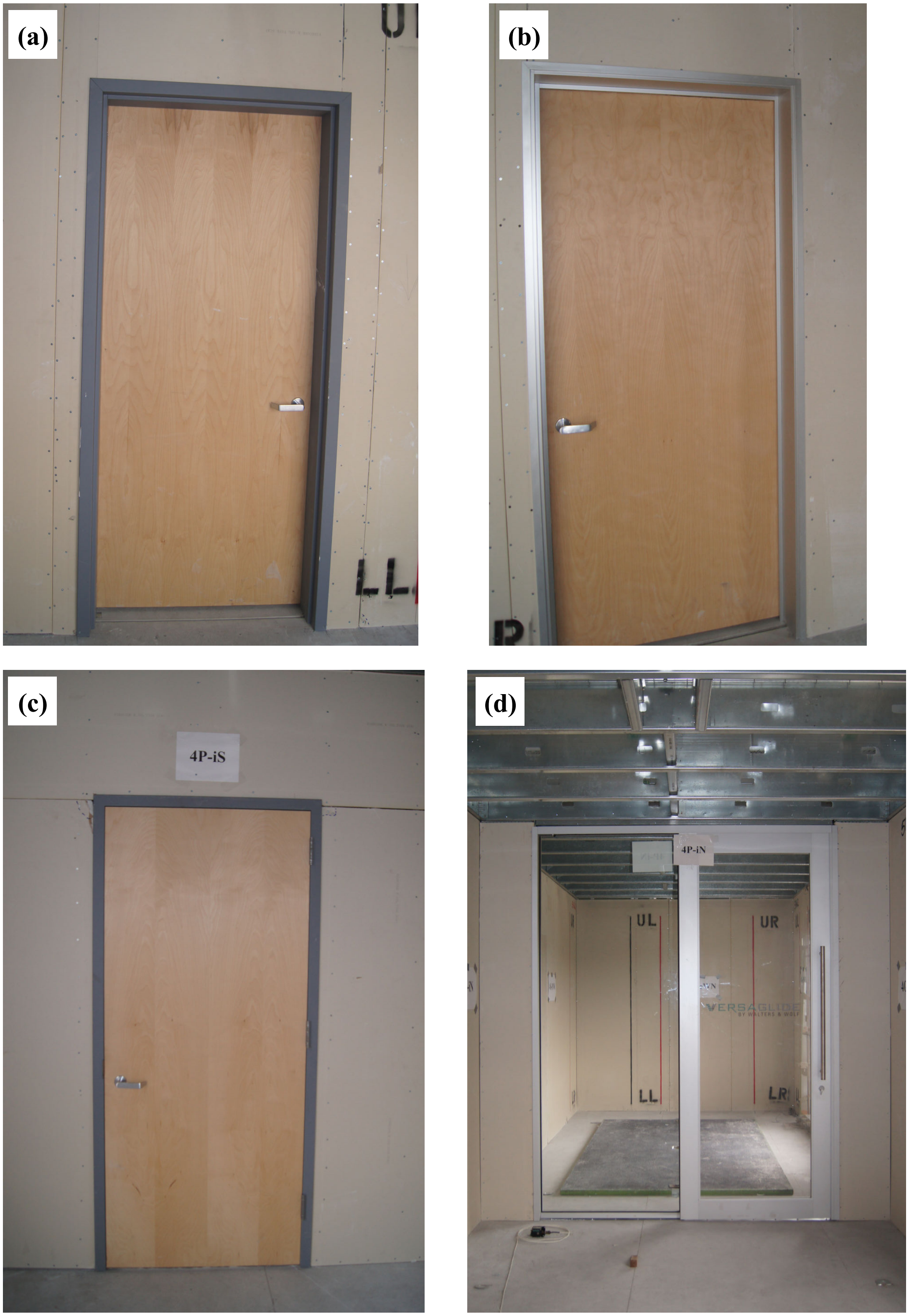

Figure H.4. Doors at level 4: (a) 4-SC, (b) 4-NC, (c) 4-SR, and (d) 4-NR.

Figure H.5. Doors at level 5: (a) 5-SC, (b) 5-NC, (c) 5-SR, and (d) 5-NR.

Figure H.6. Doors at level 6: (a) 6-SC, (b) 6-NC, (c) 6-SR, and (d) 6-NR.

H.2 Door Damage

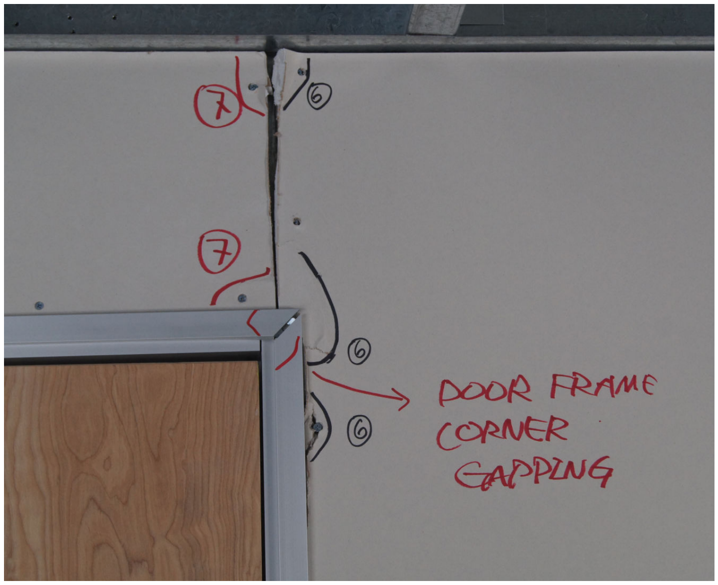

Figure H.7. Door 1-NC: door frame corner gapping following the MCE event (EQ7).

Figure H.8. Door 2-NC: buckled latch following the MCE event (EQ7).

Figure H.9. Door 3-NC: Door latch failure and door frame corner gapping following the MCE event (EQ7).

Figure H.10. Door 3-SC: Door frame screw withdrawal and loosening following the MCE event (EQ7).

Figure H.11. Door 4-NC: Door latch failure and door frame corner gapping following the MCE event (EQ7).

Figure H.12. Door 4-SC: (a) door frame partial detachment following the MCE event (EQ7), and (b) door frame detachment following the post-fire MCE event (EQ9).

Figure H.13. Door 5-SC: (a) door frame screw withdrawal following the MCE event (EQ7), and (b) door frame detachment following the post-fire MCE event (EQ9).

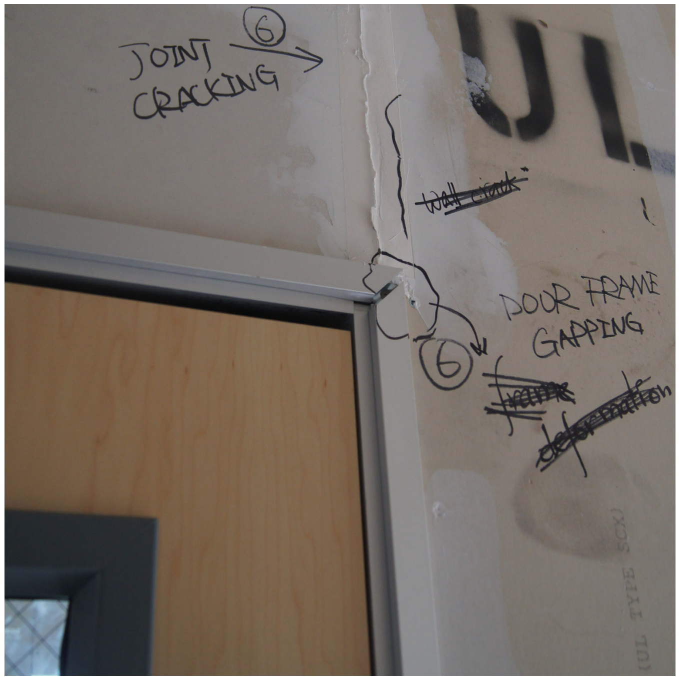

Figure H.14. Door 6-NC: door frame corner gapping following the design event (EQ6).

Figure H.15. Door 6-SC: door frame partial detachment following the MCE event (EQ7).

Figure H.16. Level 2 door damage following the fire tests: (a) 2-SC, (b) 2-NC, (c) 2-SR, and (d) 2-NR.

Figure H.17. Level 6 door damage following the fire tests: (a) 2-NC, (b) 2-NR, and (c) 2-SC.